CLRC

COUNCIL FOR THE CENTRAL LABORATORY
OF THE RESEARCH COUNCILS

Central Laser Facility

Rutherford Appleton Laboratory

Annual Report 1998-99

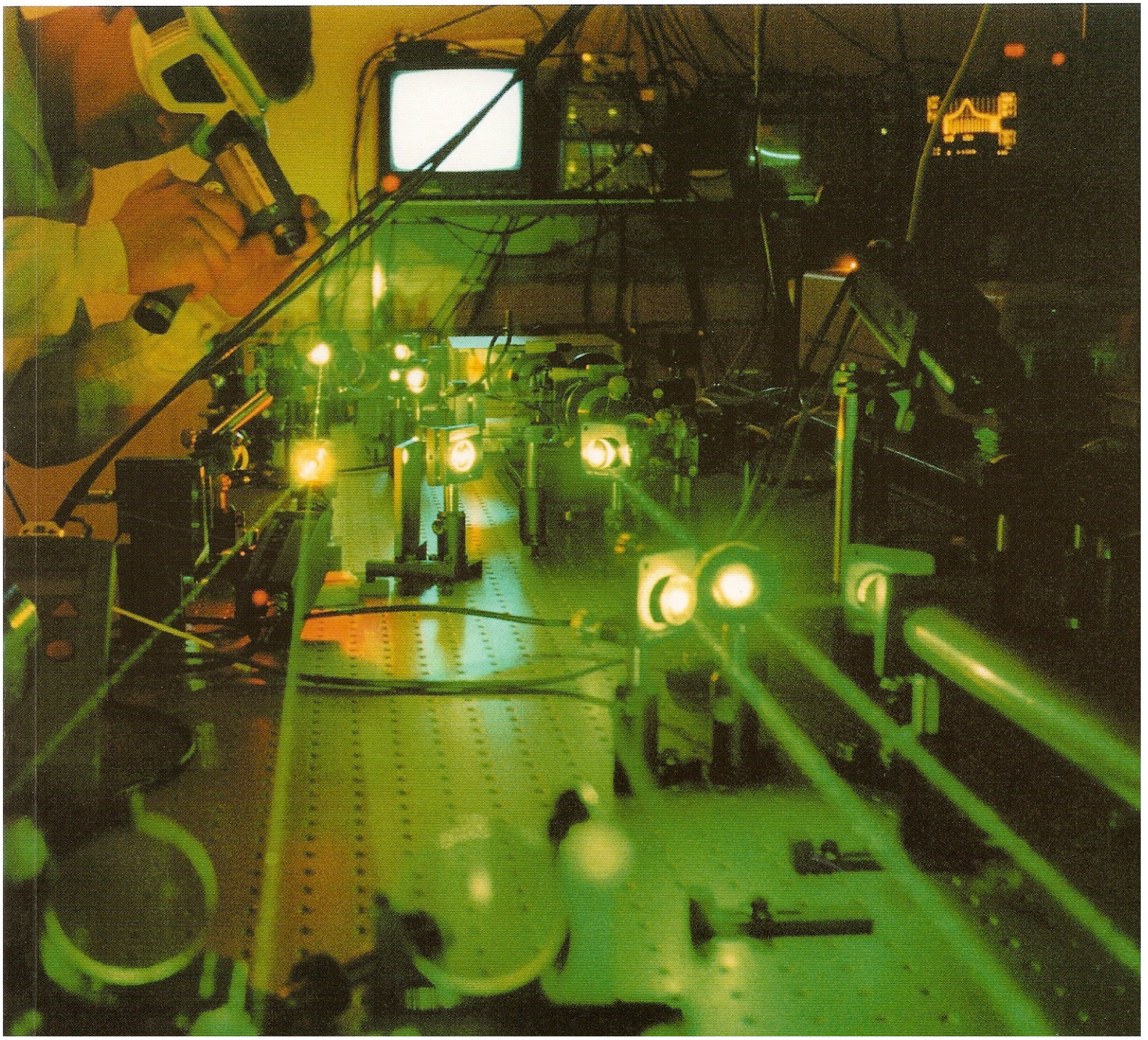

Central Laser Facility

Rutherford Appleton Laboratory

Annual Report 1998/99

Central Laser Facility
Rutherford Appleton Laboratory
Chilton, Didcot
Oxfordshire OX11 0QX
Tel. 44 (0) 1235 445655
Fax. 44 (0) 1235 445888
E-mail. clf@rl.ac.uk
Web site. http://www.clf.rl.ac.uk

RAL Report No. RAL-TR-1999-062

The front cover shows Edwin Divall aligning the first of three titanium-sapphire amplifiers in the CLF's new multi-terawatt femtosecond laser - ASTRA. (Photograph courtesy of Edwin Divall).

ISBN 0902376950

Contents

Acknowledgements

The production team for this Annual Report was as follows:

Editor	Brian Wyborn
Overall Co-ordination	Alison Brown
Production	Katharine Horton, Chris Naboulsi, Dave Burgess
Chapter Editors	David Neely, Steven Rose, Andrew Langley, Tony Parker, Colin Danson, Graeme Hirst
Section Editors	Ric Allott, Margaret Notley, David Neely, Pavel Matousek, Stanley Botchway, Waseem Shaikh, Colin Danson, Andrew Langley, Mike Towrie, Rob Clarke, Ian Ross
Technical Support	Chris Reason, Richard Williams, RAL CLEO Support.

For the third year the CLF Annual Report has been produced as an electronic document, from submission of articles, to collating, editing and the final document production.

This report is available on the CLF's Web Page Ref. http://www.clf.rl.ac.uk/.
It is also proposed to produce it on CD Rom.

The document has been reproduced by the RAL Reprographics Section.

Thanks to all the above for their contribution towards producing this report and of course to all the authors for their submissions.

Foreword

M H R Hutchinson

Central Laser Facility, CLRC Rutherford Appleton Laboratory, Chilton, Didcot, Oxon., OX11 0QX, UK

This report contains scientific accounts of the work which has been carried out at the Central Laser Facility (CLF) at the Rutherford Appleton Laboratory both by university users and facility staff during the financial year 1998/99.

The Vulcan laser has continued to provide the focus of the very strong, international research programme in laser-plasma interactions. A significant contribution to the success of this programme has been the further increase in the intensity which can be produced by Vulcan operating in the CPA mode. By improving further the beam quality and using F1 parabolic reflectors for focusing, intensities of up to 5 x 10^{19} W/cm^2 have been produced. At these very high intensities, the laser-plasma interaction gives rise to the generation of energetic electrons and ions, ultra-high magnetic fields and, by producing highly-directional beams of γ-rays, to the nuclear activation of elements via (γ,n) processes. Other areas which have been studied include the development and use of X-ray lasers for radiography of laser-produced plasma and the study of instabilities and the use of shock wave propagation in low density foams to test new concepts in inertial confinement fusion.

A very significant development has been the approval by EPSRC of a grant for £3.3M to upgrade the output power of Vulcan to 1PW. This programme will be carried out over the next three years in parallel with the users' scientific programmes. This will enable the intensity to be increased to 10^{21}W/cm^2 and will open up new areas of plasma physics to the scientific community world-wide.

The Astra laser is a 30fs, 10Hz CPA TiS laser which, during the year has been moved to a new laboratory and upgraded to produce intensities of 10^{18}W/cm^2. The new laboratory enables two user experimental areas to be operated simultaneously and this has been highly beneficial in enhancing access to this facility. A further upgrade, funded by EPSRC was commenced and this will provide target intensities of up to 10^{19}W/cm^2 to be produced in one of the two areas. The programme so far has concentrated on the interaction of intense, ultrashort pulses with neutral and ionic molecules and, with the development of the high intensity configuration, laser-plasma and short-pulse X-ray studies will become possible.

During the year, a decision was made in consultation with the users and EPSRC, the principal funding agency, to close the Titania KrF laser to permit the facility to concentrate on the new opportunities provided by the high intensity lasers, Vulcan and Astra.

The highly successful science programme has continued within the Lasers *for* Science Facility (LSF). A significant development has been the enhancement of the Raman and ps-TR^3 capability by construction of a fast Kerr gate for the rejection of fluorescence signals which obscure the Raman signal. This has enabled intramolecular electron transfer in some large organic molecules to be observed for the first time and has improved our understanding of how ultrafast changes in molecular structure influence their efficiency. The Laser Loan Pool has benefited from an ongoing investment programme in laser and diagnostic equipment which has been funded by EPSRC and has enabled state of the art lasers to be made available to university users in their own laboratories.

The science being carried out within the CLF by university colleagues from both within the UK and elsewhere in Europe continues to be of the highest quality. The very substantial capital investment made by EPSRC in Vulcan, Astra and the LSF will ensure the continuing excellence of the facilities provided at the CLF and quality of the science carried out by its users.

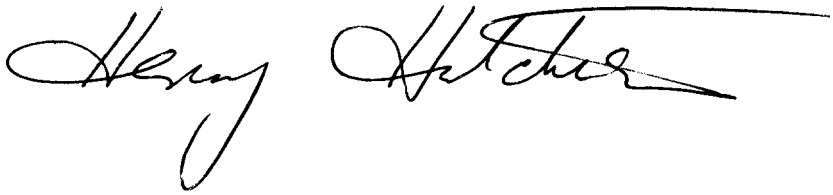

Overview of the Central Laser Facility

C B Edwards

Central Laser Facility, CLRC Rutherford Appleton Laboratory, Chilton, Didcot, Oxon., OX11 0QX.
Email C.B.Edwards@rl.ac.uk

Laser Facilities for Users

The Central Laser Facility (CLF) is one of the world's leading centres for research using lasers. Facilities available to users include the Vulcan Nd:glass laser which delivers multi-TW beams to two target areas, the Astra ultra-short pulse interaction facility based on titanium sapphire laser technology, a range of state of the art table top laser systems and specialised diagnostic instruments within the Lasers *for* Science Facility and the Laser Loan Pool.

Vulcan

Vulcan is a highly versatile large scale Nd:glass laser installation which delivers a maximum of 2.5kJ of energy in its six 10cm and two 15cm beamlines to two target areas, each of which is equipped with frequency conversion optics to enable both 1μm and 0.5μm operation of all beams. Two further target areas are available for lower energy applications. A range of pulse durations are available from 100ps to 20ns in various geometries

A short pulse (700fs) high irradiance (~$5x10^{19}Wcm^{-2}$) chirped pulse amplification (CPA) capability is available, with vacuum propagation to target and reflective beam focusing optics. Additional low energy beams, including sub-picosecond CPA probes, are provided for diagnostics with high temporal resolution. The system is fully characterised and equipped with advanced diagnostics.

Lasers *for* Science Facility (LSF)

The LSF operates a suite of state of the art table-top laser systems and associated instrumentation giving users access to highly tuneable (vuv - ir) and variable pulse width (ns to fs) laser radiation. This includes lasers for ns and ps time-resolved resonance Raman spectroscopy (TR^3), a unique dual wavelength multi-khz femtosecond synchronised pump-probe apparatus based on OPA technology, a femtosecond laboratory, a high average power laser plasma x-ray source and a fast gated (100ps) confocal microscopy laboratory.

In February 1999 funding was awarded by EPSRC for the development of the new PIRATE facility (Picosecond Infrared Absorption and Transient Excitation). The high brightness PIRATE laser, which will be tunable down to 1000 cm^{-1}, will come on line to users in 2000 for experiments in chemistry, physics, biological and material sciences.

Commercial laser systems are available from the Laser Loan Pool for periods of up to 6 months at the user's home laboratory.

Astra (HPHR)

The High Power, High Repetition Rate (HPHR) laser, now named Astra, has been upgraded in energy and installed in a new purpose-built laboratory. The pulse energy has been increased to 10mJ and, with a pulse duration of 50fs, produces intensities of greater than 10^{16} Wcm^{-2} .

The first experiment performed using the ASTRA facility was carried out by scientists from Queens' University, Belfast and the University College, London and was completed in December 1998. It studied the interactions between high intensity femtosecond laser pulses and a pulsed beam of hydrogen ions. During the year, the laser was used extensively to study short pulse interactions with atoms, ions and molecules.

Engineering Services

Mechanical, electrical and software engineering support is provided for the operation of the laser facilities at the CLF, for the experimental programmes on these facilities and for the CLF's research and development activities. Access to mechanical and electrical CAD tools and workshop facilities enable a rapid response to be provided to users.

Customers

The main customers of the Central Laser Facility are the UK Research Councils, who fund beam time primarily for grant-supported UK University researchers and their overseas collaborators. A small proportion of access is provided by the Research Councils for non-grant funded work to enable rapid access for topical and proof of principle experiments.

The EC provides beam time for European researchers through a Large Scale Facility Access contract under the TMR programme. Hiring of the facilities and access to CLF expertise is also available for industrial research and development.

Access to Facilities

90% of EPSRC access is provided to grant supported programmes through a ticket mechanism. Such grants specify the amount of facility time required, enabling the full cost of the proposals to be taken into account by the prioritisation panels convened by EPSRC. Successful proposals are allocated "tickets" for beam time, which guarantee access subject only to scheduling considerations.

The remaining EPSRC funded beam time is allocated to Direct Access for proof of principle experiments, to demonstrate feasibility or to perform urgent studies. Direct Access experiments are peer reviewed by an expert panel who advise the Director of the CLF on scientific priority, etc. Bids for Direct Access are publicised in scientific journals and on the CLF Web site. Further information is available from the Director of the CLF.

Arrangements for funding of beamtime for experiments within the remit of BBSRC programme differs from the EPSRC model and potential applicants working in these areas should contact the Director of the CLF in the first instance for further information.

European researchers are eligible for beamtime at the CLF funded by the E.C. through its Large Scale Facilities Access programme. Calls for Proposals are publicised in Physics Today and on the CLF Web site. For information on forthcoming calls for proposals, eligibility criteria, etc. please contact Dr Ric Allott (r.allott@rl.ac.uk).

The Laser Loan Pool is funded directly by an EPSRC rolling programme. These facilities are available to all UK researchers performing work falling within the EPSRC science programme. For information on forthcoming calls for proposals, eligibility criteria, etc. please contact Dr Anthony W Parker (a.w.parker@rl.ac.uk).

CLF Web site

Further information on the CLF, its facilities, and the scientific programmes is available on the CLF Web site at http://www.clf.rl.ac.uk/

Collimated Ionization Channels in Glass Targets Irradiated by Ultra-intense Laser Pulses

M Borghesi, A J Mackinnon[1], A R Bell, G Malka[2], C Vickers, O Willi

Imperial College of Science, Technology and Medicine, London,UK

[1] presently at Lawrence Livermore National Laboratory, Livermore, US

[2] presently at Université Paris-sud, Orsay, France

J R Davies

Instituto Superior Tecnico, GoLP, 1096 Lisboa, Portugal

A Pukhov, J Meyer-ter-Vehn

Max-Planck-Institut für Quantenoptik, D-85748 Garching, Germany

Main contact email address: *mbr@ic.ac.uk*

Introduction

Recent computational papers have predicted that, during the interaction of ultra-intense laser pulses with dense plasmas, collimated beams of very energetic electrons are produced[1,2)]. In particular, Particle-in-Cell (PIC) simulations predict that MeV electrons, ponderomotively accelerated along the propagation axis, are confined radially by large, self-generated magnetic fields[2)]. This confinement can lead to a well collimated electron beam propagating into the high density plasma[3)]. At high density the electrons will eventually lose their energy through collisions and will be stopped after a characteristic range depending on their energy. Recent experimental results seem to indicate that the electron beam stays collimated during its propagation through a solid plastic target[4)]. This was inferred from observations of small extent plasma plumes on the rear of 200 µm thick CH targets irradiated at 10^{19} W/cm^2. Simulations performed with a Fokker-Planck hybrid code[5)] suggest that inside the solid target the electrons are collimated by a magnetic field generated at the edge of the electron beam. The production and propagation of electron beams through high density plasmas are of topical interest for fast ignitor applications[6)]. It is essential for the fast ignitor scheme to be successful that the electron energy required to start ignition is deposited in the high density core of the compressed fusion fuel. These electrons are produced at densities close to critical and have to propagate to the core through a dense plasma. So far no direct observations of collimated electron beams have been reported.

Experimental observations of the interaction of ultra-intense laser pulses with aluminium over-coated solid glass (SiO_2) targets are reported here. Time-resolved optical probing revealed, immediately after the interaction, the presence of narrow opaque filaments in the glass. Computational modelling indicates that the observations are consistent with collimated propagation of a fast electron beam through the target.

Experimental set-up

The experiment was performed using the Vulcan Nd:glass laser operating in the Chirped Pulse Amplification mode (CPA) The targets were glass microscope slides, 250-300 µm wide and about 2 cm long. One of the narrow sides of the target was over-coated with a 1-3 µm thick aluminium layer to prevent direct laser transmission (see Figure 1). The 1.054 µm CPA interaction pulse, 1 ps in duration, with an energy of about 20 J was focused by an F/4.5 off-axis parabola (OAP) at normal incidence onto the centre of the coated side of the target. The focal spot was between 8 and 10 µm in diameter at full width at half maximum (FWHM), containing 30-40 % of the energy on target giving mean intensities up to 2×10^{19} W/cm^2.

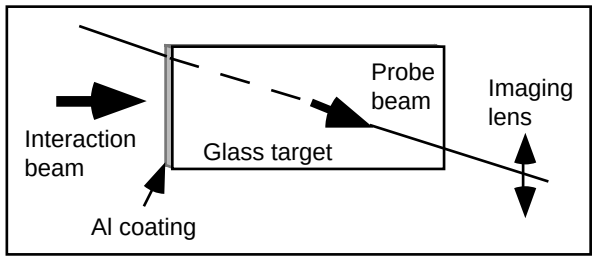

Figure 1. Schematic of the experimental arrangement

A fraction of the CPA pulse was compressed with a separate pair of gratings to a duration of 6 ps (FWHM), frequency doubled in a KDP crystal and used as a temporally independent probe. The relative timing between the probe and the interaction pulse was controlled to within a few picoseconds. A microscope objective, with an F-number of 4, imaged the target with a magnification of 55 onto photographic film resulting in a spatial resolution of 2 - 3 µm in the target plane.

Experimental results

Shadowgrams of the target were collected at different times. Before the interaction beam is focused onto the target, the glass slides are transparent to the probe radiation. Immediately after the interaction, tracks extending into the target which were opaque to the probe were observed.

A typical image is shown in Figure 2. The image has been taken with the probe nominally coincident with the interaction, i.e. integrated between $-\tau_D/2$ and $+\tau_D/2$, τ_D being the probe pulse duration. The target is mostly still transparent to the probe light, although it is becoming opaque near the interaction region (in the inner target region non-uniformities in the probe illumination affect the homogeneity of the image background). In particular a track, with a 10 µm radius, can be observed originating from the interaction region and extending into the target for 300-350 µm. Similar tracks were also observed on targets with a 3 µm aluminium overcoat. Also, on some of the images more than one track can be seen. In these cases the tracks, separated by a distance of the order of 10µm, are parallel or slightly diverging (~f/10). Typical lengths of the tracks at this timing are in the range 300 to 500 µm. In images recorded at a nominal time of + 3 ps (i.e. integrated up to 5 - 6 ps), the tracks extend up to 600-700 µm. The tracks have a roughly constant transverse size along their length, typically of the order of 10-20 µm. At about 5-8 ps after the interaction, the part of target in the field of view of the imaging system (about 1.5 mm in length) became completely opaque to the probe,

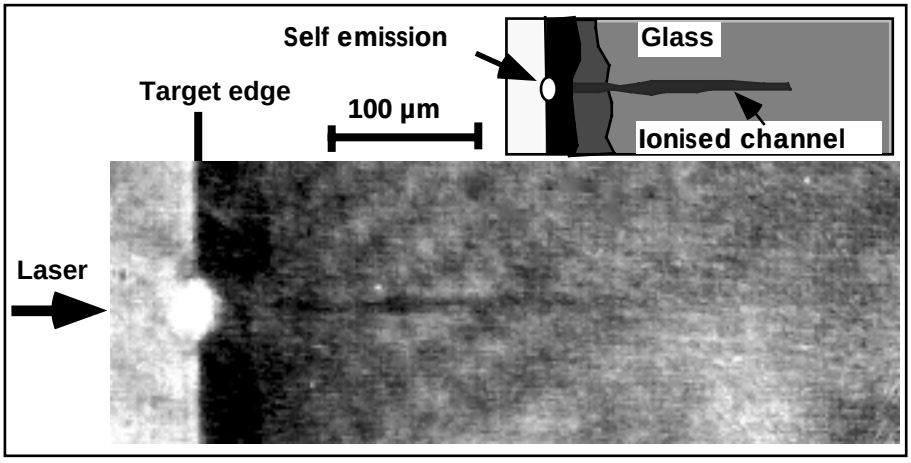

Figure 2. Shadowgram taken during the interaction of a 20 TW, 1 ps pulse with a solid glass target coated with 1 µm of Al.

limiting our experimental observations to the temporal range 0-5 ps. A similar phenomenon has been observed at lower irradiances and attributed to the propagation of a radiative ionisation front into the target[7].

Computational modelling

The opaque regions in the field of view of the probe correspond to regions in which a dense plasma is present. Under these conditions, the probe does not propagate through the plasma due to the combined effects of absorption in the plasma, reflection at the critical density and refraction due to the density gradients. It is therefore reasonable to infer that the opaque tracks correspond to localised, ionised regions inside the target. The possibility that this localised ionisation is due to the propagation through the solid of a collimated beam of hot electrons was investigated using computational codes. This hypothesis is based on experimental and theoretical evidence for the generation of high energy electrons in ultra-intense laser solid interactions[1-3,8], and on reported predictions of mechanisms leading to their collimation in overdense plasmas and solid targets [2, 3, 4, 5].

The 3-D PIC code (VLPL)[2] was used to model the electron generation in conditions close to the experiment, studying the interaction of a 10 TW, 700 fs, 6 µm radius laser pulse with a high density unionised silicon target, at an ion density of $5x10^{21}cm^{-3}$ (Silicon being similar to Aluminium and a major constituent of glass). A 3D PIC simulation using solid density and the spatial scales of the experiment is not currently possible. Barrier suppression ionisation by electric fields is included in the code, while interparticle collisions and collisional ionisation are not implemented.

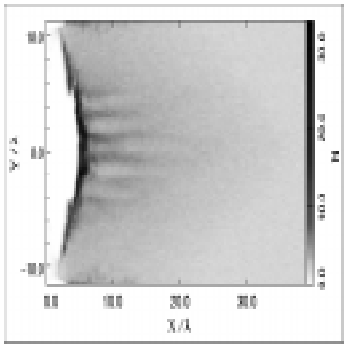

Figure 3. PIC code simulation of the interaction of a 10 TW laser pulse with unionised Si (ion density of $5x10^{21}$ cm^{-3}). The plot shows a 2D on axis cut of the electron density ($N=n/n_{cr}$) at the time of the laser pulse peak.

The simulation results are shown in Figure 3. At the left edge of the target a region of full ionisation, and compression due to the laser ponderomotive force, is clearly visible. Inside the target a series of ionised filaments are observed. These structures correspond to a current of fast electrons which splits into filaments due to the Weibel instability [2]. The electrons have a Boltzmann-like energy spectrum with an effective temperature of KT_f = 1.5 MeV. As the code does not include collisions, the ionisation is due to collective electric fields produced by the electron jets. When the electron jets propagate through a non-ionised medium, they create fields due to the associated space-charge. Also, the magnetic fields rising in time as the jets propagate induce electric fields due to Faraday's law. As a consequence, an ionised region of about 10 µm diameter with small scale filaments inside is observed. Each of the filaments is surrounded by a magnetic field, as observed in Reference 2. The electron jets propagate parallel to the laser axis, forming a closely packed bundle of ionised filaments. This would appear as a single channel opaque to transverse optical probing, as observed in the experiment.

The Fokker-Planck hybrid code described in References 5 and 9 was used to model the propagation of an electron beam through a solid SiO_2 target. The code represents the fast electrons with a Fokker Planck equation, including collisional drag and random angular scattering, which is solved using a particle, Monte Carlo method. The background electrons are represented by $\mathbf{E}=\eta\mathbf{J}_b$, where η is the resistivity and $\mathbf{J}_b$ the background current density. The set-up used was very similar to that in Reference 5 using the procedure given in Reference 9. Collision coefficients for solid SiO_2 were used. The resistivity was $\eta=1/(1/\eta_0+1/\eta_{spitzer})$ [5], with the initial, maximum resistivity $\eta_0= 2\ 10^{-6}\ \Omega m$, in agreement with experimental results (see Reference 5), and $Z\ln\Lambda=20$ in the Spitzer resistivity with the temperature given by the heating of the target. The specific heat capacity was taken from a simple fit to the results of the Thomas-Fermi model. The fast electron generation was modelled using the following parameters: peak laser intensity $2x10^{19}$ W/cm^2, spot radius 6 µm, pulse length 1 ps, giving a laser energy of about 20 J, fast electron temperature given by $KT_f=1.4(I_{19})^{1/2}$ MeV, where I_{19} is the intensity in units of $10^{19}Wcm^{-2}$. This relation for the fast electron temperature was chosen as for $I_{19}>1$ it gives KT_f approximately equal to the maximum oscillation energy of an electron in the laser electric field, as consistent with PIC results reported here and previoulsy[1]. The conversion into fast electrons was 30%, consistent with reported experimental observations[10]. The background heating 2 ps after the peak of the pulse is shown in Figure 4.

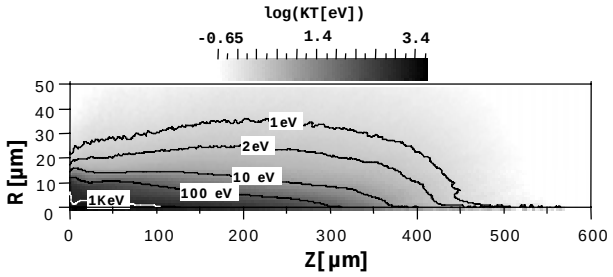

Figure 4. Profile of background heating, temperature in eV, as predicted by the hybrid code at 2 ps after the peak of the pulse.

An exact comparison with the experiment is difficult, as the code does not give the total free electron density and the experimental results will also be affected by the time integration and uncertainties in the probe timing. However, the steep temperature gradient in Figure 4 shows quite a clear boundary, and, for example, the 1 eV profile gives a reasonably good indication of the size of the heated region (i.e. of the region ionised by the passage of the electrons).

There are two strong points of comparison with the experimental results: i) the heated region has a roughly constant diameter ii) it penetrates approximately 350 µm.

The diameter of the heated region depends on the transverse size of the electron source, which in the code is taken to be of the order of the focal spot. The code predicts that 5 ps after the peak of the pulse the beam has penetrated about 500 µm into the target. By this time the electrons have lost 78% of their energy and the heat front penetration has largely stopped. These comparisons also apply to the individual tracks in the case where multiple tracks were seen. Finally it should be noted that using a fast electron temperature $KT_f = 0.46\ (I_{19})^{1/3}$MeV, as determined experimentally in Reference 11 and used in previous simulations[5)], reduced the penetration depth to about 300 µm , the propagation ceasing 3 ps after the peak of the pulse. This does not agree with the experimental observations.

Discussion

The simulations appear to confirm the hypothesis that the ionisation tracks observed in the experiment are due to magnetically collimated fast electrons. Amongst other possible causes, ionisation due to direct laser propagation is highly unlikely due to the presence of the Al coating that makes the front of the target opaque to the laser radiation. Anomalous laser transmission through Al foils has been reported[12)], however this was for thinner foils, free to expand both away and toward the laser. In these conditions decompression of the foils plays an important role in decreasing the peak density during the pulse duration, making laser transmission possible [12)]. In the conditions of the experiment reported here, due to the effect of the prepulse and the rising edge of the pulse, the main part of the pulse will interact with a short scale-length plasma, with a profile rising from underdense to highly overdense values. Ionisation due to propagation of high harmonics of the laser wavelength seems also unlikely, as, in order to propagate through the solid density plasma ahead of the interaction region, the harmonics should be in the X-UV region, and glass is opaque to radiation in this range of wavelength. However, X-UV light could propagate through a region preheated by the fast electrons, and therefore contribute to some extent to the observed experimental features.

Some information about the fast electron and target parameters can be drawn from the comparison of the experimental and computational results. The dependence of the penetration depth on fast electron temperature indicates that KT_f is of the order of a MeV, in disagreement with the experimentally determined scaling $KT_f = 0.46\ (I_{19})^{1/3}$ MeV, obtained at lower intensities[11)], but in agreement with PIC codes[1,2)] and recent experimental results [8)] . This may indicate a transition in the mechanism of fast electron generation from resonance absorption to direct ponderomotive acceleration. The code results for penetration depth are at the lower end of the range observed in the experiment. The most likely reason for this appears to be that the actual fast electron temperature was higher, due to laser irradiance higher than the nominal one. This could be due to better focusing achieved in some shots, or to self-focusing in the pre-plasma. Similarly, the observations in which more than one filament was seen, are probably due to shot-to-shot variations of the spatial distribution of the laser intensity influencing the electron source.

Conclusion

In conclusion, ionisation filaments have been observed in glass targets using optical probing techniques, following laser irradiation at intensities above 10^{19} W/cm^2. An Al coating prevented direct laser light propagation into the target. The filaments extended several hundreds microns from the target surface and maintained a roughly constant diameter of 10-20µm along this distance. Computer modelling performed with a 2-D PIC code and a Fokker-Planck hybrid code, indicated that the observed tracks are consistent with ionisation induced by magnetically collimated fast electrons. These observations are consistent with hypotheses drawn on previous experimental results and provide an important insight into the physics of the propagation of electron beams in solids and dense plasmas, a subject of topical interest in view of applications such as the fast ignitor.

Acknowledgements

The authors would like to acknowledge the help received by the staff of the Central Laser Facility while preparing and undertaking the experiment. This work was funded by ESPRC/MoD grants and a TMR Marie Curie Research Fellowship.

References

1. S C Wilks et al
Phys. Rev. Lett. 69 383, (1992)

2. A Pukhov and J Meyer-ter-Vehn
Phys. Rev. Lett. 79, 2686, (1997)

3. H Ruhl et al
Phys. Rev. Lett. 82, 2095, (1999)

4. M Tatarakis et al
Phys. Rev. Lett. 81 999, (1998)

5. J Davies, A R Bell and M Tatarakis
Phys. Rev. E 59, 6032, (1999)

6. M Tabak et al
Phys. Plasmas 1, 1626, (1994)

7. T Ditmire et al
Phys. Rev Lett. 77, 498, (1996)

8. G Malka and J L Miquel
Phys. Rev Lett. 77, 75, (1996)

9. J. Davies et al
Phys. Rev Lett. 56, 7193, (1997)

10. M Key et al
Phys. Plasmas. 5, 1966, (1998)

11. F Beg et al
Phys. Plasmas. 4, 447, (1996)

12. J Fuchs et al
Phys. Plasmas. 6, 2569, (1999).

Multi-MeV ion generation from high intensity laser interactions with underdense plasmas

K Krushelnick, E L Clark, Z Najmudin, M Salvati, M I K Santala, M Tatarakis, A E Dangor
Department of Physics, Imperial College of Science Technology and Medicine, London, SW7 2BZ, UK

V Malka
Laboratoire pour l'Utilisation des Lasers Intenses (LULI) Unité mixte n°7605 CNRS - CEA - École Polytechnique - Université Pierre et Marie Curie, France

D Neely, R Allott, C Danson
Central Laser Facility, CLRC Rutherford Appleton Laboratory, Chilton, Didcot, Oxon, OX11 0QX , UK

Main contact email address: *kmkr@ic.ac.uk*

There have been rapid advances in the use of high power, short pulse lasers over the past several years[1)] . In particular, the potential of such lasers for applications in particle acceleration[2)], x-ray generation, and inertial confinement fusion[3)] seems promising. However, much of the highly nonlinear plasma physics which occurs during such interactions is not well understood and experiments which address the fundamental physics of these interactions are required in order to properly evaluate the suitability of these intense laser-produced plasmas for such applications.

In this report, we discuss measurements of accelerated ions produced by the "Coulomb explosion" of a high intensity laser produced plasma[4)]. In this situation, ions are accelerated by electrostatic forces caused by charge separation induced by the laser ponderomotive pressure. It is found that a spatially resolved measurement of the high energy ions can provide a direct and simple estimate of the laser intensity in the plasma. By imaging the ion emission it is possible to determine how the intensity of the laser pulse changes as it propagates through the underdense plasma. In these experiments, we have measured peak ion energies of 1.0 MeV for deuterium gas interactions, 3.6 MeV for helium interactions and greater than 6 MeV for interactions with neon.

The production of energetic ions has also been inferred previously from observations of a plasma channel left trailing the high intensity laser pulse as it propagates through the underdense plasma[5,6)] . The generation of this channel is due to the expansion of energetic ions via the momentum given to them during a Coulomb explosion. As a very high intensity laser pulse propagates through an underdense plasma the strong ponderomotive force of the laser pulse forces some of the electrons from the region of highest intensity. Ions are affected much less by the ponderomotive force due to their larger mass. However, as the laser pulse passes, these ions will be given an impulse perpendicular to the laser axis and which is produced by the large space charge forces due to charge separation. After the laser pulse passes, the electrons will return to their original positions on a timescale of about $1/\omega_{pe}$, (where ω_{pe} is the plasma frequency), but the lateral momentum given to the ions will be retained and they will continue moving out of the plasma carrying low energy electrons with them. The energy of these ions is thus directly related to the intensity of the focused laser pulse and the maximum energy that can be gained by an ion during these interactions is simply given as the relativistic ponderomotive energy ($U = Zmec^2(\gamma\text{-}1)$ where Z is the ion charge and γ is the relativistic factor of the electron quiver motion in the laser field).

These experiments were performed using the Vulcan laser at the Rutherford Appleton Laboratory. This system produces laser pulses having an energy of up to 50 J and a duration of 0.9psec at a wavelength of 1.054μm (Nd:Glass). The laser pulse was focused into a gas jet target (4 mm nozzle diameter) using an f/4 off axis parabolic mirror. When helium was used as the target gas the plasma had an electron density up to about 5 x 10^{19} cm^{-3}. Deuterium and neon were also used as target gases.

In these experiments, the angular distribution of ions emitted during such high intensity laser plasma interactions was recorded using CR-39 nuclear track detectors placed at various positions surrounding the interaction region. These detectors are sensitive to ions having energies greater than about 100keV/nucleon [7)].

It was found that there was no significant variation in ion emission in the azimuthal direction (i.e., changing the laser polarisation had little effect). However, a distinct peak was observed in the emission of ions with energies greater than 300keV at 90 degrees to the axis of propagation. Measurements of the ion emission at higher energies were also obtained by using CR-39 track detectors covered with thin aluminum filters (2 μm) which blocks all signal from helium ions below about 2 MeV in energy.

Averaged measurements over 4 shots are shown in Figure 1. It is clear that the majority of ion emission occurs in the 90 degree direction, although the emission lobe also extends in the backward direction somewhat. Emission at energies greater than 2 MeV shows a narrower lobe in the 90 degree direction.

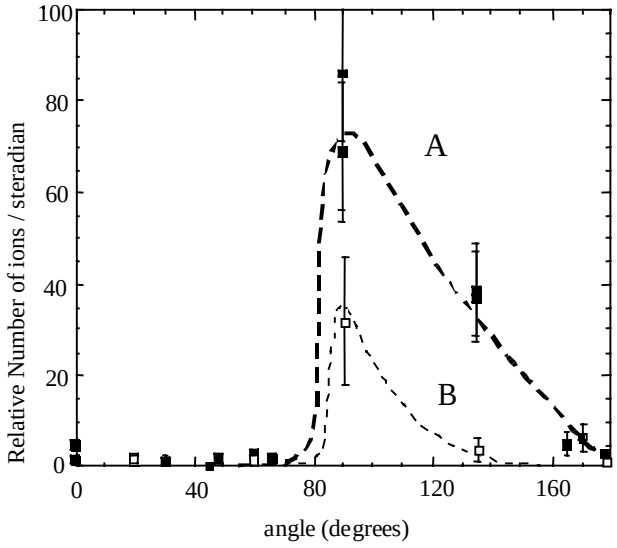

Figure 1. Angular emission of energetic ions. A) distribution of helium ions with energy greater than 400 keV B) distribution of helium ions with energy greater than 2 MeV (shown x 10). (Note that dashed lines are drawn as visual aid only) .

The spectrum of the energetic ions was measured using a Thomson parabola which spatially separates ion species having different charge to mass ratios through the use of parallel electric and magnetic fields. CR-39 was used as the detector.

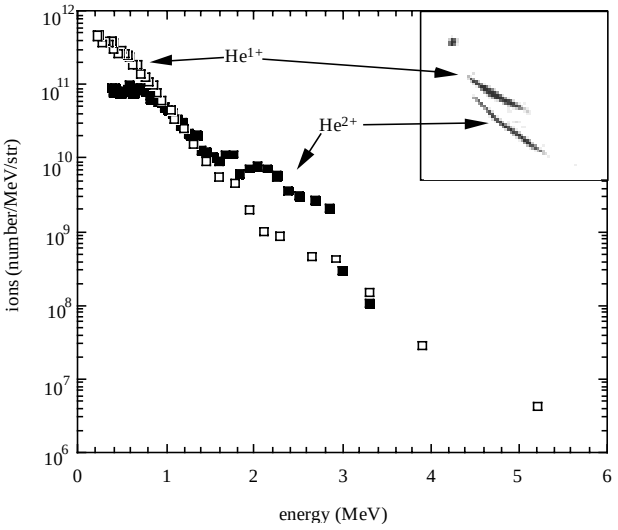

Figure 2. Typical ion spectrum from helium interaction (90 degrees). Thomson parabola tracks are shown inset.

The spectrometer was positioned at 42 cm from the laser interaction at 90 degrees from the axis of propagation and used a 250 µm diameter pinhole as the aperture. Typical experimentally measured spectra are shown in Figure 2 for helium. For the spectrum shown it is estimated that 0.25% of the incident laser energy is transferred to ions having greater than 300 keV of energy by using the previously measured ion angular emission profiles.

The spectrum in Figure 2 also shows good qualitative agreement with a recent calculated ion spectra at an intensity of 2 x 10^{18} W/cm^2 [8] (i.e., which also shows the "plateau" structure evident in our measurements).

The maximum ion energy, such that there were more than 108 ions/MeV/sterradian, was found to be 3.6 MeV for helium, 1.0 MeV for deuterium and greater than 6 MeV for neon. It is possible to use these measured energies as a diagnostic of the peak laser intensity during the laser plasma interaction. These interactions are well above the critical power threshold for relativistic self-focusing (P_{crit} = 17 (n_{crit}/n_e) GW = 1.7 TW for plasmas of densities 10^{19} cm^{-3}) so that it is expected that there will be a significant enhancement of the peak laser intensity

during the interaction. Such self-focusing occurs because of the change in plasma refractive index due to the relativistic mass increase of electrons in the intense laser field.

Enhancement of the laser intensity is precisely what is observed if we calculate the necessary laser intensity to produce the measured ion spectra. In Figure 3, a plot of the laser intensity in the plasma (obtained from the peak ion energy) versus the "expected" laser intensity from the measured laser parameters (pulse length, energy, focusability) is presented. It is clear that the effect of the plasma is typically to increase the laser intensity in the interaction region. All of the data from our measurements are presented here and it should be noted that there is a significant shot-to-shot variation in these results - probably due to the nonlinear nature of the self-focusing processes.

The process of relativistic/charge-displacement self-focusing is not exactly reproducible from shot to shot since it is sensitive to small changes in density gradients in the gas jet as well as fluctuations in the initial beam profile of the incident laser. The estimates of the laser intensity during the interactions with neon gas (less than the "vacuum" intensity) suggest that the effects of ionization induced diffraction can also counteract any self-focusing process and cause the intensity to be reduced during such interactions.

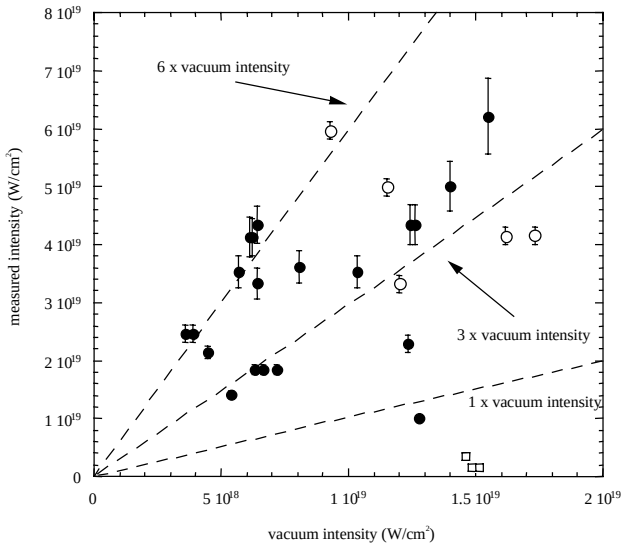

Figure 3. Experimentally estimated laser intensity in plasma (from peak ion energy) vs. expected "vacuum" intensity (from simultaneous measurements of laser parameters) Black circles - helium, white circles - deuterium, squares – neon. Dashed lines are drawn as a visual aid only.

In conclusion, these experiments have shown that energetic ions are produced primarily in the 90 degree direction during high intensity laser interactions with underdense plasmas and that the generation mechanism can be understood as a result of Coulomb explosion processes. We have shown that neon ions greater than 6 MeV can be generated. From these measurements it is likely that the laser pulse undergoes significant self-focusing as a result of relativistic and charge-displacement effects throughout the interaction region.

References

1. M Perry and G Mourou
Science 264, 917 (1994).

2. T Tajima and J M Dawson
Phys. Rev. Lett. 43, 267 (1979); P. Sprangle *et al.,* Appl. Phys. Lett. 53, 2146 (1988); K. Nakajima *et al.*, Phys. Rev. Lett. 74, 4428 (1995); C. Coverdale *et al.,* Phys. Rev. Lett. 74, 4659 (1995); D. Umstadter *et al.,* Science 273, 472 (1996); A. Modena, *et al.*, Nature 377, 606 (1995); A. Ting *et al.*, Phys. Plasmas 4,1889 (1997).

3. Tabak *et al*
Phys. Plasmas 1, 1626 (1994).

4. N H Burnett and G D Enright
IEEE J. Quant. Electron. 26, 1797 (1990).

5. K Krushelnick *et al*
Phys. Rev. Lett. 78, 4047 (1997).

6. S Y Chen *et al*
Phys. Rev. Lett. 80, 2610 (1998); G. S. Sarkisov *et al.,* (submitted for publication).

7. A P Fews
Nucl. Instrum. Methods Phys. Res., *Sect. B* 71, 465 (1992); 72, 91 (1992).

8. G Pretzler *et al*
Phys. Rev. E , 58, 1165 (1998).

Measurements of the Inverse Faraday effect in high intensity laser produced plasmas

M Tatarakis, K Krushelnick, Z Najmudin, E L Clark, M Salvati, M I K Santala, A E Dangor

Department of Physics, Imperial College of Science Technology and Medicine, London SW7 2BZ, UK

V Malka

Laboratoire pour l'Utilisation des Lasers Intenses (LULI) Unité mixte n°7605 CNRS - CEA - École Polytechnique - Université Pierre et Marie Curie, UK

D Neely, R Allott, C Danson

Central Laser Facility, CLRC Rutherford Appleton Laboratory, Chilton, Oxon, OX11 0QX, UK

Main contact email address: *m.tatarakis@ic.ac.uk*

The generation of magnetic fields in laser-produced plasmas has recently been the subject of increasing attention both theoretically and experimentally[1)]. One particular phenomenon , the inverse Faraday effect (IFE) , has been a source of some controversy as theoretical predictions are in disagreement[2,3)]. IFE is a magneto-optical phenomenon in which the propagation of circularly polarised radiation through a non-linear medium induces an axial magnetic field along the direction of propagation. Relatively small fields generated in this way were measured in solid state materials using lasers at low powers in early experiments[4)] and in the early 1970s magnetic fields were induced in plasmas through the use of circularly polarised microwaves[5)] . It has been postulated that using circularly polarised light at much higher intensities, time averaged azimuthal currents in near critical density plasmas could be generated which might produce an extremely large axial magnetic field [2,3)]. For 1 µm laser radiation at I = 10^{19} Watts/cm^2 and a plasma density of 8 x 10^{20} cm^{-3} recent calculations[3)] predict a magnetic field of greater than 10 MG which should be localised in space to the focal region of the intense laser pulse. There have been recent measurements of fields due to this effect at lower intensity (~ 10^{14} W/cm^2)[6)] which disagree significantly with theoretical predictions.

In this paper, we report the first time-resolved measurements of multi-MegaGauss magnetic fields generated by the IFE in an underdense plasma by a laser focused at relativistic intensities of ~10^{19} Wcm^{-2}. The experiments were performed using the CPA beam of the Vulcan laser at the Rutherford Appleton Laboratory. The laser pulse was at a wavelength of 1.054 µm and had an energy of 60 J, a duration of 0.9 ps, and had a 3.5 times diffraction limited focal spot. A detailed description of the laser system can be found in Reference 7. In these experiments the laser pulse was focused into a helium gas-jet target using a f/4 off axis parabolic mirror. Several diagnostics were run simultaneously during these experiments in order to measure the laser parameters (i.e., focal spot diameter, pulse length, pulse energy) and the vacuum intensity was found to be about 5x10^{18} Wcm^{-2}. A λ/4 wave plate was placed inside the vacuum chamber (after recompression) to change the laser polarisation from linear to circular for the purpose of the IFE measurements.

A small fraction of the pulse was split from the uncompressed main beam, recompressed using a separate pair of gratings and subsequently frequency doubled to 527 nm for use as a probe beam. The pulse length of the probe could be adjusted by changing the separation of the recompression gratings. The minimum pulse duration was 1.3 ps. For the purpose of the IFE experiments the probe gratings were adjusted to give a pulse length of ~15 ps duration. A Hamamatsu fast streak camera (1ps resolution) was used to measure the pulse duration of the probe beam and to time the probe beam with the main beam. Several other diagnostics were used during the experiments to provide information on laser propagation and plasma dynamics. In particular, Moire deflectometry and measurements of forward Raman scattering shadowgraphy were implemented to observe the laser plasma interaction region and density gradients in the plasma. Moire deflectometry and shadowgraphy

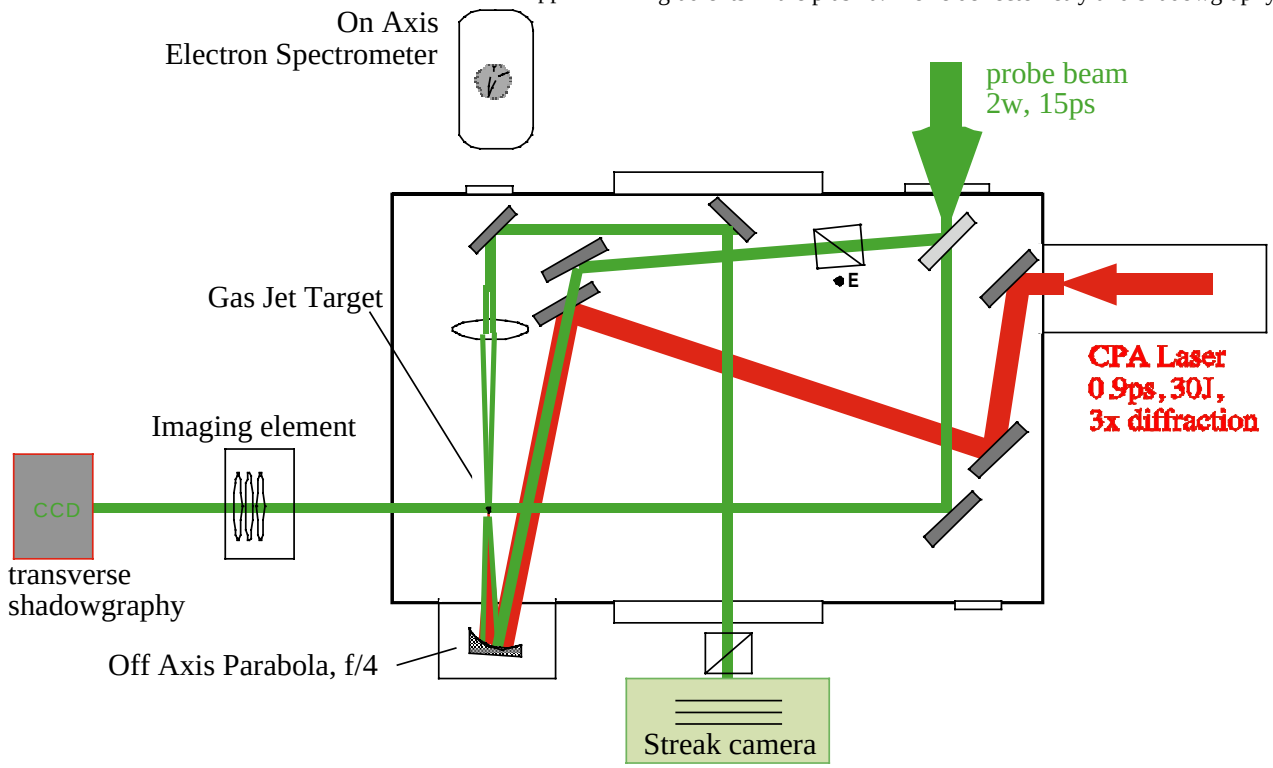

Figure 1. Experimental setup.

were performed using the same probe beam but with the pulse length adjusted to be about 1.5 ps. Furthermore, for these two diagnostics the probe pulse was transversely directed into the plasma. These images were then relayed by a high resolution (~5 μm) optical element onto CCD cameras. When helium gas was used as the target the electron density was found to be about 10^{19} cm^{-3}. The electron density could be adjusted to lower or higher values by changing the backing pressure of the gas jet.

When the probe was used collinearly it was linearly polarised and was directed onto the same parabolic mirror used to focus the interaction beam into the gas jet target (see Figure 1). Far field monitors were used to ensure that the focal regions of the two beams overlapped. The collinear probe was then imaged onto the slit of the Hamamatsu streak camera, which was used as the detector. A polarimetric system (a pair of high extinction ratio polarisers) was responsible for detecting polarisation changes of the probe due to the magnetic field generated in the plasma interaction region by the pump beam. The effect of the rotation of the plane of polarisation of a linear polarised probe propagating into a magnetised plasma (Faraday rotation) can be found in Reference 8. The angle of rotation of the electric field vector is given by;

$$\phi(\mathrm{deg}) = 3.02 \times [\lambda_p(\mu\mathrm{m})]^2 \int \frac{n(\mathrm{cm}^{-3})\, B_z(\mathrm{MG})\, dz(\mu\mathrm{m})}{10^{21}\left(1 - \frac{n}{n_{cr}}\right)^{1/2}}$$

where n and B are the electron density and magnetic field strength respectively and λ_p is the plasma wavelength (= c/ω_p).

Figure 2 presents a typical streak camera signal. The light line (top) shows the measurement when no analyser was used and the streak camera captured the probe light unaffected by the analyser. The duration is 15 ps as expected. The dark line (lower) was the signal obtained when the analyzer was set to transmit only light rotated due to the axial magnetic field light. The signal duration was about 1-3ps – which is about the duration of the high intensity laser pulse (to within the streak camera resolution). In the absence of an axial magnetic field the polarisation of the probe radiation would remain unchanged

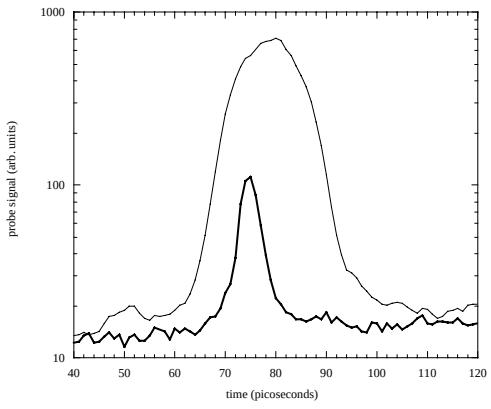

Figure 2. Lineout of the streak camera signal. Light line (top signal) indicates signal without analyser. Dark line (lower signal) indicates Faraday rotated signal (using analyser).

and therefore light would not be transmitted through the analyser. Shots without gas but with probe, or with gas but without probe were taken and only background light at noise level was observed. Furthermore, when linear polarised light was used no rotation of the probe radiation was observed. This clearly demonstrates that the source of the axial magnetic field is the circularly polarised light and is due to the IFE. It should be noted that the direction of the field (± z) was not determined in these experiments.

The magnetic field can be calculated from the intensity ratio between shots with the analyser crossed and those with the analyser parallel to the initial polarisation of the probe (Figure 2). In order to calculate the magnetic field the propagation length of the probe in the plasma is needed and this was measured by the other probe diagnostics (shadowgraphy, Moire deflectometry) as well as by imaging the second harmonic emission from the plasma. The "effective length" (the region in the plasma where the magnetic field is strong enough to significantly rotate the probe) is likely smaller than that seen by the above diagnostics, so this magnetic field measured is the estimated minimum.

The Faraday rotation angle was measured to be 19 ± 5 degrees which gives a magnetic field of ~ 9 ± 3 MG for an electron density of 10^{19} cm^{-3} and a propagation length of 0.5± 0.1 mm.

An important aspect of this measurement is that it shows that magnetic fields due to the inverse Faraday effect have a duration which is only for about that of the intense circularly polarised laser pulse which generates the field. The dissipation/ convection time for this magnetic field is clearly very short and is on the order of a picosecond. Also, there was no definite evidence of very large magnetic fields in the "wake" of the high intensity laser pulse where turbulent fields (vortices) have been predicted to exist[9] . However, from the asymmetry of the signal in Figure 2 there is some indication that much smaller fields (an order of magnitude less than that due to IFE) may exist in this wake.

In conclusion, we have performed the first time-resolved measurements of the Inverse Faraday Effect in which we measure fields of 9 ± 3 MG from interactions at intensities $5x10^{18}$ W/cm^2. The field was generated by a 0.9 ps duration laser pulse and lasted for a duration of 1-3 ps. These measurements are in reasonable agreement with theory.

Such fields may be useful for applications of laser plasma accelerators in order to reduce propagation instabilities of laser-accelerated electron beams through plasmas and perhaps improve their emittance.

References

1. M Perry and G. Mourou, Science 264, 917 (1994).

2. V Y Bychenkov, V I Demin and V T Tikhonchuk Sov. Phys. JETP 78, 62 (1994); A. D. Steiger and C. H. Woods, Phys. Rev. A 5, 1467 (1972); T. Lehner, Physica Scripta 49, 704 (1994); L. M. Gorbunov and R. R. Ramazasvili, JETP 87, 461 (1998).

3. Z M Sheng and J Meyer-ter-Vehn, Phys. Rev. E 54, 1833 (1996).

4. J P van der Ziel et al, Phys. Rev. Lett. 15, 190, (1965).

5. J Deschamps, M Fitaire and M Lagoutte Phys. Rev. Lett. 25, 1330 (1970).

6. Y Horovitz, S Eliezer, Z Henis, Y Paiss, E Moshe, A Ludmirsky, M Werdiger, B Arad and A Zigler Physics Letters A 246, 329 (1998); Y. Horovitz, S. Eliezer, A. Ludmirsky, Z. Henis, E. Moshe, R. Shpitalnik, and B. Arad, Phys. Rev. Lett. 78, 1707 (1997).

7. C N Danson et al, J. Modern Optics 45, 1653 (1998).

8. M Tatarakis, R Aliaga-Rossel, A E Dangor and M G Haines, Physics of Plasmas 5, 682 (1997)

9. Z M Sheng, J Meyer-ter-Vehn, and A Pukhov Physics of Plasmas 5, 3764 (1998).

First observations of the laser hosing instability

Z Najmudin, K Krushelnick, E L Clark, M Salvati, M I K Santala, M Tatarakis, A E Dangor
Department of Physics, Imperial College of Science Technology and Medicine, London SW7 2BZ, UK

V Malka
Laboratoire pour l'Utilisation des Lasers Intenses (LULI) Unité mixte n°7605 CNRS - CEA - École Polytechnique - Université Pierre et Marie Curie, France

D Neely, R Allott, C Danson
Central Laser Facility, CLRC Rutherford Appleton Laboratory, Chilton, Didcot, Oxon, OX11 0QX , UK

Main contact email address: *zn1@ic.ac.uk*

Propagation of ultra-high intensity laser beams in plasmas has recently received much attention with regard to potential applications such as x-ray lasers, plasma based accelerators, and "fast-ignition" of compressed Inertial Confinement Fusion pellets. For all of these applications, it is crucial that a high intensity beam can be propagated controllably, often over long distances. In the simplest case, it has been proposed that a laser beam can overcome the natural limits of refraction, and can remain focused due to its own non-linear interaction with the plasma. In particular, the relativistic quiver velocity of electrons in an intense laser field can lead to an increased on-axis index of refraction. This, in conjunction with the increase in refractive index from the reduction of on-axis electron density due to the ponderomotive force of the intense pulse, leads to the formation of a self-focusing structure. This can balance or even overcome the natural diffraction of the laser beam to give long-distance propagation of the beam or higher peak intensities than could be achieved by focusing in vacuum.

A simple treatment, for an idealised Gaussian beam, gives a critical power at which the natural diffraction is balanced by self-focusing. This critical power is $P_{cr} = 17(n_{cr}/n_e)$ GW, where n_e is the initial plasma density and n_{cr} is the critical density [1].

We report here on an experiment to study the propagation of an ultra-high power laser beam. In particular, to study the initial channel formation, we performed shadowgraphy of the laser beam focused into a supersonic gas jet. For this a second short pulse low energy frequency-doubled laser beam is passed orthogonal to the direction of propagation of the channel-forming beam as a probe. The collimated probe beam passes through the plasma and is collected by a lens, which re-images the scattered light from this beam onto a CCD camera. The refractive index of a plasma is given by $\eta = (1 - n_e/\gamma n_{cr})^{1/2}$, where n_e/n_{cr} is the ratio of electron density to critical density and γ is the Lorentz factor of plasma electrons quivering in the electric field of the laser. Thus, when a plasma is formed by the driving beam, density gradients are created which diffract the probe beam away from regions of low refractive index. Hence, shadowgraphy can measure both density gradients produced by plasma formation, as well as those resulting from plasma displacement due to the ponderomotive force of the laser beam.

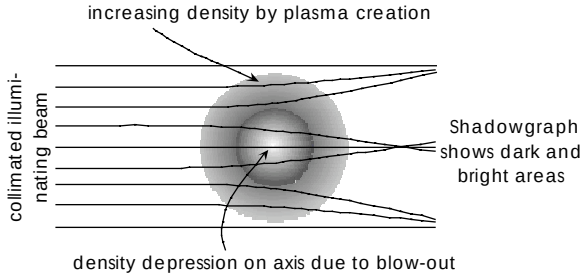

Figure 1. Schematic of probe shadowgraphy of plasma.

These experiments were performed using the Vulcan laser at the Rutherford Appleton Laboratory. This system produces laser pulses having an energy of up to 40 J on target and a duration of 0.9 psec at a wavelength of 1.054 µm (Nd:Glass). The laser pulse was focused into a gas jet target (4 mm nozzle diameter) using an $f/4$ off-axis parabolic mirror. In vacuum the laser can be focused to a 10 µm diameter spot. With helium as the target gas the plasma had electron densities up to about 5×10^{19} cm^{-3}.

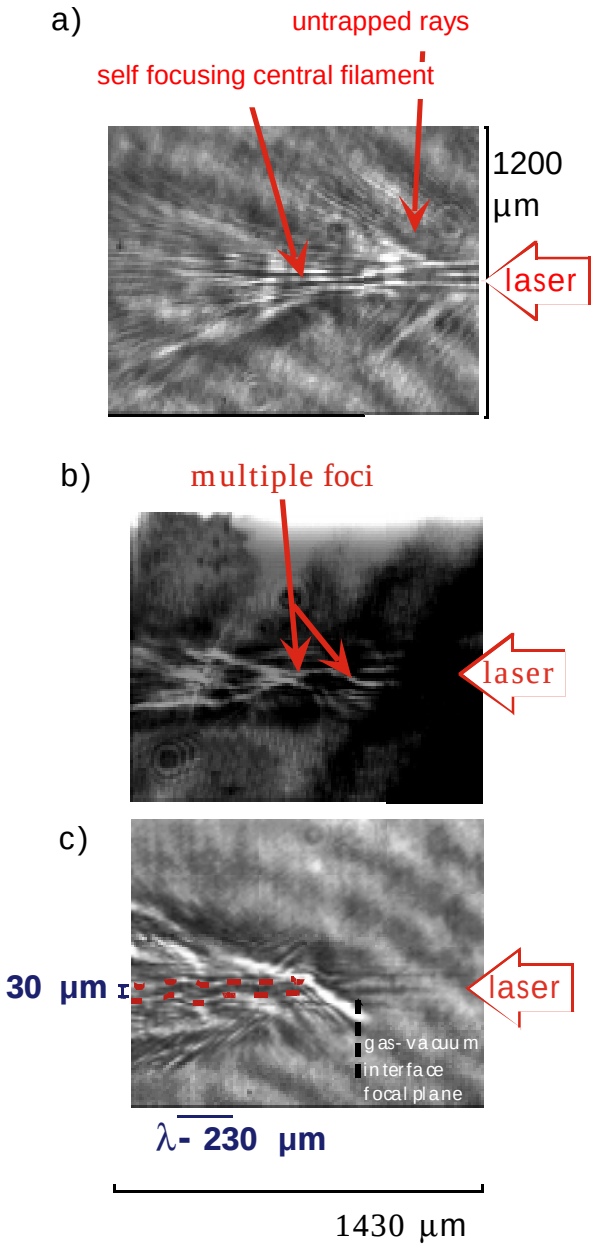

Figure 2. Shadowgraphs taken with $n_e = 2\text{-}3 \cdot 10^{19}$ cm^{-3}.

Figure 2a is typical of the shadowgrams taken during the experiment. The incoming laser beam forms a wide column of plasma which has a density minimum on axis, either due to ponderomotive or thermal expansion of the plasma within the

10 ps length of the probe beam. This accounts for the bright centre, since a density minimum would form a weakly focusing converging lens. As the laser propagates further into the gas jet, this channel becomes narrower and deeper, such that the rays towards the centre are focused so sharply that there is actually an intensity dip on axis. Noticeably, away from this channel there are a few weak filaments of fixed angle of 30°. This light is further evidence of the presence of a focusing channel on axis. Light travelling within the channel of a self-focusing beam can be diffracted by processes such as ionisation defocusing or Raman side scatter. But the self-focusing channel behaves like an optical fibre of fixed numerical aperture. Rays of light, which are bent at angles outside of this numerical aperture, will escape the channel, rather than being totally internally reflected. Since the amount of light falls off rapidly with increasing angle, most of the observed light will be at close to the angle which is just beyond the acceptance angle of this natural fibre. Relativistic effects alone cannot account for the increase in refractive index required, so that there must also be a greatly enhanced density at the edges of the channel.

As the beam travels further into the gas, it is seen to break up into a great many filaments. As can be seen in Figure 2 the laser power in each filament is much less than the critical power for self-focusing. Hence, such filaments cannot be produced by relativistic self-focusing effects. It is likely that the filaments remain intact due to the non-linear susceptibility of the unionised or partially ionised gas. For helium at close to atmospheric this atomic self-focusing is exhibited at intensities of only 10^{15} Wcm^{-2}, close to the tunnel ionisation threshold of helium[2]. This can account for the filaments remaining sufficiently focused to cause enough ionisation to be observed with shadowgraphy. Recent work by Antonsen *et al.*[3], suggests that this filamentation is initiated by ionisation. A non-ideal beam (such as the Vulcan high intensity beam), will have high intensity modulations close to focus, which result in different ionisation rates across the focal plane. Hence the plasma acts as a phase plate causing interference in the propagation of the beam, which further enhances the intensity modulations. Therefore, there is a feedback mechanism and the beam becomes unstable to this process. The highest growth-rate for this instability[3] occurs when the angle of the scattered beam is close to k_p/k_0. This is often observed to be the case for $n_e/n_{cr}(\sim k_p/k_0) \approx 0.1$, but the angle of spread of the filaments is seen to increase with density.

In the simulations[3] the interaction medium was helium. With gases having lower ionisation potentials, one expects this effect to be even more pronounced. This is the case in our experiments. For example, when hydrogen or neon were used in the gas jet, filaments were detected over a much wider range.

Sometimes the channel is observed to extend beyond the edge of our field of view. More significantly the filament has been observed by Thomson scattering[4] to extend for over 10 Rayleigh lengths at high intensity - although this only occurs when the laser power exceeds the critical power by a factor of 10 or more. It appears then that the effect of the filamentation is to prevent whole beam self-focusing of such ultra-intense pulses at powers close to P_{cr}.

However, there is a great variation in the characteristics observed. This evidently is due to imperfections in beam quality, which are typical of such ultra-high power laser pulses. One such example of anomalous behaviour is shown in Figure 2b. In this case, no filaments are observed outside the initial central channel. Indeed the whole beam seems to refocus itself at a second point about 300 µm in to the gas jet. After this, the beam appears to filament in a much more typical way. This type of 'sausaging' of a high intensity laser beam is a characteristic of beams of power well above the threshold for relativistic self focusing, and has been observed with other diagnostics such as Thomson scattering and plasma wave scattering.

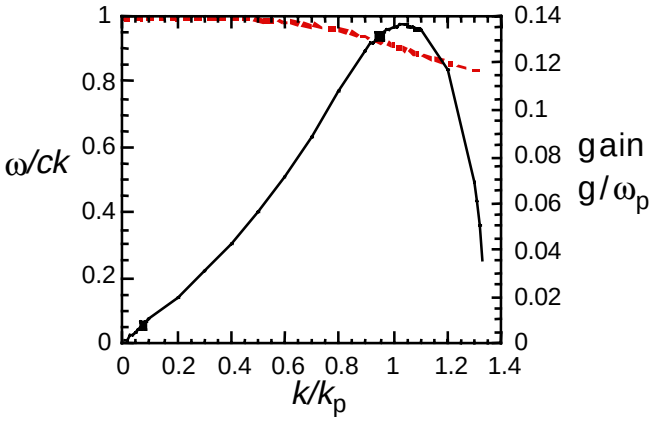

Figure 3. Growth rate (solid line) and phase velocity (dashed line) of laser hosing as a function of wavevector.

Figure 2c shows another shadowgraph showing a long propagating central filament, (this time over 3 Rayleigh lengths). However, this channel once again shows peculiar behaviour. Before entering the gas jet one can see that the plasma generated in the low-density gas outside the supersonic jet of the gas-jet has straight walls as expected. However, after crossing the boundary of the supersonic flow, the plasma channel has a transverse structure which oscillates either side of the direction of propagation, and which has a wavelength of about 230 µm. The "hosing" motion grows slightly as the pulse propagates. This type of 'laser hosing' has been predicted [5,6]. However, previous theories consider only the interaction of a laser pulse with the high amplitude plasma wave generated by the pulse, or the motion of the pulse in a pre-created guiding channel. In each of these cases the wavelength of the oscillation is predicted to be that of the plasma wave ($k_p \approx \omega_p/\omega_0 * k_0$), which in our experiments corresponds to $\lambda_p \approx 7\mu m$. This would be quite difficult to observe with our diagnostics.

Recently, however, Duda *et al.*[7] have considered a fully relativistic treatment of the electron response to a laser pulse, and find that if one considers the non-linear response of the plasma to an intense laser pulse, then longer wavelength hosing has a finite growth rate. (This is a 2D analogue to the relativistic modulational instability). In simulations, they find that at late times, the propagation of the laser pulse can be dominated by the longer wavelength hosing. In Figure 3 we plot the growth rate and phase velocity of the transverse whole-beam oscillations. It is clear that at sufficiently long wavelengths (small k_p) the oscillation velocity ω/k is close to c, the speed of light. In the time it takes the pulse to travel one (hosing) wavelength, the centre of beam motion will have moved tranversely through one cycle. Hence the oscillation will appear stationary in the lab frame, as will the channel created by the normal ponderomotive force of the laser – as we appear to see. (This would not be the case for $k \sim k_p$). Figure 2c, therefore, appears to be the first experimental evidence of laser hosing.

References

1. G Sun *et al*, Phys. Fluids 30, 526 (1987).
2. H R Lange *et al*, Optics Letters 23, 120 (1998).
3. T M Antonsen, Z G Bian, Phys Rev Lett. 82, 3617 (1999).
4. C E Clayton *et al*, Phys Rev Lett. 81, 100 (1998).
5. G Shvets, J S Wurtele, Phys Rev Lett. 73, 3540 (1994).
6. P Sprangle *et al*, Phys Rev Lett. 73, 3544 (1994).
7. B J Duda *et al*, Private Communication, (1999).

Evidence of seeding mechanisms for the convective Raman side-scattering instability

Z Najmudin, K Krushelnick, E L Clark, M Salvati, M I K Santala, M Tatarakis, A E Dangor

Department of Physics, Imperial College of Science Technology and Medicine, London SW7 2BZ, UK

V Malka

Laboratoire pour l'Utilisation des Lasers Intenses (LULI) Unité mixte n°7605 CNRS - CEA - École Polytechnique - Université Pierre et Marie Curie, France

D Neely, R Allott, C Danson

Central Laser Facility, CLRC Rutherford Appleton Laboratory, Chilton, Didcot, Oxon, OX11 0QX , UK

Main contact email address: *zn1@ic.ac.uk*

Recent experiments have demonstrated the potential of using under-dense plasmas as a source of high (multi - MeV) energy electrons[1]. These electrons are accelerated by the electric fields associated with large amplitude electron plasma waves (EPW) generated in the plasma by an intense laser pulse. If the plasma wave is relativistic (i.e., has a phase velocity close to the speed of light) electrons trapped within the wave can also be accelerated to relativistic energies.

Several schemes exist for the production of large amplitude relativistic EPW[2]. The most straightforward of these is the self-modulated wake-field accelerator. In this scheme, an intense laser pulse is focused into an under-dense plasma. Noise level plasma waves cause modulation of the laser pulse wavepacket due to variations of the plasma's refractive index (which is dependent on the plasma density). Since low density plasma has a higher refractive index, the laser intensity is larger in the troughs of the EPW. Such variations in laser intensity further enhance the plasma density modulations through the action of the ponderomotive force. Hence, a feedback mechanism is created – which results in growth of the plasma wave and modulation of the laser envelope in the plasma. The spectrum of the laser beam therefore exhibits satellites separated from the fundamental frequency by the plasma frequency, so that - in analogy to atomic physics - this process is referred to as Stimulated (Forward) Raman Scattering (FRS).

If the plasma wave reaches an amplitude where the density depression is of the order of the initial density ($\delta n/n_0 \approx 1$), then the orbits of electrons from successive buckets of the plasma wave can overlap. Hence an electron, rather than feeling its returning force, can continue its trajectory in the same direction and will be further accelerated by the electric field of the plasma wave. So the plasma wave in this limit not only acts as an accelerating structure but also the injection source of accelerated particles. In previous experiments we have measured 10^{12} electrons self-trapped and accelerated to energies above 2 MeV, with a maximum energy of up to 94 MeV [3].

Important questions remain about how this mechanism can grow to wave breaking levels in the time of our laser pulse, which is typically 1 ps. For such pulses, the growth of the instability has a maximum of about 10^7psec^{-1} growth for a laser intensity of $a_0 \approx 1.4$. - where a_0, the normalised vector potential, is a measure of the laser's electric field. For $a_0 >> 1$, the quiver velocity is close to the speed of light and the growth rate actually stops increasing due to the relativistic mass increase of the electrons. Hence, to reach wave breaking, one must initiate the scattering from a noise EPW of the order of at least 10^{-7} of the wave breaking limit. Since the EPW related to FRS is relativistic, the thermal noise source is small.

Several other possibilities have been suggested which would account for the elevated amplitude of the noise EPW. These include generation of a leading edge wake-field through the action of ionisation or other parametric instabilities such as Raman side and back scatter [4]. Hence, the study of these secondary mechanisms is vital in understanding the production of large amplitude plasma waves.

In this paper, we report on the study of self-scattering and propagation of a high intensity laser beam in an underdense plasma. In particular, we emphasise the importance of ionisation and Raman side-scatter and their importance in the evolution of the self-modulated wake-field accelerator.

Experimental set-up

The primary diagnostics discussed here are the images of the self-scattered light produced orthogonal to the propagation of the laser beam, perpendicular to its plane of polarisation. At this angle the scattering has a maximum. The spectrum of this scattered light is obtained by putting a transmission grating in front of the last imaging lens. With the rulings in line with the direction of propagation the image is spectrally dispersed orthogonally to this direction. This diagnostic is used to view the interaction of the Vulcan laser pulse with a helium gas-jet.

The Vulcan laser system produces pulses having an energy of up to 40 J on target and a duration of 0.9 psec at a wavelength of 1.054 µm (Nd:Glass). The laser pulse was focused into a gas jet target (4 mm nozzle diameter) using an $f/4$ off axis parabolic mirror. In vacuum the laser can be focused to a 10 µm diameter spot. When helium was used as the target gas the plasma had an electron density up to about 5×10^{19} cm^{-3}.

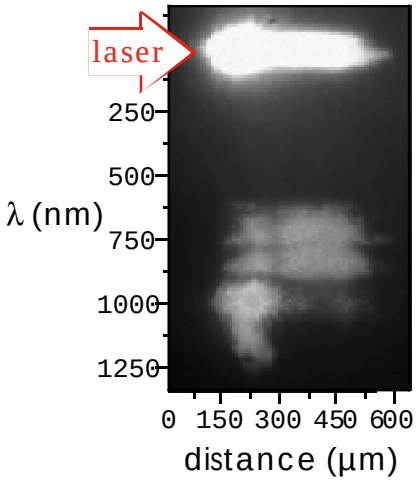

Figure 1. Spectrally dispersed images of interaction of Vulcan with helium gas-jet.

Results

A typical image of the interaction is shown in Figure 1, although the characteristics of the images can change considerably from shot to shot.

It is important to note that the scattering is initially only at the fundamental frequency, ω_0. Clearly the light scattered at the fundamental frequency has a characteristic v-shape along the direction of propagation. This indicates the presence of filaments of scattered light (see Najmudin *et al.*, in this report),

and it is likely that the filamentation is a result of ionisation scattering instability [5].

As the laser light propagates, the spectra shows light shifted away from the fundamental frequency, both at shorter and longer wavelength. The separation of the scattered satellites is at multiples of the plasma frequency and these higher order harmonics appear to increase in intensity as the pulse propagates further into the gas jet. Such multiple satellites are typical of the signal one expects from Raman Side scatter.

Noticeably at about 200 μm into the jet, the fundamental frequency and longer wavelength scattering (Stokes satellite) is reduced significantly, and the satellites on the blue side (anti-Stokes satellites) are greatly reduced. However, the blue satellites reappear later, while the red one and the λ_0 feature do not. The development of multiple orders of blue satellites is an indication that the Raman side scattering instability has become non-linear (involving 4 or more waves) – and that the instability is convective in this situation (i.e., the scattering grows as the laser pulse moves through the plasma).

The rapid large volume ionisation is a feature of the initial part of the interaction only. It appears that the ionisation scattering instability enhances the seeding of the Raman side scattering instability. Such instabilities are vital for providing the pulse shaping and electron seeding for the self-modulated wakefield accelerator.

References

1. T Tajima and J M Dawson
   Phys. Rev. Lett. 43, 267 (1979);
   P. Sprangle *et al*
   Appl. Phys. Lett. 53, 2146 (1988).

2. E Esarey *et al*
   IEEE Trans. Plasma Sci. 24, 252 (1996) and references therein.

3. D Gordon *et al*
   Phys, Rev Lett. 80, 2133 (1998).

4. J F Drake *et al*
   Phys. Fluids 17, 778 (1974);
   D W Forslund *et al*., *Phys. Fluids* 18, 1002 (1975).

5. T M Antonsen, Z G Bian
   Phys. Rev. Lett. 82, 3617 (1999).

Multi Megagauss magnetic field generation and proton transport through solids from ultra-intense laser-plasma interactions

E L Clark[1], K Krushelnick, M Zepf, M Tatarakis, F N Beg, M I K Santala, I Watts, A E Dangor

Blackett Laboratory, Imperial College of Science, Technology and Medicine, London SW72BZ,UK

[1]Radiation Physics Department, AWE plc , Aldermaston, Reading, RG7 4PR

J R Davies

GoLP (Grupo de Lasers e Plasmas), Instituto Superior Tecnico, 1900 Lisboa, Portugal

P A Norreys

Central Laser Facility, CLRC Rutherford Appleton Laboratory, Chilton, Didcot, Oxon, OX11 0QX,UK

A Machacek

Department of Physics, Clarendon Laboratory, University of Oxford, Oxford, OX1 3PU,UK

Introduction

In this paper, we report the use of an innovative diagnostic technique to measure magnetic fields in solid density plasmas produced by ultra-high intensity lasers (5×10^{19} W/cm^2). These measurements are obtained by recording the deflection of energetic protons produced simultaneously in the interaction which indicate that fields inside the target must be in excess of 30 MG. This paper reports the highest recorded magnetic fields generated in the laboratory, the first measurements of magnetic fields produced in overdense regions of plasma, as well as the first measurements of high energy proton generation (up to 18 MeV) and propagation into the target during intense laser plasma interactions.

Experimental Measurements

The results reported here were obtained during experiments at the Rutherford Appleton Laboratory using the CPA beam of the VULCAN laser This laser system produces pulses up to 50 J at a wavelength 1.053µm and with a pulse duration of 0.9 - 1.2 ps. The beam was p-polarized and was focused using an f/4 off axis parabolic mirror onto a thin (125 µm) aluminium target positioned at 45 degrees to the axis of laser propagation. The intensity on target was up to 5×10^{19} W/cm^2 and was determined by simultaneous measurements of the pulse energy, duration, and focal spot size. Behind the target, at a distance of 25 mm, and aligned with the normal to the target we placed a "sandwich" of several pieces of radio-chromic film and CR39 plastic track detectors.

Radio-chromic film is a transparent material (typically nylon) which is coated with an organic dye. Upon exposure to ionising radiation the film undergoes a colour change. The optical density of the film is subsequently measured at a particular wavelength and is calibrated against dose (Gy) using a known ^{60}Co source. The equivalent dose from protons at a particular energy is calculated and hence, the total number of protons passing through the film at each point can be determined.

CR39 is a plastic nuclear track detector. It is only sensitive to ions with energies greater than 100 keV/nucleon. In this experiment, it was sensitive primarily to protons as the front piece of radio-chromic film (110 µm thick) will transmit protons having energies greater than 2.8 MeV, but will stop all but the highest energy aluminium ions. After exposure, the CR39 is developed in concentrated sodium hydroxide solution which etches a pit at the location on the surface where each proton has stopped and released its kinetic energy. The stopping range of protons in CR39 and radio-chromic film is easily calculated and consequently, this allows a direct determination of the energy range for those protons which produce a particular series of pits. CR39/radiochromic film "sandwich" detectors can therefore provide both spatial and spectral information of protons emitted from the rear of the target.

Figure 1(a) shows a scanned image from a piece of radio-chromic film. The film contains signal only within a well-defined radius from the central hot-spot. The angle subtended by the perimeter of this circle covers a cone half angle of 30 degrees and the mark at the centre of the film indicates a region where the film has been saturated. Radio-chromic film is also sensitive to both electrons and x-rays which were also measured to be emitted from the rear of the target during these experiments. However, it is clear from the images shown in Figure 1(b)-(e) that the signal on the radio-chromic film coincides with that on the CR39 which is sensitive only to ions. Therefore, it is likely that the signal on the film is predominantly due to energetic ion emission. With this assumption, the measured proton emission is ~10^{12} protons/shot with energies greater than 2 MeV. Ion signal on the CR39 shows a ring pattern such that the diameter of the ring decreases with increasing ion energy up to a maximum of 17.6 MeV. The central position of each ring is coincident with the target normal. The outer extreme of the radio-chromic film signal, can therefore be seen to be a sharp lower energy proton cut-off below which no protons are observed. This "ion ring" structure was observed consistently from a series of shots at an intensity of ~ 5 x 10^{19} W/cm^2. The central hot spot is correlated with the highest energy ions which exhibit collimated propagation. Indeed it must be noted that all the protons must have been initially highly collimated to produce such well defined rings

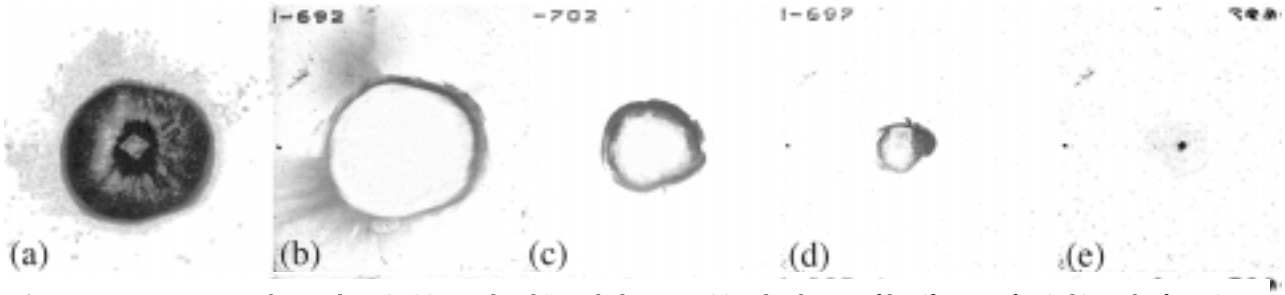

Figure 1. Ring structure observed on CR39 "sandwich" track detectors (a) radiochromic film (front surface) (b) tracks from 3 MeV protons (c) 8.9 MeV (d) 11.6 MeV (e) 17.6 MeV proton (track detectors were 5 cm x 5 cm x 0.75 mm

and the highest energy protons are hardly deflected.

It is likely that this relationship between the energy of the emitted protons and the angle at which they are emitted is caused by large azimuthal magnetic fields within the solid target material that develop and persist during the first few picoseconds after the laser pulse. The protons are consequently deflected like charged particles in a magnetic spectrometer. It is clear that such magnetic fields must be generated by an electron current – which would tend to focus a beam of electrons – but defocus or scatter ions. Such large fields have been predicted and have been shown to contribute to the focusing of electrons at the rear of such targets resulting in plasma formation.

The source of the energetic protons measured in this experiment originate from hydrocarbon contaminants on the surfaces of the aluminum target.

It is probable that the energetic protons are generated at the front surface and are subsequently transported through the target. Previous measurements of the expansion velocity of plasmas created on the rear surface during similar interactions indicate that the ion velocities produced would be much lower than the protons measured in the present experiment. The existence of a "beam" of high energy ions travelling into the target is also consistent with previous measurements of beam-plasma fusion reactions from high intensity laser interactions with CD_2 targets.

A calculation to determine the energy of the protons leaving the rear of target as a function of the energy they have entering shows an apparent lower energy cut-off of about 2 MeV, which is consistent with the ion energy measurements with the CR39 as well as the radio-chromic film data. From this evidence it is probable that protons are transported into the target from the front surface and escape at the rear with a minimum energy which consequently produces a sharply defined image on the radio-chromic film.

To obtain an estimate for the magnetic field strength required to deflect the protons as measured with the CR39, a charged particle tracking code was developed to simulate the transport of a 12 μm radius proton beam into the target. The magnetic field for these simulations was constant in the z direction through the target (125 μm), but had a profile in the r direction which was zero at r = 0 μm, rose to 30 MG at r=10 μm and then fell off as $1/r^2$. This radial dependence for the magnetic field is similar to that observed in previous detailed numerical simulations. In this case, incident protons with an energy of 10MeV are used to simulate the experimentally observed ring pattern produced by 8.9 MeV protons - since energy losses within the target will result in these protons leaving the target with an energy of 8.9 MeV. Figure 2(a) shows the measured data which is replicated remarkably well in the simulation (Figure 2(b)).

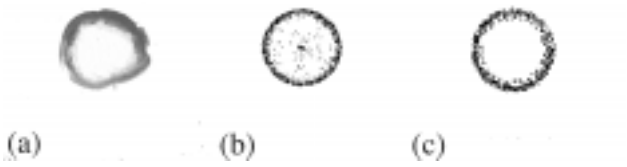

Figure 2. (a) experimental ion ring (E = 10 MeV), (b) simulated ring structure from best fit magnetic field (30 MG) (c) ion ring from field structure calculated from electron propagation simulations

Figure 3 shows the magnetic fields generated from a Fokker-Planck simulation at an incident laser intensity of I = 5×10^{19} W/cm^2, 50 J laser energy, 30% laser conversion into a fast electron population with a temperature of 1.5 MeV , 6 μm spot size at a time 1 ps after the peak of the laser pulse. The number of electrons and the fast electron temperature were determined from previous experimental measurements. It was observed that average fields of 15 to 20 MG (Figure 3) are produced and in the simulation fields up to 30 MG are possible.

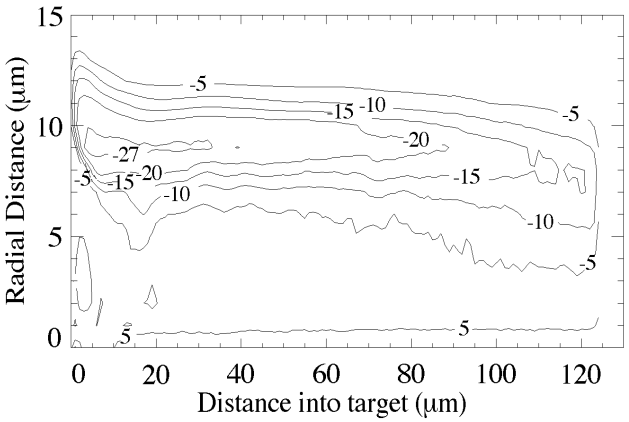

Figure 3. Simulated magnetic field structure (MGauss) from Fokker-Planck calculation

Using a qualitatively similar magnetic field distribution (although increased by a scaling factor of 3), 10 MeV protons were launched into the target in a 9 μm spot, and the resulting proton distribution at the detector plane was calculated (Figure 2 (c)). The resulting deflection pattern was observed to be very similar to that observed in the experiment with fields of 40 to 60 MG in the bulk of the target and a peak field of 90 MG required to reproduce the deflection. 10 MeV protons were chosen as they should be most affected by the magnetic fields inside the target before dissipation and compare directly to the experimental results. Similarly, the measured deflection of lower energy protons can be reproduced using this field configuration. Higher energy protons, however, are typically deflected too much by these fields to agree with the experimental observations. This is because the highest energy protons are able to penetrate far into the target before large magnetic fields have been formed, and are consequently deflected less.

Conclusions

In conclusion, these measurements are the first observations of the structure and magnitude of the magnetic field generated within a solid target during an ultra-high intensity laser interaction. These experiments suggest that the plasma exhibits an anomalous resistivity at the very high current densities which are produced from these interactions.

Improvements in the source characteristics of harmonics from plasma surfaces using higher contrast ratio laser pulses

I Watts, M Zepf, E Clark, M Santala, M Tatarakis, K Krushelnick, A E Dangor

Imperial College of Science, Technology and Medicine, The Blackett Laboratory, Prince Consort Road, London SW7 2BZ

A Machacek, J S Wark

Department of Physics, University of Oxford, Clarendon Laboratory, Parks Road, Oxford OX1 3PU

P A Norreys, R Clarke, R Allott, C N Danson, D Neely

Central Laser Facility, CLRC Rutherford Appleton Laboratory, Chilton, Didcot, Oxon OX11 0QX, UK

Introduction

At high intensities the harmonics generated by the laser-solid interaction suffer from a low source brightness due to spectral broadening and a large angular emission distribution. Previously it has been found that the conversion efficiencies depend on the scalelength L/λ of the plasma formed before the arrival of the main pulse, and at high values of $I\lambda^2$ the low source brightness has been associated with the prepulse and contrast ratio of the incident laser beam.[1)] A method that would effectively increase the contrast ratio of the incident laser would therefore reduce the deleterious effects of any pre-plasma formation and approach the conditions necessary for the theoretical predictions of specular emission and transform limited bandwidths. This is important since the harmonics emitted by the interaction of an intense laser pulse with a solid target represent a promising source of coherent short wavelength radiation, with high conversion efficiencies observed both experimentally and in simulations. [2,3,4)]

One way of increasing the contrast ratio of the incident laser is to use a 'plasma mirror'. This consists of a transparent optical flat placed at a point after the final focusing optic where the intensity is approximately 10^{14} Wcm^{-2}. Any prepulse below this plasma formation threshold is transmitted, while above this value a plasma is formed and the light is reflected from the critical surface close to the peak of the pulse. Since the plasma expansion length ($c_s\tau$ = 0.1 μm, where τ is the main pulse duration and c_s is the sound speed) is small compared to the laser wavelength the reflectivity is consistent with a sharp plasma-vacuum boundary and the plasma acts as a plane mirror. In this way the contrast ratio of the laser pulse can be increased by a factor of 100 - 1000.

Experimental Arrangement

A schematic of the experimental arrangement is shown in Figure 1. The experiment was performed in Target Area West of the VULCAN Nd:glass laser system, using the CPA beam 8. The CPA configuration delivered 700 fs – 1 ps pulses at 1.053μm with energies on target in the range 20 – 60 J. The laser was focused by using either a f/1.7 on-axis or f/3.25 off-axis parabolic mirror, which resulted in intensities of up to $3x10^{19}$ Wcm^{-2}. On target intensities were estimated by both CR39 plastic nuclear track detectors and a soft X-ray penumbral imaging camera. Focal spot sizes (from the penumbral image) were combined with the shot energy to yield the focussed intensity, and the CR39 track analysis provided maximum ion energies associated with the plasma expansion which gave another measure of the shot intensity. The targets consisted of optically polished fused silica slabs at 45^o angle of incidence with the beam p-polarised.

The harmonics were detected by a slitless flat-field XUV spectrometer with a Hitachi variable line-spaced (1200 l/mm) grating. After the grating the dispersed light in the wavelength range 540 - 276 Å was directed by a 45^o gold coated mirror onto a double microchannel plate detector coupled to an intensified CCD camera. Shorter wavelength light in the range 272 - 85 Å traveled straight through and was detected by a backthinned XUV CCD camera. This arrangement of detectors allowed harmonic orders in the range $20 < n < 120$ to be detected on a shot to shot basis. In addition to the XUV spectrometer an optical spectrometer was used to measure the spectrum of the 3rd harmonic, at 351 nm, viewing along the direction of the target normal. The configurations of the plasma mirrors are also shown in Figure 1, the particular arrangement depending on which focusing parabola was being used at the time.

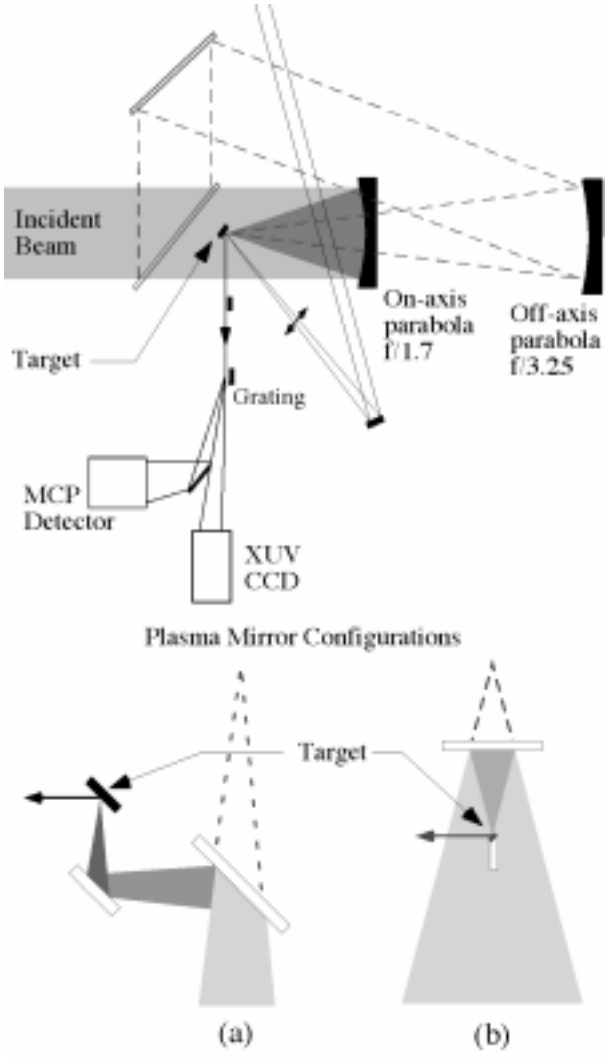

Figure 1. The Experimental Arrangement - The configurations for the plasma mirror refer to the particular focusing optic employed: (a) with the off-axis parabola and two mirrors both at 45 ^{o} and (b) with the on-axis parabola using a single mirror at normal incidence.

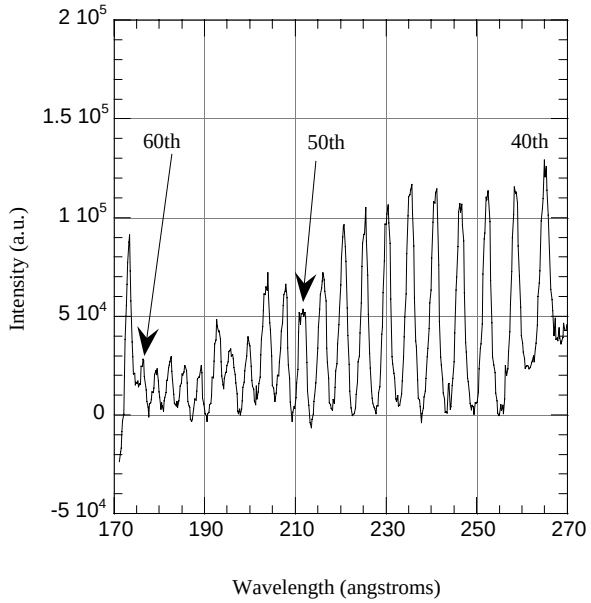

Figure 2. Typical lineout of the harmonic spectrum measured on the XUV CCD.

Results

An example of the spectra obtained by the XUV spectrometer is shown in Figure 2. Harmonics up to the 61st of the fundamental were observed in first order diffraction. The soft X-ray penumbral image established that the focal spot size was ~10 μm (FWHM) yielding an intensity on target of ~1x10^{19} Wcm^{-2}. (Note that the signal at 173 Å is an Oxygen plasma emission line)

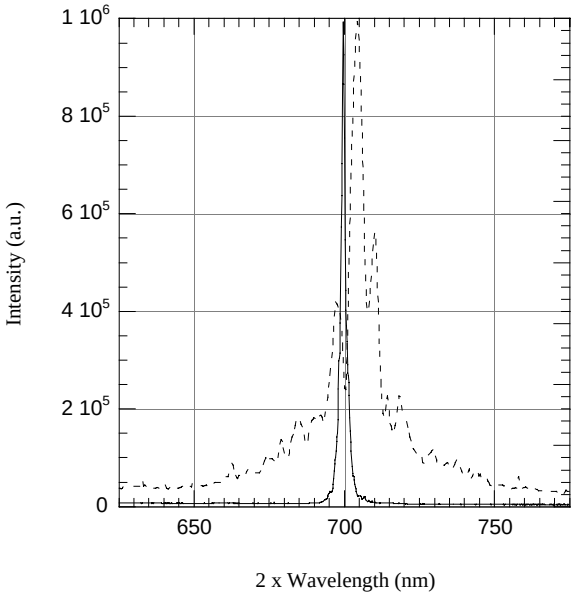

Figure 3. The spectrum of the 3rd harmonic. The solid line represents the plasma mirror, with the dashed line representing a 'normal' glass slab target.

Bandwidth Measurements

Figure 3 shows the spectrum of the third harmonic of the fundamental in second order. We can see an immediate difference between the two shots; one a 'normal' glass slab target and the other using the plasma mirror. Both shots had a similar intensity on target as inferred by the penumbral imaging camera (~ 5 x 10^{18} Wcm^{-2}). The normal shot is slightly red shifted with v/c ~ 0.003, which is in good agreement with previous measurements of the hole boring velocities for similar intensities.[5] When using the plasma mirror, however, the result is a slight blue shifting of the signal (again with v/c ~ 0.003). This can be interpreted as evidence for the production of extremely short scale-length plasma with $L/\lambda << 1$. In this case the excursion distance of electrons in the laser field ($\delta = c/\omega_p$, where ω_p is the plasma frequency) extends across the whole vacuum-plasma boundary and the laser effectively interacts with a solid density plasma. Since the plasma pressure at almost solid densities is higher than the light pressure of the incident pulse, a consequence is the blue shifting of the harmonic. On the other hand, for larger scale-lengths, the laser interacts solely at critical densities where the laser pressure is superior to the plasma pressure and the result is hole boring and red shifting of the harmonic.

Further evidence for a short scale-length using the plasma mirror is the absence of any significant self-phase modulation in the case of the plasma mirror. The bandwidth of the normal target is 5.5 nm while the plasma mirror produces a bandwidth of 0.7 nm. This compares to the transform limited bandwidth ($\Delta\lambda_n = \Delta\lambda_o/n^2$ where $\Delta\lambda_n$ is the bandwidth of the nth harmonic and $\Delta\lambda_o$ is the bandwidth of the fundamental) of 0.2 nm and suggests that very little spectral broadening takes place in any underdense plasma.

Conversion Efficiencies

The conversion efficiencies of the 20th and 21st harmonics are shown in Figure 4. The conversion is seen to be at least one order of magnitude greater in the case of the plasma mirror. (The open triangles on the graph represent the plasma mirror targets assuming 100% conversion across the mirrors). There are two possible reasons for this increase in conversion using the plasma mirror.

Firstly a difference in the angular distribution of harmonic emission between the two types of targets would reduce the observed efficiency for the normal targets. A large angular distribution is due to the Rayleigh-Taylor like instability rippling the density profile as the critical surface is locally steepened. The high laser pressure pushing back the critical surface leads to further growth of this instability. With an increase in the contrast ratio using the plasma mirror the preformed plasma has less time to expand and any instability growth of the critical surface is correspondingly lower: the laser then interacts acts with an essentially smooth flat surface and short scale-length plasma. In this way the angular distribution using the plasma mirror is reduced and results in an increase in the observed efficiencies.

Furthermore, a reduction in the plasma scale-length would also result in an increase in conversion efficiency since to maximise harmonic generation it is necessary that the laser pulse interacts close to the critical surface and the conversion is correspondingly increased for shorter scale-lengths. Low pre-plasma formation is also indicated by the broadening of plasma emission lines observed on the XUV CCD when using the plasma mirror, suggesting a higher density and temperature, as well as shorter scale-length, than without the plasma mirror. The above two points, together with the near-transform limited bandwidth and blue shifting of the 3rd harmonic, are a result of the reduced scale-length and increased contrast ratio when using the plasma mirror targets.

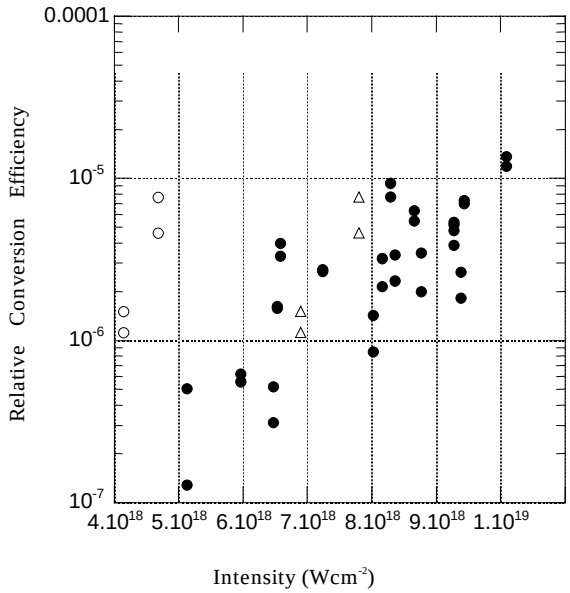

Figure 4. The conversion efficiencies of the 20th and 21st harmonics. Solid circles represent normal targets, open circles and triangles plasma mirror targets.

Conclusions

In summary we have demonstrated a technique for increasing the contrast ratio of the incident laser pulse and the concurrent effects on the harmonic generation mechanism. Previous experiments with pulse durations on the order 150 fs have shown that broad harmonic bandwidths and large angular distribution are certainly associated with the prepulse of the laser and that the contrast ratio plays an important role in maximising the source brightness of the harmonics.[1)] The results presented here suggest that the plasma mirror can be used as an effective method to reduce the deleterious effects of the expanding critical surface which leads to spectral broadening, a large angular distribution and hence lower brightness of the harmonic source.

Another way to increase the contrast ratio of the incident laser is by frequency doubling the fundamental, where the contrast ratio is given by: $I_{2\omega} \sim I_{\omega}^2$. Future work being planned on the Vulcan laser will be doing this and should allow the prepulse level to be reduced to less than 10^{10} Wcm^{-2} on target at full intensity.

References

1. M Zepf *et al*
Phys. Rev. E, 58 , R5253, (1998)

2. P Norreys *et al*
Phys. Rev. Lett., 76, 1832, (1996)

3. P Gibbon
Phys. Rev. Lett., 76, 50, (1996)

4. R Lichters *et al*
Phys. Plasmas, 3, 3425, (1996)

5. M Zepf
Phys. Plasmas, 3, 3242, (1996)

Measurement of the direction of fast electrons versus plasma scale-length

M I K Santala, E Clark, I Watts, F N Beg, M Tatarakis, M Zepf, K Krushelnick, A E Dangor
The Blackett Laboratory,Imperial College, London SW7 2BZ, United Kingdom

T McCanny, I Spencer, R P Singhal, K W D Ledingham
Department of Physics and Astronomy, University of Glasgow, Glasgow G12 8QQ, United Kingdom

S C Wilks
University of California, Lawrence Livermore National Laboratory, L-39, Livermore, CA 94550,US

A C Machacek, J S Wark
Clarendon Laboratory, Parks Road, Oxford OX1 3PU,United Kingdom

R M Allott, R J Clarke, P A Norreys
Central Laser Facility, CLRC Rutherford Appleton Laboratory, Chilton, Didcot, Oxon, OX11 0QX, UK.

Main contact email address: *m.santala@ic.ac.uk*

Introduction

The angular distribution of bremsstrahlung γ-rays produced by fast electrons accelerated in relativistic laser-solid interaction has been studied by photo-neutron activation in copper. We show that the γ-ray beam moves from the target normal to the direction of the laser **k**-vector as the scale-length is increased. Similar behaviour is found also in 2D-PIC simulations.

Experiment

Large numbers of high energy electrons are generated in laser-solid interactions at 10^{19}-10^{20} W/cm^2 as predicted by computer simulations[1,2] and confirmed by a number of experiments[3-6]. There are many potential mechanisms for fast-electron generation, e.g. classical and Brunel-type resonance absorption[7,8], ponderomotive acceleration[1] (possibly affected by a self-generated azimuthal magnetic field)[2] and wakefield acceleration[9,10]. Differing angular distributions of the electrons are expected for different mechanisms: the resonance absorption processes are expected to produce electrons mainly in the direction of the density gradient for p-polarised light while the other two mechanisms would produce electrons mainly in the laser beam propagation direction **k**-laser.

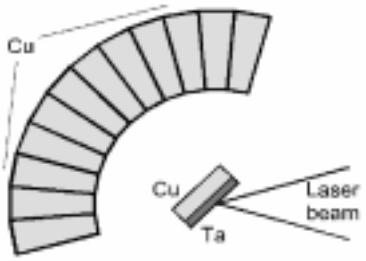

Figure 1. Schematic drawing of the target set-up.

We have experimentally studied the angular distribution of >10MeV electrons under different plasma scale-lengths[11,12]. We have done this by measuring activation induced by photo-neutron reactions in copper by bremsstrahlung. The experiment was carried out using the p-polarised, 50J, 1ps CPA beam of the Vulcan Nd:glass laser system at Rutherford Appleton Laboratory (RAL)[13]. The laser beam was incident on target at 45° angle of incidence. The targets (see Figure1) were 1.75mm thick tantalum slabs backed by 3mm of copper. These were surrounded by 12 copper wedges subtending a total angle of 120° for determination of the angular distribution. The activation ^{62}Cu, ($t_{1/2}$ =9.74min, β^+ decay) of the Cu pieces was measured after each shot by coincidence counting of the positron annihilation gamma-ray photons. The plasma scale-length was determined by shadowgraphic imaging of the inaccessible region of pre-plasma 30ps before the main pulse.

In total, simultaneous angular distributions and scale-length data were collected on 17 shots. Most of the shots were with a relatively small pre-pulse resulting in a plasma scale-length L<10μm. On three shots a very large pre-plasma was created by a pre-pulse having 6 % of laser energy which preceded the main pulse by 0.3---1.5ns. The measured angular distributions were corrected for decay and fitted with a Gaussian distribution to estimate the main γ-ray beam direction. The scale-length was estimated from the shadowgraphic images by assuming an exponential density profile.

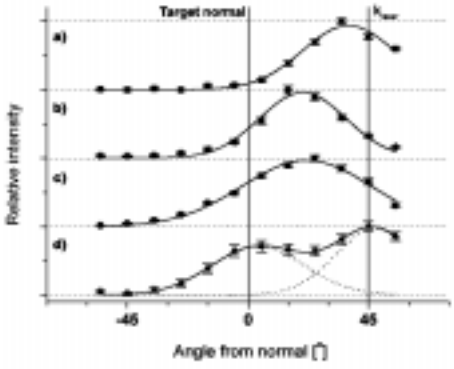

Figure 2. Four normalised angular distributions fitted with Gaussian distributions, offset for clarity. Top two plots show cases with large scale-length (a, L=5.9μm) and small scale-length (b, L=2.6μm). The lower two plots show evidence of two different electron beams as a very wide single peak (c) and as a double-peaked distribution (d).

Figure 2 displays some angular spectra obtained in the large L, (a), and the intermediate L, (b) case. The width of these distributions is 35-40° (FWHM). Very wide, (c), width =56°or double-peaked, (d), distributions were sometimes observed. This can be seen as evidence of generation of two separate electron beams, that generate two partially overlapping γ-ray beams.

To find if there is correlation between the plasma scale-length and the direction of main γ-ray emission, the peak of γ-ray emission is plotted against the measured size of the pre-plasma in Figure 3. It can be observed that these two are nearly linearly correlated (r^2=0.81) for L less than about 10μm. However, at

very large L (obtained with large pre-pulse) no correlation is observed.

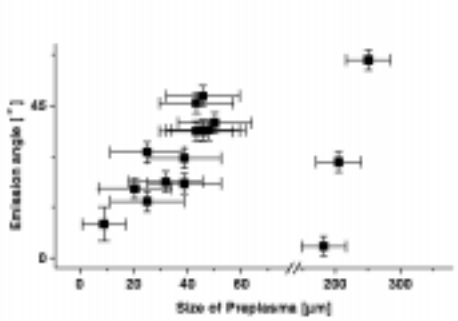

Figure 3. The direction of the main gamma-ray emission versus the size of preplasma (the distance x from the ablation front to the edge of the inaccessible region). For exponential density profile plasma scale-length L=x/9.

Discussion

The observed correlation between L and electron angular distribution could be explained by Brunel-type resonance absorption being the dominant absorption mechanism in plasmas with a steep density gradient (L\λ). As the plasma scale-length increases, the **j**×**B** type mechanism becomes the main absorption mechanism. This simple picture breaks down at shallow density gradients (L\λ>>1). The converging laser beam has to traverse a large distance in coronal plasma which results in an essentially random angular distribution. This may be due to filamentation and self-focusing of the laser beam in the under-dense plasma[14] or e.g. the hosing instability[15].

The absolute activation in the reference copper piece showed large shot-to-shot variations. The initial activity ranged from 6 to 2200Bq. The average was 460Bq, standard deviation 510Bq and median 300Bq. Below 10^{18} W/cm^2 there was little activation but otherwise there was no correlation with intensity. The activation yield showed no correlation to plasma scale-length either suggesting that the different mechanisms have similar efficiency of fast electron production. However, even if there was a correlation it might be lost in practice as only the electrons far in the tail of distribution can produce γ-rays with a sufficient energy to induce activation.

Fields in excess of 500T have been predicted in the solid over distances of tens of micrometers due to current of fast electrons[16]. In the interaction region even higher fields exceeding 10^4 T are predicted[17,18]. The Larmor radius r_L=p/(qB) of a 10 MeV electron in a 500T field is ~ 65μm and in a 10^4 T field only 3.3μm. Depending on the structure of the fields, it appears likely that the fast electrons can change their direction while traversing such fields or that two beams could coalesce altogether.

In conclusion, we have shown a correlation between the plasma density scale-length L and the main direction of fast (>10MeV) electron generation using photo-neutron reactions in copper. That is to say, for very small L\λ the γ-ray beam is normal to the target, for intermediate L\λ~5 the beam is along **k**-laser and for long L\λ, the beam direction is uncorrelated. We have found the photo-neutron activation technique to be a powerful diagnostic for measurement of >10MeV electrons.

References

1. S.C.Wilks *et.al*
   Phys. Rev. Lett. 69, 1383 (1992).
2. A.Pukhov and J.Meyer-ter-Vehn
   Phys. Plasmas 5, 1880 (1998).
3. G.Malka and J.L.Miquel
   Phys. Rev. Lett. 77, 75 (1996).
4. T.Feurer *et.al*
   Phys. Rev. E 56, 4608 (1997).
5. G.Malka, E.Lefevbre, and J.L.Miquel
   Phys. Rev. Lett. 78, 3314 (1997).
6. K.B.Wharton *et. al*
   Phys. Rev. Lett. 81, 822 (1998).
7. F.Brunel
   Phys. Rev. Lett. 59, 52 (1987).
8. S.C.Wilks and W.L.Kruer
   IEEE J. Quan. Elec. 33, 1954 (1997).
9. T.Tajima and J.M.Dawson
   Phys. Rev. Lett. 43, 267 (1979).
10. F.Amiranoff *et.al*
    Phys. Rev. Lett. 81, 995 (1998).
11. P.A.Norreys *et al*
    Phys. Plasma 6, 2150 (1999).
12. M.I.K.Santala *et al*
    Sub. to Phys. Rev. Lett. (1999).
13. C.N.Danson *etal*
    J of Mod. Opt. 45, 1653 (1998).
14. C.E.Max, J.Arons, and A.B.Langdon
    Phys. Rev. Lett. 33, 209 (1974).
15. K.C.Tzeng *et. al*
    Phys. Plasma 6, 2105 (1999).
16. J.Davies
    Accepted to Phys. Rev. E (1999).
17. A.Pukhov and J.Meyer-ter-Vehn
    Phys. Rev. Lett. 76, 3975 (1996).
18. R.J.Mason and M.Tabak
    Phys. Rev. Lett. 80, 524 (1998).

Multi MeV heavy ion emission from ultra-intense laser-plasma interactions

E L Clark[1], K Krushelnick, M Zepf, M Tatarakis, F N Beg, M I K Santala, I Watts, A E Dangor

Blackett Laboratory, Imperial College of Science, Technology and Medicine, London SW72BZ,UK

[1]Radiation Physics Department, AWE plc , Aldermaston, Reading, RG7 4PR 1

P A Norreys

Central Laser Facility, CLRC Rutherford Appleton Laboratory, Chilton, Didcot, Oxon, OX11 0QX,UK

A Machacek

Department of Physics, Clarendon Laboratory, University of Oxford, Oxford, OX1 3PU,UK

This paper reports measurements of the high energy ions and protons emitted from the front of solid targets, of various materials, produced from ultra-intense laser-plasma interaction. Heavy ions with energies up to 420 MeV have been observed from the ablating plume of the plasma, the maximum energies observed being for the ions with the highest mass number and charge state. The proton spectra show a peaked structure and the angular distribution of the protons indicates the presence of a low energy "ion ring".

Targets including aluminium, glass and lead were irradiated with the CPA beam of the VULCAN laser. Vulcan delivers about 50 J in a pulse of approximately 1 ps duration at a wavelength of 1.053 μm. The beam was p-polarised and was focused on to the target at 45 degrees using a f/1.6 on-axis parabola. The intensity on target was determined from the laser beam diagnostics and by using a penumbral camera to measure the spot size resulting in a maximum intensity on target up to 5×10^{19} W/cm^2.

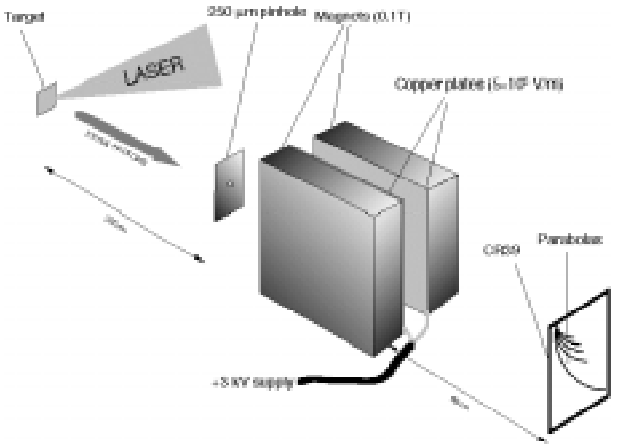

Figure 1. Thompson parabola spectrometer aligned to 15 degrees from the front target normal.

The main diagnostic used in this experiment was an E‖B Thompson parabola spectrometer. The detector views the front of the target at an angle of 15 degrees off the target normal. Protons and other ions emitted from the target are collimated and pass through a 250 μm pinhole into the detector. The detector consists of two opposing magnets, between which, attached to the inside surfaces, are copper plates. When a high voltage is applied to the plates, parallel electric and magnetic fields exist between the plates, serving to deflect the ions and protons according to their charge to mass ratio. Each species with a particular charge to mass ratio describes a parabola on the detector plane and the position along the parabola gives the energy. At the detector plane a piece of CR39 is positioned which is sensitive to ions and protons with energies greater then 100 keV/nucleon. The CR39 is etched in Sodium Hydroxide solution and where ions were incident on the surface, pits are etched which can be counted and a spectrum is determined from the energy dispersion along the parabola.

To measure the angular distribution of the protons at the front of the target, a "sandwich" of radiochromic film and CR39 was placed in front of the target. The radiochromic film is a transparent substrate coated in an organic dye which turns blue according to the dose of the ionising particles passing through it. The optical density is calibrated as a function of dose against a ^{60}Co source. The dose is then related to the equivalent number of protons per square millimetre as a function of optical density. Radio-chromic film is sensitive to electrons and photons too, but in this measurement, the signal is mainly due to protons.

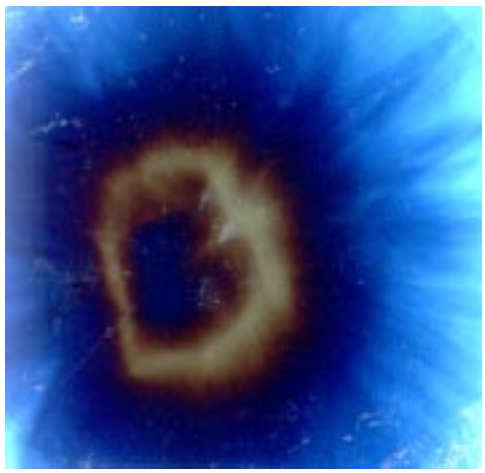

Figure 2. Image from radio-chromic film indicating a low energy "ion ring"

Figure 2 shows a typical image from a piece of radio-chromic film placed in front of a 125 μm thick aluminium target. Most of the signal is contained in an area which subtends a half angle of 15 degrees at the target.

The ring that is visible is due to protons of about 3 MeV energy, which have saturated the film. This ring pattern is observed over a series of shots but is not observed for the higher energy protons. The ring is slightly shifted away from the target normal which is aligned with the centre of Figure 2. This ring may be formed by magnetic fields deflecting the lower energy protons. The magnetic fields are generated by currents produced from perpendicular density and temperature gradients in the ablated plasma.

Higher energy protons are recorded on the CR39. This indicates a complicated distribution but generally the more energetic protons are ejected more towards the target normal. The origin of the protons is derived from hydrocarbon contaminants on the surface.

Figure 3. Raw data on a CR39 track detector from an aluminium target. A single proton parabola and many parabolas from different charge states of aluminium ions can be observed. All the parabolas have their origin on the mark left by neutral particles in the top left corner

Figure 4 shows a proton spectrum and ion spectra from a lead target. The protons show a maximum energy of just over 11MeV. Higher proton energies could not be recorded with this diagnostic. However, other measurements using a wedge filter on a piece of CR39 indicated energies up to 17 MeV.

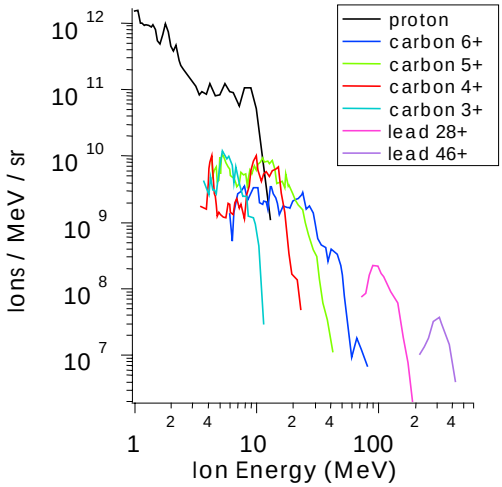

Figure 4. Spectra from a thick lead target showing lead ions and ions from hydrocarbon contaminants

The proton spectrum shows quite distinct peaks, which tend to occur in the 1 to 10 MeV range. Carbon energies up to 80 MeV have been observed as well as lead ions up to 420 MeV. The highest ion energies occur with the highest charge states and these ions have similar velocities consistent with the expansion velocity of the plasma as observed with probing diagnostics.

Aluminium targets show ion energies up to 150 MeV with fully stripped Al^{13+} . These ions are thought to be produced from the space charge effect created by electrons escaping the target dragging the ions behind them, Figure 5.

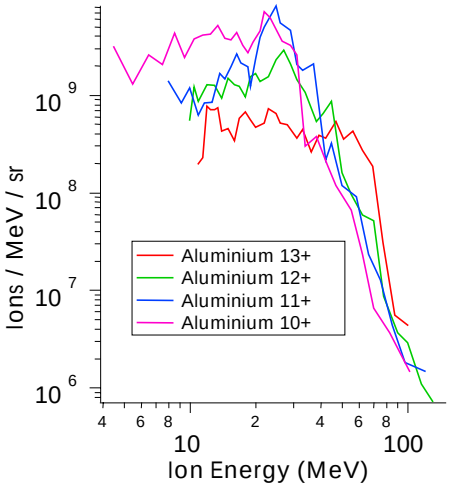

Figure 5. Spectra of aluminium ion measured from thin aluminium targets showing the four highest charge states only.

In conclusion, the highest energy ions yet observed from a laser-produced plasma have been measured from a variety of target materials.

Quantitative Measurement of Suprathermal Electron Temperature in Ultra-intense Laser-Solid Interactions via Nuclear Activation Techniques

I Spencer, R P Singhal, K W D Ledingham, T McCanny

Department of Physics and Astronomy, University of Glasgow, Glasgow G12 8QQ, United Kingdom

M I K Santala, E Clark, I Watts, F N Beg, M Zepf, K Krushelnick, M Tatarakis, A E Dangor

Blackett Laboratory, Imperial College, Prince Consort Road, London SW7 2BZ, United Kingdom

P A Norreys, R Allott, D Neely, R J Clarke

Central Laser Facility, CLRC Rutherford Appleton Laboratory, Chilton, Didcot, Oxon OX11 0QX, UK.

A Machacek, J S Wark

Clarendon Laboratory, University of Oxford, Parks Road, Oxford OX1 3PU, United Kingdom

A J Cresswell, D CW Sanderson

Scottish Universities' Research and Reactor Centre, East Kilbride, Glasgow G75 0QU, United Kingdom

J Magill

European Commission, Institute for Tranuranium Elements, Postfach 2340, D-76125, Karlsruhe, Germany.

Main contact email address: *i.spencer@physics.gla.ac.uk*

Introduction

With remarkable advancements in laser technology in recent years, due to the development of chirped-pulse amplification techniques (CPA)[1,2], focused intensities of 10^{19} – 10^{20} Wcm^{-2} are now achievable.

When these intensities are incident on a solid target, free electrons can quiver relativistically with ponderomotive energies in the MeV range. These fast electrons can produce bremsstrahlung in high Z targets. These bremsstrahlung photons can then be used to induce photo-nuclear reactions.[3,4,5]

The study of high intensity laser-plasma interactions is of current interest in many fields of research e.g. the Fast Ignitor scheme for inertial confinement fusion (ICF)[6], plasma particle accelerators[7-12] and astrophysics as well as laser-induced nuclear effects described above. The temperature of electrons produced in the laser-plasma interactions is a fundamental parameter and hence it is of great importance to measure it experimentally. This report describes a procedure which can be used to determine this value, using the measured activities of isotopes which have been produced by the laser induced photon beam.

Experimental

The ultra-intense beam-line of the Vulcan Nd:Glass laser[13] was employed in this experiment. The beam was incident on a solid tantalum target, 10x10x1.75 mm in dimension, and at an angle of 45°. The light was p-polarised, and the target was maintained in vacuum. The experimental set-up and the diagnostics involved are described in greater detail in another publication[14].

The horizontal and vertical distribution of the bremsstrahlung beam was determined under fixed laser conditions, using copper activation techniques[15]. Different materials were placed in the photon beam (directed along laser direction) to undergo nuclear activation. A copper piece was always placed directly behind the tantalum target and was used as a reference in these measurements (Figure 1). These samples had dimensions ~10x10x3 mm.

In addition to the tantalum target, seven different samples underwent (γ,n) reactions – the isotopes ^{11}C, ^{38}K, ^{63}Zn, ^{106}Ag, ^{140}Pr, ^{62}Cu and ^{64}Cu were produced. All of these isotopes (with the exception of ^{180}Ta) emit positrons, which annihilate at rest with free electrons in solids, to produce two 511 keV gamma rays at 180° to each other. These gamma rays were detected via two NaI scintillation counters operated in coincidence. Thus a measure of the activity of the samples immediately after the laser pulse could be obtained, since the efficiency of the coincidence system and the half lives of the activated samples were known (Table 1).

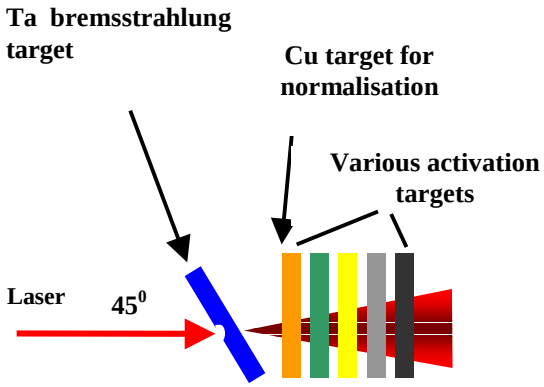

Figure 1. Schematic of activation set up. The copper sample was always placed behind tantalum target as a reference.

Reaction	Half-life	Q-value (MeV)	Peak σ (mb)
$^{63}Cu(\gamma,n)^{62}Cu$	9.7 mins	10.9	75
$^{12}C(\gamma,n)^{11}C$	20.5 mins	18.7	13.1
$^{65}Cu(\gamma,n)^{64}Cu$	12.7 hours	10.9	65
$^{107}Ag(\gamma,n)^{106}Ag$	24 mins	9.5	155
$^{141}Pr(\gamma,n)^{140}Pr$	3.4 mins	9.4	335
$^{39}K(\gamma,n)^{38}K$	7.6 mins	13.7	11
$^{64}Zn(\gamma,n)^{63}Zn$	38.1 mins	11.7	123

Table 1. Nuclear reactions produced in this experiment and their associated properties.

Analysis and Discussion

The supra-thermal electron temperature T was obtained for a given shot by calculating theoretical values for the activity of the copper samples compared to another sample with a different Q-value in the activation stack for a given value of kT (MeV), and comparing this ratio with the experimental value. As an example, the activity ratio of ^{11}C / ^{62}Cu is taken here.

The theoretical Carbon/Copper activity ratio was calculated in the following way:

The relativistic electron energy distribution is given by

$$N_e(E) = N_0 E^2 e^{-\left(\frac{E}{kT}\right)} \qquad (1)$$

where $N_e(E)$ is the number of electrons at energy E, N_0 is a constant, E is the electron energy, k is Boltzmann's constant, and T is the electron temperature. Figure 2 shows this electron distribution for E=0 to 25 MeV, kT = 1.63 MeV, N_0=1.

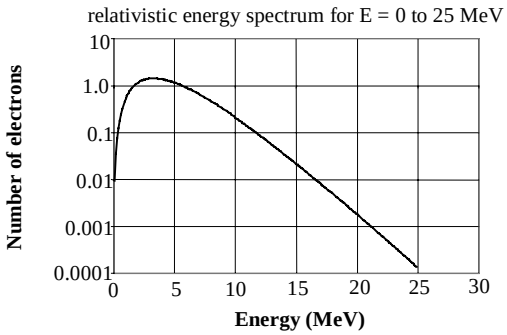

Figure 2. The shape of the relativistic electron energy distributions with N_0=1, kT=1.63 MeV.

Electrons of energy E MeV produce a gamma-ray energy spectrum in tantalum. This spectrum was calculated using the analytical expression in reference[16] Figure 3 shows examples of gamma-ray spectra produced along the electron (and hence the laser) direction in a tantalum target by 15 MeV and 20 MeV electrons.

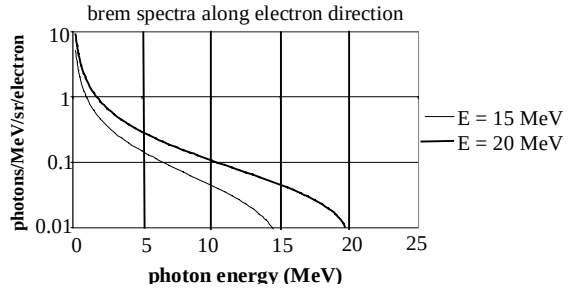

Figure 3. Bremmstrahlung spectra along relativistic electron beam direction for electrons of a) 15 MeV and b) 20 MeV.

The induced activity of a sample may be obtained from equation (2),

$$A = \left(\frac{\ln(2)}{T_{1/2}}\right) \sum_{E_\gamma} N_\gamma(E_\gamma)\sigma_{\gamma n}(E_\gamma)N \qquad (2)$$

where $T_{1/2}$ is the half-life of the radioisotope, $N_\gamma(E_\gamma)$ is the number of photons in the energy bin of width 0.5 MeV at energy E_γ, $\sigma_{\gamma n}(E_\gamma)$ is the (γ,n) cross-section at energy E_γ[17], and N is the number of nuclei present. The summation in (2) extends from the Q-value for the reaction to 25 MeV beyond which the cross-section is negligible for the reactions considered.

The total number of photons of energy E_γ incident on both the copper and carbon samples was calculated by integrating over θ=0 to 30.5° for copper, and θ=0 to 14° for the carbon sample, according to the geometry of the system. The activity ratio of $^{11}C/^{62}Cu$ was then calculated for electron temperature kT MeV and compared with the experimental value. The calculation was then repeated with different kT values until the data fitted the experimental ratio.

The $^{11}C/^{62}Cu$ activity ratio is shown as a function of kT in Figure 4, with three typical measured activity ratios from different laser shots, at nominally 10^{19} Wcm^{-2}, plotted as points corresponding to kT values of 1.43, 1.63, and 2.06 MeV.

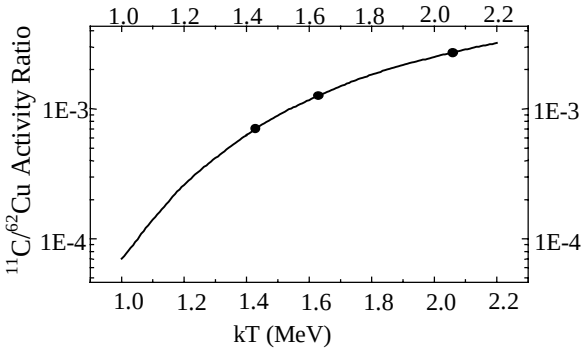

Figure 4. Activity ratio as a function of kT with three experimental ratios plotted against their corresponding kT values.

Summary

A procedure to determine the temperature of fast electrons in high-intensity ($10^{19}Wcm^{-2}$) laser-solid interactions, based on nuclear activation techniques, has been described. For large-scale, single-shot laser facilities such as VULCAN, this method can be used to calculate the temperature between shots, making a shot-to-shot comparison of the electron temperature easily attainable.

References

1. D Strickland, G Morou, Opt. Comm. 56, 219 (1985)
2. M.A. Perry, G. Morou, Science, 264, 917 (1994)
3. K. Boyer, T.S. Luk, C.K. Rhodes, Phys. Rev. Lett. 60, 557 (1988)
4. K W D Ledingham et al, CLF Annual Report 1997/98, 41
5. K W D Ledingham et al, to be published
6. M Tabak et al, Phys. Plasmas 1, 1626 (1994)
7. T Tajiama, J.M. Dawson, Phys. Rev. Lett. 43, 267 (1979)
8. M Dawson, Scientific American, March 34 (1989)
9. D Umstadter et al, Science 273, 1996
10. A Modena et al, Nature 377, 206
11. F Amiranoff et al, Phys. Rev. Lett. 81, 995 (1998)
12. R Wagner et al, Phys. Rev. Lett. 78, 3125 (1997)
13. C N Danson et al, J. Modern Optics 45, 1653 (1998)
14. P A Norreys et al, Phys. Plasmas 6, 2150 (1999)
15. M I .K Santala et al, to be published
16. D J S Findlay, Nucl.Inst. and Meth. A726, 598 (1989)
17. EXFOR www database – http://www-nds.iaea.or.at/exfor

Energy transport in high intensity laser solid interactions

M Zepf, F N Beg, E Clark, A E Dangor, K Krushelnick, MTatarakis, I F Watts

Blackett Laboratory, Imperial College of ScienceTechnology and Medicine, London SW7 2BZ

J R Davies

GoLP (Grupo de Lasers e Plasmas), Instituto Superior Tecnico , 1900 Lisboa, Portugal

P Norreys

Central Laser Facility, CLRC Rutherford Appleton Laboratory, Chilton, Didcot, Oxon. OX11 0QX, UK

A Machacek, J S Wark

Clarendon Laboratory, University of Oxford, OX1 3UP

Main contact email address: *m.zepf@ic.ac.uk*

Introduction

Energy transport in high intensity laser-solid interaction has been a focus of interest particularly in connection with the Fast Ignitor Scheme for Inertial Confinement Fusion[1]. Briefly, the idea underpinning this scheme is to separate the heating of the fusion pellet from its compression, thereby making the fusion process more efficient and possibly easier to achieve. The heating of the fusion pellet to sufficiently large temperatures (> 10 keV) is then achieved using the fast electrons (~MeV) generated in high intensity $>10^{19}$ Wcm^{-2} laser solid interactions. Very large amounts of energy (>> 1kJ) need to be deposited in a small fraction of the fuel pellet in a very short period of time (~10ps). PIC code simulations have predicted large conversion efficiencies from laser radiation into fast electrons and their existence has been confirmed experimentally[2]. However in a typical fusion scenario the electrons will be generated a long distance from the compressed core (~100µm). Understanding the physics underlying the electron transport and energy deposition in these interactions is therefore paramount.

The currents required (>50 MA) far exceed the Alfvén-Lawson limit for the propagation of an electron beam in vacuum (~0.1MA for a relativistic γ=5). Therefore the beam has to be almost perfectly compensated by a return current to enable propagation. Consequently the process of electron propagation and energy deposition cannot be approximated by the trajectory of a single electron but instead has to be viewed as a collective phenomenon dominated by the fields and currents set up by the fast electron beam. In this report we will show the first quantitative measurements of the energy deposition by a fast electron beam in a solid glass target.

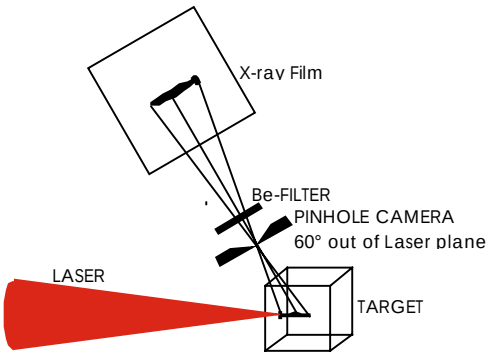

Figure 1. Experimental Layout

The Vulcan laser was focused with an f/1.5 on-axis parabola and delivered up to 50 J in a 1 ps pulse to target. The peak intensity was around 2 10^{19} Wcm^{-2}. The laser was incident at an angle of 45° onto a 10x10x 0.5 mm glass slab target. The X-ray image was taken using a pinhole camera and recorded using Kodak DEF film. The pinhole camera was elevated 60° out of the laser plane and situated directly above the focusing laser beam. A schematic diagram of the experimental layout is shown in Figure 1.

Results

Figure 3(top) shows the X-ray image obtained from the experiment. The dimensions of the X-ray emission region are 150µmx10µm. Because the data was recorded with a single X-ray pinhole camera the spatial orientation of the X-ray emission region cannot be determined unambiguously. It is therefore possible, in principle, that the observed X-ray signal corresponds to the energy distribution of the laser on the target surface. However the longitudinal dimension of the X-ray emission region is significantly larger than the focal spot of the laser (about 10-15µm diameter), which makes it highly improbable that the observed X-ray source is on the surface of the target. Also the quality of the focal spot was monitored on a shot to shot basis using an equivalent plane monitor and the aspect ratio of the major to the minor axis never exceeded 2.

Recent experimental work suggested that the electrons propagate in a narrow filament which roughly corresponds to the focal spot size[3]. Theoretical work by Davies *et al.* [4] has also suggested that the fast electrons generated around the critical surface propagate into the target in a narrow filament which roughly corresponds to the focal spot diameter in size. The formation of the filament can be understood as follows:

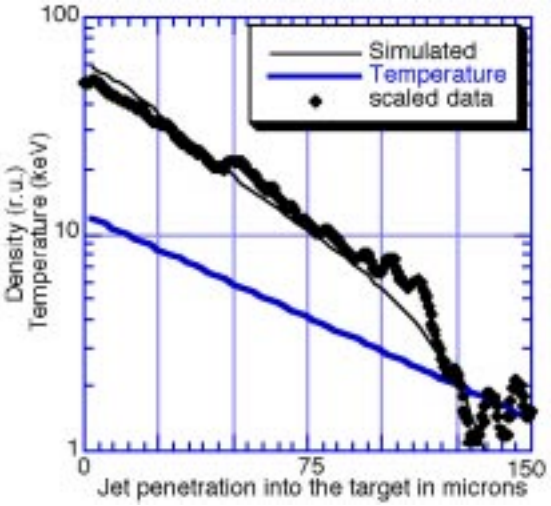

Figure 2. Line-out of the experimental data compared with simulated film density assuming an exponential temperature profile.

initially the transport of the fast electrons is inhibited by a large electric field due to the large resistivity of the cold target. This leads to strong heating of the background electrons and the formation of a low resistivity channel, which then allows a return current to flow and the fast electrons to propagate. This process is more efficient along the axis of the fast electron beam, as the current density is higher there. The electrons are

confined to this filament by the self-generated magnetic field of the fast electron current. This magnetic field reaches magnitudes of several thousand Tesla for our experimental conditions. Direct experimental evidence for these large magnetic fields was observed in the same experiment[5].

As mentioned above the fast electron current has to be almost perfectly compensated by a return current in order to propagate. This return current is colder and far more collisional than the fast electrons, which in turn leads to a strong heating of the background plasma. Davies *et al.* have predicted background temperatures of several keV in a filament which can extend to several hundred microns depth[4].

To test this hypothesis it was assumed that the X-ray filament is in the laser plane. This assumption is justified by the observation of other signatures of the electron beam, which lie in the laser plane. These include large magnetic fields, γ-ray emission cones and the observation of a filament in the target using an optical probe [5,2,6] (all in this report). We can then determine the orientation of the filament and find that it is rotated 15 degrees from the target normal towards the laser axis. Using the attenuation of the X-rays in the glass target and the film response for Kodak DEF x-ray film[7] we can calculate the temperature of the filament at different depths into the target.

A simple exponential temperature dependence reproduces the experimental data well and is in accordance with the predictions of Davies *et al*. Figure 2 shows a comparison of the lineout of the X-ray image compared to the calculated film density at different depths in to the target. One of the striking features of the data is the sudden drop in film density at around 100 µm depth. This is due to the combined effect of the rapid drop in film sensitivity to X-rays below 3 keV and the increasing attenuation by the glass target. The fact that this feature is well reproduced by the simulated film response gives credence to our interpretation that we are indeed observing the hot channel observed in the simulations.

Figure 3 shows a comparison of the simulations for our experimental conditions to the data. The pulse had a FWHM of 1ps and a peak intensity was 1.8×10^{19} Wcm^{-2} (corresponding to 50J in a 10µm radius focal spot). The fast electron distribution was assumed to contain 30% of the total laser energy and had the shape of a simple exponential. The electrons were injected with a divergence of 30°. The time dependent fast electron temperature was scaled to the intensity of the laser pulse as $(I)^{1/2}$ and the pulse-shape was assumed to be Gaussian. The bottom image shows the temperature distribution predicted by the simulation. The middle image shows the simulation data convolved with a 5µm pinhole function to facilitate the comparison with the pinhole image.

The overall agreement between the experimental data and the simulation is remarkably good, especially since the treatment of the fast electron generation is not self-consistent in the code and there are no laser dynamics included. This may go some way to explaining the difference between the experimental results and the simulation. In the experimental data we observe somewhat higher peak temperatures and a steeper gradient than in the simulation. The most likely reason is that the simple exponential distribution is a reasonable approximation only at large electron energies. Bremsstrahlung measurements conducted simultaneously with this experiment suggest that there is also a cold electron population (~100 keV temperature), which increases the total number of electrons at low energies significantly over that assumed in the code. These cold electrons would be stopped far earlier on in the target and lead to a steeper, more highly peaked distribution. This will be investigated in more depth at a later date.

It is also important to note that the simulated temperature distribution represents a snapshot taken at 2ps after the peak of the pulse. This is the point at which most of the electrons injected at the target surface have traversed the region of interest. The data, by contrast, is a time-integrated image of the X-ray filament. This may suggest that the hot plasma region remains confined by the magnetic field for long enough to prevent blurring due to lateral heat transport. Indeed this hypothesis is also supported by the relative magnitudes of the magnetic field pressure and the plasma pressure. Both the magnetic field measurements by Clark *et al.*[5] and simulation[4] suggest that $P_{plasma} \sim P_{mag}$ for our conditions. This question cannot be resolved with our current time integrated diagnostics and requires time-resolved X-ray imaging.

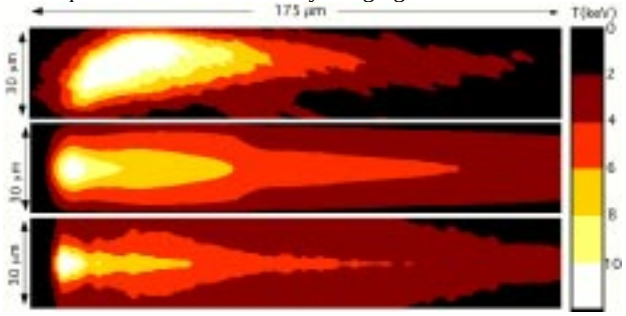

Figure 3. Comparison of experimental data (top) and simulation (bottom) and of the simulation convolved with the 5µm pinhole function (middle). The simulation represents a snapshot at 2ps after the peak of a 1ps FWHM pulse, the experimental data is time integrated **.**

The total energy contained in the filament is ~5.5 J or 11% of the total laser energy, corresponding to 20-30% of the total energy in the fast electron distribution. The technique discussed in this report allows quantitative measurements of the propagation and energy deposition resulting from the fast electrons generated in high intensity laser-solid interactions. Significant further research is needed to be able to transfer our findings to a Fast Ignitor scale experiment. Remaining issues are the scaling with background plasma conditions, e.g. target Z and initial temperature, and also the pulselength of the laser. The latter may prove particularly crucial since the scalelength of lateral diffusion scales as $\sqrt{\eta\tau}$, where η is the resistivity and τ is the pulse duration[8]. This would result in less collimated flow of the fast electrons and might become relevant for the >10ps duration pulses envisaged in the Fast Ignitor concept.

Conclusion

We have shown quantitative evidence of fast electron transport and energy deposition into the target in laser-solid interactions. The electron beam propagates in a narrow filament penetrating large depths into the target, in good agreement with previous theoretical work. This is of great importance to the Fast Ignitor scheme because it suggests that it may be possible to transport a large fraction of the initial beam energy through large lengths of plasma without significant spreading. However, this also emphasizes the need to create plasma conditions where the directionality of the electron beam and its propagation stability are well controlled, as such a small beam could easily miss the compressed core of a fusion target completely.

References

1. Tabak *et al,* Physics of Plasmas, 1, pp.1626 (1994)
2. Santala *et al,* this report.
3. Tatarakis *et al,* Phys. Rev. Lett., 81, 999 (1998)
4. Davies *et al,* Phys. Rev. E., 59, 6032 (1999)
5. Clark *et al,* this report
6. Borghesi *et al,* this report
7. Rockett *et al,* Appl. Opt., 24, pp. 2536 (1985)
8. Davies *et al,* Phys. Rev. E, 52, 7193 (1997)

Studies of Novel Laser-Solid Interactions at High Intensities on Vulcan using Nuclear Techniques

K W D Ledingham, I Spencer, T McCanny, R P Singhal
Department of Physics and Astronomy, University of Glasgow, Glasgow G12 8QQ, UK

M I K Santala, E Clark, I Watts, F N Beg, M Zepf, K Krushelnick, M Tatarakis, A E Dangor
Blackett Laboratory, Imperial College, Prince Consort Rd., London SW7 2BZ, UK

P A Norreys, R Allott, D Neely, R J Clarke
Central Laser Facility, CLRC Rutherford Appleton Laboratory, Chilton, Didcot, Oxon, OX11 0QX, UK

A Machacek, J S Wark
Department of Physics, University of Oxford, Clarendon Lab.,Oxford OX1 3PU, UK

A J Cresswell, D C W Sanderson
Scottish Universities Research/Reactor Centre, East Kilbride, Glasgow G75 0QU, UK

J Magill
European Commission, Institute for Transuranium Elements, Postfach 2340, D-76125, Karlsruhe, Germany.

Introduction

The last few years have witnessed a dramatic upsurge in short pulse laser technology with its concomitant high achievable peak powers. This has been brought about by the development of chirped-pulse amplification (CPA)[1,2]. Now table-top terrawatt lasers are to be found in many university and national laboratories and recently the first petawatt laser has been developed at Livermore[3] with others being proposed elsewhere. With these high power lasers, focused intensities between 10^{19}-10^{20} Wcm^{-2} have been achieved.

At these intensities free electrons can quiver in a laser focus totally relativistically with ponderomotive energies of MeV. A number of mechanisms are proposed which can cause the electrons in plasmas to be accelerated to many times the ponderomotive potential such as wakefield acceleration[4,5], plasma wave breaking[6], vxB acceleration in the presence of an azimuthal magnetic field[7], and resonance absorption[8].

The reason for the current and burgeoning interest in high intensity laser-plasma interactions is their relevance to a number of diverse fields e.g. advanced concepts of plasma high energy particle accelerators[9,10], laser induced nuclear photo-physics, astrophysics and inertial confinement fusion (ICF)[11]. Specifically the question of carrying out nuclear physics using a laser source has been addressed by a number of authors using high repetition rate, fs lasers[12-14] and by using single shot ultra-high intensity lasers like the petawatt laser at the NOVA facility and Vulcan [3,15-17]. A seminal theoretical paper written by Boyer, Luc and Rhodes more than ten years ago predicted the possibility of optically induced nuclear fission[18]. The first quantitative measurement of bremsstrahlung photons with energies > 2 MeV from the interaction of a laser with matter was reported by Sherman, Burnett and Enright[19]. They showed that they were produced by relativistic electrons when a 600ps, CO_2 laser pulse interacted with thick targets. Recently more energetic electrons have been produced by terawatt and petawatt lasers of 1 μm light in ≤ ps pulses [16,17].

The motivation for writing the present letter is to show how a 50 TW laser (Vulcan) can be used to carry out (γ,n) and (γ,f) reactions. These reactions are the simplest photo-nuclear reactions for γ-ray beams with an end-point up to about 30 MeV, generated by bremsstrahlung from the energetic electrons produced by laser intensities of about $10^{19}Wcm^{-2}$. Typically (γ,n) reactions produce proton rich isotopes which decay to stability by positron emission, electron capture (EC) or both[20] and have thresholds for production (Q values) which are typically >8MeV. The (γ,f) reactions are also energetically favoured having thresholds of about 4 MeV.

Experimental

The experiment used the ultra-intense beam-line of the Vulcan Nd: glass laser[21] incident on a tantalum target, 1.75mm thick, at 45^o with p-polarised light within an evacuated target chamber. The experimental arrangement has been described in greater detail elsewhere[16] as well as the principal diagnostics employed. Briefly the Vulcan laser delivered pulses on target up to 50 J with pulse lengths about 1 ps. A 95% reflecting turning mirror located after the recompression gratings was used to steer the beam on target focused by a f/1.7, 22cm focal length on-axis parabolic mirror. This turning mirror permitted 5% transmission of the laser energy for measurements of the laser spectrum, the pulse duration by a single shot autocorrelator and the focal spot quality by an equivalent plane monitor. The contrast ratio between the peak and ASE energies was measured by a third order autocorrelator to be $1{:}10^{-6}$. Equivalent plane images showed that the diameter of the focal spot was 9μm, containing 35% of the laser energy when the target holder was placed in the beam. The focused intensity on target for each shot was monitored by a penumbral imaging camera.

Firstly the angular distribution of the high energy γ rays following the laser irradiation of the tantalum bremsstrahlung target was measured. The energy loss to bremsstrahlung when the laser induced electrons slowed down in the target scales as Z^2 (atomic number) and hence high Z targets are favoured. In the present case tantalum (1.75 mm thick) was chosen.

Pieces of copper were placed around the target such that both horizontal and vertical distributions of the γ-rays could be determined. The γ-rays interact with the copper, inducing the photo-neutron reaction $^{63}Cu(\gamma,n)^{62}Cu$ with a 9.74 min half life. The β^+ activity in each piece of copper was measured separately, corrected to time zero for decay (laser shot time) and the angular distributions determined. This is the subject of a paper (published elsewhere[22]) dealing with the plasma physics implications of this observation. The laser was operated with a plasma scale length of ~ 7μ corresponding to the main γ emission being along the laser beam propagation direction. This is contrary to the observations reported in reference 19.

Results and Discussion

A number of (γ,n) reactions from different targets were carried out (Figure1). Positrons slow down in materials and annihilate at rest with electrons producing two back-to-back photons of 511 keV energy.

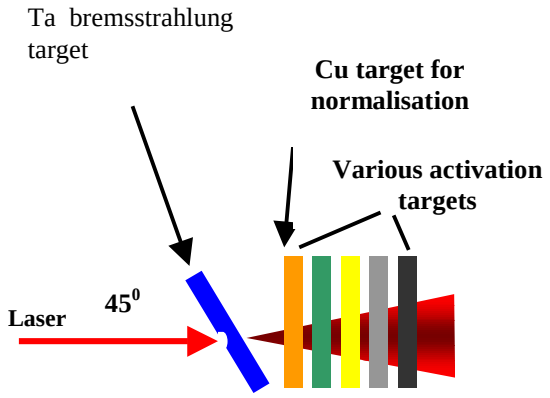

Figure 1. The arrangement for irradiating a number of different targets simultaneously. All samples had dimensions ~10x10x3mm. The copper target was used for normalisation of activities.

These were detected with high efficiency and signal to noise ratio using either two 3"x 3" or 2"x2" NaI scintillators operated in coincidence. The absolute efficiency of these systems was determined using a calibrated ^{22}Na source. The activity of the sources was corrected to time zero and knowing the (γ,n) cross sections[23,24], the number of high energy photons produced by each laser shot could be determined from which could be estimated the number of initial high energy electrons. Typically ~10^{8-9} γ-rays were generated from the highest activity sources ~ 5kBq. Table 1 presents a list of the isotopes activated, the half lives, the Q values, the peak (γ,n) cross sections. In earlier works[15,16], the activity produced in the copper sample was analysed for two hours and hence any long lived ^{64}Cu activity from the ^{65}Cu(γ,n)^{64}Cu reaction was difficult to measure unambiguously. In this letter the activity was analysed for many hours and is shown in Figure 2. The half-lives determined from the two gradients of the activity agree well with the accepted values of 9.7m and 12.7h.

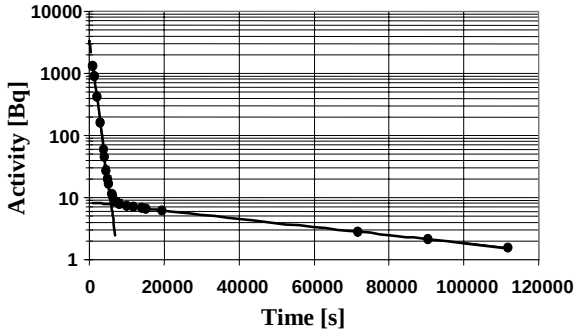

Figure 2. The half-lives of the two isotopes of Cu: ^{62}Cu, ^{64}Cu following the irradiation of Cu at 10^{19}Wcm^{-2}. The half-lives agree well the accepted values of 9.7m and 12.7h.

Figure 3 shows the activity measured as a function of time for the other isotopes listed in Table1, ^{11}C, ^{38}K, ^{63}Zn, ^{106}Ag and ^{140}Pr. Because of the differing Q values for the isotope production, the activities can be used to establish the shape of the bremsstrahlung spectrum and hence the temperature of the energetic electrons. Thus nuclear activation can be used as a powerful plasma diagnostic technique. For laser intensities of about 10^{19} Wcm^{-2}, isotopes with half-lives with up to ~24 hrs can be readily detected for medium A isotopes. For large A isotopes, longer lived activities can be measured since the (γ,n) cross sections increase with A.

Nuclear reaction	$T_{1/2}$	Q (MeV)	Peak σ(mb)	Radiation measured
^{12}C(γ,n)^{11}C	20.5m	18.7	13.1	β^+
^{39}K(γ,n)^{38}K	7.6m	13.7	11	β^+
^{63}Cu(γ,n)^{62}Cu	9.7m	10.9	75	β^+
^{64}Zn(γ,n)^{63}Zn	38.1m	11.9	123	β^+
^{65}Cu (γ,n)^{64}Cu	12.7 h	10.9	65	β^+
^{107}Ag(γ,n)^{106}Ag	24m	9.5	155	β^+
^{141}Pr (γ,n)^{140}Pr	3.4m	9.4	335	β^+
^{181}Ta(γ,n)^{180}Ta	8.2h	7.6	367	EC Hf X-rays
^{238}U(γ,f)^{134}I ^{238}U(γ,f)^{138}Cs ^{238}U(γ,f)^{92}Sr	53m 32.3m 2.7h	7.8	150	847 keV γ 884 keV γ 1436 keV γ 1384 keV γ

Table 1. (γ,n) and (γ,f) reactions at intensities ~ 10^{19}Wcm^{-2}

Generally isotopes (Z,A) which decay by EC alone or with a small β^+ fraction can be detected by the characteristic X-rays of the element Z-1. This was carried out in the case of the Ta target using a well shielded, 16% intrinsic Ge detector to detect the Hf X-rays. The low energy γ spectrum from Ta is shown in Figure 4 with the Hf X-rays clearly visible.

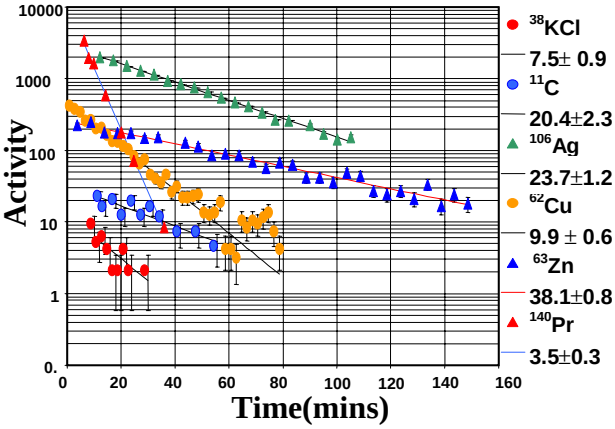

Figure 3. The activities of the isotopes listed in Table 1 as a function of time. The measured half lives agree well with the accepted values. The activities shown in this figure come from different laser shots.

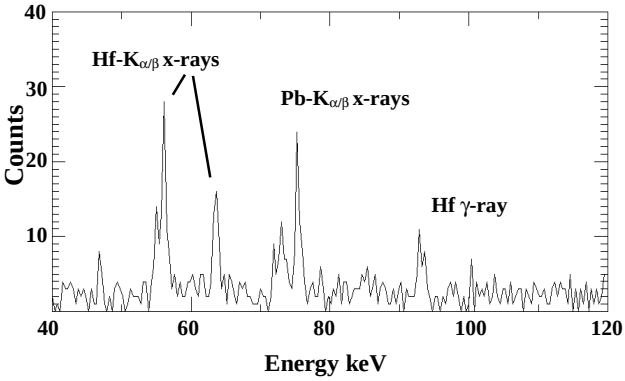

Figure 4 . The low energy γ-ray spectrum from Ta as measured by an intrinsic Ge detector. The characteristic Hf X-rays from the decay of ^{180}Ta are clearly visible. The Pb x-rays are background peaks.

Finally a ^{238}U (depleted uranium) sample of dimensions ~10×10×2mm (~3g) with a fission fragment 300μm polycarbonate foil on the front and back sides was targeted. This sandwich was shrink wrapped in plastic to contain any gaseous radioactivity and enclosed in an aluminium container.

The sample was irradiated with 3 consecutive laser shots, twenty minutes apart, of nominally 10^{19}Wcm^{-2} intensity and analysed using the Ge detector. Both (n,f) and (γ,f) reactions in fissionable materials produce a double headed asymmetric fission yield distribution of fragments with maxima at mass numbers about 95 and 140 corresponding to the neutron magic numbers of 50 and 82.

The principal fission fragments amount to about 5-6% of the total fission yield. Evidence for fission events is normally carried out by detecting the characteristic γ-rays from the principal fission fragments, detection of fission fragment tracks or fission neutrons. In the case of ^{238}U with a (γ,f) cross section which peaks at about 150mb the most abundant isotopes produced include ^{134}I, ^{138}Cs and ^{92}Sr [25] with suitable γ-ray energies and half-lives. The background activity from fissionable materials is normally sufficiently large that very careful background measurements must be taken. Specifically for ^{238}U($t_{1/2}$=4.5x10^{9}y) the background activity is 12.3 kBq/g. Two Ge γ-ray spectra in the region of 850 keV and 1400 keV are shown in Figure5 after background subtraction was performed.

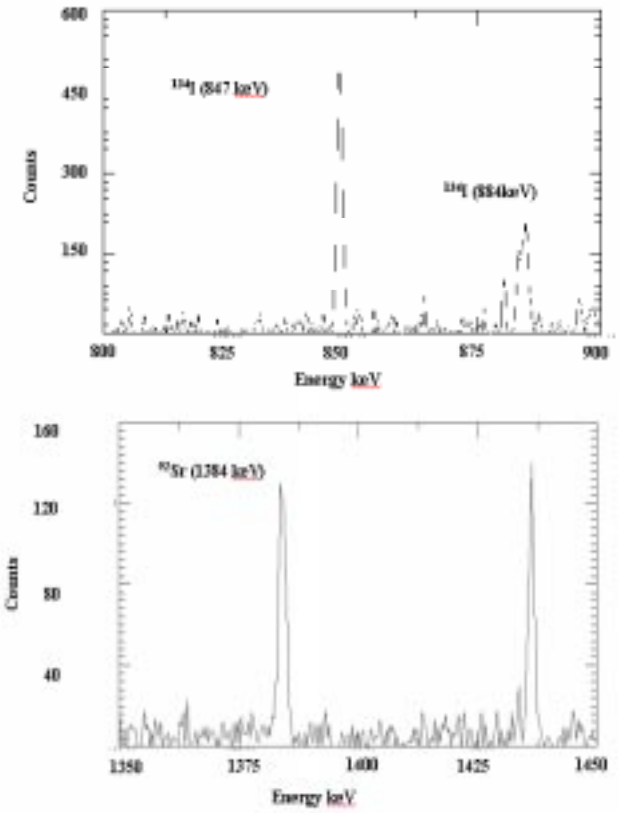

Figure 5. Some of the characteristic γ-rays emitted by three of the principal fission fragments following a ^{238}U(γ,f) reaction. The details of the isotopes and half-lives are given in Table 1.

The unambiguous characteristic γ-rays of the fission fragments I^{134}, ^{138}Cs and ^{92}Sr are indicated.

From the intensity of the ^{134}I γ-ray peak in Figure 5 using the known efficiency of the Ge detector, the fission yield to that isotope, and the (γ,f) cross section (Table1), it has been estimated that about 10^6 fission events are generated by a laser shot of ~10^{19}Wcm^{-2} in a ^{238}U target of 2 mm thickness. Any (n,f) reactions are likely to be considerably lower in intensity than the (γ, f) reactions because of the reduced numbers of neutrons[17].

In summary, it has been shown that when a beam of 1μm light at ~ 10^{19} Wcm^{-2} interacts with a high Z target, a sufficiently intense high energy γ-ray beam is generated such that photo-nuclear reactions can be carried out. ^{11}C, ^{38}K, ^{62,64}Cu, ^{63}Zn, ^{106}Ag, ^{140}Pr, and ^{180}Ta have been produced in measurable quantities up to activities of about 5kBq at the highest laser intensities. In addition photo-fission of ^{238}U has been demonstrated from the most abundant fission fragments. Some ten years ago Boyer, Luc and Rhodes[18] estimated theoretically that for 248 nm radiation at an intensity of 10^{21}Wcm^{-2}, some 10^6 fission reactions could be generated per pulse in uranium 1cm thick. This is in reasonable agreement with fission yields from U in the present experiment at 10^{19}Wcm^{-2} intensity of 1.053μm radiation.

One of the principal applications of nuclear activation to intense laser pulse interaction with solid targets is to measure the temperature of the electrons involved. In the present work the ratio of the activities from ^{62}Cu and ^{11}C will uniquely determine this quantity. In the following analysis, it was assumed that the spectrum was characterised by the relativistic electron energy distribution $E^2\exp(-E/kT)$[16] . These electrons then produce γ-radiation in the Ta target with the γ spectrum determined uniquely by the electron energy. The analysis proceeded using 0.5 MeV electron energy bins and for each, the γ spectrum was estimated[26]. This procedure allows a determination of the energy spectrum for the bremmstrahlung produced in 0.5 MeV energy bins. The corresponding (γ,n) cross sections for the ^{63}Cu and ^{12}C have been measured experimentally[24]. These cross sections and the calculated γ flux for each bin were used to evaluate the expected yields of ^{62}Cu and ^{11}C. The ratio of the two activities eliminated the need for absolute electron flux measurements. The details of this procedure will be published elsewhere[27]. Figure 6 shows a graph of the calculated ratio of the activities as a function of kT. Three typical experimental measurements for this quantity for laser intensities ~ 10^{19}Wcm^{-2} are shown as experimental points corresponding to electron temperatures of 1.43, 1.63 and 2.06 MeV for these shots. The large shot to shot variation is a particularly important result. The observed fluctuation is probably due to the highly non-linear nature of the plasma interactions at these intensities where the effects of a number of scattering instabilities play an important role.

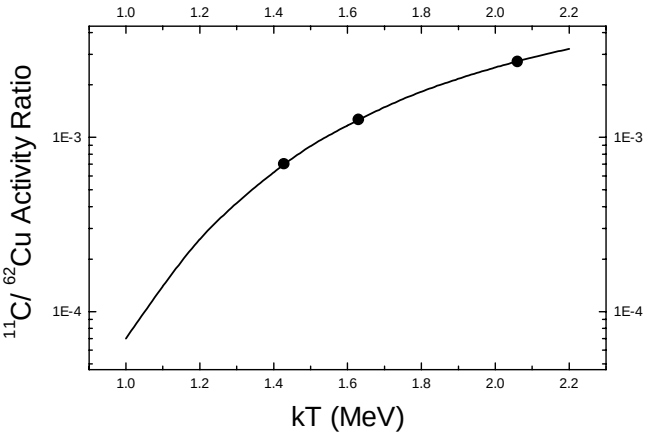

Figure 6. The calculated ^{11}C/^{62}Cu ratio as a function of kT. Three typical experimental ratios are shown for three shots at laser intensities ~ 10^{19}Wcm^{-2}.

Conclusions

It has been shown that a focused laser of wavelength 1μm can be the source of energetic electrons at intensities ~10^{19}Wcm^{-2}. These generate a highly directional γ-ray beam that can produce photo-nuclear reactions which can be used as an exciting new

diagnostic tool in plasma physics. Short lived isotope production and fission have been demonstrated. With intensities of 10^{21} Wcm^{-2} from petawatt lasers, isotopes with much higher activities and longer half-lives could be generated from a single shot. Although it is uncertain how the photon energy scales with laser intensity, pion production, energetically possible with γ-rays >140 MeV, is a distinct possibility and can be demonstrated using similar activation experiments to those described in this letter. Alternatively using CPA technology, 10Hz, 1J, 100fs lasers can deliver similar single shot intensities as the present experiment but with greatly increased activities after integrating a number of shots.

References

1. D.Strickland and G.Morou
   Opt. Commun. 56, 219 (1985).
2. M.A.Perry and G.Morou
   Science 264, 917(1994).
3. M.H.Key *et al*
   Phys. Plasmas 5, 1966 (1998).
4. T.Tajima and J.M.Dawson
   Phys. Rev. Lett. 43, 267 (1997).
5. F.Amiranoff *et al*
   Phys. Rev. Lett. 81**,**995,(1998).
6. A.Modena *et al*
   Nature 377**,** 606 (1995).
7. A.Pukhov and J.Meyer-ter Vehn
   Phys. Plasmas 5**,** 1880 (1998).
8. S.C.Wilks ,W.L.Kruer
   IEEE J. Quan. Electron. 33**,** 1954 (1997).
9. M.Dawson
   Scientific American, March**,** 34 (1989).
10. D.Umstadter, S.-Y.Chen, A.Maksimchuk, G.Morou, R.Wagner
    Science 273**,** 1996.
11. M.Tabak *et al*
    Phys. Plasmas 1**,** 1626 (1994).
12. J.D.Kmetec, *et al*
    Phys.Rev.Lett. 68**,** 15271992).
13. P.L.Shkolnikov, A.E.Kaplan, A.Pukhov, J.Meyer-ter-Vehn
    Appl. Phys. Lett 71, 3471 (1997).
14. G.Pretzler *et al*
    Phys. Rev. E. 58, 1165 (1998).
15. K.W.D.Ledingham *et al*
    RIS 98, Eds, Vickerman *et al.*, AIP, Woodbury, New York, Conference Proceedings 454, 229 (1998).
16. P.A.Norreys *et al*
    Phys. Plasmas 6**,** 2150 (1999).
17. T.A. Phillips *et al*
    Rev. Sci. Instr. 70, 1213(1999)
18. K.Boyer, T.S.Luk, C.K.Rhodes
    Phys. Rev. Lett. 60**,** 557 (1988).
19. N.K.Sherman, N.H.Burnett, G.D.Enright
    in "New Develop. in Particle Acceleration Techniques" ed. S.Turner, 2, 675, (1987) (CERN 87-11, Geneva)
20. W.Bambynek *et al*
    Rev. Mod.Phys. 49**,** 77,1977.
21. C.N.Danson *et al*
    J.Modern Optics,45**,**1653,1998).
22. M.Santala *et al*
    to be published.
23. B.L.Berman and S.C. Fultz
    Rev. Mod. Phys. 47**,** 713 (1975).
24. International Atomic Energy Agency web site: http:// www-nds.iaea.or.at/exfor.
25. D.R.Williams, High Resolution γ spectra of 40-44 MeV photon activation products: Part 2 The elements Ruthenium to Uranium
    AERE-R 9021 1978 HM Stationary Office, London.
26. D.J.S. Findlay
    Nucl. Instr. and Meth. A276**,** 598 (1989).
27. R.P. Singhal *et al*
    to be published.

Shock Wave Collisions in Low Density Foams

A Schiavi, M Borghesi, J Pasley, O Willi

The Blackett Laboratory, Imperial College of Science, Technology and Medicine, London, UK

D Neely, M Notley

Central Laser Facility, CLRC Rutherford Appleton Laboratory, Chilton, Didcot, Oxon,OX11 0QX, UK

W Nazarov

Chemistry Department, University of Dundee, UK

Main contact email address: *a.schiavi@ic.ac.uk*

Introduction

In recent years the availability of low density foams has given scientists the opportunity to investigate the formation and propagation of subsonic, transonic and supersonic waves. Such studies are of major importance for the development and testing of new ideas in Inertial Confinement Fusion[1]. Foam targets also allow direct observation of the development of shock waves. The collision of shock waves in this density regime has never been investigated before at these energy densities, and experimental data is required to test theoretical modelling.

In this experiment shock fronts were driven through a low density foam target by high intensity laser pulses. The propagation of shock waves through the target was detected by time resolved point projection absorption spectroscopy. From image processing of the exposed films and comparison with synthetic absorption spectra, it was possible to reconstruct temperature and density profiles of the shocked foam.

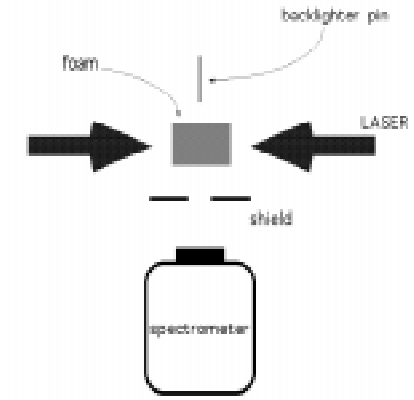

Figure 1. Experimental Setup: top view

Experimental setup

The targets consisted of triacrylate foam cylinders at a density of 50 mg/cc; the foam was doped with 25% by weight of chlorine. The average target dimensions were 200 µm in diameter and 250 µm in length. The target was mounted in the centre of the TAE target chamber of the Vulcan laser facility.

The laser pulse had a flat-top profile with 1 ns FWHM duration and was frequency doubled using a KDP crystal to obtain a 0.527 µm wavelength.

Two beams were focused on each side of the foam producing a typical irradiance of 5 10^{14} W/cm^2. Phase plates were used to smooth spatial non-uniformities in the laser beam.

The back-lighter target was a 15 µm diameter bismuth coated gold pin. The pin was irradiated by two simultaneous 0.527 µm laser pulses focused on to the pin with f/2 lenses. The pulse length, and consequently the duration of x-ray flash produced, was 90 picoseconds, allowing resolution of the evolution and propagation of the shock fronts. Different stages of the shocks' interaction were recorded by changing the delay between the main pulse and the back-lighter pulse. Radiographs were taken with a flat RbAP crystal spectrometer; the crystal was aligned so as to record on film the spectrum from 2.2 to 3.8 keV.

In this spectral range it was possible to detect the 1s2p and 1s3p absorption lines of chlorine. The spectrometer was aligned to record the central part of the foam with a 50x spatial magnification. An aluminium shield with a central window (Figure 1) was mounted between the target and the spectrometer aperture to screen the intense self-emission of the plasma at the foam edges.

An optical streak camera system looking at the interaction centre allowed timing of the main pulse with back-lighter pulse and recorded the delay between those two pulses for each shot.

Experimental results and analysis

Films were scanned to high resolution with a microdensitometer and the images were corrected for the actual film sensitivity. Film chemical fog, and radiation background present inside the spectrometer, were subtracted from the intensity image to obtain the original x-ray intensity signal. On each film two main features were present: the back-lighter flash and the foam self-emission. The self-emission was time and space integrated, and its spectrum was dominated by chlorine He-like and H-like α-lines and was used to calibrate in energy each scanned film. Figure 2 shows two shock fronts just before collision.

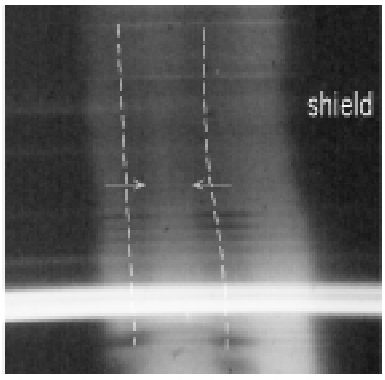

Figure 2. Radiograph of colliding shocks: the white band across is the strong self-emission corresponding to He_α lines of chlorine

The bismuth spectrum emitted by the back-lighter pin is an M shell quasi continuum emission[2] that enables detection of absorption lines of the chlorine. This is necessary for a precise measurement of temperature, because the absorption pattern changes considerably within a few eV, whilst changes in density of a factor of 2 or more are needed to cause an

experimentally detectable difference at our spectral and spatial resolution (Figure 3).

The data analysis consisted in working out the density profile by comparing transmission in the continuum (2.4-2.6 keV) of different parts of the foam along the shock propagation direction.

Temperature profiles were obtained by comparison of actual transmission profiles with synthetic profiles from the sepSAHA[3)] code: this programme simulates absorption features of chlorinated CH foams assuming local thermal equilibrium; populations of different ion configurations are calculated using Saha-Boltzmann statistics and a detailed absorption spectrum is obtained (Figure 4).

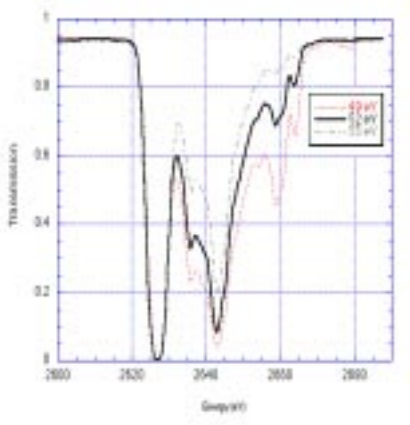

Figure 3. Synthetic transmission profiles for chlorinated foam; sensitivity to foam temperature is shown at the energy of 1s2p lines of Cl.

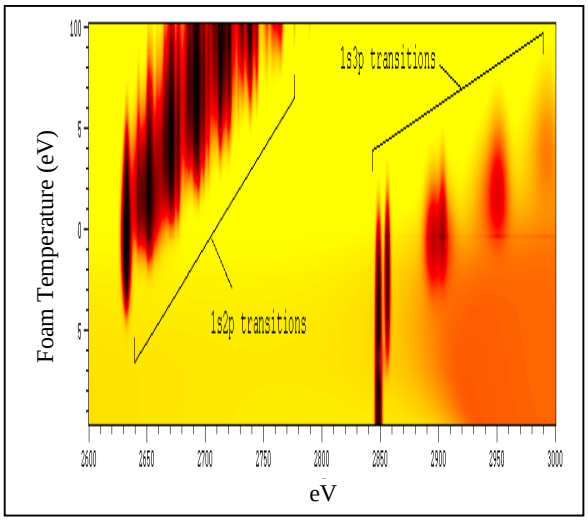

Figure 4. Synthetic (computed) transmission

Conclusions

At the time of this publication the analysis of collected radiographs is still in progress; an attempt has been made to reproduce the behaviour of observed shocks using a 1D Lagrangian code, but there is significant disagreement at times after collision of the two shocks. It seems then necessary to adopt a two dimensional approach, to take into account the energy and mass loss in the transverse direction during collision.

Acknowledgements

We would like to thank the staff of the Central Laser Facility for the valuable assistance in the setting up and running of the experiment; we would also like to thank Dr D. Hoarty of AWE Aldermaston for useful discussions and the loan of equipment. This experiment was funded by EPSRC/MoD grants; A Schiavi was supported by a Padua University Scholarship.

References

1. J Lindl
Inertial Confinement Fusion, Springer-Verlag (1998)

2. Willi
Diagnostic and experimental methods of laser produced plasmas, SUSSP Proceedings (1988)

3. D J Hoarty
Ph.D. thesis, University of London (1997)

Reverse Shocks Caused by Expanding Plasmas Impacting Upon Foams

C Vickers, A Iwase, J Pasley

Imperial College, London, SW7 2BZ, United Kingdom

D Hoarty

Atomic Weapons Establishment, Aldermaston, Reading, United Kingdom

Main contact email address: *ce.vickers@ic.ac.uk*

Introduction

Recent theoretical studies of exploding Type I supernovae[1,2,3] have suggested that as the supernova ejecta interacts with the circumstellar medium, e.g. that left over from the stellar wind of the progenitor, a blast wave is formed. When this blast wave interacts with the bow shock caused by the interaction of the stellar wind with the interstellar medium, a forward shock results. Ejecta material tends to stagnate at the impact site and the pressure from this can cause a reverse shock to form in the expanding ejecta. Little physical evidence to back this up is available and most of our knowledge comes from computer-based simulations. The ejecta of the supernova remnant, SN 1987A, is expected to impact upon its circumstellar ring sometime in the next six years[4] (in fact the Hubble Space Telescope has already seen the beginnings of the impact). The impact is expected to give new details on both the nature of the interstellar medium and the history of the supernova progenitor. Experimental studies into the phenomenon will help improve the computational models and give a better overview of the radiation profile expected from the collision and allow an optimum observation strategy to be developed.

Fortunately some simple situations can be scaled down to laboratory levels and experiments can be performed that will provide a basis for enhancement of the simulation codes. We outline details of such an experiment carried out that applies to the case where the expanding material follows a power-law density profile that interacts with a stationary medium of constant density.

We used an exploding chlorinated foil to impact upon a low-density chlorinated foam. Spatially resolved point projection x-ray spectroscopy methods were used to record the optical density of the system around the Chlorine K-band. Analysis of this data gives detailed information about the density and temperature of the system at given times.

Experimental Arrangement

The experiment was performed using the Vulcan Nd:glass laser facility. The YLF long pulse oscillator was used to give six beams with laser energy of 200 Joules, in a 1ns FWHM flat-topped pulse, at a laser wavelength of 1054nm. These were then frequency doubled using KDP crystals to give a laser wavelength of 527nm and energy of 70J per beam. These beams were focused onto a thin CHCl foil with a focal spot of 200µm to give a laser irradiance of $3x10^{14}W/m^2$. The laser irradiated foil then exploded and impacted upon a cylindrical foam of 175µm diameter, lying close to the rear of the foil. The foams used were triacrylate of density 50mg/cc, doped with chlorinated triacrylate to give 25% chlorine by weight. Most of the data taken was with either 7.5µm or 30.0µm foils. For the 7.5µm foils the foam-foil distance was roughly 100µm and for the 30.0µm foils, the foam-foil distance was roughly 200µm.

The YLF short pulse oscillator was used to give two additional beams of 80J of laser energy in an 80ps FWHM flat-topped pulse, at a wavelength of 1054nm. These were then frequency doubled using KDP crystals to give a wavelength of 527nm and energy of 25J per beam. The beams were focused onto the tip of an 18µm diameter, gold backlighter pin coated with 1µm of bismuth to give a laser irradiance of $5x10^{16}W/m^2$. The backlighter emitted a burst of x-rays, which passed through the foam and entered an x-ray crystal spectrometer set to look around the chlorine K-edge (2.8 keV). A Rubidium Acid Phthalate crystal with a 2d spacing of 26.12 angstroms was used in the spectrometer. 12.5µm Beryllium filters were placed at the entrance to the spectrometer and between the crystal and the film to stop sub-keV radiation fogging the film. A magnet was used to deflect hot electrons emitted by the target away from the film plane. A copper shield was used to block x-rays produced from the laser irradiation of the chlorinated foil fogging the film and an 80µm tungsten wire was used to block x-rays from the immediate rear of the foil.

The backlighter emits x-rays in the 3keV energy region only appreciably for the duration of the laser, giving an 80ps 'snapshot' of the foam and foil. The timings of the backlighter beams with respect to the six heating beams were changed from shot to shot to create a sequence showing the temporal evolution of the system. The timing differences were measured on every shot with an optical streak camera.

The x-ray spectral data was taken on Kodak Industrex CX-type film and then converted to optical density with a densitometer. Chemical fogging from the development process was accounted for by detracting the ambient background. A known calibration wedge was then used to convert the data to photon flux. The data was then compared with the backlighter spectrum to give the x-ray transmission.

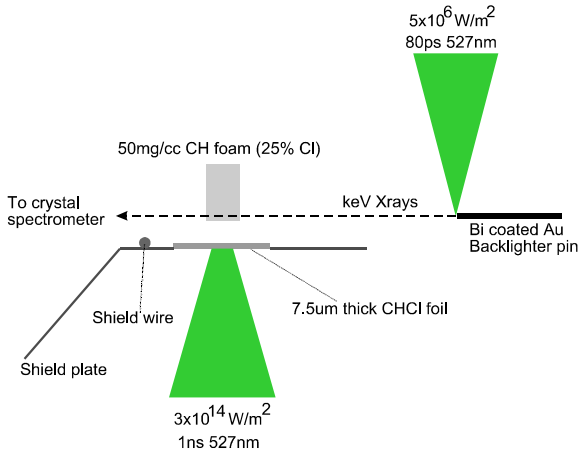

Figure 1. Schematic of the experimental setup

Modelling

The experiment was designed using the 1D lagrangian hydrocode, Medusa, modified to include multigroup radiation transfer[5]. A slight modification was also made to model the expansion of chlorinated foils more accurately. Planckian opacities used in the simulations were calculated using the detailed opacity code IMP[6].

Preliminary simulations suggest that with the 7.5µm foils, the impact occurs and a forward shock is launched ahead of the impacting material. After the impact, there is not enough material left in the expanding foil to cause a big enough build up at the impact site for a reverse shock to occur.

With the 30µm foils, however, the simulations suggest that the initial impact occurs and the forward shock is launched. Pressure from the material build-up at the impact site causes a reverse shock to form in the expanding plasma.

Current analysis of the transmission data uses the following procedure.

The line structure observed is compared with a simulated spectrum to obtain the local temperature. Local thermodynamic equilibrium (LTE) is assumed and the simulated spectra are calculated using the steady state Saha-Boltzman opacity code, Sepsaha[7]. The atomic data used in this code was calculated with the Multi-Configurational Dirac Fock treatment (MCDF) used in the General Relativistic Atomic Structure Package (GRASP)[8].

The density profile is found by comparing the transmission away from the line structure with that calculated with the IMP code. Where possible, input temperatures for the code are found from the above step, otherwise they are taken from the simulations. The errors are mostly negligible as for this situation, the background transmission is only weakly coupled to the temperature.

Results

Only preliminary results are available as detailed analysis has yet to take place. The results suggest that further modifications to the simulation code are needed concerning the expansion of the foils. That taken into consideration, it seems that with the 7.5µm foils, only a forward shock was seen. With the 30.0µm foils, however, preliminary analysis suggests that reverse shocks were seen behind the stagnant ejecta on a few of the shots. Further analysis is needed before accurate conclusions can be drawn.

References

1. K J Borkowski, J M Blondin, C L Sarazin
   The Astrophys. Journ., 400 222 (1992)
2. R A Chevalier
   The Astrophys. Journ., 258 790 (1982)
3. C F McKee, J K Truelove
   Phys. Reports, 256 157 (1995)
4. K J Borkowski, J M Blondin, R McCray
   The Astrophys. Journ., 477 281 (1997)
5. M J Edwards
   Radiation Transport & Short Pulse Interaction in Laser Irradiated Targets (thesis), Imperial College (1989)
6. S J Rose
   Appl. Phys. B, 25 1667 (1992)
7. S J Davidson et al
   Appl. Phys. Lett., 52 847 (1988)
8. K G Dyall et al
   Comp. Phys. Comms, 55 435 (1989)

Measurement of the change in XUV opacity of Al due to shock compression

E Wolfrum, A M Allen, P D S Burnett, J S Wark

Department of Physics, Clarendon Laboratory, Parks Road, University of Oxford, Oxford OX1 3PU, UK.

R Keenan, R M N O'Rourke, C L S Lewis

School of Mathematics and Physics, Queens University, Belfast, BT7 1NN, UK.

S Dobosz, G J Tallents

Department of Physics, University of Essex, Colchester CO4 3SQ

S J Rose, A Djaoui

Central Laser Facility, CLRC Rutherford Appleton Laboratory, Chilton, Didcot, Oxon, OX11 0QX, UK

M H Key, T W Barbee Jr.

Lawrence Livermore National Laboratory, Livermore California 94550, USA.

Main contact email address: *E.Wolfrum@rl.ac.uk*

Introduction

The opacity of shock-compressed material in the XUV spectral region is of general scientific interest for laboratory and astrophysical plasmas[1)] and of particular interest in inertially confined fusion (ICF) research.

Radiography with laser produced plasma x-ray sources is widely used in ICF research to probe the hydrodynamics of spherical shell implosions or accelerated planar foil analogues, driven at megabar pressures either directly by laser light or indirectly by thermal XUV radiation in a laser-heated hohlraum[2)]. Recently both thermal[3)] and laser[4,5)] XUV sources have been used to study the very small-scale hydrodynamic perturbations induced by laser speckle. To interpret such experiments, knowledge of the opacity of shock-compressed material is required.

We present here the first experimental determination of the increase in the mass absorption coefficient for shock compressed aluminium. Experiments which were carried out to study imprint and subsequent Rayleigh Taylor (RT) growth due to single mode imprint[6)] yielded radiographs showing two dominant features. These were, firstly, the large amplitudes in optical depth due to the single mode imprint, which was the quantity we wanted to measure, and, secondly, an increase in the total opacity following the envelope of the single mode Fraunhofer interference pattern. As we were mainly interested in the development of the single mode pattern after shock breakout, i.e. in the RT growth phase, we only gathered a few data points before shock breakout, where the aluminium foil is compressed to its highest density. On analysis of the data, we decided that it was worth dedicating a full radiography experiment to the measurement of the change in opacity due to shock compression, this time using a drive beam with a single smooth spot, omitting the single mode interference pattern. Great care was taken to take a temporal series of shots during the compression phase, i.e. before shock breakout. This experiment and its results are described below.

As a full XUV-laser radiography experiment is rather complicated and restricted to a few wavelengths because of the limited availability of appropriate high quality XUV mirrors, an alternative method of measuring the change in opacity due to shock compression was tested. Instead of imaging the Al foil via XUV mirrors onto a CCD, a flatfield spectrometer was used to take the data. We give details of this experiment and compare its results with those acquired with XUV-laser radiography.

Experiment – Radiography

The experiment was conducted with a 19.6 nm XUV laser producing an intense monochromatic 50 ps[7)] pulse which illuminated an Al foil. The foil was shocked by irradiation with 530 nm laser light and probed by the XUV laser at different times relative to the 200 ps shock transit time. Transmission through shocked and un-irradiated parts of the foil was compared to determine the change in opacity.

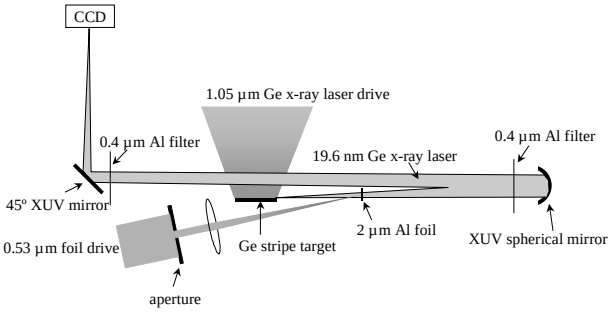

Figure 1. Experimental setup for XUV laser radiography

The experimental arrangement is shown in Figure 1. It includes a standard configuration to produce the Ge XUV laser using five beams of the Nd glass laser Vulcan at the UK's Rutherford Appleton Laboratory. Al foil targets, 2 µm thick, were positioned 3.5 cm from the exit plane of the Ge laser normal to the beam, where the beam illuminated an area approximately 750 µm by 500 µm. A Mo/Si multi-layer XUV mirror of 100 cm radius of curvature was placed at less than 0.6 degree from normal incidence 53 cm behind the Al foil in line with the XUV laser beam. The XUV mirror was protected by a 0.4 µm Al filter and imaged the transmission through the foil. It produced an image with 5 µm resolution at 18 x magnification via a plane XUV mirror at 45 degrees and 0.4 µm Al filter onto a back thinned XUV CCD detector with 1024x1024 pixels of 24 µm size. One other 11 cm aperture beam of Vulcan with an independently controlled pulse shape and synchronisation was used to irradiate the front surface of the Al target at 16 degrees from normal incidence. This beam was operated with conversion to the 530 nm second harmonic in a pulse of 100 ps rise-time and 1 ns duration. A beam block with a rectangular aperture was placed in the beam and it was focused with a 3.5 m focal length lens onto the Al foil. The average drive intensity at the centre of the irradiation was 7×10^{12} Wcm^{-2} or 1.1×10^{13} Wcm^{-2} in two data sets recorded. For the two irradiances different aperture sizes were used, 11x15 mm and 16x20 mm. The size of the aperture was small enough to produce a diffraction limited spot at the focal plane with FWHM of the central maximum in two perpendicular directions of 120 x 103 µm and 110 x 87 µm, respectively. The relative timing of the 75 ps XUV laser drive pulse and the 1 ns foil irradiation was determined by optical streak camera measurements and was adjustable with mechanical mirror slides. In the following we denote as time t = 0 the time when the drive pulse has risen to half of its maximum intensity. The corresponding ablation pressure determined from the numerical

modelling was 1 to 4.5 Mbar. A typical radiograph is shown in Figure 2. The most obvious feature is the reduction in transmission in the region of the foil, which is shocked. The ratio of the intensity in the un-irradiated and irradiated regions was determined and the logarithm of this ratio gave the change in opacity relative to the cold opacity.

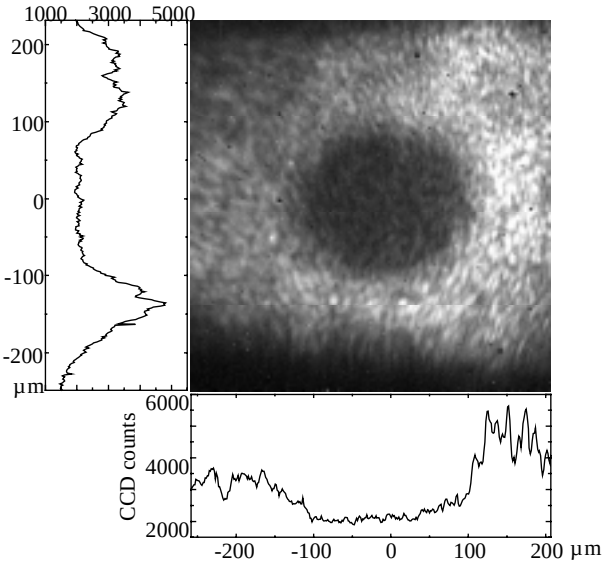

Figure 2. Typical radiograph. Probing time t=400 ps.

Results

The experimentally determined change in opacity is shown in Figure 3a) and b) for intensities of $7x10^{12}$ Wcm^{-2} or $1.1x10^{13}$ Wcm^{-2} respectively. Also shown in these figures are the results from previous single mode experiments (open symbols), which agree very well with the present results.

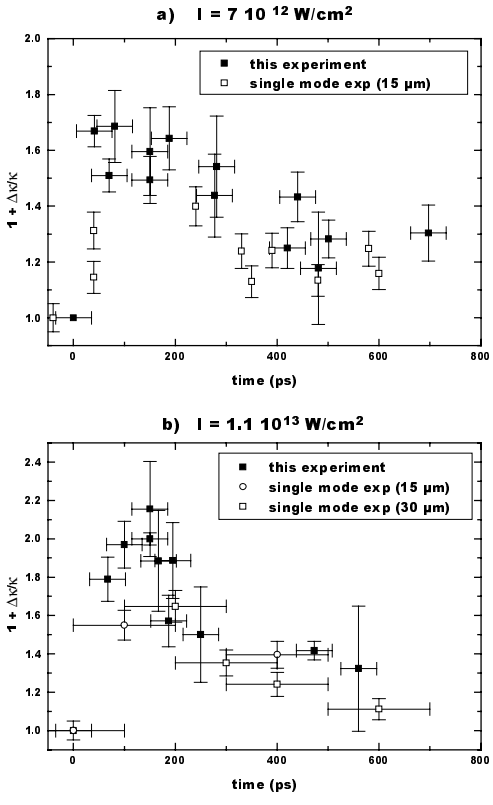

Figure 3. Relative change in opacity for a) 7 10^{12} W/cm^2 and b) 1.1 10^{13} W/cm^2.

A steep increase in the opacity can be seen at the start of the laser pulse leading to a maximum, which is consistent with maximum compression of the foil. After shock breakout the Al foil is accelerated and decompression starts at the rear side of the foil. This is reflected in the data by the rapid decrease in opacity at t = 240 ps for I = $7x10^{12}$ Wcm^{-2} and at t = 200 ps for I = $1.1x10^{13}$ Wcm^{-2}.

Experiment – Flatfield

The same 19.6 nm XUV laser was used to illuminate a 2 µm thick Al foil, which was shocked by 530 nm laser light in the geometry described above. The experimental setup is shown in Figure 4.

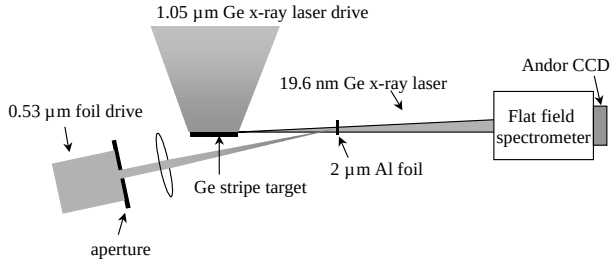

Figure 4. Experimental setup with flatfield spectrometer.

A flatfield spectrometer with a 1200 l/mm grating was placed on axis with a back-thinned Andor CCD camera as detector. The size of the detector was 28 mm by 7 mm consisting of 1024 by 256 pixel, respectively, and was placed with the long side parallel to the horizontal. This ensured that the horizontal divergence of the XUV laser was captured completely.

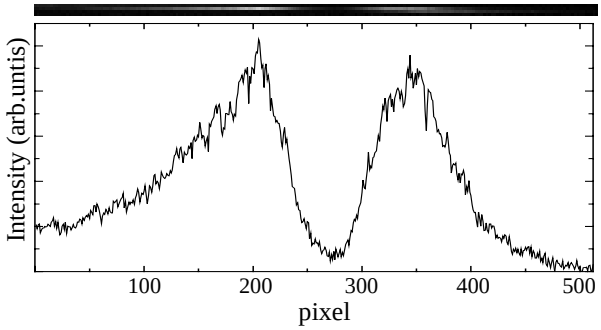

Figure 5. Spatially resolved Ge XUV laser line with the shadow of a solid 125 µm wide gold wire.

Figure 5 shows the Ge XUV laser line with a 125 µm thick gold wire placed vertically in the plane of the Al foil. The dip in intensity is clearly visible, but the XUV light is not completely blocked out. About 6% of the maximum laser intensity is detected in the center of the shadow area due to refraction effects. This introduces a rather large error, which could be avoided by imaging the horizontal plane with a gold-coated grazing incidence mirror [8].

Similarly, the shocked region in the Al foil led to higher absorption of the XUV laser, visible as a dip in the intensity. As the other dimension on the detector is the wavelength and the grating is focussing the laser light into a three-pixel wide line, the vertical spatial resolution is not available. Therefore, we had to make sure that no XUV laser light from above or below the irradiated spot could be seen by the flatfield spectrometer. To ensure this, we used a 10 x 4 mm aperture together with a 1m focal length lens to produce a spot on the Al foil, which was oblong in the vertical direction (54 µm horizontal by 136 µm vertical, FWHM). Furthermore, we reduced the entrance slit of the spectrometer to 1.5 mm. A spectrum together with its lineout is shown in Figure 6 for a probing time of 200 ps.

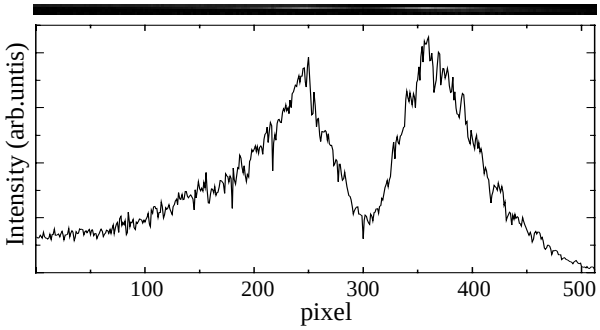

Figure 6. Spatially resolved Ge XUV laser line passing through a shocked 2µm thick Al foil. Probing time t = 200 ps.

Because the horizontal dimension of the focussed drive beam is only half as wide as the solid gold wire, the data have been evaluated assuming a 10% background due to refraction effects. The uncertainty of this estimate is expressed in the large error bars of the data points. In Figure 7 we plot the data taken with the flatfield spectrometer together with data acquired by XUV laser radiography.

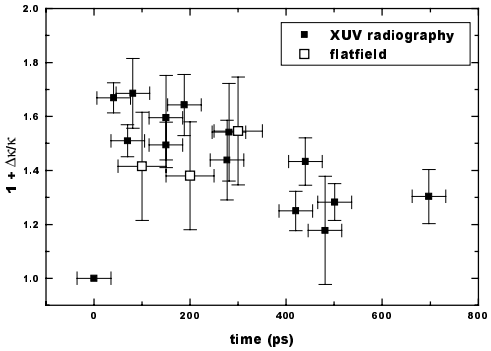

Figure 7. Comparison of experimental data for the change in opacity measured by means of XUV laser radiography (solid symbols) and with a flatfield spectrometer (open symbols).

The two data sets agree quite well with each other, showing that – in principle – it is possible to measure the change in opacity with the simpler setup.

Conclusions

Using the technique of XUV radiography we measured the change in opacity in aluminium at a wavelength of 19.6 nm due to shock compression for two different irradiances. For our conditions an increase of the opacity by up to a factor of 2 was determined. A test of a simpler setup involving a flatfield spectrometer instead of monochromatic XUV multi-layer imaging optics has been carried out, showing that the same experiments can be performed, yielding similar results. The quality of the data taken with the flatfield spectrometer is inferior, which could be overcome by imaging in the horizontal plane, thus reducing the error significantly.

References

1. M.H. Key, T.W. Barbee Jr., L.B. DaSilva, S.G. Glendinning, D.H. Kalantar, S.J. Rose and S.V. Weber. J. Quant. Spectrosc. Radiat. Transfer 54, 221 (1995)

2. D. C. A. Iglesias and S. J. Rose, Ap. J. Letts. 446, L115 (1996).

3. See e.g. S.G.Glendinning, P. Amendt, K.S. Budil, B.A. Hammel, D.H. Kalantar, M.H. Key, O.L. Landon, B.A. Remington, D.E. Desenne. In Ultra-high and high speed photography, videography and photonics '95, SPIE proceedings 2523, Publ. SPIE Bellingham, WA. p.29 (1995)

4. R.J. Taylor, J.P. Dahlburg, A. Iwase, J.H. Gardiner, D.E. Fyffe, and O. Willi, Phys. Rev. Lett. 76, 1643 (1996)

5. M.H. Kalantar, M.H. Key, L.B. DaSilva, S.G. Glendinning, J.P. Knauer, B.A. Remington, F. Weber and S.V. Weber. Phys. Rev. Lett. 76, 3574 (1996)

6. E. Wolfrum, J. Wark, J. Zhang, D. Kalantar, M.H. Key, B.A. Remington, S.V. Weber, D. Neely, S. Rose, J. Warwick, A.G. MacPhee, C.L.S. Lewis, A. Demir, J. Lin, R. Smith, G.J. Tallents. Physics of Plasmas 5, 227 (1998)

7. J. Zhang, P.J. Warwick, E. Wolfrum, M.H. Key, C. Danson, A. Demir, S. Healy, D.H. Kalantar, N.S. Kim, C.L.S. Lewis, J. Lin, A.G. MacPhee, D. Neely, J. Nilson, G.J. Pert, R. Smith, G.J. Tallents, and J.S. Wark, Phys. Rev. A, 54, R4653 (1996)

8. D. Neely, A. Damerell, R. Parker, and M. Zepf, RAL-TR-95-025, p113.

Optical Source Model for the 23.2-23.6 nm Radiation from the Multielement Germanium Soft X-ray Laser

R E Burge, X-C Yuan, G E Slark, M T Browne and P Charalambous

Cavendish Laboratory, University of Cambridge, Cambridge, CB3 OHE, UK and *Physics Department,* King's *College London, Strand, London,* WC2R 2LS, UK

C L S Lewis, G F Cairns and A G MacPhee

School of Maths and Physics, Queen's University, Belfast, BT7 1NN, UK

D Neely

Central Laser Facility, CLRC Rutherford Appleton Laboratory, Chilton, Didcot, Oxon, OX11 OQX, UK

Introduction

We are concerned with the optical properties of the J=0-l and 2-1 lasing spectral lines, particularly the 19.6nm and 23.2/23.6nm lines, using planar slab targets in the collisionally pumped neonlike germanium XXIII soft X-ray laser (XRL). We consider here, for the partially coherent J = 2-1 unresolved spectral lines at 23.2 and 23.6nm without prepulse, a description for the source size (distribution of source intensity) in two dimensions from experimental data averaged over the time period of a single pulse of radiation.

The spatial coherence properties of an XRL are usually referred to the horizontal and vertical planes. The experimental results introduced below refer to three- and four-target arrangements [1]. We add to previous data [1] results for spatial coherence in the vertical plane.

Assessing the published image data eg [2-4] the source size (FWHM) for the two J=2-1 lines without prepulse, taken with ~150μm wide line focus irradiation at the target from the driver lasers, is ~60 to ~100μm horizontally and ~200μm vertically, dependent on specific experimental conditions. The peak laser intensity for both these lines in the absence of prepulse is centred some 100 to 150μm from the target surface.

Methods of measurement of XRL beam spatial coherence have used the visibility of interference fringes from slits in a uniformly redundant array [URA, References[5]], a periodic array of pinholes [6], and we have used a series of Young slit pairs stationed at between 4 and 7 locations across the diverging laser beam [1]. Separate experiments in the horizontal and vertical directions are accomplished by rotating the diagnostic through 90 degrees. We use a method to determine fringe visibility which reduces film sensitometric errors and the errors in assessing background levels in the fringe patterns. The method is based on the Wiener-Khinchin theorem.

We use one-dimensional source models to fit separately the optical coherence properties in the horizontal and vertical directions. The interference fringe visibility $V = \frac{I_{\max} - I_{\min}}{I_{\max} + I_{\min}}$.

For equal Young slits, as in our experimental conditions the connection between central fringe visibility and the partial spatial coherence between radiation from two slits separated by distance u is given by $V(u) = |\gamma(u)|$ 1, the modulus of the complex degree of source coherence for the given slit separation. The phase of $-\gamma(u)$ can be determined by measurement of fringe displacement. Using a gaussian model the source distribution of the form $I = I_0 \exp\left(-\frac{x^2}{2\sigma^2}\right)$ the $FWHM = 2.35\sigma$ of the source can readily be calculated from the fringe visibility.

Experimental data

Experimental data from Kodak 104.02 film, each set taken in a single XRL shot using either four targets (horizontal direction [1]) or three laser targets (vertical direction) were selected, corrected for (revised) non-linearity, and made centrosymmetrical by averaging. Fringe visibility values were available for slit pairs with separations d of 100, 75, 100, 150μm horizontal [1], and 50, 100, 150, 200, 250μm, vertical, as stationed across the beam. The Young slit pairs were disposed at angular separations of 4.3mrad giving reasonable coverage across the diverging (~15 mrad FWHM horizontal, ~25 mrad FWHM vertical) XRL beam.

In our previous study of spatial coherence in the horizontal direction for four targets [1] only the central visibility values were considered; here we consider the full intensity distributions. Because of flux limitations in the diverging laser beam the slits to film separation z corresponded formally to far-field conditions $\left(z > 2d^2/\lambda\right)$ only for d=75μm.

Patterson (autocorrelation) functions

The intensity distribution in a slit diffraction pattern (power spectrum), and its Fourier transform (FT) (autocorrelation function), are related as Fourier pairs by the Wiener-Khinchin theorem. The Wiener-Khinchin theorem is a general relationship, but in far-field conditions the FT of the diffracted intensity is equivalent to the Patterson function of x-ray crystallography. The Patterson function provides the autocorrelation function in the plane of the Young slits.

The Patterson function $P(u)$ relates to the plane of the Young slits, spatial coordinate u. Let the slit transmission function be $T(u)$ with two equal slits of width a and centre to centre separation d. We will show below that for four target data the experimental results for d=75, 100, 150μm are all sufficiently close to far-field conditions to justify the use of the Patterson function to describe the x-ray transmission in the slit plane. $P(u)$ represents the average product of the transmission between points separated by a chosen distance. Neglecting constants of proportionality:

$$P(\upsilon) = \int_0^d T(\omega)T(\omega + \upsilon)d\omega \quad (1)$$

Peaks in the Patterson function are expected at the origin, u = 0, corresponding to the sum of the products of the transmission of each slit with itself, and at u = ± d, the slit separation. For equal slit widths the peak at u = ± d will have width 2a, measurements of the slit separation and slit width axe thus separated.

For equal slits in partially coherent radiation, the fringe visibility is a function of t, $V(t)$ where t is the time difference at a point Q on the recording plane between waves initially in phase at the two slits. The general expression [7] for the scattered intensity at point Q where the separate slits produce

respectively transmitted intensities I_1 and I_2 in monochromatic light, may be written as the sum of two terms. One term describes the coherent superposition of two beams of intensity $V(t)xI_1$ and $V(t)xI_2$ producing intensity modulation due to interference in accordance with the phase difference. The other term is due to the incoherent superposition of two beams of intensity $(1-V(t))xI_1$, and $(1-V(t))xI_2$. The coherent intensity, with fax-field fringes of 100% visibility within the limits of a constant value for the visibility, is revealed by an inverse Fourier transform using the central Patterson peak (only) with fractional weight V together with the Patterson peak at u = ± d. The incoherent intensity corresponds to an inverse transform of the remaining part $(1-V)$ of the energy of the central peak only.

A more practical way to optimise V from a curve of coherent diffraction was found to vary V until the fringe visibilities were closest to 100% over the full angular range.

Experimental and calculated Patterson distributions Horizontal direction (four target data)

Patterson functions axe compared in Figure 1 (a-d). Model calculations were made for both z=0.58m (the experimental slits to film distance) and z=3m, and are indistinguishable except for d=150μm which is furthest away from the farfield condition. The Patterson features are as expected. The general level of agreement between experiment and model intensity calculations is good.

Slit separation (μm) Nominal/Fitted	100/92	75/73.5	100/92	150/138
Visibility (%) fitted	64	76	78	77
FWHM (μm) (± 2μm)	52	52	39	26
Angular deviation from maximum intensity (mrad)	-4.3 →	~0 increasing	+4.3 refraction	+8.6

Table 1. Model FWHM values and visibility values: four target data

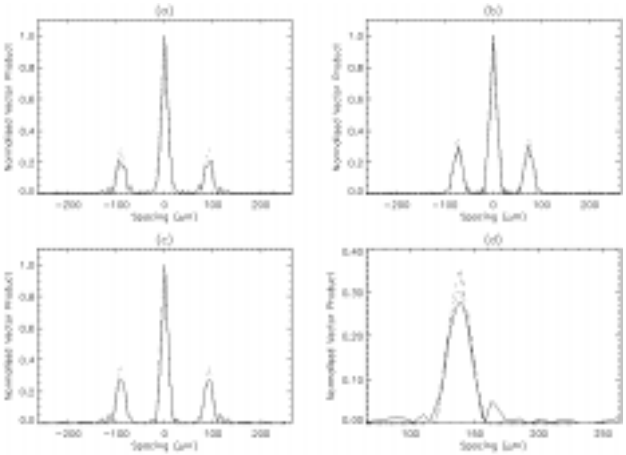

Figure 1. Patterson vector products across the angular range compared between theory and experiment (four target data). (a) to (c) respectively correspond to slit separations of 100, 75, 100 μm. (d) shows an expanded version of the principal Patterson peak for the nominal slit separation of 150 μm. Wavelength 23.3 nm. Full line experiment. Near-field calculation, z=0.58m, dotted. Far field calculation, z=3m, dash dot.

Using initially the central fringe visibility values to divide the energy in the central Patterson peak, the separated fringe intensity distributions for the coherent and incoherent components were adjusted by varying V to show good agreement when compared respectively in Figure 2(a,b) for experimental and model data for the 75μm slit separation and correspondingly for the 150μm separation in Figure 2(c,d). The parameters are given in Table 1. The values of V, following the fitting procedure, differed from the central fringe values by up to 5%.

The visibility values of the fringes in the coherent intensity component are not all 100% on moving outwards from the pattern centre in both experimental and model data due to near-field effects.

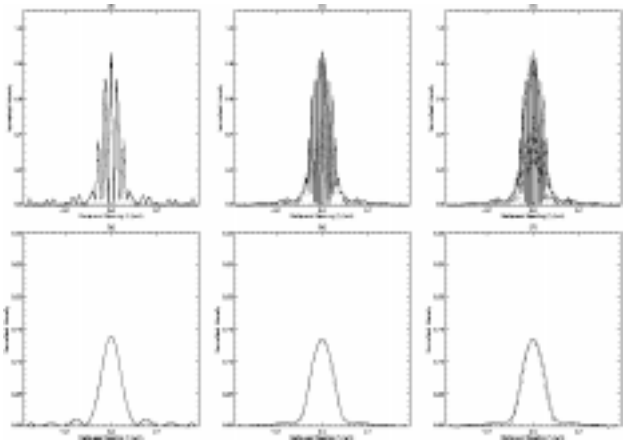

Figure 2. Separated near-field (z=0.58m) experimental (full line) and theoretical (dotted line) coherent and incoherent intensity components for four target data and slit spacings d= 75μm (a,b) and 150μm (c,d), vertical axes are normalised intensities, horizontal axes reciprocal spacings in μm^{-1}.

The incoherent components equivalent to the slit form factors from the experimental and calculated (slit width = 18 μm) data, were obtained by Fourier-inverting only the scaled central peak of the Patterson function.

It is known that the two interfering XRL beams from the slits have a complex space-time structure, which may not, on average, produce uniform slit illumination. This may be the explanation for the differences in the shapes of the Patterson peaks in Figure 1.

Vertical direction (three target data)

The experiments on the vertical source size were done at separate times from those in the horizontal direction, with similar laser pump energies and laser focus but with different configuration of the laser target [1)] and with different diagnostics, but the same nominal source width. These data, for the three target case, included interference fringes from six independent patterns for d = 150μm spread over the angular range of the vertical beam divergence. The close constancy of the fringe visibility, despite strong intensity variations across the beam, indicates a constant source size unlike in the horizontal plane. The three target data at the pattern centre, with a fringe visibility of 25%, have an intensity minimum rather than a maximum. This indicates [7)] that the dependence at the slit plane on point to point separation of the modulus of the complex degree of coherence passes through a zero value at a slit separation of less than 150μm. This may be understood as being due to the argument of $|\gamma(u)|$ flipping from zero to π at the zero of the modulus causing a reversal of the fringe contrast.

A satisfactory fit, (Figure 3) of the time-averaged data to a simple model came from a uniform source of length 125μm. The sign of the complex degree of coherence alternates from loop to loop of the transform, being positive at small slit separations and for high fringe visibility.

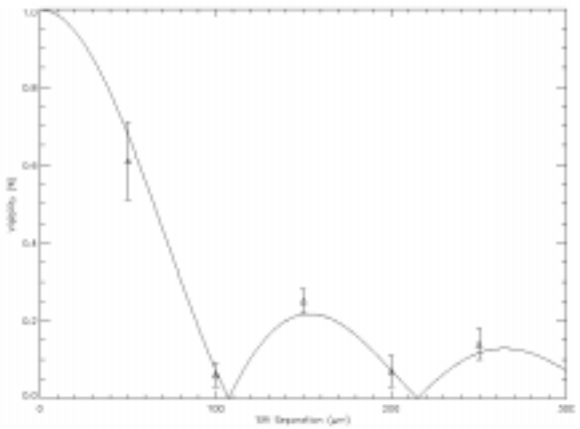

Figure 3. Experimental (points) and model visibility values for slit separations in the three target case (vertical source distribution). Source to slit distance 580 mm, slit to film distance 650 mm. Calculations for wavelength 23.2 nm.

A comparison between the experimental interference fringes for the 150μm slit separation and fringes calculated from a source model with a uniform source 125μm long is shown in Figure 4(a). The fit of the near-field intensities is good. Also shown are the Patterson function (4(b)) and the separate coherent and incoherent intensity distributions (4(c,d) respectively). The experimental and model Patterson functions are closely similar. As expected the Patterson functions display only a central peak and two symmetrical peaks at ±150μm each ~40μm wide. Accounting for noise, the agreement is good between the incoherent patterns l(b,d) and 4(d) for similar slit widths; the non-zero minima are near field effects.

Conclusions

Spatial coherence measurements for a four target X-ray laser in the horizontal direction show variations in apparent source size with beam angular divergence. In the vertical direction, for a three target source with similar excitation to the four target source, the spatial coherence is consistent with a uniform source and is constant across the diverging laser beam.

Table 1 shows for the four target configuration a smallest source size in the horizontal direction at the maximum measured refraction of 26μm, revised from 33μm [1)], which is the same value corresponding to the same model at similar high refraction for the three target system [1)]. This value is considerably smaller than that found by direct imaging. Our results give the source dimension in the vertical direction for the three target system as 125μm, closely similar to the width (~120μm) of the line focus of the driver laser as also used in the four target case, generally consistent with direct imaging.

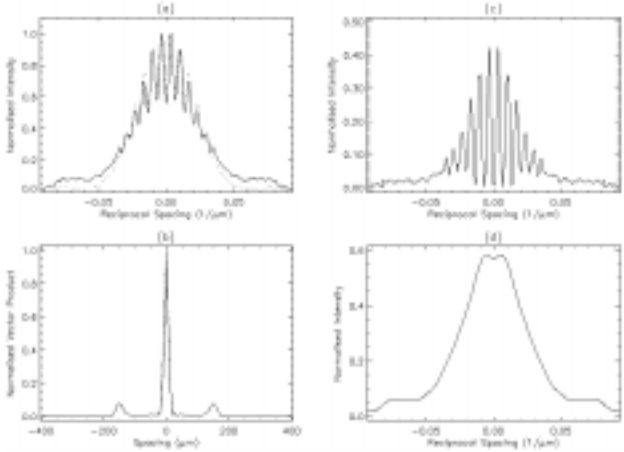

Figure 4. (a) Experimental fringe intensity distribution for three target data (full line) for slit separation 150μm superimposed on calculated (dotted) distributions for a uniform source 125 μm long. (b) Patterson functions calculated from the two near-field curves of Figure 4(a). (c) Coherent intensity distribution corresponding to experimental diffraction from Young slits. (d) Experimental incoherent intensity distribution. (c,d) in near field conditions.

Acknowledgements

We are grateful to the EPSRC for access to the Vulcan laser at the Rutherford Appleton Laboratory and to the Leverhulme Trust and the Royal Society for financial support.

References

1. R E Burge, G E Slark, M T Browne, X-C Yuan, P Charalambous, X-H Cheng, C L S Lewis, G F Cairns, A G MacPhee, and D Neely J.Opt.Soc.Am. B 15, 2515 (1998).

2. P B Holden, S B Healy, M T M Lightbody, G J Pert, J A Plowes, A E Kingston, E Robertson, C L S Lewis and D Neely J. Phys. B 27, 341, (1994).

3. J C Moreno, J Nilsen, Y Li, P Lu and E E Fill Optics Lett. 21, 866, (1996).

4. Y Li, G Pretzler, E E Fill and J Nilsen J. Opt. Soc. Am. 13, 742, (1996).

5. J E Trebes, K A Nugent, S Mrowka, R A London, T W Barbee, M R Carter, J A Koch, B J MacGowan, D L Matthews, L B Da Silva, G F Stone, and M D Feit Phys. Rev. Lett, 8, 588, (1992).

6. Y Kato, M Yamanaka, H Daido, H Shiraga, H Azuma, K Murai, G Yuan, E Miura, T Kanabe, M Takagi, S Nakai, C L S Lewis, D M O'Neill, D Neely, M Niibi, N Tsukamoto and Y Fukuda in X-ray Lasers 1992, E E Fill ed, 125, of Institute of Physics Conference Series (IOP, Bristol, UK, 1992), 9.

7. M Born and E Wolf Principles of Optics (Pergamon, Oxford 1993) Chap 10.

Saturated X-ray lasers at 196Å and 73Å pumped with CPA travelling wave excitation

A G MacPhee, C L S Lewis, R Keenan, R M N O'Rourke

School of Mathematics and Physics, Queen's University of Belfast, Belfast BT7 1NN, UK

G J Tallents, S J Pestehe, F Strati

Department of Physics, The University of Essex, Colchester CO4 3SQ, UK

G J Pert, S P McCabe, P Simms

Department of Physics, The University of York, Heslington, York YO1 5DD, UK

D Neely, R Allott

Central Laser Facility, CLRC Rutherford Appleton Laboratory, Chilton, Didcot, OXON OX11 0QX, UK

Main contact email address: *a.macphee@qub.ac.uk*

The efficiency of pumping soft x-ray lasers based on a laser-produced plasma medium has increased by more than 3 orders of magnitude in the last decade through a combination of novel experimental design and detailed theoretical modelling guidance [1,2]. Scaling to shorter wavelength operation has been achieved through the use of higher Z targets allowing the efficient operation of Ni-like, as well as Ne-like ion XRLs [3]. Pre-formed plasmas and curved targets have been among the principle experimental techniques which have had a major impact on these recent achievements in the development of X-ray lasers. A new and significant advance in the field has been the demonstration of transient gain in neon-like ions at the Max Born Institute in Berlin [4]. This technique has subsequently been developed and extended to nickel-like ions at the Rutherford Appleton Laboratory [5,6], at LLNL and at LULI. Here we report demonstration of a travelling wave pumping technique which enables us to achieve saturated output intensities at the shortest wavelength to date[7], pumped in the very efficient transient gain mode.

The transient gain scheme decouples the two main phases in generating inversion and gain [8]. A long pulse is used to produce and ionise a plasma of desired atomic composition as before, but it does not have to heat the plasma to high temperature. The temperature reached is just sufficient to produce a large fractional abundance of the required ionisation stage, which is usually neon-like or nickel-like, but is too low to cause significant excitation of the upper laser levels. The plasma is allowed to expand hydro-dynamically to a point where the correct ion stage is located in a region of optimum electron density (usually 1-6x10^{20} cm^{-3}) and minimum possible density gradient. At this point the population inversion is pumped by injecting an ultra-short pulse of picosecond duration and at high intensity (e.g. up to 2x10^{15} W/cm^2) into the pre-prepared plasma. This raises the electron temperature very rapidly to values in excess of a kilovolt and leads to transient collisional excitation (TCE) and extremely large values of gain coefficient. Typical simulations for both Ne-like and Ni-like ions indicate gain coefficients in excess of 100 cm^{-1} are achieved on picosecond timescales and only before the system equilibriates through collisional mixing and ionises [9]. The penalty paid in this scheme is that the short-lived gain duration, T_G , means the amplifier length cannot be longer than about cT_G, unless a travelling wave pump is used to keep the excitation in phase with the amplifying group of photons. Saturation of output may be achieved with relatively short (several mm) amplifier lengths. This leads to bright XRL output with picosecond duration pulses and a pump requirement that is modest in terms of both the nsec and psec drive pulses.

In this experiment the picosecond pump pulse, with energy up to ~50 J, is generated in the Vulcan laser amplifier chain using chirped pulse amplification (CPA) technology [10]. Guided by simulations, the basic pumping scheme had three laser pulses. Two 280 ps FWHM Gaussian pulses with average intensity ~10^{12} Wcm^{-2} (first pulse) and ~10^{13} Wcm^{-2} (second pulse) and separated by 2ns were used to prepare the pre-formed plasma. The third pulse was <3 ps FWHM, at intensity >10^{15} Wcm^{-2} and arrived to interact with the pre-formed plasma during the trailing edge of the second pulse. Each pulse was focussed to a common line focus of ~100 μm width and ~12 mm length. Targets were made from either Ge or Sm evaporated onto polished glass substrates with length ranging from 1 mm up to 9 mm and were centred in the line focus. All three pulses were derived from the same YLF oscillator. The CPA pulse was stretched, amplified and then compressed prior to entering the target chamber. The 280 ps heating pulses were split from the CPA line after stretching, diverted to an alternative amplifier chain and then directed into the target area. This eliminated jitter in the arrival time of the three laser pulses on target.

To achieve pumping with the picosecond pulse in an excitation wave travelling at the speed of light, c, it is necessary to tilt the wavefront of this beam so that it intercepts the target plane at 45° and there are a number of ways to do this. The method adopted at RAL for travelling-wave pumping combines the intrinsic tilt in the wavefront inherent to the off-axis focussing optics used and an additional component introduced using a diffraction grating [12,18]. Without the diffraction grating, the intrinsic travelling wave speed was 2.9c and we henceforth refer to this condition as the non-travelling wave mode. For Ge the intrinsic non-travelling wave pulse length was (1.0 ± 0.2) ps but was (2.7 ± 0.2) ps when the travelling wave was introduced. For Sm, the pulse length was (0.8 ± 0.2) ps for non-travelling wave mode and (1.0 ± 0.2) ps for travelling wave mode. The difference in pulse length was due to different degrees of optimisation of the pulse stretcher and its correction to compensate for the travelling wave grating dispersion.

Two grazing incidence, flat-field spectrometers with 16-bit, back-thinned CCDs [11] recorded the soft X-ray signal from the plasma. The spectrometers were mounted axially to observe the X-ray laser signals emitted in both the preferred, travelling wave direction (N end) and in the opposite direction (S end). Uniformity of the pump laser heating along the target was monitored by two space-resolving Bragg crystal spectrometers. All observed X-ray lasing action was initiated by the CPA pulse since the pre-plasma alone could not generate enough gain to produce a detectable output at the lasing wavelength.

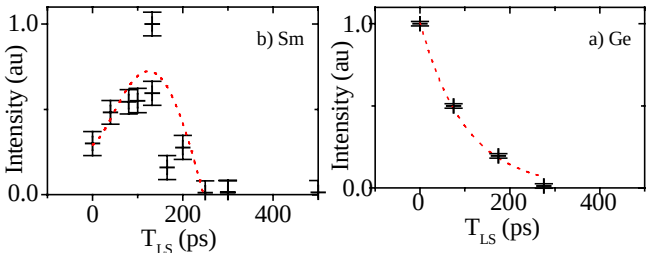

Figure 1. XRL output dependence on arrival time,TLS, of short CPA pulse relative to peak of long pulse for 9 mm targets. (a) Ge (196Å) ; (b) Sm (73Å).

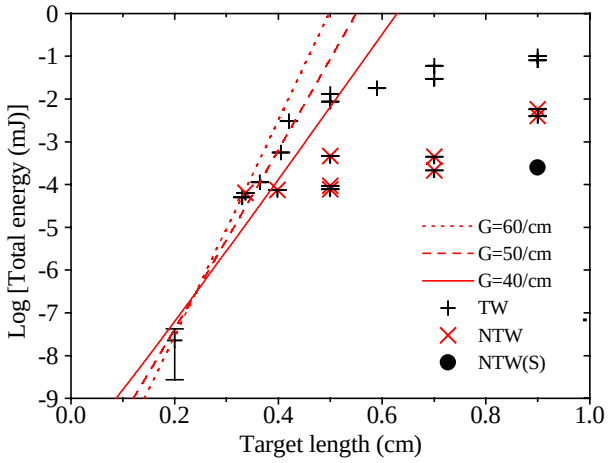

Figure 2. Experimental data showing growth curve for 196Å Ge signal with SSG >40cm^{-1} leading to strongly saturated output of ~0.1mJ when pumped with travelling wave (V=c). For non-travelling wave (V=2.9c), outputs at each end of target (N and S) are consistent with a gain duration of ~10ps.

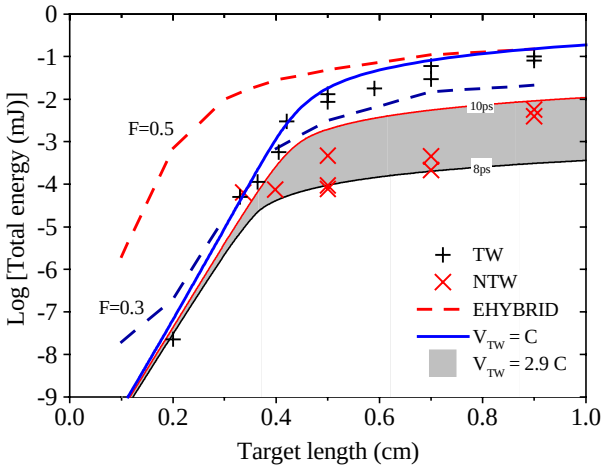

Figure 3. Model fits to Ge data. Dotted lines refer to absolute output from RAYTRACE code, post-processing EHYBRID code. Solid line (TW) is from analytical model with α_0 = 50cm^{-1} and normalised to F=0.5 at 9mm. Shaded area is for NTW with gain duration times from 8ps (lower bound) to 10ps.

A sequence of shots on 9mm long Ge targets was taken to determine the optimum delay, T_{LS}, between the main long pulse and the short pulse with the travelling wave switched on. The CPA pulse intensity was ~1.5×10^{15} Wcm^{-2}, the main long pulse intensity was ~5×10^{12} Wcm^{-2} and a 10% pre-pulse arrived 2 ns early. The intensity and position of the pre-pulse were fixed for the Ge data set and therefore not necessarily optimised. The X-ray laser signal from the system as a function of T_{LS} is shown in Figure 1, but no measurements were made for settings where the CPA pulse arrived before the peak of the long pulse. It is possible therefore that a more efficient system could have been produced, requiring less energy in the long pulse drive beam.

The two data sets in Figure 2 represent the X-ray laser output measured under travelling wave and non-travelling wave conditions with T_{LS}-80 ps and the absolute energy scale, based on best estimates of grating efficiency, CCD quantum efficiency and filter transmission, is believed to be systematically accurate to better than a factor of two. The signal growth curves are similar for short target lengths but diverge for $\ell \geq$ 3.5mm. The X-ray transit time for a target of ~3.5 mm length is therefore characteristic of the duration of gain on the transition and hence we infer that the gain duration is ~10 ps. Figure 2 also shows analytic growth curves based on the Linford formula [12] for a range of small signal gain coefficients, indicating that the peak gain coefficient achieved is >40 cm^{-1}. The total output energy from the 9 mm target was ~100 μJ and was determined by integrating over solid angle using the angle-resolved CCD signal, as illustrated later in Figure 4b, and assuming similar vertical beam divergence. With a 10 ps XRL pulse length and an exit pupil aperture of dimensions 25 μm horizontal and 55 μm vertical (taken from simulations using the 1.5D, fluid and atomic code EHYBRID [13]), this corresponds to an intensity in the plasma of ~7 x 10^{11} Wcm^{-2}, which is well into the saturated regime [14]. Parameters calculated numerically within EHYBRID such as the gain recovery time and the transition linewidth indicate that the saturation intensity is ~2 x 10^{10} Wcm^{-2}. This is in very close agreement with an estimate derived from Figure 3 when the derivative of a fourth order polynomial fit to the travelling wave data is used to locate the point where the small signal gain coefficient is reduced to half its peak value. The saturation intensity is reached with a target of ~4.5 mm length. Measurements made on the South flat-field spectrometer in the counter-propagating direction to the travelling wave showed negligible output of the X-ray laser line, as would be expected for a ~10 ps duration gain period. The S-channel had ~1/8 the sensitivity of the N-channel and the only measurable signal was for a 9 mm target irradiated in the non-travelling wave mode. This corresponded to ~5 % of the nearly saturated output observed on the N-channel for the same shot and is consistent with expectation. We can note that for simultaneous pumping along the target length (i.e. infinite travelling wave speed) we expect N and S outputs to be the same and independent of length for $\ell \geq$ 3 mm and that the output for $\ell \leq$ 3 mm is not sensitive to the travelling wave speed.

The experimental data has been compared to outputs from both numerical simulations and simple analytical models, as illustrated in Figure 3. The numerical simulations derive from a 3-D raytrace post-processing the inhomogeneous space-time output of the 1.5-D fluid and collisional-radiative atomic code EHYBRID [2,13]. The RAYTRACE code, which includes saturation effects, simulates the travelling wave case by assuming the peak gain conditions are presented at all times to the propagating pulse. The code predicts a gain duration of ~10 ps FWHM. It is important to note that the absolute energy values from the numerical model and best estimates from experimental measurements are derived independently and show very good agreement in the long target travelling wave case. The EHYBRID code has been very successfully used before to simulate soft XRL action in the QSS regime with long pulse drive, where it was found necessary to use a correction factor F=0.5 to multiply the actual incident laser energy to account for unmodelled energy loss channels in the absorption process [15]. For the present TCE case, where interactions are at intensities ~100X higher, we find that a corresponding factor F=0.3 gives a better fit to data in Figure 3, mainly by reducing the source function and the peak gain coefficient. Also shown in Figure 3 are the scalings from a simple analytical model [16] which tracks a single ray through a homogeneous gain medium with specified constant gain coefficient, α_0, and gain duration, T_G, where the region of gain travels in the ray direction at a speed $V_{TW} \geq c$ [17]. The ratio of the saturation intensity to a variable spontaneous emission intensity is a free parameter but both are fixed, along with α_0, by fitting to the travelling wave (V_{TW} = c) data and normalising to numerical output for the 9 mm case. Keeping these parameters fixed, the non-travelling wave output (V_{TW} = 2.9c), which is now sensitive to T_G, is calculated as shown in Figure 3. The plots indicate that the gain duration is T_G = 9±1 ps, in reasonable agreement with the numerical model.

Having established the effectiveness of the travelling wave pump we shot Sm coated targets in this mode but at ~2X higher pump intensity. Although initially guided by modelling which also used a prepulse we found that, for Sm, a 10% pre-pulse on

the long-pulse beam-line damaged the conditions for gain at 73Å, typically reducing the potential output by a factor of ~3. Our transient gain data for the travelling wave pumped Ni-like Sm X-ray laser was produced using a single 280ps heating beam and a single CPA beam. The arrival time of the CPA pulse relative to the peak of the long pulse was optimised as shown in Figure 1(b), by taking a sequence of shots with different delays on the long-pulse beam-line. The optimum pulse separation was found to be ~130ps. A further sequence of shots was taken to measure the gain coefficient at the optimum pulse separation as shown in Figure 4(a). A gain coefficient of ~19 cm^{-1} was measured for this transition. The maximum integrated XRL output energy for the 73 Å Sm laser was ~1.5μJ and based on modelling parameters this corresponds to an

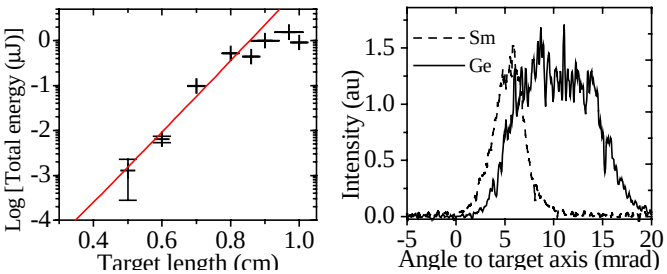

Figure 4. (a) Growth curve for Sm at 73Å with SSG ~19cm^{-1} shown by Linford fit. (b) Horizontal angular distributions for outputs from 9mm targets of Ge and Sm.

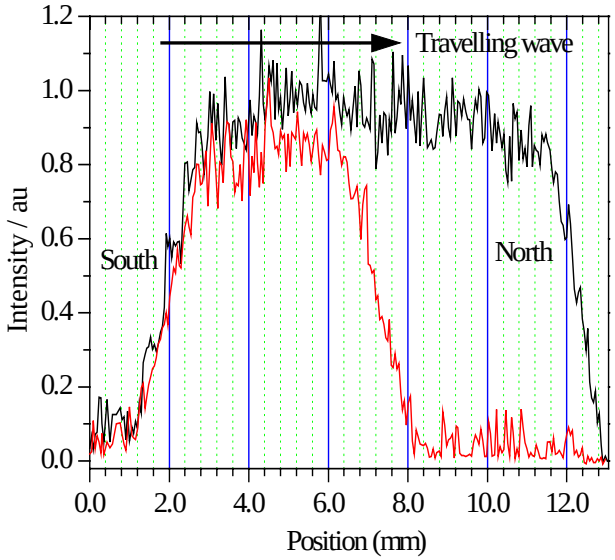

Figure 5. Time integrated Ni-like 3p-4d emission at ~1.5keV as a function of position for 5mm and 9.7mm Sm slabs.

output intensity of ~10^{10} Wcm^{-2}. It should be noted that saturation might have been achieved with the longest Sm targets, as the rolling over of the signal at about 9 mm was not due to reduced CPA heating pulse intensity at the end of the target. This is illustrated in Figure 5 which shows line-outs of the Ni-like 3p-4d emission from 5mm and 9.7mm Sm targets. The slope at the edges of both data sets corresponds to the instrument slit. No signals were detected from Sm targets on the South flat-field spectrometer, again confirming the effectiveness of the matched travelling wave pump. Figure 4(b) shows typical angle-resolved line-outs from the North flat-field spectrometer for 9mm Ge and Sm targets with travelling wave. Compared to the Ge data, the Sm laser has much reduced divergence and refraction. This is expected, due to the reduced refraction effects at the shorter wavelength.

To conclude, saturated operation of Ne- and Ni-like X-ray lasers pumped by ~1 ps laser pulses in the transient collisional excitation regime has been demonstrated with a travelling wave pump. Transient gain at 196 Å was confirmed by observation of both forward and backward XRL beams from a Ge plasma under ideal and non-ideal travelling wave conditions. A gain coefficient of >40 cm^{-1} at 196 Å was produced, sufficient to saturate the $2p^5_{1/2}3p_{1/2}$ J=0 to $2p^5_{1/2}3s_{1/2}$ J=1 transition in a target ≥5 mm long. The overall behaviour was shown to be consistent with numerical and semi-analytical modelling. When Ni-like Sm targets were pumped under optimised travelling wave conditions, a small signal gain coefficient of ~19 cm^{-1} was observed at 73 Å on the $3d^9_{3/2}4d_{3/2}$ J=0 to $3d^9_{5/2}4p_{3/2}$ J=1 and saturation effects were observed for targets ≥8 mm long. This lasing is at approximately double the photon energy previously observed in transient pumping and is a direct consequence of a true travelling wave pump.

References

1. J Nilsen *et al*
Phys. Rev. A 48, 4682 (1993).

2. J A Plowes, G J Pert and P B Holden
Opt. Commun. 116, 260 (1995); Opt. Commun. 117, 189 (1995); J A Plowes et al Opt. Quant. Elect. 28, 219 (1996).

3. J Zhang *et al*
Phys. Rev. Lett. 78, 3856 (1997); Science 276 , 1097 (1997).

4. P V Nickles *et al*
Phys. Rev. Lett. 78, 2748 (1997).

5. M P Kalachnikov *et al*
Phys. Rev. A 57, 4778 (1998).

6. P J Warwick *et al*
J. Opt. Soc. Am. B 15, 1808 (1998).

7. A G MacPhee *et al*
Submitted to Phys.Rev.Lett. May 1999

8. Yu V Afanasiev *et al*
Sov. J. Quantum Electron. 19, 1606 (1989); V.N. Shylaptsev *et al.*, Proc. SPIE 2012, 111 (1993).

9. S B Healy *et al*
Opt. Commun. 132, 442 (1996); J. Nilsen, Phys. Rev. A 55, 3271 (1997).

10. C N Danson *et al*
in *Superstrong Fields in Plasmas*, edited by M. Lontano, G. Mourou, F. Pegoraro, and E. Sindoni, AIP Conf. Proc. 426, 473 (1998).

11. Andor Technology Ltd, 9 Millennium Way, Springvale Business Park, Belfast T12 7AL, Northern Ireland.

12. G J Linford, E R Peressini, W R Sooy and M L Spaeth
Appl. Opt. 13, 379 (1974).

13. G J Pert
J. Fluid Mech. 131, 401 (1983).

14. L B Da Silva *et al*
Optics Lett. 18, 1174 (1993).

15. P B Holden *et al*
J. Phys. B 27, 341 (1994); G.F. Cairns *et al.*, 29, 4839 (1996).

16. F Strati *et al*
"Traveling wave effects on short pulse pumped x-ray lasers", this report.

17. P J Warwick and C L S Lewis
Central Laser Facility Ann. Rept. RAL-TR-97-045 [ISBN 0902376705], 99 (1998).

Preliminary Investigations into Non-linear Optics with X-Ray Lasers

R M N O'Rourke, R Keenan, C L S Lewis, A G MacPhee, B Moore

School of Mathematics and Physics,The Queen's University of Belfast, Belfast BT 7 1NN, Northern Ireland.

S Dobosz, G Tallents,

Department of Physics, University of Essex, Colchester CO4 3SQ.

A Djaoui, D Neely,

Central Laser Facility, CLRC Rutherford Appleton Laboratory, Chilton, Didcot, Oxon, OX11 0QX, UK

E W Wolfrum,

Clarendon Laboratory,University of Oxford, Oxford OX1 3PU.

Main contact email address: *r.orourke@qub.ac.uk*

Introduction

Following on feasibility studies[1,2] into the subject, experimental exploration began in January 1999. The initial experiment, carried out in target area east of Vulcan, was to exact preliminary tests on the viability of a four wave mixing process. This scheme involved the combination of two XRL photons at 23.12 nm from Ne-like Ni with one optical photon at 1.06 µm in a Na-like Ar plasma to give an output at near the second harmonic of the XRL input. This article aims to outline some of the uncertainties which faced us prior to the experimental run and the progress made into understanding the best way in which to approach the experiment in the future.

Pre-experiment modelling

Modelling of the susceptibility has been dealt with extensively elsewhere[1,2,3,4]. The composition of the ionised gas jet, and the irradiation conditions needed to get it to the required Na-like state were assessed using MED 103 in planar geometry. Initially an inspection was performed to assess the temporal stability of the desired ionisation stage for a particular atom density and various input intensities. Results shown below, Figure 1, indicate that for an electron density of 10^{19} cm^{-3} with a 100 ps pulse, one should aim for laser intensity in the region of 10^{13} to 10^{14} W cm^{-2} incident on the gas jet. Plots are against time and the ionisation stages are relatively uniform across the spatial extent of the plasma.

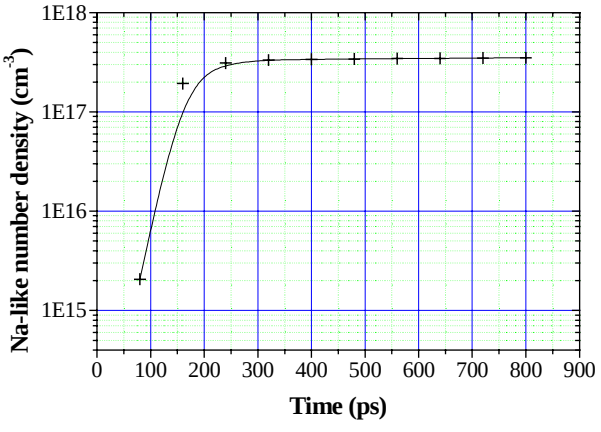

Figure 1. Modelling of mixing medium.

This would result in ionisation to a sodium-like state between 300 and 500 ps after the heating pulse is turned on. At this time the temperature of the plasma is in the region of 20 to 25 eV, allowing a reasonable population of the 3p level in the Na-like ions (the base from which the process is defined to start). An extensive scan was performed to create a matrix of data incorporating irradiance level, atom density and ionisation stage population. These results are shown in Figures 2 and 3 and indicate the regions of interest where one should aim to work in order to maximise the sodium-like number density. All of the data shown in these two figures are taken as a snapshot at 400 ps after the heating pulse has been switched on.

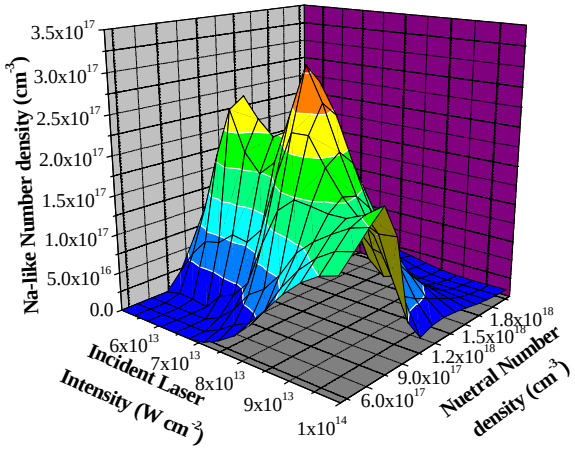

Figure 2. 3-D surface colour map of MEDUSA results.

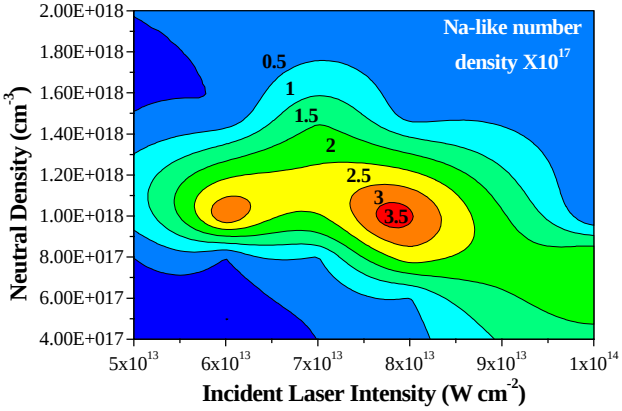

Figure 3. Contour map of MEDUSA output.

Issues to be resolved in the experiment.

Could we produce a reliable Ne-like Ni XRL? Could the XRL be driven into saturated operation? If driven to saturation, what output power could we achieve?

Would there be a problem with the pumpdown of such a large volume (as in Figure 4 below)? Would using extra pumps cause unfavourable vibration affecting the alignment of the system?

How would we monitor the ionisation stage of the gas jet?

Would we be able to split the XRL to provide the two beams required for phase matching?

How would we align the split beamlets back into the gas jet some 2 m away to tens of microns accuracy?

Would the optical mixing beam destroy the glass splitting plate as it focused into the jet?

Would the self-emission of the gas jet swamp out the non-linear signal?

Experiment and Results.

A schematic of the experiment is shown in Figure 4. The Ne-like Ni XRL was created using the five sided illumination technique with standard pulse lengths of 100 ps and a line focus of 100 µm by up to 35 mm. The gas jet was prepared by a line focus using cylindrical optics which provided on target intensities of up to 5 x 10^{14} Wcm^{-2}. The remaining beam from the main six was focused down and used as the mixing beam thus eliminating arrival time jitter with respect to the XRL beams. On exit from the target the XRL was split in two by a Lloyds mirror arrangement. The split beam was incident on one

We could not analyse the ionised jet in the same way, since the damage threshold of the interferometer did not allow a probe beam with sufficient brightness. A preliminary attempt to measure ion number density distributions within the gas jet using a Dy target backlighter in a point projection spectroscopy (PPS) set-up failed due to a dominant self-emission signal.

As a result we had to rely on the emission spectroscopy as the sole diagnostic for the gas jet. Some typical spectra from the emission spectrometer from which Na-like resonance lines can be detected are shown in Figure 6. The analysis does not however give us an actual ion density as the PPS would have.

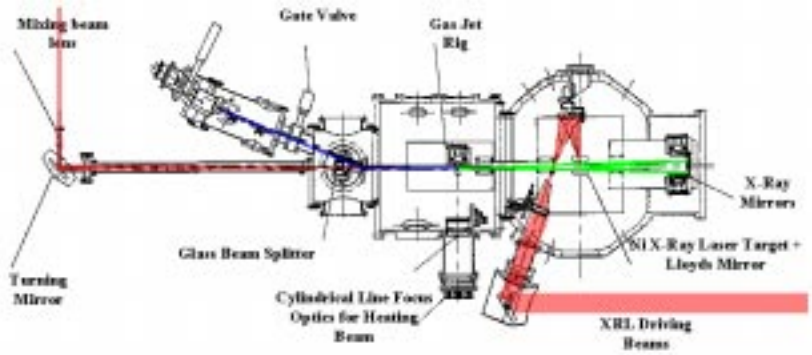

Figure 4. Experimental schematic.

50 mm diameter, 1 m ROC x-ray multilayer mirror and focused into the gas jet (by this time a plasma of Na-like Ar). In the plasma the mixing of the 2 XRL photons with one Nd:YAG occurred. The output would then travel along the axis to the beam splitter, which redirects it to the flat field spectrometer for detection. The use of one XRL mirror minimised uncertainty in the alignment of the split beams into the gas jet, which was 2 m downstream of the exit plane.

The Mixing Medium

The experiment began with an investigation of the gas jet. We used a Normarski interferometer to analyse the neutral density of the gas jet. Our analysis of the neutral atom density was consistent with that of previous experiments carried out using Nitrogen. Shown below in Figure 5 is an interferogram taken at the operating pressure during the experiment (20 bar). The accompanying graph outlines the density distributions from the nozzle tip outward. The image is of a 1.3 mm circular gas jet nozzle used in the experiment.

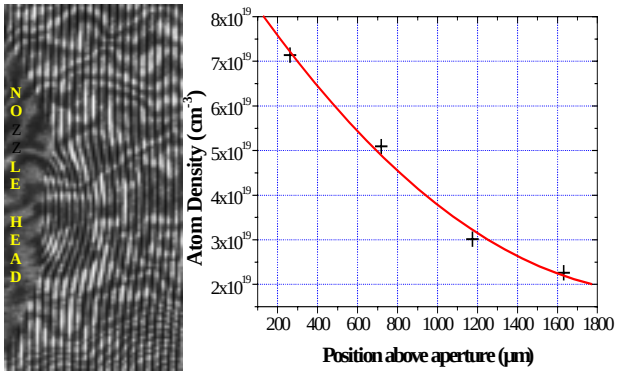

Figure 5. Gas jet interferometry.

In short, to operate in the region we required (electron density below 10^{20} cm^{-3}, to avoid refraction of the optical beam) the gas jet must be set 2mm below the mixing plane and at a reservoir pressure of 20 bar. This was extrapolated from the data, as we did not have a wide enough window to see 2 mm from the tip at this magnification.

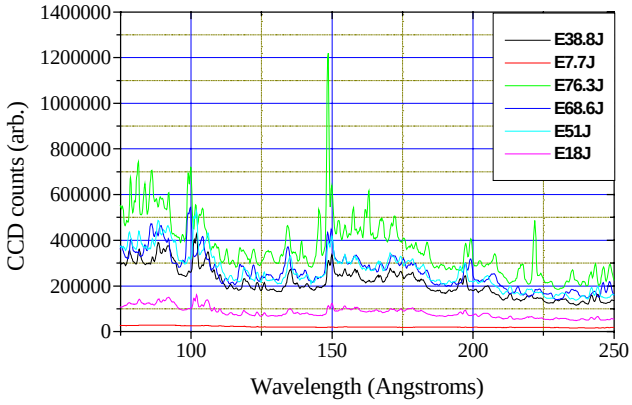

Figure 6. Typical emission spectra.

Attempts to streak the output from the emission spectrometer were unsuccessful, due to the gas jet causing cathode grid flashover prior to the ionisation of the gas jet.

The Ne-like Ni X-ray laser

We compared slab and stripe targets of Ni. The slabs were found to be reliable, though output did vary with quality of finish.

One obvious advantage with the slabs is that the chamber does not need to be let to air for several shots. In this run up to 6 shots per pumpdown were possible, limited by the design of the target mount.

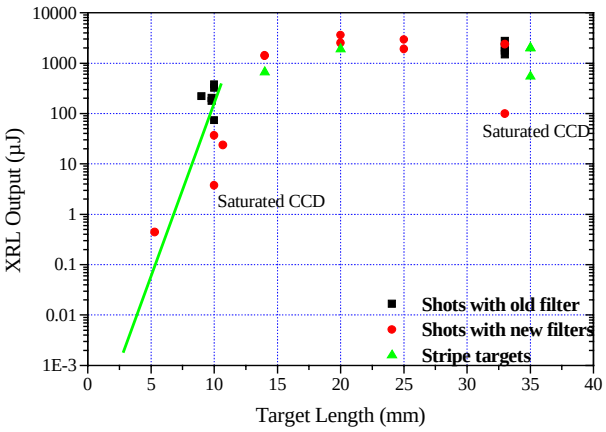

Figure 7. Gain-length scan for the Ne-like Ni XRL.

The stripe targets were less reliable, but mainly due to coating problems which have since been resolved. The output from the slab targets reached 3mJ and that from the stripe target averaged about 1.5 to 2 mJ. The length scan on the slab target is shown in Figure 7 above. A Linford fit to the data indicated saturation occurred at between 12 and 15 mm and gave a small signal gain coefficient of 14 cm^{-1}.

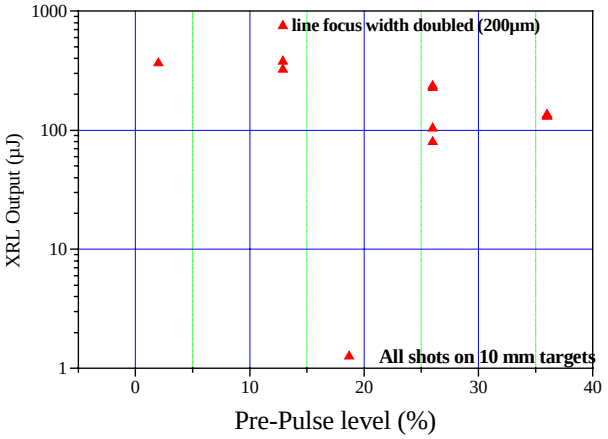

Figure 8. Pre-pulse scan.

A pre-pulse scan indicated the output was not sensitive to the level of pre-pulse as shown in Figure 8 above with a fixed pre-pulse to main pulse delay of 2 ns. This scan was done with short targets operating in the SSG regime to enhance any sensitivity to pre-pulse.

Alignment techniques

We are satisfied with our alignment of the split beams into the gas jet. This was simulated using a visible diode laser coupled to an optical fibre, the output of which was placed at the exit plane of the XRL accurately using the offline target alignment system. At the gas jet plane a camera with a microscope lens was mounted on a Sony Magnascale mount. The alignment was checked for flexing during pumpdown and calibrated.

We successfully split the XRL and aligned it back into the spectrometer via the glass beam splitter at the north end of the chamber. This was our penultimate shot. Our final shot was an attempt at FWM. The XRL beam was focused into the gas jet to an intensity of ~ 10^{10} W cm^{-2}; the optical to $1x10^{14}$ Wcm^{-2}. Modelling has shown that such a pulse (optical) will not decrease the Na-like population through over-ionisation appreciably over the timescale of the interaction (50 ps). Therefore we should expect a near second harmonic signal with an intensity exceeding 10^4 W cm^{-2}, which should be detectable on the spectrometer[1,2]. In the event no detectable signal was produced.

Conclusions and prognosis

Self Emission:

The concept of using a CPA pulse to reduce the self emission has been shelved as the short pulse would result in a colder plasma with very few ions in the 3p state. It may be worthwhile constructing a pinhole arrangement for the FFS collecting the mixed signal. This could make PPS more feasible.

Alternative mixing schemes

To date our modelling of schemes has been restricted to the Na-like sequence. It has been pointed out that the Cu-like sequence might provide higher conversion rates due to the higher oscillator strengths in such an ion[3]. With some adaptation for relativistic effects, our atomic simulation codes will output the orbital reduced matrix elements which will be required to set up the susceptibility codes for energy scans.

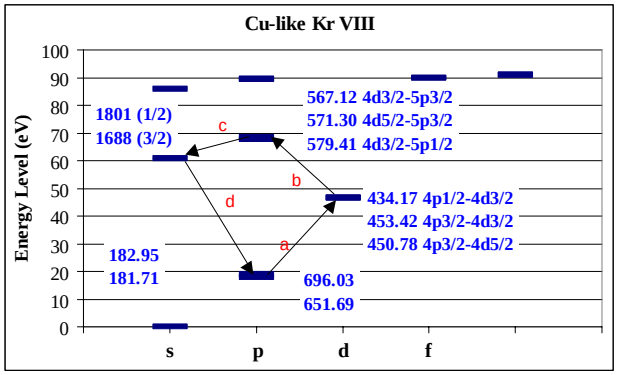

Figure 9. The Cu-like Kr level structure.

Preliminary investigations of the Cu-like sequence have shown that the optical transition will not be matched in this scheme. It is quite feasible though, that this mismatch will be offset by the higher oscillator strengths provided when working at lower n (in comparison to the Na-like sequence). In addition analysis shows that mismatch is less critical in the long wavelength leg of the process.

The mixing process would demand an appreciable population of the 4p level. This should be satisfied as the gas mixing plasma is expected to have an electron temperature in excess of 20 eV. The two XRL photons would stimulate transitions to the 4d and 5p levels. The optical photon then polarises the transition to 5s; decay to 4p gives a near second harmonic output. The scheme illustrated in Figure 9 applies to longer wavelength systems such as the plasma discharge devices[1]. Obviously to apply it to shorter wavelengths would require a more highly ionised species.

We have ironed out many of the problems that faced us and achieved a number of the aims we set ourselves.

(i) We have driven the Ne-like Ni XRL into saturation with a gain coefficient of 14 cm^{-1} and an output energy of 2 to 3 mJ. We can now be confident that metal slab targets are an option at RAL. This will increase our turnaround time greatly in future experiments.

(ii) The emission of the gas jet has proved to be bright enough for analysis of the ionised species. If we can reduce the self-emission or change to a brighter backlighter then we could cross calibrate the systems and have an on-line Na-like ion count.

(iii) We can split the XRL into the required two beams using a Lloyds mirror. With a small number of shots we will be able to ensure equal intensity in both beams.

(iv) Our alignment strategy is reliable and can be set up quite quickly. The flexing of the chamber can be accounted for. We have demonstrated that we can align one of the split

fundamental beams through the gas jet onto the glass splitter and into the spectrometer at the north end.

(v) The glass splitting plate survives the focusing mixing beam.

A great deal has been learned from this preliminary run which will increase the prospect of successfully demonstrating NLO effects in a follow up experiment in August 1999.

References

1. R.M.N. O'Rourke, C.L.S. Lewis and A. Hibbert, Near Frequency Doubling through Four Wave Mixing in Plasma, *CLF Annual Report 1988-99*, D. Neely ed. Oxfordshire, Rutherford Appleton Laboratories, (1999)
2. R.M.N. O' Rourke, C.L.S Lewis and A. Hibbert, Near Frequency Doubling through Four Wave Mixing in Plasma; *Institute of Physics Conference Series*, 159, 687-690 (1999).
3. M.H. Muendel and P.L. Hagelstein; Four-wave frequency conversion of coherent soft x rays in a plasma, *Phys. Rev. A* 44 (1991): 7573-7579.
4. P.L. Shkolnikov, A.E. Kaplan, M.H. Muendel and P.L. Hagelstein; X-ray laser frequency near-doubling and generation of tunable coherent x rays in a plasma, *Appl. Phys. Lett.* 61, 17 (1992): 2001-2003.
5. J.J. Rocca, D.P. Clark, J.L.A. Chilla and V.N. Shlyapstev; Energy Extraction and Achievement of the Saturation Limit in a Discharge-Pumped Table-Top Soft X-Ray Amplifier, *Physical Review Letters* 77, 8 (1996): 1476-1479.

Five Beam Irradiance of a Single Sm X-ray Laser

R Keenan, R M N O'Rourke, C L S Lewis

School of Mathematics and Physics, The Queen's University of Belfast, Belfast, BT7 1NN, UK

E Wolfrum, J Zhang

Clarendon Laboratory, Department of Physics, University of Oxford, Oxford, OX1 3PU, UK

S J Pestehe

Department of Physics, University of Essex, Colchester, CO4 3SQ, UK

Main contact email address *r.keenan@qub.ac.uk*

Introduction

The Ni-like Sm x-ray laser (7.3nm) has been shown to saturate at plasma medium lengths of ~18mm [1] using a double pulse configuration, where a prepulse produces a cold preformed plasma which increases energy absorption from the main heating pulse and reduces refraction. However, for lengths beyond 18mm, into saturation mode, a double target arrangement [2] had been used to compensate for refraction. The alignment of the double targets is critical for coupling of the small gain regions close to the target and precision surface displacement is required for maximum output. Also, the Sm laser has a narrow divergence so when imaging back past the target, as in radiography[3], the beam is close to the axis and the double target creates a wide obstruction in the chamber centre for the beam to get past. For these reasons we have tried a single Sm target, 25mm long, driven with 5 overlapped beams each 20mm long. This length was chosen since 25mm is well into saturation, where output increases linearly with length, but short enough that uniformity and an intensity of $5x10^{13}$ W/cm^2 can easily be achieved.

Experimental

5 beams of Vulcan at 1.05µm, pulse duration 75ps, were used in a standard off-axis geometry, each producing a line focus 20mm long and 100µm wide. These beams were displaced axially and overlapped on a 25mm target to produce a uniform irradiance of $5x10^{13}$ W/cm^2 (Figure.1). From the optimisation of the double pulse pumping of Sm a 1% or 10% prepulse was used arriving 2ns early [4].

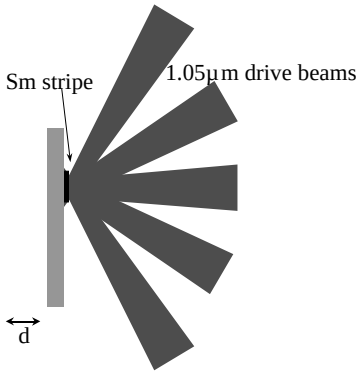

Figure 1. 5 beams focussed on target.

The targets were 25mm long by 100µm wide Sm stripes of ~1µm thickness coated on glass. The beams were focussed on the stripe and the target could then be retracted a distance d (Figure 1). This allowed the extreme beams to heat different regions of the preformed plasma.

The exit plane of the x-ray laser was imaged using a spherical multilayer mirror at near normal incidence providing a ~8x magnification onto a CCD (Figure 2). Uniformity along the line focus was monitored by a space-resolving, time integrated crystal spectrometer.

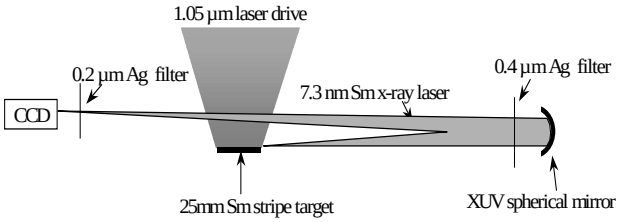

Figure 2. Imaging setup.

Results

Figure 3 shows images of the XRL at various target retractions, d, and the output in the half-maximum (HM) area for a 1% prepulse. The total output also increases with increasing target retraction.

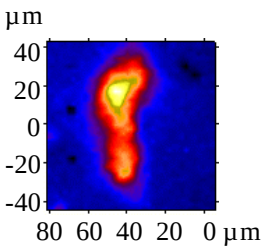

(a) output = 0.43µJ

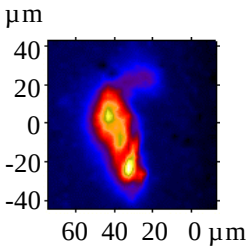

(b) output = 0.55µJ

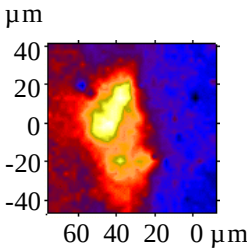

(c) output = 0.85µJ

Figure 3. Image of Sm XRL with output in HM (a) target retraction d = 0µm (b) d = 20µm (c) d = 60µm.

When the target is at zero two lobes can be seen where the beams from top and bottom create 2 separate gain regions. As the target is pulled back the double lobes reduce to one bright

central region as the 5 beams overlap and heat in the same region of the pre-plasma. Shots were also taken with a 10% prepulse where the pre-plasma is larger and here the output also increased when the target was retracted 30µm The degree of uniformity achieved along the line focus is indicated in Figure 4. which is a line out of the Ni-like 3p-4d emission from a 25mm Sm target.

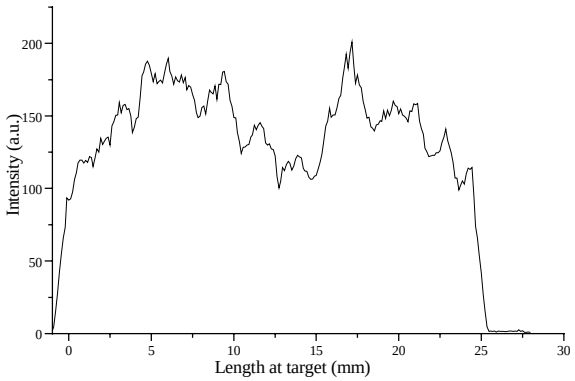

Figure 4. Intensity along line focus.

Conclusions

5-sided illumination of a long target is an easy method for producing a saturated Sm XRL output. Alignment is less critical than for a double target and so the output is more reliable. It is also better for imaging as there is less of an obstruction on axis. This method has now been used to produce saturated Ne-like Ni and Ge XRLs at RAL[5,6]. Also target retraction of ~50µm increases the output of the XRL and provides a better beam profile. This is important for radiography where high output is needed for probing thick foils and good beam profile is required to ensure the imprint on the foil is probed by the brightest part of the XRL.

References

1. J.Zhang, A.G.MacPhee, J.Lin, E.Wolfrum, R.Smith, C.Danson, M.H.Key, C.L.S.Lewis, D.Neely, J.Nilsen, G.J.Pert, G.J.Tallents, and J.S.Wark. Science 276, 1097 (1997).

2. C.L.S.Lewis, D.Neely, D.M.O'Neill, J.O.Uhomoibhi, M.H.Key, Y.Al Hadithi, G.J.Tallents, and S.A.Ramsden. Opt. Comm. 91, 71 (1992)

3. E.Wolfrum, J.S.Wark, J.Zhang, R.M.N.O'Rourke, R.Keenan, C.L.S.Lewis, A.G.MacPhee, D.Kalantar, M.H.Key, B.A.Remington, D.Neely, A.Djaoui, S.J.Rose, G.Eker, J.Lin, R.Smith, G.J.Tallents. Proceedings of the 6th International XRL conference, IOP, 657 (1998).

4. J.Lin, G.J.Tallents, R.Smith, G.Eker, S.J. Pestche, A.G. MacPhee, R.Keenan, C.L.S. Lewis, R.M.N.O'Rourke, J. Zhang, E Wolfrum, J.S. Wark, D.Neely and G.J. Pert. CLF annual report, 1998.

5. R.M.N.O'Rourke et al CLF annual report, 1999.

6. E. Wolfrum et al CLF annual report, 1999.

Parametric Instabilities and Harmonic Generation at the Relativistic ¼ Critical Density of Ultra-intense Laser Light

P. Mason, H. C. Barr, D. Parr

Department of Physics, Wivenhoe Park, Colchester, Essex, CO4 3SQ

Main Contact email address: *pmason@essex.ac.uk*

Introduction

At non-relativistic intensities the two plasmon decay instability (TPD)[1] arises at the quarter critical density (n_c /4). For a linear polarized laser driver, optimum coupling is in the plane of polarisation of the laser beam. At the same time, one of the TPD plasmons can participate in higher harmonic generation at half-harmonic frequencies $\omega = (N+1/2)\omega_0$. At non-relativistic intensities the process is parasitic to TPD. At relativistic intensities it arises as a stimulated ("Raman") harmonic generation (SRHG) process in its own right (and arises across all densities from quarter critical plasma up to the laser cut-off). The results below show the hybrid TPD/SRHG process which occurs at ultra-high intensities at the "relativistic critical density" $n_0 = n_{cr}/4$ where $n_{cr} \approx n_c\ \gamma_q$, $\gamma_q = (1+q^2/2)^{1/2}$. The numerical approach to all electronic parametric instabilities as developed by Barr, Mason and Parr[2] is used to obtain the results presented here.

Discussion

The anharmonic laser driver is a superposition of harmonics ($l\omega_0$, $\mathbf{k}_0 = 0$) where l is any integer. This couples any fluctuation ($\omega, \mathbf{k}$) to the modes ($\omega+\omega_0, \mathbf{k}$). If any pair or more of these is either an electron plasma wave $\omega = \omega_p$ or a light wave $\omega^2 = \omega_p^2 + k^2c^2$ then a resonant three-wave parametric instability with resonant modes coupled through intermediate non-resonant modes may ensue. At relativistic intensities the modes are strongly coupled so that a wide range of higher order harmonic generation processes emerges with large growth rates. Let ω_{pr} be the mean relativistic plasma frequency (averaged over the laser period). Then $\omega_{pr} = G(q)H(q)\omega_0 \approx \omega_0$ where $H(q)$ is also a function of order unity. Laser harmonics satisfy a dispersion relationship $\omega^2 = \omega_{pr}^2 + k^2c^2$; plasma waves, by contrast, generally have a complex multimode composition. A quick examination of 3-wave phase matching indicates the wide range of parametric instability regimes which may emerge at ultrahigh intensity. If this pair corresponds to a plasma wave $\omega_1 = \omega_{pr}$ and a scattered light wave such that $\omega_2^2 = (\omega_1 - l\omega_0)^2 = \omega_{pr}^2 + k^2c^2$ then this is akin to a higher order Raman mechanism which we refer to as stimulated Raman harmonic generation (SRHG). For N-th harmonic generation this is satisfied for wavenumbers where $k^2c^2 \approx N^2 - 1$ ($N > 1$). These circles are included to guide the eye in Figure 1 (over page). The decay into two plasma waves is possible provided that $\omega_{pr} = 1/2$. This is the usual TPD instability occurring near the relativistic quarter critical density.

In addition, instability arises not only due to coupling between such resonant modes but also due to nonresonant modulations.

At ultra-high intensities, large growth rates and frequency shifts arise so that single Fourier modes satisfying either of the above dispersion relations usually will not occur; instead the normal mode is a complex superposition of many strongly coupled Fourier modes. In the case of SRHG, however, there is a single dominant resonant Fourier mode satisfying $\omega^2 = \omega_{pr}^2 + k^2c^2$ coupled to a complex longitudinal response, none of whose Fourier modes satisfy the plasma wave dispersion relation. At weakly relativistic intensities ($q<1$), the growth factor $\Gamma/\omega_0 = 3q^2/16$ occurs for decay into coupled longitudinal-transverse modes.

Results

The patterns of SRHG seen for underdense plasma persist at all densities except that the inner ellipse - the usual SRS[3,4] - degenerates to a point at $n_{0,lab} = n_c$ /4 ($u = \sqrt{3}/2$) and is of course absent at higher densities. The remaining ellipses now correspond to harmonic generation at near half-harmonic frequencies (as seen in the laboratory frame). At the quarter critical density, when $K_y \neq 0$, TPD coupling arises. As predicted from three-wave theory, there is TPD growth at all wavenumbers for which $K_y \neq 0$ with growth maximizing along the hyperbola $K_x^2 = 4K_y^2 + 3$. Figure 1(a) is a typical growth pattern for TPD for low to moderate intensity drivers. However, the TPD growth is now overlain by an almost orthogonal pattern of SRHG showing a coincidence in the conditions for these two processes. At low intensity there is now a resonant triplet of modes along the ellipses. SRHG, being a higher order process, is essentially parasitic to TPD and hence grows with TPD. One can therefore expect in-plane half-harmonic emission to grow with TPD and that its presence to be an indication of the existence of the quarter critical density. As seen in Figure 1(a) TPD growth is maximum close to the maximum K_y values on the SRHG ellipses and corresponds to exact side-scattering of the SRHG emission; this is precisely where growth is reduced to zero for in-plane SRHG in underdense plasma (see reference [2]). The presence of TPD means that in-plane SRHG sidescattering is dominant for low to moderate intensities $q \leq 1$. For example, due to TPD, one can expect measurable 3/2-harmonic generation in the laser plane of polarization and predominantly at 90º, i.e. emitting along v_{0y}. Figure 2(a) is a typical spectrum showing a resonant triplet when q=0.5 for emission at $\omega_s = 7/2$. The dominant mode in b_z satisfies the EM dispersion relation while the two dominant peaks in ϕ satisfy the plasma wave dispersion relation $\omega = -u\,k_x \pm 1/4$.

When $q > 1$, TPD and SRHG arise on equal terms (see Figure 1(b)-(d)). Strongest growth, $\Gamma \approx 0.3\Omega_0$, for the combined TPD and SRHG processes produces emission at near half-harmonics into a wide range of angles in the backscattering quadrant. Figure 2(b)-(d) illustrates the complex multimode nature of these interactions. Figure 2(b) shows a case of essentially pure TPD at high intensity (not close to an SRHG ellipse), while Figs. 2(c) and (d) correspond to the peak growth points for 5/2 and 7/2 harmonic emission where the dominant resonant harmonic is evident in the b_z spectrum.

Figure 3 shows the out-of-plane growth where TPD coupling is absent. This is similar to the underdense plasma case. However, it is clear that the peak growth points lie well away from, indeed almost midway between, the SRHG ellipses predicted by low intensity phase matching arguments. In consequence, the emission, in contrast to the in-plane harmonic emission, emerges at frequencies closer to integer harmonics than the anticipated half-harmonic frequencies.

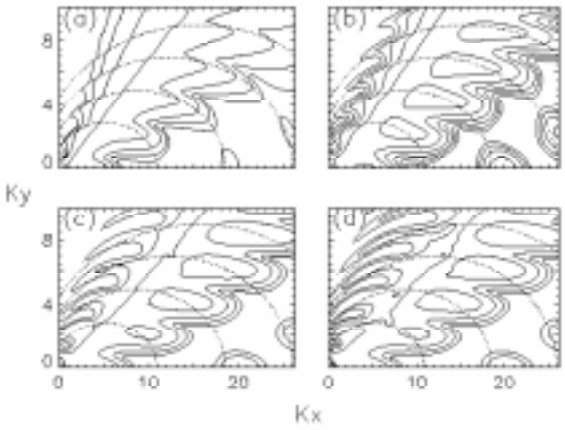

Figure 1. Contour plot of the pulse frame growth rate Γ / Ω_0 at the relativistic quarter critical density ($u = \sqrt{3} / 2$) for wave-numbers in the laser plane of polarization (K_z=0). The contour interval is 0.04. The minimum and maximum contours shown, and the laser amplitude q are respectively:
(a) 0.04, 0.16, q=1, (b) 0.04, 0.24, q=2,
(c) 0.16, 0.28, q=5 and (d) 0.16, 0.28, q=10.

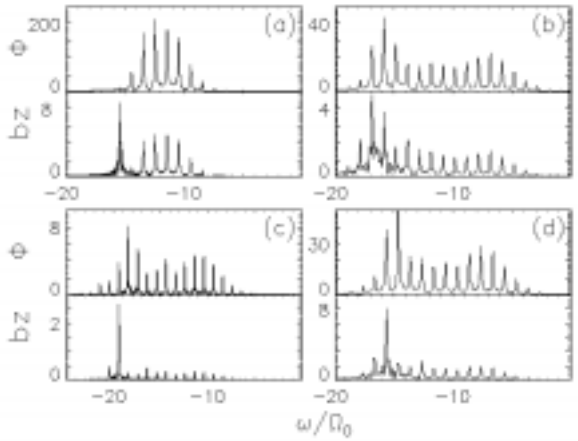

Figure 2. Spectra of b_z and ϕ (arb. units) at the relativistic quarter critical density where (a) (q=0.5), K = (13.8,6.8,0), Γ/Ω_0 = 0.07), (b) (q=5), K = (14.3,8.2,0)\), Γ/Ω_0 = 0.23\), (c) (q=5), K = (18.3,6.4,0), Γ/Ω_0 = 0.31 and (d) (q=5), K = (14.0,6.9,0), Γ/Ω_0 = 0.26.

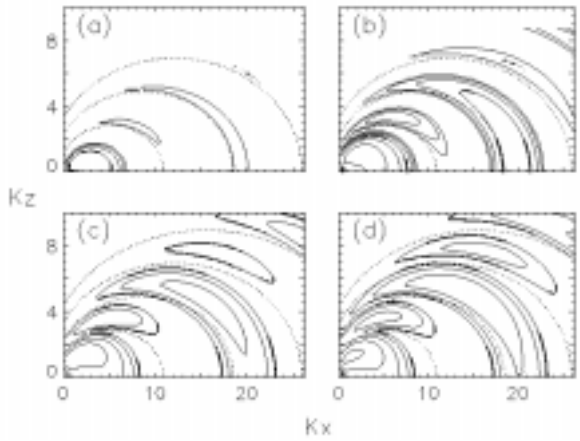

Figure 3. Contour plot of the pulse frame growth rate Γ / Ω_0 at the relativistic quarter critical density ($u = \sqrt{3} / 2$) for wavenumbers out of the laser plane of polarization (K_y=0). The contour interval is 0.04. The minimum and maximum contours shown, and the laser amplitude q are respectively (a) 0.04,0.16, q=1, (b) 0.04,0.24, q=2, (c) 0.16,0.28, q=5 and (d) 0.16,0.32, q=10.

References

1. B. Langdon, B. F. Lasinski, and W. L. Kruer, Phys. Rev. Lett., 43, 133 (1979).
2. H. C. Barr *et al*., CLF Annual report (1997/8)
3. J. F. Drake, P. K. Kaw, Y. C. Lee, G. Schmidt C. S. Liu and M. N. Rosenbluth, Phys. Fluids, 17, 778 (1994).
4. D. W. Forslund, J. M. Kindel, and E. L. Lindman, Phys. Fluids, 18, 1002 (1975).

Parametric Instabilities and Harmonic Generation in overdense Plasma at the Cutoff for ultra-intense Laser Light

D M Parr, H C Barr and P Mason

Department of Physics, University of Essex, Colchester, CO4 3SQ

Main contact email address: *dparr@essex.ac.uk*

Introduction

Classically overdense plasma is accessible to ultra-intense laser light due to self-induced transparency caused by the relativistic electron mass increase. Here we examine the electron parametric instability of linearly polarised light at its cut-off, where the 'relativistic critical density' $n_{cr}=n_c G^2(q)\gamma_q$, $q=eA_0/mc^2$ is the peak normalised vector potential of the laser light and $G(0)=1$, $G(q>>1)\approx 1.07$. At n_{cr} the linearly polarised laser light is a non-linear anharmonic pure transverse oscillation[1] (induced longitudinal motion is negated by self-consistent fields), with the electron velocity approaching a rectangular waveform when $q>>1$. Such waveforms are unstable in a variety of ways[2,3]: modulationally, to a second order two plasmon decay mechanism, and to stimulated harmonic generation. These derive from a combination of charge-displacement and relativistic mass increase modulations/fluctuations. A general and unified treatment applicable to all electronic parametric instabilities, described in last year's Annual Report[4] and there applied to underdense plasma, is used.

Discussion

The anharmonic laser driver is a superposition of harmonics $(l\omega_0,\boldsymbol{k}_0=0)$ where l is any integer. This couples any fluctuation $(\omega,\boldsymbol{k})$ to the modes $(\omega+l\omega_0,\boldsymbol{k})$. If any pair or more of these is either an electron plasma wave $\omega=\omega_p$ or a light wave $\omega^2=\omega_p^2+k^2c^2$ then a resonant three-wave parametric instability with resonant modes coupled through intermediate non-resonant modes may ensue. At relativistic intensities the modes are strongly coupled so that a wide range of higher order harmonic generation processes emerges with large growth rates. Let ω_{pr} be the mean relativistic plasma frequency (averaged over the laser period). Then $\omega_{pr}=G(q)H(q)\omega_0\approx\omega_0$ where $H(q)$ is also a function of order unity. Laser harmonics satisfy a dispersion relationship $\omega^2=\omega_{pr}^2+k^2c^2$; plasma waves, by contrast, generally have a complex multimode composition. A quick examination of 3-wave phase matching indicates the wide range of parametric instability regimes which may emerge at ultra-high intensity.

If this pair corresponds to a plasma wave $\omega_1=\omega_{pr}$ and a scattered light wave such that $\omega_2^2=(\omega_1-l\omega_0)^2=\omega_{pr}^2+k^2c^2$ then this is akin to a higher order Raman mechanism which we refer to as stimulated Raman harmonic generation (SRHG). For N-th harmonic generation this is satisfied for wavenumbers where $k^2c^2\approx N^2-1 (N>1)$. These circles are included to guide the eye in Figure1.

The resonant decay into a pair of light waves at integer or half-integer harmonics is also possible: then $\omega_1=-\omega_2=M\omega_0/2$ and $k^2c^2\approx M^2/4-1$. This decay can only be achieved for second and higher order processes $(M\geq 2)$.It is well known that three light waves cannot be phase-matched in first order. This is a symmetric coupling between positive and negative integer or half-integer harmonics (or, a coupling between oppositely travelling waves with the same frequency and wavenumber, i.e. standing waves). We refer to this as stimulated electromagnetic harmonic generation (SEHG).

Finally there is the decay into two plasma waves provided that $\omega_{pr}=l/2$. When $l=1$ this is the usual TPD instability near the relativistic quarter critical density. When $l=2$, a second order TPD process occurs at the relativistic critical density.

It is also possible for two or more of (A), (B) and (C) to have Fourier modes in common. Near the relativistic critical density all three of the above processes can be coupled together so that there is a resonant quadruplet: (B) involves the N-th harmonic light wave $\omega=\pm N\omega_0$, which is a 2 N-th order process; (A) involves the N-th harmonic light wave $\omega=\pm N\omega_0$ coupled to the plasma wave $\omega=\omega_0$, which is an $(N+1)$-th order process; (C) couples together the plasma waves $\omega=\pm\omega_0$ and is second order (N is any positive integer). Thus, even in low intensity regimes, higher order processes may be evident by a parasitic coupling to a lower order process. At relativistic intensities these distinct mechanisms can be equally strong in their own right.

In addition, instability arises not only due to coupling between such resonant modes but also due to non-resonant modulations. At ultrahigh intensities, large growth rates and frequency shifts arise so that single Fourier modes satisfying either of the above dispersion relations usually will not occur; instead the normal mode is a complex superposition of many strongly coupled Fourier modes. In the case of SRHG, however, there is a single dominant resonant Fourier mode satisfying $\omega^2=\omega_{pr}^2+k^2c^2$ coupled to a complex longitudinal response, none of whose Fourier modes satisfy the plasma wave dispersion relation. At weakly relativistic intensities $(q<1)$, the growth factor $\Gamma/\omega_0=3q^2/16$ occurs for decay into coupled longitudinal-transverse modes.

Results

Large growth rates, a significant fraction of the laser frequency, occur at similar levels across a wide range of harmonics. Figure 1 shows the characteristic growth pattern of the dominant instabilities which emerge at the laser cutoff. We show these results in the (k_x,k_y)-plane only since there is symmetry about the k_y axis. The largest growth at low intensity is seen in Figure 1(a) for $K_y=0$, and for $q>>1$, this growth rate reaches $\Gamma\approx 4\omega_0$. The interaction involves six Fourier modes, the electromagnetic modes at $\omega=\pm\omega_0$, and electrostatic modes at $\omega=\pm 2\omega_0$,. This branch has the largest growth of any at all intensities although only marginally so at ultrahigh intensity as Figures 1(a)-(d) demonstrate.

What appears, in addition, is a combination of the three processes described above. The SRHG ellipses are given by $k^2c^2=(N^2-1)\omega_0^2$ for N>1 while those corresponding to SEHG give that $k^2c^2=(M^2/4-1)\omega_0^2$ where M is any integer greater than 2. These processes coincide when $M=2N$ giving emission into laser harmonics.

Branches involving only SEHG with emission into half-harmonics are seen but have weaker growth. The second order TPD process (C) is also evident; for example, the branch on the $N=2$ ellipse in Figure 1(a) which shows scattering into the second harmonic involves a quadruple resonance comprising all three processes (A), (B) and (C) coupling resonant light waves at $\omega=\pm 2\omega_0$ and resonant electron plasma waves at $\omega=\pm\omega_0$. The spectra for all branches are symmetric about $\omega=0$ indicating standing wave solutions. N-th harmonic emission includes modes up to $|l|\leq N$. Figure2 shows the symmetric spectra for $q=5$ at the first four peak growth points corresponding to emission into the first four harmonics.

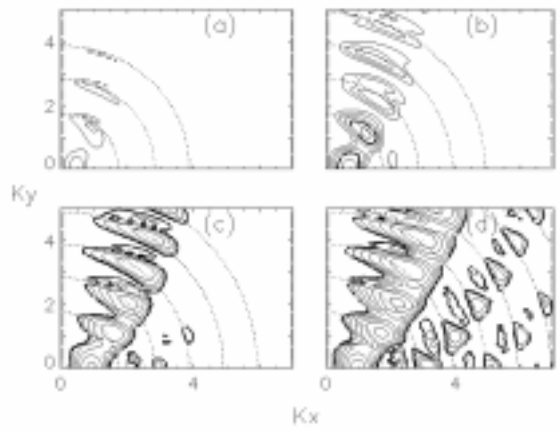

Figure 1. Contour plot of the pulse frame growth rate Γ/Ω_0 at the relativistic critical density (u=0,ω_0=1) for wavenumbers in the laser plane of polarization (k_z =0). The contour interval is 0.04. he minimum and maximum contours shown, and the laser amplitude q are respectively (a) 0.04,0.08, q=1, (b) 0.04,0.20, q=2,(c) 0.16,0.32, q=5 and (d) 0.16,0.40, q=10.

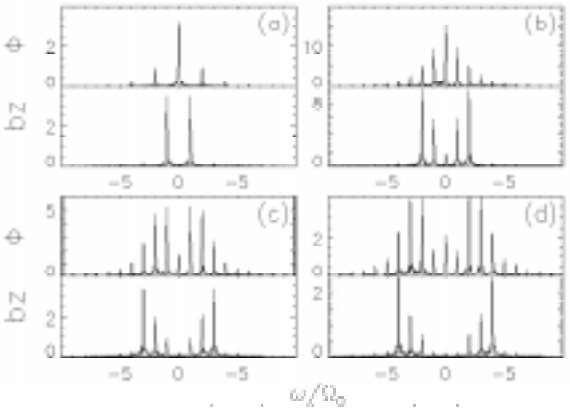

Figure 2. Spectra of b_z and ϕ (arb. units) at the relativistic critical density for q=5 at the peak growth points of Figure1(c) corresponding to emission into the first four harmonics.
(a) $\boldsymbol{K}$ = (0.9,0,0), Γ/Ω_0 =0.37,
(b) $\boldsymbol{K}$ = (1.6,1.1,0), Γ/Ω_0 = 0.35,
(c) $\boldsymbol{K}$ = (2.0,2.1,0), Γ/Ω_0 = 0.34 and
(d) $\boldsymbol{K}$ = (2.4,3.1,0), Γ/Ω_0 = 0.31.

References

1. C E Max and F Perkins
Phys. Rev. Lett. 27, 1342 (1971); C. E. Max, Phys.Fluids 16, 1277 (1973).

2. N L Tsintsadze
Sov. Phys. JETP 32, 684 (1971).

3. S Guerin, P Mora and G Laval
Phys. Plasmas, 5, 376 (1998).

4. CLF Annual Report 1997/98.

Suppression of Raman Gain by Finite Level Ion Acoustic Waves in Inhomogeneous Plasma

A.V. Lukyanov

Tamm Theoretical Physics Department, Lebedev Institute, Moscow

H.C. Barr and T.J.M. Boyd

Department of Physics, University of Essex, Colchester CO4 3SQ

Main contact email address: *barrhc@essex.ac.uk*

Introduction

The influence on stimulated Raman scattering (SRS) of secondary decays and stimulated Brillouin scattering (SBS) has received much experimental and theoretical attention in recent years on account of its relevance to ICF experiments[1)]. Mostly, analytic studies were restricted to homogeneous plasma. Here we report the outcome of a study of the influence of secondary decays on Raman gain levels in inhomogeneous plasma when a finite level of ion acoustic waves is present.

Discussion

Two secondary decays are considered: the decay of the primary Raman electron plasma wave into a secondary plasma wave and an ion acoustic wave - the Langmuir decay instability (LDI) - or, the decay of the primary Raman plasma wave into a secondary scattered light wave and an ion acoustic wave, which we refer to as the electromagnetic decay instability (EDI). Such decays are local processes in inhomogeneous plasma so that we consider situations where the primary and secondary decays are coincident. Attention is confined to 1D backscattering.

In isolation, the Raman gain is given by the Rosenbluth gain factor $G_R=\pi\gamma_R^2/V_{L1}V_1|K_R'|$ where γ_R is the Raman homogeneous plasma growth rate, $V_{L1}(V_1)$ is the plasma wave (scattered wave) group velocity and K_R is the wavenumber mismatch factor between the three waves. In the absence of the laser driver, the secondary decay in the presence of a finite level of ion acoustic wave would not produce instability but merely give rise to a nonlinear frequency shift $\Delta_N=\omega_p N/2$ where $N=\delta n/n_0$ is the ion acoustic fluctuation level assumed finite at some level above noise. However, the ion acoustic wave causes the other two waves to exchange energy through the resonance. This can be expressed in terms of a negative 'gain' which for the LDI process is $G_N=\pi\Delta_N^2/V_{L1}V_{L2}|K_L'|$ where V_{L2} is the secondary Langmuir wave group velocity and K_L is the mismatch factor for the LDI. Similarly, for EDI, $G_N=\pi\Delta_N^2/V_{L1}V_2|K_E'|$ where V_2 is the group velocity of the secondary scattered light wave and K_E is the EDI mismatch factor. Mismatch factors depend on gradients in the density, flow velocity and temperature. Below we give an expression for the net Raman gain G subject to both these mechanisms in terms of the 'gain' factors G_R and G_N and the noise levels of the source waves.

Let the source levels from which the waves amplify be δ_{L1} for the primary Langmuir wave entering the resonant region from the left (say), δ_{L2} for the secondary Langmuir wave entering from the right (LDI), δ_1 for the Raman backscattered wave, and δ_2 for the secondary scattered wave (EDI). In general, the light wave source levels are small by comparison with the Langmuir wave noise levels.

The model used is a WKB coupled-mode representation of the 5-wave interaction between the three SRS waves and the three secondary LDI or EDI waves where the Raman Langmuir wave is common to both processes. Laser pump depletion is neglected and the ion acoustic wave is likewise assumed to be at a level that variation in its amplitude through the coincident resonances can be ignored. It is the evolution and gain in the remaining three source waves that are sought by, in principle, integrating the equations through the resonance. In practice, the gain can be obtained by integrating along a contour in the complex plane which bypasses the resonance and uses asymptotic solutions which are easily obtained. This makes use of Stokes' theory, whose details, somewhat lengthy, we omit here.

For the SRS/EDI process, it is found that the net gain in the primary Langmuir wave (say) depends weakly on the source levels so that

$$G = G_R - G_N$$

In other words, the secondary EDI decay can be very effective in suppressing the Raman gain.

For the SRS/LDI process, the net gain G satisfies

$$e^{2G} = e^{2G_R-2G_N} + \left(\frac{\delta_{L2}}{\delta_{L1}}\right)^2 \frac{V_{L2}}{V_{L1}}\left(e^{2G_R} - e^{2G_R-2G_N}\right)$$

We see that the net gain depends sensitively on the relative source levels of the two Langmuir waves entering the resonance from opposite sides. Usually, one would expect these to be at comparable levels, $\delta_{L1}\approx\delta_{L2}$, and since $V_{L1}\approx V_{L2}$ we obtain that $G\approx G_R$ (exact when $(\delta_{L2}/\delta_{L1})^2V_{L2}/V_{L1}=1$) showing that the secondary decay has little if any effect on Raman backscattering. On the other hand, there may be good reasons for the source levels of the Langmuir waves entering the resonance from opposite sides to be different. Figure 1 illustrates how the net gain G varies with G_N for a range of the ratio of the Langmuir source wave amplitudes.

For parameters typical of recent experiments (Labaune et al. 1997), with a Raman gain factor G_R=5, an ion acoustic wave level of $N\approx0.25\%(1\%)$ is sufficient to give an equal negative gain G_N=5 for LDI (EDI).

If the source of the finite level of ion acoustic waves is stimulated Brillouin scattering, then the SRS/LDI process has coincident resonances for densities approaching the quarter critical density. On the other hand, SBS can act as the ion wave source for the SRS/EDI process in underdense plasma. Of course, there are no such limitations if the density fluctuations are seeded from an external source.

This theory may thus provide an explanation for many features of the observed interplay between SRS and SBS in laser-produced plasmas. For instance, in[1)] the SRS instability was observed to switch off during the presence of an SBS signal and reappeared when the ion acoustic density fluctuation level went below some critical value. Such behavior may correspond to the case where the LDI mechanism is in operation, i.e. when the gain factor experiences a fast transition from

$$G = G_R$$

to

$$G = G_R + 0.5\ln\left(\frac{\delta_{L2}^2}{\delta_{L1}^2}\frac{V_{L2}}{V_{L1}}\right)$$

Another interesting observation connected with the influence of density fluctuation on SRS signal was the observed dependence

of the SRS signal on the damping of ion-acoustic wave[2,3]. Since the SRS gain factor depends on the ion acoustic density fluctuation level, it is in turn sensitive to the ion-acoustic wave damping rate. In terms of the theory presented here, the ion acoustic wave damping reduces N thus diminishing G_N leading to an increase of the SRS signal.

Thus in conclusion one can say that it is shown that there are two basic mechanisms which are responsible for the coupling between SRS and density fluctuations. Both mechanisms may be present in laser-produced plasma and become important at almost the same level of density fluctuations.

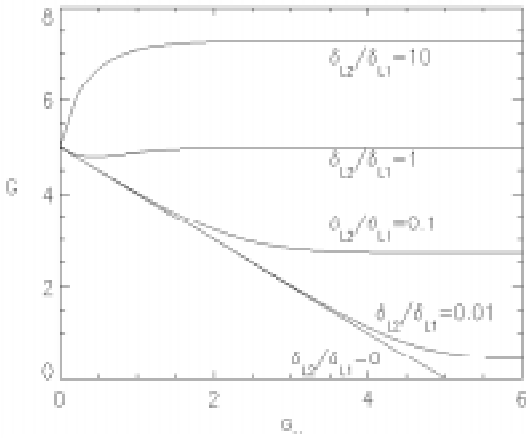

Figure 1. The net gain G for the SRS/LDI mechanism versus G_N for various ratios of the Langmuir wave source levels. The SRS / EDI mechanism corresponds to the curve where $\delta_{L2}/\delta_{L1}= 0$.

References

1. C. Labaune, H.A. Baldis, N. Renard, E. Schifano, A. Michard, Phys. Plasmas, 4 423 (1997).
2. R.K. Kirkwood et al., Phys. Rev. Letters, 77 2706 (1996)
3. Juan C. Fernandez et al., Phys. Rev. Letters, 77 2702 (1996).

Atomic number scaling of Ni-like lasers

G Eker, G J Tallents*

Department of Physics, University of Essex, Colchester CO4 3SQ, UK

**From September 1999 at Department of Physics, University of York, York, YO1 5DD*

Main contact email address: *geker@essex.ac.uk*

One of the important objectives of X-ray laser development is to achieve a coherent, monochromatic, and saturated laser output at short wavelengths. Saturated soft X-ray amplification in Ne-like ions has been demonstrated at wavelengths between 24 nm to 15 nm. The required pumping laser energy increases rapidly with Ne-like ions as the wavelength becomes shorter towards the water window region (2.5 nm –4.4 nm). With Ni-like ions the pumping laser energy is reduced for a given X-ray laser wavelength as the quantum efficiency (the laser transition energy/the excitation energy) for Ni-like ions is higher than that for Ne-like ions of similar X-ray laser wavelength.

With multi pulse pumping, the efficiency of soft X-ray lasers produced from laser plasma media has increased. Shorter wavelength lasing has been achieved using higher Z targets in Ni-like and Ne-like ions. Multi pulsing works well with ~100 ps pulses, where the gain is quasi-steady state. Collisional pumping into the upper lasing level is balanced by radiative decay [1-3].

In this report, Ni-like X-ray lasers with atomic numbers between 47 (Ag) and 92 (U) and lasing wavelengths between 14 nm and 2.5 nm are examined. We calculate the gain coefficients and the required pumping conditions for the Ni-like ions as a function of atomic number using the 1½D hydrodynamic with atomic physics code EHYBRID and the atomic data tabulated by Daido et al [4].

The energies of lasing levels and the oscillator strengths of transitions have been calculated by Daido et al for Ni-like ions from Z=47 to 92. There are two 4d-4p J=0-1 lasing transitions for Ni-like ions. The lasing transition oscillator strengths are approximately equal for dysprosium (Z=66), but become increasingly unequal at higher and lower Z so that the dominant lasing transition switches from the long wavelength line to the short wavelength line with increasing Z. Given excitation cross-sections as a function of incident electron energy, an excitation rate coefficient can be calculated for a Maxwellian electron velocity distribution. The excitation rate coefficient is given by

$$< \sigma v >= 1.58 x 10^{-5} \frac{n p(b) \exp(-b)}{\Delta E \sqrt{T}} \qquad (1)$$

where ΔE is the transition energy in eV, T is the electron temperature in eV, b=ΔE/T, and n is a multiplier. The p(b) function is tabulated by Daido et al in terms of A_0, A_1, A_2 and A_3 using

$$p(b) = \exp\left(A_0 + A_1 \ln b + A_2 (\ln b)^2 + A_3 (\ln b)^3\right).$$

We can write for the pumping rate into an excited quantum state

$$R = < \sigma v > n_e n_i \qquad (2)$$

where n_e is the electron density and n_i is the ion ground state density. Daido have calculated the electron temperature and density producing the maximum Ni-like fractional population (see Figure 1).

For these conditions we have evaluated the collisional excitation rate coefficient for pumping into the upper Ni-like lasing level and the pumping rate R according to equation (2).

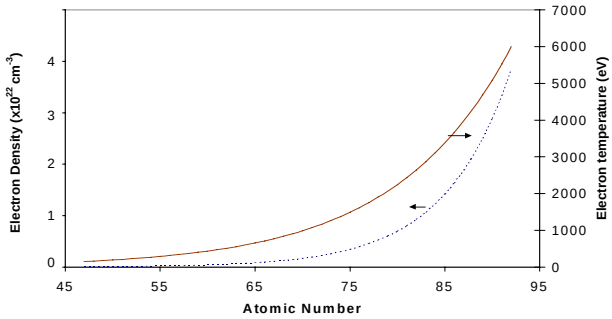

Figure 1. The temperature and density producing maximum fractional Ni-like population.

A simple 4 level laser model with a Doppler broadened laser gain profile predicts that the small gain coefficient is given by

$$G_0 = \frac{\lambda^3}{8\Pi\sqrt{\Pi}} \sqrt{\frac{M}{2kT_i}} R \left[1 - \frac{g_2 A_{21}}{g_1 A_{10}}\right] \qquad (3)$$

where λ is the lasing wavelength, M is the ion mass, Ti is the ion temperature, A_{21} is the radiative transition probability for transitions between the upper and lower lasing level and A_{10} is the radiative transition probability to the ground state of the lower lasing level. The parameters g_1 and g_2 are the respective level degeneracies.

The small signal gain coefficient G_0 is calculated using equation (3) assuming an ion temperature of 200 eV for the plasma conditions of optimum Ni-like fraction population. We assume that a fraction δ= 0.5 of the total ions are Ni-like. The required length L for saturated output is deduced from the gain length product at saturation (G_0L=15).

It remains to determine the laser irradiance conditions needed to produce the plasma electron temperature and density for maximising the Ni-like population and assumed for the evaluation of G_0 and L.

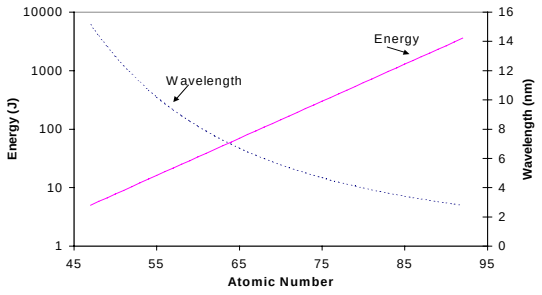

Figure 2. Calculated wavelength for the most intense 4d-4p lasing transitions for Ni-like X-ray lasers and the estimated pump laser energy in a 75 ps pulse required to produce lasing in Ni-like ions as a function of atomic number Z.

The EHYBRID fluid and atomic physics code is used for this. Assuming a double pulse pumping configuration with a pre-pulse of 10% timed 2 ns before the main pulse, a pulse width of

75 ps and a focal width on target of 100 μm, the laser irradiance needed to achieve the electron temperature producing maximum Ni-like population can be calculated.

The laser energy needed to achieve saturated X-ray output for Ni-like ions is determined using the necessary L values (Figure 2). Allowance is made for overspill of the line focus length, so that 2/3 of the laser energy is incident on the target and for a 50% loss in the laser absorption. The analysis predicts, for example, that Ni-like Dy lasing at 5.86 nm requires ~90 J on target to achieve saturation in agreement with the experimentally obtained value [5].

References

1. J Nilsen, B J MacGowan, L B DaSilva and J C Moreno
   Phys. Rev. A48, 4682 (1993).
2. J Nilsen and J C Moreno
   Phys. Rev. Lett. 74, 337 (1995).
3. J Y Lin et al
   Optics Commun. 158, 55 (1998).
4. H Daido et al
   Intern. J. Mod. Physc. B11, 945 (1997).
5. R Smith, G J Tallents, J Zhang, G Eker, S McCabe, G J Pert and E Wolfrum
   Phys. Rev. A59, R47 (1999).

Multiphoton Ionization of He and H_2

D H Glass, J Colgan, P G Burke

Department of Applied Mathematics and Theoretical Physics, The Queen's University of Belfast, Belfast, BT7 1NN

Main contact email address: *D.H.Glass@qub.ac.uk*

Introduction

For a number of years the *R*-matrix-Floquet[1] theory of multiphoton processes has been used to study multi-electron atoms and atomic ions in intense laser fields. Use of this approach has led to a greater understanding of a number of phenomena, such as laser-induced degenerate states (LIDS), which have been discussed in previous reports[2]. Although much progress has been made it has been difficult to study realistic laser parameters for atoms such as He due to the large numbers of photons which must be absorbed for ionization to occur. In the present report this problem is considered by studying the multiphoton ionization of He at the KrF laser wavelength of 248 nm and intensities up to 6×10^{14} Wcm^{-2}.

Recently the *R*-matrix-Floquet theory and computer programs have been extended to treat the multiphoton ionization of diatomic molecules[3,4]. This area of work is of particular interest due to the extra degrees of freedom arising from the nuclear motion which introduces new processes not found in atoms such as dissociation and bond-softening. To date most other theoretical work on molecules in intense laser fields has focussed on H_2^+, but given the power of *R*-matrix theory in its application to multi-electron systems the present approach will enable more complex molecules to be studied. An illustration of this is given by results obtained for H_2.

Since an outline of the theory has been given previously[2] and more details can be found elsewhere[1,3,4] only the present calculations will be discussed below.

Multiphoton Ionization of He

At low intensities absorption of five photons is sufficient to ionize the He atom, but as the intensity increases the ionization threshold moves up by approximately the ponderomotive energy, U_p, of a free electron which is given in atomic units by

$$U_p = \frac{E_0^{\,2}}{4\omega^2} \qquad (1)$$

where E_0 is the electric field strength and ω is the laser frequency. If the intensity is sufficiently high channel closing occurs so that six photons are required to ionize the atom. Figure 1 gives the energy level diagram for He in both the low and high intensity cases. It can also be seen that in the high intensity case intermediate five photon resonances can occur between the ground state and excited bound states.

The calculations were carried out adopting a single state, the 1s, to represent the residual He^+ ion. The accuracy of this approximation was confirmed by calculating ionization rates for several intensities using a three state approximation to allow for additional correlation effects to be included. The rates obtained from the two approximations differed by less than 5%.

In Figure 2 the total ionization rate is given as a function of the laser intensity for a wavelength of 248 nm. At low intensity the total rate obeys the perturbative power law for five photon ionization.

At an intensity of 6.7×10^{13} Wcm^{-2} channel closing occurs as discussed above and as the intensity increases further five photon resonances occur between the ground state and excited bound states of odd parity. This series of intermediate resonances culminates with the largest resonance due to the 1s2p ^{1}P^o excited state at an intensity of 5×10^{14} Wcm^{-2}.

The present results are of particular interest given recent experimental work[5] which has been carried out on He at 248 nm. For this reason further calculations are underway on the investigation of the 1s2p ^{1}P^o resonance which becomes even more pronounced at neighbouring wavelengths. In addition, a comparison is underway between the present time-independent approach and time-dependent calculations[6] also being carried out at Queen's University.

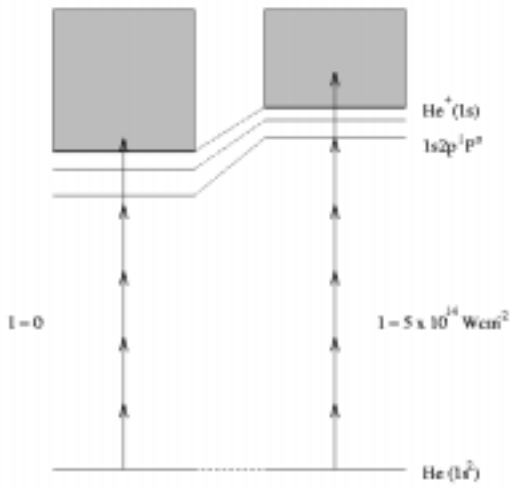

Figure 1. Energy levels for He at zero intensity and 5×10^{14} Wcm^{-2}. The shaded area represents the continuum.

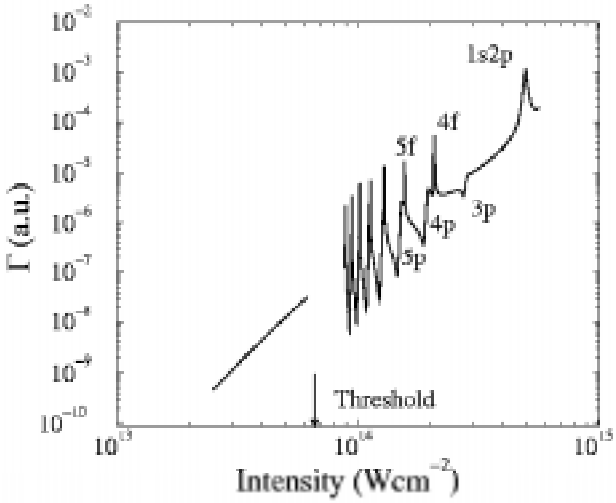

Figure 2. The total ionization rate as a function of laser intensity. The arrow marks the intensity where channel closing takes place.

Multiphoton Ionization of H_2

Two target states of the residual H_2^+ ion were retained in the expansion of the wavefunction, corresponding to the X $^2\Sigma_g^+$ ground state and the $^2\Sigma_u^+$ first excited state. These were represented as LCAO-MO-SCF wavefunctions constructed from a 1s-2s-2p STO σ basis as used by Tennyson *et al*[7] in their study of low energy electron scattering by H_2^+.

The potential curves for this system are shown in Figure 3. Also marked on this figure are the Rydberg bound states converging to the H_2^+ ($^2\Sigma_g^+$)ground state and the Rydberg resonances converging to the H_2^+ ($^2\Sigma_u^+$) excited state.

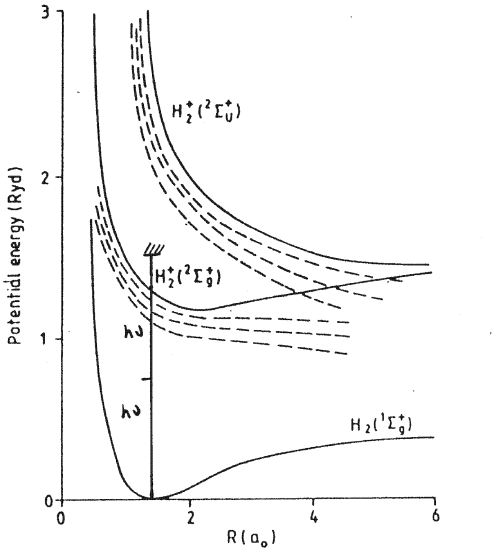

Figure 3. Potential energy curves for H_2 and H_2^+.

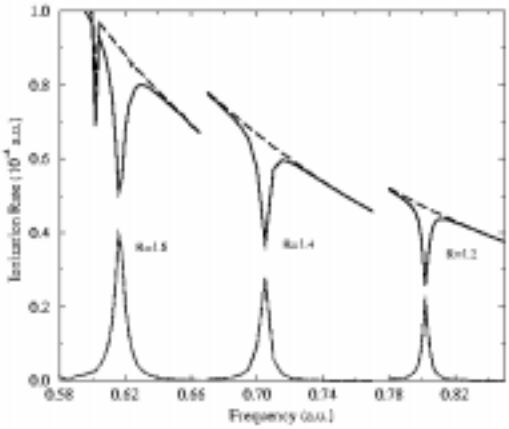

Figure 4. Contribution of the two photon rate to the total rate at different internuclear separations. The dashed line is the total ionization rate, the solid line is the one-photon contribution to this and the dotted line is the two-photon contribution.

Initially single photo-ionization results at low intensities were calculated for this system, and the positions of the doubly excited states corresponding to the Rydberg series converging to the H_2^+ ($^2\Sigma_u^+$) were found to be in good agreement with previous work[7].

The contributions of the one and two photon ionization rates were extracted from the total ionization rates for calculations carried out at an intensity of 10^{12} Wcm^{-2}. These are illustrated in Figure 4. A strong enhancement of the two photon ionization rate can be clearly seen at each inter-nuclear separation considered (1.2, 1.4 and 1.6 au). This is due to the presence of a core resonance, where the frequency is such that it brings the ground state into resonance with the first excited state.

The calculation of two photon ionization rates is also being carried out for a range of inter-nuclear separations for H_2. We also hope to investigate three photon ionization at a laser wavelength of 248 nm, in order to compare more closely with experiment.

The computer programs used in this work have been developed for a general diatomic molecule. We therefore intend to begin calculations of multiphoton ionization rates for other molecules of interest such as N_2 and CO.

Acknowledgements

The authors acknowledge with thanks support from the EPSRC through a rolling grant and support by DENI for a studentship to JC.

References

1. P. G. Burke, P. Francken and C. J. Joachain
   J. Phys. B 24, 761, (1991)
2. D H Glass, P G Burke and C J Noble
   RAL-TR-1997-045 82, (1997);
   D H Glass, J Colgan, P G Burke and C J Noble
   RAL-TR-1998-080 51, (1998)
3. J Colgan, D H. Glass, K Higgins and P G Burke
   Comput. Phys. Commun. 114, 27, (1998)
4. P G Burke, J Colgan, D H Glass and K Higgins
   J. Phys. B, submitted
5. D Charalambidis, D Xenakis, C J G J Uiterwaal, P Maragakis, J Zhang, H Schröder, O Faucher and P Lambropoulos
   J. Phys. B 30, 1467, (1997)
6. J S Parker, E S Smyth and K T Taylor
   J. Phys. B 31, L571, (1998)
7. J Tennyson, C J Noble and S Salvini
   J. Phys. B 17, 905 (1984).

Fast and Anomalous Electron Transport in Intense Short Pulse Laser-Matter Interactions

M. G. Haines

Blackett Laboratory, Imperial College, London SW7 2BZ

Main contact email address: *m.haines@ic.ac.uk*

Introduction

When an intense short pulse laser is incident on dense matter the electromagnetic energy is converted with high efficiency to energetic electrons[1]. The subsequent transport of these fast electrons has been studied theoretically by three types of model: a fully PIC code[1], a hybrid code (collisionless fast electron component in a resistive electron fluid background)[2], and analytically in 1-D for a similar hybrid model[3]. In this report further analytic work will be presented, showing how the return cold electron current will excite an anomalous resistivity as in a related paper[4], and the associated skin depth leads to an estimate of the net current and the self-generated magnetic field.

Importance of the electric field, E

In conventional e-beam-plasma interactions[5] it is assumed that the electric field, set up by charge separation, and in 2-D modified by induction, is too small to affect the beam itself. The condition for validity of this depends on the penetration length l, given by

$$\frac{3}{2}T_h = \frac{1}{2}m_e v_h^2 = eEl = e\frac{J_c}{\sigma}l \qquad (1)$$

where T_h, v_h are the hot electron temperature and speed, J_c is the return cold current density and σ is the background plasma electrical conductivity. Quasi-neutrality ensures that the hot (or fast) electron current density J_h is equal and opposite to J_c, while the absorbed laser intensity I_{abs} is $7T_hJ_h/2_e$. The critical length that arises then in eq.(1) is $^3/4z_0$, being the length scaling arising in Bell[3]. For a target length greater than this critical value the hot electrons are reflected from a moving potential slope. Furthermore, for a narrow focussed laser deposition, 2-D effects will lead, through a non-zero curl $\underline{E}$, to the generation of an azimuthal magnetic field.

Heating and the drift parameter

In Bell's model[3] the heating of the background electrons in a time Δt leads to temperature change of the cold electrons of density n_c,

$$\Delta t_c = \frac{8}{21}\frac{J_{abs}}{n_c z_c}\Delta t \qquad (2)$$

A typical example of T_c = 100eV for Al, $\sigma=10^6\omega^{-1}m^{-1}$, I_{abs} = $10^{18}W\text{cm}^{-2}$, T_h = 200keV leads to z_0 = 28μm; while for Δt = 1ps and n_c = 7.8 x $10^{29}m^{-3}$ gives ΔT_c = 1.1keV. Clearly T_c is not constant, and indeed in Davies' hybrid code is allowed to vary. The initial drift parameter, v_d/c_s is ~ 1.7, where $v_d = J_c/n_c e$ and c_s is the ion acoustic velocity. At higher intensity eg. $10^{19}W/\text{cm}^2$, ΔT_c will rise to 11 keV and v_s/c_s will be 5.3. In such cases an anomalous resistivity will be generated either due to ion-acoustic turbulence for $ZT_e >> T_i$, Z being the ionic charge, or, in the presence of the generated magnetic field, lower hybrid turbulence.

1-D model with anomalous resistivity

Equations (3) and (4) represent the fast electron pressure balance and continuity respectively:-

$$\underline{E} = -\frac{T_h \nabla n_h}{e n_h} \qquad (3)$$

$$\frac{\partial n_h}{\partial t} = \nabla\cdot\left(\frac{\underline{J}_h}{e}\right) = -\nabla\cdot\left(\frac{\underline{J}_c}{e}\right) \qquad (4)$$

as in Bell, but Ohm's law is replaced by

$$J_c = \alpha n_c e c_s \qquad (5)$$

and T_c is now varying according to

$$\frac{3}{2}n_c\frac{\partial T_c}{\partial t} = \underline{J}_c\cdot\underline{E} \qquad (6)$$

From these we arrive at a coupled pair of time varying equations in c_s and $n_{\underline{h}}$

$$\frac{\partial c_s}{\partial t} - \alpha\frac{T_h}{n_h}\frac{Z}{3m_i}\frac{\partial n_h}{\partial z} \qquad (7)$$

$$\frac{\partial n_n}{\partial t} = -\alpha n_c\frac{\partial c_s}{\partial z} \qquad (8)$$

On eliminating c_s we arrive at a non-linear *wave* equation

$$\frac{\partial^2 n_h}{\partial t^2} = \alpha^2 n_c\frac{ZT_h}{3m_i}\frac{\partial}{\partial z}\left(\frac{1}{n_h}\frac{\partial n_h}{\partial z}\right) \qquad (9)$$

in contrast to the non-linear *diffusion* equation found in Bell. This gives a characteristic velocity of propagation, u

$$u = \left[\frac{\alpha^2 n_c Z T_h}{3m_i n_h}\right]^{1/2} \qquad (10)$$

A numerical example, pertinent to ref.6, α = 2, n_c/n_h = 100, T_h = 200keV, Z = 6, m_i = $12m_p$ gives u = 3.6 x 10^7ms^{-1} or a transmission time through 140μm of plastic of 4ps.

A self-similar solution can be found for eq.(9) giving

$$T_c \propto n_h \propto \frac{t^2}{(z+z_0)^2} \qquad (11)$$

for $I_{abs} \propto t$ and $z_0 = \frac{7}{3}\alpha^2 T_n^2\frac{n_c Z t}{m_i I_{abs}}$.

Skin depth and magnetic field

Space charge neutralisation in a background plasma occurs on a time scale $(4\pi\sigma)^{-1}$, while in absence of an induced plasma current a relativistic electron beam will be limited to the Alfvén-Lawson value $\beta\gamma mc^3/e$. When a cold electron return current is driven, the usual model[5] leads to a skin depth δ of $c(t/\sigma)^{1/2}$. In contrast a cold collisionless background plasma will have a skin depth of c/ω_{pe} where ω_{pe} is the cold electron plasma frequency, while a hot plasma will have an anomalous skin depth that we can estimate to be $\left(c^2 v_c \pi t / w_{pe}^c\right)^{1/3}$. This last case is appropriate for the PIC simulations[1] and gives good agreement of $\delta \approx 3.6c/\omega_{pe}$.

However when we ask if the lower hybrid turbulence will be important we find that in such a PIC simulation v_d is much greater than c_s. Employing the anomalous collision frequency[7,8] we find it has a value of $2 \times 10^{15} s^{-1}$ for $T_i = 0.1T_e$, $(v_d/v_i)^2 = 10$, B = 250MG and $\beta_e \sim 1$. Its growth rate is only 1% of the laser (angular) frequency ω_0 and its saturation time is $\sim 10^3\omega_0^{-1}$. A very fine mesh $\leq 0.1\lambda_D$ (λ_D is the Debye length) would be required to simulate this, but we can estimate that the skin depth will be increased by a significant factor to a value of $c/\alpha\omega_{pi}$ and hence the magnetic field will also rise by this factor.

However before then the magnetic pressure might exceed the plasma pressure and pinching of the channel will occur. The experimental evidence for magnetic channelling of the electron beam itself is now very strong as shown by the hot plasma breakout on the rear surface[6] and more recently from the emerging energetic proton deflection[9].

References

1. S C Wilks et al.
   Phys. Rev. Lett. 69, 1383 (1992)
2. J R Davies et al.
   Phys. Rev. E. 56, 7193 (1997)
3. A R Bell et al.
   Plasma Phys. Control. Fusion 39, 653 (1997)
4. M G Haines,
   Phys. Rev. Lett. 78, 254 (1997)
5. R B Miller,
   'An Introduction to the Physics of Intense Charged Particle Beams',
   Plenum Press, New York (1982)
6. M Tatarakis et al.,
   Phys. Rev. Lett. 81, 999 (1998)
7. J V Brackbill et al.
   Phys. Fluids 27, 2682 (1986)
8. J F Drake et al.
   Phys. Fluids 27, 1148 (1986)
9. E L Clark et al.,
   (submitted for publication).

Fokker-Planck Coefficients for Ion-Electron Collisions in an Electro-magnetic Field

G J Pert

Department of Physics, University of York

Main contact email address: *gjp1@york.ac.uk*

Introduction

Fokker-Planck modelling provides a convenient method for calculating the electron distribution function following ionisation by a strong electro-magnetic field. In contrast to Monte-Carlo simulation the method allows a more accurate calculation of the distribution in the high velocity tail without unacceptably high computational overheads, a condition important for the investigation of electron excitation and ionisation. The calculation of electron-electron elastic collisions follows the usual MacDonald,-Judd-Rosenbluth form. However unless the simulation is to be performed on the time scale of the field oscillation, some averaging over the ion-collision rate is required. This report shows how this requirement can be met when the electron distribution is isotropic, and yields (yet again) the high field inverse bremsstrahlung heating rate.

Electron-Ion Scattering

We consider the scattering of oscillating electrons by heavy, fixed ions of charge Z and density N_i. In this case in the absence of an electric field, the electron velocity is unchanged in the collision, since an elastic rotation in the isotropic case leaves the speed unaltered. When the field is present, we require the scattering averages parallel and perpendicular to the electron velocity: $\Delta v_{\|}$, $\Delta v_{\perp}$ (= 0 in a symmetric system), $\Delta v_{\|}^2$, $\Delta v_{\perp}^2$. Transforming to the frame with the ions moving with quiver velocity -u and the electrons with their thermal speed v we can obtain these averages directly from Chandrasekhar[1)] (equations (2.352), (2.421), (5.723) and (32) p.256) accurate to the 'dominant term' in the Coulomb logarithm. Each term omits smaller logarithmic and other terms, in particular we lose the behaviour of the log with respect to u and v together. This will lead to problems at low fields, where the variation of the Coulomb log is crucial in determining the rate of energy absorption. The mean velocity changes per unit time, calculated from $\Delta v = \Delta v_{\|} + \tfrac{1}{2}\Delta v_{\perp}^2 / v$ and $\Delta v^2 = \Delta v_{\|}^2$, obtained with this level of approximation are:

$$\Delta v = \frac{4\pi}{3} N_i \frac{(Ze^2)^2}{m^2}\frac{1}{v^2}\begin{cases} -\dfrac{u^2}{v^2}\ell n[\Lambda(v)] & \text{if } v>u \\ 2\dfrac{v}{u}\ell n[\Lambda(u)] & \text{otherwise}\end{cases}$$

$$\Delta v^2 = \frac{8\pi}{3} N_i \frac{(Ze^2)^2}{m^2}\frac{1}{v}\begin{cases} \dfrac{u^2}{v^2}\ell n[\Lambda(v)] & \text{if } v>u \\ \dfrac{v}{u}\ell n[\Lambda(u)] & \text{otherwise}\end{cases}$$

the velocity used to calculate the Coulomb logarithm should be the averaged relative impact speed, but this presents intractable problems. Consistently with Chandrasekhar, we use the larger of the two individual values, namely Max(u,v). The Coulomb logarithm for electron/ion collisions in an applied field takes a different form from that of the electrons as a consequence of the changed outer impact parameter over which energy absorption can take place. In either classical or quantum scattering we obtain the forms $\ell n[\Lambda(v)] = \ell n\{\sqrt{[1 + (b_{max}/b_{min})^2]}\}$ where $b_{min} \approx \mathrm{Max}[(Ze^2/mv^2),(h/mv)]$ and $b_{max} \approx v/\omega$ are the inner and outer impact parameters respectively; the inner parameter is either the Landau parameter or the electron wavelength depending on the nature of the scattering process. The mean energy gain per unit time $\Delta E = m[v\,\Delta v + \tfrac{1}{2}\Delta v^2]$ is zero for v > u. This is clearly un-physical since inverse bremsstrahlung is present at low intensity, and is due to the neglect of higher order terms referred to earlier. Proceeding to the next order for v > u we find Δv is modified to:

$$\Delta v = \frac{4\pi}{3} N_i \frac{(Ze^2)^2}{m^2}\frac{1}{v^2}\begin{cases} \dfrac{d}{dv}\left\{\dfrac{u^2}{v}\ell n[\Lambda(v)]\right\} & \text{if } v>u \\ 2\dfrac{v}{u}\ell n[\Lambda(u)] & \text{otherwise}\end{cases}$$

but Δv^2 remains unchanged. Hence the mean energy gain per unit time:

$$\Delta E = \frac{4\pi}{3} N_i \frac{(Ze^2)^2}{m}\begin{cases} \left(\dfrac{u}{v}\right)^2 \dfrac{d}{dv}\{\ell n[\Lambda(v)]\} & \text{if } v>u \\ 3\dfrac{1}{u}\ell n[\Lambda(u)] & \text{otherwise}\end{cases}$$

If the field is off, u = 0, the mean energy change ΔE = 0 consistent with elastic collisions. These results are in excellent agreement with the elementary impact model. To obtain the net energy gain we must average over the field cycle, i.e. over a period of the quiver velocity, $u = u_0\sqrt{[\tfrac{1}{2} - |\phi - \tfrac{1}{2}|\cos(2\theta)]}$. To do this we introduce two parameters R(v) and S(v) which form the averages over the phase, θ, when v> u or v < u respectively:

$$R(v) = \begin{cases} \dfrac{1}{2} & v>u_{max} \\ \dfrac{2}{\pi}\displaystyle\int_0^{\theta'} \frac{u^2(\theta)}{u_0^2} d\theta & u_{max}>v>u_{min} \\ 0 & u_{min}>v \end{cases}$$

$$S(v) = \begin{cases} 0 & v>u_{max} \\ \dfrac{2}{\pi}\displaystyle\int_{\theta'}^{\pi/2} \frac{u_0}{u(\theta)}\ell n[\Lambda(u(\theta))] d\theta & u_{max}>v>u_{min} \\ \dfrac{2}{\pi}\displaystyle\int_0^{\pi/2} \frac{u_0}{u(\theta)}\ell n[\Lambda(u(\theta))] d\theta & u_{min}>v \end{cases}$$

For a beam with polarisation coefficient φ, we obtain the maximum, $u_{max} = u_0\sqrt{[\tfrac{1}{2} + |\phi - \tfrac{1}{2}|]}$, and minimum, $u_{min} = u_0\sqrt{[\tfrac{1}{2} - |\phi - \tfrac{1}{2}|]}$, quiver velocities, and the phase angle, θ′, at which the velocity equals the instantaneous quiver speed is given by:

$$\theta' = \begin{cases} \pi/2 & v>u_{max} \\ \arcsin\left\{\sqrt{(v^2 - u_{min}^2)/(u_{max}^2 - u_{min}^2)}\right\} & u_{max}>v>u_{min} \\ 0 & u_{min}>v \end{cases}.$$

We note the following properties: R(v) and S(v) are continuous over the entire domain of v; although their derivatives are discontinuous at $v = u_{max}$ and $v = u_{min}$. The combination $\dfrac{u_0^2}{v}\ell n[\Lambda(v)]\dfrac{dR(v)}{dv} + \dfrac{v^2}{u_0}\dfrac{dS(v)}{dv}$ is continuous for all v. For R(v) we have the explicit form

$$R(v)=\begin{cases}\tfrac{1}{2} & v>u_{\max}\\ \tfrac{1}{\pi}\left[\arcsin\left\{\dfrac{v^2-u_{\min}^2}{u_{\max}^2-u_{\min}^2}\right\}-\dfrac{1}{u_0^2}\sqrt{\left(u_{\max}^2-v^2\right)\left(v^2-u_{\min}^2\right)}\right] & u_{\max}>v>u_{\min}\\ 0 & u_{\min}>v\end{cases}.$$

However for S(v) no simple analytic form is available, although simple approximations can be developed for plane polarised (ϕ=0,1) and nearly circular light ($\phi\approx$0.5).

Hence we obtain after averaging over the period:

$$\Delta v=\frac{4\pi}{3}N_i\frac{\left(Ze^2\right)^2}{m^2}\frac{1}{v^2}\left\{\frac{d}{dv}\left\{\left(\frac{u_0}{v}\right)^2\ell n[\Lambda(v)]\right\}R(v)+2\frac{v}{u_0}S(\Delta,v)\right\}$$

$$\Delta v^2=\frac{8\pi}{3}N_i\frac{\left(Ze^2\right)^2}{m^2}\frac{1}{v}\left\{\left(\frac{u_0}{v}\right)^2\ell n[\Lambda(v)]R(v)+\frac{v}{u_0}S(\Delta,v)\right\}$$

The corresponding Fokker-Planck equation becomes:

$$\frac{\partial f}{\partial t}=\frac{4\pi}{3}N_i\left(\frac{Ze^2}{m}\right)^2\frac{1}{v^2}\frac{\partial}{\partial v}\left\{\begin{array}{l}\dfrac{u_0^2}{v}\dfrac{\partial}{\partial v}[R(v)f(v)]\ell n[\Lambda(v)]+\\ \dfrac{v^2}{u_0}\dfrac{\partial}{\partial v}[S(\Delta,v)f(v)]\end{array}\right\}$$

The Energy Integral

The inverse bremsstrahlung absorption rate is obtained by calculating the rate of increase in the total energy integrated over the distribution:

$$\frac{\partial}{\partial t}\int\frac{1}{2}mv^2f(v)4\pi v^2dv$$
$$=16\pi^2mN_i\left(\frac{Ze^2}{m}\right)^2\int\left[\frac{1}{3}u_0^2\frac{d}{dv}\{\ell n[\Lambda(v)]\}R(v)+\frac{v^2}{u_0}S(v)\right]f(v)dv$$

in agreement with earlier results in high and low fields. At low fields, $u_0 \ll v_T$, the term in S(v) does not contribute strongly and R(v) $\approx$ ½. At high fields R(v) $\approx$ 1/3 $(v/u_0)^3$, and the term in R(v) is therefore much smaller than that in S(v). Hence we note that the term R(v) makes only a small contribution to the absorption in high fields and S(v) in low.

If the Coulomb logarithm is held constant then the energy absorption rate obtained by integrating over the distribution does not depend on the term R(v), which integrates to zero provided $\lim_{v\to 0}\ell n[\Lambda(v)]\to 0$, as predicted by the value of ΔE and simple analysis.

The integrals may be evaluated in the limit of weak fields $u_0 \ll v_T$ where v_T is the mean thermal speed ($\sqrt{}$ 2kT/m for a Maxwell-Boltzmann distribution of temperature T). Writing R(v) and S(v) explicitly in terms of their integrals , reversing the order of integration and noting that f(v<u_0) $\approx$ f(0) we obtain:

$$\int_0^\infty\frac{d}{dv}[\ell n\Lambda(v)]R(v)f(v)dv\approx\frac{1}{2}\int_{u_{\max}}^\infty\frac{d}{dv}[\ell n\Lambda(v)]f(v)dv+$$
$$f(0)\int_0^{\pi/2}[\ell n\Lambda(u_{\max})-\ell n\Lambda(u)]u^2(\theta)d\theta$$

and

$$\int_0^\infty S(v)f(v)v^2dv\approx\frac{1}{3}f(0)\int_0^{\pi/2}\ell n\Lambda(u)u^2(\theta)d\theta$$

Hence after integration by parts and using the result $\lim_{v\to 0}\ell n[\Lambda(v)]\to 0$ we obtain:

$$\int_0^\infty\left\{\frac{1}{3}u_0^2\frac{d}{dv}[\ell n\Lambda(v)]R(v)+\frac{v^2}{u_0}S(v)\right\}f(v)dv$$
$$\approx-\frac{1}{6}u_0^2\int_{u_{\max}}^\infty\ell n\Lambda(v)\frac{d}{dv}[f(v)]dv$$

which for a Maxwell-Boltzmann distribution yields:

$$\frac{dE}{dt}=\frac{4\pi^{1/2}}{3}\frac{mN_iN_e}{v_T^3}\left(\frac{Ze^2}{m}\right)^2\left\{\ell n\left(\bar{\Delta}^2\right)-3\gamma\right\}\quad as\ u_0\to 0$$

is accordance with earlier results, where $\Lambda(v) = \Delta v^3$, $\bar{\Delta} = \Delta v_T^3$ and γ is Euler's constant (= 0.677215665). This result confirms the importance of using the next order term in Δv.

The other case in which the integral can be analytically evaluated is the high field limit where $u_0 \gg v_T$. In this case R(v) $\approx$ 0 when f(v) $\neq$ 0 and S(v) is given by its high field value. For plane polarised light we may use the approximation noted earlier which integrates to give for a thermal Maxwell-Boltzmann distribution:

$$\int_0^\infty\frac{v^2}{u_0}S(v)f(v)dv\approx\frac{N_e}{2\pi u_0}\left\{\begin{array}{l}\ell n\left(\bar{\Delta}\right)[\ell n(2x)+(\gamma/2+\ell n2-1)]+\\ 3/2\left\{[\ell n(2x)]^2-(\gamma/2+\ell n2-1)^2-5\pi^2/24\right\}\end{array}\right\}$$

Comparing this result with that from the full calculation for this particular case, we see a difference only in the term $5\pi^2/24$, which replaces $\pi^2/24$. The source of this discrepancy is the cut-off introduced in the term ℓn [Λ(v)] when v = u, and gives a measure of the inaccuracy introduced thereby.

References

1. S Chandrasekhar
Principles of Stellar Dynamics,
Dover Publications (New York) 1960.

Designing Cylindrical Targets to Measure the Radiative Properties of High Density and Temperature Plasmas

Y Xu, S J Rose

Central Laser Facility, CLRC Rutherford Appleton Laboratory, Chilton, Didcot, Oxon, OX11 0QX, UK

Main contact email address: *y.xu@rl.ac.uk*

Introduction

Cylindrical implosion is of great interest because of its excellent diagnostic access [1,2,3]. In this paper we investigate whether it is possible to achieve a high density and temperature plasma with a relatively low temperature and density gradient using a cylindrical implosion directly-driven by a high-power laser [4,5]. We present 1-D numerical simulations to explore the plasma conditions that may be achieved. Our long-term aim is to design an experiment that will allow a measurement of the radiative opacity of the compressed plasma, with a view to assessing the accuracy of current opacity calculations.

Results

We use the one-dimensional hydrocode MED103 with a laser wavelength of 0.35µm and a pulse length of 10nsec. MED103 employs flux-limited Spitzer thermal transport (with a flux limiting factor of 0.1 for our simulations) and a corrected (to give correct solid density) Thomas-Fermi equation of state. Two initial foam densities (160mgcm^{-3} and 250mgcm^{-3}) are used in the simulations. We wish to achieve a compressed core density above 100gcm^{-3} and for successful diagnosis we require a minimum compressed core diameter of about 50µm. Therefore the minimum initial cylinder radius must be 625µm and 500µm corresponding to the two initial densities respectively.

We present here some of the results of our calculations. A schematic diagram of the cylindrical target for which results are presented is shown in Figure 1.

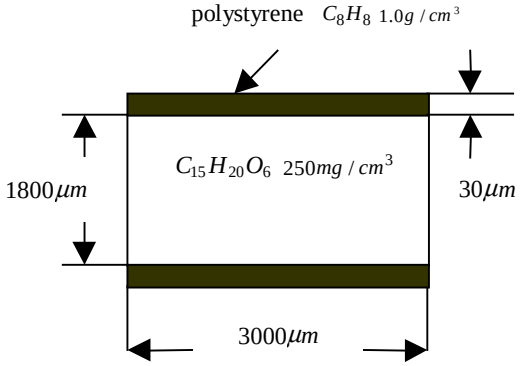

Figure 1. Schematic diagram of cylindrical target for which results are presented.

Figure 2 shows our simulations of the density variation in the foam at different times during the implosion of the cylinder shown in Figure 1, uniformly irradiated by 500kJ of laser energy. From Figure 2 we see that a compressed core density above 100gcm^{-3} can be achieved. The foam is found to be relatively uniform in both density and temperature. This is confirmed in Table 1 which shows the spatial average and standard deviation of both the density and temperature in the foam at two times near peak compression.

To investigate the influence of pulse shape, we have compared the results of using either a Gaussian or a flat-top shape. For the same laser energy a Gaussian pulse produces a plasma with a lower temperature whilst a flat-top pulse produces a plasma which varies more slowly in time.

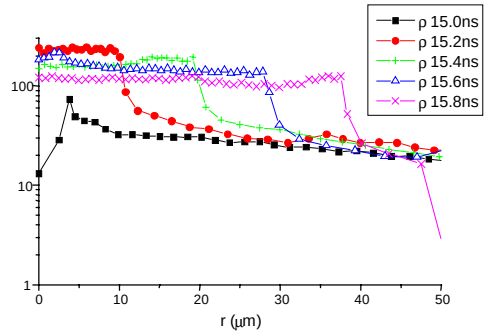

Figure 2. Variation of density (gcm^{-3}) for the cylindrical target in Figure 1 heated by a Gaussian laser pulse.

Future work will involve an assessment of the effect of instabilities on the implosion and the design of an experimental arrangement that will allow diagnostic access along the axis to measure the radiative opacity of higher-Z material doped into a section of the foam.

time (nsec)	T	ΔT	ρ	$\Delta\rho$
15.4	76.4	5.3	167.0	17.8
15.8	59.3	2.7	114.4	7.9

Table 1. Average and standard deviation of foam density (gcm^{-3}) and temperature (eV) at two times during the cylindrical implosion.

References

1. W W Hsing and N M Hoffman
Phys. Rev. Letts. 78, 3876 (1997).

2. W W Hsing, C W Barnes, J B Beck and N M Hoffman
Phys. Plasmas, 4, 1832 (1997).

3. C W Barnes, D L Tubbs, J B Beck et al
Rev. Sci. Instrum. 70, 471 (1999).

4. S J Rose
Physics World, April, 56 (1994).

5. S J Rose
Laser and Particle Beams, 9, 869 (1991).

Travelling Wave Effects on Short Pulse Pumped X-ray Lasers

F Strati and G J Tallents*

Department of Physics, University of Essex, Colchester, Essex, CO4 3SQ

**Now at Department of Physics, University of York, York, Y01 5DD*

Main contact email address: *fstrati@essex.ac.uk*

Introduction

There has been an increasing interest in transient collisional excitation[1)] of soft x-ray lasers. The advent of high intensity, short pulse (~1 ps), lasers has enabled experimental investigation of the feasibility and characteristics of this approach. The first transient excitation demonstration was achieved at the Max Born Institute in Berlin[2)] with neon-like ions. The technique has subsequently been successfully developed and extended in a number of experimental investigations at the Rutherford Appleton Laboratory[3,4,5)] (RAL), at LLNL[6)] and at LULI[7)]. In a recent experiment at RAL[8,9)] saturation has been achieved on the 196 Å Ge neon-like and, for the first time, on the 73 Å Sm nickel-like transitions using a traveling wave technique[10)] for the optical pulse pumping. The efficiency of the traveling wave optical pumping of the lasing medium has been investigated for the 196 Å Ge neon-like x-ray laser by irradiating a solid target with different traveling wave velocities.

The principal aim of this report is to review a simple semi-analytical Amplified Spontaneous Emission (ASE) model, accounting for homogeneous broadening, in order to investigate the active medium length-scaling of the energy output through saturation and the effects of traveling wave pumping on general ASE devices, to which the soft x-ray lasers belong.

Experimental Results

A plane solid Ge target strip was irradiated in a line focus geometry setup of ~12 mm length and ~100 μm width by a multiple pulse arrangement where two long pulses (~280 ps FWHM), of average intensities of ~10^{12} W/cm^2 (first pulse) and ~10^{13} W/cm^2 (second pulse), separated by a 2 ns delay, preceded a ~3 ps CPA pulse of ~10^{15} W/cm^2 from the Vulcan Nd:glass amplifier laser chain. The CPA pulse timing was adjusted so that the short CPA pulse was incident on target ~80 ps after the peak of the second long pulse.

The main effect of the two long pulses is to prepare a pre-formed plasma of the correct ionisation stage and long hydrodynamic scale-length for the arrival of the short CPA pulse that will pump the population inversion on the x-ray laser transition by transient collisional excitation[1)]. As the gain on the x-ray laser transition is of short time duration, T_G, the amplifier length cannot be greater than cT_G (where c is the speed of light) unless a traveling wave pump along the line focus is set up to keep the excitation in phase with the group of photons traveling in the amplifying laser produced plasma medium.

To this effect, traveling wave pumping has been set up by combining the intrinsic tilt in the wavefront of the CPA pulse, inherent to the off-axis focusing optics used, with an additional tilt component given by introducing in the CPA beam line a diffraction grating[10)]. An intrinsic traveling wave pumping speed along the line focus of 2.9c was measured when the diffraction grating was not in place, while an ideal condition of traveling wave speed close to 1.0c was achieved with the diffraction grating inserted in the CPA beam line. In Figure 1 is shown the x-ray laser energy output scaling with target length for the 196 Å Ge transition for the ideal, $V_G = 1.0c$, traveling wave pumping and for the non-ideal, intrinsic, $V_G = 2.9c$, case. Also in Figure 1 are represented some of the predictions of the ASE model to be discussed later in this report. For further details and discussion of the experimental setup and results we refer the reader to MacPhee *et al.*[8,9)].

The ASE Model

We model the x-ray laser device with an idealized monodimensional ASE element consisting of a homogeneous rod of isotropically emitting, amplifying medium of length L, following Pert[11)]. We restrict ourselves to the discussion of homogeneous broadening of a single amplified beam along the active medium but we include the time evolution of the ASE output.

The radiative transfer equation for the frequency dependent ASE intensity is given by:

$$\left(\frac{\partial}{\partial z}+\frac{1}{c}\frac{\partial}{\partial t}\right)I(\nu;z,t)=G(\nu)I(\nu;z,t)+E(\nu) \tag{1}$$

where $G(\nu)$ is the gain and $E(\nu)$ the spontaneous emission rate in the frequency interval $(\nu,\nu+d\nu)$ and z the distance along the rod in the direction of propagation.

As discussed by Pert[11)], in the quasi steady-state approximation for a two-level atom system, the gain and the spontaneous emission rate can be approximated by the following expressions:

$$G(0)=\frac{G_0}{1+I_{ave}/I_S}$$
$$E=\frac{E_0}{1+I_{ave}/I_S} \tag{2}$$

where $G(0)$ is the gain at the line profile center, G_0 the small signal gain at the line center, E_0 the small signal spontaneous emission rate, $f(\nu)$ the line profile (assumed to be identical for spontaneous and stimulated emission), and

$$I_{ave}=\int I(\nu)\left(f(\nu)/f(0)\right)d\nu=\int I(\nu)\Phi(\nu)d\nu \tag{3}$$

is the intensity averaged over the line profile. I_S designates the saturation intensity.

Hence, in quasi steady-state, the following relation holds between the gain and spontaneous emission rate:

$$E(\nu)/G(\nu)=\left(E_0/G_0\right)f(0)\equiv I_0 f(0) \tag{4}$$

where we introduce the *constant* spontaneous emission intensity, I_0, along the rod.

To account for a temporal evolution of the ASE output signal, we assume that the spatial and time dependence can be "lumped" in a given small signal gain profile, while we retain the relation (4) between saturated gain and spontaneous emission rate. This amounts to closing the radiative transfer equation by assuming that the rate equations can be accounted for in the approximations:

$$G_0=G_0(z,t)\quad E(\nu)/G(\nu)=I_0 f(0)=const. \tag{5}$$

These expressions are to be used, along with (2), as source terms for the ASE signal in (1).

The radiative transfer equation then reads:

$$\left(\frac{\partial}{\partial z}+\frac{1}{c}\frac{\partial}{\partial t}\right)I(\nu;z,t)=G(0)\Phi(\nu)\left[I(\nu;z,t)+I_0 f(0)\right] \tag{6}$$

where $G(0)$ is as given in (2).

Assuming the ansatz:

$$I(\nu)=I_0 f(0)\left[\exp(y\,\Phi(\nu))-1\right] \tag{7}$$

for the frequency dependent intensity, where y will play the role of an actual gain-length product, eq. (6) transforms to:

$$\left(\frac{\partial}{\partial z}+\frac{1}{c}\frac{\partial}{\partial t}\right)y=G(0)=\frac{G_0(z,t)}{1+I_{ave}/I_S} \tag{8}$$

where the frequency dependence is now absorbed into the line profile averaged intensity.

As shown by Pert[11], upon the ansatz (7), we can define an amplification function $\alpha(y)$ so that the following relationship holds between the total frequency independent intensity and the intensity averaged over the line profile:

$$\begin{aligned} I_T &= I_0\int d\nu\, f(0)\left[\exp(y\,\Phi(\nu))-1\right]\equiv I_0\,\alpha(y)\\ I_{ave} &= I_0\int d\nu\,\Phi(\nu)\, f(0)\left[\exp(y\,\Phi(\nu))-1\right]\equiv I_0\,\beta(y)\\ \frac{d\alpha}{dy} &= \beta+1 \end{aligned} \tag{9}$$

and eq. (8) finally transforms into a closed form for y:

$$\left(\frac{\partial}{\partial z}+\frac{1}{c}\frac{\partial}{\partial t}\right)y=\frac{G_0(z,t)}{1+r\,\beta(y)} \tag{10}$$

where $r\equiv I_0/I_S$ is the ratio of the spontaneous emission intensity to the saturation intensity.

Using relation (9) among intensities, eq. (10) is readily integrated by the method of characteristics[12] with general solution:

$$(1-r)\,y(L,t)+r\,\alpha(y(L,t))=\int_0^L dz\,G_0(z,\tau)H(\tau)\equiv\gamma(L,t) \tag{11}$$

where $\tau\equiv t-(L-z)/c$ is the retarded time and H is Heaviside's unit step function.

The solution (11) has the form of an implicit, transcendental, equation for the actual gain-length product $y(L,t)$ and it obeys the following initial and boundary conditions imposed on the intensity:

$$\begin{cases} I(\nu;z=0,t\ge 0)=0 & \text{(boundary condition)}\\ I(\nu;z\ge 0,t=0)=0 & \text{(initial condition)}\end{cases}.$$

The general solution (11) forms the basis of the present ASE model. It describes the build-up of an ASE signal from a spontaneous emission intensity I_0, constant along the rod length L, that is switched on at times $t>0$, and where the saturation effects are accounted for assuming a saturated gain of the form given in (2), with a spatial and temporal dependent small signal gain profile $G_0=G_0(z,t)$. The laser line homogeneous broadening influence on the total output intensity is then completely determined by the functional form of the amplification function $\alpha(y)$.

Model Predictions

To model the experimental results presented so far and to exemplify in the simplest case the predictions of the developed model, we first specialize solution (11) to the case of a square-wave small signal gain profile of finite time duration T_G traveling towards positive z with a speed $V_G\ge c$, as given by:

$$G_0(z,t)=g_0\,H(t-z/V_G)H(z/V_G+T_G-t) \tag{12}$$

where g_0 is the flat-top value of the small signal gain and H denotes again Heaviside's unit step function. Inserting (12) in the r.h.s. of (11), defining $1/V_{eff}\equiv(1/c-1/V_G)$ an effective speed and $T_{eff}\equiv L/V_{eff}$, we get: (13)

for $L\le V_{eff}T_G$

$$\gamma(L,t)=\begin{cases} g_0V_{eff}\left[T_{eff}+t-L/c\right] & \text{for } t\in\left[L/c-T_{eff},L/c\right]\\ g_0V_{eff}T_{eff} & \text{for } t\in\left[L/c,L/c+T_G-T_{eff}\right]\\ g_0V_{eff}\left[L/c+T_G-t\right] & \text{for } t\in\left[L/c+T_G-T_{eff},L/c+T_G\right]\\ 0 & \text{otherwise}\end{cases}$$

while for $L>V_{eff}T_G$

$$\gamma(L,t)=\begin{cases} g_0V_{eff}\left[T_{eff}+t-L/c\right] & \text{for } t\in\left[L/c-T_{eff},L/c+T_G-T_{eff}\right]\\ g_0V_{eff}T_G & \text{for } t\in\left[L/c+T_G-T_{eff},L/c\right]\\ g_0V_{eff}\left[L/c+T_G-t\right] & \text{for } t\in\left[L/c,L/c+T_G\right]\\ 0 & \text{otherwise}\end{cases}$$

and for the trivial case $V_G=c$ the solution reduces to $\gamma(L,t)=g_0L$ for $t\in\left[L/c,L/c+T_G\right]$.

It can be noted that in the particular case of the profile (12) the solution (13) exhibits discontinuities in the first derivative propagating, as usual, along the characteristics at speed *c* and, also, with the speed V_G characteristic of the profile discontinuities.

For the specification of the amplification function we assume the simple analytical approximation given by the widely used Linford formula[13], which is strictly valid in the case of integration over a Gaussian frequency line profile in (9) and is given by:

$$\alpha(y)\cong\frac{(\exp(y)-1)^{3/2}}{(y\exp(y))^{1/2}}.$$

Integrating the total intensity output I_T over time for the total energy output at the end of the rod, *L*, we can compute the scaling with length of the ASE signal by numerically solving eq. (11) with the r.h.s. given in (13) by means of a standard root-finding technique, the model results will then depend on the five parameters $g_0, I_0, r=I_0/I_S, T_G, V_G$.

In Figure 1 we present the results of the model for the square-wave profile given in (12) as well as the experimental results described before. Here the model parameters g_0, I_0, r are first fitted to the matching traveling wave pump speed $V_G=c$ by assuming a temporal duration T_G of 10 ps as suggested by simulations with the Ehybrid (1+1/2) hydrodynamics code[14] and by the observation that the experimental ASE output for lengths up to 3.3 mm is independent of the excitation speed V_G. We, then, investigate the effects on the ASE output through saturation of a mismatched traveling wave pump speed $V_G=2.9c$ and of small variations in the small signal gain time duration T_G. In this last case, it is necessary to refit the first

3 parameters g_0, I_0, r to the matching wave speed $V_G = c$ experimental results allowing for the change in T_G. As the total output intensity is constant in time, only the parameter I_0 needs to be changed by a scaling factor.

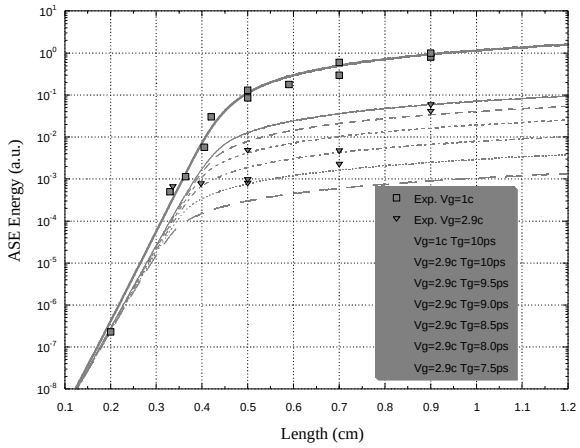

Figure 1. Experimentally measured Ne-like Ge X-Ray laser output at 19.6 nm (taken from[8]) as a function of target length with traveling wave pumping $V_G = c$ (squares) and $V_G = 2.9c$ (triangles). Computed variation from the model assuming a square temporal gain profile of different time durations are plotted (as labelled).

The solution (11) allows for the specification of an arbitrary small signal gain profile. We explored the effects on the ASE signal output of the shape of a traveling wave profile with speed V_G given as $G_0(z,t) = g_0(t - z/V_G)$. The results are shown in Figure 2 and Figure 3, where the temporal shape $g_0(t)$ was either a square-wave of duration 10 ps as discussed above (shape A), an exponential tail of (1/e) relaxation time of 10 and 20 ps (shapes B and C, respectively), a symmetric trapezoid (shape D) or, finally, the peak gain results of an Ehybrid simulation of typical conditions in the experiment (shape E). In Figure 2 the parameters in the model for each of the profiles listed (A,B,C) were first fitted to the matching pump speed $V_G = c$ experimental results and then used to predict the scaling with length of the ASE signal for a mismatched situation where $V_G = 3c$, while in Figure 3 we compare the scaling of the symmetric trapezoid (D) having a FWHM similar to that of the peak gain temporal profile from Ehybrid simulation (E).

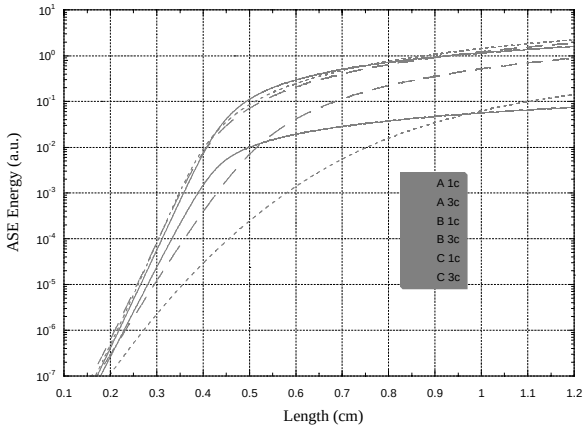

Figure 2. Variation from the model of the ASE output signal for different shapes (A,B,C) of the small signal gain profile as a function of target length, as explained in the text.

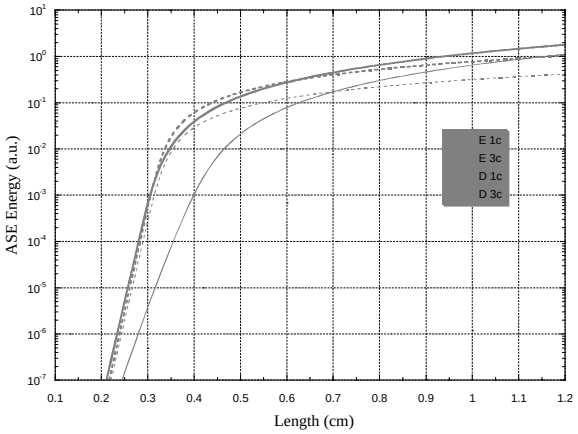

Figure 3. Variation from the model of the ASE output signal for different shapes (D,E) of the small signal gain profile as a function of target length, as explained in the text.

From these results we can see that the ASE output signal does not depend critically on the shape of the temporal profile of the small signal gain when $V_G = c$, while the mismatching condition $V_G > c$ produces in all cases a more dramatic reduction in the available output energy and more pronounced differences for different shapes of the small signal gain profile.

Conclusions

Deploying a simple approximation to the solution of the rate equations for a two-level atom system, we were able to find a solution in closed form for the governing equation of a single-beam ASE signal build-up and propagation in a monodimensional active medium. The model accounts for saturation effects and homogeneous broadening of the laser line and has enabled us to investigate in a quantitative way the effects of a mismatching traveling wave pumping excitation. Indeed both experimental results[8,9] and the present modeling show that a matching condition, $V_G = c$, for the pumping of soft x-ray lasers in the transient collisional regime[1] is a critical issue for enhanced ASE output if the length of the active medium needed to attain saturation is greater than cT_G, where T_G represents a measure of the excitation time duration.

The model also predicts a variation in the temporal evolution of the output ASE pulse for different traveling wave pump speeds as a consequence of the form of the term on the r.h.s. of (11). The main effect is a growth in the pulse-width as the traveling wave pump speed increases due to the different velocities between the excitation and light pulses along the active medium. This feature was not investigated in the experiment.

The approximation (5) is good for laser schemes where the lower level population is rapidly depleted by depopulating mechanisms. However, the investigation of some phenomena is precluded. For example, the description of pulse distortion effects involves a detailed modeling of the rate equations for the atomic specimen coupled to the radiative transfer equation (1).

The model is consistent with previous work aimed at the investigation of the effects of a mismatching condition in the traveling wave pumping of ASE devices. If we restrict ourselves to the particular case of a square-wave profile for the small signal gain, avoid saturation effects and assume a Milne line profile, then we arrive at the same results presented by Warwick *et al.*[15]. Letting $y(L,t) = \gamma(L,t)$, with γ as given in (13), for the actual gain-length product (i.e. neglecting saturation) and integrating the total intensity $I_T = I_0 \alpha(y)$ over time with the amplification function given by

$\alpha(y) = (\exp(y) - 1)$ (i.e. assuming a Milne line profile), gives the scaling with length, *L*, of the output ASE signal and results in agreement with Warwick *et al.*[15].

The present approach allows for both saturation and homogeneous broadening effects to be incorporated and, in the limits discussed above, permits the investigation of general temporal profiles for the small signal gain.

References

1. Yu V Afanasyev and V N Shlyaptsev
   Sov. J. Quantum Electron., 19, 1606, (1989)
2. P V Nickles *et al*
   Phys. Rev. Lett., 78, 2748, (1997)
3. M P Kalachnikov *et al*
   Phys. Rev. A, 57, 4778, (1998)
4. P J Warwick *et al*
   J. Opt. Soc. Am. B, 15, 1808, (1998)
5. A G MacPhee *et al*
   In *X-Ray Lasers 1998*, edited by Y. Kato and H. Daido, IOPP Conf. Series, 159, 75, (1999)
6. J Dunn *et al*
   Phys. Rev. Lett., 80, 2825, (1998)
7. A Klisnick *et al*
   in *X-Ray Lasers 1998*, edited by Y. Kato and H. Daido, IOPP Conf. Series, 159, 107, (1999)
8. A G MacPhee *et al*
   submitted to Phys. Rev. Lett.
9. A G MacPhee *et al*
   "Saturated X-ray lasers at 196Å and 73Å pumped with CPA travelling wave excitation" in the X-Ray laser section of these proceedings.
10. C N Danson *et al*
    in *Superstrong Fields in Plasmas*, edited by M. Lontano, G Mourou, F. Pegoraro and E. Sindoni, AIP Conf. Proc., 426 473, (1998)
11. G J Pert
    J. Opt. Soc. Am. B, 11, 1425, (1994)
12. E Zauderer
    Partial Differential Equations of Applied Mathematics, chap. 10, 778-808, Wiley Interscience, New York, 1998
13. G J Linford E R Peressini W R Sooy and M L Spaeth
    Appl. Opt., 13, 379, (1974)
14. G J Pert
    J. Fluid Mech., 131, 401, (1983)
15. P J Warwick and C L S Lewis
    Central Laser Facility Ann. Rep. RAL-TR-97-045 [ISBN 0902376705], 99, (1998).

Manipulation of Bond Hardening in H_2^+ by Chirping of Intense Femtosecond Laser Pulses

L J Frasinski, J H Posthumus, J Plumridge, K Codling

J. J. Thomson Physical Laboratory, The University of Reading, Whiteknights, Reading RG6 6AF, UK

P F Taday, A J Langley

Central Laser Facility, CLRC Rutherford Appleton Laboratory, Chilton, Didcot, Oxon, OX11 0QX, UK.

Main contact email address: *L.J.Frasinski@reading.ac.uk*

Intuition suggests that a sufficiently strong laser field can weaken molecular bonds and induce dissociation. This mechanism known as *bond softening*[1] is uncontroversial and well understood in H_2^+ (see, for example, *Topical Review*[2]). The opposite effect, also called molecular stabilisation, vibrational trapping, creation of light-induced bound states or *bond hardening*, has the same theoretical origin[1], but the history of its experimental verification has been confusing. Two manifestations of bond hardening in H_2^+ near one-photon[3] and three-photon[4] resonances were inferred from rather noisy data in the early 1990s. They were received with great interest, as at that time the stabilisation of the molecular bond was a candidate for a universal mechanism explaining the invariance of ion kinetic energies with changes of intensity and pulse duration[5,6]. Later, it was established that this invariance is a signature of rapid, sequential ionisation at the critical internuclear distance[7-9]. Since then there has been a surprising lack of clear-cut confirmation of the bond hardening effect. With more recent work casting doubt on the existence of light-induced bound states[10-11], the idea of bond hardening has become again only a remote theoretical possibility. Against this trend of scepticism, we present an experimental observation of bond hardening in H_2^+.

In these experiments, chirped pulses from a Ti:sapphire laser[12] were amplified to 10 mJ in energy and compressed to about 50 fs duration at a repetition rate of 10 Hz. The pulse bandwidth had an almost perfect gaussian shape centred at 792 nm and an extent of 22 nm, full width at half maximum (FWHM). The pulse length was varied by scanning the separation of the two compressor gratings and introducing some uncompensated chirp. The linearly polarised beam, 5 mm in diameter, was focused in an ultra high vacuum chamber using an f/4 parabolic mirror to give a peak intensity of the order of 10^{14} W/cm^2. Hydrogen gas was introduced into the vacuum chamber via simple effusion, raising the ambient pressure to about 10^{-6} torr. At this pressure and intensity no space charge effects were observed. Following the process of multiphoton ionisation of H_2, an external electric field directed 'forward' and 'backward' fragment ions into a vertical, 13 cm-long drift tube. Ions were detected by microchannel plates with a 10-mm circular restriction in front to improve the energy and angular resolutions. The ion time-of-flight (TOF) spectrum and pulse energy were recorded at each laser shot by a digital oscilloscope and stored in a computer.

Figure 1 shows ion TOF spectra recorded at several pulse lengths. For each grating separation the peak intensity was adjusted to about 150 TW/cm^2, i.e. below saturation of any ion channel[13]. At each laser pulse the ion signal and the pulse energy were stored, but ion signals from only a narrow energy window were selected for the TOF plots. The position of the window was slightly adjusted to give the same height of the H_2^+ peak and highlight amplitude changes in the H^+ peaks. The lowest energy channel, 1ω, involves dissociation of H_2^+ via one-photon absorption. The next channel, 2ω, is a similar process but involves absorption of three photons and an emission of one of them. The (1, 1) channel is the Coulomb explosion of two protons following H_2^+ ionisation. This peak shifts to higher kinetic energies with pulse shortening, because shorter rise time initiates Coulomb explosion at a smaller inter-nuclear distance. A similar dynamic shift is observed in the 1ω peak but the details are quite different; bond hardening is involved.

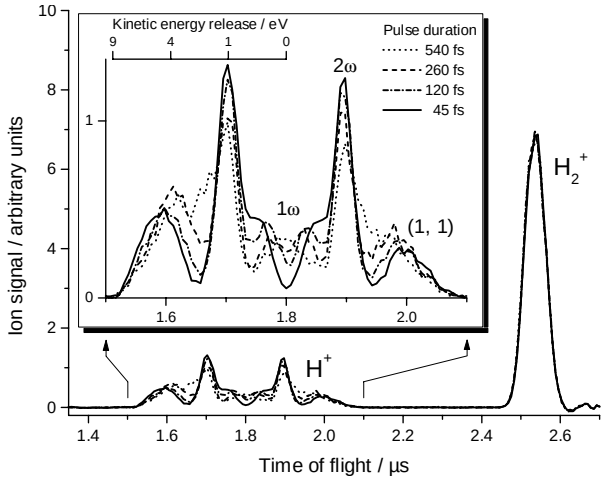

Figure 1. Bond hardening manifests itself as a shift in the low-energy proton peak labelled 1ω, from 0.0 to 0.3 eV of kinetic energy release when the laser pulse is shortened from 540 to 45 fs.

Potential energy curves for H_2^+ dressed in the photon field are shown in Figure 2, which was adapted from Reference 2 by adjusting the photon wavelength to 792 nm. It is sufficient to consider only the two lowest molecular ion states: the attractive $1s\sigma_g$ and repulsive $2p\sigma_u$ states. Since the system, H_2^+ and photons, must be considered as a whole, the molecular curves must be repeated at all discrete energies of the photon field. Zero energy is set at some arbitrarily large number of photons and the states are labelled with $n\omega$, where n is the number of photons absorbed. Due to selection rules, the photon interaction couples only half of the states, alternating between $1s\sigma_g$ and $2p\sigma_u$ for even and odd n. These diabatic states, shown in Figure 2 as solid lines, describe the system correctly at low laser intensity. When the intensity increases, the curve crossings become anticrossings and a widening of the energy gap between the upper and lower branches of the new, adiabatic states (broken lines) occurs.

On the lower branch the electronic charge oscillates in phase with the laser field, decreasing the energy of the system; on the upper branch these oscillations are in antiphase. At the centre of the gap almost the entire electronic charge oscillates between the two protons. As the system moves away from resonance, the amount of oscillating charge diminishes, in sympathy with the reduced mixing of the $1s\sigma_g$ and $2p\sigma_u$ states. At the 1ω crossing the charge oscillates with the laser frequency; at the 3ω crossing the charge oscillations are three times faster. Strictly speaking, this adiabatic picture is valid only for a slowly evolving system. Nevertheless, it allows us to understand the dynamics of H_2^+ on a time scale an order of magnitude slower than the oscillations of the laser field.

In Figure 3 the process of bond hardening is illustrated with the relevant potential curves copied from Figure 2. The ionisation of the neutral molecule starts at about 50 TW/cm^2 on the leading edge of the laser pulse creating a wave packet composed of a few of the lowest vibrational states of H_2^+. The interesting part of this wave packet has energy just below the 1ω dissociation limit (see Figure 3 (a)). It crosses the potential well in about 10 fs and arrives at the 3ω gap while the gap is still rather small. The Landau-Zener transition probability[14] (for a convenient formula) tells us that most of the wave packet crosses the gap diabatically. The wave packet slows down in the shallow part of the potential well, turns back and arrives again at the 3ω crossing, when the gap is much wider and the probability of a diabatic crossing is small. Now the wave packet is trapped in the laser-induced adiabatic state (see Figure 3 (b)), essentially completing the process of bond hardening.

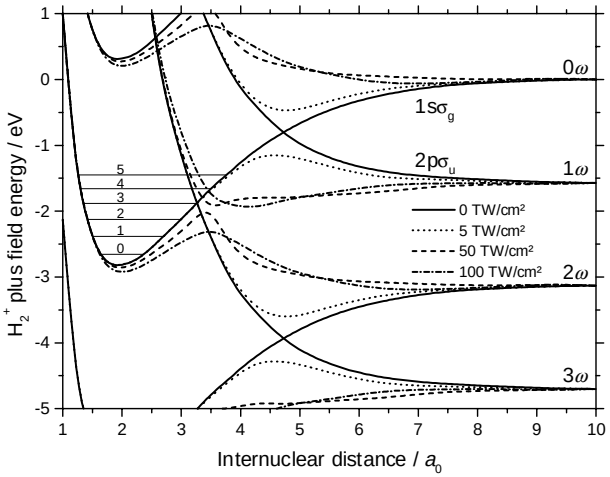

Figure 2. Molecular potential energy curves of H_2^+ dressed in a photon field of 792 nm wavelength. With increasing laser intensity curve crossings become anti-crossings. A nuclear wave packet with kinetic energy corresponding to the 3rd and 4th vibrational levels of a free molecule can be trapped in the potential well created by intensities of 100–200 TW/cm^2 at 4 a_0.

Of particular interest is the decay of the bond-hardened state. As the intensity falls on the trailing edge of the laser pulse, the shape of this state changes from concave to convex (see Figure 3 (c)); it now becomes the bottom part of the 1ω anti-crossing. In this process the trapped wave packet is lifted up and about a half of it falls back into the $1s\sigma_g$ well, but the other half spills out to the 1ω dissociation limit. Clearly, the faster the intensity fall time, the higher the wave packet is lifted and the larger is the kinetic energy it gains. This dynamic process is responsible for the shift of the 1ω peak shown in Figure 1.

Chirping laser pulses change the wavelength at the leading and trailing edges of the pulse. To test if this wavelength variation affects the 1ω peak, the grating separation was scanned to give a chirp variation from positive to negative. The recorded TOF spectra shown in Figure 4 are symmetrical with respect to the zero-chirp grating separation, $s = 0$. (The somewhat larger noise compared to Figure 1 reflects the lack of windowing of the pulse energy.) To test further for a possible wavelength effect, a slit selecting only a part of the optical spectrum was inserted in the compressor and several TOF spectra were recorded at various wavelengths. It was found that only the reduced bandwidth and not the central wavelength affected the kinetic energy of the 1ω peak. These tests show that chirped pulses are just as good as bandwidth-limited ones for manipulating the dynamics of bond hardening. Reducing the pulse intensity to well below the saturation level does not shift the position of the 1ω peak. This suggests an absence of dynamic effects near the peak of intensity and indicates that the wave packet is released from the bond-hardened state on the *trailing* edge of the laser pulse. Such intensity independence of the 1ω peak contrasts with the behaviour of the (1, 1) peak. Here dissociation of H_2^+ on the *leading* edge[13] is followed by further ionisation and Coulomb explosion, with the kinetic energy release being affected by the magnitude of the peak intensity.

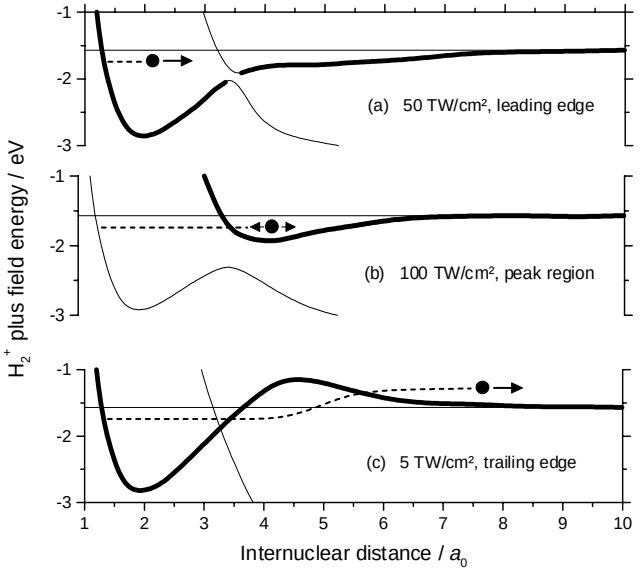

Figure 3. The dynamics of bond hardening. H_2^+ is created on the leading edge of the laser pulse and the wave packet jumps the anti-crossing gap (a). As the intensity increases, the gap widens and the wave packet is trapped (b). Falling intensity flexes the well upwards and the wave packet is released (c). The kinetic energy release depends on the speed of the intensity fall.

The threshold for population trapping in the bond-hardened state is experimentally estimated to be about 100 TW/cm^2. This population trapping is expected to cease above 200 TW/cm^2 due to increasing probability of ionisation[13] rather than shallowness of the bound state. Even if the state cannot support any vibrational levels at high intensity, the spreading of the wave packet is too slow to disperse the population before the intensity drops again.

It is interesting to note the complex *electron* dynamics of the bond-hardened state, which is the result of the combined mixing of the $1s\sigma_g$ and $2p\sigma_u$ states at 1ω and 3ω frequencies. At large inter-nuclear distances the electron charge oscillates in phase with the laser field and the attractive force of the bond comes from the diminishing of these oscillations with increasing inter-nuclear distance. At small distances the charge oscillations become three times faster and in anti-phase, but the repulsive force on the nuclei is dominated by the anti-bonding nature of the $2p\sigma_u$ state.

Energy conservation deserves a brief comment. The dashed trajectory in Figure 3 (c) indicates that the H_2^+ ion gains a fraction of a photon energy in the bond-hardened state. This can be explained by absorption of photons from the high-energy end of the spectrum and re-emission at the low-energy end, a dynamic Raman effect within the laser bandwidth (45 meV FWHM).

The interpretation of the shift in the 1ω peak in terms of the bond hardening process depicted in Figure 3 is supported by previous theoretical work. Figure 19(b) in Reference 2 shows the evolution of a wave packet exposed to a pulse of 150 fs duration, 150 TW/cm^2 peak intensity and 780 nm wavelength. The simulation starts from the $v = 4$ vibrational level of H_2^+.

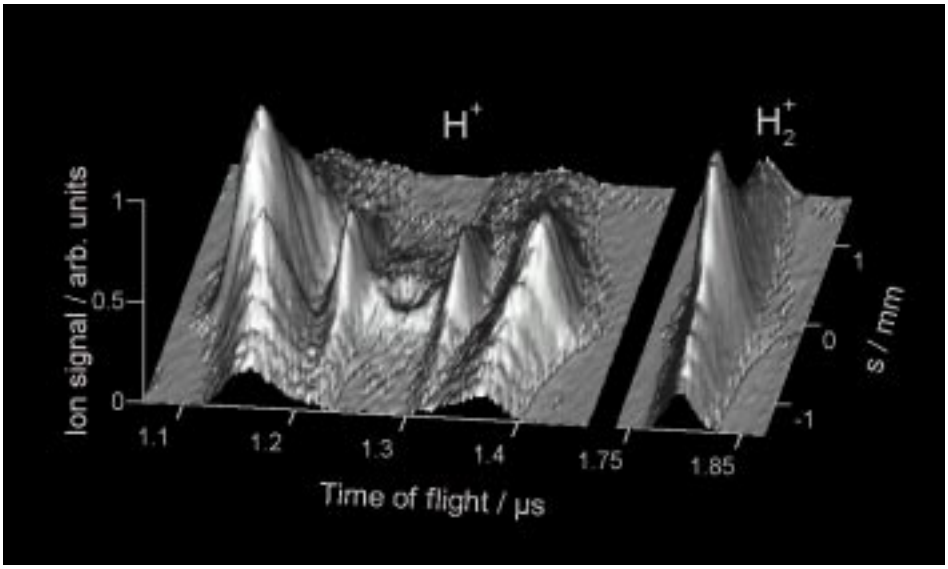

Figure 4. The variation of ion TOF spectra with grating separation offset, *s*, shows the dynamic Raman effect as a 'crater' in the middle of the proton peaks. The variation of the pulse duration (FWHM) with *s* is given by Δt/fs = $\sqrt{(42^2 + (350\ s/\text{mm})^2)}$. The symmetry of the crater with respect to the $s = 0$ position (the shortest pulse) shows that the dynamics of the bond-hardening is independent of the chirp direction.

As the intensity increases, one half of the population escapes with high kinetic energy to the 2ω dissociation limit whereas the other half gets trapped at an inter-nuclear distance of between 4 and 5 a_0 for about 100 fs. When the intensity falls, about a half of the trapped population is released with energy of 0.1 eV to the 1ω limit. It is remarkable that this population is lifted from just below the dissociation limit, providing a theoretical basis for the dynamic Raman effect. The calculated proton energy spectrum (figure 20(b) of Reference 2) clearly shows the 1ω and 2ω peaks we observe in Figure 1. It would be interesting to repeat these simulations for a range of pulse duration in order to confirm the existence of this dynamic shift of the 1ω peak.

A lower range of vibrational levels of H_2^+ seems to be populated than expected from the Franck-Condon overlap with the ground state of H_2 (see, for example Figure 3 of Reference 15). This indicates that bond softening also takes place in the neutral molecule and the first ionisation occurs at a relaxed inter-nuclear distance. The $v = 0$ level is expected to be highly populated but its tunnelling probability through the bond-softened barrier is small (see Figure 2). Higher vibrational levels dissociate with increasing efficiency through the 3-photon gap to the 2ω limit. Trapping in the bond hardened state is expected to start at $v = 3$ and be quite efficient at $v = 4$. The population of $v \geq 5$ levels, which are above the 1ω dissociation limit, is probably negligible. We therefore believe that almost all population of the 1ω peak shown in Figure 1 is lifted from *below* the dissociation limit by the dynamic process depicted in Figure 3(c).

With hindsight we suggest that peaks B in Figure 2 of Reference 11 are a signature of the bond-hardened state, despite the authors' claim that their experimental conditions cannot populate such states. This state is the same one allegedly observed much earlier[4)] but it turns out that it is populated without the initial molecular wave packet bouncing back and can be observed in the low-energy 1ω channel rather than the energetic (1, 1) channel (see Figures 2 and 3 of Reference 4).

We are pleased to acknowledge the Engineering and Physical Sciences Research Council (UK) for their financial support.

References

1. A D Bandrauk and M L Sink
J. Chem. Phys. 74, 1110 (1981).

2. A Giusti-Suzor, F H Mies, L F DiMauro, E Charron, and B Yang
J. Phys. B: At. Mol. Opt. Phys. 28, 309 (1995).

3. S W Allendorf and A Szöke
Phys. Rev. A 44, 518 (1991).

4. A Zavriyev, P H Bucksbaum, J Squier and F Saline
Phys. Rev. Lett. 70, 1077 (1993).

5. K Codling, and L J Frasinski
J. Phys. B: At. Mol. Opt. Phys. 26**,** 783 (1993).

6. M Schmidt, D Normand and C Cornaggia
Phys. Rev. A 50, 5037 (1994).

7. J H Posthumus, L J Frasinski, A J Giles and K Codling
J. Phys. B: At. Mol. Opt. Phys. 28**,** L349 (1995).

8. T Seideman, M Yu Ivanov and P B Corkum
Phys. Rev. Lett. 75, 2819 (1995).

9. T Zuo and A D Bandrauk
Phys. Rev. A 52, R2511 (1995).

10. T D G Walsh, F A Ilkov and S L Chin
J. Phys. B: At. Mol. Opt. Phys. 30**,** 2167 (1997).

11. G N Gibson, M Li, C Guo and J Neira
Phys. Rev. Lett. 79**,** 2022 (1997).

12. S Backus, C G Durfee III, M M Murmane and H C Kapteyn, Rev. Sci. Instr. 69, 1207 (1998).

13. J H Posthumus, J Plumridge, P F Taday, J H Sanderson, A J Langley, K Codling and W A Bryan
J. Phys. B: At. Mol. Opt. Phys. 32, L93 (1999).

14. A Zavriyev and P H Bucksbaum
in *Molecules in Laser Fields*, edited by A. D. Bandrauk, published by Marcel Dekker Inc., New York (1994)

15. T D G Walsh, F A Ilkov, S L Chin, F Châteauneuf, T T Nguyen-Dang, S Chelkowski, A D Bandrauk and O Atabek, Phys. Rev. A 58, 3922 (1998).

Multiply Charged Intact Ions of Polyatomic Cyclic Molecules Generated by Strong Laser Fields

C Kosmidis, P Tzallas

Physics Department, University of Ioannina, 45110 Ioannina, Greece

K W D Ledingham, T McCanny, R P Singhal

Department of Physics and Astronomy, University of Glasgow, Glasgow G12 8QQ, UK

P F Taday, A J Langley

Central Laser Facility, CLRC Rutherford Appleton Laboratory, Chilton, Didcot, Oxon, OX11 0QX, UK

Main contact email address: *kkosmid@cc.uoi.gr*

Introduction

The interaction of strong laser fields with atoms and molecules leads to the production of multiply charged species. The observation of highly charged atomic ions produced by intense laser beams has been reported a few years ago [1-3] and has later been extended to molecular ions[4,5].

Multiply charged molecular ions may offer significant advantages in quantitative analysis and structure determination, notably isomer distinction and peptide analysis. Recently, multiply charged intact ions induced by femtosecond (fs) lasers have been observed for some polyatomic molecules[6-8]. This observation, in conjunction with the potential of femtosecond laser induced mass spectrometry discussed earlier[8] may have an important bearing on analytical applications.

The mechanism for the production of these species is not clear yet. Two main mechanisms have been proposed for the production of multiply charged atomic ions. According to the first mechanism, called stepwise ionization, initially only one electron is detached from the atom while the second electron is subsequently ejected from the singly charged ion. The second mechanism is a non-sequential one and is referred to as the simultaneous detachment of two electrons. Cornagia and Hering[9] have reported non-sequential ionization for a number of small molecules.

In the present work the interaction of some cyclic polyatomic molecules with strong laser beams (10^{15}-10^{16}W/cm^2) is studied. De Witt and Levis[10-11] have concluded that ionization yield of the parent molecule is related to the molecular structure.

The main aim of the present work is to explore the role of molecular structure in multiply charged intact ion generation under strong laser irradiation and the influence of the frequency and the intensity of the laser beam. The molecules have been chosen in such a way as to investigate the influence, if any, of aromaticity for some homo- and heterocyclic compounds. It is important also to check the significance of the nature of the higher occupied molecular orbitals (MO).

Experimental Details

The experimental set up used is described in detail elsewhere[7]. The specifications of the laser pulses were: pulse width 50 fs, wavelengths 790 and 395 nm. Both wavelengths were vertically polarized. Controlled attenuation of the beam energy was achieved by a variable neutral density filter. Laser intensities were estimated to be accurate to 10-15%.

The time of flight (TOF) mass spectrometer is of conventional linear arrangement with ion optics based on a Wiley-McLaren design and an Einzel lens placed immediately after the extraction optics to increase the ion transmission through the system. The samples were admitted effusively from the inlet system to the vacuum chamber via a needle valve.

The laser beam was focused using a concave mirror of focal length 3cm at about 4mm from the repeller. The mass resolution was typically 200 at 100D.

Results and Discussion

In Figure 1 the mass spectra of cyclopentanone, cyclohexanone, furan, pyridine and aniline are presented. These spectra have been recorded at 790nm. Cyclopentanone (CP) and furan have a five-members ring, while cyclohexanone (CH), pyridine and aniline a six-member one. Except CP and CH, the other three molecules are aromatic and only aniline is a homocyclic aromatic molecule. CP, CH and pyridine have a n-MO as HOMO while aniline a π-type MO.

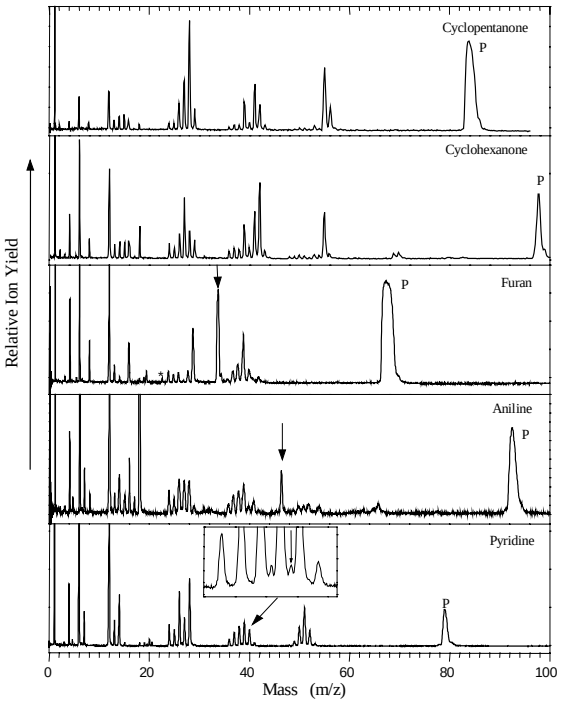

Figure 1. The TOF mass spectra induced at 790nm (I~4x10^{14}W/cm^2). The parent ion is denoted by a P, the P^{2+} by an arrow and P^{3+} by a star.

Multiply charged intact ions have been observed only for aromatic molecules. This observation holds also at λ=395nm (Figure 2).

In Figure 3, the ratio P^{2+}/P^{+} as a function of laser intensity at λ=790 and 395nm is presented for a furan, pyridine and aniline. For furan the ratio P^{3+}/P^{+} is also presented. It is worth noting that triply ionized hydrocarbons have rarely been observed. For furan and pyridine the ratio P^{2+}/P^{+} increases as a function of intensity and at higher laser intensities becomes more or less constant (plateau) for 790nm. The latter is not observed for 395nm. The ratio P^{2+}/P^{+} for aniline has an inverse wavelength dependence compared to that observed for furan. Moreover, it is found for pyridine that the abundance ratio P^{2+}/P^{+} is higher at 395nm than that at 790nm. These differences suggest that the

mechanism for multiple ion production is not the same for all species and could be related to molecular structure.

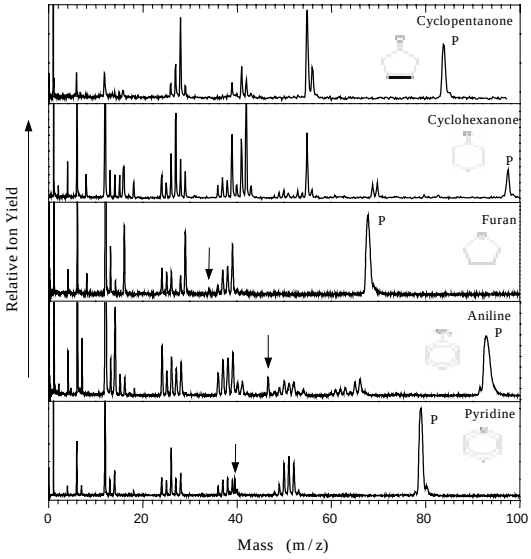

Figure 2. The TOF mass spectra at 395nm. The parent ion peak is denoted by a P and the doubly charged parent ion by an arrow.

Molecular ionization could be attributed to multiphoton ionization processes (MPI) and/or to a field ionization mechanism. Of course, in any case, MPI is expected to contribute to ion production on the laser pulse wings. At the laser pulse peak intensity, even for the lower intensities employed, the Keldysh parameter γ is found to be smaller than 1 for both wavelengths used (for furan γ is estimated to be 0.44 at γ=790nm and 0.55 at 395nm). These γ values are indicative of tunneling ionization and the single ionization is attributed to a field ionization mechanism.

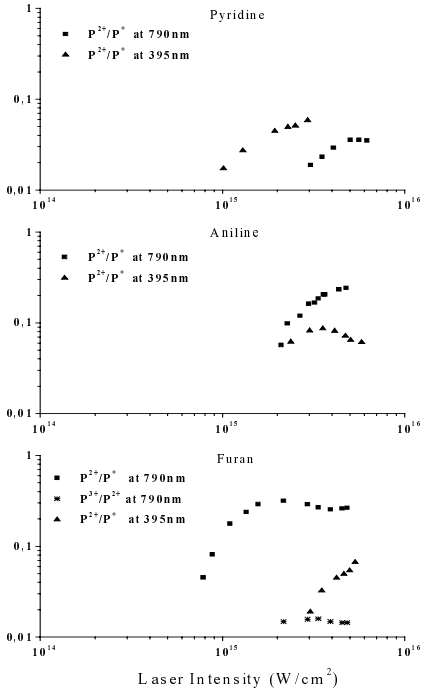

Figure 3. The abundance ratios of P^{2+}/P^{+} for furan, aniline and pyridine at 790 and 395 nm. For furan the ratio of P^{3+}/P^{2+} at 790nm is also shown.

It is possible that the recorded double and triple intact ion have been produced through a simultaneous detachment or a stepwise process. As mentioned before, double ionization of some small molecules has been attributed to simultaneous ejection of two electrons. For multiple, non-sequential ionization two different mechanisms have been proposed. Corkum[12] proposed a re-scattering model while Fittinghoff et al[13] proposed an alternative explanation known as the shake-off model.

In Figure 4 the dependence of the total ion signal, the parent ion, the doubly and triply charged parent ion on the laser intensity at λ=790 and 395nm is presented for the case of furan. No doubly charged intact ions could be recorded for laser intensities where the yield of the single charged parent ion was not close to saturation. This observation is valid for both wavelengths and could be considered as evidence, although not a proof, for a stepwise (sequential) ionization process, involved in the production of the P^{2+} ion. The same observation is valid for the P^{3+} production (P^{3+} observed for laser intensities above the saturation of P^{2+}).

If the re-scattering mechanism was involved in the multiply charged ion production, then the maximum kinetic energy of the returning electron is expected to be 3.17Up, [where Up is the ponderomotive potential, $Up=9.33\times10^{-14}I\lambda^2$, (I in W/cm^2 and λ in μm)] and this energy should be enough to eject the second electron i.e. higher than the ionization potential for P^{2+} generation. Tsai and Eland[14] have found a good correlation between single and double ionization energies for aromatic molecules: double ionization energy is 2.8±0.1 times that of single ionization. The maximum kinetic energy of the returning electron at the determined intensity thresholds for furan should be 148 eV at 790nm and 138 eV at 395nm, while the IP^{2+} is estimated to be only 25 eV. It is clear that from this point of view, the re-scattering mechanism could be also involved in the doubly charged ion production although the maximum kinetic energy of the electron corresponds to much higher energies than those needed for P^{2+} generation. The above conclusion is valid also for aniline and pyridine. It is believed that the polarization dependence of the ion yield will provide further information on the details of the ionization mechanism.

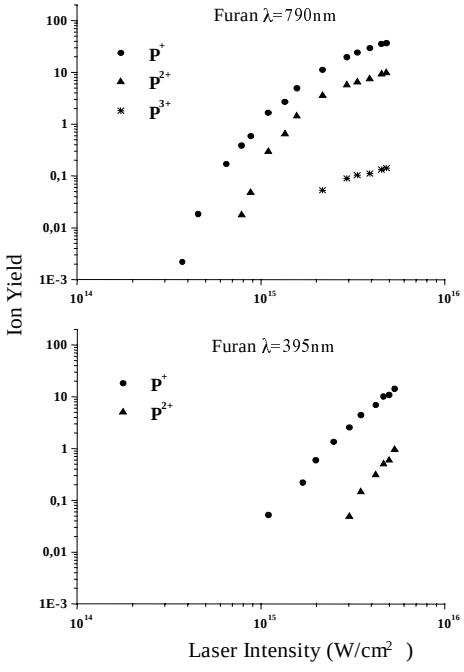

Figure 4. The intensity of the total ion yield, the P^{+}, P^{2+}, P^{3+} of furan is presented at 790 and 395 nm.

Finally, for the triply charged intact furan ion, it should be noted that the observed threshold intensity is relatively close to that estimated by the barrier suppression ionization model (BSI)[15] . The intensity threshold for BSI is given by:

$$I_{BSI} = \frac{E_i^4}{16 Z^2}$$

and corresponds to the minimum laser intensity required for a bound electron to escape without tunneling. In practical units $I_{BSI}(W/cm^2)=4x10^9[E_i^4 (eV)/Z^2]$, where E_i is the ionization potential and Z the ionic charge state. Despite the weakness of not including the influence of the laser pulse duration, this model predicts reasonably well the yield of higher charged ions for the heavier noble gases, created by sequential processes. For furan the E_i for the triply charged ion can be estimated by an empirical rule, which relates, for closed shell molecules, the single and triple ionization energies by the relationship: $IP^{3+}=(5.0 \pm 0.2)$ x IP^{+} [16]. The calculated IP^{3+} is 44.4 ± 0.2 eV. Thus, a value of $I_{BSI}=1.7x10^{15}W/cm^2$ is estimated which is close to that experimentally determined ($I=2.9x10^{15}W/cm^2$).

Conclusions

The multiply charged intact ion production from cyclic polyatomic molecules has been studied by means of strong laser pulses at 790 and 395nm. It is found that molecular aromaticity favors the multiply charged intact ion generation regardless of the nature of the HOMO. Doubly charged intact ions were observed for homo- and heterocyclic molecules with five- and six-member ring at both wavelengths in high abundance. No evidence for multiply charged intact ions exist in the mass spectra of cycloketones studied in this work.

There is evidence that multiply charged ion production is taking place through a sequential process, although the re-scattering model cannot be excluded.

An unambiguous triply charged intact molecule is recorded for furan at 790nm. The intensity threshold for P^{3+} was found to be relatively close to that predicted by the barrier suppression model, assuming a sequential ionization process.

References

1. L A Lompre, G Mainfray, C Manus, S Repoux, J Thebault J. Phys. Rev. Lett., 36, 949, (1976)
2. A L'Huillier, L A Lompre, G Mainfray, C J Manus Phys. B,16, 1363, (1983)
3. B Sheehy, L F DiMauro, Annu. Rev. Phys. Chem., 47, 463, (1996) and references therein
4. L J Frasinski, K Codling, P Hartherly, J Barr, I N Ross, W T Toner, Phys. Rev. Lett. **,** 58, 2424, (1987)
5. K W D Ledingham, R P Singhal, D J Smith, T McCanny, P Graham, H S Kilic, W X Peng, S L Wang, A J Langley, P F Taday, C Kosmidis, J.Phys. Chem A, 102, 3002, (1998)
6. D J Smith, K W D Ledingham, R P Singhal, H S Kilic, T McCanny, A J Langley, P F Taday, C Kosmidis Rapid Commun. Mass Spectrom.**,** 12, 813, (1998)
7. D J Smith, K W D Ledingham, H S Kilic, T McCanny, W X Peng, R P Singhal, A J Langley, P F Taday, C Kosmidis C. J.Phys. Chem A, 102, 2519, (1998)
8. K W D Ledingham, H S Kilic, C Kosmidis, R M Deas, A Marshall, T McCanny, R P Singhal, A J Langley, Shaikh, W. Rapid Commun. Mass Spectrom., 9,1522, (1995)
9. C Cornagia, Ph Hering J.Phys. B, 31, L503, (1998)
10. M J De Witt, R J Levis J.Chem. Phys., 102, 8670, (1995)
11. M J De Witt, R J Levis J.Chem. Phys., 108, 7045, (1998); *ibid.* 108, 7739, (1998)
12. P B Corkum Phys. Rev. Lett. **,** 71, 1994, (1993)
13. D N Fittinghoff, P R Bolton, B Chang, K C Kulander Phys. Rev. Lett. **,** 69, 2642, (1992)
14. B P Tsai, J H Eland Intern. J. Mass. Spectrom. Ion Proc., 36,143, (1980)
15. S Augst, D D Meyerhofer, D Strickland, S L Chin J.Opt.Soc. Am.B, 8, 858,(1991)
16. R G Kingston, M Guilhaus, A G Brenton, J H Beynon Org. Mass Spectrom., 20, 406, (1985)

Uniform Molecular Analysis Using Femtosecond Laser Mass Spectrometry

X.Fang, K.W.D.Ledingham, P.Graham, D.J.Smith, T. McCanny, R.P.Singhal

Department of Physics and Astronomy, University of Glasgow, Glasgow G12 8QQ

A.J.Langley, P.F.Taday

Central Laser Facility, CLRC Rutherford Appleton Laboratory, Chilton, Didcot, Oxon, OX11 0QX, UK

Main contact email address: *X.Fang@udcf.gla.ac.uk*

Introduction

Laser mass spectrometry permits ultra-sensitive detection and analysis of atoms and molecules, and has become an important analytical tool in many areas [1-3]. This technique is based on the analysis of ion information from irradiated atoms or molecules. Therefore the procedure and mechanism of ion production plays a key role in its analytical ability. Generally, preceding the ion detection by mass spectrometers and particularly by time of flight (TOF) mass spectrometers, a laser ionises the atoms or molecules in samples either by resonance (including resonance enhanced) or by non-resonance ionisation. For elements such ionisation is a simple up-pumping of atomic levels to ionic states. However ionisation of molecules is often accompanied by and/or competes with molecular dissociation which leads to the production of fragments.

As ultra-fast (ps to fs) pulse lasers generating intense fields, 10^{12}-10^{15} Wcm^{-2} and even higher, have become increasingly available in a few research laboratories, ultra-fast/high intensity laser mass spectrometry is being carried out. More and more interest is being shown by scientists in analytical areas who are trying to take advantage of the great potential of FLMS to overcome the difficulties experienced in the nanosecond regime.

The Glasgow group [4-11] has carried out a wide series of investigations on high-intensity laser non-resonance multiphoton ionisation TOF mass spectrometry. A number of different molecular species have been studied to develop a general ultra-trace analytical technique with ultra-high sensitivity. It was concluded that under irradiation by ultra-fast/intense lasers, the dissociative states of molecules can be bypassed and hence parent ions, being characteristic of the molecules, are more easily produced and often dominate the mass spectra of all the molecules under study. Ionisation saturation of species can be reached and it is possible that the species are ionised with similar efficiencies. Therefore it is expected that FLMS may be used as a general ultra-trace analytical technique. The data are presented here to demonstrate the general applicability of FLMS for uniform analysis of a number of molecules. The TOF mass spectra for a number of molecular species with their corresponding RSFs have been investigated using the upgraded high intensity femtosecond lasers (>1.6×10^{16} Wcm^{-2}) now available at the Rutherford Appleton Laboratory.

Experimental arrangement

The basic arrangement of the femtosecond laser TOF MS system is shown in Figure 1. The details of the femtosecond laser and TOF mass spectrometer have been described in reference [12] and [13] respectively.

Briefly, laser pulse energies up to 10 mJ per pulse, with the duration of about 50 fs, are provided by the Ti: Sapphire fs-laser system. The laser beam profile was imaged by a CCD camera to measure the beam diameter as 10 mm. A focusing mirror of 10 cm focal length was fixed behind the ion extraction region to allow the laser beam focus to lie very close to the sample entrance hole in the pusher electrode. The intersection space between the focus and the sample stream is defined as the ionisation volume where photoions are produced. Conventionally, the strength of a laser beam used for photo-ionisation is measured in term of average power density over the beam waist, or laser intensity.

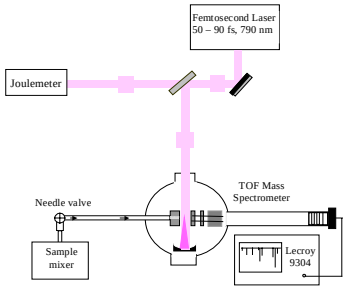

Figure 1. Basic arrangement of the femtosecond laser TOF MS system.

The TOF is a conventional linear system with an ion flight length of 1.2 m pumped by a turbo pump to a base pressure of 10^{-8} Torr. The operational parameters of the extraction optics are based on a Wiley McLaren design[14], and an einzel lens was placed immediately after the extraction optics to increase the ion transmission through the system. The mass resolution was typically 200 at 100D. A sample, one species or a mixture, was admitted effusively to a high vacuum system through a needle valve and then into the TOF through a tiny hole in the pusher plate. Ion signals were detected and amplified by a Thorn EMI (Ruislip, UK) electron multiplier which was coupled to a Lecroy (Chestnut Ridge, NY, USA) 9304 digital oscilloscope, and hence the mass spectra averaging over a minimum of 300 shots were recorded for data analysis.

Results and analysis

The mass spectra for a number of different molecules and vapours were measured as a function of laser intensity and compared with the spectra for argon. This was carried out for a mixture of the two gases at the same partial pressures ($2.1\text{x}10^{-6}$ torr) and for the two gases at the same pressures separately. From these spectra the relative sensitivity factor (RSF) was calculated for each gas.

The relative sensitivity factor is a very important parameter for this analysis[5,15], which evaluates the quantification capability of the mass spectrometry. For a species A in a sample with reference to species B, the RSF is defined as

$$RSF\ (A) = \frac{I_A / [A]}{I_B / [B]}$$

Here I_A and I_B are the summed ion signal intensities of species A and B in all charged states respectively, which are measured by peak area integration in their TOF mass spectra and proportional to the photo-ion populations of these species, and [A] and [B] are the concentrations of species A and B in the mixture sample.

Hence a value of unity for RSF demonstrates that similar ionisation efficiencies of the species are achieved in spite of any difference in ionisation potentials. Such an RSF would represent a complete, uniform detection sensitivity and reliable quantification.

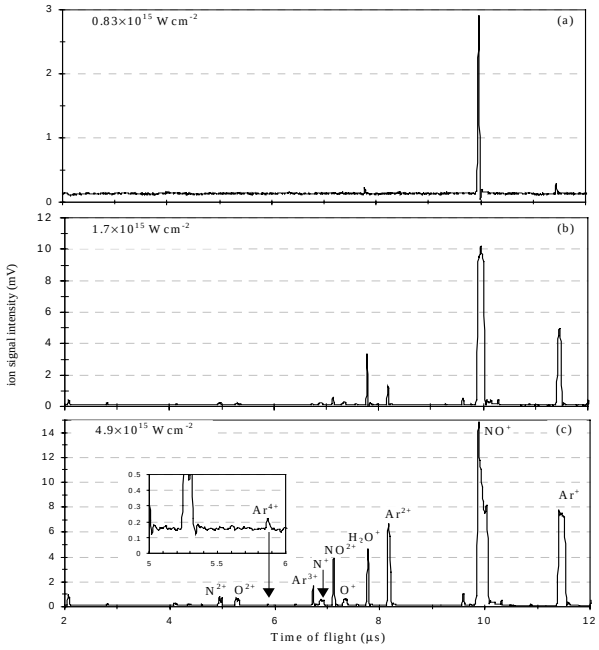

Figure 2. Time of flight mass spectra for the molecule NO at laser intensities of (a) 0.83×10^{15} Wcm^{-2}, (b) 1.7×10^{15} Wcm^{-2} and (c) 4.9×10^{15} Wcm^{-2} respectively.

Figure 2 (a-c) show the mass spectra of a sample of NO mixed with the reference gas Ar at the same partial pressure (2.1×10^{-6} Torr) at the laser intensities of 8.3×10^{14} Wcm^{-2}, 1.7×10^{15} Wcm^{-2} and 4.9×10^{15} Wcm^{-2}. In Figure 2(a), the NO^+ ion signal is far larger than the Ar^+ signal. Their peak area integrations are 0.1 nVs and 0.005 nVs respectively and hence the RSF for NO/Ar is ~20/1. The IEs are 9.25eV for NO, requiring six photons for ionisation and 15.76 for Ar, requiring ten photons for ionisation. The laser intensity is not high enough to achieve similar ionisation efficiencies for the two species. When the laser intensity is increased to 1.7×10^{15} Wcm^{-2}, the RSF of NO relative to Ar is 3.2 and the ionisation efficiencies for these species is becoming more similar. At the laser intensity of 4.9×10^{15} Wcm^{-2}, the signals from multiply charged parent ions and the fragment ions become stronger. The summed peak area of NO^{2+}, NO^+ and N^+ is 2.1 nVs and that of Ar^{4+}, Ar^{3+}, Ar^{2+} and Ar^+ is 1.8 nVs. Derived from the peak area integration the RSF is 1.17, which is close to unity. At this level of laser intensity or higher a uniform ionisation for these species can be obtained.

Figure 3 (a-c) shows the RSFs as a function of laser intensity, for the molecules CO, CH_4, NO with the presence of Ar in the species respectively. Uncertainties of 11% for the RSFs of gas were carefully estimated and are shown by error bars in the figures. These uncertainties result from the measurement errors of gas pressures and peak area integration of TOF spectra. The sample pressure was 4.2×10^{-6} Torr with the same partial pressures for the two species in each mixture of CO/Ar, CH_4/Ar, and NO/Ar. From these figures it is seen that the RSFs decrease as the laser intensities increase and approach unity when the laser intensities are about 4×10^{15} Wcm^{-2} for CO, 3.6×10^{15} Wcm^{-2} for CH_4 and 4.9×10^{15} Wcm^{-2} for NO respectively. At these laser power levels or higher, uniform ionisation efficiency is achieved and quantification is reliable.

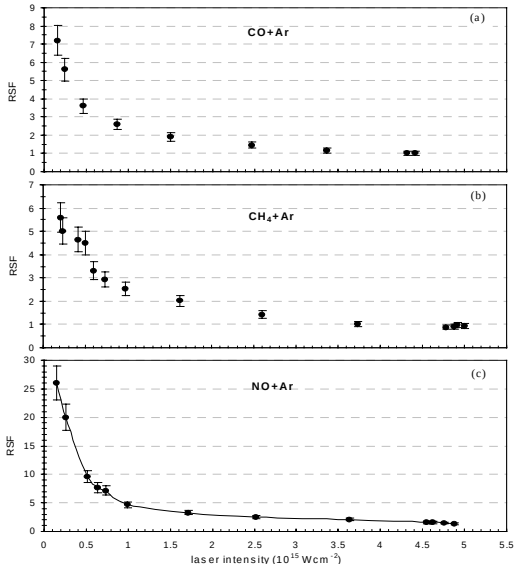

Figure 3. RSFs relative to Ar, versus laser intensity, of molecules (a) CO, (b) CH4 and (c) NO with the presence of Ar in the mixtures. The error bars indicate the estimated measurement errors of 11%.

Due to the different ionisation potentials of CO, CH_4, NO and Ar: 14.01eV, 12.6eV, 9.25eV and 15.76eV respectively, the numbers of photons required for ionisation are different being 9, 8, 6 and 10 respectively for a 790 nm photon (equivalent energy 1.57eV). At lower laser intensities, the probability of ionisation is different which causes the RSFs to have different values. In Figure 3c, the difference between the numbers of photons required for ionisation of NO and Ar is larger than those for CO and Ar in Figure 3a and for CH_4 and Ar in Figure 3b. As a result the RSFs of NO are higher than the other two at the same laser intensities before the onset of ionisation saturation.

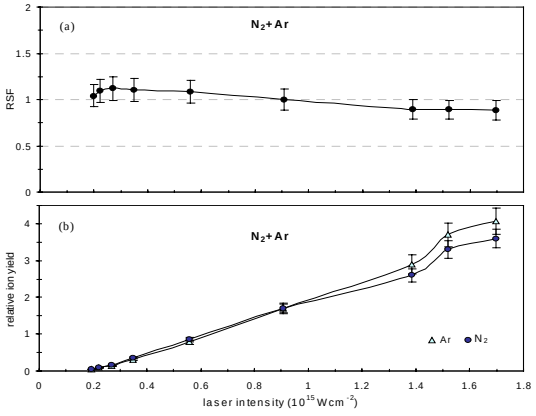

Figure 4. (a) RSFs relative to Ar, versus laser intensity, of N_2 with the presence of Ar in the mixture; (b) the ion yields of species N_2 and Ar versus laser intensity. The error bars indicate the estimated measurement errors of 11%.

The case of the nitrogen molecule is interesting. This species has a high ionisation potential (15.58 eV) which is very close to the IE of Ar (15.76 eV), and ten photons are needed to ionise either a N_2 molecule or Ar. Thus the two species would be expected to have similar ionisation cross-sections and ionisation efficiencies. Figure 4a shows the RSFs relative to Ar with the error bars of 11%, versus laser intensity, obtained from the spectra of the mixture sample ($4.2x10^{-6}$ Torr) of N_2 and Ar with the same partial pressures. The RSFs change only slightly as the laser intensity increases, lying close to unity throughout the range. Figure 4b shows the ion yields of both of the species as

a function of laser intensity, from which it is seen that the ion yields increase slowly. This indicates that the ionisation volume still increases slightly with increasing laser intensity indicative of the fact that a sharply defined ionisation volume has not been achieved.

For liquid-phase molecular species, a difficulty arises when the RSFs are measured for a mixture of the reference species with its vapour, because of sticking of the vapour to the walls of the transfer capillary tube. Such vapours were separately measured at identical pressures to the reference gas. Figure 5a,b show the RSFs, with their error bars of 13%, of CH_3I and CS_2 relative to Ar versus laser intensity. The RSFs approach unity with increasing laser intensity.

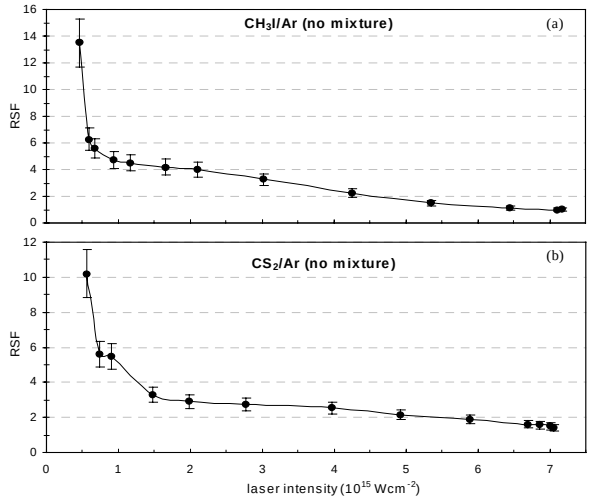

Figure 5. RSFs, versus laser intensity, of liquid-phase molecule (vapour) CH3I and CS2 relative to Ar (gas-phase) when these species were separately used for their mass spectrometry. The error bars indicate the estimated measurement errors of 13%.

In Figure 6(a-b), the RSFs, relative to Ar, of N_2O and CO_2 versus laser intensity are shown with their error bars of 11% when separate (non-mixture) species N_2O, CO_2 and Ar were used respectively to obtain their spectra for peak area integration. For the ionisation of these molecules nine photons are required. RSFs of the two species keep decreasing and approach unity when the laser intensities are about 4.5×10^{15} Wcm^{-2} for both CO_2 and N_2O. Thus uniform ionisation has been reached at this intensity.

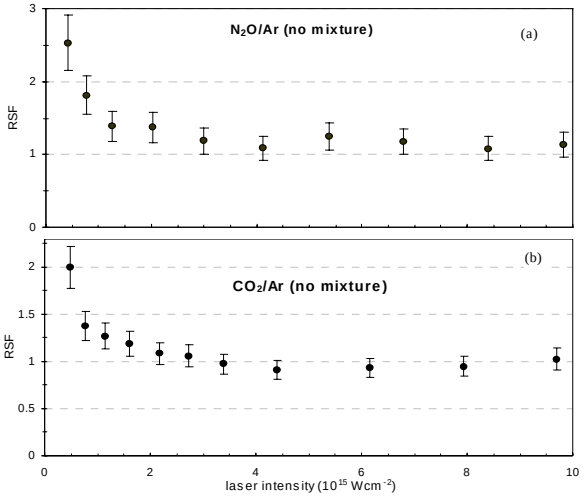

Figure 6. RSFs relative to Ar, versus laser intensity, of molecules N2O and CO2 when these species were separately used for their mass spectrometry.

The error bars in Figure 6 indicate the estimated measurement errors of 11%. In this Figure the data for laser intensities up to 10^{16} Wcm^{-2} is shown. The reason for this is because the laser was upgraded before this data was taken and intensities up to a few times 10^{16} Wcm^{-2} are now available.

Poly-atomic molecules were also studied using the femto-second laser. Figure 7a-b show the RSFs for the molecules C_6H_6 and C_7H_8 respectively versus laser intensity. The ion yields of these three species C_6H_6, C_7H_8 and Ar were separately measured from their time-of-flight spectra for the RSF calculations. In Figure 7a, the ionisation saturation is reached at the laser intensity of 7×10^{15} Wcm^{-2} where the RSF is unity. While in Figure 7b, the RSF of C_7H_8 decreases down to a value of about 1.0 at the laser intensity of about 6×10^{15} Wcm^{-2} where uniform ionisation is reached.

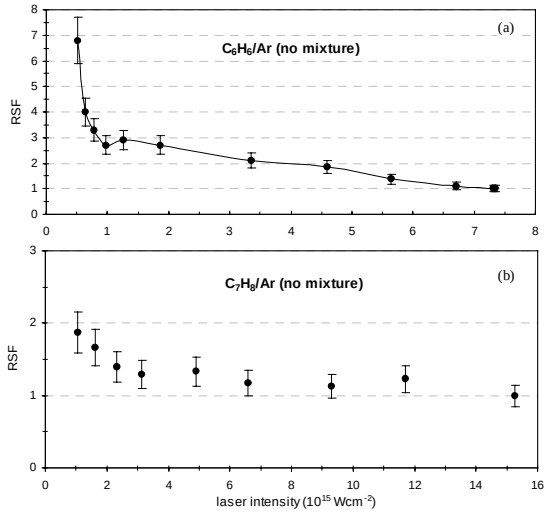

Figure 7. RSFs, relative to Ar, of molecules of C6H6 and C7H8 versus laser intensity when these were separately used for their mass spectrometry. The error bars indicate the estimated measurement errors of 13%.

It would appear that uniform ionisation efficiency has been demonstrated at laser intensities about 7×10^{15} Wcm^{-2} for the gases studied and hence FLMS has considerable potential for quantitative molecular analysis. The Glasgow group will continue this work for many more types of molecules to ascertain the generality of the technique.

Conclusions

Using a femtosecond laser with high intensity at the wavelength of 790 nm coupled to a TOF mass spectrometer, a series of molecules, CO, CH_4, NO, N_2O, CO_2, N_2, CH_3I, CS_2, C_6H_6, and C_7H_8, with very different ionisation potentials have been investigated. The detailed analysis of RSFs against laser intensities, up to 1.6×10^{16} Wcm^{-2}, has demonstrated that most of the molecules have reached their ionisation saturation status. At intensities of about 7×10^{15} Wcm^{-2} uniform ionisation efficiencies were reached resulting in RSFs tending to unity. Therefore the possibility of quantitative chemical analysis for these types of molecular samples has been demonstrated and more work will be carried out to test the generality of the procedure.

Acknowledgements

We would like to express our thanks to Rutherford Appleton Laboratory for excellent facilities and assistance, and to EPSRC for the financial support and a studentship for P.G.

References

1. D. M. Lubman (Ed.)
   Laser and Mass Spectrometry, Oxford University Press, New York (1990)
2. Vertes, R. Gijbels and F. Adams
   Laser Ionisation Mass Analysis, Chemical Analysis Ser. Vol.124, John Wiley and Sons, New York (1993)
3. K. W. D. Ledingham, in: D. L. Andrews and A. A. Demidov (Eds.)
   An Introduction to Laser Spectroscopy, Plenum Press, New York, pp.187 – 227 (1995)
4. D. J. Smith, K. W. D. Ledingham, R. P. Singhal, H. S. Kilic, T. McCanny, A. J. Langley, P. F. Taday and C. Kosmidis
   Rapid Commun. Mass Spectrom., 12, 813 (1998)
5. K. W. D. Ledingham and R. P. Singhal
   Int. J. Mass Spectrom. Ion Proc. 163, 149 (1997)
6. K. W. D. Ledingham, R. P. Singhal, D. J. Smith, T. McCanny, P. Graham, H. S. Kilic, W. X. Peng, S. L. Wang, A. J. Langley, P. F. Taday and C. Kosmidis
   J. Phys. Chem., A102, 3002 (1998)
7. P. Graham, K. W. D. Ledingham, R. P. Singhal, D. J. Smith, S. L. Wang, T. McCanny, H. S. Kilic, A. J. Langley, P. F. Taday and C. Kosmidis
   Proceedings of the 9th Symposium on RIS (1998)
8. K. W. D. Ledingham, D. J. Smith, R. P. Singhal, T. McCanny, P. Graham, H. S. Kilic, W. X. Peng, A. J. Langley, P. F. Taday and C. Kosmidis
   J. Phys. Chem., A103, 2952 (1999)
9. D. J. Smith, K. W. D. Ledingham, R. P. Singhal, T. McCanny, P. Graham, H. S. Kilic, P. Tzallas, A. J. Langley, P. F. Taday and C. Kosmidis
   Rapid Commun. Mass Spectrom., 13, 1366 (1999)
10. Kosmidis, P. Tzallas, K. W. D. Ledingham, T. McCanny, R. P. Singhal, P. F. Taday and A. J. Langley
    to be published
11. X. Fang, K. W. D. Ledingham, P. Graham, D. J. Smith, T. McCanny, R. P. Singhal, A. J. Langley, P. F. Taday
    Rapid Commun. Mass Spectrom., 13, 1390 (1999)
12. P. F. Taday, I. Mohammed, A. J. Langley and I. N. Ross
    Annual Report 1997/1998, Central Laser Facility, Rutherford Appleton Laboratory, p.179
13. K. W. D. Ledingham, H. S. Kilic, C. Kosmidis, R. M. Deas, A. Marshall, T. McCanny, R. P. Singhal, A. J. Langley and W. Shaikh
    Rapid Commun, Mass Spectrom. 9, 1522 (1995)
14. W. C. Wiley and I. W. Mclaren
    Rev. Sci. Instrum. 26, 1150 (1955)
15. He, J. Basler, A. Paul and C. H. Becker
    J. Vac. Sci. Technol. A14(3), 1433 (1996)

Unusual Angular Distribution Anisotropies of Fragment Ions from the Dissociation of N_2O and H_2S

P Graham, K W D Ledingham, R P Singhal, T McCanny, X Fang

Department of Physics & Astronomy, University of Glasgow, Glasgow, G12 8QQ, Scotland, UK.

A J Langley, P F Taday

Central Laser Facility, CLRC Rutherford Appleton Laboratory, Chilton, Didcot, Oxon, OX11 0QX, UK

C Kosmidis, P Tzallas

Department of Physics, University of Ioannina, GR-45110, Ioannina, Greece.

Main contact email address: *K.Ledingham@physics.gla.ac.uk*

Introduction

As lasers have become increasingly more intense, and able to provide power in pulses of shorter duration, so the highly non-linear processes induced by the laser/matter interaction such as bond-softening, Above Threshold Ionisation (ATI), and alignment of molecules[1-5] can be studied. This last topic has become the focus of much recent research activity as the spatial control of molecules has very deep and wide-ranging implications in a variety of different fields.

By utilising chirped-pulse amplification[6] (CPA) Astra provides strong E-fields which distort the molecular structure and which may align the molecule with the field.

Such distortions may polarise a molecule, which induces a dipole moment. The field interacts with the molecule via the dipole to produce a torque which tends to align the molecule. As the polarisability increases with charge-state of the parent ion, the torque is increased also and thus aligns the molecule more tightly. This narrows the angular distribution of the exploding fragments from these highly charged transient parent ions. Furthermore, in an ensemble of molecules with randomly orientated dipoles, those molecules which lie along the direction of the ToF axis and laser polarisation are more efficiently ionised/dissociated and detected. Either or both of these processes can account for the observed anisotropy of the fragment ions.

In this report some angular distributions are presented for the N_2O and H_2S molecules which exhibit unusual behaviour regarding the N- and S-fragment ions. The data were taken using the ultra-intense femtosecond Astra Ti:S laser facility at RAL.

Experimental

The laser system used is based on a 20 fs Ti:S oscillator pumped by a Spectra-Physics Millenia solid-state laser[7]. It produces output pulses of 790nm, 50fs and an energy/pulse of 5mJ after being stretched, amplified in 2-stages in a Ti:S rod amplifier pumped by two frequency-doubled Spectra-Physics GR-270 Nd:YAG lasers, and then re-compressed to 50fs. The laser polarisation was rotated with respect to the lab frame using a polariser and $\lambda/2$ wave-plate.

Gas-phase samples are admitted effusively from an inlet system into a high-vacuum chamber. The sample pressures were of the order of 10^{-6} Torr. The ToF system is a conventional linear mass spectrometer based on the Wiley-McLaren configuration, the field-free region being of length 1.2m. Ions are detected by an electron multiplier connected to a LeCroy digital oscilloscope.

Results and Discussion

Angular distributions for the molecule N_2O are presented for a laser intensity of 10^{16} Wcm^{-2} and 50 fs. The distributions for both N_2O^+ and N_2^+ are isotropic (not shown) indicating that the efficiency of ionising and detecting the parent ion is independent of the polarisation orientation. The isotropy of N_2^+ is surprising however as the distribution for CS^+ from CS_2 is anisotropic. The N_2O molecule has a linear N-N=O structure. Thus, the N-N diatomic breaks away from the O-atom to produce N_2, in a similar fashion to C-S breaking away from the other S-atom in the case of CS_2. This suggests that the N_2 ion must have a very low kinetic energy in order to account for the isotropy observed. The isotropy also occurs due to bending in the field, as this fragment has been observed to become more isotropic as the rotational levels increase in a bent configuration[8].

The distributions for NO^+ and NO^{2+} are shown in Figure 1. Both distributions are peaked in the 0-180° direction. Similarly for CS^+ and CS^{2+} from CS_2[9], the NO^+ distribution is anisotropic but possessing an isotropic component; whereas the NO^{2+} is markedly anisotropic. This suggests that NO^+ comes from N_2O^+ or N_2O^{2+}; but that NO^{2+} originates from a higher charged precursor of the parent molecule.

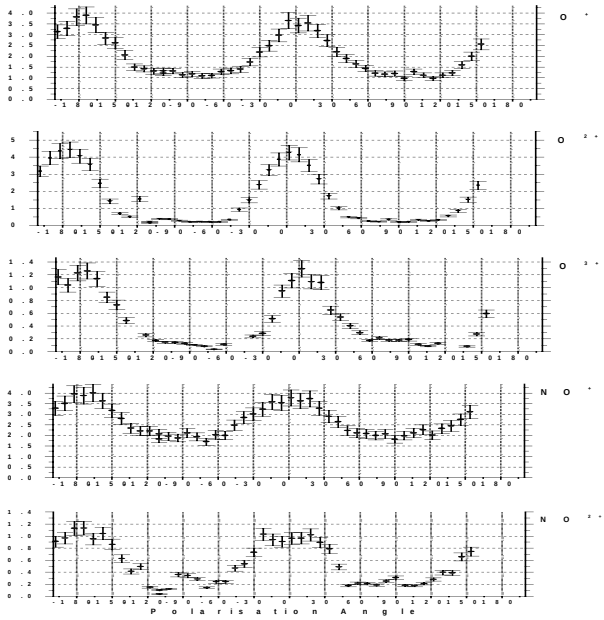

Figure 1. Angular distribution of O and NO fragments.

The distributions of the O-fragments are also shown in Figure 1. It can be seen that all are anisotropic. Interestingly, it would also appear that the distributions narrow slightly for increasing charge-states. This is similar to results reported for CO_2[10] and since O and N have similar molecular weights, and that the bond lengths are similar in both molecules, the moments of inertia of both are similar. Thus, as CO_2 may be aligning within the 50 fs laser pulse it is reasonable to expect that N_2O may also. The angular distributions of N^{p+} ($p \leq 4$) are shown in Figure 2. The distributions show a highly unusual behaviour. All are anisotropic but the distributions are peaked in both the 0-180°, as well as the $\pm 90^o$ direction, although this orthogonal distribution diminishes with decreasing charge-state.

These two peaks in the distributions arise from the fact that the molecular structure is N-N=O. The peripheral N-atom is responsible for the peak along the ToF axis direction, whilst the central N-atom is responsible for the perpendicular peak, in a similar fashion to the central C-atom in CS_2 being peaked perpendicular to the ToF axis[9]. The molecule is initially linear but, as the central N-atom is ejected orthogonally this lends support to the molecule bending in the field.

The perpendicular peak of the distribution increases with the charge of the N-fragments because when the polarisation is at right angles to the ToF axis, the highly charged peripheral N-ions are ejected in this perpendicular direction with increasing kinetic energy. So the probability of detecting them along the ToF axis is small, compared to that of the central N-ion, which flies down the drift tube to the detector, and hence is more efficiently detected. Thus, the peaks at ± 90° grow relatively to those at 0 and 180°.

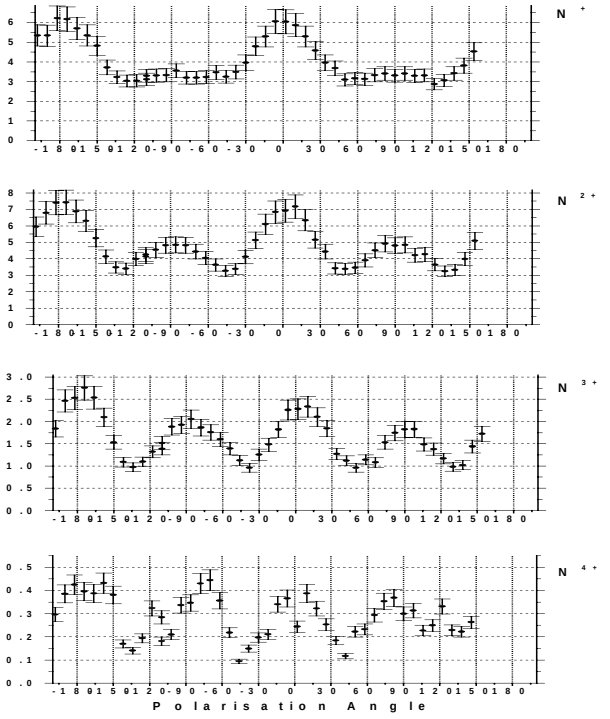

Figure 2. Angular distribution of N fragment ions.

The S-ion distributions observed from the ionisation and dissociation of the H_2S molecule at an intensity of 10^{16} W cm^{-2} and 50 fs are shown in Figure 3. As seen in the diagram, the polar-plots of the S^{2+} to S^{5+} ions show a definite isotropic distribution. The S^{6+} distribution (not shown) is less clear to interpret. The S^{6+} shows isotropy, although less obviously so. The results for S^+, HS^+, and H_2S^+ were not obtainable due to these peaks being saturated.

The H^+ distribution (not shown) is similar to that for the S^+ from CS_2 , being anisotropic and peaking along the 0-180° direction. The H^+ ion may come from 'soft' dissociation of the parent molecule, being ejected along the direction of polarisation with small kinetic energy. Obviously, higher charge-states of H-atoms are impossible. What makes H_2S different from CS_2 is that the peripheral H-ions are considerably lighter and hence more easily aligned with the laser field due to a reduced moment of inertia.

Also, both N_2O and CS_2 are initially linear molecules that are thought to be slightly bent in the laser field, producing ions peaked in the (± 90°) direction; whereas H_2S starts off with a H-S-H angle of about 93°. In order for the S-ions up to S^{6+} to be isotropic, it has to behave as an 'observer' in the break-up of the molecule. Thus, the isotropic S distributions observed are indicative of a straightening of the H_2S molecule when it interacts with an intense field of a laser.

Even more interesting however, and quite unexpected, is the appearance of an S^{7+} ion with a corresponding angular distribution, which to the authors' knowledge is the first time it has been observed. As can be seen, its distribution is highly anisotropic, and furthermore was the only fragment peak in the mass spectra to possess a split structure, perhaps indicating forward- and backward-directed ions occurring from Coulomb explosion. Unlike the central atom in CS_2 however, it is peaked along the 0-180° direction and is a minimum at ± 90°.

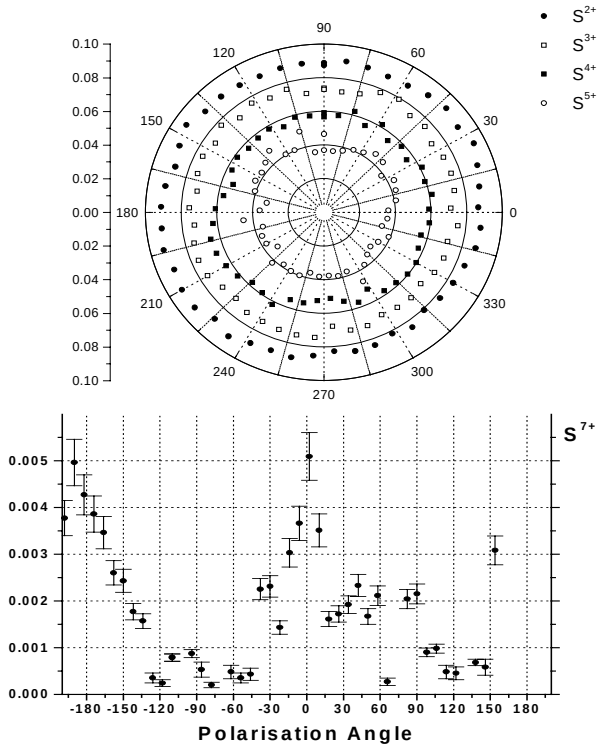

Figure 3. Angular distributions of S fragment ions.

Conclusion

The angular distributions of N_2O and H_2S were studied at an intensity of 1×10^{16} W cm^{-2}, and in the femto-second regime (50 fs). The laser field may induce a sufficiently large dipole moment to effect a torque strong enough to orientate the molecular axis within the duration of the 50 fs laser pulse used.

Several of the distributions show unusual behaviour that has not been observed before. In particular the N-distributions from N_2O consist of a peak at 0 and 180° from the peripheral N-atom, and another perpendicular to this at ± 90° from the central N-atom, which grows relatively to the first as the charge of the N-ion increases. Furthermore, a split S^{7+} peak and a corresponding anisotropic angular distribution is presented which is a maximum along the ToF direction, in stark contrast to the S^{2+}-S^{6+} ion peaks, which are isotropic.

References

1. H J Loesch, F Steinkemeier
   1993 J. Chem. Phys., 98, 9570
2. M J J Vrakking, S Stolte
   1997 Chem. Phys. Lett., 271, 209-215
3. A H Zewail
   1996 Abstracts of Papers of the American Chemical Society, 211, 153
4. C Mainos
   1996 Phys. Rev. A, 54, 4226-4235
5. B Friedrich, D Herschbach
   1995 J. Phys. Chem., 99, 15686-15693
6. D Strickland, G Mourou
   1985 Opt. Commun., 56, 219
7. P F Taday, I Mohammed, A J Langley, I N Ross, K Codling, K W D Ledingham, W R Newell, S Preston, D Riley, I Williams
   1998 Central Laser Facility, RAL Annual Report 1997/98, 179.
8. D W Neyer, A J R Heck, D W Chandler
   1999 J. Chem. Phys., 110, 3411-3417
9. P Graham, K W D Ledingham, R P Singhal, T McCanny, A J Langley, P F Taday, C Kosmidis
   to be published.
10. J H Sanderson, R V Thomas, W A Bryan, W R Newell, A J Langley, P F Taday
    1998 J. Phys. B: At. Mol. Opt. Phys., 31, L599-L606

High Harmonic Generation in Organic Molecules

N Hay, E Springate, K Mendham, J P Marangos

LASPII, Blackett Laboratory, Imperial College of Science, Technology and Medicine, London, SW7 2BZ,UK

M Castillejo, R de Nalda

Instituto de Química Física Rocasolano,CSIC, Serrano 119, 28006 Madrid, Spain

P F Taday, E J Divall, A J Langley

Central Laser Facility, CLRC Rutherford Appleton Laboratory, Chilton, Didcot, Oxon, OX11 0QX, UK

Main contact email address: *n.hay@ic.ac.uk*

Introduction

We present preliminary results of an investigation into high harmonic generation (HHG) in organic molecules. Benzene and cyclohexane vapours were compared with monatomic xenon in two complementary studies using near infrared pulses generated by titanium sapphire chirped pulse amplification laser systems. Pulses of duration 70 fs at 795 nm and 240 fs at 780 nm were provided by Astra and the Blackett Laboratory Laser Consortium titanium sapphire laser respectively. The two studies covered an intensity range from ~4×10^{13} to ~5×10^{15} Wcm^{-2}.

HHG in monatomic gases has been studied for some time and is now reasonably well understood[1]. Small molecules, diatomics in particular, have also received some attention[2]. Their behaviour is generally similar to atoms – the familiar plateau and cut-off are present in the harmonic spectra, with the position of the cut-off approximately predicted by the I_p+3U_p rule. Very few studies have included larger molecules[3].

We were motivated to study HHG in organic molecules for several reasons. Organic molecules can be highly polarisable. The presence of π-delocalised electrons in some organics such as benzene and butadiene, can increase the polarisability. There is evidence from previous work comparing butane and butadiene that this can increase the harmonic conversion efficiency[4]. Some species, such as cyclohexane, exhibit a giant resonance. The cyclohexane giant resonance at 10.4 eV is potentially much more accessible to multiphoton excitation by near-infrared photons (~1.5 eV) than the giant resonances present in atoms that have excitation energies typically ~100 eV. Recent studies using ion time of flight spectroscopy to study ionisation and dissociation of organic molecules have shown that they can be remarkably stable when exposed to high intensity ultra-short laser pulses[5]. Benzene, for example, can remain essentially intact at intensities approaching 5×10^{14} Wcm^{-2}.

Experiment

Typical HHG experiments use pulsed valves to deliver the (gaseous) non-linear medium to the target area. Benzene and cyclohexane, however, are both liquids at room temperature. This required the development of a heated valve that was capable of delivering gas pulses at a variety of pressures. Its major features were an integrated gas valve and sample reservoir, which were temperature controlled from ambient to 470 K with a temperature stability of ±0.1 K. A heated capacitance manometer measured the vapour pressure created in the reservoir. A schematic is shown in Figure 1.

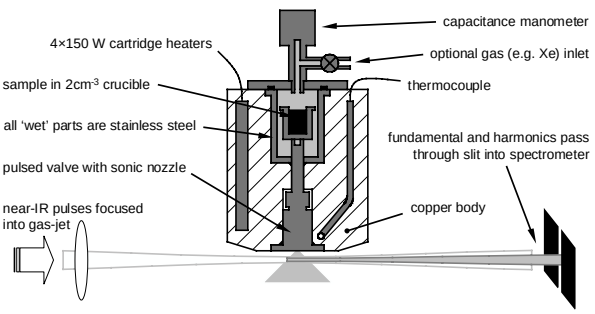

Figure 1. Schematic of heated pulsed gas valve and the laser interaction region.

The heated pulsed valve was mounted on a small vacuum chamber attached to a VUV spectrometer and pumped by a turbo-molecular pump. The laser pulses were focused into the gas jet by a 300 mm focal length lens mounted immediately before the 3 mm thick fused silica entrance window. The spectrometer was fitted with a 600 lines.mm^{-1} grating and an electron multiplier tube (EMT) detector. A calibrated fast photodiode fitted to an integrating sphere was used to measure the laser pulse energy. A boxcar gated integrator received the signals output from the EMT and the energy monitor diode after every laser shot, digitised them and transferred them to a PC.

Results

Harmonic spectra were recorded for benzene, cyclohexane and xenon under nominally identical conditions. These results are shown in Figure 2 for 240 fs pulses at a peak intensity in the focus of 2×10^{15} Wcm^{-2}. The gas density in the laser focus was ~2×10^{17} molecules.cm^{-3}.

The most striking feature of this data is that the strengths of the harmonic signals from the organic molecules are comparable to those from xenon atoms, one of the most efficient HHG media studied to date.

Figures 3a to 3c show intensity dependences for harmonics q=7-13 in xenon and q=7-11 in benzene and cyclohexane using 240 fs pulses. The form of the xenon harmonic yields shown in Figure 3a is typical of HHG. All the harmonics were observed in the plateau region. The roll-over at higher intensity (>9×10^{14} Wcm^{-2}) was primarily due to depletion of the neutral species by ionisation.

As with xenon, the benzene harmonic yields in Figure 3b first increase with a slope ~2 before beginning to roll-over as the intensity approaches 7×10^{14} Wcm^{-2}. At this point the intensity dependences diverge. The roll-over is most pronounced for q=7

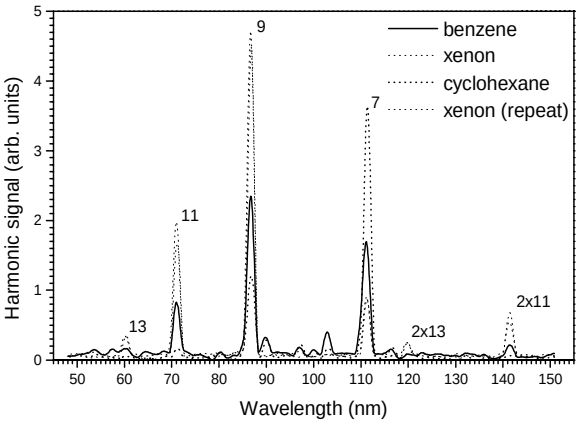

Figure 2. Benzene and cyclohexane harmonic spectra for q=7-13 compared with xenon under nominally identical conditions.

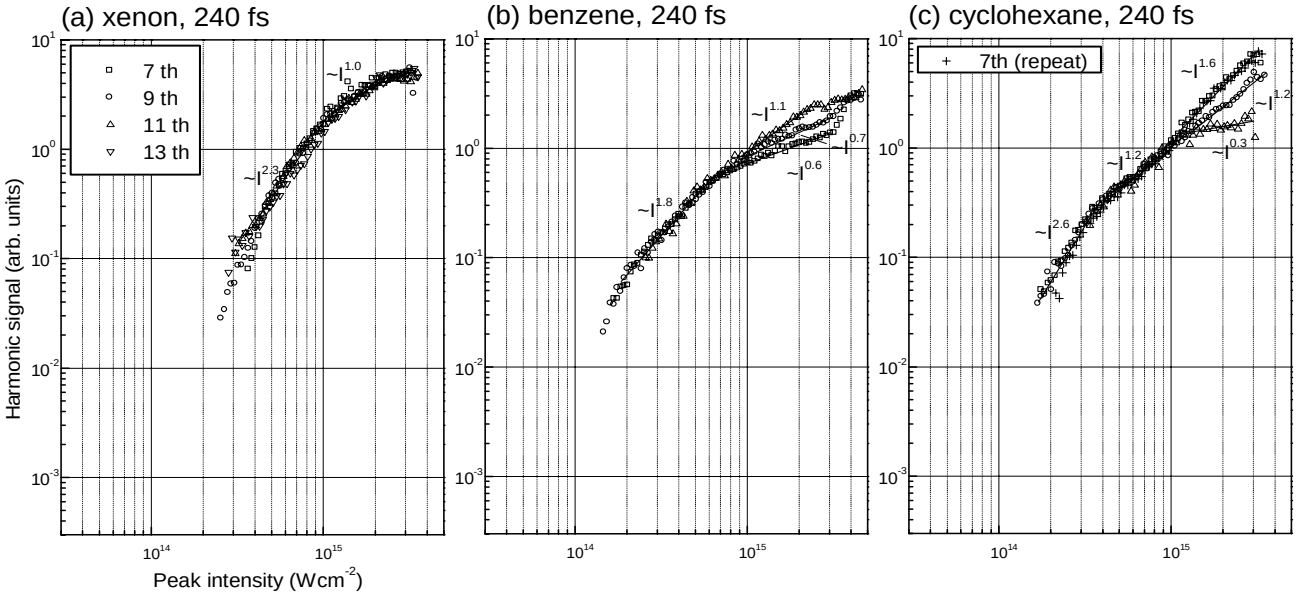

Figure 3. Harmonic yield intensity dependences using 240 fs, 780 nm pulses (a) xenon, (b) benzene and (c) cyclohexane.

and becomes less for higher q. This is the opposite to the expected consequence of free-electron dispersion, which is stronger at shorter wavelengths. From 2×10^{15} to 4×10^{15} Wcm^{-2} the curves reconverge.

For cyclohexane (Figure 3c) all harmonics again follow the same initial intensity dependences. Above ~1×10^{15} Wcm^{-2} the curves diverge. The 11th harmonic rolls-over to become almost constant with increasing intensity. There is no change of slope in the 9th harmonic and the 7th harmonic actually exhibits steeper intensity dependence. This compares with xenon (Figure 3a) where all the harmonic yields have stopped increasing at this intensity. We illustrate the repeatability of the data by plotting a second, independent 7th harmonic dataset.

Figure 4 shows the results of an identical experiment using 70 fs pulses. Although the intensity range covered in this experiment is lower, improved environmental conditions increased the dynamic range of our detection apparatus by at least an order of magnitude. This enabled us to measure the weaker 13th harmonic of the organic molecules and also to observe the initial steep intensity dependence of the harmonic signal. Where the intensity ranges of the two experiments overlap, we can see that the behaviour of all the molecules appears to be similar. The intensity dependences are all ~I^2 at I~2-4$\times10^{14}$ Wcm^{-2} (with the exception of q=11 for cyclohexane). The change in pulse duration seems to have had little effect. We would, however, expect it to make a difference at higher intensity where it would affect the ionisation/dissociation of the molecules and would modify the anomalous behaviour seen in the organics using 240 fs pulses.

References

1. P Antoine, M Gaarde, P Salières, B Carré, A L'Huillier , M Lewenstein, Inst. of Phys. Conf. Series, 154 142, (1997)
2. Y Liang, A Talebpour, C Y Chien, S Augst and S L Chin J. Phys. B: At. Mol. Opt. Phys., 30 1369, (1997)
3. C Lynga, A L'Huillier and C-G Wahlström J. Phys. B: At. Mol. Opt. Phys., 29 3293, (1996)
4. D J Fraser, M H R Hutchinson, J P Marangos, Y L Shao, J W G Tisch and M Castillejo, J. Phys. B: At. Mol. Opt. Phys., 28 L739, (1995)
5. K W D Ledingham, D J Smith, R P Singhal, T McCanny, P Graham, H S Kilic, W X Peng, A J Langley, P F Taday, C Kosmidis, J. Phys. Chem. A, 103 2952, (1999)

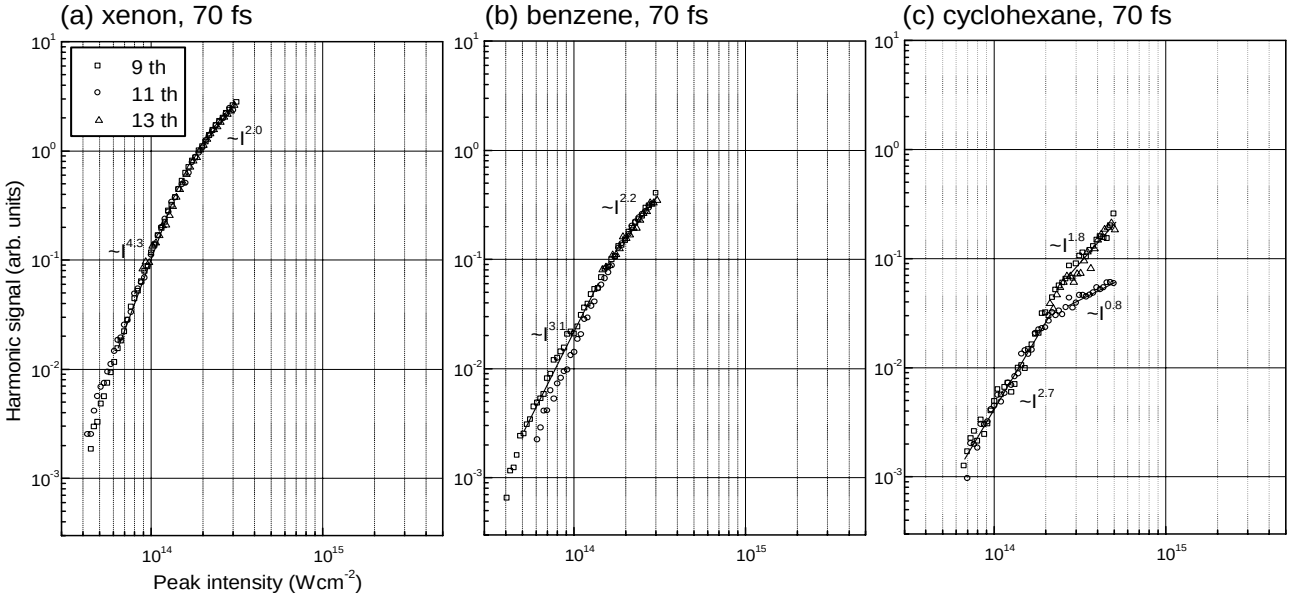

Figure 4. Harmonic yield intensity dependences using 70 fs, 795 nm pulses (a) xenon, (b) benzene and (c) cyclohexane.

Dissociation and Dissociative Ionization of H_2^+ using a Crossed Femtosecond Laser and Ion Beam Technique

I D Williams, P McKenna

Queens University of Belfast, BelfastBT7 1NN

J H Sanderson, W A Bryan, A El-Zein, W R Newell

University College London Gower Street London WC1E 6BT

P F Taday, E Divall, A J Langley

Central Laser Facility, CLRC Rutherford Appleton Laboratory, Chilton, Didcot, Oxon, OX11 0QX, UK

Main contact email address: *i.williams@qub.ac.uk*

Introduction

Theoretical interpretations of the dissociation and dissociative ionisation of H_2^+ in an intense femtosecond laser pulse quite reasonably all begin with the molecular ion H_2^+, generally in a Franck-Condon vibrational distribution[1] . In other words it is assumed that the initial ionization of the neutral H_2 molecule by the leading edge of the laser pulse is totally independent of the subsequent dynamics of the H_2^+ ion. Experimental studies however all begin with a neutral H_2 molecule[2] , and assume that the ionisation process and presence of the ionised electron are not important.

To test this very important assumption, we herein report on the first experimental study of a beam of H_2^+ molecular ions in an intense femtosecond laser pulse. By producing a fast beam of H_2^+ ions to interact with the laser pulse, the precursor H_2 neutral state is avoided and furthermore fast product neutral H atoms can be detected as well as protons. This is the first time that neutral dissociation products have been detected in the study of molecules in strong laser fields.

Experimental

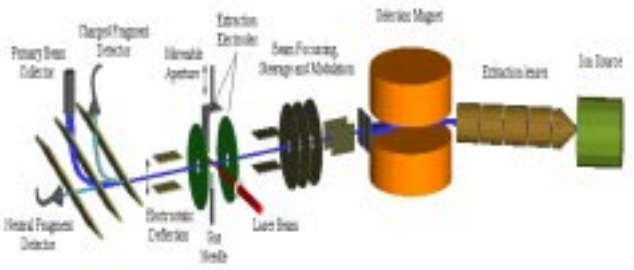

Figure 1. Crossed femtosecond laser beam and ion beam.

H_2^+ ions were formed in a plasma discharge ion source, with a 1 keV beam extracted and momentum analysed. At the point of interaction, the H_2^+ ion beam of diameter 1 mm (full width at half maximum) was intersected at 90° by a linearly polarized laser pulse with a spatial Gaussian profile, focussed by an f/10 lens to a spot of 10μm diameter. With the axis of polarization set mutually perpendicular to both beams, proton fragments, predominantly ejected along the polarization vector, were energy analysed by applying a variable electric field across a pair of deflection plates. The energy selected protons were then deflected in a 45° parallel plate analyser and detected in an off-axis channel electron multiplier. The parallel plate analyser served to separate and baffle the primary H_2^+ beam from the proton signal. The Ti-sapphire laser operated at a fundamental wavelength of 790 nm, delivering 65 fs duration pulses of maximum focussed intensity 10^{15} Wcm^{-2} at 10 Hz repetition rate.

H atom fragment yields were measured by rotating the axis of polarization of the laser, such that the E vector was colinear with the ion beam axis. The fast neutral products passed undeflected through the parallel plate analyser and were detected in an on-axis channel electron multiplier.

Measured energy spectra for both proton and H atom fragments from an H_2^+ molecular ion beam are shown in Figure 2. The similarity between the main peaks in the proton and neutral spectra is immediately apparent. Clearly these peaks are due to

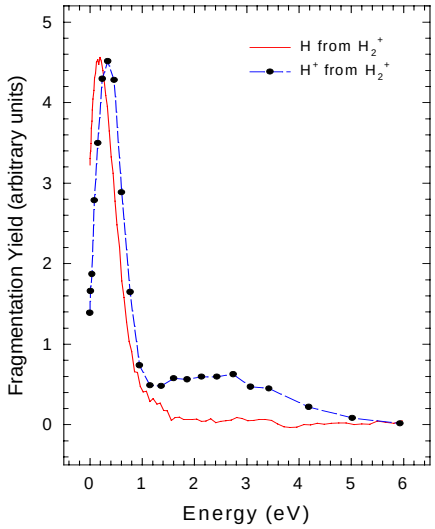

Figure 2. Energy distributions of H and H^+.

the dissociation channel:

$$H_2^+(1s\,\sigma_g, v) + nh\nu \rightarrow H^+ + H(n, l) \quad \ldots \quad (1)$$

leading to a proton plus an H atom with equally shared dissociation energy. However the second distribution in the proton energy which is not present for the neutral H is clearly due to the coulomb explosion channel:

$$H_2^+(1s\,\sigma_g, v) + nh\nu \rightarrow H^+ + H^+ + e^- \quad \ldots \quad (2)$$

leading to two protons. The energy of this distribution is consistent with the theory of enhanced ionisation, however differences between the energy distributions[2] and those of Figure 2 indicate that the effect of the initial ionisation is not completely negligible. This is currently the subject of investigation.

References

1. T Zuo and A D Bandrauk
Phys. Rev. A 52, 2511,(1995).

2. G N Gibson et al
Phys. Rev. Lett 79, 2022, (1997).

An Investigation of the Angular Distributions of Fragment ions from Coulomb Explosion of the Linear CS_2 Molecule

P Graham, K W D Ledingham, R P Singhal, T McCanny, S M Hankin, X Fang, D J Smith

Department of Physics & Astronomy, University of Glasgow, Glasgow, G12 8QQ, Scotland, UK.

A J Langley, P F Taday

Central Laser Facility, CLRC Rutherford Appleton Laboratory, Chilton, Didcot, Oxon, OX11 0QX, UK

C Kosmidis, P Tzallas

Department of Physics, University of Ioannina, GR-45110, Ioannina, Greece.

Main contact email address: *K.Ledingham@physics.gla.ac.uk*

Introduction

As theoretical and experimental study of triatomic molecules subjected to intense laser beams[1-13] gains momentum, useful insights are obtained into the dynamical processes involved. The experiments are becoming increasingly sophisticated and include alignment and trapping[14-17] of molecules. Indeed, the ability to control the alignment of the overall molecular dipole moment with the laser field can have significant implications in the control of chemical reactions (steric effects) and hence is receiving intensive contemporary interest from several groups[16-28].

A dramatic upsurge in short pulse laser technology, with its concomitant high achievable peak powers, has been observed in the last few years. This has largely been due to the development of chirped-pulse amplification (CPA) techniques[29]. Using the ultra-intense ($I \approx 1\times10^{16}$ W cm^{-2}) Astra femtosecond (τ = 50fs) laser facility at RAL, we have studied the effect of this ultra-intense laser/matter interaction. Specifically we have observed the angular distribution of fragment ions from the parent molecules subsequent to Coulomb explosion, and the mechanism responsible for the observed anisotropy – alignment or preferential ionisation.

Experimental

Gas-phase samples were admitted effusively to the high-vacuum chamber pumped to a base pressure of ~10^{-8} Torr by a turbomolecular pump. The chamber pressure was maintained at ~10^{-6} Torr when a sample was admitted in order to avoid space-charge effects and pressure broadening of the ion peaks. The ToF system employed in this work was a conventional linear mass spectrometer based on the Wiley-McLaren configuration. The field-free drift region had a length of 1.2 m. Ions were detected using an electron multiplier (Thorn EMI) connected to a LeCroy (9344C, 500MHz) digital storage oscilloscope (DSO). The extraction fields used were of the order of 500 V cm^{-1}.

The femtosecond laser system used was based on a Spectra Physics Ti:S oscillator pumped by an Ar-ion laser[30] producing pulses of 9 μJ pulse^{-1} at 790 nm and 50 fs duration. The pulses were then stretched to ~300 ps. The stretched pulse was then amplified in a multi-pass confocal amplifier consisting of a 7 mm long Ti:S rod (Crystal Systems) pumped with 67 mJ from the second harmonic of a Spectra Physics GCR 270-10 Nd:YAG laser. The pulse train is then recompressed to 50 fs using a pair of gratings and the final beam energy is 5mJ. When focussed using a f/3 spherical mirror this gives intensities of 10TW cm^{-2}. Measurement of the angular distributions of the fragments was achieved by rotating a λ/2 wave-plate in the path of the beam placed immediately before the quartz window of the target chamber, in order to avoid polarisation-dependent transmission losses through the beam-splitters, etc.

Results and Discussion

A polar plot of the CS_2^{n+} ($n \leq 3$) peaks (not shown) exhibits a uniform signal intensity for all polarisation angles (isotropic). The isotropy shows that the intact parent ions, ionised up to the triply-charged state, are detected with equal efficiency regardless of polarisation orientation.

The angular distributions of specific fragment ions exhibit a significantly different behaviour from that of the multiply-charged parent ions. The angular distributions for the CS^+ and CS^{2+} fragment ions are shown in Figure 1.

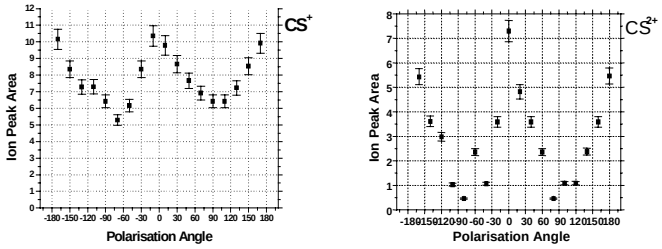

Figure 1. Angular distribution of the CS fragment ions.

The CS^+ exhibits weak anisotropy, whereas the doubly-ionised fragment CS^{2+} clearly shows only an anisotropic distribution. Bond-breaking in CS_2^+ is not a Coulomb explosion process and only imparts a small kinetic energy to the S^+ or CS^+ ions and the neutral counter-fragment. This is termed 'soft' dissociation. The resulting low kinetic energy fragment ions remain within the collection volume of the ToF analyser and are detected efficiently. Conversely, the anisotropic distributions for CS^+ and CS^{2+} are derived from the fragmentation of higher ionised states of the CS_2 molecule resulting in Coulomb explosions. These explosions yield two ionised fragments that may possess sufficient kinetic energy to escape the collection volume of the ToF analyser. The anisotropy in the ion signal is a measure of the initial momentum of the exploding fragments; those fragments ejected pseudo-parallel to the ToF axis are detected with greater efficiency.

The angular distributions for S^{n+} ($n \leq 6$) from CS_2 are shown in Figure 2. It is evident from these data that all the fragments are markedly anisotropic, peaking along the parallel direction (0 and 180^o). The minimum ion count for each graph in Figure 2 is near zero for all charge-states, except S^+. Similar to CS^+ (Figure 1) the S^+ distribution has an underlying isotropic component originating from the low energy fragmentation of CS_2^+ and CS_2^{2+} ions (both isotropically distributed). The angle where the maximum ion count occurs is the same for all S^{n+} fragments and is parallel to the ToF axis (0° and 180°). Furthermore, the FWHM value is equal for all S-fragments (~60°). If the CS_2 molecules were aligning in the electric field of the laser beam, one would expect the distributions to narrow for higher charged fragments due to the higher induced dipole moment, and hence aligning torque acting on the precursor molecule. That this is not the case in the present work indicates that there is little evidence for alignment of CS_2 within the 50 fs pulse, regardless of the transient charge-state of the molecule.

The origin of the anisotropic signal maxima is a result of preferential ionisation/detection occurring when the laser polarisation is efficiently overlapped with the molecular axis of the triatomic parent molecule and the ToF axis. Hence, both ionisation/dissociation and Coulomb explosion are enhanced, apparent through the preferential detection of the CS^{n+} and S^{n+} fragments ejected within ca. ±30° of the ToF axis.

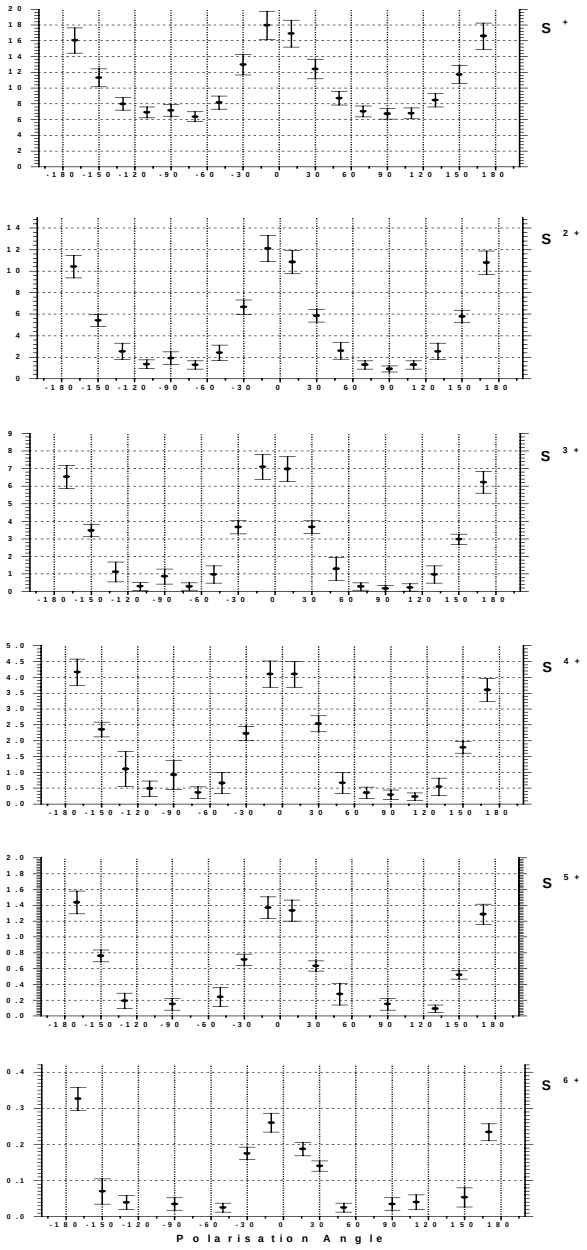

Figure 2. Angular distribution of the S fragment ions.

Comparison of the angular distributions for S and C fragments reveals that the molecular structure is distorted by the presence of the laser field. Diametrically opposite behaviour for the ejection of S and C fragments is clearly shown in the angular distributions of Figures 2 and 3. This polarisation-dependent effect arises from the preferential ionisation of those molecules whose molecular axes are pseudo-parallel to the laser field. The distributions are maximised along the perpendicular direction (± 90°). A similar underlying isotropic component to that of S^+ and CS^+ is observed for C^+. The origin of the diametrically opposite behaviour for C- and S-fragment ions is a result of the molecular geometry in the ion state. The CS_2 ion molecule is slightly bent when excited, with the S-C bonds at small angles to the electric field of the laser. When the laser field is collinear with the ToF axis, the S^{n+} ions are ejected along the polarisation direction (actually along the bonds) and along the ToF axis resulting in efficient detection. The greatly reduced C^{m+} signal is a result of the fragments being ejected perpendicular to the laser polarisation after Coulomb explosion. The anisotropy of the multiply-charged carbon atoms can be traced to the molecular axis being bent such that a momentum transfer from the Coulomb exploding S atoms occurs and results in the C^{m+} intensity peaking at 90°. Conversely, when the polarisation is perpendicular to the ToF axis the high energy S^{n+} ions are lost and detected with reduced efficiency. In an attempt to elucidate the question of whether the CS_2 molecule can rotate within the laser pulse, angular distributions were carried out at different pulse lengths. Figure 4 shows the C^+ distributions for three pulse lengths of 150 fs, 1 ps and 300 ps. Data obtained with the two shorter pulse lengths exhibited little change from that recorded at 50 fs. However, the distribution recorded with the longer pulse length (300 ps) became markedly isotropic. A similar finding was obtained for the S fragments. The alignment of CS_2, proposed by Couris et al.[31] to occur at pulse durations of 200 fs, could not be reproduced at 50 fs, 150 fs or 1ps.

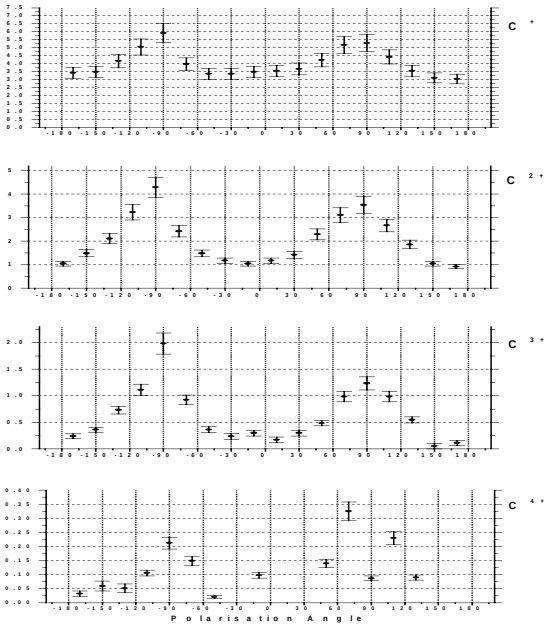

Figure 3. Angular distribution of C fragment ions.

This orthogonal ejection of peripheral and central ions from triatomic species has been confirmed by numerous groups for molecules such as NO_2, H_2O, COS and CO_2[31-33].

Conclusions

An investigation of the ionisation/dissociation process of the linear CS_2 molecule has been carried out using 50 fs, 790 nm laser pulses at an intensity of 1×10^{16} W cm^{-2}. The S^{n+} fragment peaks are broader than those for C^{m+} fragments indicating that they possess more energy in the break-up as expected from Coulomb explosions of highly-charged CS_2 molecular ions. This is especially obvious in the ToF mass spectrum recorded using horizontal polarisation. In addition, the maximum charge-state attained by S^{n+} (n = 6) is greater than that for C^{m+} (m = 4). To access the much more tightly bound 5+ state in C and 7+ state in S requires 392 and 281 eV respectively. Clearly these energies are not available from a laser beam of intensity 1×10^{16} W cm^{-2} with a ponderomotive potential of 186 eV.

The angular distributions for the CS_2^+, CS_2^{2+}, CS_2^{3+}, CS^+, CS^{2+}, S^{n+} and C^{m+} ions were analyzed by measuring peak areas with respect to the polarisation vector of the laser pulse as it was

rotated. The CS_2^+, CS_2^{2+}, CS_2^{3+} parent ion distributions are all isotropic. The CS^+, C^+ and S^+ distributions exhibit a significant underlying isotropic component in addition to anisotropy. All other multiply-charged fragments display totally anisotropic behaviour. The S^{n+} and CS^{2+} distributions are maximised parallel to the ToF-axis, whereas the C^{m+} ions are ejected orthogonally. This is accounted for by a field-induced bending of the initially linear CS_2 molecule and subsequent momentum transfer.

The FWHM values for the S^{n+} and C^{m+} peaks are approximately of equal width. This suggests that the observed anisotropies are not in fact due to the alignment of the molecule within the laser pulse, but to the preferential ionisation of those molecules that have their axes initially aligned with the laser field. The isotropic component observed for S^+, C^+, and CS^+ is associated with low energy 'soft' dissociation. Thus, the conclusion drawn for CS_2 (and heavier molecules) is that the initial orientation is responsible for the observed anisotropy, the molecule being unable to be aligned within the 50 fs laser pulse. This is further borne out by results for CS_2 and CH_3I, having similar degrees of alignment in a nanosecond pulse[16].

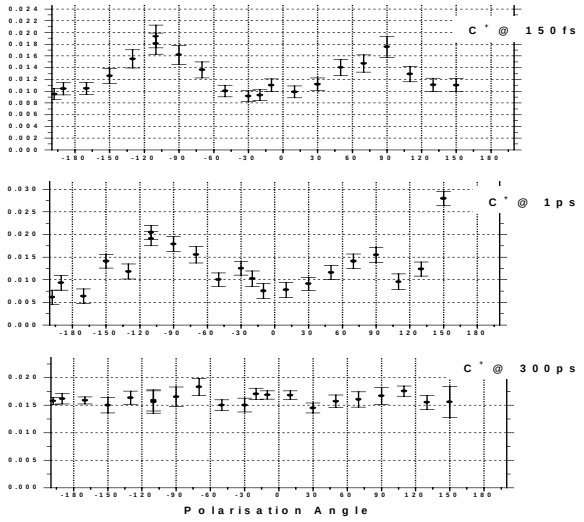

Figure 4. Angular distribution of C^+ at 150 fs, 1 ps and 300 ps.

Finally, angular distributions are shown for C^+ from CS_2 for laser pulse lengths of 150fs, 1ps and 300ps. At the longest pulse length the distribution becomes markedly isotropic whereas the two shorter pulse widths are anisotropic and very similar to the results obtained at 50 fs. The distribution width is similar for both 50 and 150 fs, in contrast to another recent report[31]. The spectra corresponding to longer pulse durations also show increased fragmentation over those for shorter pulses. This effect is also observed by Koudoumas et al.[34].

In summary, the orientation of the inter-atomic axes with respect to the electric field of the laser is crucial for efficient energy transfer leading to ionisation/dissociation. Molecules which are initially oriented along the direction of laser polarisation contribute most to the observed ion signal through the preferential ionisation process, as mentioned above. Further work is being carried out for other molecules (e.g. H_2S, N_2O, CH_3I) under a range of experimental conditions, i.e. variable pulse widths and linear/circular polarisation. The results of this work will be published elsewhere[35]. It is hoped that this will lead to a greater understanding of the mechanisms for alignment/enhanced ionisation, and ultimately to steric control of chemical reactions.

References

1. K Vijayalakshmi, V R Bhardwaj, D Mathur
1997 J. Phys. B: At. Mol. Opt. Phys. 30, 4065-4085

2. J H Posthumus, J Plumridge, M K Thomas, K Codling, L J Frasinski, A J Langley, P F Taday
1998 J. Phys. B: At. Mol. Opt. Phys. 31, L553-L562; Posthumus JH, Giles AJ, Thompson M, Shaikh W, Langley AJ, Frasinski LJ, Codling K 1996 *J. Phys. B: At. Mol. Opt. Phys*. 29, L525-L531

3. A Hishikawa, A Iwamae, K Hoshina, M Kono, K Yamanouchi
1998 *Chem. Phys*. 231, 315-329; Hishikawa A, Iwamae A, Hoshina K, Kono M, Yamanouchi K 1998 *Chem. Phys. Lett*. 282, 283-291

4. L A Lompre, P Monot, T Auguste, G Mainfray,C Manus
1993 *Journal de Chimie Physique et de Physico-Chimie Biologique* 90, 1275-1282

5. M J DeWitt, R J Levis
1998 *J. Chem. Phys*. 108, 7739-7742

6. A Talebpour, S Larochellem S L Chin
1997 *Laser Physics* 7, 851-857

7. D Normand, S Dobosz, M Lezius, P D'Oliviera, M Schmidt
1997 *I.O.P Conf. Series* 154, 287-297

8. M Y Ivanov, D R Matusek, J S Wright
1996 *Phys. Rev. A* 54, 3235-3244

9. Cornaggia C 1996 *Phys. Rev. A* 54, R2555-R2558

10. S Chelkowski, A Conjusteau, T Zuo, A D Bandrauk
1996 *Phys. Rev. A* 54, 3235-3244

11. F A Ilkov, T D G Walsh, S Turgeon, S L Chin
1995 *Phys. Rev. A* 51, R2695-R2698

12. G R Kumar, P Gross, C P Safvan, F A Rajgara, D Mathur
1996 *Phys. Rev. A* 53, 3098-3102

13. A E Kando, W J Meath
1991 *Molecular Physics* 74, 113-129

14. B Friedrich, D Herschbach
1995 *J. Phys. Chem*. 99, 15686-15693

15. A D Bandrauk, Ruel
1999 *J. Phys. Rev. A* 59, 2153

16. H Sakai, C P Safvan, J J Larsen, K M Hilligsoe, K Hald, H Stapelfeldt
1999 *J. Chem. Phys*. 110, 10235

17. H Yu, T Zuo, A D Bandrauk
1998 *J. Phys. B: At. Mol. Opt. Phys*. 31, 1533-1551

18. H J Loesch, A Remscheid
1990 *J. Chem. Phys*. 93, 4779-4790

19. A H Zewail
1996 *Abstracts of Papers of the American Chemical Society* 211, 153

20. M J J Vrakking, S Stolte
1997 *Chem. Phys. Lett*. 271, 209-215

21. C Mainos
1996 *Phys. Rev. A* 54, 4226-4235

22. S J Garrett, D H Fairbrother, V P Holbert, E Weitz, P C Stair
1994 *Chem. Phys. Lett*. 219, 409-415

23. D Mathur, V R Bhardwaj, P Gross, G R Kumar, F A Rajgara, C P Safvan, K Vijayalakshmi
1997 *Laser Physics* 7, 829-838

24. J H Posthumus, J Plumridge, L J Frasinski, K Codling, A J Langley, P F Taday
1998 *J. Phys. B: At. Mol. Opt. Phys*. 31, L985-L993

25. J H Sanderson, R V Thomas, W A Bryan, W R Newell, A J Langley, P F Taday
1998 *J. Phys. B: At. Mol. Opt. Phys*. 31, L599-L606

26. J M Rost, J C Griffen, B Friedrich, D R Herschbach
1992 *Phys Rev. Lett*. 68, 1299-1301

27. H J Loesch, F Steinkemeier
1993 *J. Chem. Phys*. 98, 9570

28. B Friedrich, D Herschbach
1995 *J. Phys. Chem*. 99, 15686-15693

29. D Strickland, G Mourou
1985 *Opt. Commun*. 56, 219

30. P F Taday, I Mohammed, A J Langley, I N Ross, K Codling, K W D Ledingham, W R Newell, S Preston, D Riley, I Williams
1997/98 *Central Laser Facility RAL Annual Report* 179

31. S Couris, E Koudoumas, C Fotakis
1999 *J. Phys. B: At. Mol. Opt. Phys*. *to be published*

32. J H Sanderson, R V Thomas, W A Bryan, W R Newell, A J Langley, P F Taday
1998 *J. Phys. B: At. Mol. Opt. Phys*. 31, L599-L606

33. J V Ford, Q Zhong, L Poth, A W Castleman Jr
1999 *J. Chem. Phys*. 110, 6257-6267

34. E Koudoumas, R DeNalda, C Fotakis, S Couris
1999 *Laser Chemistry* at press

35. P Graham, K W D Ledingham, R P Singhal, T McCanny, A J Langley, P F Taday, C Kosmidis
To be published.

Ultrafast Time-resolved UV-Visible Absorption Study of Photochemical Radical Formation from [Re(R)(CO)$_3$(dmb)]; R = Me or Et

I R Farrell, A Vlcek, Jr.

Department of Chemistry, Queen Mary and Westfield College, University of London, London, E1 4NS. United Kingdom.

P Matousek, M Towrie

Central Laser Facility, CLRC Rutherford Appleton Laboratory, Chilton, Didcot, Oxon, OX11 0QX, UK

Main contact email address: *A.Vlcek@qmw.ac.uk*

Introduction

Metal complexes of the general formula [Re(R)(CO)$_3$(dmb)]; R = Me, Et, ^{i}Pr, Bz; α-diimine = R-DAB, bpy, dmb, etc. often react via a Re–R homolysis to give the radical photoproducts [Re(S)(CO)$_3$(α-diimine$^{\cdot-}$)] and R·. Re–R homolysis quantum yields for the Et, ^{i}Pr and Bz complexes all approach unity whereas the methyl complex reacts with a quantum yield of only 0.4, which is found to be heavily dependent on temperature. [1)]

The objects of this study are the two complexes [Re(R)(CO)$_3$(dmb)]; R = Me or Et; dmb = 4,4'-dimethyl-2,2'bipyridine. It is hoped that time-resolved spectroscopy on the ultrafast timescale will unravel further the mechanism behind the homolysis reaction and reveal the factors which limit the homolysis quantum yield for the methyl complex.

Experimental

The ultrafast spectrometer at RAL has been described before in great detail.[2,3)] Pump-probe spectroscopy was used to generate high concentrations of transient species and examine them in one of two ways:

(1) Time-resolved spectra were taken by passing a white-light probe beam through the excited part of the sample and dispersing it onto two 512 pixel diode arrays. This allowed absorption spectra of the transient species to be recorded in the range 475–650 nm.

(2) For a more accurate determination of the decay kinetics, single wavelength kinetic profiles were recorded by selecting portions of the white-light probe beam using 10nm wide bandpass filters and directing this onto photodiode detectors.

Nanosecond time-resolved spectra were recorded at the University of Amsterdam using a well described experimental setup.[1)]

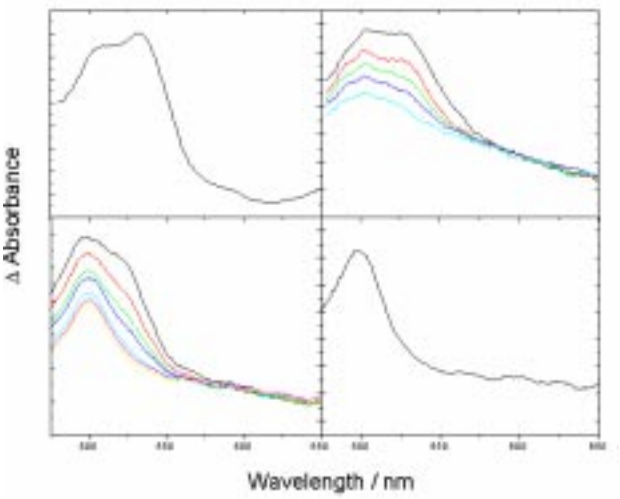

Figure 1. Time-resolved spectra of [Re(R)(CO)$_3$(dmb)]
Left: R = Me; top: 2 ps; bottom: 0, 10, 20, 30, 50, 70 and 80 ns.
Right: R = Et; top: 2, 50, 100, 200, 700 ps.

Results and Discussion

The time-resolved absorption spectra of the methyl and ethyl complexes are depicted in Figure 1. Ultrafast experiments show that the two bands, corresponding to the radical photoproducts (510 nm) and MLCT trapping state (530 nm), are completely formed within the resolution of the instrument (≤ 400 fs). The time-resolved spectra of the ethyl complex, however, show an interesting time evolution on the ultrafast timescale. The spectrum immediately after excitation (2 ps) displays two bands. One of these is persistent (505 nm) on the ultrafast and nanosecond timescales and is assigned to [Re(S)(CO)$_3$(dmb$^{\cdot-}$)]. The other band (530 nm) decays with a lifetime of 186 ps seemingly with the concurrent production of photoproduct (the quantum yield for homolysis is 1).

This behaviour is essentially the same as that observed for the methyl complex[1)], but on a timescale almost 150 times faster. Accordingly, the decaying, 530 nm species is assigned as a ^{3}MLCT trapping state, similar in nature to that found for [Re(Me)(CO)$_3$(dmb)] but lying at higher energy. It is thought that the ^{3}MLCT trapping state in the methyl complex lies below both the initially populated, Franck-Condon MLCT state and the reactive σπ* state. Hence it provides an efficient, deactivation pathway. In the corresponding ethyl complex, the ^{3}MLCT state lies higher in energy than the reactive σπ* state, but lower in energy than the Franck-Condon state. In this way the "trap" does not act as a deactivation route, but as an alternative, delayed pathway to homolysis.

References

1. C. J. Kleverlaan, D. J. Stufkens, I. P. Clark, M. W. George, J. J. Turner, D. M. Martino, H. van Willigen, A. Vlcek, Jr. J. Am. Chem. Soc. 120, 10871, (1998)

2. P. Matousek; A. W. Parker; P. F. Taday and M. Towrie; Opt. Comm. 127, 307, (1996)

3. M. Towrie; A. W. Parker; W. Shaikh and P. Matousek Meas. Sci. Technol. 9, 816, (1998)

A Femtosecond Spectroscopic Study of MLCT Excited States Dynamics of $[Cr(CO)_4(bpy)]$: Excitation Energy Dependent Branching Between CO dissociation and Relaxation

I R Farrell, A Vlcek, Jr.

Department of Chemistry, Queen Mary and Westfield College, University of London, London E1 4NS. United Kingdom

P Matousek, M Towrie

Central Laser Facility, CLRC Rutherford Appleton Laboratory, Chilton, Didcot, Oxon, OX11 0QX, UK

Main contact email address: *A.Vlcek@qmw.ac.uk*

Introduction

The metal complex $[Cr(CO)_4(bpy)]$ has an intense metal-to-ligand charge transfer (MLCT) absorption band at *ca.* 500 nm. Population of this MLCT state leads to the dissociation of an axial CO ligand with a temperature and excitation wavelength (λ_{ex}) dependent quantum yield of 0.1 – 0.2[1)]. The present study investigates the mechanism for this, in particular the rate of CO loss and factors that limit and affect quantum yield.

Experimental

The ultrafast spectrometer at RAL has been described before in great detail.[2,3)] Pump-probe spectroscopy was used to generate high concentrations of transient species and examine them in one of two ways:

(1) Time-resolved spectra were taken by passing a white-light probe beam through the excited part of the sample and dispersing it onto two 512 pixel diode arrays. This allowed absorption spectra of the transient species to be recorded in the range 560–720 nm.

(2) For a more accurate determination of the decay kinetics, single wavelength kinetic profiles were recorded by selecting portions of the white-light probe beam using 10nm wide bandpass filters and directing this onto photodiode detectors.

This experiment relied on the technical specification of the RAL ultrafast setup. The facility to individually tune the pump and probe laser pulses independently of each other was crucial for excitation wavelength dependence experiments.

Results and Discussion

Solutions of $[Cr(CO)_4(bpy)]$ in pyridine were excited at 500 nm. Time resolved spectra at various intervals after excitation are shown in Figure 1.

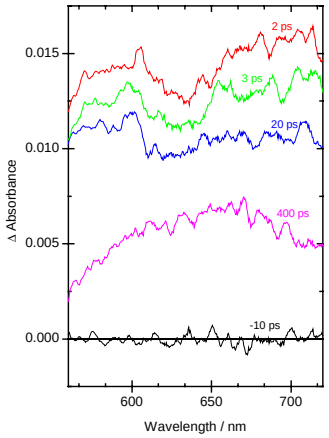

Figure 1. Time-resolved spectrum of $[Cr(CO)_4(bpy)]$ in pyridine solution after 2, 3, 20 and 400 ps.

Spectra recorded at long times after excitation (> 250 ps) have an apparent maximum at 660 nm. On the basis of previous nanosecond work this band is assigned to the *fac*-$[Cr(CO)_3(bpy)]$ photoproduct. Spectra recorded at earlier times after excitation are broad and featureless, extending far into the red. This is characteristic of the bpy$^{\cdot -}$ chromophore, which has been characterised by spectroelectrochemistry. Consequently, the time-resolved spectra at early delay times are thought to consist of two components: the 660 nm photoproduct band and absorptions due to MLCT states, which are characterised by their bpy$^{\cdot -}$ chromophore.

Kinetic profiles, measured at various wavelengths throughout the spectral range, indicate that this time evolution fits well to double exponential decay kinetics, yielding two lifetimes of 8 ± 1 and 87 ± 3 ps. These values were found to be independent of pump and probe wavelength, however variation of λ_{ex} did affect the relative proportions of photoproduct and MLCT states produced.

Shortening the excitation wavelength from 580 nm to 400 nm increased the relative amount of the initially formed photoproduct from 1.5 % of the total change in absorbance to 7.9 % (see Figure 2).

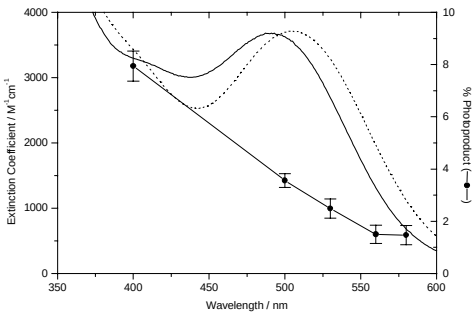

Figure 2. Absorption spectra of $Cr(CO)_4$ (bpy) in pyridine (——) and CH_2Cl_2 (·····) solutions shows together with the photoproduct contribution to the initial (t=0) transient absorption, C_o, measured at various excitation wavelengths (•).

This is an important mechanistic result and one that mirrors the previously observed quantum yield dependence on λ_{ex}. A relationship between the amount of product formed and the excitation wavelength implies that the reacting species must have a "memory" of the excitation energy. This effectively precludes the possibility of any relaxation before CO loss and suggests that the branching ratio between formation of the photoproduct and population of the MLCT trapping state (and consequently the CO loss quantum yield) is decided at the very earliest time after excitation.

References

1. J. Vichova; F. Hartl and A. Vlcek, Jr. J. Am. Chem. Soc. 114, 10903, (1992)

2. P. Matousek; A. W. Parker; P. F. Taday and M. Towrie; Opt. Comm. 127, 307, (1996)

3. M. Towrie; A. W. Parker; W. Shaikh and P. Matousek Meas. Sci. Technol. 9, 816, (1998)

The Ultrafast Dynamics of [Mn(Br)(CO)$_3$(^{i}Pr-DAB)]: The First Stages of *fac* → *mer* Isomerisation

I R Farrell, A Vlcek, Jr.

Department of Chemistry, Queen Mary and Westfield College, University of London, London, E1 4NS. United Kingdom.

P Matousek, Mike Towrie

Central Laser Facility, CLRC Rutherford Appleton Laboratory, Chilton, Didcot, Oxon, OX11 0QX, UK

Main contact email address: *A.Vlcek@qmw.ac.uk*

Introduction

The organometallic complex *fac*-[Mn(Br)(CO)$_3$(^{i}Pr-DAB)] has a low lying halide-to-ligand charge transfer transition from where it undergoes a *fac* → *mer* isomerisation. The first stage of this isomerisation process is believed to be the concerted loss of an equatorial carbonyl ligand and migration of the axial halide into the equatorial plane, the isomerisation process being completed by the recombination of the dicarbonyl fragment with free CO.[1)]

This study examines the events that lead to this isomerisation process on the ultrafast timescale and hope to unravel the kinetics and mechanism of the process.

Experimental

The ultrafast spectrometer at RAL has been described before in great detail.[2,3)]

Pump-probe spectroscopy was used to generate high concentrations of transient species and examine them in one of two ways:

(1) Time-resolved spectra were taken by passing a white-light probe beam through the excited part of the sample and dispersing it onto two 512 pixel diode arrays. This allowed absorption spectra of the transient species to be recorded in the range 525–675 nm.

(2) For a more accurate determination of the decay kinetics, single wavelength kinetic profiles were recorded by selecting portions of the white-light probe beam using 10nm wide bandpass filters and directing this onto photodiode detectors.

Results and Discussion

The time-resolved spectrum at 2 ps after excitation at 500 nm shows one fairly broad band centered at approximately 620 nm (see figure 1). This band decays concurrent with the formation of another with an apparent maximum at 560 nm. The presence of near isosbesticity at ca. 575 nm indicates a clean conversion between the two bands. The spectra recorded at later time delays (50 – 200 ps) also show the presence of a band growing in at around 700 nm with kinetics that are obviously not identical to those of the decaying 620 nm band. A small "blue-shift" of the 560 nm band to around 540 nm is also observed on this timescale.

Single wavelength kinetic profiles show that 620 nm band decays with single exponential kinetics, having a mean lifetime of 11.1 ± 0.7 ps. The formation of the 560 nm band, however, fits well to double exponential kinetics: the first lifetime identical to that above and the second equal to 23.4 ± 5.9 ps. The latter is consistent with the single exponential formation of the absorption at longer wavelengths (700 – 800 nm) which has a risetime of 20.6 ± 1.2 ps.

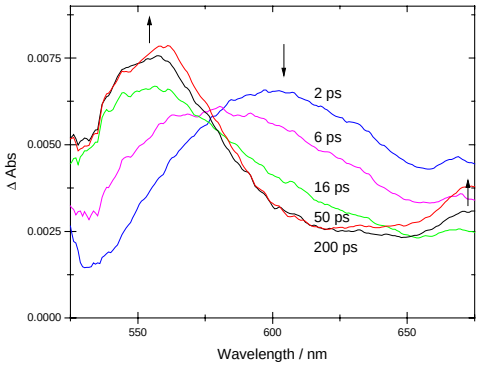

Figure 1. Time-resolved absorption spectrum of fac-[Mn(Br)(CO)$_3$(^{i}Pr-DAB)] in pyridine solution after 500 nm XLCT excitation.

We assign the observations described above to an A→B→C type mechanism in which "A" represents the initially populated XLCT excited state and "B" represents the weakly solvated CO loss product, [Mn(Br)(CO)$_2$(^{i}Pr-DAB)]…py. "C" is thus assigned as the stable (and previously characterised) photoproduct [Mn(Br)(py)(CO)$_2$(^{i}Pr-DAB)] which is formed in preference to the *mer*-tricarbonyl species in such a coordinating solvent as pyridine.[1)]

This rather slow time for CO dissociation (11 ps) is somewhat of an exception for CO loss from an excited state of an organometallic. Such processes usually happen much more quickly than this.[4)] The slow rate of CO loss is consistent with a resonance coupling mechanism to "escape" from a completely bound excited state to a fully relaxed, dissociative ground state.[5)]

References

1. G. J. Stor; S. L. Morrison; D. J. Stufkens and A. Oskam. Organometallics 13 ,2641 (1994).
2. P. Matousek; A. W. Parker; P. F. Taday and M. Towrie; Opt. Comm. 127, 307, (1996)
3. M. Towrie; A. W. Parker; W. Shaikh and P. Matousek Meas. Sci. Technol. 9, 816, (1998)
4. A. Vlcek, Jr. Coord. Chem. Revs. 177, 219 (1998)
5. A. Rosa; G. Ricciardi; E. J. Baerends and D. J. Stufkens. J. Phys. Chem. 100, 15346, (1996).

Interligand Electron Transfer in MLCT-Excited State of $[Re(MQ^+)(CO)_3(dmb)]^{2+}$: Kinetics and Medium Effects

D J Liard, A Vlcek, Jr.

Dept. of Chemistry, Queen Mary and Westfield College, University of London, London E1 4NS, United Kingdom

P Matousek

Central Laser Facility, CLRC Rutherford Appleton Laboratory, Chilton, Didcot, Oxon, OX11 0QX, UK

Main contact email address: *A.Vlcek@qmw.ac.uk*

Introduction

The ultrafast excited state dynamics of $[Re(MQ^+)(CO)_3(dmb)](PF_6)_2$ and $[Re(4\text{-}Etpy)(CO)_3(dmb)](PF_6)_2$, where dmb = 4,4'-dimethyl-2,2'-bipyridine, MQ^+ = *N*-methyl-4,4'-bipyridinium, 4-Etpy = 4-ethylpyridine, were studied in acetonitrile and ethylene glycol. The rate of electron transfer was determined for the excited state, interligand, electron transfer:

$$**[Re^{II}(MQ^+)(CO)_3(dmb^{\bullet-})]^{2+} \longrightarrow *[Re^{II}(MQ^{\bullet})(CO)_3(dmb)]^{2+}$$

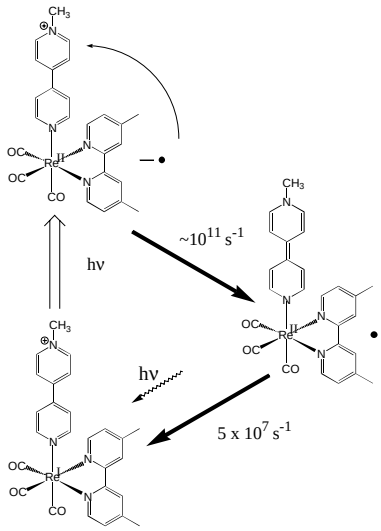

Figure 1. Interligand electron transfer.

Experimental

We made $[Re(MQ^+)(CO)_3(dmb)](PF_6)_2$ and $[Re(4\text{-}Etpy)(CO)_3(dmb)](PF_6)_2$ according to literature procedures.[1)]

Time-resolved transient absorption spectra were generated using the system of lasers in the ultrafast spectroscopy laboratory at RAL.[2)] Samples are irradiated at both 400nm and 330nm, which is within the range of the MLCT absorption band of the excited states and monitored using pump-probe techniques. Both beams are generated from the 800nm fundamental output of a Ti:Sapphire laser, producing a pulse typically 250fs in length. The pump beam of 400nm is generated by frequency doubling the fundamental laser light, while the beam at 330nm requires an OPA in addition to frequency doubling.

The pump and probe beams are focussed in a 2mm flow-cell containing the sample. The probe beam is then dispersed on the diode array using a diffraction grating. For studies at single probe wavelength, the probe beam passes through a filter of 10nm width at the desired wavelength.

Results and Discussion

Time-resolved transient absorption spectra of $[Re(4\text{-}Etpy)(CO)_3(dmb)]^{2+}$ shows a very weak, broad absorption at about 450 nm due to the (Re→dmb) MLCT excited state, which is very long lived. On the other hand, for $[Re(MQ^+)(CO)_3(dmb)]^{2+}$, this excited state undergoes an interligand electron transfer: to form the (Re→MQ^+) MLCT excited state, characterised by an intense, structured absorption band at about 630 nm due to the $MQ^{\bullet}$ radical.(Figure 2)

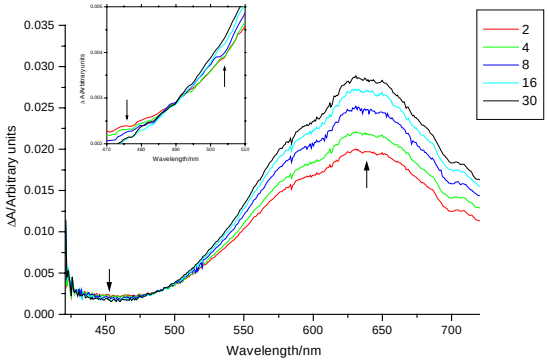

Figure 2. Time-resolved transient absorption spectra of $[Re(MQ^+(CO_3)(dmb)]^{2+}$ in acetonitrile. Inset : isosbestic point after smoothing.

Electron transfer rate constants of $1.3x10^{11}$ s^{-1} in acetonitrile and $6.7x10^{10}$ s^{-1} in ethylene glycol were determined. In the former solvent, the shape of the $*[Re^{II}(MQ^{\bullet})(CO)_3(dmb)]^{2+}$ absorption band is already fully developed at 2 ps, while in the latter, the vibrational structure starts to appear only after 4 ps.

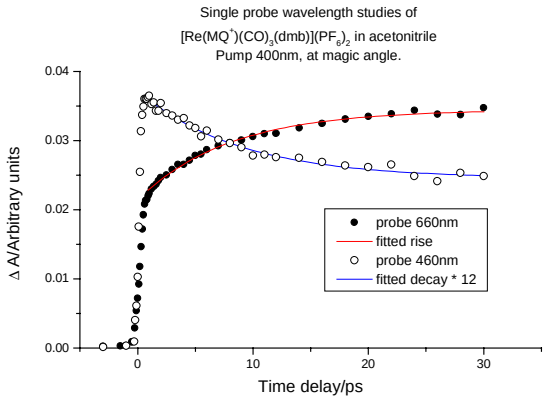

Figure 3. Single probe wavelength studies of $[Re(MQ+)(CO)_3(dmb)]^{2+}$ in acetonitrile showing rate of formation of transient is equal to rate of decay of MLCT excited state.

Conclusion

The difference between the two solvents indicates that the electron transfer process is nonadiabatic in rapidly relaxing acetonitrile, while it could become adiabatic in ethylene glycol. It is also wavelength independent. As far as we are aware, this is the first time that interligand excited state electron transfer kinetics have been observed directly.

References

1. S L Mecklenburg, K A Opperman, P Chen, T Meyer J. Phys. Chem. 100, 15145, (1996)

2. P Matousek, A W Parker, P F Taday, W T Toner, M Towrie Optics Communications, 127, 307, (1996)

Picosecond Time-Resolved Photoelectron Angular Distributions from S_1 para-difluorobenzene

K L Reid, T A Field

School of Chemistry, University of Nottingham, Nottingham, NG7 2RD

M Towrie, P Matousek

Central Laser Facility, CLRC Rutherford Appleton Laboratory, Chilton, Didcot, Oxon, OX11 0QX, UK

Main contact email address: *Katharine.Reid@nott.ac.uk*

Introduction

It has been known for some time that photoelectron angular distributions (PADs) can provide a probe of the alignment of the state that is ionized[1-4]. The use of time-resolved PADs to monitor the evolution of excited state alignment following (1+1) resonance-enhanced multiphoton ionization (REMPI) was proposed and demonstrated on a nanosecond time-scale for atoms by the groups of Lambropoulos[1] and Berry[2] and for molecules by our group[5-6] The use of picosecond time-resolved PADs following laser excitation as a means of probing the effects of rotation-vibration coupling in an excited electronic state was originally suggested in a theoretical paper by Noguchi et al.[7] Although time-resolved photoelectron spectroscopy has been used as a method of examining intra-molecular dynamics by the groups of Reilly[8], Knee[9] and Stolow[10] among others, to date these groups have not measured photoelectron angular distributions. In recent years the idea of measuring picosecond or even femtosecond time-resolved PADs has been given impetus by the development of the "velocity mapping " technique by Eppink and Parker[11] in which emitted photoelectrons are imaged, and also by some very recent theoretical work[12-13].

In this report we present picosecond time-resolved PADs measured following excitation of the $3^1 5^1$ level in S_1 para-difluorobenzene in a (1+1) REMPI scheme. We employed field-free time-of-flight photoelectron spectroscopy, which enabled us to monitor all the ion states formed simultaneously and also to define a photoelectron ejection direction. Angular distributions were mapped out by rotating the polarization vectors of the exciting and ionizing laser beams together in essentially the same technique as that described by Leahy et al.[14]

Experimental

Para-difluorobenzene (Aldrich, 99%) was introduced at room temperature through a hypodermic needle into one end of a doubly mu-metal shielded drift tube. The effusive beam was photoionized with co-propagating laser beams (pump and probe) perpendicular to the axes of the drift tube and the hypodermic needle. A triple microchannel plate electron detector (Photek) was mounted at the other end of the drift tube to detect photoelectrons ejected along its axis. Precautions were taken to reduce electric fields to an absolute minimum in the drift tube by coating the inside of the drift tube. The operating pressure in the chamber was around 3×10^{-6} torr, thus providing a collision-free environment.

A 1 kHz titanium sapphire regenerative amplifier (Spectra-Physics, Spitfire) was configured for the chirped pulse amplification of picosecond pulses. The output was tripled to give ~ 1 ps pulses at 257 nm with pulse energies of ~ 20 μJ. The 257 nm beam was split into two parts one of which, acting as the probe, was sent down a computer controlled optical delay line. Each beam was passed through a computer controlled rotatable double Fresnel rhomb which enabled its polarization to be independently determined. Both pump and probe beams were loosely focused and had pulse energies of around 2-3 μJ in the interaction region, and beam diameters of around 100 μm as determined by a CCD camera. These conditions ensured that there was no saturation of either the excitation or the ionization step. The two beams were then passed through a masked chopper which alternately passed the pump beam, then the probe beam, then both beams, and was used to trigger the laser system. The flight times of photoelectrons were recorded with a time-to-digital converter (TDC, LeCroy 2277).

In the experimental runs ten polarization geometries were chosen corresponding to five photoelectron ejection directions; $\theta = 0°$, 22.5°, 45°, 67.5° and 90°, where θ is the angle between the polarization vector of the probe and the direction of photoelectron ejection. For each value of θ spectra were taken with the pump and probe polarizations parallel and perpendicular to each other, in other words to map out an angular distribution the two beam polarizations were rotated together either mutually parallel or mutually perpendicular. This experiment was repeated for six different pump-probe time delays (0, 20, 40, 60, 80 and 100 ps) as determined by the delay line.

Figure 1 shows a spectrum of photoelectron counts versus the internal energy of the paradifluorobenzene ion deduced from the time-of-flight spectrum. The four major ion vibrational peaks (3^1, $3^1 6^1$, $3^1 5^1$ and $3^1 5^2$) already assigned by Sekreta et al.[15] were fitted to accurately determined energies of these states from the ZEKE work of Reiser et al.[16]

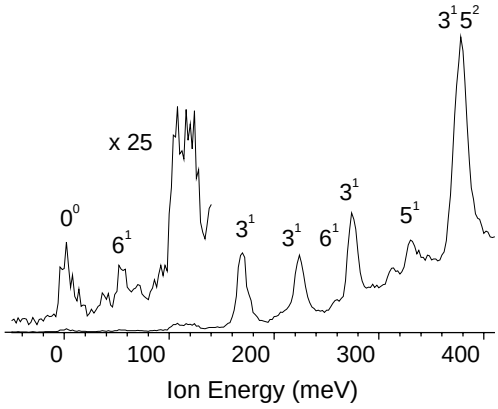

Figure 1. Photoelectron spectrum following excitation of $3^1 5^1$.

Analysis of data

The peaks in the photoelectron spectra (see Figure 1) were fitted to Lorentzian lineshapes, using a least squares fitting routine developed at the Rutherford Appleton Laboratory[17] which varied the positions, widths and heights of each peak and allowed for a rising baseline. The area of each Lorentzian is related to the number of photoelectron counts associated with one ion peak at one time delay and one polarization geometry. In order to determine the number of photoelectrons corresponding to excitation by the pump beam followed by ionization by the probe beam for the four chosen peaks the photoelectron spectra due to pump and probe beams alone were subtracted from the photoelectron spectrum due to both beams together. These subtracted data were then fitted to the function

$I(\theta,\phi) = \sum_L \beta_{L0} Y_{L0}(\theta,\phi)$ where $Y_{L0}(\theta,\phi)$ is a spherical harmonic with $M = 0$. β_{L0} values were determined from the experimental data by linear least square fitting using Single Value Decomposition as described by Press et al.[18)]

Discussion

Figure 2 shows PADs for the ion peak assigned to 3^1 for parallel pump and probe polarizations at six time delays. Data for other ion states and polarizations are presented in a forthcoming publication[19)].

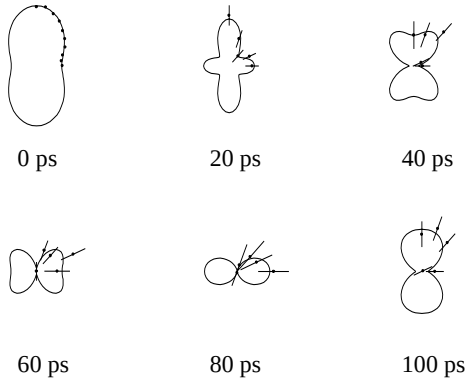

Figure 2. Photoelectron angular distributions as a function of time-delay.

PADs depend on molecular axis alignment and on photoionization dynamics.[4,20)] The photoionization dynamics do not depend on the time delay between pump and probe except in so far as they reflect the changing composition of the ionized rotational envelope in S_1 (providing no electronic changes occur, such as intersystem crossing). Therefore any changes in PADs are a direct probe of either changing rotational populations or changing molecular axis alignment, both of which indicate rotation-vibration coupling in the S_1 band excited. As can be seen from the polar plots in Figure 2 there are substantial changes in PADs as a function of time-delay which are well within error bars. The changes seen indicate that the PADs are very sensitive to intermediate alignment because, as mentioned above, the photoionization dynamics should be the same at each time delay. Rotational recurrences cannot explain the dramatic changes in PADs that are seen because the PADs change at times that are not predicted by rotational wavepacket evolution. Therefore we believe that the best explanation for the observed time-dependent behaviour of the observed PADs is rotationally mediated intramolecular vibrational energy redistribution (IVR).

Conclusion

We have demonstrated that picosecond time-resolved PADs can be used as a method of monitoring an evolving alignment in a polyatomic molecule. This in turn means that such measurements can probe the involvement of molecular rotation in IVR processes, providing that care is taken to predict the effect that the evolution of a pure rotational wavepacket will produce. Our results suggest that, in agreement with Nathanson and McClelland[21)], rotation has a role in mediating IVR in S_1 para-difluorobenzene. Further analysis to quantify this will be presented in a future publication.

Acknowledgements

We are very grateful to Nicholas Pedge for his assistance with this experiment. KLR would like to thank the EPSRC for an Advanced Fellowship.

References

1. A T Georges and P Lambropoulos
Phys. Rev. A, 18 , 1072, (1978).
2. M P Strand, J Hansen, R -L Chien and R S Berry
Chem. Phys. Lett., 59, 205, (1978).
3. J W Winniczek, R L Dubs, J R Appling, V McKoy and M G White, J. Chem. Phys., 90, 949, (1989).
4. D J Leahy, K L Reid and R N Zare
J. Phys. Chem., 95, 8154, (1991).
5. K L Reid, Chem. Phys. Lett., 215, 25, (1993).
6. K L Reid, S P Duxon and M Towrie
Chem. Phys. Lett., 228, 351, (1994).
7. T Noguchi, S Sato and Y Fujimara
Chem. Phys. Lett., 155, 177, (1989).
8. X Song, M Yang, E R Davidson and J P Reilly
J. Chem. Phys., 99, 3224, (1993).
9. X Zhang, J M Smith and J L Knee
J. Chem. Phys., 100, 2429, (1994).
10. V Blanchet and A Stolow
J. Chem. Phys., 108, 4371, (1998).
11. A T J B. Eppink and D.H. Parker
Rev. Sci. Instr., 68, 3477, (1997).
12. T Seideman, J. Chem. Phys., 107, 7859, (1997).
13. S C Althorpe and T Seideman
J. Chem. Phys., 110, 147, (1999).
14. D J Leahy, K L Reid and R N Zare
J. Chem. Phys., 95, 1757, (1991).
15. E Sekreta, K S Viswanathan and J P Reilly
J. Chem. Phys., 90, 5349, (1989).
16. G Reiser, D Rieger, T G Wright, K Müller-Dethlefs and E W Schlag, J. Phys. Chem., 97, 4335, (1993).
17. P Matousek, A W Parker and M Towrie
Raman analysis program, Rutherford Appleton Laboratory Report, RAL-95-028 (1995).
18. W H Press, S A Teukolsky, W T Vetterling and B P Flannery
Numerical Recipes in Fortran (Cambridge University Press, UK, 2nd Ed. 1994), p. 670.
19. K L Reid, T A Field, M Towrie and P Matousek
J. Chem. Phys., in press.
20. K L Reid, D J Leahy and R N Zare
J. Chem. Phys., 95, 1746, (1991).
21. G M Nathanson and G M McClelland
Chem. Phys. Lett., 114 441, (1985).

Ps-TR^3 Studies into Photoelectron Transfer Processes in Metallo-based Cyclophanes, Catenanes and Ruthenium Intercalates

A C Benniston

Chemistry Department, Joseph Black Building, University of Glasgow, Glasgow, G12 8QQ

P Matousek, A W Parker

Central Laser Facility, CLRC Rutherford Appleton Laboratory, Chilton, Didcot, Oxon, OX11 0QX, UK

Main contact email address: *andrewb@chem.gla.ac.uk*

Introduction

Over the past years the advances in laser spectroscopy have resulted in the development of improved time-resolved tools for probing ultra-fast photochemical processes. Picosecond time-resolved resonance Raman spectroscopy (TR^3) is one such method which permits the probing of structural alterations in molecular assemblies over ultra-fast timescales[1)]. Figure 1 illustrates a selection of molecular systems which we have been studying using picosecond TR^3 spectroscopy, and more recently the new Kerr-gated (K-TR^3) method[2)]. In all the cases the ruthenium(II) polypyridyl moiety is the photoactive centre able to relay an electron to the electron acceptor site(s) in the molecular assemblies. The systems 1-4 were studied primarily as models of the photosynthetic reaction centre, and our interest is in using this series of compounds to prove whether directional electron transfer is possible[3)].

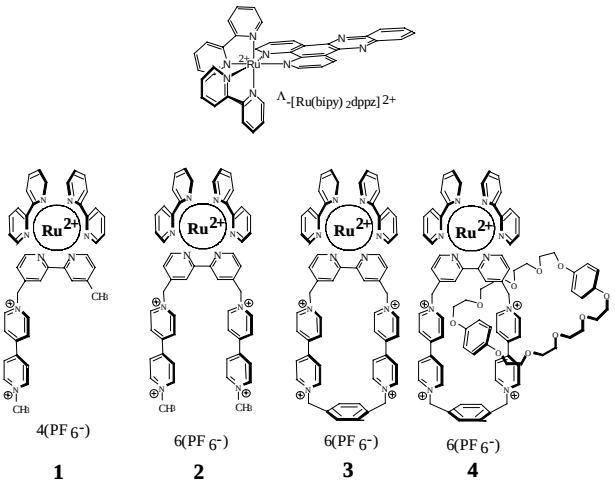

Figure 1. Molecular systems studied.

The elucidation of the excited-state structure of Λ-[Ru(bipy)$_2$dppz](BF$_4$)$_2$ was undertaken as the first step into fully understanding the mechanism of the on/off luminescence which the complex displays in the presence and absence of DNA. This part of the work is discussed in detail in the Results section.

Kerr-gated Picosecond Time-Resolved Resonance Raman

K-TR^3 represents a substantial technological advancement in the measurement of resonance Raman spectra from samples that strongly fluoresce. Detailed description of the setup is given elsewhere in this Report. In brief, the Kerr-gate comprises two crossed polarizers and a Kerr medium activated to propagate the light of interest by and intense linearly polarized laser pulse (gating pulse). The relative angle of polarization between the two beams is 45^o. Interaction of the gating pulse with the Kerr medium induces a transient anisotropy through a non-linear optical effect. This transforms the polarization of the light (fluorescence + Raman) propagating through the medium from linear to elliptical. The propagation length through the Kerr medium can be chosen so that polarization of the Raman light is transformed back to being linearly polarized but rotated by 90^o with respect to its original polarization direction. In this instance, the Kerr medium acts as a λ/2 waveplate and the light is transmitted through a cross polarizer onto the spectrometer slit. With this set up the fluorescence emitted after the gate is closed becomes blocked by the polarizers. For the first time (see later) we have applied this Kerr gating technique to also break the degeneracy of the single colour set-up by gating out the probe Raman spectrum only, and blocking the TR^3 spectrum from the pump beam.

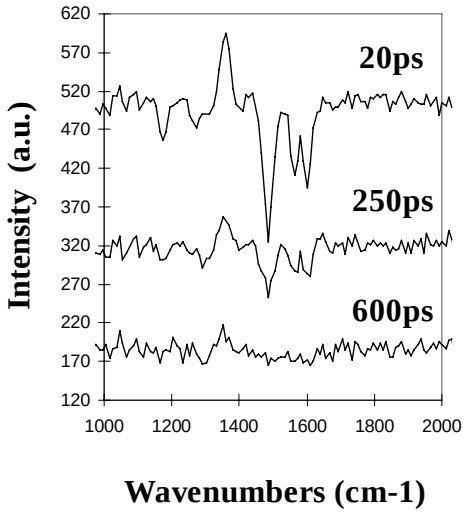

Figure 2. Transient K-TR^3 spectra obtained following photoexcitation of Λ-[Ru(bipy)$_2$dppz](BF$_4$)$_2$ in water.

Results

Depicted in Figure 2 are the transient K-TR^3 Raman bands observed at three different time delays following optical excitation (λ_{ex} = 415 nm, λ_{prob} = 415 nm) of Λ-[Ru(bipy)$_2$dppz](BF$_4$)$_2$ with a 1 ps (fwhm) laser pulse. Under these conditions the pump photons excite exclusively the MLCT band whilst the probe pulse interrogates the excited-state transient. There are two main bleach regions (1150 - 1300 cm^{-1} and 1480 - 1600 cm^{-1}) which are attributed to depletion of ground-state resonance Raman bands of the complex. The additional peak at 1361 cm^{-1} is assigned to resonance enhancement of a band solely associated with the excited state. The fully corrected spectrum when ground-state bleaching has been taken into account displays three main peaks at 1361 cm^{-1}, 1438 cm^{-1} and 1572 cm^{-1}, which are the resonance Raman bands of the excited state. Identical experiments were also performed in the less polar solvent acetonitrile. The corrected excited-state spectrum is depicted in Figure 3. The spectrum is somewhat different from that obtained in water with one main band at 1390 cm^{-1}. These results unequivocally show that the excited-state structure of the complex is different in the two solvents. Furthermore, we have now been able to rationalise the non-emissive behaviour of Λ-[Ru(bipy)$_2$dppz](BF$_4$)$_2$ by invoking a hybrid excited-state model in which the solvent

influences where the transferred electron is located within the dppz ligand[4].

Overall, the technique of time-resolved resonance Raman spectroscopy has pushed forward our understanding of photo-processes in exotic complexes. The newly developed Kerr gate has allowed TR^3 spectra to be obtained from strongly fluorescent samples. However, the work highlighted the need to continue to develop this unique apparatus to enable faster accumulation times and extend the technique to investigating transients with weaker absorption cross sections ($\varepsilon \leq 5x10^3$). The planned improvements are expected to also enhance spectral resolution and signal-to-noise profiles enough to observe subtle changes in resonance Raman bands induced by differences of the environment of the electron acceptor and begin to address our programme on directional electron transfer process.

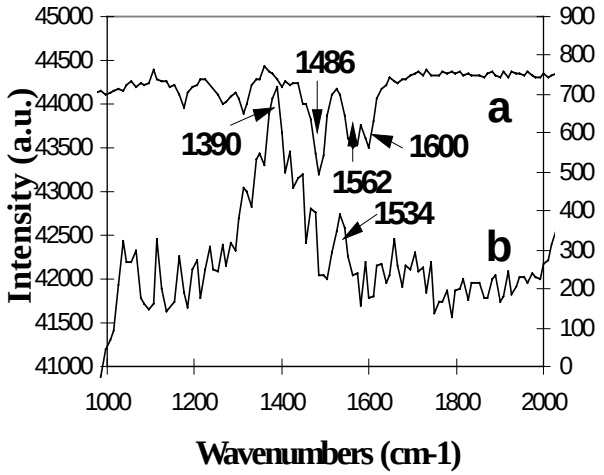

Figure 3. (a) Raw and (b) corrected transient K-TR^3 spectra following photoexcitation of Λ-$[Ru(bipy)_2dppz](BF_4)_2$ in acetonitrile

Acknowledgements

This work was supported by the University of Glasgow and the EPSRC who funded access to the Central Laser Facility at RAL.

References

1. M Towrie, A W Parker, W Shaikh and P Matousek Meas. Sci. Technol., 9 , 816, (1998).
2. P Matousek, M Towrie, A Stanley and A W Parker Applied Spectroscopy 1999, in press.
3. A C Benniston, P R Mackie, A Harriman, Angew. Chem. Int. Ed., 39 , 354, (1998).
4. A C Benniston, P Matousek, A W Parker,J. Am. Chem. Soc., 1999, submitted.

Time-Resolved Fluorescence of Cyano-Terphenyl in Solution

W T Toner

Department of Physics, Clarendon Laboratory, Parks Road, Oxford OX1 3PU

W M Kwok, C Ma, D Phillips

Department of Chemistry, Imperial College, Prince Consort Road, London

P Matousek, M Towrie, A W Parker

Central Laser Facility, CLRC Rutherford Appleton Laboratory, Chilton, Didcot, Oxon, OX11 0QX, UK

Main contact email address: *W.T.Toner@rl.ac.uk*

Time resolved fluorescence spectra of cyano-terphenyl (CTP) have been obtained as part of a programme to identify and quantify the effects of relaxation on fast reactions initiated by photo-excitation, and complement our earlier work on this subject[1]. The Kerr gate system[2] was modified to reduce dispersion, enhance time-resolution and extend the spectral range to the UV. The first collection lens was replaced by a mirror, and benzene was used instead of CS_2 as the Kerr medium, in a 1 mm rather than a 2 mm cell. The gate was formed by an UV sheet polariser, the Kerr cell, and a crossed Glan Taylor polariser. "Magic angle" conditions were used. The instrument response time was ~ 3 ps (rise from 10% to 90%). A 1 mm cell with copper sulphate solution in water was used in front of the spectrometer to block the residual gating pulse. Figure 1 shows data for CTP in cyclohexane, 1-octanol and acetonitrile, uncorrected for substantial wavelength dependence of sensitivity. Preliminary inspection indicates that there are no large time-dependent spectral distortions.

Qualitative features of the spectra clearly indicate a progressive change with solvent properties in the balance between solvation due to the dipole moment of charge-separated CTP(S1) and that due to molecular polarisability. Detailed analysis will be needed to quantify the effects, and the outline given here is provisional. The cyclohexane spectra are characteristic of solvation dominated by polarisability differences, which has much longer time-scales than polar solvation[3]. In these cases, the bandshape of each vibronic component has a sharp edge on one side and an approximately exponential tail on the other. The data suggest that S1 is less polarisable than S0, resulting in a red tail, and in slow frequency shifts to the blue during relaxation. The slowness may owe something to competition with polar effects. In contrast, all the acetonitrile spectra are characteristic of the solvation of a polar molecule, which produces Gaussian line broadening and a related Stokes shift that is too fast to resolve. The observed slow shift to the blue is attributed to residual polarisability. The octanol spectra have mixture of the two characteristics. Polar solvation behaviour is seen at late times, but the Stokes shift is smaller than for acetonitrile, indicating a weaker CTP(S1) dipole - solvent interaction. The early time spectra have significant structure in the region around 28000 cm^{-1}, suggesting competition between polar and polarisability effects up to ~ 20 ps. This is interpreted as due to incomplete charge separation at early times: the weaker dipole interaction is partly balanced by polarisability change, lengthening a Marcus-like time-scale for full charge separation. This competition also accounts for the long time-scale of the polar solvation Stokes shift.

The interpretation of the early time intensity excess at frequencies < 25000 cm^{-1}, seen in the cyclohexane and Oligophenyl spectra, is complicated. We have previously observed that cooling differs from relaxation in quaterphenyl and in stilbene[1]. Vibronic components from thermally populated modes whose S0 and S1 frequencies are different can produce effects that are indistinguishable from polarisability change. Moreover, possible dynamic changes in molecular parameters (polarisability or frequency ratios) alter the band-shape in the same way as changes in energy. However, the relatively small excess intensity in the region above 30000 cm^{-1} (28000 cm^{-1} in acetonitrile), seen in all spectra at the earliest times, is thought likely to be due to IVR on the <<1 ps time-scale, with the effect scaled down by the ratio of τ_{IVR} to the instrument time resolution.

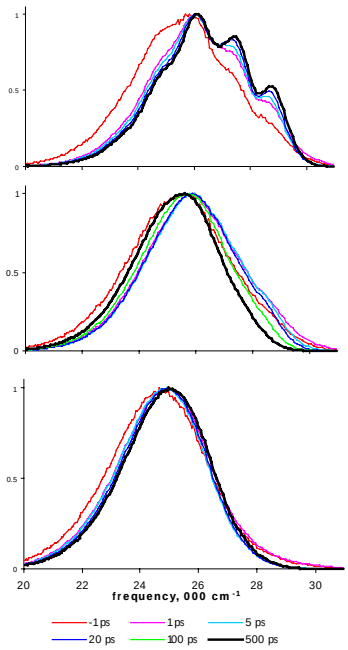

Figure 1. Time-resolved fluorescence spectra of CTP in cyclohexane (top), 1-octanol (middle) and acetonitrile (bottom). Times do not indicate true delay from excitation, due to pulse temporal profile effects.

References

1. R E Hester *et al.*
Chem Phys Lett, 208 471 (1993).
P Matousek *et al.*,
J Chem Phys, 107 9807 (1998).
G D Scholes *et al*
J Phys Chem. A, 102 1431 (1998).

2. P Matousek *et al.*,
Development Section, this Report (1999).

3. B D Bursulaya *et al.*
J Phys Chem. 99 10069 (1995).

Photoluminescence of 5-Cyanoindole Electropolymer Films

P Jennings, A C Jones, A R Mount

Department of Chemistry, The University of Edinburgh, West Mains Road, Edinburgh, EH9 3JJ.

Main contact email address: *a.c.jones@ed.ac.uk*

Introduction

Electropolymerised 5-substituted indoles are new examples of photoluminescent conjugated polymer systems. The occurrence of efficient luminescence in conjugated polymers has become of technological interest since the discovery that electro-luminescence could be produced from poly(phenylene vinylene) in thin-film light-emitting diode structures[1)] Electroluminescent polymer films have potential applications in the development of large-area light-emitting displays.

The aim of this research project was to carry out a detailed investigation of the photophysical properties of electro-polymerised 5-substituted indoles, with particular emphasis on the factors influencing their photoluminescence efficiency. The electropolymerisation of 5-substituted indoles proceeds via a trimeric intermediate and the polymer consists of linked trimer units [2,4)]. Previously, we have reported on the fluorescence properties of the polymers and their constituent trimers in solution phase[5,6)] and of intact polymer films[6)]. In this report we focus on the photoluminescence properties of electro-polymerised 5-cyanoindole films.

As discussed previously, the photoluminescence efficiency of 5-cyanoindole polymer films shows a dramatic dependence on redox state[6)]. The films are highly fluorescent in the reduced (neutral) state but non-fluorescent in the oxidised (cationic) state. The fluorescence of the non-emitting oxidised film is restored when the film is dissolved, indicating that it is the morphology of the film, not the redox state of the polymer chains, that is responsible for the quenching of fluorescence.

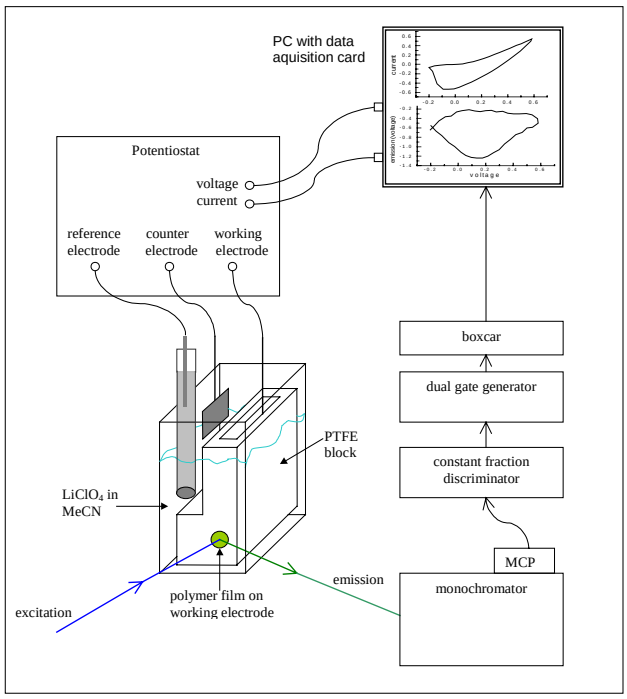

Figure 1. Experimental arrangement for in-situ cyclic voltammetry/fluorescence experiments. The dimensions of the fused silica cuvette containing the electrochemical cell are 20mm x 40mm x 40mm.

To gain a better understanding of the processes occurring when the polymer film is cycled between the reduced and the oxidised states, an electrochemical cell was constructed in a fused silica cuvette to carry out in-situ fluorescence measurements at the working electrode. The experimental arrangement is illustrated in Figure 1. This enabled simultaneous recording of the cyclic voltammogram and the variation in fluorescence intensity.

Results and Discussion

A series of 5-cyanoindole polymer films, produced under a range of electropolymerisation conditions to give different proportions of polymer and trimer, were studied. The emission intensity was measured as a function of voltage, at sweep rates from $2mVs^{-1}$ to $200mVs^{-1}$, as the film was cycled between reduced and oxidised states. Electrochemical data and fluorescence data were collected simultaneously.

The results for a film containing a low proportion of polymer, cycled at a low sweep rate are shown in Figure 2. These

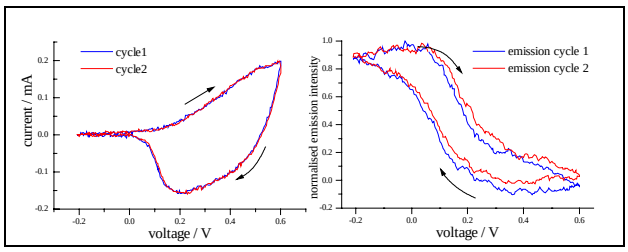

Figure 2. Cyclic voltammogram and "fluorescogram" for a 5-cyanoindole film (low polymer content), for two cycles at a sweep rate of 20 mVs^{-1}. The arrows indicate the direction of the cycle.

illustrate both the electrochemical reversibility of the redox cycle and the corresponding reversible change in fluorescence intensity. Apart from a very small difference in the emission intensity for each cycle, they are almost identical. This is still the case even after multiple cycles. The longest period for which a film was examined was 5 hours of repeated cycling, over which time there was no apparent drop in the emission intensity. The decrease in emission intensity as the film is oxidised and the subsequent increase as it is reduced can be seen clearly. In order to relate the emission intensity to the extent of oxidation of the film, the charge passed was calculated. In Figure 3, plots of charge against voltage and emission intensity against charge are shown for the first cycle.

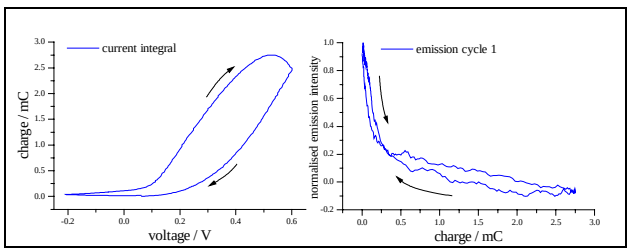

Figure 3. Plots of charge against voltage and emission intensity against charge for a 5-cyanoindole film (low polymer content) with a sweep rate of 20 mVs^{-1}. The arrows indicate the direction of the cycle.

From the plot of emission against charge, it can be seen that the maximum emission intensity is shown by the film in its fully reduced state. As the film is oxidised the emission intensity decreases, falling to zero in the fully oxidised state. The majority loss of fluorescence intensity occurs after only

approximately 10 % of the film has been oxidised, suggesting that oxidation of only a small fraction of the film opens an efficient non-radiative channel. When the sweep is reversed and the film reduced, the fluorescence intensity is restored, with a steep increase in intensity once approximately 90% of the film has been re-reduced, closing the efficient non-radiative channel. The emission intensity shows a reversible dependence on the oxidation state of the film and, at this sweep rate, the relationship between emission intensity and charge is very similar for the forward (oxidation) and reverse (reduction) sweeps. Upon oxidation, anions move into the film to balance the charge (hence doping the film) and upon reduction these anions are expelled to give an undoped film. Previous studies[7] have shown that in the oxidised (doped) state, the films are more conducting than in the reduced (undoped) state. It is possible that the efficient non-radiative mechanism, present in the oxidised films, is associated with the increased conductivity, providing an efficient channel for electron transfer.

At slow sweep rates, the change in emission intensity is very similar on forward and reverse sweeps; however, as the sweep rate increases, a significant difference develops. This is seen most clearly on the plots of emission intensity against charge. As the sweep rate increases, the initial steep drop in intensity, as the fully reduced film is oxidised, becomes less evident. The behaviour of the same film at the highest sweep rate, 200mVs^{-1} is shown in Figure 4. A gradual decline in fluorescence intensity is seen as the oxidation proceeds. On reversal

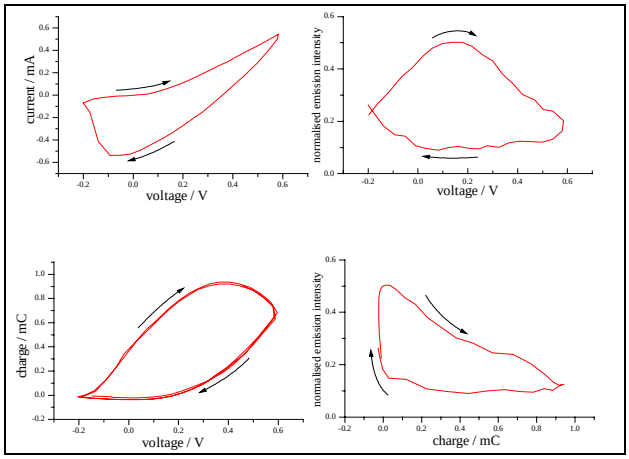

Figure 4. Plots of current, current integral and emission intensity against voltage, and emission intensity against current integral for a 5-cyanoindole film (low polymer content) with a sweep rate of 200 mV/s. The arrows indicate the direction of the cycle.

of the sweep, the intensity continues to decrease initially and does not start to increase until late in the reduction sweep. The intensity recovers at the greatest rate at the end of the reduction sweep and as the sweep is reversed. This recovery of intensity occurs over part of the cyclic voltammogram where very little charge is passed, and is seen on the plot of intensity against charge as a very sharp rise. Thus, there is a time-lag in the response of the emission to the change in redox state of the film. This hysteresis results in a separation (along the intensity axis) of the fluorescence-charge response curves for the forward and reverse sweeps; the greater the hysteresis the greater the separation. The hysteresis increases as the sweep rate increases. The observation of hysteresis implies that the dependence of fluorescence intensity on the redox state of the film is not simply a function of the redox charge, but is due to a change in the structure of the film, associated with the change in redox state. At high sweep rates, the rate of structural rearrangement is slower than the rate of oxidation (or reduction) of the film, leading to the hysteresis in fluorescence response. As the sweep rate increases the charge passed decreases and the oxidation is incomplete. Consequently, as the sweep rate increases, the difference in emission intensity between the reduced and oxidised states decreases.

Increasing the polymer content of the film has a significant effect on the response of emission intensity to change in redox state. Whereas there is negligible hysteresis apparent in low-polymer films at a sweep rate of 20mVs^{-1} (Figure 2), there is a considerable hysteresis in the fluorescence response of high-polymer films at this sweep rate. For high-polymer films, the hysteresis only becomes insignificant at sweep rates of 5 mVs^{-1} and below. These results imply that films with a higher polymer content have a greater barrier to structural re-organisation, and hence change in emission intensity, than films with a low polymer (high trimer) content. This is consistent with the intuitive expectation that the greater the polymer content of the film, the less flexible will be the structure and the greater the resistance to re-organisation.

Conclusion

A new, in-situ, technique has been developed which allows the photoluminescence of intact polymer films in the working electrochemical cell to be examined and the emission properties to be related to electrochemical observations. The dependence of fluorescence intensity on redox state was investigated for films of 5-cyanoindole polymer as they were cycled between the reduced (fluorescent) and oxidised (non-fluorescent) states. It was found that at faster sweep rates there is a time-lag in the response of the emission to the change of redox state of the film, observed as hysteresis in the fluorescence-charge response curves. This implies that the variation in emission intensity with redox state is not simply a function of the redox charge, but is associated with a change in the structure of the film. Films with a higher polymer content display a greater hysteresis, implying that the presence of extended polymer chains are a barrier to structural re-organisation of the film.

Acknowledgements

This work was funded by EPSRC grant GR/K12625.

References

1. J H Burroughs, D D C Bradley, A R Brown, R N Marks, K Mackay, R H Friend, P L Burns and A B Holmes Nature, 347, 539, (1990).
2. J G Mackintosh and A R Mount, J. Chem. Soc. Faraday Trans., 90, 1121, (1994).
3. J G Mackintosh, C R Redpath, A C Jones, P R R Langridge-Smith, D Reed and A R Mount, J. Electroanal Chem., 375, 163, (1994).
4. P Jennings, A C Jones, A R Mount and A D Thomson, J. Chem. Soc. Faraday Trans., 93, 3791, (1997).
5. P Jennings, A C Jones and A R Mount, J. Chem. Soc. Faraday Trans., 94, 3619, (1998).
6. P Jennings, A C Jones and A R Mount, CLF Annual Report 1997/98.
7. M Robertson, *PhD Thesis*, The University of Edinburgh 1998.

Study of Amphiphilic Polymers at Oil/Water Interfaces using Vibrational Sum-frequency Spectroscopy

J Bowers, A Zarbakhsh

Department of Chemistry, University of Durham

J R P Webster

ISIS Facility, CLRC Rutherford Appleton Laboratory, Chilton, Didcot, Oxon, OX11 0QX, UK

M Towrie, I P Clark

Central Laser Facility, CLRC Rutherford Appleton Laboratory, Chilton, Didcot, Oxon, OX11 0QX, UK

Main contact email address: *a.zarbakhsh@durham.ac.uk*

Sum frequency spectroscopy (SFS) is a non-linear, surface-specific technique that measures the vibrational spectrum of molecules assembled at a surface or interface [1]. In the experiment, two pulsed laser beams (one visible, the other infrared) are overlapped on the surface and the intensity of the generated sum-frequency output is measured as a function of the incident infrared frequency. By polarisation selection of the three beams, molecular orientation and bonding processes at the interface can be inferred. SFS has been applied at solid/liquid [1], air/liquid [2], and liquid/liquid [3] interfaces.

Since surfactants and polymers appear in a wide range of domestic and industrial applications we sought to make a comparative study of the adsorption of polymers with different molecular architecture at an oil/water interface using SFS. The method exploited thus far to study liquid/liquid interfaces limits the choice of oil. In order to develop a new method of studying liquid/liquid interfaces utilising thin, stable oil films (based on a method we have established for complementary neutron reflectivity studies), we have used the LSF's lasers.

In the experiment conducted in the Nanosecond Laboratory, the visible beam (1-2 mJ, Nd:YAG 532nm) was overlapped with a counter-propagating IR beam (0.5 mJ, generated by mixing output from a dye laser, ~800nm, with the Nd:YAG 1064 nm fundamental in a $LiNbO_3$ crystal in an Inrad Difference Frequency Unit). The sum-frequency (SF) radiation (~460 nm) was gathered from the surface and focussed onto the chip of a Princeton Instruments CCD camera. Due to the extremely low intensity of the SF radiation, good imaging of the SF beam is an essential feature of the experiment. SF radiation from a GaAs (110) crystal surface was used to align the beams and detection system.

Standard systems (a self-assembled octadecyl-mercaptan monolayer on gold [4], an insoluble decan-1-ol monolayer on water [2], and a soluble sodium dodecyl-sulphate monolayer on water [5]) were used to test the set-up. The spectra given in the literature were obtained. We were unable to extend the experiments to the liquid/liquid interface due to some general technical problems which we were unable to overcome in the time-frame of the experiment. Most notably we often encountered a signal at the same frequency and level of intensity as the SF radiation. We believe that this could be a result of ablation of dust particles in the intense visible beam we were using to compensate for the relatively weak IR beam.

However, from the lessons learned in this experiment, suggestions for improving the experimental set-up and sample environment can readily be made. Principally, it is desirable to be able to increase the IR intensity and lower the visible intensity to achieve a good SF signal without encountering the spurious signal (without taking it to the other extreme whereby sample heating from the IR occurs). This aspect of the experiment would certainly benefit from the potential development of an SFS set-up in the Ultrafast Laboratory. Conservative estimates reveal that the SF signal intensity could be increased by a factor of 100 without incurring practical problems. Furthermore, this offers the potential of measuring a broad-band spectrum rather than measuring each point individually. In terms of sample environment, it would be favourable to use a thin (~μm thick) oil layer on, for example, a water-free quartz support. This offers two advantages: first, absorption of the radiation is reduced, and secondly, deuterated oil can be readily and inexpensively used. This latter point potentially allows the study of C-H stretching at the oil/water interface in addition to the O-H stretching.

We would like to thank Colin Bain for useful discussions.

References

1. C D Bain
J. Chem. Soc: Faraday Trans. 1995, 91, 1281.

2. B D Casson, R Braun, C D Bain
Faraday Disc. 1996, 104, 209.

3. D.E. Gragson, G.L. Richmond
J. Phys. Chem. 1998, B102, 569.

4. T Hui Ong , P B Davies, C D Bain
Langmuir 1993, 9, 1836.

5. D E Gragson, B M McCarty, G L Richmond
J. Phys. Chem 1996, 100, 14272.

Nanosecond Time-Resolved Resonance Raman Studies (TR^3) on Solvent Effects on Organometallic Charge Transfer Excited States at both Room and Cryogenic Temperatures

X Z Sun, S M Nikiforov, M W George

School of Chemistry, University of Nottingham, University Park, Nottingham, NG7 2RD

I P Clark

Central Laser Facility, CLRC Rutherford Appleton Laboratory, Chilton, Didcot, Oxon, OX11 0QX, UK

Main contact email address: *mike.george@nottingham.ac.uk*

Introduction

Electron transfer is a fundamental process important for a wide range of biological and chemical processes. Time-resolved infrared spectroscopy (TRIR), a combination of UV flash photolysis with fast infrared detection, is particularly useful in studying excited states of transition metals containing moieties such as CO or CN. These groups have very high IR extinction coefficients and act as probes of the electron distribution in the excited state.[1)] The lowest electronic excited state of the tricarbonyl, $ClRe(CO)_3(bpy)$, is an MLCT state, involving charge-transfer from the central Re atom to the bpy ligand. We have used TRIR to show how IR can probe the charge-transfer transition, since it reduces the Re-CO backbonding and hence shifts the ν(CO) to higher frequency.[2)] On lowering the temperature of solutions of coordination compounds in glass-forming materials through the glass transition temperature, there is a sharp variation in some photophysical properties, explained by the change in viscosity. In particular, the emission for long lived charge-transfer states shifts to the blue (*luminescence rigidochromism*).[3)] We have studied the C-O vibrations of the MLCT excited state of $ClRe(CO)_3(bpy)$ in both solution and rigid glass phases.[4)] A temperature dependence of the position of the excited state ν(CO) was observed; this *new* phenomenon was referred to as *infrared rigidochromism*. In fluid solution the average shift in ν(CO), Δν(CO), upon MLCT excitation for $ClRe(CO)_3(bpy)$ is 58 cm^{-1}, while in a rigid glass Δν (CO) is only 38 cm^{-1}, Figure 1. This observation can be explained by the inability of the rigid solvent to assist in the charge-transfer process. In a fluid environment, the solvent molecules are free to rotate and can reorientate themselves to accommodate the charge separation created upon MLCT excitation.

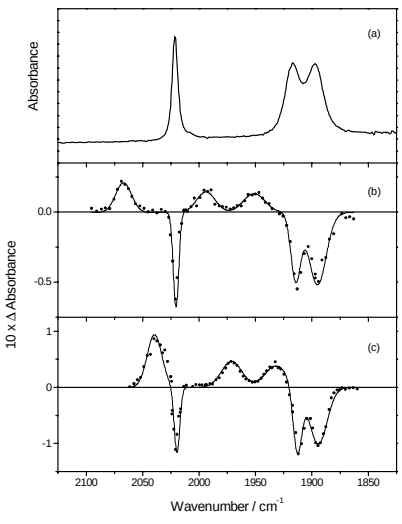

Figure 1. (a) Room temperature FTIR spectrum of $ClRe(CO)_3(bpy)$ (1×10^{-3} M) in n-PrCN/n-EtCN (5:4, v:v). (b) and (c) show TRIR spectra of the same solution at 135 and 77 K respectively. Both TRIR spectra were recorded at ca 100 ns after photolysis (355 nm).

Here we have used Time-Resolved Resonance Raman Spectroscopy (TR^3) at the Laser *for* Science Facility to probe the excited state ν(C-O), ν(C-N) and ν(C=C) in order to investigate the extent of charge-transfer above and below the glass transition temperature.

Experimental: Construction of the TR^3 cold cell.

A variable temperature cold cell (for solid matrices) and low temperature jet for Raman spectroscopy were successfully designed, produced and tested. The cold cell consisted of a hollow copper block with quartz windows in the base and in one side (allowing both conventional 90° and back scattering geometries to be used for Raman spectroscopy). A 'U'-shaped copper tube, through which the coolant - liquid N_2 - was passed, was inserted through the lid of the block. The samples, contained in quartz tubes, were held in a snug fitting copper tube that was joined to this tube. To prevent condensation forming on the cell windows the inside of the cell was evacuated.

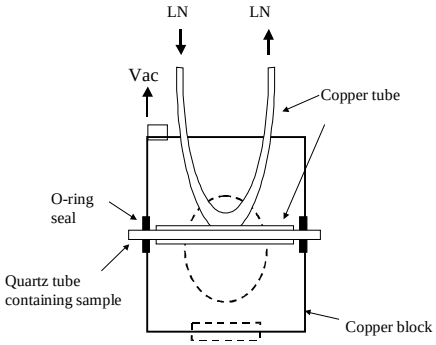

Figure 2. Cross-section through the copper block, showing the cell used to collect data. Dashed lines indicate the location of the quartz windows.

The low temperature jet consisted of a length (30-50 cm) of 1/16" stainless steel tubing coiled and enclosed in a metal box, encased in an insulating polystyrene layer. Using a Micro-pump the sample is flowed through the coil to the jet which is enclosed in an open-ended quartz cell. Temperature control is achieved by pulsing liquid nitrogen, using a solenoid valve on the liquid outlet of a 50 litre dewar, into the metal box. The flow of the coolant is regulated using an in-line type-K thermocouple positioned immediately before the jet. By keeping the distance between the cooler and the jet to a minimum (ca 0.5 m) a constant temperature of 223 K was achieved while flowing the methanol solution.

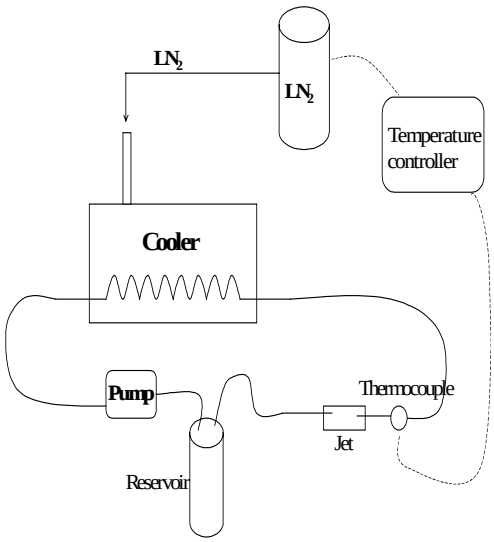

Figure 3. Schematic showing the low temperature jet and cooling system.

Results and Discussion

Figure 4 shows TR^3 spectra of $ClRe(CO)_3(bpy)$ in PrCN/EtCN (5:4, v:v) recorded during the laser pulse (10 ns) using 355 nm (pump and probe) at 298K and ca 140 K (10 K below the glass-to-fluid transition of the solvent mixture). Since the MLCT transition is directed towards the bpy ligand one would expect the Raman peaks corresponding to the bpy vibrations to show a similar temperature dependence to the ν(CO) bands observed in the TRIR experiments. The TR^3 spectra obtained at 298 K and 140 K do appear to be different, Figure 3. However, the spectrum obtained at 298 K is almost purely MLCT excited with very little contribution due to the ground state bands. The spectrum obtained at 140 K has a large contribution from ground state absorptions. We find that there is no significant shift in the MLCT excited state Raman bands of $ClRe(CO)_3(bpy)$ in PrCN/EtCN upon glass formation.

It was necessary to ensure that the heat deposited in the sample by the 355 nm YAG beam was not melting the bulk of the glass and allowing the solvent molecules to rotate and therefore leading to a "fluid-like" spectrum at both "low" and "high" temperatures. The repetition rate of the YAG laser was reduced and the TR^3 spectrum of $ClRe(CO)_3(bpy)$ in PrCN/EtCN was recorded. Again we found no significant shift of the MLCT Raman bands of $ClRe(CO)_3(bpy)$ upon glass formation. The results obtained from the TR^3 experiments appear to contradict the TRIR data in that there is no rigidochromism effect on the Raman bands. However we cannot completely eliminate the possibility that the intense laser beam melts the glass locally.

There is clearly more to learn about solvent effects on charge transfer and time-resolved vibrational spectroscopy will prove increasingly useful for this purpose. Further work is in progress to understand the rigidochromic effect on vibrational spectra of $ClRe(CO)_3(bpy)$ in PrCN/EtCN.

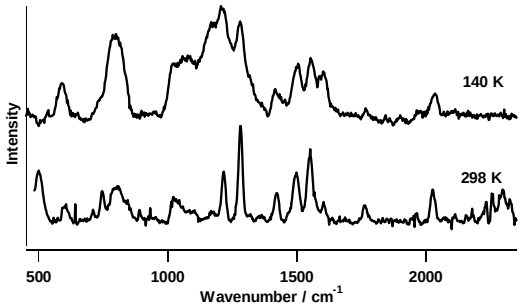

Figure 4. TR^3 spectrum of $ClRe(CO)_3(bpy)$ in PrCN/EtCN (5:4, v:v) recorded using 355 nm (pump and probe) at 298K and ca 140 K

Acknowledgements

We would like to thank Drs A.W. Parker, M. Towrie and P. Matousek for helpful discussions. We thank the Royal Society for funding (SMN visit).

References

1. M W George, M Poliakoff and J J Turner, The Analyst 119, 551, (1994).
2. M W George and J J Turner, Coord Chem. Rev.177, 201, (1998).
3. M S Wrighton and D L Morse J. Am. Chem. Soc., 96, 998, (1974).
4. I P Clark, M W.George, F P A Johnson and J J Turner Chem. Commun., 1587, (1996).

Nanosecond Step-scan FTIR Spectroscopy in Conventional and Supercritical Fluids

X Z Sun, S M Nikiforov, M W George

School of Chemistry, University of Nottingham, University Park, Nottingham, NG7 2RD

Main contact email address: *mike.george@nottingham.ac.uk*

Introduction

Time-resolved IR spectroscopy (TRIR) is a technique for probing the rate and mechanism of photochemical reactions. It involves the use of a pulsed UV/visible laser to initiate the reaction, and fast IR detection to monitor the generation of short-lived intermediates.[1)] The technique is becoming widespread and has already made a major impact on the study of organic and organometallic reactions both in the gas phase and in solution. Traditionally the TRIR apparatus at Nottingham has consisted of an IR diode laser which is tuned to a particular IR frequency and is used to monitor changes in IR absorption of a reaction solution following a UV laser pulse. The IR laser is then re-tuned to another frequency and the process is repeated. Thus IR spectra are built up *point-by-point* by plotting change in absorbance versus wavenumber. The relatively narrow line-widths of absorptions make it possible to monitor several key species in solution at the same time; destruction of reactants and formation of excited states, intermediates and products can all be followed. Our current *point-by-point* laser-based approach to TRIR limits the IR range that can be studied due to the long acquisition time required for a complete spectrum (indeed, recording a 300 cm^{-1} spectrum is a whole day's work). However, many problems can only be solved by obtaining data over a much wider IR range.

Step-scan FTIR spectroscopy offers a very attractive approach to obtain fast time-resolved IR measurements since this technique covers the entire mid-IR region allowing simultaneous measurement at all frequencies maintaining the high throughput and multiplex advantage of FTIR. The time-resolved *step-scan* FTIR technique involves the moveable mirror of the interferometer being displaced in a step-wise manner. At each mirror position, the time-dependent change in IR intensity following excitation is measured producing time-dependant interferograms. Fourier transformation of an interferogram at a particular time delay following excitation of the reactions yields the spectral intensity changes at that particular time slice and this can be easily converted to the corresponding absorption spectra. Repeating this process at a variety of time delays following excitation results in a series of time-resolved spectra. Kinetic traces can be obtained by plotting the change in absorbance at any frequency as a function of time. However the acquisition of time-resolved step-scan FTIR data has required a large amount of signal averaging (up to weeks) to improve signal-to-noise. This is due in part to imprecision in stopping the moving mirror. Consequently time-resolved IR investigations have been largely restricted to cyclic or photoreversible reactions such as bacteriorhodopsin, halorhodopsin, photosynthetic reaction center, myoglobin and hemoglobin.[2)] Here we have used a combination of *new* interferometer design, with increased precision in mirror position, and a nanosecond Nd:YAG laser (Laser *for* Science Facility) to construct a *new* nanosecond *step-scan* time-resolved IR spectrometer.[3] Our objective is to construct a time-resolved *Step-scan* spectrometer that can obtain ns-TRIR spectra without the need for extensive signal averaging, thus opening up this technique to study chemical reactions rather than photo-reversible systems.

Experimental Set-up

Step-scan FTIR experiments were conducted using a combination of a Nicolet Magna 860 Interferometer and a Nd:YAG laser (Spectron SL805G) from the laser loan pool, Figure 1. Synchronisation of the Nd:YAG laser with data collection was achieved using a pulse generator (Stanford DG535).

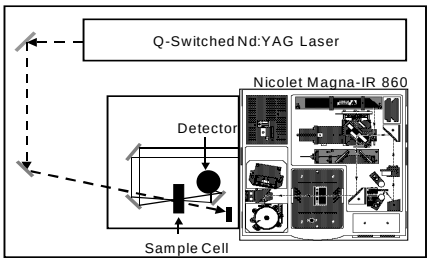

Figure 1. Experimental set-up for step-scan TRIR experiments.

The interferometer is equipped with both an internal 100 kHz 16-bit digitiser and an external 100 MHz 12-bit digitiser. In these experiments two different photovoltaic MCT detectors were used. A 0.5 mm detector with a 50 MHz preamplifier was used for measurements < 50 ns and a 1.0 mm detector with a 20 MHz preamplifier was used for measurements > 50 ns. These detectors have both AC and DC outputs and both outputs are digitized simultaneously to ensure proper phase matching. Single sided interferograms were obtained using only one laser pulse at each mirror position.

Results and Discussion

We have recently shown that the combination of TRIR and super-critical fluids allows the detection of organometallic noble gas complexes in solution at room temperature. $M(CO)_5(Xe)$ and $M(CO)_5(Kr)$ (M = Cr, Mo and W) were generated by flash photolysis of $M(CO)_6$ in supercritical Xe (scXe) or Kr (scKr) solution.[4)] We will use the formation of $W(CO)_5(Xe)$ in scXe as a diagnostic of our new instrument. Figure 2 shows the step-scan FTIR spectrum following irradiation of $W(CO)_6$ in scXe (3100 psi) in the presence of CO (30 psi).

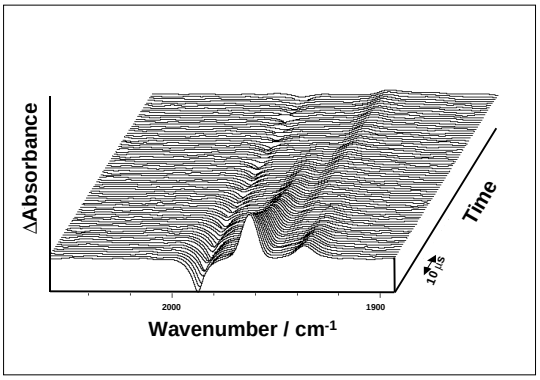

Figure 2. Time-resolved Step-scan FTIR spectra obtained in 1 μs time-slices following irradiation of $W(CO)_6$ in scXe. These data were obtained from one scan of the interferometer.

The parent $W(CO)_6$ absorption is clearly bleached and two new ν(C-O) bands are formed and can be assigned to $W(CO)_5(Xe)$ by comparison to previous TRIR studies. We were intentionally not completely rigorous in the preparation of the solution of

$W(CO)_6$ in scXe. $W(CO)_5(Xe)$ decays to reform the parent and a new species with a band at 1944 $cm^{-1.}$ This new species can be assigned to $W(CO)_5(H_2O)$ and indicates the presence of a H_2O impurity[5] in the Xe solution. This result emphasises the advantage of using step-scan FTIR for kinetic measurements since using a diode laser (at a single frequency) to obtain the decay kinetics of $W(CO)_5(Xe)$ may have missed the formation of $W(CO)_5(H_2O)$ and anomalous results may have been obtained. The simultaneous acquisition of both spectral and kinetic information results helps address this problem. We have used the formation of $W(CO)_5(Xe)$ to probe the risetime of our instrument, which was found to be 10 ns, Figure 3.

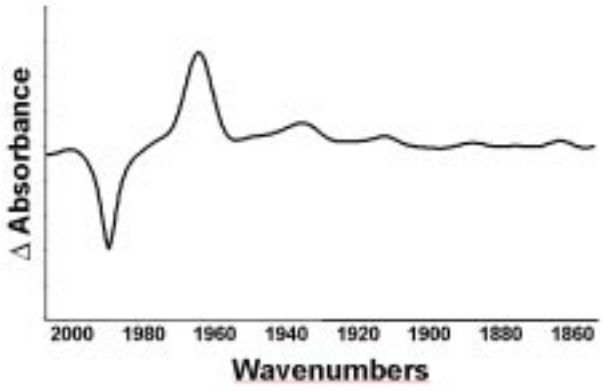

Figure 3. Time-resolved Step-scan FTIR spectrum obtained in 10 ns following irradiation of $W(CO)_6$ in scXe. These data were obtained from co-adding four scans of the interferometer.

We have used the photochemistry of *trans*-$[CpMo(CO)_3]_2$ in supercritical CO_2 ($scCO_2$) as a model system to compare the step-scan FTIR instrument with IR diode lasers for obtaining kinetics information. The photochemistry of *trans*-$[CpMo(CO)_3]_2$ in $scCO_2$ has recently been investigated using TRIR.[6)]

Visible irradiation (532 nm) of *trans*-$[CpMo(CO)_3]_2$ in $scCO_2$ results only in cleavage of the Mo-Mo bond to produce $CpMo(CO)_3$ radicals. The $CpMo(CO)_3$ radicals recombine at a diffusion controlled rate to form both *trans*-$[CpMo(CO)_3]_2$ and the unstable *gauche*-$[CpMo(CO)_3]_2$, Figure 4. This is followed by slow isomerisation of *gauche*-$[CpMo(CO)_3]_2$ to *trans*-$[CpMo(CO)_3]_2$. The IR spectra shown in Figure 4 are averaged over 4 scans.

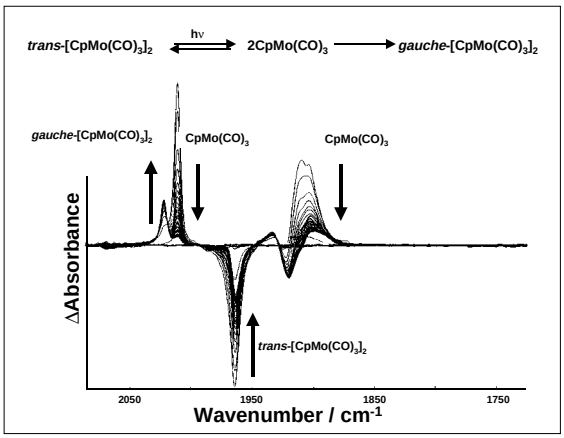

Figure 4. Step-scan FTIR spectra obtained in 500 ns increments following irradiation (532 nm) of *trans*-$[CpMo(CO)_3]_2$ in $scCO_2$.

This system is particularly suited to comparing the different approaches for obtaining kinetic information in that the $CpMo(CO)_3$ radicals decay by a second order process on the microsecond timescale and the isomerisation of *gauche*-$[CpMo(CO)_3]_2$ to *trans*-$[CpMo(CO)_3]_2$ is a first order process on the millisecond timescale. In principal the use of diode lasers for the measurement of kinetics at one IR frequency should produce better *signal-to-noise* ratio because of the higher IR photon flux these lasers provide. The TRIR decay traces of $CpMo(CO)_3$ in $scCO_2$ are compared in Figure 5. It can be seen that under these conditions both approaches produces excellent kinetic information and using both approaches the decay of $CpMo(CO)_3$ is second order. Similarly, on a slower timescale there is no difference between using the two techniques for obtaining the first order decay of *gauche*-$[CpMo(CO)_3]_2$ to *trans*-$[CpMo(CO)_3]_2$. From this we conclude that comparable kinetics can be obtained from using step-scan FTIR and IR diode lasers for TRIR measurements.

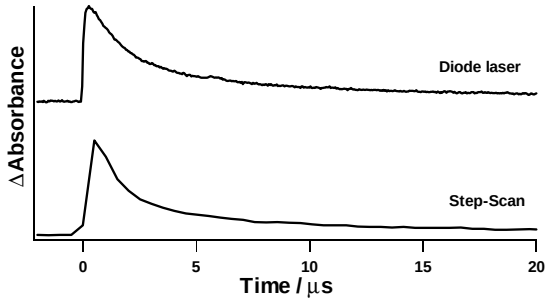

Figure 5. Comparison of TRIR decay traces of $CpMo(CO)_3$ radical (2012 cm^{-1}) using diode laser and step-scan based TRIR spectrometer.

Wavenumber resolution is also an important factor in time-resolved step scan FTIR measurements. The majority of time-resolved step scan FTIR experiments have used relatively low spectral resolution (typically 8 cm^{-1}). The main reason for not using higher resolution for time-resolved step scan FTIR is the much greater number of data points required for the interferogram which becomes prohibitive when a large amount of signal averaging is required to obtain a satisfactory signal-to-noise ratio.

We have chosen to study the photochemistry of $[CpFe(CO)_2]_2$ in *n*-heptane solution following visible excitation using step-scan FTIR. Visible irradiation of $[CpFe(CO)_2]_2$ causes cleavage of the Fe-Fe bond and formation of $CpFe(CO)_2$ radicals. These radicals recombine in 5-10 μs to form either *cis*-$[CpFe(CO)_2]_2$ or *trans*-$[CpFe(CO)_2]_2$ thus producing a non-equilibrium concentration of *cis*-$[CpFe(CO)_2]_2$.[7)] Slowly *cis*-$[CpFe(CO)_2]_2$ isomerises to the more stable *trans*-$[CpFe(CO)_2]_2$. Early TRIR measurements using CO lasers showed that the radicals had ν(C-O) bands at ~ 2005 and 1938 cm^{-1} in *n*-heptane. The high frequency ν(C-O) band could not be accurately determined because of the strong overlap with the absorption of the parent. Hochstrasser and co-workers investigated the photochemistry of or *trans*-$[CpFe(CO)_2]_2$ in cyclohexane using picosecond TRIR and detected a transient with absorption maximum at 1933 cm^{-1} and claimed that the 5 cm^{-1} shift was significant and assigned the 1933 cm^{-1} to a precursor of the radical.[8)] The original microsecond TRIR experiments were carried out using a CO laser and were therefore quoted with an error of ± 4 cm^{-1}. High resolution TRIR experiments using the diode laser based TRIR spectrometer demonstrated that the $CpFe(CO)_2$ radicals had a ν(C-O) absorption at 1935 cm^{-1} in *n*-heptane and 1933 cm^{-1} in cyclohexane and the difference between the microsecond and picosecond TRIR results was due to a solvent shift in the ν(C-O) bands of the $CpFe(CO)_2$ radical.[9)] Figure 6 shows the step-scan TRIR spectra obtained following irradiation of *trans*-$[CpFe(CO)_2]_2$ in *n*-heptane solution. It is clear that we can obtain TRIR spectra with excellent signal-to-noise ratio even at

high resolution 0.5 cm^{-1}). The correct band position was only obtained using high spectral resolution (<2 cm^{-1}).

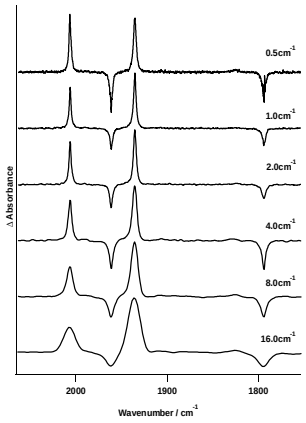

Figure 6. Step-scan FTIR spectra obtained 1μs after irradiation of *trans*-$[CpFe(CO)_2]_2$ in *n*-heptane solution at 16,8,4,2,1 and 0.5 cm^{-1} resolution.

All the experiments described above have used time-resolved step-scan FTIR to probe the photochemistry of metal carbonyl complexes, which have very intense ν(C-O) bands in the infrared. We have also been interested in applying TRIR to organic photochemistry, particularly to azides and benzoyl radicals. Benzoyl radicals are key intermediates in many photopolymerisation reactions and have a characteristic band at 1800-1850 cm^{-1} depending upon the nature of the substituents on the benzene ring.[10] Here we have used the photochemistry of (1-hydoxycyclohexyl)phenyl ketone to probe the capability of our step-scan spectrometer to detect transient species with weak IR bands in irreversible photochemical systems. Irradiation of (1-hydoxycyclohexyl)phenyl ketone in *n*-heptane generates benzoyl radicals recombine to reform the parent or couple together to form the other products.

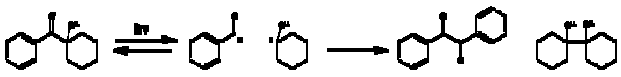

Figure 7 shows the step-scan FTIR spectrum obtained 1 μs following irradiation of (1-hydoxycyclohexyl)phenyl ketone in n-heptane. In this experiment a low UV laser power was used to produce small IR transients. The spectrum obtained 1 μs after photolysis clearly shows depletion of the parent absorption and the production of the benzoyl radical at 1827 cm^{-1}. The data shown in Figure 7 was obtained by averaging 32 scans.

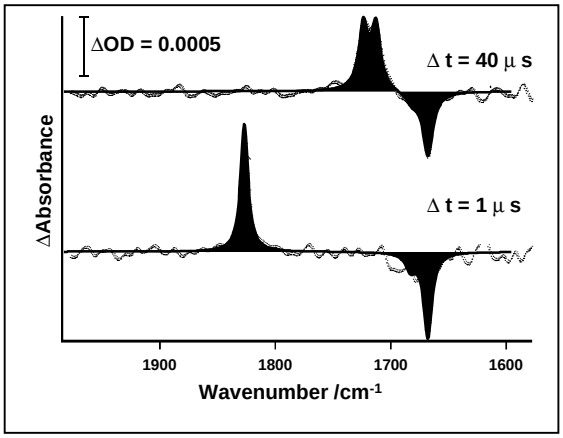

Figure 7. Step-scan FTIR spectra obtained following irradiation of (1-hydoxycyclohexyl)phenyl ketone in n-heptane.

We have achieved 1 μs TRIR spectra of very small absorptions (ΔOD < 5 $x10^{-4}$ with a signal-to-noise ratio > 10 in a few hours).

The benzoyl radicals recombine to reform the parent and the benzoin photoproduct. The TRIR decay trace (1827 cm^{-1}) of the benzoyl radical is shown in Figure 8.

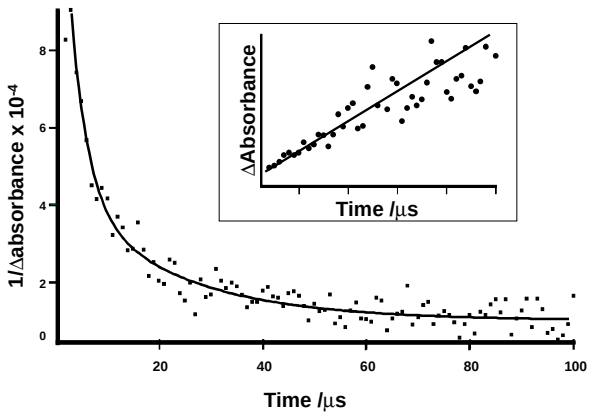

Figure 8. Decay of benzoyl radical (1824 cm^{-1}) obtained using step-scan FTIR.

Conclusions

We have constructed a *new* nanosecond *step-scan* time-resolved IR spectrometer. We have demonstrated this instrument can obtain TRIR spectra with high signal-to-noise ratio ((ΔOD < 5 $x10^{-4}$) and high time-resolution (10 ns). We have demonstrated that this step-scan FTIR can be used to probe a variety of chemical reactions.

Acknowledgements

We are extremely grateful to the Laser *for* Science Facility Laser loan pool for supply of the Nd:YAG laser. We would like to thank Drs A.W. Parker, M. Towrie, I. P. Clark and P. Matousek for helpful discussions. We thank the Royal Society for funding (SMN visit).

References

1. M W George, M Poliakoff and J J Turner
The Analyst 119, 551, (1994). *See April Appl. Spectr. (1997)*.

2. M W George,
Signal-to-News, Nicolet Instruments 119, 5 (1998).

3. X Z Sun, M W George, S G Kazarian, S M Nikiforov and M. Poliakoff,
J. Am. Chem. Soc 118, 10525 (1996).

4. H Hermann, F-W Grevels, A. Henne and K Schaftner,
J. Phys. Chem. 86, 5151, (1982).

5. X Z Sun, S M Nikiforov and M W George,
Organometallics *to be submitted*.

6. B D Moore, M B Simpson, M Poliakoff and J J Turner,
Chem. Commun. 972, (1984).

7. J N Moore, P A Hansen and R M Hochstrasser,
J. Am. Chem. Soc. 111, 4563, (1989).

8. A J Dixon, M W George, C Hughes, M Poliakoff and J J Turner
J. Am. Chem. Soc. 114, 1719, (1992).

9. G W Sluggett, C Turro, M W. George, I V Koptyug, and N. J Turro,
J. Am. Chem. Soc. 117, 5148, (1995).

Ultrafast Studies of the Photochemistry of Phenols

R H Bisby

Department of Biological Sciences, University of Salford, Salford M5 4WT

P Matousek, M Towrie, A W Parker

Central Laser Facility, CLRC Rutherford Appleton Laboratory, Chilton, Didcot, Oxon, OX11 OQX, UK

Main contact email address: *r.bisby.staff@salford.ac.uk*

Introduction

α-Tocopherol (vitamin E) protects lipidic systems (membranes and lipoproteins) against oxidative damage by acting as a chain-breaking antioxidant [1]. The kinetics of oxidation of α-tocopherol and the reduction of the tocopheroxyl radical have been studied in the micro- and milli-second time regions by nanosecond laser flash photolysis [2-4]. These studies showed that the tocopheroxyl radical (T-O$^{\cdot}$) was formed by photoionisation. Time-resolved resonance Raman spectroscopy indicated that the tocopheroxyl radical cation (T-OH$^{+\cdot}$), with a pK_a of –1.4, was the predominant species in strongly acidic solutions [5]. Furthermore, the radical cation is expected to be an intermediate not only in the photoionisation reaction, but may also participate in biological oxidations of vitamin E.

$$\text{T-OH} + h\nu \rightarrow \text{T-OH}^{+\cdot} \rightarrow \text{T-O}^{\cdot} + H^{+}$$

However, the pK_a value of the radical cation indicated that the lifetime would be of the order of picoseconds in neutral solution and so femtosecond laser studies should provide an ideal approach to kinetic studies of radical cation formation and decay.

Results and Discussion

Previous femtosecond transient absorption experiments at single wavelengths mainly at ca. 800 nm indicated that the hydrated electron formed from photoionisation of water-soluble vitamin E analogues was formed in two stages. Picosecond time-resolved resonance Raman spectra confirmed the intermediate formation of the radical cation [6]. In the present report some results are presented using the newly developed multi-wavelength picosecond transient absorption spectrometer system outlined in the 1997-98 Annual Report [7].

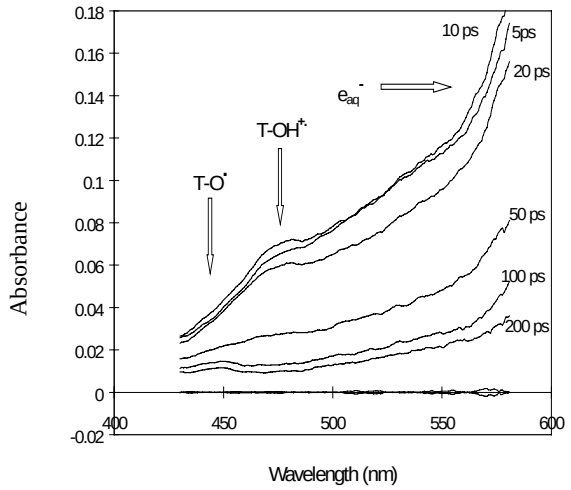

Figure 1. Transient absorption spectra from femtosecond laser photolysis (277 nm) of Trolox C in aqueous solution at neutral pH.

Figure 1 shows the transient absorption spectra recorded from a solution of Trolox C (a water soluble Vitamin E analogue) in aqueous solution at pH 7 after photolysis by a 300 fs pulse at 277 nm. The main feature is the broad red and infrared absorption of the hydrated electron formed by photoionisation. The kinetics of formation and decay of the hydrated electron decay within the initial 200 ps period following the laser pulse have been well characterized in the previous single wavelength experiments at 830 nm [6]. Using the diode array spectrometer, an additional absorption peak at 450-500 nm is observed in the 10 ps spectrum due to the tocopheroxyl radical cation. This decays together with the hydrated electron, until at 200 ps after the laser pulse another absorption in the region of 440 nm is discernable and readily ascribed to the neutral tocopheroxyl radical. The results therefore show that the de-protonation of the tocopheroxyl radical cation at neutral pH occurs on a time-scale of about 20 ps, and are consistent with the previous TR^3 measurements.

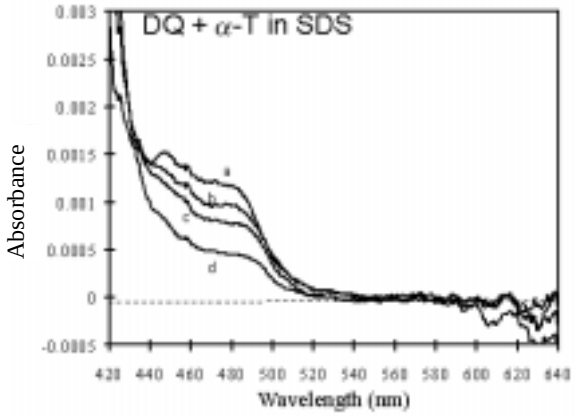

Figure 2. Transient absorption spectrum from femtosecomd laser photolysis of duroquinone and a-tocopherol in sodium dodecyl sulfate (SDS) micelles. Spectra were recorded at a) 30 ps, b) 250 ps, c) 500 ps and c) 2000 ps after excitation with a laser pulse at 390 nm.

One advantage of the OPA lasers in the Ultrafast Laboratory is the ability to pump the sample over a wide wavelength range. This is illustrated in Figure 2 which shows transient absorption spectra obtained after excitation of the charge transfer complex formed between duroquine (DQ) and α-tocopherol in sodium dodecyl sulfate (SDS) micelles. Photo-excitation of this complex allows us to observe a reaction more closely related to that occuring in nature, but on an ultra-fast time scale. Whereas in the nanosecond laboratory TR^3 experiments revealed only formation of the neutral tocopheroxyl radical on oxidation by triplet duroquinone, the present results appear to demonstrate intermediate absorption in the region of 480 nm due to the tocopheroxyl radical cation. Unfortunately at present it is not possible to bridge the gap in time-scales between those accessible in the Ultrafast Laboratory (up to ca 2 ns) and those in the Nanosecond Laboratory (> ca 10-20 ns).

The related compound 4-hydroxycinnamate has also been investigated because of its importance as a component in the light-sensing prokaryotic photo-active yellow protein (PYP) [8]. Experiments in the nanosecond laboratory showed that the phenoxyl radical of 4- hydroxycinnamate could be formed by sensitized photo-oxidation with duroquinone, but not by direct

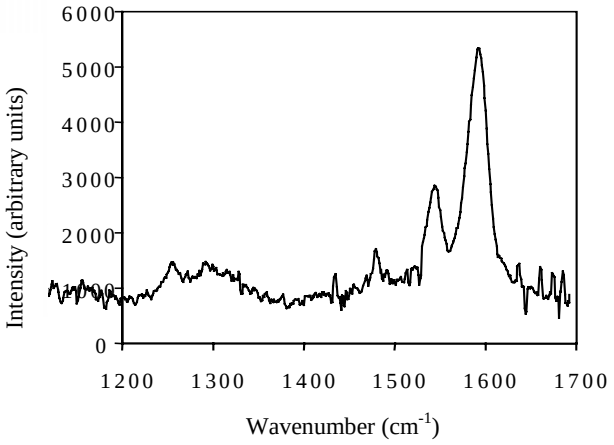

Figure 3. Resonance Raman spectrum of the phenoxyl radical from 4-hydroxycinnamate in methanol/water (50/50 v/v), probe wavelength 600 nm.

photolysis in the ultraviolet (266-308 nm). Unsubstituted phenoxyl radicals generally only show resonance enhancement of the C-O stretching vibration in the TR^3 spectrum [9], whereas 4-alkoxyl substituted phenoxyl radicals [10], including the tocopheroxyl radical [5], show additional strong enhancement of the ring C-C stretching vibration. This is due to delocalisation of the unpaired electron to the oxygen atom in the 4-substituent.

Figure 3 shows that in addition to the C-O vibration at 1544 cm^{-1}, the C-C stretching vibration at 1592 cm^{-1} is also strongly enhanced in the TR^3 spectrum of the 4-hydroxycinnamate phenoxyl radical. The conjugated double bond allows radical delocalisation if the same way as in 4-methoxyphenoxyl.

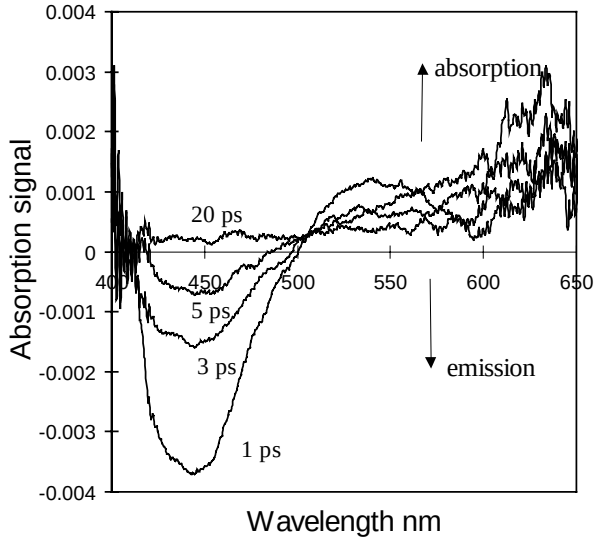

Figure 4. Transient emission observed after excitation at 277 nm of 4-hydroxycinnamate in aqueous solution at pH 7.

The nanosecond experiments using direct photolysis revealed no transients due to excited states, so the experiment was repeated with the superior sensitivity in absorbance in the Ultrafast Laboratory with 300 fs pulses at 277 nm. The results of this experiment are shown in Figure 4. Instead of the transient absorptions seen in the previous experiments with Trolox, the data with 4-hydroxycinnamate shows a stimulated emission which decays with a lifetime of about 2 ps. It is thought that this may involve formation of the photo-excited transition state which leads to isomerisation in this compound, and which might be an important intermediate in the mechanism of PYP.

References

1. G W Burton and K U Ingold
Acc.Chem.Res.19, 194, (1986)

2. R H Bisby and A W Parker
FEBS Letters 290 , 205, (1991)

3. R H Bisby and A W Parker
Arch.Biochem.Biophys. 317,170, (1995)

4. R H Bisby and A W Parker
J. Amer.Chem.Soc. 117,5664, (1995)

5. A W Parker and R H Bisby
J.Chem.Soc. Faraday Trans. 89,2873, (1993)

6. M Towrie, G Gaborel, P Matousek, A W Parker, W Shaikh and R H Bisby
Laser Chem., 19, 153, (1999)

7. M Towrie, P Matousek, A W Parker, S Jackson and R H Bisby
CLF Annual Report 1997-98, (RAL Report RAL-TR-1998-080) p. 183.

8. W D Hoff et al
Biochemistry 35, 1274, (1996)

9. G N R Tripathi and R H Schuler
J.Chem.Phys. 81, 113, (1984)

10. G N R Tripathi and R H Schuler
J.Phys.Chem. 92, 5129, (1988)

Discharge-flow Studies of the Kinetics of the Reactions of Br, Cl, BrO and ClO with CH_3O using LIF detection

C E Canosa-Mas, N J Hendy, D Shah, A Vipond, R P Wayne

Physical and Theoretical Chemistry Laboratory, University of Oxford, South Parks Road, Oxford, OX1 3QZ, UK

Main contact email address: *vipond@physchem.ox.ac.uk*

Introduction

It is now well established that the rapid spring-time depletion of stratospheric ozone over the Antarctic is due to catalytic cycles involving XO radicals, where X = Cl or Br. The reactions of CH_3O_2 with XO are of potential importance in the stratosphere. Under low ozone conditions, the reaction of Cl atoms with CH_4 is favoured, leading to the formation of CH_3O_2, which in turn may react with XO. It has been proposed that the reactions with ClO and BrO could both possess channels that promote the chain decomposition of ozone[1,2].

The study of reactions of CH_3O_2 in the laboratory also requires the investigation of possible side chemistry involving the CH_3O radical; the latter species is always present in non-negligible concentrations when CH_3O_2 is produced in low pressure reactors, such as the one used in this work. The CH_3O radical itself is a key intermediate in the atmospheric oxidation of methane and also in combustion systems. However, there are relatively few kinetic data for its reactions with other radicals. In this work, the reactions

$$CH_3O + Br \rightarrow \text{products} \quad (1)$$
$$CH_3O + Cl \rightarrow \text{products} \quad (2)$$
$$CH_3O + BrO \rightarrow \text{products} \quad (3)$$
$$CH_3O + ClO \rightarrow \text{products} \quad (4)$$

have been investigated at room temperature. The work was prompted by the lack of agreement in the literature over the values of the rate constants. In the case of reactions (1) and (3), rate constants are required for the interpretation of subsequent work on the reaction of CH_3O_2 with BrO.

Experimental Details

The experiments were carried out using a discharge-flow tube (Figure 1) equipped with a double sliding injector and six static side injectors, described previously[3]. The tube was operated at P = 2 – 2.3 Torr and T = 296 ± 1 K.

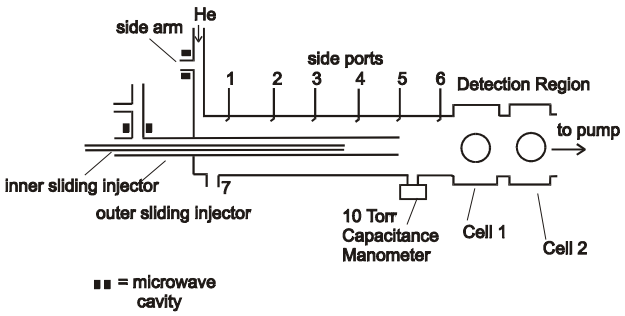

Figure 1. Schematic diagram of apparatus.

Generation of species

A number of different methods of generation of the reactants were used. CH_3O was generated in the sliding injector by one of two reaction pathways:

$$F + CH_3OH \rightarrow CH_3O + HF \quad (5)$$
or
$$F + CH_4 \rightarrow CH_3 + HF \quad (6)$$
$$CH_3 + NO_2 \rightarrow CH_3O + NO \quad (7)$$

For reactions (5) and (6), F atoms were generated in the outer sliding injector by subjecting F_2 in helium to a microwave discharge. CH_3OH or CH_4 was delivered through the inner sliding injector, in sufficient excess to consume all the F atoms. In reaction (7), NO_2 was added to just surpass the maximum of the CH_3O signal, ensuring complete consumption of the CH_3 radicals. Typical concentrations of F_2, CH_3OH, CH_4 and NO_2 were < 5 H 10^{11}, 4 H 10^{13}, 4 H 10^{14}, 5 H 10^{12} molecule cm^{-3}. Typical concentrations of CH_3O were (0.5 – 1.5) H 10^{11} molecule cm^{-3}.

The halogen atom species, X, was generated by several methods. In the simplest case, a flowing mixture of X_2 in helium was subjected to a microwave discharge, in the side arm of the flow tube. Other methods included:

$$F + X_2 \rightarrow X + FX \quad (8)$$
$$F + C_2H_3Br \rightarrow Br + C_2H_3F \quad (9)$$
$$Cl + C_2H_3Br \rightarrow Br + C_2H_3Cl \quad (10)$$

The precursor, X_2 or C_2H_3Br, was introduced in excess *via* port 1 to completely consume the atomic co-reactant, generated in the side arm. Typical concentrations of X were (0.5 – 2.5) H 10^{12} molecule cm^{-3}.

The halogen oxide species, XO, was formed by addition of excess ozone to react with X, the latter being generated by one of the methods described above.

$$X + O_3 \rightarrow XO + O_2 \quad (11)$$

Ozone (*ca*. 5 H 10^{13} molecule cm^{-3}) was delivered through port 2. Typical concentrations of XO were (0.5 – 2.5) H 10^{12} molecule cm^{-3}.

Detection of Species

The flow tube was coupled to two detection cells. The first permitted the detection of CH_3O radicals by laser-induced fluorescence (LIF) of the ($\tilde{A}\ ^2A_1 – X\ ^2E_1$) transition at λ = 292.8 nm. The excitation beam was produced using a dye laser (Spectra-Physik, PDL-2), with Rhodamine 610 chloride dye, pumped by a Nd-YAG laser (Quanta-Ray, GCR-11). The fluorescence passed through two filters (Schott UG11 8 = 270 – 380 nm band pass and Andover Corporation 8 ∃ 305 nm) and was detected by a photomultiplier (EMI B2F/RFI6443), positioned orthogonal to the laser beam. The signal was processed through a box car integrator (EG & G 162) and output to a chart recorder.

In order to quantify the concentration of CH_3O, the LIF signal was calibrated through a series of experiments. It should be emphasised that, since the CH_3O was the kinetic species, only an approximate calibration was required. In each experiment, a constant excess of CH_3 (from reaction 6) was allowed to react over a fixed contact time, with a range of known concentrations of NO_2. A different concentration of CH_3 was used in each experiment, to determine the maximum slope, m, from the series of plots of LIF signal *versus* [NO_2]. The value of 1/m yields the approximate calibration factor. The sensitivity of the LIF detection system was *ca*. 6 x 10^9 molecule cm^{-3}.

The second cell allowed the detection of Br or Cl atoms by resonance fluorescence (RF). The atoms were observed at wavelengths of 148 – 158 nm and 138 nm, respectively. The exciting radiation was provided by a lamp in which a dilute

flow of Br_2 or Cl_2 in argon was subjected to a microwave discharge. The radiation passed through a window of sapphire (for Br) or of CaF_2 (for Cl), into the centre of the cell. The resonance fluorescence from the Br or Cl atoms passing through the detection zone of the flow tube was detected by a photomultiplier (Hamamatsu, R1459), positioned orthogonal to the lamp.

Determination of the concentration of X required the accurate calibration of the RF signal. Both RF systems were calibrated by the stoicheiometric conversion of known concentrations of precursor (HCl for Cl, and C_2H_3Br or HBr for Br) to X, by reactions with excess F or Cl atoms.

$$F + HCl \rightarrow HF + Cl \qquad (12)$$
$$Cl + C_2H_3Br \rightarrow Br + C_2H_3Cl \qquad (10)$$
$$F + HBr \rightarrow HF + Br \qquad (13)$$

A plot of signal *versus* the concentration of precursor yields a calibration factor from 1/*m* (where *m* = slope). The sensitivity of the calibration systems for Br and Cl were 4 H 10^9 and 5 H 10^9 molecule cm^{-3}.

The concentration of XO was determined by introducing excess NO (> 3 H 10^{14} molecule cm^{-3}) *via* port 6, to stoicheiometrically convert XO to X, the latter being observed by RF.

$$XO + NO \rightarrow X + NO_2 \qquad (14)$$

Experimental Procedure

All experiments were performed under *pseudo* first-order conditions with excess X or XO formed in the main flow of the tube. The kinetic species, CH_3O, was generated in the sliding injector and introduced into the main flow at a number of different positions, corresponding to contact times of up to 30 ms. The rate constants were obtained by one of two methods.

Method 1: Absolute determination

The absolute method was used for reactions 1, 2 and 4. The LIF signal was measured in the absence and presence of X or ClO for each contact time (signals S_0 and S_t, respectively). Experiments were conducted for a range of concentrations of X or ClO, measured using RF.

Method 2: Relative determination

The second method obtained rate constants for reactions 3 and 4 relative to those for reactions 1 and 2. The LIF signal was measured in the absence and presence of X and XO, consecutively. The concentrations of X and XO were equal; XO was obtained by complete conversion of X by reaction with O_3 (reaction 11).

Treatment of Data and Results

Throughout the rest of the paper, the second-order rate constants for reactions (1) to (4) will be labelled k_{Br}, k_{Cl}, k_{BrO} and k_{ClO}.

Method 1: The experimental data were treated using a simple *pseudo* first order approach

$$\ln\left\{\frac{S_o}{S_t}\right\} = k_X' t \qquad (I)$$

where $kN_X = k_X[X]$. The slope of a plot of $\ln\{S_0/S_t\}$ *versus* contact time, *t*, yields the value of kN_X. Plotting kN_X *versus* [X] yields the second-order rate constant from the slope. Figure 2 shows the second-order plot for reaction (1), giving a value of k_{Br} of $(5.0 \pm 0.3) \times 10^{-11}$ cm^3 $molecule^{-1}$ s^{-1}, where the errors are the 95% confidence limits of the line of regression.

In the study of reaction 2, CH_3O was generated by reactions (6) and (7). However, the Cl atoms also react with CH_4

$$Cl + CH_4 \rightarrow CH_3 + HCl \qquad (15)$$
$$k_{15} = 1.1 \text{ H } 10^{-11} \text{ cm}^3 \text{ molecule}^{-1} \text{ s}^{-1}$$ [4)]

Although the extent of reaction (15) has negligible effect on the concentration of Cl, the CH_3 leads to the formation of CH_3O by reaction with NO_2 (reaction 7). The first-order treatment of the experimental data was modified in order to take into

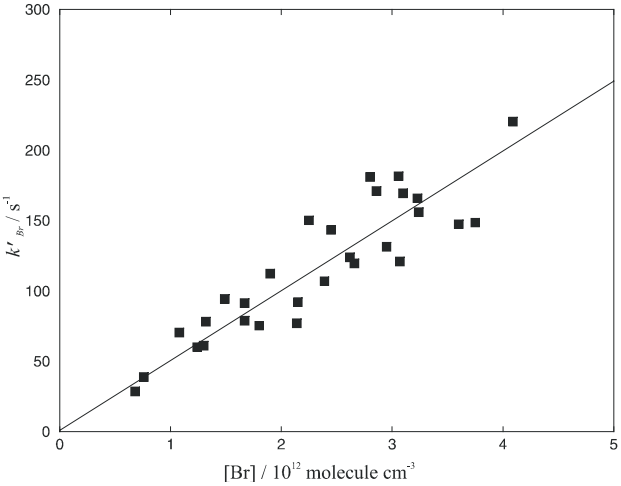

Figure 2. Second-order plot for the reaction of CH_3O with Br.

consideration the additional CH_3O resulting from reaction (15)

$$\ln\left\{\frac{S_0 - S_{CH4,t}}{S_t}\right\} = k_{Cl}' t \qquad (II)$$

where $S_{CH4,t}$ is the signal observed from only the reaction of Cl with CH_4 in the presence of NO_2, over time *t*.

A second order plot of k'_{Cl} *versus* [Cl] yields a value of k_{Cl} of $(9.0 \pm 0.9) \times 10^{-11}$ cm^3 $molecule^{-1}$ s^{-1}, where the errors are the 95% confidence limits of the line of regression (Figure 3).

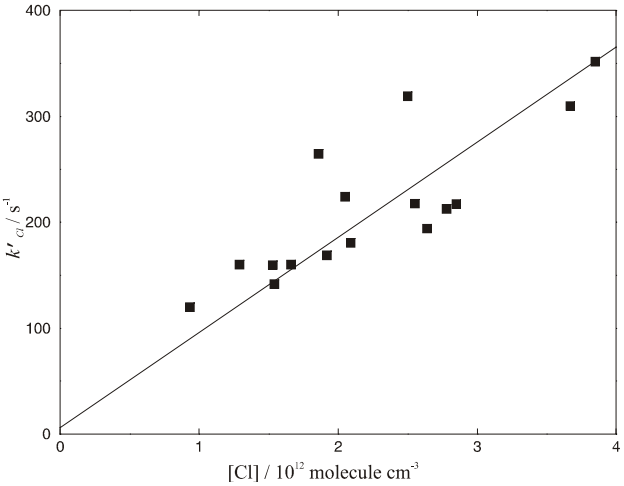

Figure 3. Second-order plot for the reaction of CH_3O with Cl.

In the reaction of CH_3O with ClO (reaction 4), the Cl atoms used to generate ClO were completely consumed by reaction with O_3, and thus could not initiate the formation of additional CH_3O by reaction (15). Therefore, the experimental data were treated using equation (I). Figure 4 shows a second-order plot, where the value of k_{ClO} was found to be $(4.1 \pm 0.5) \times 10^{-11}$ cm^3 $molecule^{-1}$ s^{-1}.

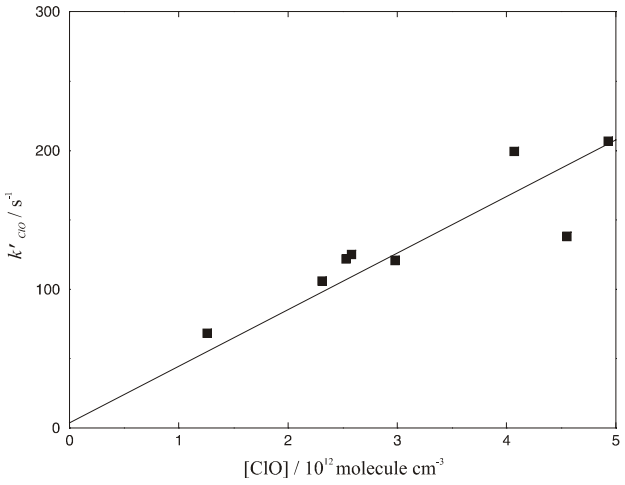

Figure 4. Second-order plot for the reaction of CH_3O with ClO.

Method 2: The first-order rate constants for X and XO were determined using equation 1 (for Br, BrO and ClO) or equation 2 (for Cl), as described in the previous section. The ratio of the rate constants is expressed

$$\frac{k'_{XO}}{k'_{X}} = \frac{k_{XO}[XO]}{k_{X}[X]} \qquad \text{(III)}$$

Since the concentrations of X and XO are the same (XO being generated by the stoicheiometric conversion of X in reaction 11), equation (III) can be simplified so that the ratio of the second-order rate constants is the same as that of kN_{XO}/kN_X. In fact, the concentration of BrO was only *ca*. 85 - 90% that of [Br] under the conditions of the experiment, as a result of the reproduction of Br atoms by the relatively rapid BrO self reaction[4]. However, thanks to the similarity of the rate constants k_{Br} and k_{BrO}, the correction to take into account the concentration of Br atoms in the BrO system was negligible.

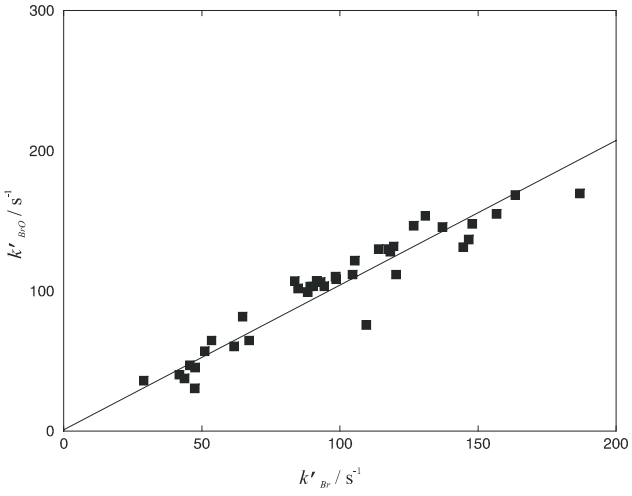

Figure 5. Relative plot of kN_{BrO} *versus* kN_{Br}.

Figures 5 and 6 display plots of kN_{XO} *versus* kN_X, where X is Br or Cl. The ratios of k_{BrO}/k_{Br} and k_{ClO}/k_{Cl} were found to be (1.03 ± 0.04) and (0.45 ± 0.03) respectively, where the errors

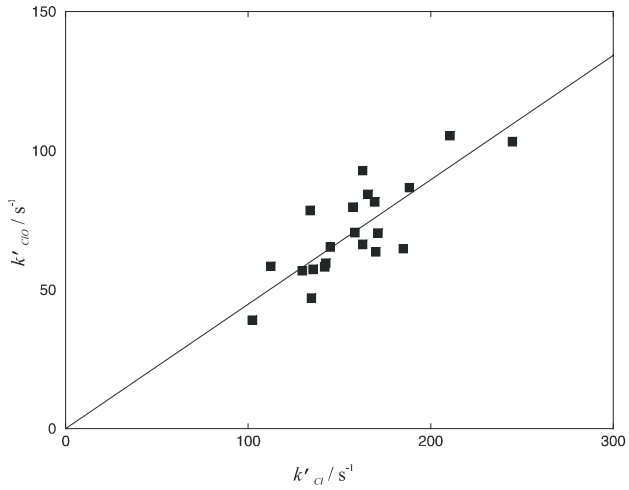

Figure 6. Relative plot of kN_{ClO} *versus* kN_{Cl}.

are the 95% confidence limits of the lines of regression. Inserting the values of k_{Br} and k_{Cl} found in the absolute determination (method 1) into the appropriate ratios, yields k_{BrO} = (5.2 ± 0.5) × 10^{-11} cm^3 molecule^{-1} s^{-1} and k_{ClO} = (4.1 ± 0.7) × 10^{-11} cm^3 molecule^{-1} s^{-1}. Errors include 95% confidence limits of the gradients in figures 5 and 6 and the errors in k_{Br} and k_{Cl}.

Discussion

A summary of the rate constants found in this work and the present literature values for the reactions with CH_3O is presented in Table 1. There are some differences between the values determined here and those in the literature. However, there is particularly good agreement between the values obtained for k_{Br} and k_{Cl} and those determined by Szilagyi *et al.*[6] and Jungkamp *et al.*[7]. The reason for the discrepancy between other values is not clear.

Co-reactant	Rate constant k / 10^{-11} cm^3 molecule^{-1} s^{-1}	
	This work	Literature
Br	(5.0 ± 0.3) [a]	(7.0 ± 0.4) [5] 5.0 [6]
Cl	(9.0 ± 0.9) [a]	(10.0 ± 0.2) [7] (1.9 ± 0.4) [8] (2 ± 1) [9]
BrO	(5.2 ± 0.5) [b]	(3.8 ± 0.4) [5]
ClO	(4.1 ± 0.5) [a] (4.1 ± 0.7) [c]	(2.3 ± 0.3) [8] (1.3 ± 0.3) [9]

a Absolute determination, b Relative to *k*Br, c Relative to *k*Cl.

Table 1. Summary of results.

The products of the reactions have not been observed in this kinetic study. However, it seems likely that HX will be a major product in reactions (1) and (2). Indeed, the other plausible channel is pressure dependent, and thus is unlikely to occur under the low pressure conditions of the flow tube.

$$CH_3O + X \rightarrow HX + CH_2O \qquad (16a)$$
$$CH_3O + X + M \rightarrow CH_3OX + M \qquad (16b)$$

Reactions (3) and (4) have four possible channels.

$$CH_3O + XO \rightarrow CH_2O + HOX \quad (17a)$$
$$\rightarrow CH_3O_2 + X \quad (17b)$$
$$\rightarrow CH_2O_2 + HX \quad (17c)$$
$$\rightarrow CH_3X + O_2 \quad (17d)$$

Daële *et al.*[8] found HOCl to be a major product of reaction (2). It seems likely that HOBr will similarly be a major product of reaction (1).

Inspection of the results shows that while Cl reacts faster than Br with CH_3O, the trend is reversed for the halogen monoxides where BrO reacts faster than ClO. One possible explanation comes from a simple consideration of the mechanism of reaction. The mechanism by which CH_3O reacts with X is likely to involve simple hydrogen abstraction and may be favoured by the more electrophilic Cl atom. The order of reactivity also follows the order of exothermicity (data from DeMore *et al*. [4])

$$CH_3O + Cl \rightarrow HCl + CH_2O \quad)H_{2a} = -340.0 \text{ kJ mol}^{-1} \quad (2a)$$
$$CH_3O + Br \rightarrow HBr + CH_2O \quad)H_{1a} = -273.5 \text{ kJ mol}^{-1} \quad (1a)$$

On the other hand, in the case of the reaction of CH_3O with XO, it may be postulated that the reaction proceeds *via* a five-membered transition state (Figure 7), where it is the oxygen atom of XO which abstracts the H atom from CH_3O, generating HOX as a major product, a process which is favoured by the less electrophilic Br atom.

$$CH_3O + ClO \rightarrow HOCl + CH_2O \quad)H_{4a} = -304.1 \text{ kJ mol}^{-1} \quad (4a)$$
$$CH_3O + BrO \rightarrow HOBr + CH_2O \quad)H_{3a} = -273.5 \text{ kJ mol}^{-1} \quad (3a)$$

The transition state may also be more stable for BrO. The five-membered structure incorporating the smaller ClO might be more strained, leading to lower reactivity.

At present there are no data for reactions of CH_3O with I and IO, so it is not possible to confirm whether the same trends hold for the iodine species.

As mentioned in the introduction, the main motivation for the study of the reactions of CH_3O was the need to determine their rate constants in order to interpret results from reaction systems containing CH_3O_2. In our laboratory, we have conducted experiments on CH_3O_2, generated by the reactions

$$F + CH_4 \rightarrow CH_3 + HF \quad (6)$$

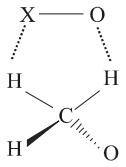

Figure 7. Five-membered transition state.

$$CH_3 + O_2 + M \rightarrow CH_3O_2 + M \quad (18)$$

The CH_3O radical is present in the system as a result of the reactions

$$CH_3 + CH_3O_2 \rightarrow CH_3O + CH_3O \quad (19)$$
$$CH_3O_2 + F \rightarrow FO + CH_3O \quad (20)$$

Observation of CH_3O by LIF, followed by the conversion of CH_3O_2 to CH_3O with excess NO and observation of the resultant LIF signal, showed that the ratio of the concentrations of CH_3O to CH_3O_2 was *ca.* 1:2. Therefore, when investigating the atmospherically significant reaction of CH_3O_2 with BrO, the reactions of CH_3O must be taken into consideration. Indeed, the one literature value[1] for the reaction of CH_3O_2 with BrO of (5.7 $\pm$ 0.6) H 10^{-12} cm^3 molecule^{-1} s^{-1} points to a comparatively slow reaction, whereas the CH_3O species present in the system will react much more rapidly with BrO and Br, causing substantial side chemistry.

Summary

A discharge-flow tube has been used to determine the rate constants for the reactions of CH_3O with Br, BrO, Cl and ClO at room temperature and a pressure of *ca*. 2 Torr. A number of different methods were used to generate the radicals. RF and LIF detection techniques were employed. The results revealed Cl to be more reactive than Br, and BrO to be more reactive than ClO, towards CH_3O. The rate constants for the reactions of Br and BrO are relatively large, thus indicating that secondary chemistry of CH_3O in systems to investigate the reaction of CH_3O_2 with Br or BrO is likely to be significant.

Acknowledgements

We wish to thank the European Union for funding the research as part of the COBRA project. Miss Shah thanks the NERC for funding under grant GT 04/97/273/MAS. We thank the Rutherford Appleton Laboratory for loaning the laser systems.

References

1. A Aranda, G Le Bras, G Laverdet and G Poulet
Geo. Phys. Res. Lett., 24, 2745 (1997)

2. F G Simon, J P Burrows, W Schneider, G K Moortgat and P J Crutzen
J. Phys. Chem., 93, 7807 (1989)

3. P Biggs, C E Canosa Mas, D E Shallcross, A Vipond and R P Wayne
J. Chem. Soc. Faraday Trans., 93, 2701 (1997)

4. W B DeMore, S P Sander, C J Howard, A R Ravishankara, D M Golden, C E Kolb, R F Hampson, M J Kurylo and M J Molina
JPL Publication, 97-4 (1997)

5. A Aranda, V Daële, G Le Bras and G Poulet
Int. J. Chem. Kinet., 30, 249 (1998)

6. I Szilágyi, S Dóbé and T Bérces
Presentation at the 15th International Symposium on Gas Kinetics, Bilbao (1998)

7. T Jungkamp, A Kukui and R N Schindler
Ber. Bunsenges. Phys. Chem., 99, 1057 (1995)

8. V Daële, G Laverdet and G Poulet
Int. J. Chem. Kinet., 28, 589 (1996)

9. P Biggs, C E Canosa-Mas, J-M Fracheboud, G Marston, D E Shallcross and R P Wayne
J. Chem. Soc., Faraday Trans., 91, 3045, (1995)

Competition Between the Br and Br* Channels in the A-band Photodissociation of CH_3Br

J Underwood, I Powis

School of Chemistry, University of Nottingham, Nottingham, NG7 2RD

Main contact email address: *Ivan.Powis@nottingham.ac.uk*

Introduction

The A-band dissociation of the methyl halides provides a prototype for the theoretical and experimental investigation of polyatomic molecular photodissociation. Absorption of a single photon in this continuum results in a broad, unstructured absorption band leading to two reaction channels: $CH_3 + X^*$ $^2P_{1/2}$ and $CH_3 + X$ $^2P_{3/2}$. The excitation gives rise to two electronic states in the limit of weak spin-orbit coupling, but splits into five components under strong spin-orbit interaction. In C_{3v} symmetry curve crossing between these components results, but Jahn-Teller-like distortion creates a conical intersection. The surface crossing can thus play a key role in determining the branching between the two asymptotic decay channels.

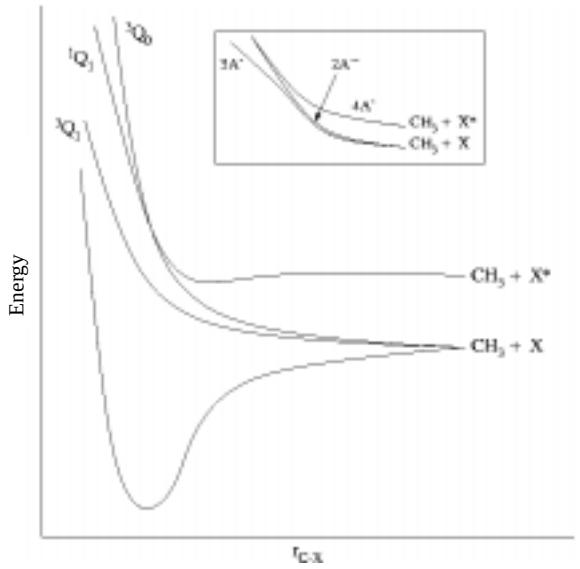

Figure 1. Schematic diabatic potential in C_{3v} symmetry relevant to A-band dissociation. Inset shows avoided crossing on reduction to C_s symmetry.

While the A-band dissociation of CH_3I has been extensively studied, much less attention has been devoted to blue-shifted CH_3Br band. Amongst other reasons, this should provide interesting comparisons because of reduced spin-orbit interaction Initial Br photofragment anisotropy studies in the blue[1] suggested that surface crossings were unimportant with differing β parameters for the two channels arising solely from isolated decay on two surfaces. Later Br atom photofragment imaging studies[2,3] in the 200-230 nm region demonstrate a clearer role for surface crossing: while the Br* fragment recoil parallel to the dissociation laser resulting from excitation to, and dissociation along a $^3Q_0$ surface, the Br fragment is more nearly isotropic, but with marked wavelength dependence revealing mixed perpendicular and parallel excitation and surface crossing in the latter case.[3]

Kitsopoulos *et al.*[3] also examined the CH_3 fragments using non-resonant, non-state-selective detection. Both channels display evidence for internal excitation, more so for the Br channel.

The work described here extends these measurements deep into the red wing of the absorption band, where it might be expected that curve-crossing will have a substantial influence on the dynamics. In addition to extending Br and Br* photofragment studies into this region we report vibrationally state-selective probing of the methyl fragment.

Experimental

One and two colour pump-probe experiments were performed using photolysis wavelengths in the 240-270 nm region. Fragments were detected in a time-of-flight apparatus by state-selective REMPI ionization. The majority of measurements were made using an effusive source of CH_3Br, but additionally a cold (50 K) molecular beam of CD_3Br was also employed for experiments probing the methyl fragment.

Results

Measurements on Br* display a pronounced anisotropy, with the TOF peakshape depending markedly on the dissociation laser polarization direction (Figure 2).

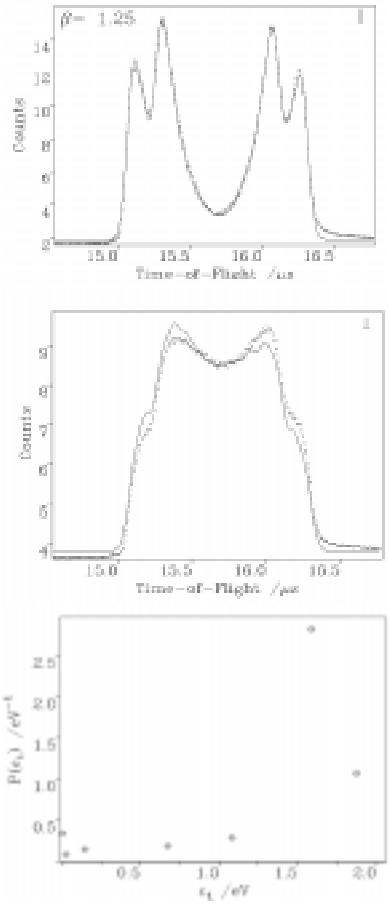

Figure 2. Br* Fragment TOF at 251 nm for two polarization geometries. Structure on peaks reveals Br isotopes**.** Bottom is the distribution of kinetic energy. Solid lines are fit to data.

The derived β parameters are nevertheless reduced at these longer wavelengths indicating an increased role for surface crossings . The Br results are very different, with no perceptible

anisotropy, confirming expectations of substantially mixed perpendicular/parallel excitation for this channel.

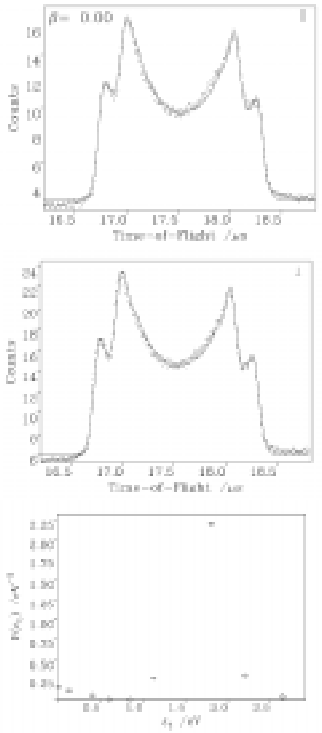

Figure 3. As previous figure for Br photofragment at 250 nm.

REMPI/TOF spectra of 250 nm methyl photofragments were obtained using a second laser to probe the 0_0^0 and 2_1^1 $X \rightarrow 3p_z$ transitions. Attempts were also made to use the corresponding $X \rightarrow 4p_z$ bands, though here there were problems with photolysis induced by the probe laser. Attempts to observe v_2=2 levels via the 2_2^2 band were unsuccessful. Only the central Q branches were observed, despite the successes of these methods in obtaining rotationally resolved branches in CH_3I studies.[4,-6)] Attempts were repeated using jet-cold CD_3Br, for which predissociative losses of intermediate CD_3^* should be much reduced, but again only the intense Q branches were observed.

We ascribe this failure to obtain the known OPRS branch structure to the production of rotationally highly excited methyl fragments, in both the Br and Br^* channels. As a consequence there should be very little population in individual levels with individual transition lying in the noise. The central Q branch is observable first because of the coincidence of many transitions, and second because the line strength factors are two orders of magnitude greater for this branch. Simulations of the observed Q-branch profile support this view, suggesting a rotational temperature of up to 1000 K. In the case of CH_3I it has been shown that the dynamics of curve crossing induce rotational excitation[6)] and the enhanced curve crossing in the red here seems to be even more effective.

The 0_0^0 and 2_1^1 Q-branch REMPI-TOF spectra have been fit with a model which includes the characteristic energy release for fast (Br) and slow (Br^*) channels, an energy width for each, an anisotropy β parameter for each and a Br^*:Br branching ratio. The latter were found to be 0.98±0.18 for v_2=0 and 0.61±0.20 for v_2=1. The energy parameters are freely varied in this fitting, yet they accord well with known constraints: the Br and Br^* channels differ by the known Br spin-orbit splitting of 4.94 eV, the vibrational differences agree with the known v_2 quantum, and the kinetic energy accompanying the ground state methyl in the Br channel is the full excess energy ($h\nu$-D_0) of 1.9 eV.

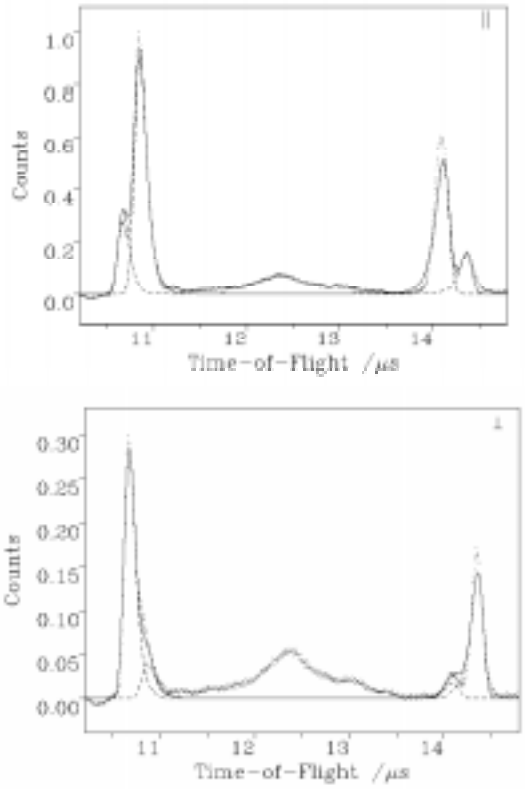

Figure 4. CH_3 (v_2=0) TOF spectrum at 251 nm. Solid line is a fit to experimental data. The non-resonant background signal at 12.3 μs is excluded from the fitting operation.

	CH_3 (+ Br)	CH_3 (+ Br^*)
v_2=0	0.08 ± 0.09	1.88±0.04
v_2=1	0.2±0.2	1.9±0.1

Table 1. Anisotropy parameters, β, obtained from methyl REMPI -TOF at 251 nm.

The low-v methyl fragments in the Br^* channel thus have higher β values than the non-selective Br^* TOF measurements, suggesting that the higher v levels must be more isotropic. Overall we may rationalise these findings in terms of distortion fron C_{3v} symmetry and consequent curve crossing mechanisms, producing rotational and vibrational excitation, along with comparable oscillator strengths for perpendicular and parallel excitations in the extreme red wing of the A-band.

References

1. G N A van Veen, T Baller and A E de Vries, Chem. Phys. 92, 59, (1985)
2. W P Hess, D W Chandler and J W Thoman, Chem. Phys. 163, 277, (1992)
3. T Gougousi, P C Samartzis and T N Kitsopoulos, J. Chem. Phys. 108, 5742, (1998)
4. R O Loo, H P Haerri, G E Hall and P L Houston, J. Chem. Phys., 90, 4222, (1988)
5. D W Chandler, J W Thoman, M HM Janssen and D H Parker, Chem. Phys. Lett., 156, 151, (1989)
6. I Powis and J F Black, J. Phys. Chem., 93 (1989)

Rate coefficients for reactions of C(^{3}P) at the temperatures of interstellar clouds

D Chastaing, P L James, I R Sims, I W M Smith

The University of Birmingham, School of Chemistry, Edgbaston, Birmingham, B15 2TT

Main contact email address: *i.r.sims@bham.ac.uk*

Introduction

Ground state atomic carbon, C ($2p^2\ ^3P_J$), has been detected in a wide range of astronomical environments, and is particularly abundant in dense interstellar clouds (ISCs). Dense by interstellar standards, where the average gas density is ~1 cm^{-3}, these clouds correspond to the laboratory equivalent of an ultra high vacuum, with gas densities of the order of 10^4 cm^{-3}. They are also extremely cold, with temperatures in the range 10 - 50 K. However, owing to their great size, they may contain typically the equivalent of 10 - 100 times the mass of our Sun, and it is within these clouds that the richest variety of interstellar molecules has been observed, including many carbon-containing radicals. The largest confirmed interstellar molecule is $HC_{11}N$, but it is highly probable that much larger species such as polyaromatic hydrocarbons (PAHs) and fullerenes exist as well.

Neutral-neutral reactions of atomic carbon with various hydrocarbon species have been identified by Herbst and co-workers as potentially of great importance in the *synthesis* of larger carbon-containing species, employing successive insertion-elimination reactions of the type: [1)]

$$C + C_nH_m \rightarrow C_{n+1}H_{m-1} + H \qquad (1)$$

Following the kinetic measurements of Husain and co-workers on reactions of atomic carbon with a wide range of hydrocarbon species at room temperature, the theoretical work of Clary and co-workers has pointed to the continued rapidity of such reactions down to the temperatures prevailing in dense ISCs.[2,3)]

Our studies of the kinetics of neutral-neutral reactions at extremely low temperatures are conducted in the Birmingham CRESU apparatus, one of only two such facilities world-wide which enable accurate rate coefficients for such reactions to be measured down to the temperatures prevailing in dense ISCs. CRESU is a French acronym standing for *Cinétique de Réaction en Ecoulement Supersonique Uniforme* or *Reaction Kinetics in Uniform Supersonic Flow*.

The experiments of Husain and co-workers[2-6)] employed time-resolved atomic resonance absorption spectroscopy to monitor the C(^{3}P) concentration directly via the ($3s^3P - 2p^3P$) resonant transition at 166 nm. Carbon atoms were created by VUV photolysis ($\lambda \leq 160$ nm) of carbon suboxide (C_3O_2) using a coaxial flash lamp. The authors report rapid room temperature rates for reactions with unsaturated hydrocarbons, NO and O_2. Becker and co-workers[7)] used the PLP-LIF technique to study kinetics of the reactions of atomic carbon with NO and O_2 in a flow cell at room temperature. Ground state carbon atoms were produced by multiphoton dissociation of CH_2Br_2 at 248 nm, and monitored by two-photon laser induced fluorescence at 143.5 nm ($^3P_2 - {}^3D_3$ transition).

Experimental

The CRESU method, as applied to neutral-neutral reactions, has already been described in detail by Sims *et al.*[8)] Full specifications of the Birmingham CRESU apparatus have also been given recently by James *et al.*[9)]

The heart of the CRESU apparatus is an axisymmetric Laval nozzle. It is mounted on a reservoir equipped with a perforated Teflon disc to ensure laminar flow and good mixing of the gas streams entering the reservoir. All the temperatures in the gas flows were achieved by the isentropic expansion of the gas mixture prepared in the reservoir through the nozzle and into the main chamber. This expansion generates a supersonic flow of gas in which the Mach number, the temperature, the density of the gas, the mole fraction of the co-reagent and the velocity of the gas stream are constant along the axis of the flow.

C(^{3}P) atoms were created by the pulsed laser photolysis of carbon suboxide, C_3O_2, using the 193 nm radiation from one of two similar excimer lasers (Lambda-Physik, Compex 102 or Compex 202, from the LSF Loan Pool), equipped with unstable resonator optics to give the required low-divergence beam, and operating on ArF at a repetition frequency of 10 Hz.

C_3O_2 was synthesised via the dehydration of *bis*(trimethylsilyl) malonate (Aldrich), and stored in a collection vessel. When required, the collection vessel was surrounded by an acetone / dry ice slush. The C_3O_2 has a vapour pressure of approximately 20 Torr at this temperature (–60 °C).

A cylinder of high purity argon (Air Products) provided a regulated flow (~10—100 standard cm^3 $minute^{-1}$) of buffer gas, which bubbled through the liquid C_3O_2 and was saturated with C_3O_2 vapour. The absolute concentration of C_3O_2 within the CRESU flow was estimated to be $\leq 10^{10}$ molecules cm^{-3}.

The progress of reaction was monitored by a chemiluminescent marker technique, resembling that used in our study of the kinetics of C_2H radical reactions in the CRESU apparatus.[10)] In each series of experiments, a constant concentration of NO_2 was added to the CRESU flow, along with the C_3O_2 precursor, and appropriate reagent and buffer gases. C(^{3}P) atoms produced in the photolysis then reacted at a constant rate with the NO_2, which was in large excess over the C_3O_2:

$$C(^3P) + NO_2 \rightarrow CO + NO \qquad (2)$$

Dorthe *et al.*[11)] observed chemiluminescence resulting from both NO($B^2\Pi$) and NO($A^2\Sigma^+$) products from this reaction. The chemiluminescence was gathered in the CRESU apparatus by an optically fast collection arrangement, and the (0,8) β-band NO($B^2\Pi$—$X^2\Pi$) emission isolated using an interference filter centred at 320 nm (10 nm FWHM), before being imaged on to the photocathode of a sensitive photomultiplier tube (Electron Tubes, type 9125 MgFlB). The radiative lifetime of NO ($B^2\Pi$; $v' = 0$) is short (2.0 μs) relative to the lifetime of the kinetic decays, and so its concentration rapidly reached a steady state value which was directly proportional both to the intensity of the emission and to the concentration of the carbon atoms. The resulting signal was transferred via an appropriate load resistor to a 200 MHz digital oscilloscope (Tektronix, model TDS350), which averaged emission traces from 128 laser shots before the resultant data were transferred to a PC. Typically, this procedure was repeated four times, so that the traces that were analysed were the result of 512 individual experiments. In addition, under some conditions it was necessary to perform a background subtraction to allow for the effects of scattered light. The background trace was recorded by omitting NO_2 from the gas mixture, leaving all other conditions the same.

The flows of NO_2 (SIP Gases), the co-reagent (O_2, C_2H_2, C_2H_4 or C_3H_6; Air Products), and the carrier gas (He, Ar or N_2; Air Products) were taken directly from the cylinders and regulated by means of mass flow controllers (MKS). The C_2H_2 was passed through a trap immersed in cooled methanol at –40 °C to remove any residual acetone resulting from the storage method.

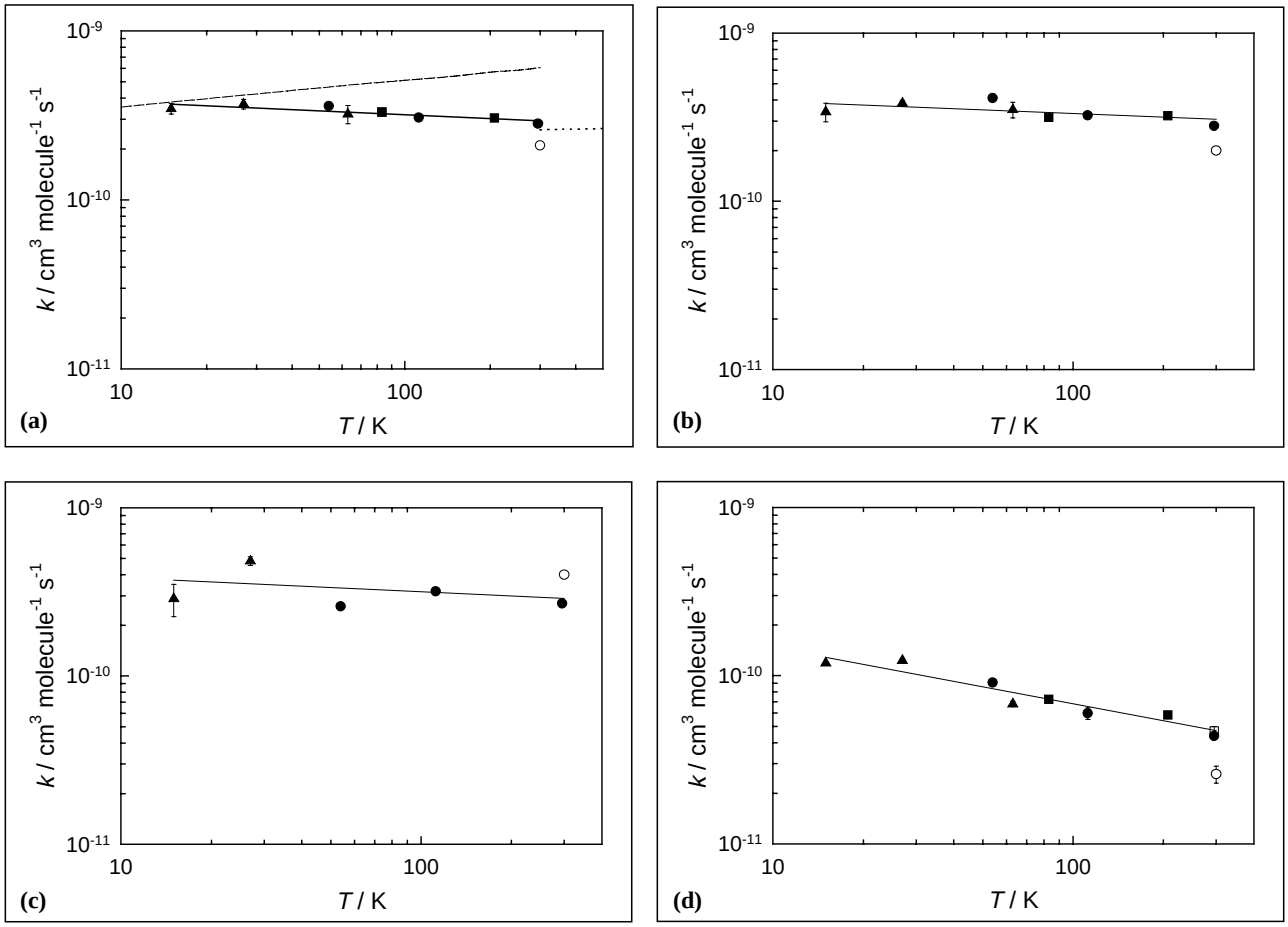

Figure 1. Rate coefficients *k* for the reaction of C(^{3}P) atoms plotted on a log-log scale against temperature. The filled symbols show the results of this work: circles (●) denoting Ar carrier gas; squares (■) N_2; and triangles (σ) He: **(a)** C + C_2H_2: the room temperature result of Haider and Husain[2] is shown as an open circle (○). The solid line shows the result of a non-linear least-squares fit to the data giving $k = 2.9 \times 10^{-10}$ $(T / 298\ K)^{-0.08}$ cm^3 molecule^{-1} s^{-1}. The dashed line (– – –) shows the results of a capture calculation performed by Liao and Herbst,[14] while the dotted line (· · · ·) represents the VRRKM calculation of Guadagnini et al..[13] **(b)** C + C_2H_4: the room temperature result of Haider and Husain[2] is shown as an open circle (○). The solid line shows the result of a non-linear least-squares fit to the data giving $k = 3.1 \times 10^{-10}$ $(T / 298\ K)^{-0.07}$ cm^3 molecule^{-1} s^{-1}; **(c)** C + C_3H_6: the room temperature result of Haider and Husain[5] is shown as an open circle (○). The solid line shows the result of a non-linear least-squares fit to the data giving $k = 2.9 \times 10^{-10}$ $(T / 298\ K)^{-0.08}$ cm^3 molecule^{-1} s^{-1}; **(d)** C + O_2: the room temperature results of Husain and Young[6] and Becker et al.[7] are shown as an open circle (○) and an open square (□) respectively. The solid line shows the result of a non-linear least-squares fit to the data giving $k = 4.7 \times 10^{-11}$ $(T / 298\ K)^{-0.34}$ cm^3 molecule^{-1} s^{-1}.

Results and Discussion

Experiments to determine the kinetic behaviour of carbon atom reactions with a reagent R (R = O_2, C_2H_2, C_2H_4 or C_3H_6) were performed both at room temperature in a subsonic flow, and at low temperatures ranging from 15 K to 204 K in He, Ar or N_2 buffer gases, using a number of Laval nozzles. The flows contained a small concentration of C_3O_2 (estimated to be less than 10^{10} molecule cm^{-3}), a constant concentration of NO_2 (~10^{14} molecule cm^{-3}), and a variable concentration of reagent, R (ranging up to ~10^{14} molecule cm^{-3}), in a buffer gas of density in the approximate range 10^{16} - 10^{17} molecule cm^{-3}.

Values of the second-order rate coefficients k_R were established by a series of experiments in which [R] was varied whilst [NO_2] was kept constant. The temperature-dependence of the rate coefficients for these reactions of C(^{3}P) is displayed in Figure 1.

The magnitudes of the rate coefficients for the reactions of carbon atoms with C_2H_2, C_2H_4 and C_3H_6, and their very slight increase as the temperature is lowered, are consistent with the initial formation of an energised complex in which the radical attacks a π-orbital in the unsaturated hydrocarbon with a rate which is determined by capture on a potential energy surface (or potential energy surfaces) with no barrier. This mechanism is supported by the crossed molecular beam experiments of Kaiser *et al.*[12] who report the explicit identification (under single collision conditions) of the reaction products corresponding to carbon atom insertion followed by rapid hydrogen elimination, i.e. C_3H (from C_2H_2), C_3H_3 (from C_2H_4) and C_4H_5 (from C_3H_6). The overall reactions may be represented as:

$$C + C_nH_m \rightarrow C_{n+1}H_{m-1} + H \qquad \text{(1 above).}$$

Atomic carbon has, as noted above, three closely spaced spin orbit states. C($^3P_1$) lies 16.4 cm^{-1} (≡ 23 K) above the ground state $^3P_0$, and the upper spin orbit state, $^3P_2$, lies 43.4 cm^{-1} (≡ 62 K) above ground. At room temperature, all of these states will have an appreciable population. However, at the lowest temperatures of the present experiments, only the lowest $^3P_0$ state will be appreciably populated. A strong negative temperature dependence for such reactions would suggest that collisions between reactant and carbon atoms in the lowest spin orbit state are more likely to lead to reaction than collisions between reactant and carbon atoms in the higher spin orbit states. However, these reactions show only a very slight temperature dependence, which suggests that reaction can occur with similar probabilities from all spin orbit states. Furthermore, the magnitude of the rate coefficients suggests that reaction occurs essentially on every collision.

The reaction of $C(^3P)$ with C_2H_2 has been the subject of two recent theoretical studies, employing differing but complementary techniques. Guadagnini, Schatz and Walch[13] performed high-level ab-initio calculations along the minimum-energy reaction path, and then calculated rate coefficients in the range T = 300—1000 K using the variational RRKM (VRRKM) method. They obtained a value for the rate coefficient at room temperature of ($k = 2.6 \times 10^{-10}$ cm^3 molecule^{-1} s^{-1}), in very good agreement with the result from this present study. Furthermore, they found essentially no temperature dependence up to 1000 K.

Liao and Herbst[14] performed capture calculations using the ACCSA approach of Clary and co-workers, and obtained rate coefficients which, while they are too large at higher temperatures, do converge with experiment at the lowest end of the temperature range. Capture theories based on long-range potentials would be expected to work best at the lowest temperatures, and this is also in accord with findings for CN reactions. The products of this reaction are almost certainly C_3H + H. Both cyclic and linear forms of C_3H are seen in the cold, dark cloud TMC-1, and this reaction may be responsible for their abundance. Clearly, direct measurements of product branching ratios at ultra-low temperatures are required.

The finding that carbon atoms react rapidly with simple unsaturated hydrocarbons lends strong support to the proposal that such reactions could play an important role in the chemistry of cold interstellar clouds. The synthesis of carbon-rich hydrocarbon radicals in the interstellar medium via reactions of type (1) appears to represent a more realistic route than the previously postulated ion-molecule reaction networks. The much higher concentrations of neutral species compared to ions would more than compensate for the somewhat greater rate coefficients of ion-molecule reactions at the temperatures of dense ISCs.

The rate coefficients for the reaction of ground state atomic carbon with the diradical O_2 ($X\ ^3\Sigma_g^-$) are lower than those for the reactions of $C(^3P)$ with the unsaturated hydrocarbons and display a stronger, though still slight, negative temperature dependence ($T^{-0.34}$). This behaviour is characteristic of radical-radical reactions occurring on attractive potential surfaces. [8]

The only published calculation of rate coefficients for the reaction between $C(^3P)$ atoms and O_2, to our knowledge, is the 1977 study of Kinnersly and Murrell.[15] They derived an analytical form for the relevant potential surfaces, and performed classical trajectory calculations to obtain the rate coefficient over the temperature range 300 - 800 K. They obtained a result in reasonable agreement with experiment at room temperature ($k = 1.92 \times 10^{-11}$ cm^3 molecule^{-1} s^{-1}), but predicted a mild positive temperature dependence, in disagreement with our results extrapolated to higher temperatures. Clearly, it would be interesting to compare our results with calculations performed on *ab-initio* potential surfaces calculated using the latest methods.

Summary and Conclusions

We have measured rate coefficients for the reactions of ground-state carbon atoms, $C(^3P)$, with C_2H_2, C_2H_4, C_3H_6 and O_2 at temperatures from 295 down to 15 K in a CRESU apparatus, using a combination of pulsed laser photolysis to generate, and a chemiluminescence marker technique to follow the concentration of, $C(^3P)$ atoms. The rate coefficients for all four reactions increase as the temperature is lowered, and those for reactions with the unsaturated hydrocarbons exceed 2×10^{-10} cm^3 molecule^{-1} s^{-1} at all temperatures below 300 K. These reactions would appear to proceed via an addition-elimination mechanism, resulting in an increase in carbon chain length, and must take place on potential surfaces without significant barriers to initial complex formation. It therefore seems likely that these reactions – and similar ones involving $C(^3P)$ atoms and other hydrocarbons – play an important role in forming species with long carbon chains in dense interstellar clouds.

Acknowledgements

We are grateful to EPSRC for a substantial research grant to construct the CRESU apparatus, and for an Advanced Fellowship to one of us during the time these experiments were performed (IRS). We also thank EPSRC and the EU (under its TMR programme) for studentships (PLJ and DC, respectively). The EPSRC Laser Loan Pool at the Rutherford Appleton Laboratory provided one of the excimer lasers, for which we express our thanks. We are also very grateful to Dr Bertrand Rowe and his colleagues at Rennes for valuable advice and discussions, to Dr Sébastien Le Picard for discussions and assistance with the CO relaxation measurements, and to Stuart Arkless, Tony Rothin and Steve West for their skilled technical assistance.

References

1. R. P. A. Bettens and E. Herbst
Astrophys. J., 478, 585, (1997)

2. N. Haider and D. Husain
J. Photochem. Photobiol., A, 70, 119, (1993)

3. D. C. Clary, N. Haider, D. Husain, and M. Kabir
Astrophys. J., 422, 416, (1994)

4. D. Husain and L. J. Kirsch
Trans. Faraday Soc., 67, 2025, (1971)

5. N. Haider and D. Husain
J. Chem. Soc., Faraday Trans., 89, 7, (1993)

6. D. Husain and A. N. Young
J. Chem. Soc., Faraday Trans. 2, 71, 525, (1975)

7. K. H. Becker, K. J. Brockmann, and P. Wiesen
J. Chem. Soc. Faraday Trans. 2, 84, 455, (1988)

8. I. R. Sims, J. L. Queffelec, A. Defrance, C. Rebrion-Rowe, D. Travers, P. Bocherel, B. R. Rowe, and I. W. M. Smith
J. Chem. Phys., 100, 4229, (1994)

9. P. L. James, I. R. Sims, I. W. M. Smith, M. H. Alexander, and M. B. Yang
J. Chem. Phys., 109, 3882, (1998)

10. D. Chastaing, P. L. James, I. R. Sims, and I. W. M. Smith
Faraday Discussions, 109, 165, (1998)

11. G. Dorthe, J. Caille, S. Burdenski, P. Caubet, M. Costes, and G. Nouchi
J. Chem. Phys., 82, 2313, (1985)

12. R. I. Kaiser, D. Stranges, Y. T. Lee, and A. G. Suits
Astrophys. J., 477, 982, (1997)

13. R. Guadagnini, G. C. Schatz, and S. P. Walch
J. Phys. Chem. A, 102, 5857, (1998)

14. Q. Liao and E. Herbst
Astrophys. J., 444, 694, (1995)

15. S. R. Kinnersly and J. N. Murrell
Mol. Phys., 33, 1479, (1977)

Rate Coefficients for the Reaction and Relaxation of H_2O in Specific Vibrational States with H Atoms and H_2O

P Barnes, P Sharkey, I R Sims, I W M Smith

School of Chemistry, University of Birmingham, Edgbaston, Birmingham B15 2TT, U.K.

Main contact email address: *i.w.m.smith@bham.ac.uk*

Introduction

The notion of selectively promoting chemical reactions by the excitation of particular vibrational modes in the reagents has been proposed for some years. In order to explore this possibility it is necessary to proceed beyond the generic three-atom reaction A + BC → AB + C, where there is only one reagent vibration. In recent years, the exothermic reaction between OH radicals and H_2, and the reverse endothermic reaction between H atoms and H_2O

$$OH + H_2 \rightarrow H_2O + H \qquad \Delta_rH^\theta = -63.3 \text{ kJ mol}^{-1} \qquad (1, -1)$$

has become the prototype of four-atom reactions for both experiment and theory. The groups of Crim [1] and Zare [2] have demonstrated dramatic bond selectivity in reaction (-1) by exciting H_2O to specific vibrational levels by overtone band absorption. Among other things, Crim et al. showed that, whereas OH is formed in v = 0 when H atoms react with H_2O ($|04>^-$), it is formed mainly in v = 1 when H atoms react with H_2O ($|13>^-$), demonstrating that the two OH stretching modes in H_2O act essentially as 'local modes', so that sufficient excitation deposited in one of them can lead to selective breaking of that bond in reaction with H atoms. This conclusion was beautifully confirmed by experiments on the reaction between H atoms and HOD in which it was demonstrated that the reaction products were either OD + H_2 or OH + HD, depending on whether the OH or OD stretching mode in HOD was excited.

Although the work of Crim and Zare showed that reaction (-1) is dramatically accelerated by excitation of the H_2O molecule in its stretching vibrations, they made no attempt to quantify this enhancement. The aim of our experiments is to determine rate coefficients for reaction between H atoms (and ultimately other radical atoms) with H_2O in specified vibrational states. This is accomplished by performing kinetic experiments in a discharge-flow system containing known steady-state concentrations of H atoms. LIF is then observed from the OH produced in reaction (-1) as a function of time following the firing of a pulsed laser which excites H_2O molecules to a specific local mode state. In this way we have obtained data for five levels of H_2O: $|04>^-$, $|13>^-$, $|03>^-$, $|12>^-$ and $|02>^-2>$. Our results have been reported in a preliminary communication[3] and at the Faraday Discussion on Stereochemistry and Control in Chemical Reactions.[4]

Experimental Method

Full details of our experimental method can be found in References 3 and 4. In brief, the experiments use (i) a discharge-flow system to prepare mixtures of H atoms (and undissociated H_2) and H_2O diluted in Ar, and (ii) two pulsed tunable lasers, one to prepare H_2O in a selected vibrational level and the other to observe either the OH (v=0) or OH (v=1) product of reaction. The concentration of H atoms is determined by titration with NO_2 and a known concentration of H_2O is introduced into the flowing gas using a combination of a 'bubbler' and a trap maintained at a lower constant temperature than the bubbler. For each H atom concentration, a series of measurements were made, each at a different concentration of H_2O.

The 'pump' laser radiation is either produced directly from a tunable dye laser or, for longer wavelengths, is generated by shifting the frequency of radiation from a dye laser by the stimulated Raman effect in H_2. The 'probe' laser excites 'off-resonance' LIF signals from OH. Thus to observe OH (v=0), formed in reactions where all the excitation of the H_2O stretching vibrations was in one local mode, LIF was excited at 282 nm and observed at 308 nm. OH (v=1) was observed by exciting LIF at 312 nm and observing at 282 nm. Signals were recorded as the time delay between pairs of pulses from the pump and probe lasers was systematically varied. Typical traces are displayed in Figure 1.

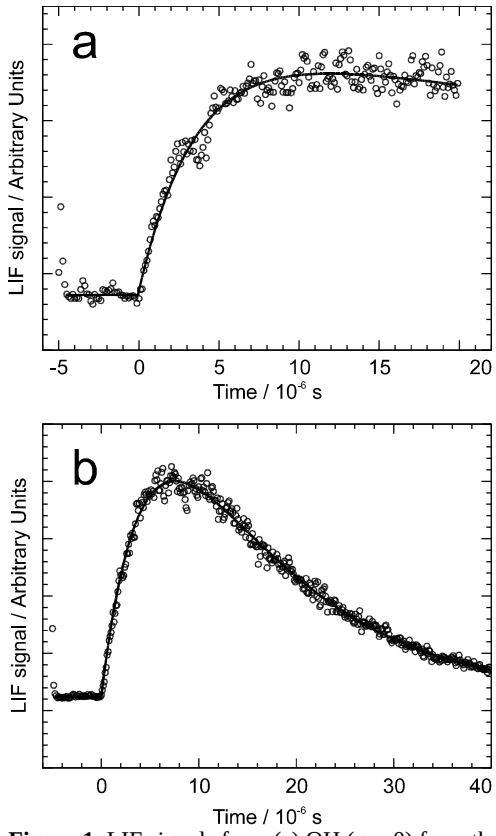

Figure 1. LIF signals from (a) OH (v = 0) from the reaction of H atoms with H_2O ($|04>^-$), and (b) OH (v = 1) from H + H_2O ($|13>^-$).

Results and Discussion

Traces like those shown in Figure 1 are fitted to generate two first-order rate constants, one for loss of vibrationally excited water and one either for removal of OH (v=0) by diffusion or for relaxation of OH (v=1).

In each series of experiments, the first-order rate constants are plotted against the concentation of H_2O present. The gradients of these lines give second-order rate coefficients for the relaxation of H_2O in the selected vibrational state and, where appropriate, for relaxation of OH (v = 1) by collisions with H_2O molecules. The intercepts yield information about the processes involving H atoms: removal of H_2O and relaxation of OH (v=1).

The final results of these analyses are given in Table 1.

	removal of excited H_2O		relaxation of OH(v = 1)	
	by H atoms	by H_2O	by H atoms	by H_2O
$H_2O\|04\rangle^-$	4.3 ± 1.6[a] (16.7)	2.0 ± 0.8 (24.0)	–	–
$H_2O\|13\rangle^-$	3.0 ± 0.8 (11.7)	1.7 ± 0.4 (20.4)	1.5±0.4 (5.8)	0.2
$H_2O\|03\rangle^-$	3.0 ± 1.0 (11.7)	3.7 ± 1.4 (44.4)	–	–
$H_2O\|12\rangle^-$	0.48 ± 0.12 (1.9)	1.7 ± 0.5 (20.4)	1.4 ± 0.12 (5.4)	0.4 ± 0.14
$H_2O\|12\rangle^-2\rangle$	0.8 ± 0.3 (3.1)	1.5 ± 0.3 (18.0)	–	–

TABLE 1. Rate constants (10^{-10} cm^3 $molecule^{-1}$ s^{-1}) and, in brackets, thermally averaged cross-sections ($Å^2$) for removal of vibrationally excited H_2O and relaxation of OH (v = 1).

The data listed in Table 1 are essentially unique - there are very few similar results, from experiment or theory, with which to compare. Nearly all the rate coefficients listed in Table 1 are near to their gas kinetic limiting values; that is, the collisional probabilities are close to unity. The unusually high efficiency of the vibrational self-relaxation of H_2O has been observed before for lower lying vibrational levels, and it presumably arises because of the strong, anisotropic, dipole-dipole forces that act between water molecules.

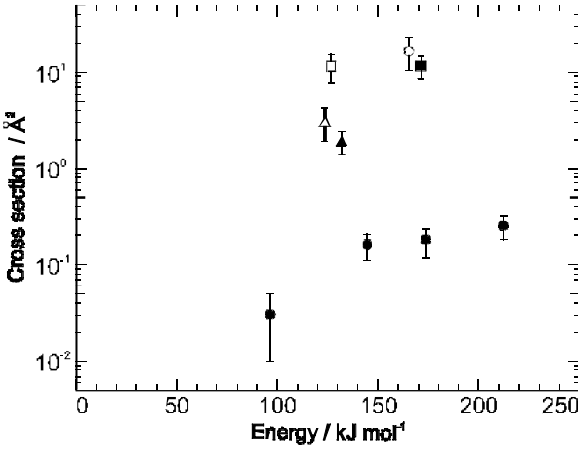

Figure 2. Comparison between the thermally averaged cross-sections derived from our rate coefficients for removal of H_2O from specific vibrational levels by H atoms: $|13\rangle^-$, ■; $|04\rangle^-$, ○; $|03\rangle^-$, □; $|02\rangle^-2\rangle$, Δ; $|12\rangle^-$, ▲ with those determined by Wolfrum and co-workers (●) for the reaction of translationally 'hot' H atoms with H_2O.

It is important to appreciate that our measurements on the removal of vibrationally excited H_2O by H atoms do not distinguish between reaction and relaxation, and our rate coefficients therefore correspond to sums of those for these two processes. However, in contrast to earlier studies, the latest calculations of Schatz's group [5] give large rate coefficients for reaction and suggest that reaction occurs at rates that are, at least comparable, to those of relaxation.

If our measured rate coefficients arise predominantly through reaction, then the reaction is accelerated by approximately 15 orders-of-magnitude compared with that between H atoms and vibrationally unexcited H_2O on excitation of the H_2O reagent to vibrational levels above threshold. However, the selectivity of energy consumption is only tested properly by comparing the cross-section for reaction from a specific vibrational state with that for reaction with the same amount of collisional energy. In Figure 2 we compare our thermally averaged cross-sections against those measured for reaction of translationally 'hot' H atoms with unexcited H_2O at collision energies from 1.0 to 2.2 eV. It can be seen that the thermally averaged cross-sections for vibrationally enhanced removal of H_2O are roughly two orders-of-magnitude larger than those where the same amount of energy is present in relative translational motion, suggesting that the reaction is selectively promoted by vibrational excitation of the H_2O reagent, a conclusion which is entirely in keeping with expectation for a strongly endothermic direct reaction.

Conclusions and Future Work

In addition to data on the relaxation of vibrationally excited H_2O and OH, we have measured the first rate coefficients for removal of H_2O in specific vibrational states in collisions with H atoms. The variation of these rate coefficients with state show that it is the energy within the most strongly excited stretching mode that determines the magnitude of the rate coefficient. This observation, as well as other evidence, suggests that reaction to produce OH + H_2 makes a major contribution to the observed rate coefficients.

A number of extensions to the present work are planned. Our first aim is to determine the branching ratio for reaction to relaxation, at least for H +H_2O ($|04\rangle^-$). This aim will be achieved by comparing the yield of OH (v = 0) from this reaction with that obtained when vibrationally excited H_2O molecules are photodissociated with a pulsed laser operating at 266 nm. Secondly, we wish to determine rate coefficients for H + H_2O ($|02\rangle^-$) where the total energy only just exceeds the minimum required for the endothermic reaction (-1).

In the longer term, we intend to extend our measurements to a wider range of systems comprising radical atoms and triatomic molecules. The first of these will be H + HOD which will provide more data on the prototypical H + H_2O system. Later we shall use other atoms, especially O(^{3}P) and Cl, and HCN, as well as H_2O in these measurements.

References

1. (a) F.F. Crim, J. Phys. Chem., 1996, 100, 12725:
(b) A. Sinha, M.C. Hsiao and F.F. Crim, J. Chem. Phys., 1991, 94, 4928;
(c) R.B. Metz, J.D. Thoemke, J.M. Pfeiffer and F.F. Crim, J. Chem. Phys., 1993, 99, 1744.

2. M.J. Bronowski, W.R. Simpson and R.N. Zare, J. Phys. Chem., 1993, 97, 2194;

3. G. Hawthorne, P. Sharkey and I.W.M. Smith, J. Chem. Phys., 1998, 108, 4693.

4. P.W. Barnes, P. Sharkey, I.R. Sims and I.W.M. Smith, Faraday Discuss. 1999, 113, in press.

5. G.C. Schatz, G. Wu, G. Lendvay, D.-C. Fang and L.B. Harding, Faraday Discuss. Chem. Soc., 1999, 113, in press.

6. A. Jacobs, H.R. Volpp and J. Wolfrum, J. Chem. Phys., 1994, 100, 1936.

Vibrational Energy Transfer in Polyatomic Molecules: Energy Transfer in Collisions of Highly Excited NCNO with He, Ar and N_2

S M A Wright, I R Sims, I W M Smith

School of Chemistry, University of Birmingham, Edgbaston, Birmingham B15 2TT, U.K.

Main contact email address: *i.w.m.smith@bham.ac.uk*

Introduction

The transfer of energy in collisions involving polyatomic molecules with large amounts of internal energy is a subject of intense interest at the present time and is much less well-understood than the vibrational relaxation of small molecules in low states of excitation. The ultimate aim is to measure the distribution function P(E'|E) which defines the distribution of final state energies E' following single collisions between the polyatomic molecule with internal energy E and the collision partner M. In practice, one currently has to be satisfied with measures of <ΔE>, the mean energy transferred from the polyatomic molecule, with <E>, the average internal energy of the ensemble of molecules. To compare with data we have obtained with 'large' molecules such as toluene and pyrazine, we have chosen to study energy transfer in nitrosyl cyanide, NCNO.

The threshold for photodissociation of NCNO has been determined as 585.3 nm, whilst its visible absorption spectrum extends from about 550 to 850 nm.[1] Thus by absorption of photons at wavelengths > 585.3 nm, NCNO molecules can be prepared that have high amounts of internal energy but that are stable with respect to dissociation. In our experiment, NCNO was excited with photons from a dye laser generally tuned to 600 nm. Following radiationless processes, this scheme prepares NCNO molecules in the electronic ground state with a well-defined amount of vibrational energy. The subsequent vibrational relaxation of NCNO was followed by observing infrared fluorescence at ca. 2170 cm^{-1}, corresponding to the CN stretch fundamental vibration in the NCNO molecule. The traces of infrared emission intensity with time were transformed into curves of <ΔE> with <E> using the methods pioneered by J.R. Barker and co-workers.[2]

Experimental Method

NCNO was synthesised by standard methods and was used in mixtures of 1 - 2% in one of the three gases He, Ar or N_2. These mixtures were irradiated with the output from a pulsed dye laser. In most experiments, the laser was tuned to 600 nm (ca. 420 cm^{-1} below the threshold for photo-dissociation) though some experiments were conducted at somewhat longer wavelengths. Infrared emission was observed using a liquid N_2 cooled InSb detector The long wavelength cut-off and the use of a long wavelength pass filter ensured that the only emission observed would be that associated with fundamental transitions in the ν_1, CN stretching, vibration. Two typical traces of this emission are shown in Figure 1.

Results and Discussion

Traces like those shown in Figure 1 exhibit a finite rise time and usually a slower decay. Although further work needs doing to establish the origin of the rise, it is consistent with the notion that, in small molecules like NCNO, the species excited by the absorption of laser photons to states of predominantly S_1 character return to the S_0 electronic ground-state by collisionally assisted processes. The decaying portion of the emission traces is interpreted as reflecting the collisional relaxation of NCNO molecules that are vibrationally excited in the electronic ground state as a result of collisions with the dilutent gas. The first part of the analysis is to fit this part of the curve to a single exponential. In order to relate the derived first-order constants to a function describing how <ΔE>, the mean amount of energy removed per collision, depends on <E>, the mean internal energy of the NCNO, it is necessary to do two things: (i) convert the first-order constants in terms of s^{-1} to a constant in terms of $(collisions)^{-1}$, and (ii) relate the relative intensities of emission to the energy content of the emitting molecules. This latter transformation was performed using the normal assumption[2] that the internal energy is statistically shared between the oscillators of the molecule at all significant internal energies. Figure 2 shows plots of <ΔE> against <E> for the three colliders that have been investigated, He, Ar and N_2.

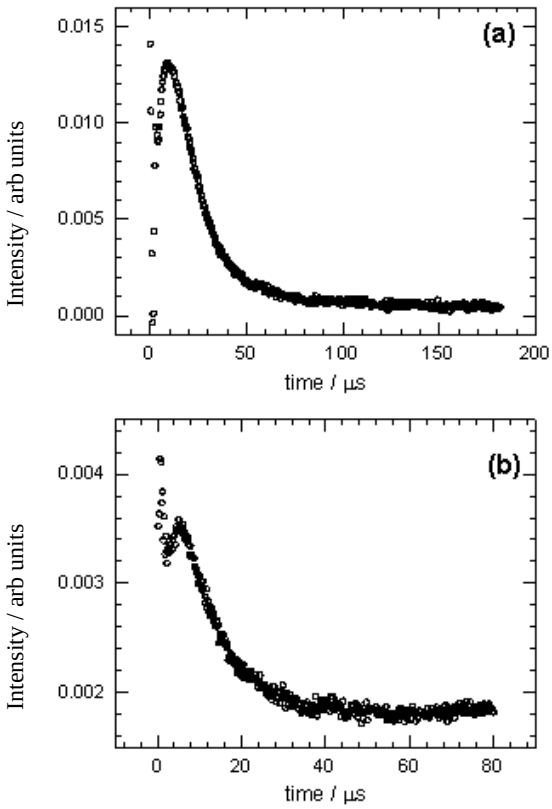

Figure 1. Decays of infrared fluorescence from NCNO excited (a) at 600 nm in a 1% mixture in Ar at 100 Torr; and (b) at 640 nm in a 2% mixture in He at 100 Torr.

There are two distinct ways in which the data which we have measured for NCNO differs from the extensive data on energy transfer in aromatic molecules such as azulene, pyrazine and toluene that has been obtained by Barker's group and ourselves.

First, the collision efficiencies of He, Ar and N_2 with NCNO are all essentially the same, whereas for the aromatic species the efficiencies increase in the order He to Ar to N_2. Secondly, the amounts of energy removed per collision are roughly two orders-of-magnitude smaller in the case of NCNO. In both respects, and not surprisingly, the present data is more akin to the results found for relaxation of NO_2, CS_2 and SO_2. One way in which the data for NCNO differ from those molecules is that we find a smooth variation of <ΔE> with <E>. In the triatomic molecules that have been studied at high levels of excitation, there is evidence that the collisional efficiency decreases when

e internal energy falls below that of low-lying electronically cited states.

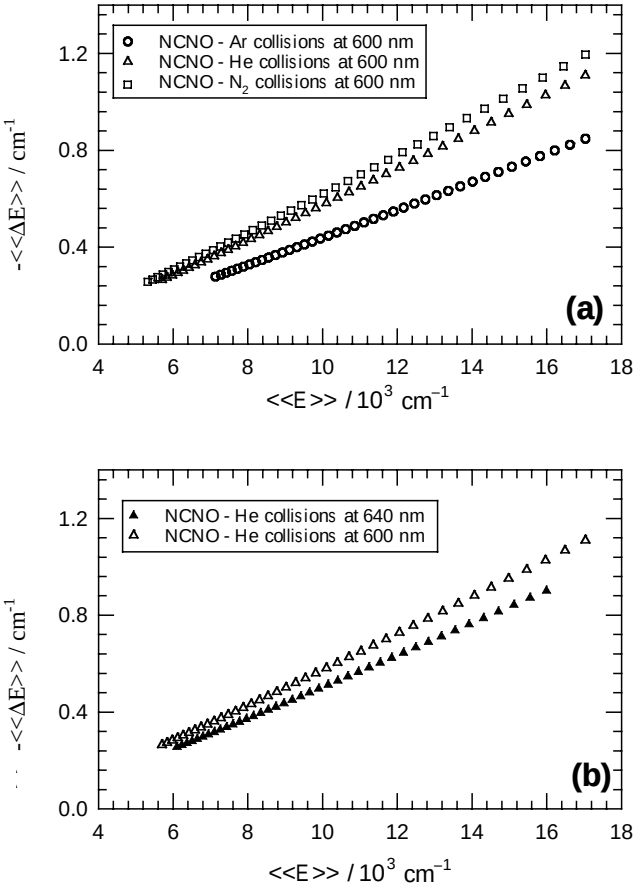

Figure 2. Plots of mean energy removed versus mean energy content: (a) deactivation by He, Ar and N_2 following excitation at 600 nm; and (b) deactivation by He following excitation at 600 nm and 640 nm

Conclusions and Future Work

The results reported here are preliminary and we hope to extend our information on collisional energy transfer in NCNO aided by future laser loans. As well as further studying relaxation at high levels of excitation by the method described here, we shall, in the near future, perform experiments to investigate collisionally-induced dissociation from levels of excitation just below the dissociation limit. In these experiments, one tunable laser will excite NCNO molecules at wavelengths only slightly longer than the threshold at 585.3 nm, and a second tunable laser will interrogate the fragments, CN and NO, of collisionally-induced dissociation.

References

1. (a) I. Nadler, J. Pfab, H. Reisler and C. Wittig, J. Chem. Phys., 1984, 81, 653;
(b) I. Nadler, M. Noble, H. Reisler and C. Wittig, J. Chem. Phys., 1985, 82, 2608.

2. (a) J.R. Barker, J. Phys. Chem., 1984, 88, 11;
(b) J. Shi, D. Bernfeld and J.R. Barker, J. Chem. Phys., 1988, 88, 6211;
(c) J. Shi and J.R. Barker, J. Chem. Phys., 1988, 88, 6219.

Conformational landscapes in molecular and biomolecular systems

J P Simons, E G Robertson, M R Hockridge

Physical and Theoretical Chemistry Laboratory, South Parks Road, Oxford, OX1 3QZ

Main contact email address: *jpsimons@physchem.ox.ac.uk*

Introduction

Inter- and *intra*-molecular hydrogen-bonded interactions are a universal feature of biomolecular architectures, influencing their electronic charge distributions, conformational landscapes and *supra*-molecular structures. There is a subtle balance between *intra*-molecular and *inter*-molecular bonding, for example between an amide group and neighbouring groups on a peptide chain, or an amide group and neighbouring solvent molecules, such as water. The free jet expansion coupled with LIF or R2PI detection and rotational band contour analysis, provides a powerful strategy for probing both conformational and *supra*-molecular structure. It becomes even more powerful when it is reinforced by ion-dip spectral 'hole-burning' experiments. Mass selected detection permits the identification of size-selected hydrated clusters (as well as their molecular hosts) while the 'hole-burning' experiments enable their spectral features to be separately isolated. Structural assignments can be achieved through analysis of the rotational and/or vibrational band contours of the isolated features, aided crucially, by the predictions of *ab initio* computation.

N-Phenyl Formamide

N-Phenyl formamide (formanilide) is one of the simplest aromatic amides and provides a model of the peptide bond. Previous work in this laboratory[1] and elsewhere[2] has shown that both the cis and trans isomers are observed in the jet expansion. We undertook a study of the hydrated clusters of formanilide using LIF, R2PI and ion-dip spectral holeburning techniques, aided by the loan of a tunable uv laser from the LSF.[3]

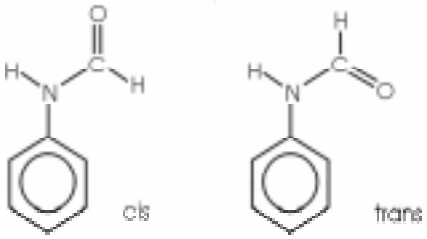

An R2PI spectrum of formanilide and associated water clusters is shown in Figure 1. The cis and trans origins of the molecule are labelled A and B. The R2PI spectra in the $FA(H2O)_n^+$ mass channels, together with the hole-burning spectra shown in Figures 2**,** reveal the presence of five distinct hydrated clusters of formanilide, labelled C-G. Under 1-colour ionisation conditions, species D and F partially fragment into the FA^+ mass channel (with efficiencies of *ca*. 25% and 60% respectively – although these percentages may be affected by 3-photon excitation processes), suggesting their assignment to 1:1 water clusters. The band system labelled 'C', which appears in both the $FA(H_2O)^+$ and $FA(H_2O)_2^+$ mass channels, is assigned to a 1:2 hydrated cluster. Species E shows no signal in the FA^+, or the $FA(H_2O)_2^+$ mass channels; if it were a 1:1 water cluster, then it would appear not to fragment at all but given the fragmentation patterns of the other hydrated clusters, a more likely assignment would be to a 1:2 water cluster that loses one water molecule with 100% efficiency. The latter assignment is supported by the change in the observed relative cluster populations as the jet expansion conditions are varied and by the rotational band contour analysis which follows.

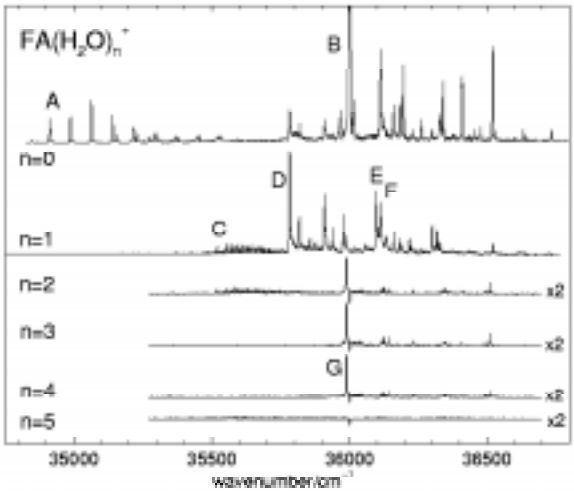

Figure 1. One-colour R2PI spectra under clustering jet conditions, probing mass channels $FA(H_2O)_n^+$: (a) n=0 (b) n=1 (c) n=2 (d) n=3 (e) n=4 (f) n=5.

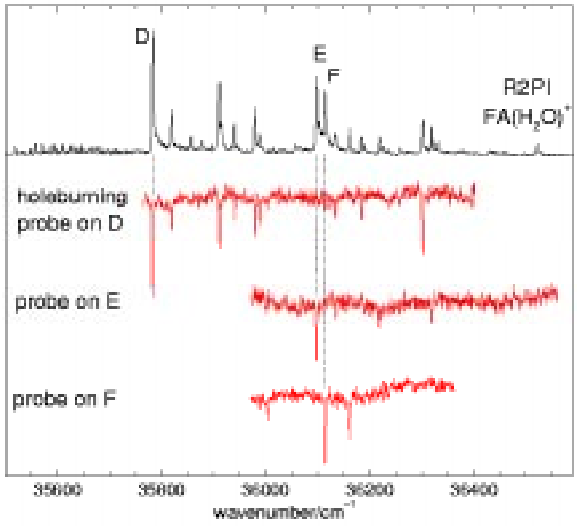

Figure 2. One-colour R2PI spectra in the region of isomer 'B' under clustering jet conditions: upper trace: mass channel $FA(H_2O)^+$. Below are R2PI holeburning spectra, probing depletion of peaks 'D', 'E' and 'F'.

Optimised structures of 1:1 water clusters of *cis*- and *trans*-formanilide are shown in Figure 3, togther with their relative energies, computed at the MP2/6-31G*//HF/6-31G* level. The predicted band contours shown alongside have distinctive (and helpful) differences which reflect changes in the TM alignments as well as the rotational constants of the hydrated clusters. Extremely good agreement between the experimental contour D and the third '*ab initio*' contour in Figure 3, allows its

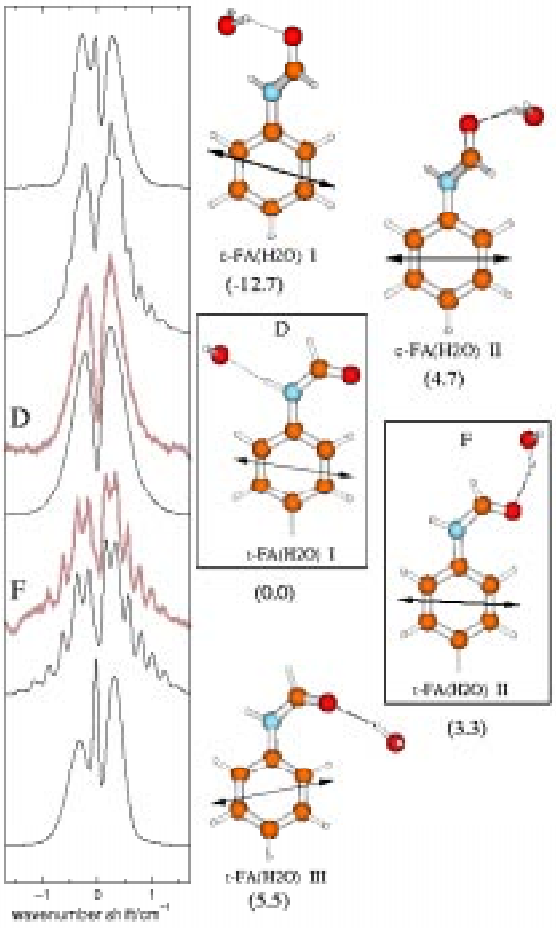

Figure 3. Experimental band contours D and F together with simulated rotational band contours for the FA(H_2O) complexes shown alongside, on the basis of HF/6-31G* and CIS/6-31G* *ab initio* data (T_{rot} = 2K, *FWHH* = 0.10 cm^{-1}). Relative energies in $kJmol^{-1}$ at the MP2/6-31G*//HF/6-31G* level are given in parentheses.

assignment to *t*-FA(H_2O) **I**, in which water is bound as a proton acceptor at the N-H site. Likewise, band F may be assigned to the cyclic hydrate, *t*-FA(H_2O) **II**, with a water proton donating to the carbonyl oxygen. The assignments of bands D and F are also consistent with the observed spectral shifts. The red-shift of peak 'D' by 218 cm^{-1} relative to the band origin of *trans*-formanilide, implies an increase in the acidity of the NH hydrogen in the electronically excited, S_1 state. Hydration of the acidic hydrogen in phenol and indole results in red-shifts of 353 cm^{-1} [4] and 132 cm^{-1}.[5] On the other hand, the 113 cm^{-1} *blue*-shift of peak 'F', associated with the hydrate in which a water molecule is bound at the HCO group, indicates that the carbonyl oxygen is a *weaker* proton acceptor in the S_1 state: the amide group shows a *lesser* tendency towards charge polarisation in S_1 than in S_0. The increased acidity of the N-H hydrogen on electronic excitation is attributed therefore, to an inductive effect, transferring electronic charge to the ring rather than the carbonyl group.

The 1:2 hydrates C and E may also be assigned by analysis of their band contours and spectral shifts. The appearance of partially resolved sub-band structure in the fluorescence excitation contour of band 'E', shown in the lower trace of Figure 4, fits only one possible structure: the cyclic H-bonded cluster shown. Band C exhibits complex vibrational structure which can be ascribed to progressions based upon three low frequency vibrational modes (29, 38 and 51 cm^{-1}), see Figure 5.

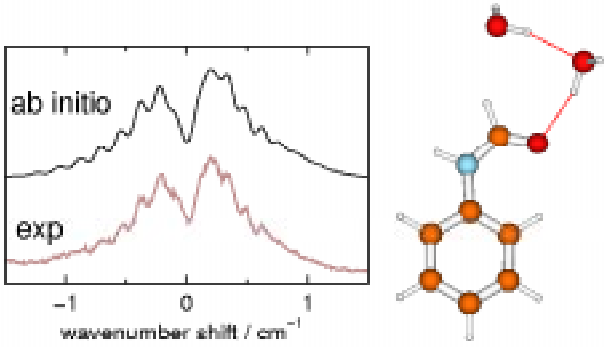

Figure 4. Lower trace: Fluorescence excitation contours of band E. Upper trace: Simulated contours based on *ab initio* data for the structure shown alongside.

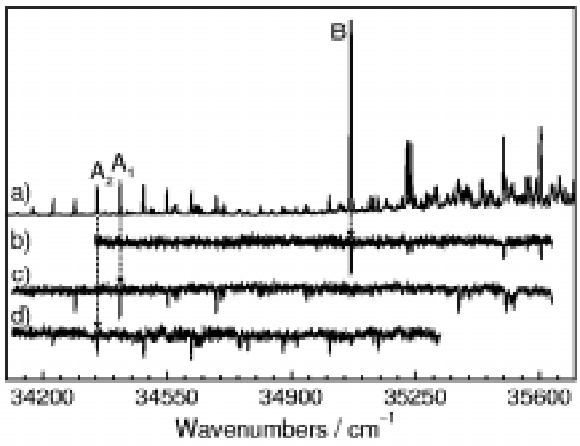

Figure 5. Upper trace: one-colour R2PI spectra in the region of peak 'C' in mass channel FA(H_2O)$^+$. Below are simulated stick spectra of the progressions based on combinations of the vibrations ν_1 (29.3 cm^{-1}), ν_2 (37.7 cm^{-1}) and ν_3 (51.2 cm^{-1}).

Consideration of this data, together with the observed spectral shift (-482 cm-1), a partially saturated band contour, and *ab initio* relative energies allows assignment to the structure shown in Figure 5, with water molecules bridging between the proton donating NH site and the proton accepting π site over the ring. The low frequency progressions are attributed to reorientation of the water dimer following changes in the π···HOH interaction induced by the π-π* excitation. The two assigned 1:2 hydrates of *trans*-formanilide follow the pattern observed in the 1:1 clusters, with waters bound alternatively to the N-H site (cluster C) and the HCO site (cluster E). Both involve cyclic hydrogen-bonded structures, in which an extra 'H-bond' is formed (HOH···π_{ring} in cluster C and H_2O···HCO in cluster E). Cooperative effects are maximised in these structures since each molecule acts as both proton donor and proton acceptor.

All of the water features C-G have been assigned to clusters of the *trans*-formanilide, leaving the question of why clusters of the *cis*-isomer have not been observed in R2PI scans down to 34480 cm^{-1}. A *cis* conformation of the amide group allows energetically favourable cyclic hydrogen-bonded structures with one or two water molecules bridging between the NH and CO sites. There is no reason why they should not be *formed* in the jet expansion, and so the question becomes why are they not *detected*? One consideration is that intermolecular vibrations of the water molecule(s) may couple to the torsional mode in formanilide, resulting in a broad Franck-Condon envelope of weakly allowed transitions, similar to that observed for cluster C. A further possibility is that resonant 1-colour two photon excitation which provides *ca*. 8.60 eV may barely be sufficient to ionise the complexes.

4-Phenylimidazole and 5-Phenylimidazole

The active site in protease enzymes such as chymotrypsin, involves the catalytic triad, serine-histidine-aspartate[6]. The central residue includes the imidazole ring, thought to play a key role in providing a 'proton relay' path between the donor, serine, and the acceptor, aspartate, which promotes charge separation and catalytic activity[6]. The phenyl ring of 4-phenylimidazole (4-PI) provides a suitable chromophore to examine hydrogen bonding to the imidazole group, and 4-phenylimidazole is itself an enzyme inhibitor.

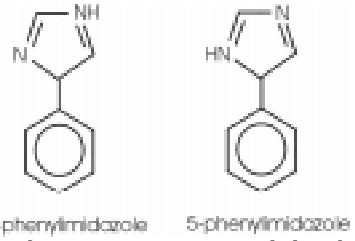

Figure 6 shows the R2PI spectrum, recorded in the 4-PI (and 5-PI) mass channel, when a sample of 4-phenyl imidazole was heated and expanded through the pulsed nozzle. Also shown, are a series of ion-dip, hole-burn spectra, centred on the two neighbouring features labelled 'A1' and 'A2' and on the isolated feature labelled 'B', appearing to the blue. The 'B' region is assigned to 4-PI, while the low frequency vibronic progression 'A' is assigned to its tautomer, 5-PI. *Ab initio* calculations suggest that the two rings of 5-PI are twisted in the ground state, but co-planar in the excited state. Compelling evidence for the non-planarity of system A is provided by the hole-burning spectra probing the peaks A1 and A2. They display *either* even (A2) *or* odd (A1) members only, of the main progression, T^n_0; the alternate features are missing. This behaviour can be understood if the low-lying torsional levels in

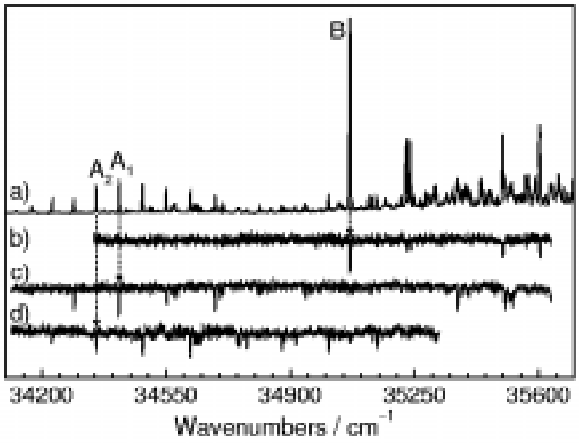

Figure 6. (a) Mass-selected R2PI spectra of 4-PI sample in the $S_1 \leftarrow S_0$ origin region (m/z=144), (b-d) ion-dip hole-burn spectra probing features 'B', 'A1' and 'A2'.

the ground electronic state are split into symmetric and anti-symmetric components by the co-planar barrier in the torsional potential, while the upper electronic state has a planar (or near planar) equilibrium geometry. Its torsional levels would then alternate between even (symmetric) and odd (antisymmetric) and the even/odd hole-burn spectra would display either the symmetric, T^{2n}_{0+}, or the antisymmetric, T^{2n+1}_{0-}, components of the upper state vibrational progression – but not both.

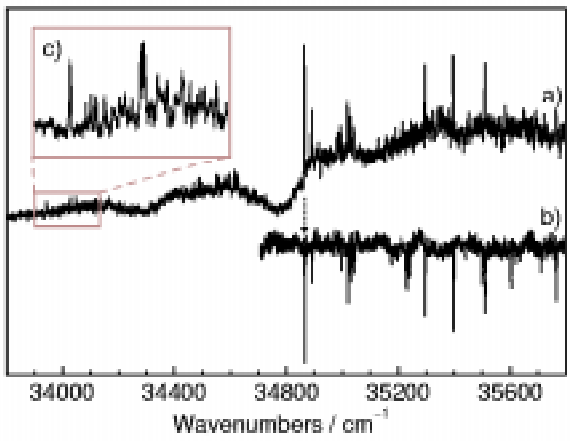

Figure 7. (a) Mass-selected R2PI spectra of 4-PI (and 5-PI) water clusters in the $S_1 \leftarrow S_0$ origin region (m/z=162), (b) ion-dip hole-burn spectra probing the peak at 34865 cm^{-1}. (c) enlargement of band system attributed to a 5-PI 1:1 water cluster.

A number of additional features can be identified in the phenyl imidazole-H_2O mass channel displayed in Figure 7(a). The hole-burn spectrum in Figure 7(b) shows that the set of peaks blue-shifted from the band origin at 34,865 cm^{-1} are associated with one particular cluster. Several of the vibronic features based upon it occur at wave-numbers which closely match those observed in system B. This encourages their assignment to a 1:1 hydrate of 4-PI, rather than its tautomer. Analysis of the partially resolved band contour of the origin (not shown) allows its assignment to a cluster in which water is bound at the NH site of the imidazole ring. The shift in the band origin, 203 cm^{-1} to the red of the origin band in the host molecule 4-PI, suggests a considerable (and plausible) increase in the acidity of the NH proton in the electronically excited $^1(\pi\pi^*)$ state. Another band system, shown in the inset of Figure 7(c), which is displaced ca. 200 cm^{-1} to the red of the origin band of 5-PI, is tentatively assigned to the corresponding hydrate of the tautomer. Further details are reported in Reference 7.

References

1. J A Dickinson, M R Hockridge, E G Robertson and J P Simons
   LSF annual report 1996/97 'Laser Spectroscopy of amide and amino acid water clusters'.

2. V P Manea, K J Wilson and J R Cable
   J. Am. Chem. Soc., 119, 2033, (1997)

3. J A Dickinson, M R Hockridge, E G Robertson and J P Simons
   J. Phys. Chem., in press.

4. H Abe, N Mikami and M Ito
   J. Chem. Phys., 86, 1768, (1982).

5. M J Tubergen, D H Levy
   J. Chem. Phys., 95 2175, (1991)

6. T E Creighton
   Catalysis, Proteins, Structures and Molecular Properties, Chap. 9, W H Freeman, NY1984.

7. M R Hockridge, E G Robertson and J P Simons
   Chem. Phys. Lett., 302, 538, (1999).

State to State Chemiluminescence in Mn + $Cl_2 \rightarrow$ MnCl* +Cl

T J Hughes, M R Levy

Department of Chemical and Life Sciences, University of Northumbria, Ellison Place, Newcastle upon Tyne NE1 8ST

Email address: *martin.levy@unn.ac.uk*

Introduction

The partly-filled d-shells of the transition metals render the electronic spectroscopy of both the atoms and the diatomic oxides and halides extremely complex. Hence, in simple gas phase atomic reactions, many potential surfaces may be accessible and interact. This complexity represents both a challenge and an opportunity for reaction dynamicists.

Over the past decade, research at this laboratory has been directed towards the investigation of chemiluminescent reactions of Mn atoms with various oxygen- and halogen-containing molecules[1-8]. Laser ablation at 1064 nm has been employed to generate a pulsed atomic beam of wide velocity range and containing several long-lived metastable states (a^6D_J, z^8P_J, a^4D_J, …) in addition to the ground state (a^6S). Translational excitation functions $\sigma(E_T^0)$ have been measured by velocity-separation over a long flight path (x = 282 mm), followed by interaction with a standing pressure of reagent gas (E_T^0 = nominal collision energy in this configuration = $\frac{1}{2}\mu(x/t)^2$, where μ = reduced mass and t = flight time). Recently, the experiments have been extended to the determination of the dependence on E_T^0 of the rotational alignment $-<P_2(\hat{\mathbf{j}}'.\hat{\mathbf{k}})>$ ($\mathbf{j}'$ = product rotation, $\mathbf{k}$ = reagent velocity vector)[8].

Where chemiluminescence is strongly endothermic, its observation at low collision energies clearly indicates the participation of excited Mn states in the beam. In other cases, and at higher energies, however, it may be difficult to assign reagent species. The reaction Mn + Cl_2 is one such case in point, since the fully ground state reaction is ~100 kJ mol^{-1} exothermic, while the various emitting states ($b^5\Pi$, $c^5\Sigma^+$, $d^5\Pi$, $e^5\Sigma^+$, $A^7\Pi$) have excitations ~141, 180, 241, 273 and 323 kJ mol^{-1}. In all channels, enhanced chemiluminescence is found at energies above the a^6S threshold.

To determine whether or not ground state atoms are responsible, a much 'colder' beam source is required. This is achieved in the present work by the use of an MnO_2 target instead of Mn. Laser-induced fluorescence has been used to determine the time-profile of the Mn pulse. For reasons of space, only the MnCl*($c^5\Sigma^+$) results are presented.

Experimental

The apparatus is essentially identical to that described previously[1,2], with the addition of (i) the LAS2050 dye laser, pumped at 355 nm by the GCR-170 Nd:YAG laser, and (ii) long baffle-arms to the reaction chamber, to minimise scattered light. Exalite 404 dye is used to tune the LAS2050 into the Mn a^6S-z^6P_J and a^6D_J-z^6D_J transitions at ~403 and 401-406 nm respectively.

With the solid Mn target, data are taken as before: light from the reaction zone is imaged via a beamsplitter onto separate photomultipliers, preceded by appropriate filters so that one measures the chemiluminescence signal $I(t)$, while the other detects the 'beam' signal $I_b(t)$ - long-lived metastable emission on the Mn $z^8P_J \rightarrow a^6S$ transition. Data are passed alternately to separate channels of a Thurlby digital storage adapter and averaged (ultimately) over several thousand laser shots.

In the MnO_2 case, the atomic metastable emission virtually disappears, so only $I(t)$ is averaged. The 'beam' signal now has to be probed by LIF, but the pulsed nature of the dye laser prevents the whole time-profile being obtained contemporaneously with $I(t)$. Instead, data are averaged at fixed delay times to build up an overall profile $I_b'(t)$.

Results, Analysis and Discussion

For the Mn target, LIF was found on the a^6S-z^6P_J transition, but with low signal intensity, confirming the suspected very low number densities in the atomic pulse. The peak signal was at ~50 μs, implying a beam temperature ~50,000 K. This is significantly less than the 80,000 K originally reported for this system[1], but is not inconsistent with most subsequent measurements using a less powerful Nd:YAG laser.

Despite an extensive search, no signal could be detected above the scattered laser light on any of the a^6D_J-z^6D_J transitions. Assuming a statistical distribution among the J-levels, this implies that the a^6D_J:a^6S ratio is ≤0.05 for this target and ablation plasma temperature.

For the MnO_2 target, the a^6S LIF as a function of delay time is displayed in Figure 1. Overall, the signal was much enhanced, and the time-profile much colder. The curve represents the best fit to the data, assuming a Maxwell-Boltzmann number density distribution, and yields a beam temperature 17,100 ± 600 K. This is consistent with the virtual disappearance of the $z^8P_J \rightarrow a^6S$ emission, suggesting that the populations of all metastable states are drastically reduced. Again, no a^6D_J LIF could be found.

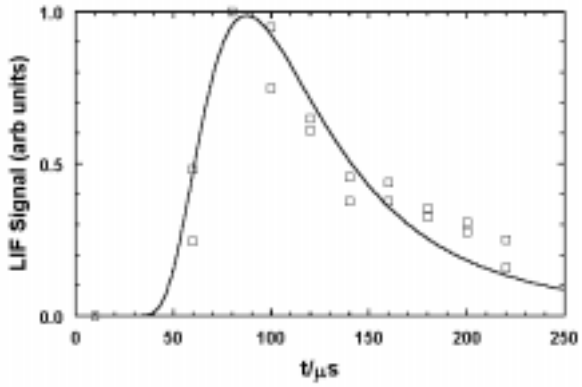

Figure 1. Number density time-of-arrival profile of Mn pulses from the MnO_2 target, by means of LIF on the a^6S-z^6P_J transition. The solid curve shows the best fit to the data assuming a Maxwell-Boltzmann velocity distribution (T ~ 17,100 K)

The chemiluminescence data for the solid Mn target were transformed as before[1] to cross sections $\sigma(E_T^0)$ by the equation

$$\sigma(E_T^0) \equiv \sigma(t) = \frac{I(t)}{I_b(t)}\Gamma(t)t \ ,$$

where $\Gamma(t)$ is the joint exponential decay factor of the two emitting z^8P_J states and the factor t converts $I_b(t)$ to flux. The data are analysed in terms of the multiple line of centres (MLC) approach[3,4]

$$\sigma(E_T) = \sum_k \sigma_k (1 - E_k / E_T) \ , \ k = 0,1,2, \ \ldots$$

where each term only operates from its threshold E_k. This is more effectively employed in its yield function form:

$$Y(E_T) = E_T\sigma(E_T) = \sum_k \sigma_k (E_T - E_k)$$

since it implies multilinear plots. The use of $Y(E_T^0) = E_T^0\sigma(E_T^0)$ instead of $Y(E_T)$ gives rise to threshold curvature, but this can be exactly calculated.

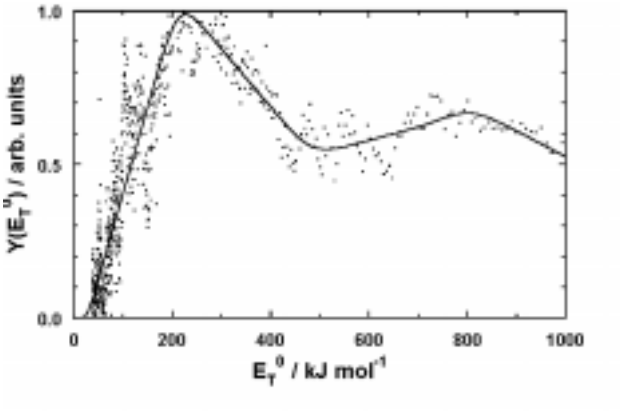

Figure 2. Yield function for production of MnCl*($c^5\Sigma^+$) from Mn + Cl_2, obtained by laser ablation of a solid Mn target. The solid line shows the best fit to the data using the multiple line of centres approach.

Figure 2 shows the yield function data for the MnCl*($c^5\Sigma^+$) product channel. The data are rather noisy, but the best fit via the MLC approach implies some 5 terms (E_4 is outside the range displayed). The derived initial threshold, E_0 = 29 kJ mol^{-1}, requires excited Mn atoms, and the negative fall-off above ~220 kJ mol^{-1} can be attributed to a forward transition state shift with increasing collision energy[3-8]. Such behaviour is commonly followed by a leveling off in the yield function at higher collision energy. The secondary rise at ~500 kJ mol^{-1} is not inconsistent with that, but it does suggest the possibility of an additional unresolved contribution, perhaps from ground state Mn atoms.

For the MnO_2 target, excitation functions should in principle be derived using the LIF-generated Mn number density distribution $I_b'(t)$:

$$\sigma(E_T^0) \equiv \sigma(t) = \frac{I(t)}{I_b'(t)}t$$

However, since the beam temperature could change with repeated ablation, we consider just the 'raw' chemiluminescence signal $I(E_T^0)$, but converted to a *modified* yield function form by multiplication by E_T^0. These data are displayed in Figure 3. The solid curve represents the least-squares best fit using the modified MLC equation

$$Y(E_T) = (I_b'(T, E_T)/t)\sum_k \sigma_k (E_T - E_k)$$

where $I_b'(T,E_T)$ is a Maxwell-Boltzmann beam flux distribution corresponding to beam temperature T and collision energies E_T.

It is immediately obvious that the quality of the data is much improved, reflecting the higher number density, at least of ground state atoms, in the beam. Whatever the beam temperature, it is also apparent that there is a significant enhancement above ~100 kJ mol^{-1}, although a small component does remain at low energy. In fact the modified MLC analysis fits the data with two production terms and one depletion, at ~29, ~119 and ~240 kJ mol^{-1}. The ratio σ_1:σ_0 ~ 2:1, and the beam temperature is found to be 16,600 ± 500 K. The two independent points of close agreement, between the initial thresholds E_0, and the beam temperature T, represent a significant justification of the current approach.

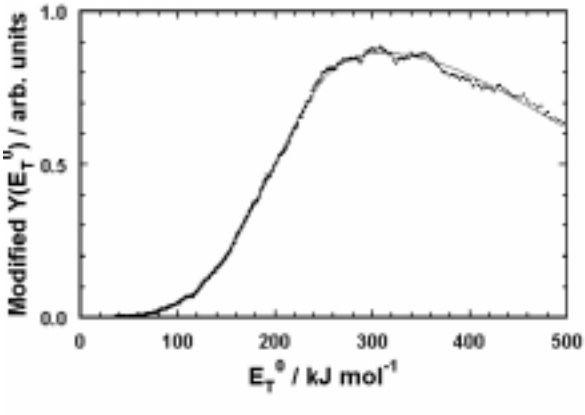

Figure 3. 'Modified' yield function for production of MnCl*($c^5\Sigma^+$) from Mn + Cl_2, obtained by laser ablation of a solid MnO_2 target. The sold line shows the best fit to the data using the multiple line of centres approach and a Maxwell-Boltzmann beam velocity distribution, whose optimum temperature is found to be ~16,600 K.

The results indicate that chemiluminescence from ground state atom reaction has a threshold ~120 kJ mol^{-1}. The initial, 29 kJ mol^{-1}, threshold is attributed to reaction of the first metastable state, a^6D_J. Given the low number density of the latter in both beams, its reaction probability above threshold must be orders of magnitude higher than that of Mn(a^6S) – a not unsurprising result in view of the different ionisation potentials. Both species do however display significant excess barriers to chemiluminescence.

Figure 2 shows no evidence for a production threshold at ~120 kJ mol^{-1}, although it could be lost in the noise. Nonetheless, comparison of the σ_k values from Figures 2 and 3 indicate that any contribution of a^6S reaction to Figure 2 must be small. This indicates that the secondary rise at ~500 kJ mol^{-1} is predominantly due to reaction of excited Mn atoms.

References

1. M R Levy
J. Phys. Chem, 93 5195, (1989)

2. M R Levy
J. Phys. Chem, 95 8491, (1991)

3. M R Levy
Res. Chem. Kinet, 1 163, (1993)

4. D A Newnham, D L Herbertson, M R Levy
Can. J. Chem., 72 850, (1994)

5. D A Newnham, M R Levy
J. Phys. Chem., 100 2799, (1996)

6. D L Herbertson, M R Levy
J. Phys. Chem., 100 2809, (1996)

7. D L Herbertson, M R Levy
J. Phys. Chem., 100 14584, (1996)

8. M A Spence, M R Levy
J. Phys. Chem., 101 7498, (1997)

Ionisation of DNA by 193 nm Light Yields Damage Mainly at Guanine by Intra-molecular Charge Migration

P.O'Neill and M. Plumb
MRC Radiation and Genome Stability Unit, Harwell, Didcot, Oxfordshire, OX11 ORD.

A.W. Parker
Central Laser Facility, CLRC Rutherford Appleton Laboratory, Chilton, Didcot, Oxon, OX11 0QX,UK

Main contact e-mail address: *p.oneill@har.mrc.ac.uk*

Introduction

Exposure of DNA to ionising radiation results in chemical modifications caused by two different processes i) direct ionisation of the DNA molecule, the direct effect, and ii) damage from radical species produced in the vicinity of the DNA, the scavengeable (indirect) effect. The advent of short wavelength ultraviolet lasers has enabled the study of the direct ionisation processes without the interaction of the ionisation products of water. Photoionisation of aqueous solutions of DNA with 193nm laser light results in the formation of a photoejected electron via a monophotonic process.[1] The DNA radicals formed by photoionisation are proposed precursors of low yields of single strand breaks (ssb),[2] which we have confirmed using Rayleigh light scattering experiments.[3] Further, migration of the electron loss centres to guanine has been demonstrated thereby enriching the yield of guanine radicals. Radical product(s) formed at guanine are indeed the precursor(s) of strand breakage which occurs in yields of less than 1% of the photoionisation events.[2,4,5] The yield of base modifications formed within plasmid DNA determined using enzymes which are selective for different damage sites and create a single strand breakage at the site of the damage are ~5x and 20x higher for damages excised by *Escherichia coli* endonuclease III (Nth) and *Escherichia coli* formamidopyrimidine-DNA glycosylase (Fpg) respectively.[5] (Fpg) excises oxidised purine modifications, including 8-oxo-7,8-dihydroguanine and 2,6-diamino-4-hydroxy-5-formamidopyrimidine (FapyGua), and it additionally has a β,δ-lyase activity that nicks DNA at apurinic/apyrimidic (AP sites).[6] Nth is known to excise oxidised pyrimidine damages[6] and has a β-lyase activity that nicks DNA at apurinic/apyrimidic (AP sites).[6]

From seqencing polyacrylamide gel electrophoresis under denaturing conditions, exposure of an aqueous, aerated solution of a double stranded DNA fragment to 193nm light leads to selective, non-random modification at guanine in the form of frank ssb and base modifications, revealed by treatment with either Fpg, Nth or hot piperidine treatment.[7] There is a similar neighbouring base sequence dependence for Fpg and Nth sensitive damage as that previously reported for both hot alkali labile damage and prompt ssb. Low yields of photoproducts, namely pyrimidine dimers are also revealed using the enzyme T4 endonuclease V. The yields of base damage at pyrimidines are very low even though these bases are ionised and would, in the absence of charge migration, yield oxidised pyrimidine damage which would be excised by Nth. Although irradiation of DNA with 193nm light causes photoionisation of all the nucleic acid bases, these results indicated that guanine is the predominant site for localisation of the oxidative damage. These findings[7] are consistent with migration of the radical cation to 'target' damage at guanine sites. The findings indicate that a common precursor to the damage is involved reflecting the similarity in the sequence distribution of the damage. These results indicate that damage at guanine and the sequence dependent yields are a signature for *direct ionisation*, which is a major component of the
damaging effect of exposure of cellular systems to ionising radiation.

Excision enzymes have proved useful tools for the determination of both the yield and the nucleic acid base specificity for 193 nm light induced DNA damage, since the site of nucleic acid base damage is revealed as a gap/ssb. This study has been extended to identify whether nucleic acid base damage occurs at guanine when in a thymine/adenine rich region of a DNA fragment of known sequence. From these studies the question arises as to whether the 193 nm light induced charge migration occurs by intra- and/or inter-molecular processes.

Experimental

To address the question of inter- and intra-strand hole migration, experiments using specific sequences have been initiated. The sequences have been synthesised and hybridised as ds oligonucleotides and subcloned into a bacterial vector.[2] As these sequences contain guanine in A/T rich environments, e.g. T_7GCGT_7 and A_7CGCA_7

```
5′CGAA TTTTTTTGCGTTTTTTT AAGCGAAGCGATGCGT
3′GCTT AAAAAAACGCAAAAAAA TTCGCTTCGCTACGCA
```

a comparison of the sequence-dependent yield of damage induced by 193 nm light can assist in the interpretation of inter- and intra-strand charge migration. Since the sequence A_7CGCA_7 contains a pyrimidine base between guanine and adenines (see above), the possible inhibitory effect of the pyrimidine may be assessed. The oligonucleotides were irradiated as double stranded oligonucleotides with 193 nm light and subsequently assessed for sequence specificity of ssb, Fpg sensitive sites and alkali-labile sites by denaturing PAGE. With all the DNA fragments studied, the induction of ssb by the hydroxyl radical is random where sequence dependent effects can be ignored.

Results

The base sequence specificity of the enzyme sensitive sites induced by 193 nm light in the oligonucleotides containing T_7GCGT_7 and A_7CGCA_7 in the complementary strand was determined using Fpg. An aqueous solution containing a 5'-^{32}P-end labelled restriction cut fragment of double stranded DNA, of known sequence, was irradiated with 193nm light (for conditions see Reference 2). The base specificities of prompt ssb (lane c), enzyme-induced ssb (lane a) and piperidine-labile sites (lane d) induced in DNA by 193nm light are shown in Figure 1. Lane b shows the Maxam Gilbert cleavage sequence for G/A. Treatment of un-irradiate DNA with these proteins does not result in the formation of ssb. As shown previously,[2] 193 nm irradiation of DNA results in prompt ssb exclusively at the guanine moieties (lane c) but the distribution of ssb is not the same for all the guanines, reflecting an influence of local structure. Damage excised by Fpg protein yields a gap (single-strand break) in the duplex (lane a) exclusively at guanine. The amount of damage of guanine in the form of prompt ssb, hot alkali labile damage and Fpg excision damage is greatest for neighbouring guanine residues. For instance in the DNA fragment containing A_7CGCA_7 base sequence, 193nm light produces ssb and Fpg sensitive sites at guanine as shown in the Figure 1. Differences in the electrophoretic mobility of the fragments representing ssb or Fpg sites, reflect a damaged sugar remnant associated with a ssb.[2,7]. Although photoionisation of adenines will occur within this A_7CGCA_7 region, damage at these adenine residues above background was not observed.

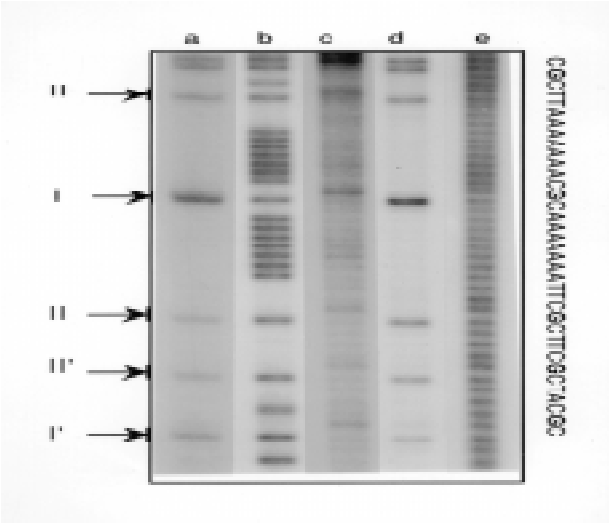

Figure 1. The base sequence specificity of prompt and Fpg induced ssb in A7CGCA7 DNA fragment by 193 nm light;, Fpg sensitive sites (a), frank ssb (c) and piperidine-labile sites (d) and Maxma Gilbert lane for A/G (b) and hydroxyl radical induced ssb (e).

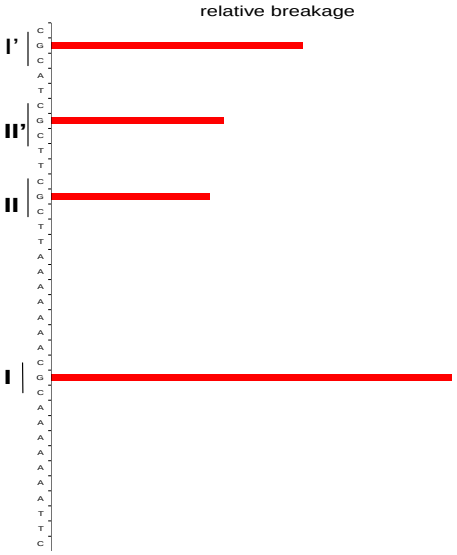

Figure 2. The relative yields of base lesions visualised as Fpg ssb induced by 193 nm light.

This is consistent with the observed charge migration from the adenine radical cation to guanine in single stranded oligonucleotides.[8] Furthermore, the extent of guanine damage at the CGC site within the adenine-rich environment ((I)) is about 1.6x greater, as shown by band intensities, than the guanine damage at the CGC (I') within the non-adenine rich sequence as shown in Figure 2.

It is inferred that charge migration occurs from the adenine radical cation to guanine (I) so that the intervening cytosine does not inhibit migration. In contrast, the neighboring base, e.g. cytosines which are less readily oxidised than guanine, do inhibit charge migration in single stranded oligonucleotides.[8] Guanine damage in the flanking site (II) are not enhanced when compared with the damage at the corresponding site (II') in the non-adenine rich region.

With the complementary strand T_7GCGT_7 the excision occurs at guanine with no apparent excision of base damage at thymine. The extent of excision at the guanine sites is similar and does not show any significant enhancement over the corresponding sites in the non-A/T rich regions. Excision of the guanines in the T_7GCGT_7 by Fpg is not enhanced. It is suggested that the yield of thymine radical cations in this region is so low[2] that any contribution to guanine damage from charge migration is insignificant.

The Scheme summarises the data showing the damaged sites, where **G** is enhanced cleavage and G non-enhanced cleavage.

```
5′......CGAA TTTTTTTGCGTTTTTTT AAGC..
3′......GCTT AAAAAAACGCAAAAAAA TTCG...
```

Within the specifically synthesised insert, the boxed region shows the sequences discussed for guanine damage by photoionisation of the ds oligonucleotide fragment. Intrastrand charge migration from the base radical cations to guanine (lower strand) occurs with enhancement of the damage at the guanine site. If transfer of the radical cation from the more distal adenine residues to the nearer guanine within the flanking sites occurs, they are suggested to transfer to more distal guanines since the amount of damage is not enhanced at these guanines. It is inferred that charge migration may occur over several base pairs involving hopping/tunnelling through the π stacked bases.[9] This migration must compete with irreversible hydration of the radical cations[3] and/or proton transfer to its complementary base.[10]

In conclusion, these preliminary studies indicate that photo-ionisation of DNA fragments results predominantly in a sequence dependent intra--strand charge migration of the radical cation of the nucleobases to the most easily oxidised base, generally guanine, located within a few base pairs of the initial site of ionisation.

References

1. L P Candeias, P O'Neill, G D D Jones, and S Steenken. Int.J.Rad.Biol., 61 15, (1992)
2. T Melvin, M A Plumb, S W Botchway, P O'Neill and A W Parker. Photochem. Photobiol., 61 584, (1995)
3. T Melvin, S W Botchway, A W Parker and P O'Neill J.Am.Chem.Soc., 118 10031, (1996).
4. Cullis P.M., Malone, M.E. and Merson-Davies, L.A. (1996) J. Am. Chem. Soc. 118, 2775-2781
5. T Melvin, S Cunniffe, D Papworth, T Roldan-Arjona and PO'Neill. Photochem. Photobiol. 65 660, (1997)
6. E C Friedberg, G C Walker and W Siede. DNA Repair and Mutagenesis, ASM Press, Washington D.C. (and references therein) (1995)
7. T Melvin, S M T Cunniffe, P O'Neill, A W Parker and T Roldan-Arjona.. Nucl. Acids Res. 26, 4935-4942 (1998).
8. T Melvin, S W Botchway, A W Parker and P O'Neill. J.Chem.Soc., Chem.Commun., 653-654, (1995)
9. E. Meggers, M.E. Michel-Beyerle, B. Giese. J. Amer. Chem. Soc. 120, 12950-12955 (1998).
10. S. Steenken. Free Rad. Res. Commun. 16, 349-379 (1992).

We acknowledge the contributions of Dr T. Melvin and the gift of Fpg protein from Dr T. Roldan-Arjona.

Further development of the laser-plasma induced x-ray source for cellular radiobiology and DNA biochemistry

M A Hill, D L Stevens, J Fulford, P O'Neill, D T Goodhead

MRC Radiation & Genome Stability Unit, Harwell, Didcot, Oxon, OX11 0RD

A Nottola, G J Tallents

Department of Physics, University of Essex, Colchester CO4 3SQ

W Shaikh, J Westhall, E Turcu*

Central Laser Facility, CLRC Rutherford Appleton Laboratory, Chilton, Didcot, Oxon, OX11 0QX, UK

**Now at JMAR Research, San Diego, CA, USA*

Main contact email address: *m.hill@har.mrc.ac.uk*

Introduction

Ultrasoft x-rays provide a unique tool for investigating the intracellular mechanisms of radiation action. They produce low energy, isolated electron tracks randomly throughout the irradiated material. These electrons have well defined energies and short tracks comparable in size to those of critical structures in the cell, such as DNA, nucleosomes and chromatin fibers. They can therefore be used as a fine probe of the energy and spatial requirements for specific types of radiation damage and so provide much needed data for understanding and modeling the processes involved. Also, these tracks are similar to the numerous secondary electrons and electron 'track ends' produced in the slowing down spectrum of more energetic electrons produced by most irradiations. Hence, they are representative of this substantial component in any ionizing irradiation.

The high intensity and broad x-ray beam produced by the RAL laser-plasma source is important in overcoming the high attenuation of these low energy x-rays to produce the sample dose rate required. The high intensity also allows greater flexibility in the range of potential biological and chemical endpoints open to investigation. The carbon Lyman α line (367 eV) is of particular interest, with an attenuation through mammalian cells and water sample not too dissimilar to that of the C_K (277 eV) and Cu_L (956 eV) produced by the MRC cold cathode source. In parallel with the redesign of the target chamber for these experiments, spectroscopy measurements have also been made, since knowledge of the spectrum is important in determining the mean absorbed dose to an irradiated sample.

Redesign of target chamber

The target chamber and tape drive mechanism has been redesigned to maximize the x-ray flux by reducing the target to sample distance from 30 cm to 5 cm through helium at atmospheric pressure. The sample is positioned in the normal direction to a moving target tape, which is struck at 45° by a focused laser pulse. Samples, which consist of mammalian cells or plasmid DNA solutions, are irradiated in glass-walled dishes (3 cm internal diameter) with a 0.9 μm mylar base. Between the target and dish is positioned a UV/light filter (0.5 μm V on 0.5μm CH) also spanning a circular area of 3 cm. A three position irradiation slide allows one sample to be changed while another is being irradiated. For dosimetry purposes the central position of the slide is occupied by a photodiode with a 0.9 μm mylar dish base filter. This is cross calibrated before and after each exposure with a second monitor photodiode with identical filters positioned at 45° from the normal of the target tape. The monitor photodiode is used to determine when the required dose to the sample has been delivered. A second slide has also been made which allows samples to be cooled.

Initial DNA studies using polypropylene target

Polypropylene tape was used as a target to produce carbon x-ray emission lines rather than a mylar tape, which would also produce higher energy oxygen lines. The attenuation of these carbon x-rays through the helium, filter and mylar results in emission lines in the ~450 eV region dominating the carbon Lyman α line. It is hoped to use a small amount of nitrogen to filter out these higher energy lines for future experiments.

These initial studies used pUC18 plasmid DNA (2686 base pairs) irradiated in solution at two different scavenging capacities determined by the concentration of Tris. Initially >95% of the plasmid is in the supercoiled form. Relaxation to the open circular form will result from a DNA single strand break (ssb), which can be produced either by the radiation interaction directly with the DNA or indirectly by reaction with an OH radical produced by the interaction of radiation with a nearby water molecule. The production of a DNA double strand break (dsb) will result in the linearisation of the plasmid. The relative proportions of the different plasmid forms can be determined by gel electrophoresis due to their differing mobilities. At a scavenging capacity of 10^{-6} s (0.66 m*M* Tris) the indirect effect dominates and the production of ssb can be used as a probe of the yield of OH radicals escaping the radiation track. The higher scavenging capacity (0.2 m*M* Tris) can be used as a model system for DNA damage in a living cell.

An 8 μm thick plasmid sample was irradiated with x-ray pulses at 5 Hz for the low scavenger and 50 Hz for the high scavenger, with a surface dose rate in the region of 0.2 Gy per shot.

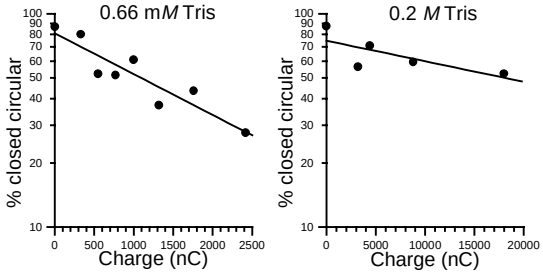

Figure 1. Dose dependence for single strand break induction.

Results

The experimentally determined dose responses for single strand break induction at the two scavenging capacities are shown in Figure 1. Absorbed dose is represented by charge collected on monitor photodiode since more measurements are needed to accurately determine the mean absorbed dose.

Summary

The successful irradiation of both plasmid and mammalian cells (data not presented) demonstrates the feasibility of cellular radiobiological and DNA biochemical experiments with the new setup and the ability of achieving high dose rates. Work still needs to be done to improve dosimetry and spectra quality.

KrF Laser Annealing of ZnS:Mn Thin Film Phosphors

E Mastio, W Cranton, C B Thomas

The Nottingham Trent University, Burton St. Nottingham, UK.

Main contact email address: *wayne.cranton@ntu.ac.uk*

Introduction

Inorganic thin films of ZnS:Mn are of importance in the field of flat screen display technology as the active light emitting layer in thin film electroluminescent displays (TFELs). Recently, the Displays Research Group at Nottingham Trent University have demonstrated the use of TFEL technology within a novel high resolution, miniature display device that utilises laterally transmitted light to produce high intensity emission at reflecting microstructures[1)], as shown in Figure 1. Miniature flat screen displays based on this technology have sufficient luminence (>3000fL) to be suitable for portable head mounted display systems, where the projected display image is bright enough to permit viewing over ambient background illumination.

Critical to the fabrication of the LETFEL, or any TFEL device is an annealing process to activate the dopant in the thin film phosphor. However, as demonstrated by the authors, thermal annealing of the device also results in a modification of the phosphor/dielectric interface region, which is detrimental to the electron transport properties within the device, limiting the performance [2)]. Hence, since 1997, the Displays Group has been working with the CLF, under EPSRC Grant No. GR/K90074, to examine the feasibility of using pulsed laser annealing (PLA) of the thin film phosphor, in order to achieve the dopant activation with minimal effect on the interface region. Following an initial period of investigation to determine the optimum experimental arrangement [3)], PLA irradiations of ZnS:Mn thin films have been demonstrated to provide enhancements in luminescence [4)], and recently we have commenced PLA of LETFEL display devices, which are currently being fabricated into fully working demonstrators. The present report covers the experimental period 98/99, when much of the work was concerned with a materials investigation into the effect of PLA on ZnS:Mn thin film crystallinity.

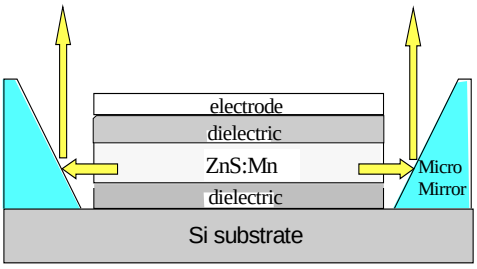

Figure 1. Schematic cross section of Laterally Emitting Thin Film Electroluminescent, LETFEL device, showing principle of reflected light emission.

Experimental Details

800 nm thick polycrystalline ZnS:Mn thin films were sputtered onto polished n-type single crystal (100) silicon wafers, from a pressed powder ZnS:Mn target. The Mn concentration of the source material is 0.45 wt%. To examine the effect of post-deposition annealing, the wafer was cleaved into twelve sections. This enables direct comparison of thermal and pulsed laser annealing of samples grown under the same conditions.

Post-deposition thermal annealing was performed on four of the cleaved samples in vacuum ($1x10^{-7}$ T) for 1 hour at temperatures of 400 °C, 500 °C, 600 °C, and at a maximum of 700°C. Limitation to 700 °C was due to thin film losses by delamination at higher temperatures. To achieve efficient absorption of the laser irradiation in the thin film, it is necessary to irradiate with photons of energy greater than the band gap (~ 3.66 eV for ZnS), since at lower energy these films are optically transparent. With KrF laser emission of 249 nm corresponding to ~ 4.98 eV, the optical absorption coefficient α has been determined to be $3.33x10^5$ cm^{-1} for crystalline ZnS [5)] and $3.15x10^5$ cm^{-1} for polycrystalline ZnS:Mn thin films[6)]. Irradiation of the samples was performed under 150 psi (13.6 bars) of Ar pressure to prevent atmospheric contamination and either laser sublimation or ablation due to the low ZnS vapour pressure at atmospheric pressure. The pressure cell in which the wafer was mounted is attached to a motorised micro-positioning stage which facilitates irradiation of different areas of the sample for comparative analysis of relative laser power density. PLA irradiation was performed using the KrF laser of the x-ray laboratory in the LSF. Energy densities of 100 - 650mJcm^{-2} were obtained over an irradiating area of 3mm diameter. Additional experimental information was obtained for this study from ZnS:Mn samples that had previously been annealed utilising the Titania high power KrF facility during 97/98 [4)].

Crystallinity analysis

X-ray diffraction analyses were performed via collaboration with Laboratory PHASE, Strasbourg to investigate the crystallinity of the films, before and after annealing, using reflections from the CuKα_1 emission line (wavelength = 0.15405981nm) into a Siemens D5000 diffractometer with front monochromator. The applied power of the x-ray tube was 35 kV x 25 mA, the angular step was 0.005 ° within the studied 25° to 68° range, and the quanta acquisition time was 5 seconds. All diffraction lines characteristics were obtained by a deconvolution programme using the Lorentzian approximation.

Results

Figure 2 shows the measured XRD patterns of non-annealed (NA), thermally annealed (700 °C) and pulsed laser annealed samples at various power densities (10.76 MW/cm^2, 15.53 MW/cm^2, 20.99 MW/cm^2, 22.04 MW/cm^2, 24.27 MW/cm^2). (Due to the long deposition time, the as-grown sample is considered to be effectively annealed thermally at the 200°C substrate temperature used during growth). The observed diffraction lines correspond to the crystal planes as indicated. The (111), (200), (220), and (311) lines correspond to the cubic phase and the (00.2), (10.1), (10.2), (11.0), (10.3), (11.2) and (20.2) lines correspond to the hexagonal phase. For the as-grown and thermally annealed ZnS:Mn structures, the lack of diffraction from any hexagonal planes indicates a predominantly cubic structure (see Figures 2a and 2b). Consequently, the observed diffraction peaks are all attributed to the cubic forms i.e. (111), (220), and (311). Analysis of their diffraction characteristics do not reveal significant grain growth or reorientation which is in agreement with previous work [7)].

XRD patterns of samples exposed to laser irradiation with optical power density greater than 10.76 MW/cm^2 exhibit pronounced cubic to hexagonal transformation via the appearance of the hexagonal (10.1), (10.2) and (10.3) lines. (see Figures 2d to 2g). In Figure 3, the diffraction characteristics of the (10.1) plane are investigated. Between about ~ 16 MW/cm^2 and ~ 21 MW/cm^2, the peak intensity $I_{10.1}$ is nearly constant before increasing rapidly beyond ~ 21 MW/cm^2 while the full width at half maximum (FWHM) and atomic spacing remain unchanged within experimental errors. Finally, evidence of the crystalline quality improvement of the phosphor thin film is clearly recognised under higher irradiation power

(> 22.02 MW/cm^2), since a secondary diffraction line recognised at around 63.63 °, (Figure 2g), corresponds to the (20.2) plane.

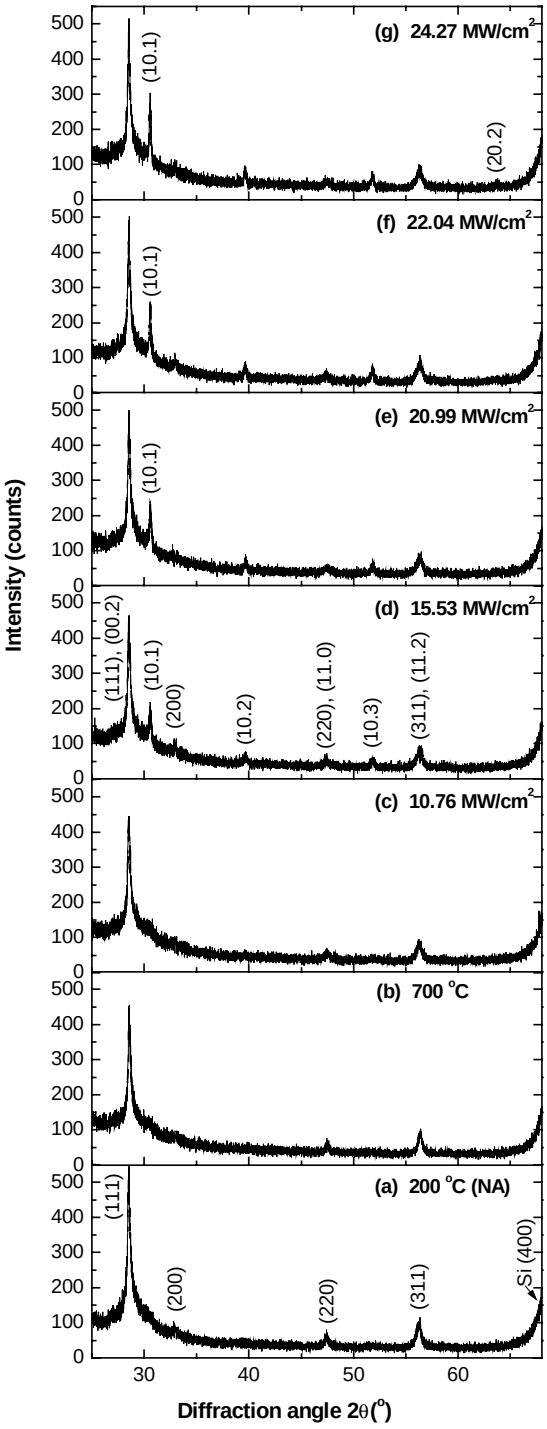

Figure 2. XRD patterns of samples as deposited (NA) at 200 °C (a), thermal annealed at 700 °C (b), and pulsed laser annealed under incident laser power densities of 10.76 MW/cm^2 (c), 15.53 MW/cm^2 (d), 20.99 MW/cm^2 (e), 22.04 MW/cm^2 (f), 24.27 MW/cm^2 (g).

Discussion and Conclusions

The major difference in the XRD patterns of laser and thermal annealed samples is the formation of the hexagonal wurzite structure, the most stable allotrope at high temperatures, suggesting strongly that the temperatures involved in the former process exceed those of the latter limited to 700 °C. Simulation of the maximal surface temperature attained using the lowest power density of 10.76 MW/cm^2 suggests an effective surface annealing temperature of 875 °C [8], which conforms to the observed crystallographic modifications.

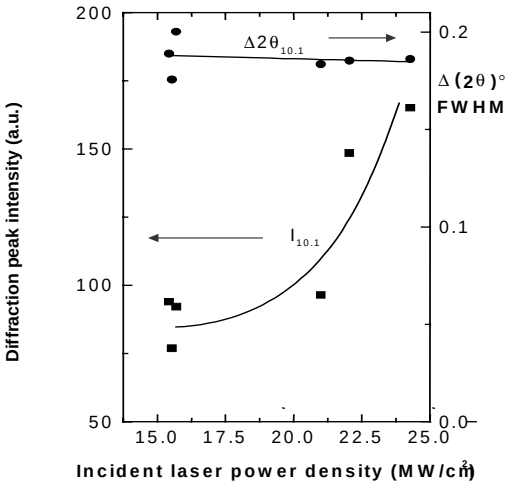

Figure 3. (10.1) diffraction line characteristics as a function of incident laser power density.

The first hexagonal lines are detected for laser annealed samples at power densities between 10.76 MW/cm^2 and 15.43 MW/cm^2, which is below the simulated phase transition threshold of 17 MW/cm^2. However this simulated value was determined using the optical and thermal parameters of single crystal ZnS. For polycrystalline thin films, as studied here, we would not expect such a sharp transition since the binding energies between atoms are less well defined. Both as grown and samples thermally annealed, up to 700 °C, exhibit the zinc blende form. Using the novel pulse laser annealing technique, it is suggested that allotropic transition from the cubic to hexagonal phase occurs between 10.76 MW/cm^2 and 15.43 MW/cm^2, i.e. below the calculated transition threshold of 17 MW/cm^2.

Analysis of the full width at half maximum of the diffraction peaks indicates that crystallite size remains constant using both annealing techniques. Considering the processing temperatures and time factors involved, we infer that the pulsed laser annealing processing time is insufficient to increase the crystalline size and that allotropic transition occurs in the solid state. It is concluded that the intensity increase of the hexagonal closed packed plane reflections is due to enhanced in-depth transformations. These transformations coincide with improvements in PL and indicated that an enhanced host environment for the dopant ions results from the induced solid state transformations.

References

1. C B Thomas, W.M. Cranton, and R. Stevens SID International Symposium 96 Digest (1996).
2. W M Cranton, R Stevens, C B Thomas, A H Abdullah, M R Craven, Proc. IEE Colloquium on Materials for Displays (1995) 7/1.
3. M Cranton, E A Mastio, C B Thomas, R Stevens, J P O Evans, CLF-RAL Annual Report, (1997) 147.
4. A Mastio, W M Cranton, C B Thomas, CLF-RAL Annual Report, (1998) 11.
5. Ozaki and S Adachi, Jpn. J. Appl. Phys. 32, 5008 (1993).
6. M Savani, M. Phil thesis, University of Bradford, 1982.
7. F Cattel, A G Cullis, Thin Solid Films 92, 211 (1982).
8. A Mastio, W M Cranton, C B Thomas, E Fogarassy, S de Unamuno, Appl. Surf. Sci. 139, 35 (1999).

Femtosecond Dynamics of Resonantly Excited Excitons in GaN

S Hess, F Walraet, R A Taylor, J F Ryan

Clarendon Laboratory, Department of Physics, University of Oxford, Parks Road, Oxford, OX1 3PU

B Beaumont, P Gibart

CNRS-Centre de Recherche sur l'Hétéro-Epitaxie et ses Applications, Rue B. Gregory, Parc Sophia-Antipolis, F-06560 Valbonne, France

Main contact email address: *r.taylor1@physics.ox.ac.uk*

Introduction

GaN and its alloys are of considerable interest for optoelectronic device applications in the blue and ultraviolet spectral regions[1)], and a detailed understanding of their optical properties is important for designing and optimizing devices such as light emitting diodes and lasers. As in all direct, wide band-gap semiconductors, the band-edge optical response of GaN is dominated by excitonic effects: the exciton binding energy is ~20 meV, and it has already been shown that excitons play an important role in the optical reflection and absorption spectra at low carrier density and low temperature[2,3)]. However, the situation at high carrier density and temperature is not so clear. The Coulomb interaction between electrons and holes is expected to become screened with increasing density, and together with phase-space filling, this should lead to a bleaching of the exciton resonance. However, excitonic gain has been reported for GaN at high excitation density[4)]. This behaviour is complicated by the fact that the emission spectrum of wide band-gap materials tends to be dominated by bound exciton recombination, and is therefore highly dependent on sample quality. Consequently, exciton dynamics are determined to a great extent by localization at impurities and defects, and only in high quality material can intrinsic relaxation and radiative recombination processes be studied.

In this communication, we present a time-resolved pump-probe study of high quality epitaxial overgrowth. In order to probe primarily the radiative exciton population, we resonantly excite excitons with a 250 fs laser pulse, resulting in an exciton population with wavevector $\mathbf{q} \sim 0$. The sharp exciton resonances in the reflectance spectrum bleach as the density of photoexcited excitons increases, and the change in intensity of the reflected light as a function of time is a measure of the $\mathbf{q} \sim 0$ exciton dynamics. At 4 K the dominant excitonic relaxation process is trapping at impurities and defects with a characteristic time $\tau^1_{\text{eff}} \sim 16$ ps. At much higher temperatures (>60 K) we observe the emergence of long-lived radiative recombination with $\tau^2_{\text{eff}} \sim 375$ ps. The longer lifetime agrees well with the predicted value for the radiative decay of thermalised excitons at the polariton bottle-neck.

Experiment

The GaN sample studied here is a nominally undoped epilayer grown by lateral epitaxial overgrowth, which is a two-step process involving both undoped and Mg-doped GaN deposition[5)]. A GaN layer is first grown by Metal Organic Vapour Phase Epitaxy (MOVPE) under atmospheric pressure on a (0001) Al_2O_3 substrate. A 30 Å dielectric film of silicon nitride is then deposited in-situ by reaction of silane and ammonia. Standard photolithographic techniques are then used to produce a periodic digital mask which exposes GaN stripes of width 5 μm and separation 10 μm. The stripes are aligned in the $[10\bar{1}0]$ direction. Finally, these patterned layers are overgrown by GaN, the growth being continued until there is a coalescence of the laterally grown areas, producing smooth and optically flat GaN layers. It has been shown that the high defect density usually found in GaN films is significantly reduced using this novel growth technique[6)].

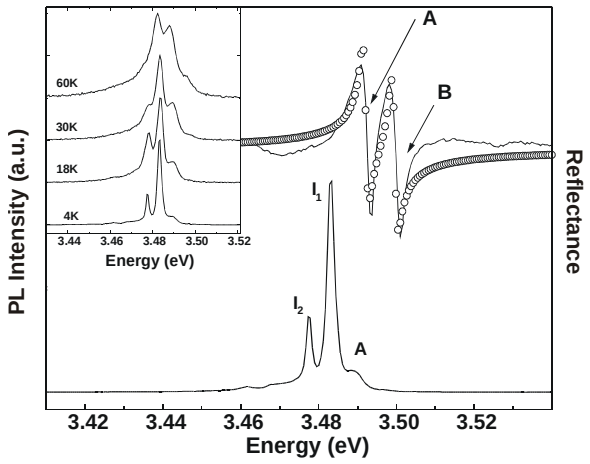

Figure 1. CW reflectance and photoluminescence spectra of GaN at 4 K. The exciton resonances are labelled A and B in the reflectance spectrum. Bound exciton peaks in the luminescence are labelled I_1 and I_2. The open circles are a fit to the reflectance data as discussed in the text. The inset shows weak excitation PL spectra at different temperatures. The curves are offset for clarity.

Figure 1 shows low-temperature photoluminescence (PL) and reflectivity spectra that exhibit characteristic excitonic behaviour. The CW PL was excited by a frequency doubled copper vapour laser (255 nm), and the source for the reflectivity measurements was a standard Xenon lamp. The reflectivity spectrum exhibits two sharp resonances at 3.492 eV and at 3.501 eV, which correspond to the Γ_7^C - Γ_9^V (A) and Γ_7^C - Γ_7^V (B) excitons respectively[7)]. The calculated reflectivity spectrum (hollow circles) is given by:

$$\varepsilon(\omega) = \varepsilon_\infty + \sum_{j=1}^{2} \frac{4\pi\alpha_j \omega_{0j}^2}{\omega_{0j}^2 - \omega^2 - i\Gamma_j \omega}$$

where $\varepsilon_\infty = 5.35$ is the high-frequency dielectric constant, ω_A = 3.492 eV and ω_B = 3.499 eV are the resonance energies, $4\pi\alpha_A = 5 \times 10^{-4}$ and $4\pi\alpha_B = 4 \times 10^{-4}$ are the polarizabilities, and $\Gamma_A = \Gamma_B = 1.5$ meV are the effective linewidths of the A- and B-excitons. The latter values are considerably smaller than the linewidths ~ 6 meV obtained from conventionally grown GaN[8)].

The PL spectrum, on the other hand, is dominated by shallow neutral donor bound excitons (I_1 and I_2), and there is no evidence of recombination from deeper impurity centres[9)]. The weak line labelled A at 3.49 eV, is assigned to the n = 1 free A-exciton state; its very low intensity relative to the bound states indicates that free excitons are localised on a timescale which is considerably faster than their recombination time. However, the inset in Figure 1 shows that the intensity of I_1 and I_2 decreases with increasing temperature, whereas the free exciton intensity increases significantly, which indicates that the bound excitons are thermally ionized and feed the free A- and B-exciton population. This thermal quenching of the I_1 and I_2 peaks is even more rapid above 60 K, consistent with excitons being only weakly bound to the neutral donors.

It is apparent from the data presented in Figure 1 that time-resolved photoluminescence will be of limited use in studying free exciton dynamics. In practice only the bound excitons can be clearly distinguished, and our streak camera measurements reveal that the risetime of the A-signal is ≤ 10 ps, the time resolution of the apparatus[10]. An alternative approach which provides direct information on free exciton behaviour is time-resolved reflectance.

The excitation source we used was an Optical Parametric Oscillator (OPO) in conjunction with a frequency-doubled amplified Ti:sapphire laser (operating at 800 nm)[11]. A fraction of the frequency-doubled blue light was mixed with the residual red light in an OPO which was tuned to resonance with the GaN band gap at 355 nm (3.495 eV). The pulse duration was 250 fs at a continuum generated in a water cell from the residual frequency-doubled Ti:sapphire pulses. Group velocity dispersion in the water cell temporally broadened the continuum, resulting in a net time-resolution for the experiment of 800 fs. The reflected light was focused into a 0.5 m spectrograph and detected using a liquid nitrogen cooled CCD.

The time-resolved reflectance spectroscopy was performed on the A- and B-exciton transitions with an average pump power of 0.1 mW. Both pump and probe beams were focused onto the sample with a polarization E ⊥ c. The spot diameter of the focused pump beam on the sample was 130 μm, while that of the probe beam was slightly smaller in order to optimize spatially homogeneity of the photoexcited exciton density. This pump power corresponds to a maximum exciton density of 2.0×10^{19} cm^{-3}, given that 83% of the incident light was transmitted into the sample and assuming that every photon excites an electron-hole pair.

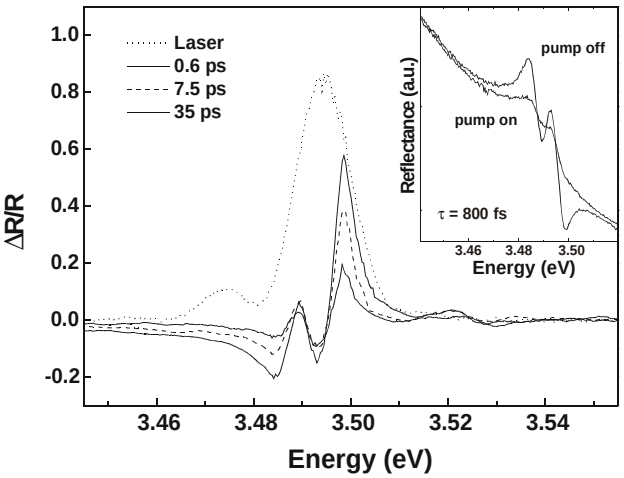

Figure 2. Differential reflectance spectra measured at various time-delays at 4 K. The laser excitation spectrum is shown as a dotted curve. The inset shows the measured reflectance spectra with and without pump at a time-delay of 800 fs.

Results

Figure 2 presents differential reflection spectra recorded at several different time-delays after the excitation pulse, showing strong bleaching of the excitonic transitions. As can be seen in the inset of Figure 2, the onset of bleaching occurs within the 800 fs time resolution of our system. The recovery of the excitonic reflectivity takes place on a slower timescale, and even after 35 ps there is a small residual bleaching. A noteworthy feature of the measurements is that the energies of the A- and B-excitons are apparently unshifted even in the presence of this relatively strong photoexcitation. This result is consistent with theoretical predictions of excitonic transitions in bulk semiconductors which include only exciton self-screening and no free carrier contribution, an approximation that is likely to apply in the present case of resonant excitation: in this model the band-gap renormalisation is exactly cancelled by the simultaneous reduction of the exciton binding energy[12]. It is also noteworthy that the C-exciton, which arises from the spin-split-off valence band, features quite strongly in the differential reflectance at 3.52 eV, although it is not apparent in the CW spectrum (c.f. Figure 1).

Figure 3 shows the amplitude of the differential reflectance signal as a function of time at a temperature of 4 K for both A- and B-excitons, which were obtained by fitting the spectra using Lorentzian line-shape functions[13]. The rise-time in each case is resolution limited indicating that the excitons are completely bleached after a few hundred femtoseconds. The decay of the differential reflectance after the initial transient can be fitted (solid line) using a single exponential with a decay time of τ_{eff} ~ 16 ps for both A- (hollow circles) and B-excitons (filled circles). This very small value for the effective lifetime suggests that excitons are trapped very rapidly into lower energy localised states, since the radiative lifetime of excitons is expected to be much longer. The value for the exciton lifetime at low temperatures agrees well with the risetime measured in our time-resolved luminescence measurements of I_1 and I_2[10], and with previously published PL data[14,15]. This trapping time is considerably longer than the sub-picosecond trapping times expected for polar optical phonon emission; however, under the present experimental conditions of resonant excitation the trapping process which applies here will involve only acoustic phonon emission considering that the optical phonon energy is ~ 90 meV.

An increase in temperature to 60 K results in the appearance of a long-lived component in the differential reflectance data: as shown in Figure 4 the decay is now clearly bi-exponential, with decay times of τ_1 ~ 16 ps and τ_2 ~ 375 ps giving a good fit to the data. Comparison with the CW data presented in the inset to Figure 1, which show that a significant free exciton population exists at 60 K in thermal equilibrium with the neutral donor bound excitons, suggests that the longer decay component is due to intrinsic radiative recombination.

Discussion

In bulk semiconductors the radiative decay of free excitons requires scattering to the photonic region of the polariton dispersion branch, and thus the radiative lifetime is practically determined by the time necessary to pass through the excitonic polariton bottle-neck region. In the absence of defects this relaxation process involves acoustic phonon scattering; because of the flat dispersion, the energies involved are small and the relaxation time can be extremely long. A theoretical analysis by Toyozawa[16] yields the following expression for the radiative lifetime:

$$\tau_{rad} = \tfrac{1}{2}(5\pi/3)^{3/5}\{\hbar^2 c^7 M^2 \alpha L^3 \upsilon_0^{-2} C^{-4} \omega_A^{-1}\}^{1/5} \omega_A^{-1}$$

where M/v_0 is the mass per unit volume of the unit cell, α is the polarizability, L is the thickness of the excited layer, $\hbar\omega_A$ is the energy of the A-exciton and C is the deformation potential. Using values of these parameters for GaN: 3014 kgm^{-3}, 4×10^{-5}, 0.1 μm, 3.492 eV and 4 eV respectively (obtained from our fit in Figure 1) and[17,18] we estimate τ_{rad} ~ 300 ps. This value is in remarkably good agreement with the experimentally observed long-lived component.

Conclusions

We have measured the lifetime of resonantly excited excitons by means of time-resolved reflectance spectroscopy. We observe strong time-dependent bleaching of the A- and B-excitons. We have measured a lifetime of ~16 ps at low temperatures, which is determined by trapping of excitons by acoustic phonon emission to defects and impurities. At higher temperatures we observe radiative recombination with a

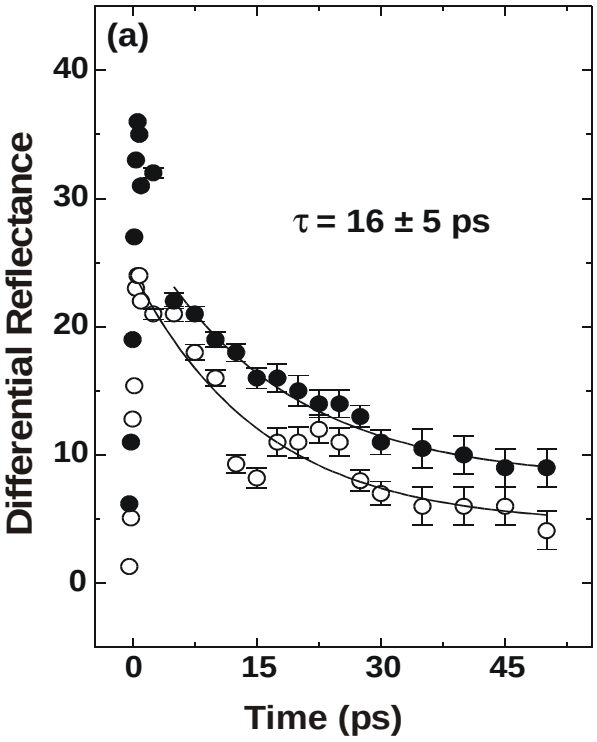

Figure 3. Time-dependence of the differential reflectance signal at 4 K from A-excitons (hollow circles) and B-excitons (filled circles). The solid lines show the results of a single exponential fit to the data (τ =16 ± 5 ps).

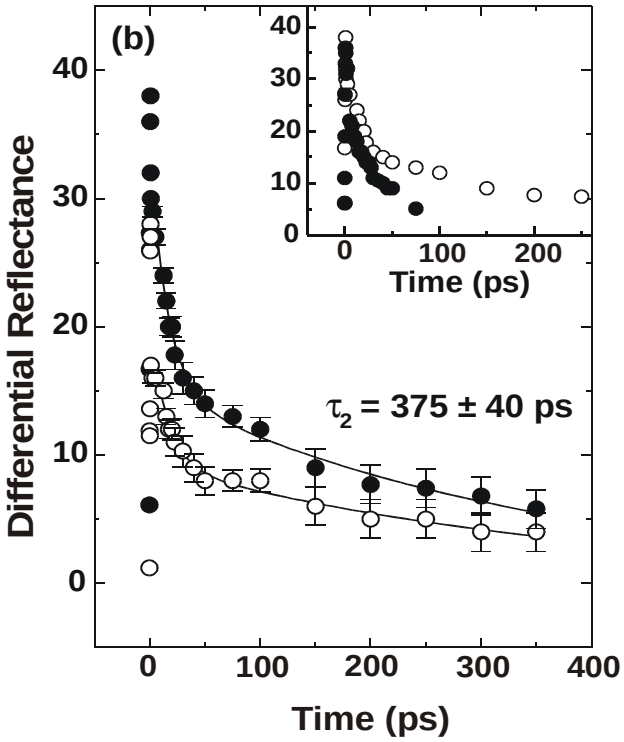

Figure 4. Time-dependence of the differential reflectance signal at 60 K from A-excitons (hollow circles) and B-excitons (filled circles). The solid lines show the results of a double exponential fit to the data (τ_1=16±5 ps and τ_2=375±40 ps). The inset shows the B-exciton signal at 4 K and 60 K, plotted on the same time axis for comparison.

lifetime of 375 ps, which is in good agreement with theoretical predictions for GaN. It will be important to extend these measurements to higher excitation densities to investigate the process of stimulated emission, and to low-dimensional structures in which direct radiative recombination is permitted due to spatial confinements. Furthermore, comparison of measurements obtained using resonant and non-resonant excitation should permit the influence of phase space filling and screening on exciton dynamics to be evaluated.

The authors wish to thank the EPSRC and Drs. P. Matousek and M. Towrie (Rutherford Appleton Laboratory) for their help in making available the OPO laser system used in these experiments.

References

1. S Strite and H Morkoç
J. Vac. Sci. Technol. B, 10(4), 1237, (1992)

2. W Shan, A J Fischer, S J Hwang, B D Little, R J Hauenstein, X C Xie, J J Song, D S Kim, B Goldenberg, R Horning, S Krishnankutty, W G Perry, M D Bremser and R F Davis
J. Appl. Phys., 83, 455, (1998)

3. A J Fischer, W Shan, J J Song, Y C Chang, R Horning and B Goldenberg
Appl. Phys. Lett., 71, 1981, (1997)

4. L Eckey, J Holst, A Hoffmann, I Broser, H Amano, I Akasaki, T Detchprohm and K Hiramatsu
Journ. of Lum. 72-74, 59, (1997)

5. B Beaumont, M Vaille, G Nataf, A Bouillé, J C Guillaume, P Vénnegues, S Haffouz and P Gibart
submitted to MRS Internet J. Nitride Semicond. Res.

6. O H Nam, M D Bremser, T S Zheleva and R F Davis
Appl. Phys. Lett., 71, 2638, (1997)

7. R Dingle, D D Sell, S E Stokowski and M Ilegems
Phys. Rev. B, 4,1211, (1971)

8. M Tchounkeu, O Briot, B Gil, J P Alexis & R-L Aulombard
J. Appl. Phys., 80 , 5352, (1996)

9. S Hess, R A Taylor, J F Ryan, N J Cain, V Roberts and J Roberts
Phys. Stat. Sol. (b), 210, 465, (1998)

10. S Hess, R A Taylor and J F Ryan, unpublished

11. M Towrie, A W Parker, W Shaikh and P Matousek
Meas. Sci. Technol., 9, 816, (1998)

12. G W Fehrenbach, W Schäfer, J Treusch and R G Ulbrich
Phys. Rev. Lett., 49, 1281, (1982)

13. D E Aspnes
in Optical Properties of Solids, edited by M. Balkanski (North-Holland, Amsterdam), Chap. 4A, (1980)

14. J Allègre, P Lefebvre, J Camassel, B Beaumont & P Gibart
MRS Internet J., 2, Art. 32, (1997) and references therein

15. J S Im, A Moritz, F Steuber, V Härle, F Scholz and A Hangleiter
Appl. Phys. Lett.,70 , 631, (1998)

16. Y Toyozawa
Progress of Theoretical Physics Suppl., 12, 111, (1959)

17. S L Chuang and C S Chang
Appl. Phys. Lett., 68, 1657, (1996)

18. A Alemu, B Gil, M Julier and S Nakamura
Phys. Rev. B, 57, 3761, (1998)

Time-resolved Band-gap Renormalization and Gain in GaN Epilayers

S Hess, R A Taylor, J F Ryan

Clarendon Laboratory, Department of Physics, University of Oxford, Parks Road, Oxford OX1 3PU

B Beaumont, P Gibart

CLRC CNRS-Centre de Recherche sur l'Hétéro-Epitaxie et ses Applications, Rue B. Gregory, Parc Sophia-Antipolis, F-06560 Valbonne, France

N J Cain, V Roberts, and J S Roberts

The Hicks Building, Department of Physics, University of Sheffield, Hounsfield Road, Sheffield S3 7RH

Main contact email address: *r.taylor1@physics.ox.ac.uk*

Introduction

Recent reports of stimulated emission from GaN[1,2] epilayers and InGaN quantum wells[3,4] have shown that there is an appreciable redshift of the stimulated emission relative to the low-density photoluminescence (PL) spectrum. Further work by Schmidt *et al.*[5] has indicated the presence of large optical non-linearities in GaN under nanosecond excitation in the region of the band-edge, including induced absorption below the band-gap at high excitation densities. These results have a direct bearing on the nature of the stimulated emission process in GaN, particularly with respect to the role of excitons versus electron-hole plasma emission. In this paper we present the results of experiments on thin films of GaN intended to investigate the optically pumped gain and the time-resolved transient absorption at high excitation densities.

Experiment

The first experiment investigated a 2 μm thick epilayer of GaN grown by atmospheric pressure MOCVD on a (0001) sapphire substrate with a 100Å AlN buffer (sample 1). A pulsed XeCl excimer laser operating at 308 nm was used to excite this sample in the standard variable-stripe-length geometry[6] for measuring optical gain and loss. The laser was focused to a 50 μm wide uniform stripe of variable length, and emission from the edge of the sample was detected.

In the second experiment, a 0.5 μm thick epilayer of GaN grown by MOCVD on an AlN buffer layer on sapphire was used (sample 2). This sample was thin enough to enable transient absorption experiments to be undertaken with sub-picosecond time resolution, using a pump and probe geometry. An amplified mode-locked Ti:sapphire laser was frequency tripled to 266 nm and used as a pump beam. The probe beam was a white-light continuum generated in a water cell from frequency doubled Ti:sapphire pulses. The net time resolution of the system was 800 fs. The transmitted continuum was dispersed using a 0.5 m spectrograph and detected using a CCD camera.

Results

The low-temperature reflectivity spectrum of sample 1 is shown in Figure 1, together with the PL spectrum obtained using weak excitation. The former shows the expected three excitonic

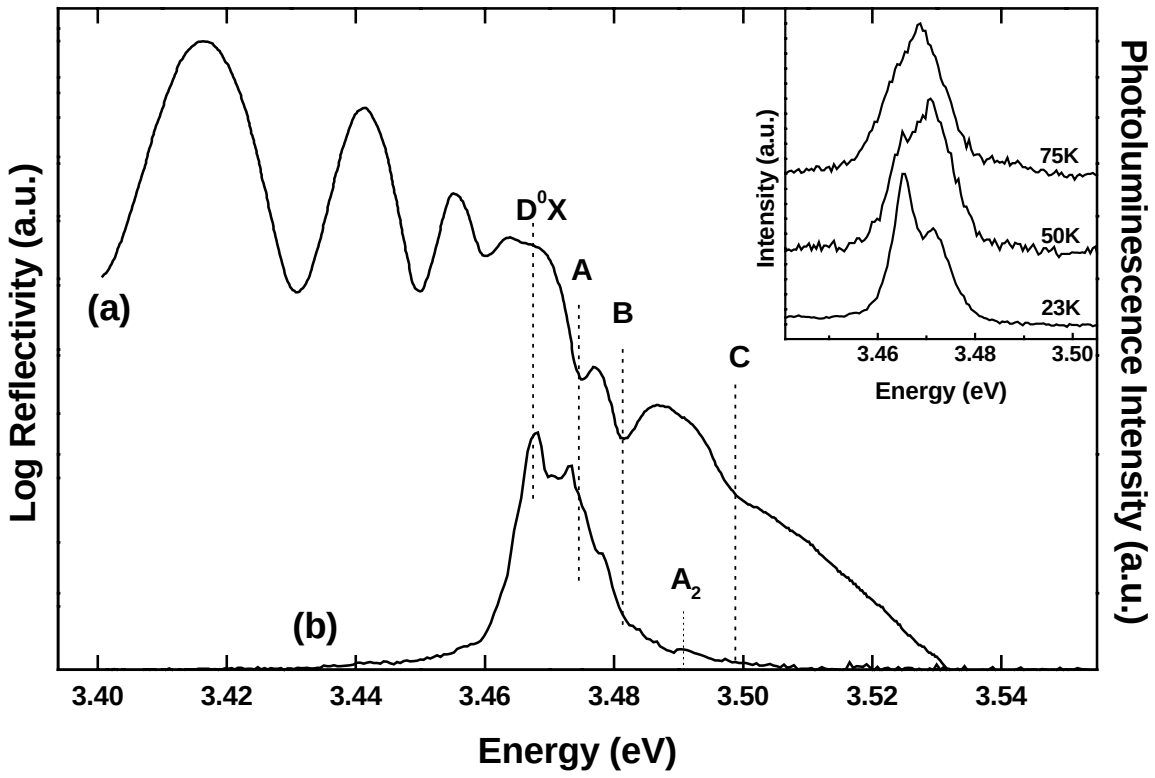

Figure 1. (a) Reflectivity spectrum of a 2 μm thick GaN epilayer. The three exciton resonances are labelled A, B and C. (b) PL spectrum measured at 8 K and low excitation density, showing a strong donor bound exciton line D^0X. The inset shows weak excitation PL spectra at different temperatures. The curves are offset for clarity.

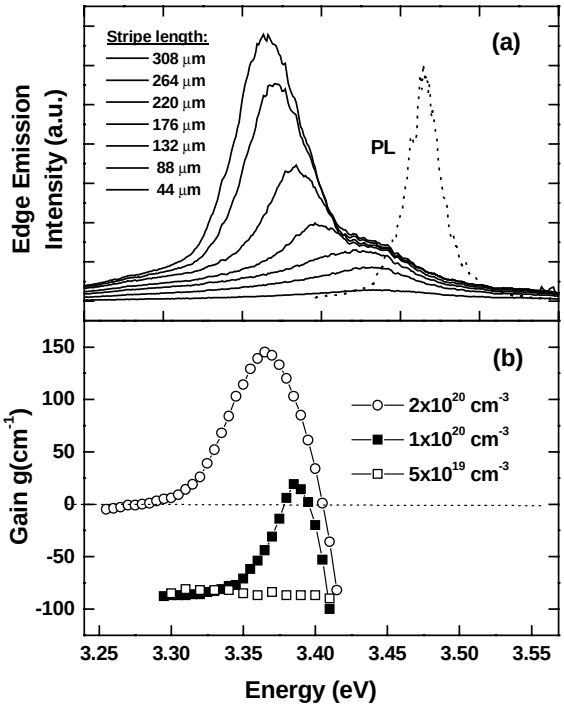

Figure 2. (a) Edge emission spectra from sample 1 for different stripe lengths and a carrier density of 2×10^{20} cm^{-3}, (b) corresponding measured gain spectra for three different carrier densities (T = 8 K).

resonances indicated by dotted lines and labelled A, B and C. The transition energies are 3.475, 3.481 and 3.499 eV, respectively. The oscillations in the low-energy region of the reflectivity spectrum are due to interference effects in the GaN layer. The PL spectrum is dominated by the neutral-donor bound exciton (D^0X). Three additional lines labelled A, B and A_2 appear at 3.473, 3.479 and 3.490 eV, which can be assigned to the $n = 1$ states of the free A and B exciton and the $n = 2$ state of the free A exciton, respectively. The inset in Figure 1 shows that the intensity of the D^0X peak decreases with increasing temperature, giving a binding energy of 5 meV. By measuring the temperature dependence of the total PL intensity it was possible to calculate the exciton binding energy in sample 1 to be 25 ± 2 meV[2].

Spectra at 8K for an excitation intensity of 9.5 $MWcm^{-2}$ (corresponding to a carrier density of 2×10^{20} cm^{-3}) are shown in Figure 2(a). The emission spectrum is a broad asymmetric band, redshifted with respect to the low-excitation PL spectrum (shown as a dotted curve). This is consistent with strong self-absorption and high internal losses, consistent with trapping at non-radiative centres. For short stripe lengths the intensity increases sub-linearly with increasing stripe length, whereas for longer stripe lengths we observe the onset of stimulated emission in the low-energy tail of the emission band. Gain spectra for various carrier densities are presented in Figure 2(b). The carrier density at the onset of stimulated emission is estimated to be ~ 9×10^{19} cm^{-3}. On doubling the excitation density the gain spectrum broadens and the measured maximum net modal gain increases from 17 to 148 cm^{-1}. This is in agreement with recent results for epitaxial GaN films[1,8]. At lower carrier densities, in the low-energy region of the gain spectrum where band-to-band absorption is negligible, the net modal optical gain approaches an energy- and density-independent value of ~ -80 cm^{-1}, which is a measure of the optical loss[7]. This is much greater than the value reported by Frankowsky et al. of ~ -10 cm^{-1} for an InGaN/GaN heterostructure with high optical confinement[7], as might be expected.

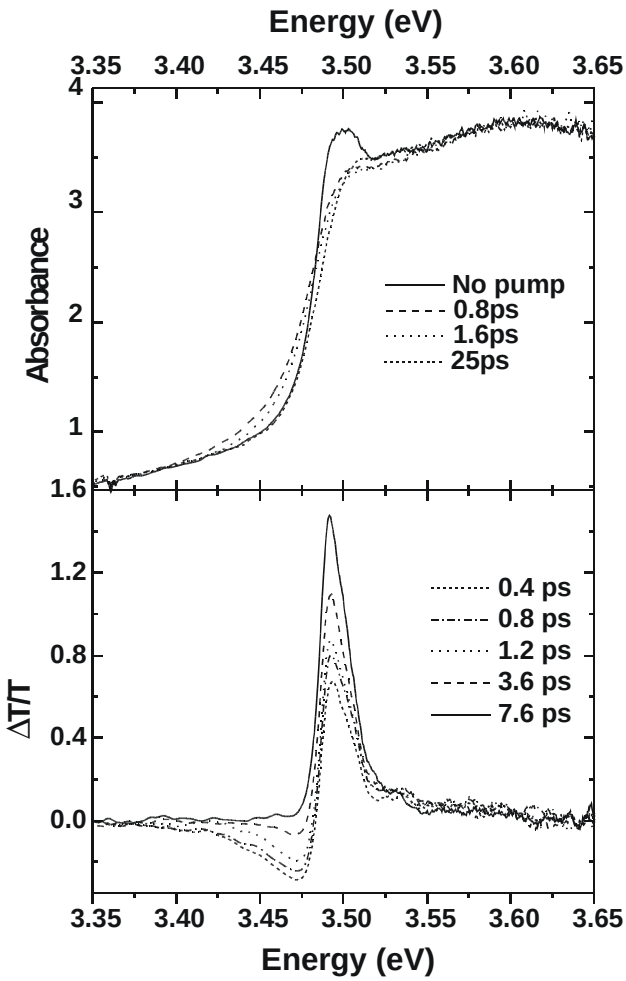

Figure 3. (a) Absorption spectra from sample 2 at various time delays. (b) Differential transmission spectra from sample 2 at 4 K for various time delays after excitation. The pump energy is 4.67 eV.

Figure 3(b) shows normalized differential transmission spectra taken at 4 K for sample 2, using the femtosecond pump-probe system described above. One prominent feature that is immediately obvious is the large induced absorption seen below the exciton energy, extending as far as 3.35 eV, 400 fs after excitation. This is nearly 180 meV below the band-edge. The feature recovers quickly, and has disappeared completely by 7.6 ps after excitation, leaving fully-bleached A and B exciton transitions, together with some induced transmission above the band-edge due to free-carrier effects. As the laser pump energy is 4.64 eV, the absorption length is very short. This implies that the sample is excited non-uniformly, and that a dense, rapidly expanding electron−hole plasma is produced. The measured transmission spectrum above the band-gap is thus complex and difficult to interpret, and further experiments with pump energies near the band-edge have been undertaken[9]. Nonetheless, any shift of the band-edge to lower energies due to the presence of an electron-hole plasma will be immediately apparent due to the rapid increase in the absorption in regions where previously the transmission was high. As can be seen clearly in Figure 3(a), which shows the measured absorption spectra for the excited GaN epilayer as a function of time, the origin of the induced absorption is band-gap renormalization due to the presence of a high density of photoexcited carriers in the band[10]. The estimated initial carrier density is 5×10^{19} cm^{-3}. This density is comparable to that at which stimulated emission is seen in sample 1, and the shift is consistent with that expected for such carrier densities[11].

Discussion

Although the two samples have different thicknesses and impurity densities, it is nonetheless likely that the large red-shift in the energy at which stimulated emission appears in sample 1 is a consequence of band-gap renormalization, since gain will be largest in regions where intrinsic and extrinsic internal losses are minimized. We see no evidence of excitonic scattering in our spectra. The relatively high density at which gain appears in our samples may be due to localisation of carriers as seen in InGaN quantum wells by Song *et al.*[3)]. It is clear from the absorption data that, at the densities where net gain is seen, the excitons are fully bleached and the electron-hole system is in the plasma phase. We thus conclude that stimulated emission from GaN epilayers such as these proceeds via the recombination of an electron-hole plasma, and that band-gap renormalization may account for the energy at which stimulated emission appears.

References

1. D Wiesmann, I Brener, L Pfeiffer, M A Khan and C J Sun
   Appl. Phys. Lett. 69, 3384 (1996)
2. S Hess, R A Taylor, J F Ryan, B Beaumont and P Gibart
   Appl. Phys. Lett. 73, 199 (1998)
3. Y–K Song, M Kuball, A V Nurmikko, G E Bulman, K Doverspike, S T Sheppard, T W Weeks, M Leonard, H S Kong, H Dieringer and J Edmond
   Appl. Phys. Lett. 72, 1418 (1998)
4. S Bidnyk, T J Schmidt, Y H Cho, G H Gainer, J J Song, S Keller, U K Mishra and S P DenBaars
   Appl. Phys. Lett. 72, 1623 (1998)
5. T J Schmidt, J J Song, Y C Chang, R Horning and B Goldenberg
   Appl. Phys. Lett. 72, 1504 (1998)
6. K L Shaklee, R E Nahory and R F Leheny
   J. Lumin. 7, 284 (1973)
7. G Frankowsky, F Steuber, V Härle, F Scholz and A Hangleiter
   Appl. Phys. Lett. 68, 3746 (1996)
8. L Eckey, J Holst, A Hoffman, I Broser, H Amano, I Akasaki, T Detchprohm and K Hiramatsu
   J. Lumin. 72-74, 59 (1997)
9. S Hess, R A Taylor, J F Ryan, F Walraet, N J Cain, V Roberts, and J S Roberts
   in preparation
10. H Schweizer, A Forchel, A Hangleiter, S Schmitt-Rink, J P Löwenau and H Haug
    Phys. Rev. Lett. 51, 698 (1983)
11. W F Brinkman and T M Rice
    Phys. Rev. B7, 1508 (1973)

X-Ray Lithography Using Novel Mask Making Technique

J A Cairns, A G Fitzgerald, G J Berry, M R Davidson

Department of APEME, University of Dundee, Dundee, DD1 4HN, UK

J Thomson

Department of Chemistry, University of Dundee, Dundee, DD1 4HN, UK

Main contact email address: *j.a.cairns@dundee.ac.uk*

Introduction

High density silicon chips are manufactured by projecting an image of their circuitry through a mask onto the silicon wafer. The masks consist of a quartz substrate coated with a chromium layer which is selectively etched to produce the desired pattern. One difficulty is to produce linewidths much narrower than 1 μm. Although the chip maker can project the image through a stepper system and thereby reduce it by a factor of 5, this imposes an ultimate limit in the linewidth of ~0.2 μm achievable on the chip. To produce next-generation integrated circuits the industry must undergo a complete paradigm shift. No less than five possible replacements have been proposed to succeed optical lithography which include: extreme ultraviolet, SCALPEL, projection ion beam lithography, X-ray lithography and electron beam direct write. The main problem preventing the implementation of these techniques is that of mask fabrication, which involves a series of complex processing steps, often onto fragile membrane-type substrates.

At the University of Dundee we have investigated a new method for the production of X-ray masks[1,2] This involves the use of a newly synthesised range of organometallic compounds which decompose under the influence of electron beam irradiation, leaving behind a metallic residue. Since electron beams can be focused down to <0.1 μm, this opens up an entirely new method of producing masks. The main aim of the experiments performed at the Lasers for Science Facility was to investigate the potential of organometallic compounds to produce X-ray masks. This report describes experiments performed using the soft X-ray source at the Rutherford Appleton Laboratory with X-ray masks produced from organometallic compounds.

Experimental

The X-ray mask blanks were supplied by Fastec Ltd, and consisted of a 7.5 mm square of silicon with a 1 mm square silicon nitride membrane of 100 nm thickness. Since the masks were going to be patterned by electron beam lithography, it was necessary to deposit an anti-static coating on top of the insulating silicon nitride. For this reason chromium was deposited to a thickness of 10 nm by sputtering.

The organometallic compounds used were cyclooctadiene platinum chloride, triphenylphosphine gold chloride and triphenylphosphine platinum fluoride. Owing to the inherent fragility of the substrates, it was decided that thermal evaporation provided the best means of thin film production. It was found that the organometallic compounds evaporated readily to form uniform films of thicknesses ranging from 0.1 to 2.5 μm.

The masks were then patterned in the electron beam pattern generator at an accelerating voltage of 20 kV, a beam current of 18 pA with a typical dose of 8 $mCcm^{-2}$ and a beam step-size of 25 nm. Typical exposures took less than 40 minutes to complete. A series of patterns were produced such that the best resolution could be achieved. Figure 1 shows a scanning electron microscope image of a pattern produced using cyclooctadiene platinum chloride.

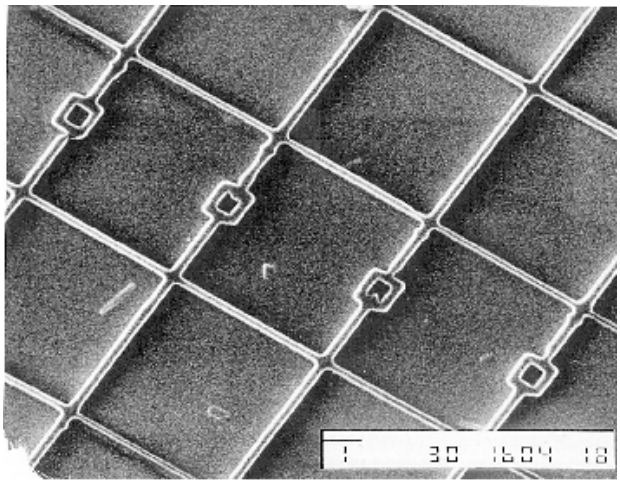

Figure 1. SEM image of absorber pattern produced from the electron beam irradiation of cyclooctadiene platinum chloride (scale bar represents 1 μm).

Using scanning electron microscopy the linewidths of the metal patterns were found to be better than 250 nm. Figure 1 clearly shows the excellent potential of the electron beam irradiation of organometallic compounds to produce high resolution patterns. Some evidence of proximity effect is observed in Figure 1. The rounding off of corners on rectangular features and the rounding off at the intersection between perpendicular lines are all caused by proximity effects.

The soft X-ray source at Rutherford Appleton Laboratory uses a system of excimer lasers which produce trains of picosecond pulses. These are focused down to a 10 μm spot onto a moving tape target material. This results in the ablation of material which is heated to typically 10^7 K, which in turn results in the thermal generation of X-rays. Two types of targets were commonly used for X-ray lithography: Mylar and copper. Copper is used to produce 1.2 nm X-rays (CuLα) and Mylar is used to produce carbon 3.67 nm X-rays (CKα). It was found to be advantageous to use carbon X-rays for pattern transfer. The reason for this is that the absorption of platinum and gold at 3.67 nm is greater by a factor of about ten than the absorption at 1.2 nm whereas the absorption of the membrane differs only by a factor of two. This results in an improvement in contrast of approximately 4 to 5 times. Figure 2 shows a photograph of the soft X-ray source at the Rutherford Appleton Laboratory.

Negative resist (AZPN114) was used which was deposited onto silicon wafers by spin coating to a thickness of 500 nm. The resist was held 23 μm from the mask using a Mylar spacer. X-ray exposure was performed in helium at 20 Torr. This is necessary since air would absorb a significant proportion of the low energy X-rays. The resist was exposed to X-rays with doses at the sample ranging from 1.3-10 $mJcm^{-2}$. Following exposure, the resist was post-baked at 105 °C for five minutes and developed in AZ 518MIF developer for fifteen seconds.

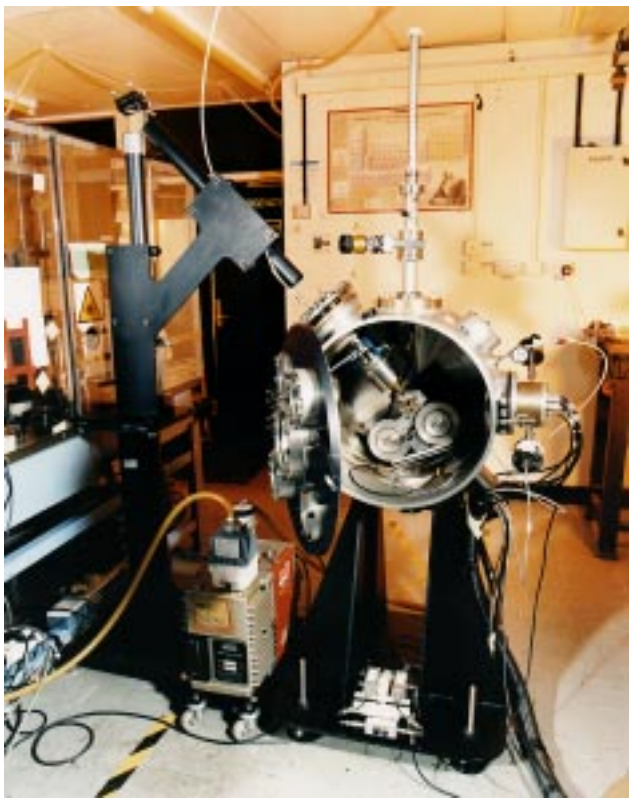

Figure 2. Photograph of soft X-ray source used at the Rutherford Appleton Laboratory.

Results and Discussion

Following the exposure and development of the resist, the patterns were found to be transferred faithfully from the mask. A typical pattern transfer is shown in Figure 3.

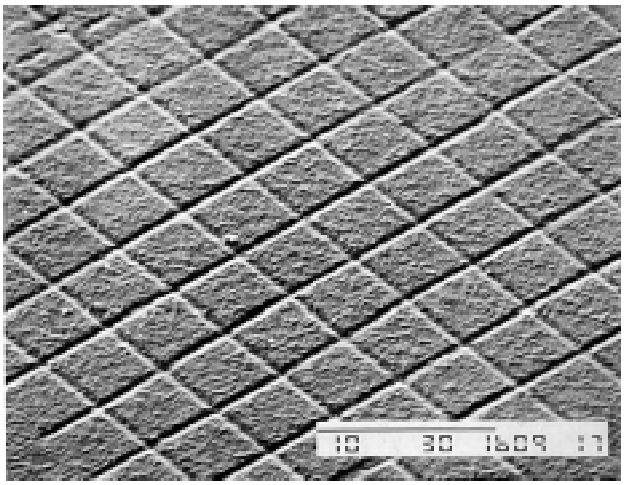

Figure 3. SEM image of a typical resist transfer, (scale bar represents 10 μm).

One concern is that the resist does not appear to be developed through to the silicon surface. This could be a result of three factors: over-exposure, under-development or an insufficient absorber thickness. Since the development and exposure parameters are standard, this effect must be a result of insufficient absorber thickness. To circumvent this problem thicker layers of organometallic must be used to increase the thickness of the deposit. This would lead to loss of resolution owing to the forward scattering of the incident electrons. A move to higher accelerating voltages such as those possible with the scanning transmission electron microscope would lessen the effect of these forward scattered electrons. An accelerating voltage of 100 kV should, in theory, permit the exposure of thicker organometallic layers with less scattering. For this reason we are currently in the process of modifying a scanning transmission electron microscope for electron beam lithography. One disadvantage with using more energetic electrons is that the organometallic is less sensitive. Another option is to use organometallic compounds containing a higher percentage of metal.

Summary

In summary, we have demonstrated the ability to produce X-ray masks with linewidths of the order 250 nm. These have been used in conjunction with the soft X-ray source at the Rutherford Appleton Laboratory for X-ray lithography. Our method of mask fabrication has significant advantages over current methods particularly in the reduced number of processing steps needed.

Acknowledgements

We gratefully acknowledge the financial support provided by the EPSRC and the technical assistance of Mr W Shaikh and Mr J Westhall.

References

1. M R Davidson, G J Berry, J A Cairns, A G Fitzgerald, B Lawrenson, J Thomson, I C E Turcu, W Shaikh, N Spencer, R M Allott and N Takeyasu, Microelectronic Eng, 41/42, 279, (1998).

2. G J Berry, J A Cairns, M R Davidson, D R G Rodley, J Thomson, I C E Turcu and W Shaikh Rev. Sci. Instrum, 69, 3350, (1998).

The Laboratory Scanning X-Ray Microscope

A G Michette, C J Buckley, S J Pfauntsch, N R Arnot, J Wilkinson, Z Wang

Department of Physics, King's College London, Strand, London WC2R 2LS

W Shaikh

Central Laser Facility, CLRC Rutherford Appleton Laboratory, Chilton, Didcot, Oxon, OX11 0QX, UK

Main contact email address: *Alan.Michette@kcl.ac.uk*

Introduction

The laboratory scanning x-ray microscope has been installed on a dedicated target chamber in the LSF x-ray laboratory, and has been used to obtain preliminary images. All components of the microscope have performed well, although some upgrading is needed in order to produce a user-friendly facility. However, two significant problems remain which degrade the quality of the images. These are vibration and electrical noise; major efforts have been taken to reduce the effects of these, but spatial resolutions are still limited to ~0.4 µm at best.

The microscope

A photograph of the microscope installed on the target chamber is shown in Figure 1, and a schematic diagram of the set-up is given in Figure 2. In common with all high-resolution x-ray microscopes, a zone plate is used to form the x-ray probe. Those used, made in-house, have tungsten zones on 50 nm thick Si_3N_4 substrates. The diameter is 93 µm with an outermost zone width of 103 nm, giving a focal length of 2.842 mm for 3.37 nm x-rays. Larger zone plates with finer outer zones can be made routinely, but were not necessary for the work carried out so far. A 40 µm diameter central stop and a 30 µm diameter order-selecting aperture (OSA) positioned 2 mm downstream of the zone plate ensure that only first-order focused x-rays reach the specimen. The zone plate is mounted on a two-axis translator 45 cm from the ~25 µm diameter source[1)], giving a demagnification of ~150 and a focal spot size of ~0.2 µm.

Figure 1. The x-ray microscope installed on the target chamber.

Specimens are mounted on a three-axis translation stage driven by motors with 1 µm step sizes. Two of the axes are used to position the specimen transverse to the x-ray beam and the third for focusing. A CCD camera (lower centre in Figure 1, in its retracted position to the right of the detector) with a ×10 objective lens is mounted on a stage collinear to the focusing stage within 1 µm over a range of 10 cm. This allows the positioning of all the components both longitudinally and transversely by first viewing the chamber exit window (500×500 µm Si_3N_4, 100 nm thick coated with 40 nm of aluminium). Secondly, the camera is moved downstream the correct distance to view the zone plate so that it can be positioned over the centre of the exit window. Thirdly, the camera is moved the correct distance downstream to view the OSA which is positioned over the centre of the zone plate. Finally, the camera is moved the correct distance downstream to view the specimen (at the x-ray focus) which is positioned to an area of interest. This procedure allows positioning of all

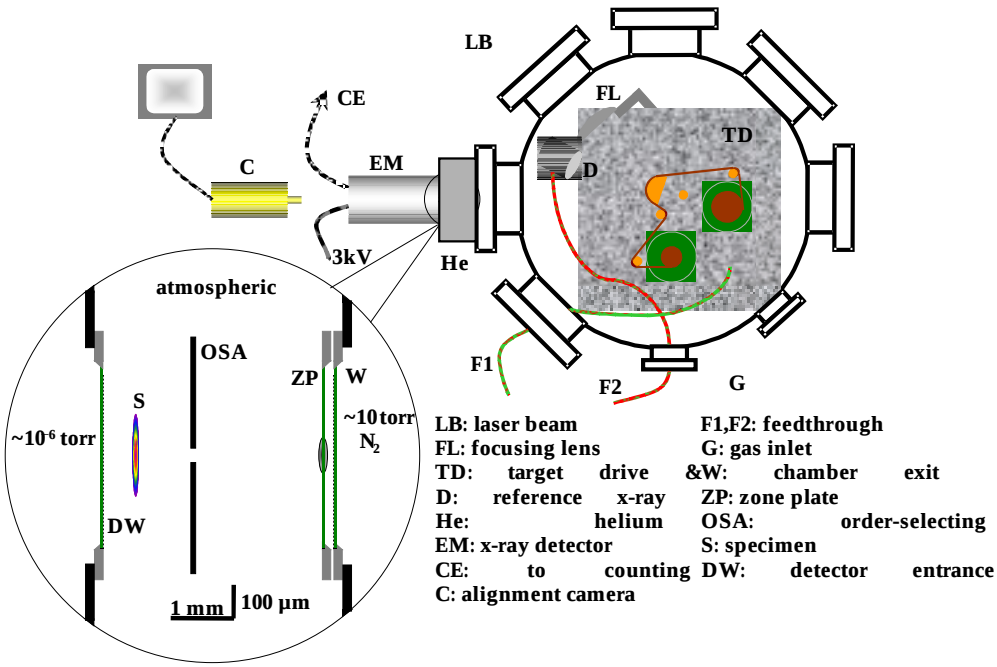

Figure 2. Schematic Diagram of the X-Ray Microscope. The inset is roughly to scale, with different vertical and horizontal scales.

components to within a few micrometres; this is sufficiently accurate for all except the OSA which has to be moved to its final position by using the x-ray signal as described later.

For well established reasons[2], thin tape targets are used in the LSF x-ray source. These give less debris than rotating solid cylinders and can easily be driven to present a fresh surface to the laser beam every pulse. Alternatives, such as liquid-drop or gas-puff targets, are much more expensive to implement and provide a smaller range of materials. Also, because the microscope was based on source rather than specimen, the target drive had to incorporate suitable motions for this, which would have been very difficult with a liquid-drop or gas-puff system. The main criteria used in the design were

1. The tape size and driving speed must be such that tape changes are infrequent, allowing large images to be acquired. Thus 12 mm wide tape was used to allow many more "tracks" (by moving the tape up or down relative to the laser beam) than for the 4 mm tape on the original LSF target drive.

2. Accuracy of movement. The $\lambda = 249$ nm laser beam is focused onto the tape surface using a 9 cm focal length aspheric lens. The laser beam is a 2×1 cm and so the depth of focus is ~±10 µm, but a plasma can be formed with the required emission parameters over a larger range of focus. Experimentally, the water-window x-ray emission was constant over a few hundred micrometres, and so the lens was positioned at the centre of this range. Scanning is achieved by moving the lens and the target surface together in two orthogonal directions. This movement is demagnifed on the specimen by the zone plate and, for an image resolution of ~0.2 µm, minimum target step sizes of ~15 µm (Shannon sampling) are needed. The motors used could be stepped at 1 µm (or less with the microstepping option).

3. The movement of the tape surface along the beam direction clearly has to be significantly less than 15 µm in order to prevent blurring. By shining a HeNe laser beam across the edge of the surface and magnifying with a microscope objective the movement could be monitored; for the original LSF tape drive, the surface was observed to oscillate with an amplitude of ~10 µm with some less regular movements of up to 50 µm. With the target drive built for the x-ray microscope no oscillations could be seen, which meant that the amplitude was much less than 1 µm.

The laser-plasma x-ray source presents a challenge for accurate detection of the numbers of photons in each pulse, since they arrive in very short bursts. Ideally, a detector should produce an output signal which is consistently proportional to the number of incident photons. Several phenomena prevent this from being the case: photon energy conversion statistics, gain statistics, noise and non-linear effects. If a detector is subject to insignificant noise, whether internal or external, and is linear over the range of operation, then the deviation from proportionality of the output is determined primarily by the Poisson variation in the number of particles generated by the incident photons. Since the LSF x-ray laboratory is noisy electromagnetically, the detector has to be shielded. It did not prove possible to achieve this with a windowless photodiode while at the same time cooling it to reduce the internal (thermal) noise. Although we are confident that, given time, this problem can be overcome, it was decided that it would be prudent to develop an alternative detector.

Photomultiplier tubes have the desired properties as they use focused dynode systems which provide linear gain over several decades of input level. An Electron Tubes Ltd 129EM photoelectron multiplier tube was removed from its glass housing and placed in a vacuum chamber with a silicon nitride entrance window. The first dynode was coated with 100 nm of caesium iodide which acted as a photoemitter and the dynode chain then provided amplification of the photoelectron signal. The detector was tested[3] on the X1A synchrotron beamline at the Brookhaven National Laboratory, USA, and at the LSF x-ray source prior to its installation on the x-ray microscope. In both cases the dynode voltage was –2.5 kV.

The synchrotron tests showed the linearity of the detector for count rates approaching 1 MHz. The data were obtained by comparing the signals with air and helium between the exit slit and detector for different slit widths. The LSF tests were compared with the signal from the reference diode (inside the target chamber, and therefore shielded) with that from the EM detector. Charge pulses from both the EM and the diode were measured and stored via a Lecroy 2249A module, a CAMAC crate and a PC. These results show a non-linearity at high count rates (the peak count rate for the LSF source is much greater than the average for the synchrotron). This is almost certainly due to inter-dynode voltage drop at higher charge pulse levels. For initial imaging with the microscope this non-linearity is not too important, as count rates are much lower than in the tests.

Image acquisition and display and computer control of the microscope (including all stage movements) are carried out using a PC with software developed using the commercial package IDL. Because of some problems with IDL drivers for Windows NT, alternative control software was written in QBASIC, which proved just as efficient though slightly cumbersome. Image data, consisting of reference diode and EM detector output, was read into the PC via the Lecroy 2249A module and CAMAC crate. The EM data is normalised by the reference diode data to remove effects of fluctuating plasma output.

Final alignment of the OSA, to ensure that the unwanted diffraction orders are fully removed, has to be carried out using the x-ray beam. First, the OSA is moved across the x-ray beam, both horizontally and vertically, while monitoring the detector signal and the points at which the signal drops to zero are noted. The OSA is then positioned in the centre of the range. Second, a pinhole is scanned across the beam downstream of the focus which, if the OSA is correctly aligned, should give a characteristic symmetric donut image. Misalignment of the OSA will allow zero (and >1) order diffracted radiation to reach the detector, giving an asymmetric image. Focusing is carried out by scanning an edge across the beam and fitting the variation in detector signal to a normal distribution; the smallest FWHM defines the focus and also gives a measure of the resolution. An example is shown in Figure 3.

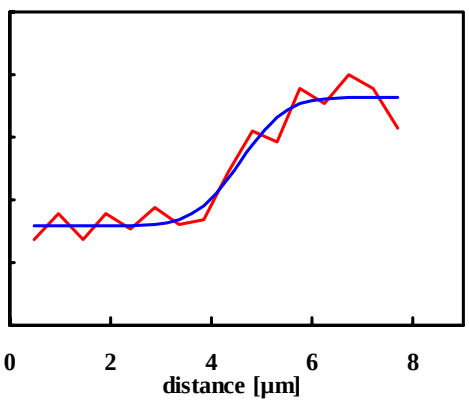

Figure 3. Result of an edge scan across the beam. The data for this example were taken when vibrations were high (rms ~0.6 µm). The fit indicates a resolution of ~0.75 µm.

Performance of the microscope

The known parameters of the x-ray source and zone plate arrangement indicate a theoretical resolution of ~0.2 µm. However, vibration monitoring indicated rms amplitudes of several micrometres, mainly due to vacuum pumps. By careful isolation of all critical microscope components using cork pads, amplitudes could be reduced to ~0.1 µm, although at times values as high as ~0.6 µm were recorded, especially during the late evening. This indicates that, at best, vibration need not be a major problem (although it will be when the microscope is reconfigured to allow better resolution capabilities), but that this could not be relied upon.

The other major problem in the use of the microscope was electromagnetic noise. The extent of this is shown in Figure 4, which is a typical EM detector output pulse. Here, the pulse height is ~300 mV and the noise has an amplitude of ~50 mV.

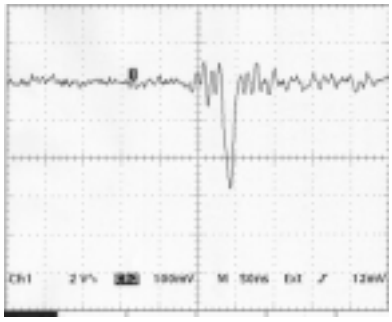

Figure 4. An output pulse from the EM detector.

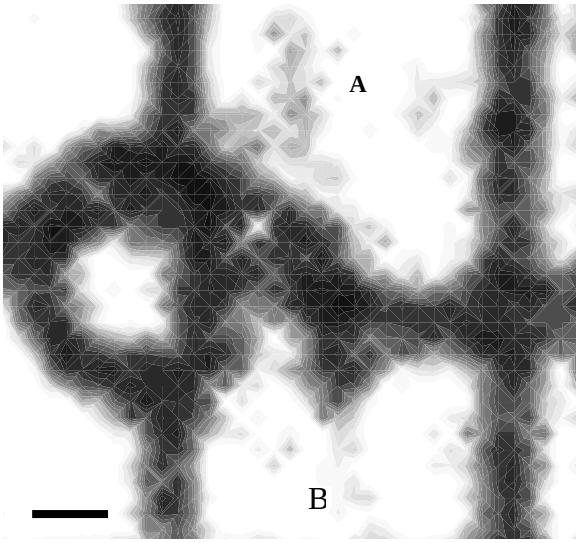

Figure 5. A low resolution image of myofibrils on an em finder grid. The figure "6" is a location mark on the grid. A cluster of myofibrils can be seen at upper centre (A), with a less dense cluster extending downwards (B). The scale bar is 10 µm.

Under favourable circumstances, the noise amplitude could be reduced to ~2 mV which, if reproducible, would have been acceptable. However, despite attempts to achieve reproducible noise and to limit its effects, the amplitude varied in an unpredictable way.

Despite the vibration and noise problems, images have been obtained, albeit at poorer resolution than would otherwise have been achievable. An example is shown in Figure 5.

Conclusions and future work

The microscope performance has clearly been severely compromised by the effects of vibrations and electrical noise. The characterisation of these and the reduction of their degrading effects will be essential in order to allow the development of the microscope as a user facility.

References

1. A G Michette et al
Annual Report of the Central Laser Facility, p119, (1998)

2. A G Michette
J. X-Ray Sci. Technol. 7, 98, (1997)

3. C J Buckley et al
X-Ray Microfocusing: Applications and Techniques, SPIE Proceedings 3449, 208, (1998)

Growth, excimer laser annealing and characterisation of ECR-PECVD Si thin films for seed layer production of crystalline Si on amorphous substrates

S Summers, H S Reehal

School of Electrical, Electronic & Information Engineering, 103 Borough Rd, South Bank University, London. SE1 0AA

G J Hirst

Central Laser Facility, CLRC Rutherford Appleton Laboratory, Chilton, Didcot, Oxon, OX11 0QX, UK

Main contact email address: *summersd@sbu.ac.uk*

Introduction

Current silicon solar cell manufacturing costs are kept high due to the use of expensive crystalline silicon substrates. The substrates account for around 50% of the cost of production and inhibit the development of photovoltaic product lines. Therefore low cost alternatives need to be used. An obvious choice is glass and this has been the choice of many research groups in this field. However glass constrains the processing temperatures in thin film crystalline silicon growth limiting traditional high temperature (>600 °C) approaches and so other techniques are required to attain the required crystallinity of material on an amorphous substrate.

Excimer laser crystallisation (ELC) has been used to produce crystalline silicon from amorphous silicon films as thin film transistors for use in active matrix LCD displays[1)]. This approach could, in principle, be extended to large area crystallisation for solar cells and is the motivation for this work.

Thin Film Growth

Sample set A. Silicon thin films with thickness' of 50, 100 and 200 nm were grown under varying conditions using electron cyclotron resonance plasma enhanced chemical vapour deposition (ECR PECVD). A schematic of the ECR PECVD reactor is given in Figure1. The growth temperature of 375 °C was kept constant for all depositions as was the microwave power at 500 W. The plasma pressure was confined to the range 5 - 5.5 mTorr while the silane to hydrogen ratio of the depositions were varied giving rise to a series amorphous films.

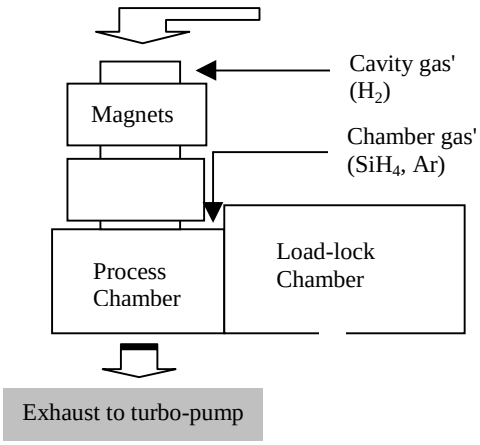

Figure 1. ECR PECVD Reactor schematic.

The gas ratios used were SiH_4:H_2, 1:10, 2:10, 3:10 and 4:10.

Each set of process parameters was repeated twice to deposit nominally identical films on two substrates. One set on SiO_2 coated (100) Si, and one set on Corning Glass 7059.

In addition depositions were also performed with Ar gas introduced into the deposition chamber. Some films were also deposited on Pd coated CG7059 and Cr coated CG7059. The metal coatings were produced by vacuum evaporation.

Sample set B. Silicon thin films with thickness' of 200 and 400 nm were investigated. The growth temperature of 400 °C was kept constant for all depositions as was the microwave power at 330 W. The plasma pressure was confined to the range 3.5 - 3.7 mTorr. The silane to hydrogen ratio of the depositions was kept constant at 30:1. The gases were mixed as 2 sccm of H_2 flowing through the cavity for plasma gas, and 1sccm of SiH_4 and 28 sccm of H_2 flowing in the process chamber for process gases.

This set of deposition parameters gave rise to microcrystalline silicon thin films. These films were deposited on two substrates. One set on SiO_2 coated (100) Si, and one set on Corning Glass 7059. Standard substrate preparations were performed before deposition to ensure high cleanliness during the process for both sets of samples. Film thickness' were measured by a Dektak Profilometer.

Excimer Laser Crystallisation

Sample set A. The deposited silicon films were irradiated by KrF excimer laser uv radiation at 248 nm wavelength. Each identical film was subjected to three irradiation regimes: i) 1 shot @ ~230 mJcm^{-2}, ii) 2 shots @ ~120 mJcm^{-2} and iii) 3 shots @ ~120 mJcm^{-2}. The samples were kept at room temperature and were irradiated under a single atmosphere of Ar gas.

Sample set B. A matrix of irradiation conditions was devised and the samples were irradiated under four fluences; 320 mJcm^{-2}, 520 mJcm^{-2}, 750 mJcm^{-2} & 1 Jcm^{-2}. Each fluence was repeated with a varying number of shots per irradiation area, ranging from 1 to 128. The samples were kept at room temperature and were irradiated under a single atmosphere of Ar gas.

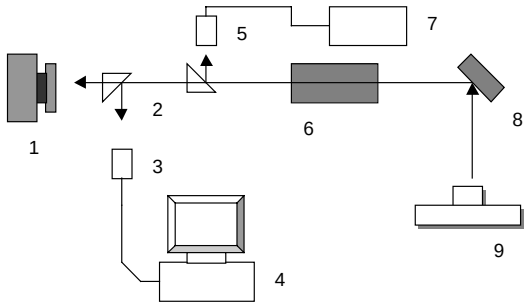

Figure 2. ELC experiment schematic.

A schematic of the ELC set-up is shown in Figure 2. The numbered components are as follows: 1. Sample chamber and stepper motor rig; 2. 8% Beam splitters; 3. CCD camera; 4. PC; 5. Gentec detector; 6. Attenuation plates; 7. Laser energy detector; 8. Mirror; 9. Laser output.

The laser used was a Lambda Physik LPX-200 KrF excimer. Targeting was achieved using a Spectra Physics Inc. 10 mW He-Ne laser set co-linearly with KrF excimer laser. Pulse fluence was controlled with the use of Hoya Corporation 8% attenuation plates allowing for minimal changes in experimental setup from shot to shot. The shot powers were calibrated and measured by Gentec ED-500 and ED-200 laser energy detectors, respectively, feeding an automated laser energy

meter. Beam profile images were also captured using a Pulnix TM765 CCD chip with 248nm filter connected to image capture equipment.

Microscopy of Irradiated Films

Light microscopy of the irradiated regions showed apparent damage effects on most of sample set A and some of sample set B. Scanning Electron Microscopy reveals possible solidification processes as the images show a network of solidified material.

Micro-Raman Spectroscopy

Raman spectroscopy of the samples reveals substantial qualitative improvement of film crystallinity on all samples. Amorphous and crystalline silicon are characterised by a wide feature centred at 480 cm^{-1} and a narrow peak at 520 cm^{-1} respectively[2]. The Raman spectroscopy was performed using a Renishaw Raman Model 1000 Microscope operating with Ar ion 488 nm laser radiation.

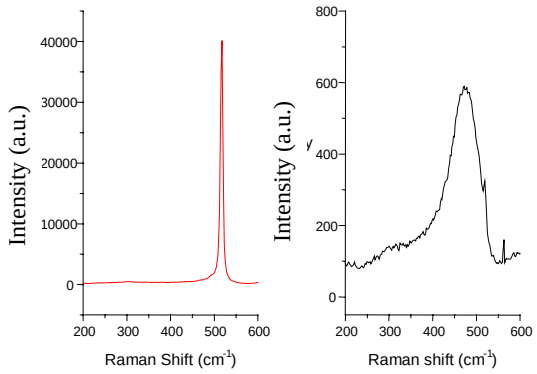

Figure 3. Post and pre-annealed Raman spectra.

Figure 3 shows the effects of laser annealing on a 50nm film from sample set A. The spectra were recorded under identical circumstances and so a radical increase in intensity is apparent as well as a shift from the amorphous phase to the crystalline phase. The post laser anneal spectrum is centred on 517 cm^{-1} indicating a tensile stress in the film. The shift also indicates that the 520 cm^{-1} peak from the substrate is not interfering with the spectrum.

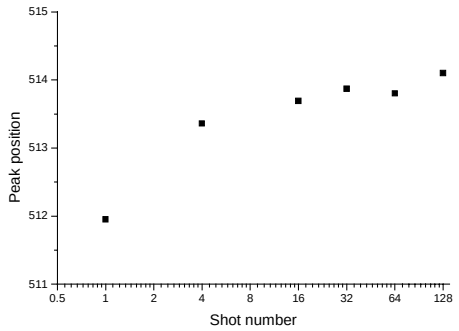

Figure 4. Raman peak intensity as a function of the number of irradiances.

Figure 4 displays the annealing effects of multiple shots a single fluence (320 $mJcm^{-2}$) on 400 nm films from sample set B. The large relative shift in the Raman peak position from 520 cm^{-1} is probably caused by a combination of internal stresses in the film and very small grain sizes[3].

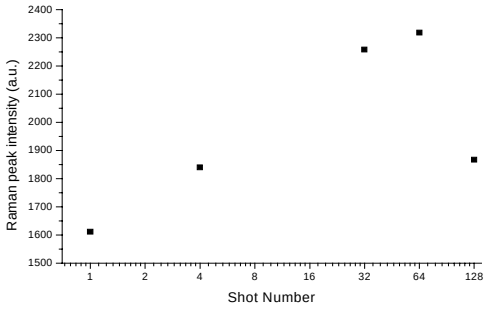

Figure 5. Raman peak position as a function of shot number.

A consistent improvement in film crystallinity as determined by Raman spectroscopy was obtained by laser annealing on all samples with the exception of the silicon films deposited on evaporated metal interlayers. The lack of improvement in these cases may be due to a number of factors. The metal films will act as a heatsink changing the thermal response of the system. Silicide phases will also form within the material and may occur inhomogeneously in the film.

The films tended to show surface damage effects at high shot fluences, which is to be expected with the film being completely melted and thermal coupling with the substrate occurring. High shot numbers also caused damage in some cases. Figure 5 shows a steady increase in peak intensity of a 200nm film from sample set B irradiated by 500 $mJcm^{-2}$ until the application of 128 shots when surface damage is apparent and the corresponding Raman spectra degrades.

Electron Recoil Detection Analysis (ERDA)

ERDA was performed on the crystallised films and showed substantial dehydrogenation of the irradiated areas compared to the pre-irradiated profiles. This confirms a proposal to use low fluence irradiations prior to the main annealing irradiation to dehydrogenate the film, potentially removing the time consuming process step of furnace annealing[4].

Future Work

The final film quality has been hampered by a small number of systematic problems, all of which can be eliminated. The films irradiated at high fluence and high shot numbers showed regions of damage consistent with non-uniformities in the incident beam profile. This will be resolved with the use of beam homogenising optics. The films often display surface features consistent with material loss. In some cases this may be due to ablative action localised in small regions corresponding to high fluence areas of the incident beam, but in general it is caused by explosive hydrogen release from the film during melting. This could be tackled with the use of a zero hydrogen film deposition technique, such as sputtering or the use of a dehydrogenation step after deposition by ECR PECVD.

Acknowledgements

The ERDA measurements were performed by N Barradas and C Jeynes of the Surrey University Ion Beam Facility. Financial support from EPSRC and BP Solar is gratefully acknowledged.

References

1. S D Brotherton *et al* IEEE Trans. Elec. Dev, 40 407, (1993)
2. P V Huong
   Analysis of Microelectronic Materials and Devices, Ed. M Grasserbauer and H W Werner , 151, Wiley (1996)
3. Jian Zi *et al*, Appl. Phys. Lett, 69 200, (1997)
4. D Sands, G Williams and P H Key
   Semicond. Sci. Technol, 12 750 (1997)

Spectra in the Range 5 to 50 Å from the X-ray Source

A Nottola[*], G J Tallents[§]

Department of Physics, University of Essex, Wivenhoe Park, Colchester, Essex, CO4 3SQ

[*] *Now at CNR-IESS, 00156 Rome, Italy*

[§] *From September 1999: Department of Physics, University of York, York YO1 5DD*

D T Goodhead, M A Hill, D L Stevens

Radiation and Genome Stability Unit, Medical Research Council, Harwell, Didcot, Oxon, OX11 0RD, UK

I C E Turcu[#], G J Hirst, W Shaikh, J Westhall

Central Laser Facility, CLRC Rutherford Appleton Laboratory, Chilton, Didcot, Oxon, OX11 0QX, UK

[#] *Now at JMAR Research, San Diego, CA, USA*

Main contact email address: *nottola@iess.rm.cnr.it*

Introduction

In order to characterise the CLF soft X-ray laser-plasma source for radiobiology experiments to be performed by the Radiation and Genome Stability Unit of the Medical Research Council, a series of spectroscopic measurements has been carried out on the X-ray source itself.

The characterisation was directed to choose materials to be used as laser targets giving the most efficient energy emission in selected X-ray regions in the range 0.2-2 keV with the narrowest bandwidth possible, to be further filtered in future experiments by means of X-ray optics or grazing incidence mirrors.

Experimental set-up

The soft X-ray laser-plasma source has been described in detail elsewhere[1,2]. The source was used in the 8-pulse configuration, each pulse lasting approximately 5 ps and with a pulse to pulse time separation of 2 ns. The laser irradiance was approximately 10^{15} Wcm^{-2}. The materials used as laser targets in this study were copper, steel (~iron), aluminium, titanium and Mylar (~carbon). Different kinds of spectrometers were used in order to record a large spectral range. A crystal spectrometer was used with flat PET, Beryl and KAP crystals. A transmission grating (TG) spectrometer was employed in order to record spectra at higher wavelengths. The spectrometers were set at an angle with the source normal, 45° for the TG and 60° for the crystal spectrometer. Both spectrometers were filtered to cut UV and visible radiation. The TG spectrometer was equipped with 0.1 μm of Al, while the crystal spectrometer had different filters depending on the spectral region under examination. We used 10 μm of Be or 1.5 or 3 μm of Al. The laser-plasma interaction chamber was filled with He gas at atmospheric pressure, in order to attenuate the debris flux from the plasma source.

Materials and methods

The spectra were recorded on Kodak DEF (Direct Exposure Film). The film was developed according to published procedures[3] making use of D19 developer and FX-40 fixer. The data were digitised using a Joyce-Loebl densitometer mod. MK III C, with a scanning spatial resolution of 10 μm. The experimental data were deconvolved by taking account of the film sensitivity, the crystal reflectivity or TG transmission, the different light paths in He for the crystal spectrometer, the filter transmission, the solid angle of emission as seen by the spectrometers and the number of laser shots. This gave spectra in units of photons/sr/Å/shot emitted from the source.

It was possible to identify a great number of spectral lines by comparing experimental data to reference tables found in the literature[4-6]. This was very useful to calibrate the wavelength scale in the spectra with some accuracy.

Results and discussion

In Figure 1 the copper spectrum obtained over the whole spectral range inspected is shown. In Figure 1(a) we can observe the continuum hard X-ray tail, measured with a PET crystal ($2d$=8.74 Å). By comparing this experimental data with the exponential slope of the bremsstrahlung emission, an electron temperature of 320 eV has been estimated for our plasma. In Figure 1(b) the spectral region obtained with a Beryl crystal ($2d$=16 Å) is shown, whereas in Figure 1(c) and 1(d) we present the result given by a KAP crystal ($2d$=26.6 Å), used at two different angles in order to extend the spectral range inspected up to 20 Å. In the last three figures there is a wavelength overlapping, so that the whole range between 7 and 20 Å has been covered. In Figure 1(e) the spectrum obtained with the TG spectrometer is shown.

Figure 2 shows the steel spectrum taken with the PET crystal, Figure (2a), Beryl crystal, Figure 2(b), KAP crystal, Figure 2(c) and TG spectrometer, Figure 2 (d).

In Figure 3(a) we show the aluminium spectrum measured with the PET crystal. In Figure 3(b) the aluminium spectrum in the region between 6.6 and 8.6 Å is presented, as obtained with the Beryl crystal. The L_α line is quite visible at 7.17 Å, whereas He_α and He_β lines are clearly visible at 7.76 Å and 6.64 Å, respectively. On the right side of the He_α line a number of satellite lines are also present. From the experimental L_α/He_α line intensity ratio, by comparison with theoretical simulations of the same quantity plotted as a function of the electron temperature[7], a value of 320 eV has been found for the electron temperature, in very good agreement with the value above mentioned for a copper target. In Figure 3(c) the spectrum obtained with the TG spectrometer is shown.

In Figure 4 the Mylar spectrum is reported. Figure 4(a) shows the KAP crystal data, with the oxygen L_β, L_γ and L_δ lines clearly visible at 16.006, 15.176 and 14.821 Å, respectively. Figure 4(b) shows the TG spectrum.

Figure 5 shows the titanium spectrum taken with the PET crystal, Figure 5(a), Beryl crystal, Figure 5(b), KAP crystal Figure 5(c), and TG spectrometer, Figure 5(d).

In Table 1 we report a summary of the maximum photon number emission from several targets. A wavelength range is given for the spectral regions considered over which various lines are emitted with an approximate bandwidth (full width) for each interval. To be noted is the extremely narrow bandwidth in the case of aluminium, due to the small number of intense isolated lines, see Figure 3(b).

Conclusions

We have described the spectroscopic characterisation of the soft X-ray laser-plasma source operating in the X-ray and UV

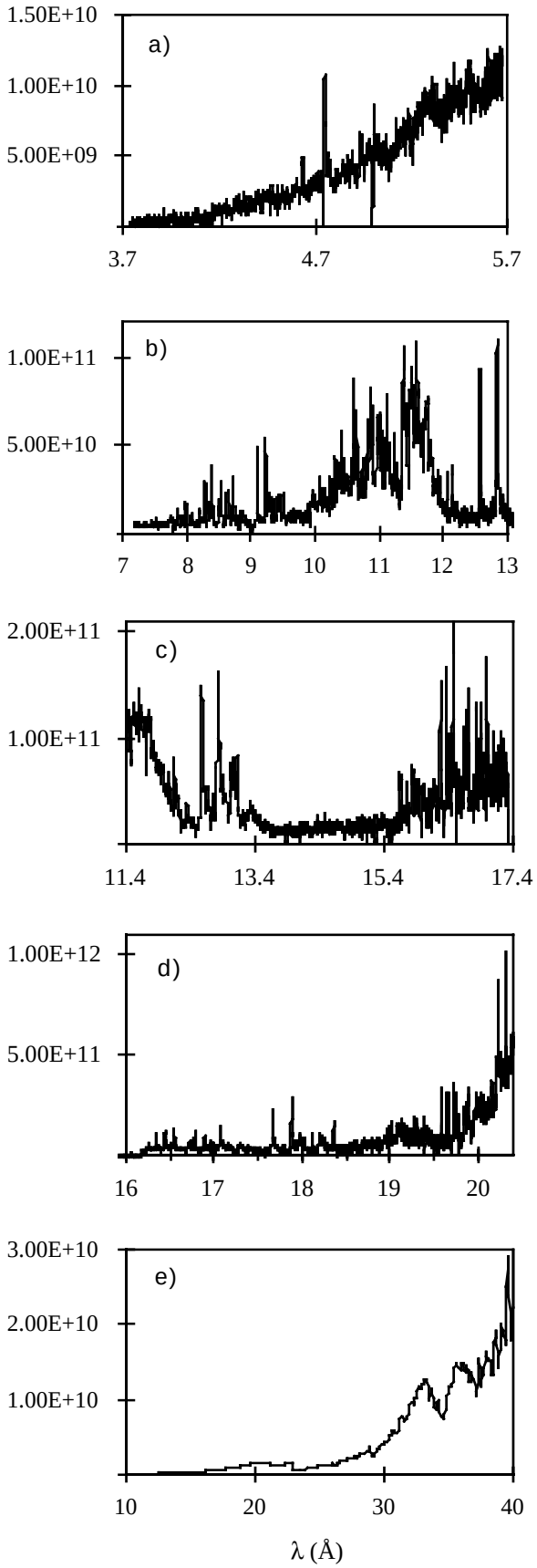

Figure 1. Copper spectra obtained with a) PET crystal, b) Beryl crystal, c) and d) KAP crystal, e) TG spectrometer. Vertical scale is in units of photons/sr/Å/shot.

laboratory of the Central Laser Facility. The study of several targets has been carried out making use of a crystal spectrometer equipped with PET, Beryl and KAP crystals, and a transmission grating spectrometer. Spectra covering the whole region between 5 and 50 Å were obtained, and using two different methods it was possible to measure the plasma electron temperature (~320 eV). A first evaluation of the absolute value of emission and its approximate spectral width from the several targets in the maximum output region has been given.

Acknowledgements

We would like to thank Mr. C. Brown and his co-workers at the CLF for their kind support in the filter making.

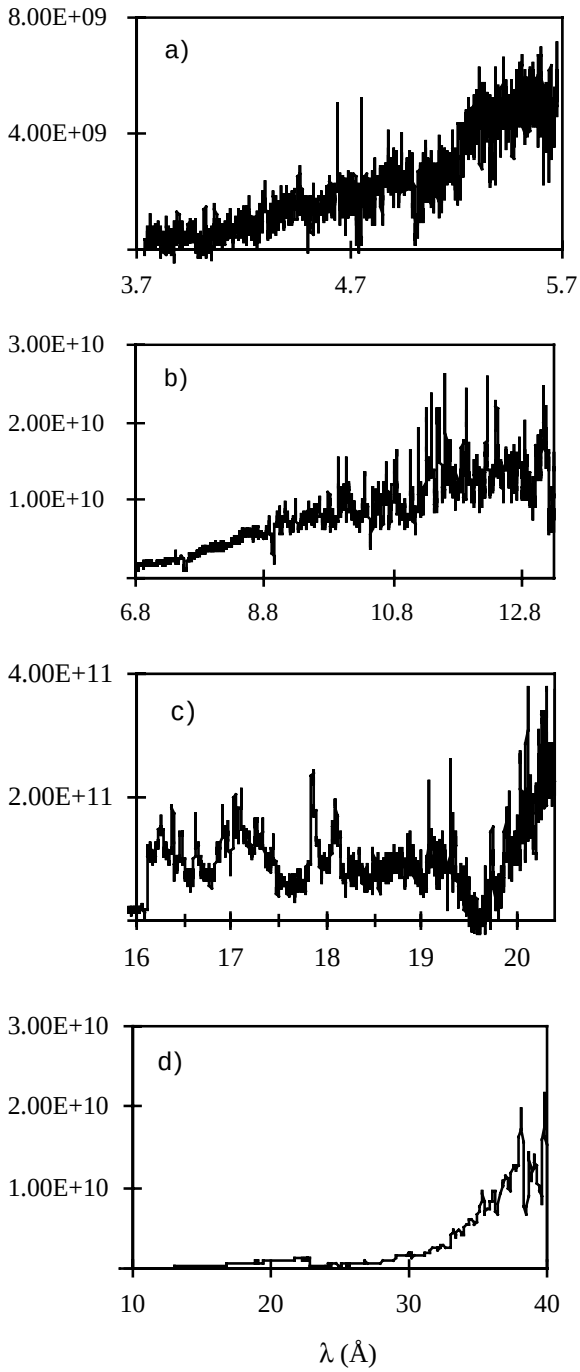

Figure 2. Steel spectrum obtained with a) PET crystal, b) Beryl crystal, c) KAP crystal, d) TG spectrometer. Vertical scale is in units of photons/sr/Å/shot.

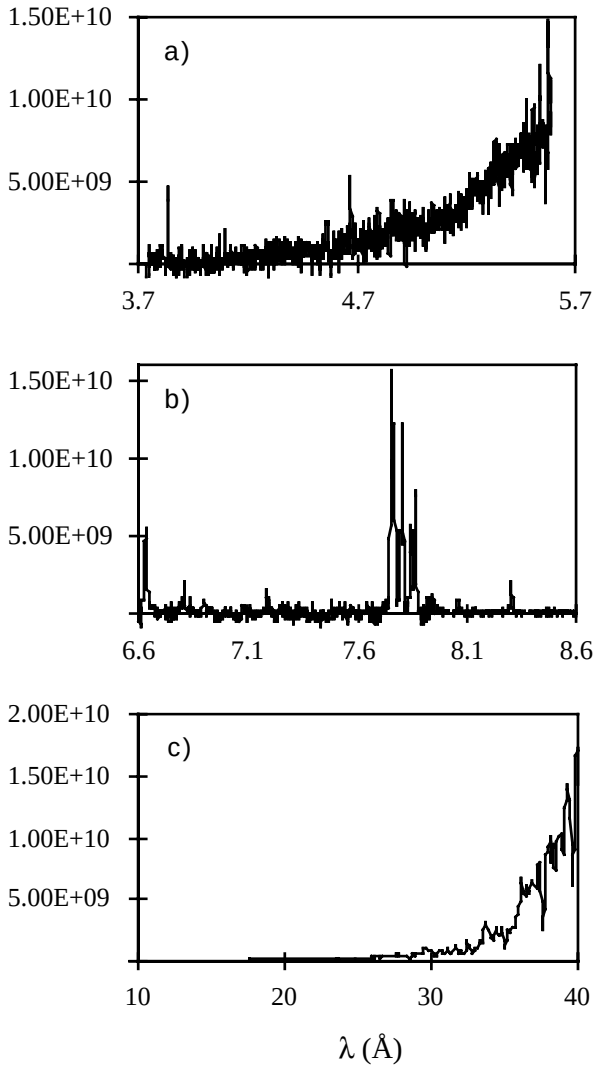

Figure 3. Aluminium spectrum obtained with a) PET crystal, b) Beryl crystal, c) TG spectrometer. Vertical scale is in units of photons/sr/Å/shot.

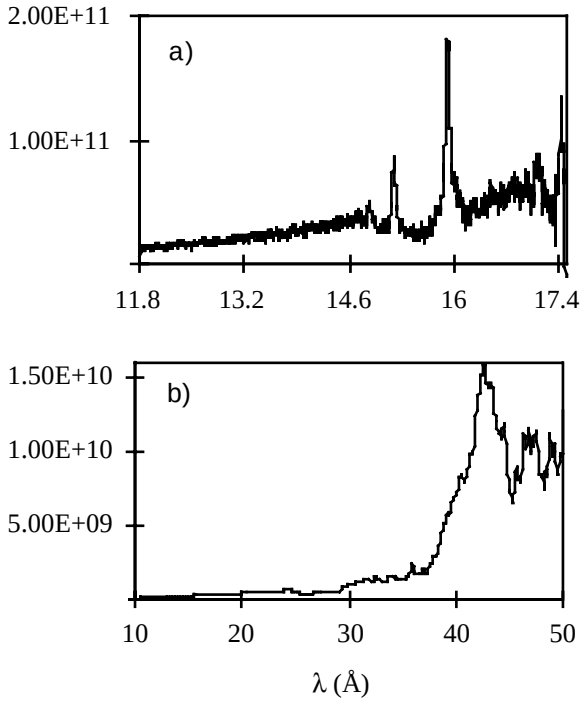

Figure 4. Mylar spectrum obtained with a) KAP crystal, b) TG spectrometer. Vertical scale is in units of photons/sr/Å/shot.

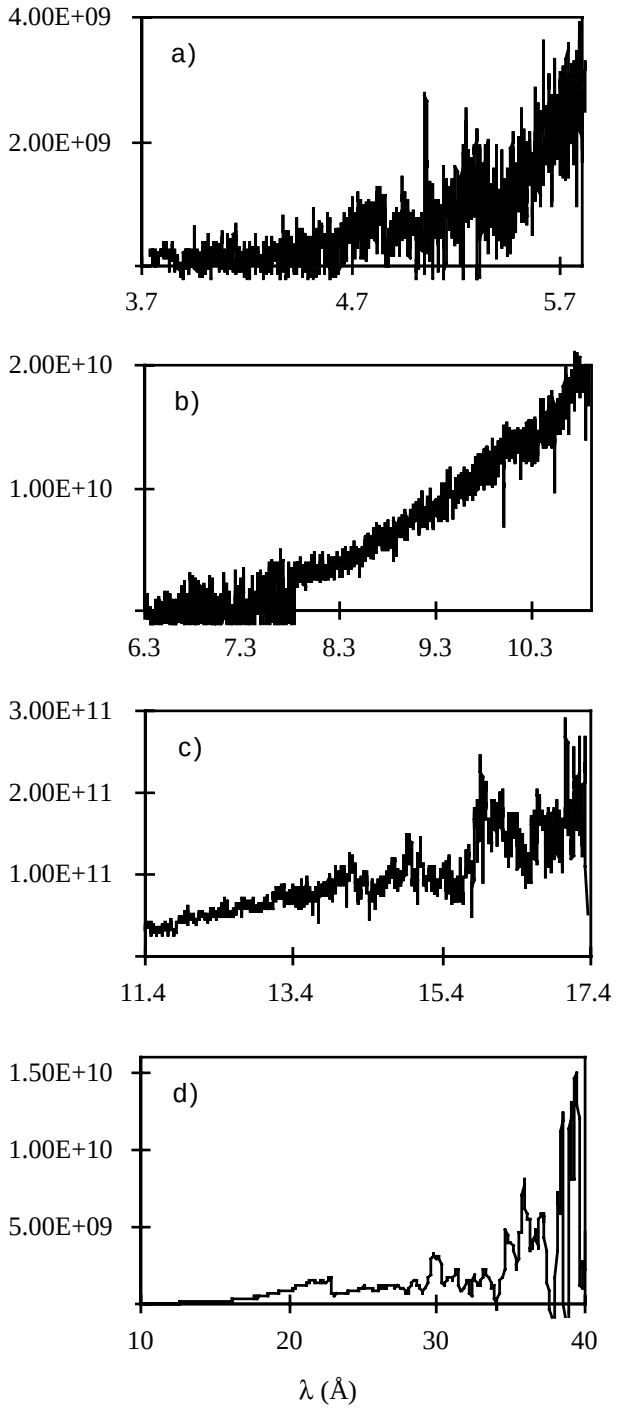

Figure 5. Titanium spectrum obtained with a) PET crystal, b) Beryl crystal, c) KAP crystal, d) TG spectrometer. Vertical scale is in units of photons/sr/Å/shot.

Target	Spectral region (Å)	Maximum flux (Photons/sr/Å/shot)	$\Delta\lambda/\lambda$ (%)
Copper	10-12	10^{11}	20
Steel	16.5-18.5	$2\cdot10^{11}$	10
Aluminium	7.75-7.9	$1.6\cdot10^{10}$	2
Mylar	14.8-16	$1.8\cdot10^{11}$	10
Titanium	15.8-17.5	$3\cdot10^{11}$	10

Table 1. Summary of the energy emission from the several targets.

References

1. I C E Turcu et al.
SPIE, 2015, 243 (1993)

2. I C E Turcu et al.
Appl. Phys. Lett., 63, 3046 (1993)

3. P D Rockett et al.
Applied Optics, 24, 2536 (1985)

4. S Bashkin and J O Stoner, JR
Atomic Energy Levels and Grotrian Diagrams, NH Elsevier (1975)

5. H Gordon et al.
J. Phys. B: Atom. Molec. Phys. 13, 1985 (1980)

6. D Batani et al.
SPIE, 1053, 479 (1991)

7. R W Lee
FLY computer code (1995)

High Density, Ultra-fast Dynamics of Quasiparticles in High Temperature Superconductors

C J Stevens

Department of Engineering Science, Oxford University, Parks Road, Oxford OX1 3PJ

D C Smith, P Gay, J F Ryan

Clarendon Laboratory, Department of Physics, Oxford University, Parks Road, Oxford, OX1 3PU

Main contact email address: *C.J.Stevens@eng.ox.ac.uk*

Introduction

Measurements of photo-excited carrier relaxation in High Tc materials provide a technique with which to investigate the fundamental quasiparticle interaction in the superconducting and quasi-metallic phases. Many measurements have been reported at low excitation powers [1)] on a range of high-T_c materials but little work has been carried out at high densities where the photo-excited population can significantly disrupt the superconducting condensate. Further almost all measurements have only studied the quasiparticle response at a few discrete wavelengths making interpretation of the probe interaction rather uncertain. In order to address these issues we have carried out measurements using the RAL Ultrafast Spectroscopy facility in order to better understand the probe interaction and the dynamics at high intensities.

Experimental

The measurements were carried out on $Bi_2Sr_2CaCu_2O_8$ thin films. The optical arrangement is detailed in Figure 1. Pump pulses at 400nm were used to excite the sample while the probe was a white light continuum generated using a flowing glycol cell. The continuum was filtered using a range of interference filters to produce a range of discrete probe energies. The probe beam was monitored using a pair of photodiodes coupled to a lock-in amplifier, which used a differential input configuration to maximize sensitivity. The pump beam was chopped at ~80Hz to obtain only the pump induced modulation to the sample reflectivity.

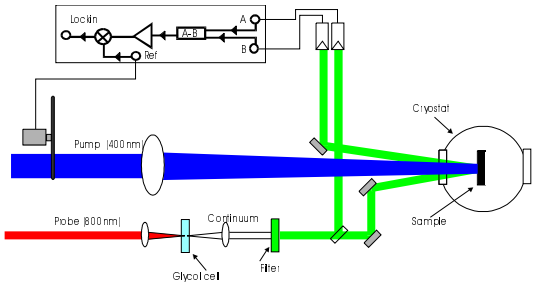

Figure 1. Experimental apparatus used in ultrafast reflection experiments.

Results

Figure 2 shows the photo-induced reflection signals recorded at probe energies of 1.46eV at the maximum of the continuum probe spectrum. In the inset to Figure 2 we show the pump intensity dependence of the low temperature (10K) dynamics of BSCCO.

To date all measurements at low intensities in Oxford and elsewhere have shown a near linear density dependence with no indication of the expected saturation of the signals with increasing photoexcitation[2)].

The very clear phase transition point in the data at ~ 5mW where the time evolution of the signal also changes dramatically is a very good indication of the saturation density which arises due to the **total** collapse of the superconducting condensate.

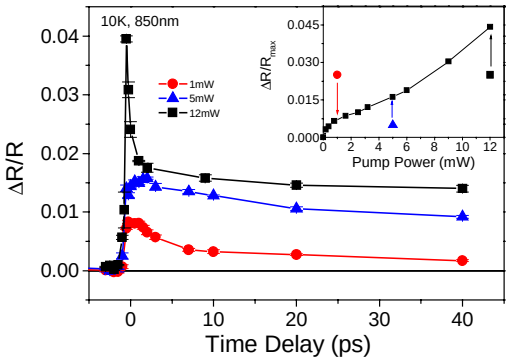

Figure 2. Ultrafast reflectance signals as a function of pump power. Inset: Peak signal versus power.

Changes in the relaxation times which are apparent in the signals of Figure 2 may relate to a number of possible sources including hot phonon effects and modifications to quasiparticle scattering arising from the loss of the condensed phase. To our knowledge this behavior is the first observation of saturation behavior in any high T_c material.

Figure 3 shows the spectral dependence of the room temperature signals, accumulated using interference filters to select a probe wavelength from the continuum.

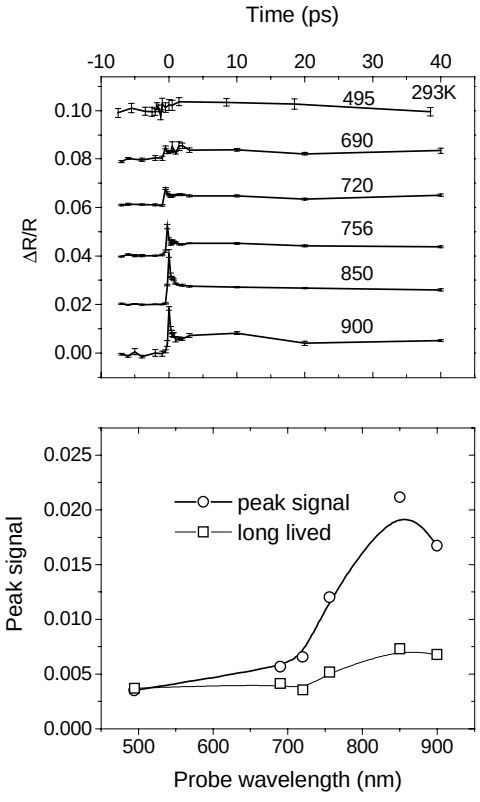

Figure 3. Top) Signals at a variety of probe wavelengths. Bottom) Peak signal spectrum.

In the strongest region of the continuum we found evidence suggesting that the threshold density of Figure 1 varies with probe wavelength.

While these signals do not in themselves make a clear picture of the probe mechanism in BSCCO they do indicate the value of improving the detection performance and hence the width of the spectral coverage. Using filters we were able to detect signals at 600nm and shorter wavelengths but a complete spectral dependence will require significantly better performance. Early indications are that there is a sign change in the photo-induced signal near 500nm.

While the spectrum extracted in the lower portion of Figure 3 should be treated with some care, the general shape seems to reflect the origin of both the peak and longer lived signals being stronger at longer wavelengths which would be commensurate with a Drude dominated response. Further work will explore this spectrum in more detail and to both shorter and longer wavelengths in order to better identify the probe interaction.

References

1. C J Stevens et al
Phys. Rev. Lett. 78 p2212 (1997)

2. P Gay et.al
Proceedings of MOS 99 Stockholm Sweden. To be published in Journal of Low Temperature Physics.(1999)

Investigation of the Nd:YAG Laser Percussion Drilling Process using High Speed Filming

P W French, †D P Hand, ‡C Peters, G J Shannon, *P Byrd, W M Steen

Laser Group, Department of Mechanical Engineering, The University of Liverpool, PO Box 147, Liverpool L69 3BX UK

†Department of Physics, Heriot Watt University, Riccarton, Edinburgh EH14 4AS UK.

‡Lumonics Ltd, Cosford Lane, Swift Valley, Rugby CV21 1QN UK

**Aerospace Group, Bristol UK.*

Introduction

Laser percussion drilling is a process that is of great interest to the aerospace industry. The speed of the drilling action makes it a prime candidate for drilling such components as combustion chambers which have between 40,000 to 50,000 holes[1)] . Other components such as turbine and guide vanes contain fewer holes, typically 50 to 200, but given the total numbers of components involved, percussion drilling still has the potential to provide significant cost-benefit. In a previous study using experimental design techniques we found that the dominant factors affecting the process are focal position, gas pressure, pulse shape and pulse energy. A high speed camera filming at speeds of 40,500 frames per second was therefore used to capture the drilling event with these factors set at different levels.

Experimental set-up

The Kodak EktaPro HS 4540 camera system with a maximum frame rate of 40,500 frames per second (f.p.s) was used in one of two positions. The first was with the camera normal to the workpiece surface, viewing the drilling event on axis and the second position was with the camera viewing orthogonal to the drilling laser. Both are shown schematically in Figure 1. The drilling events were captured using the two highest frame rates, 40,500 and 27,000 f.p.s. The target area was illuminated with an argon ion laser operating at 514 nm. An interference filter, FWHM 10 ± 2 nm was used to discriminate the scattered argon laser light from the plasma radiation emitted by the drilling process.

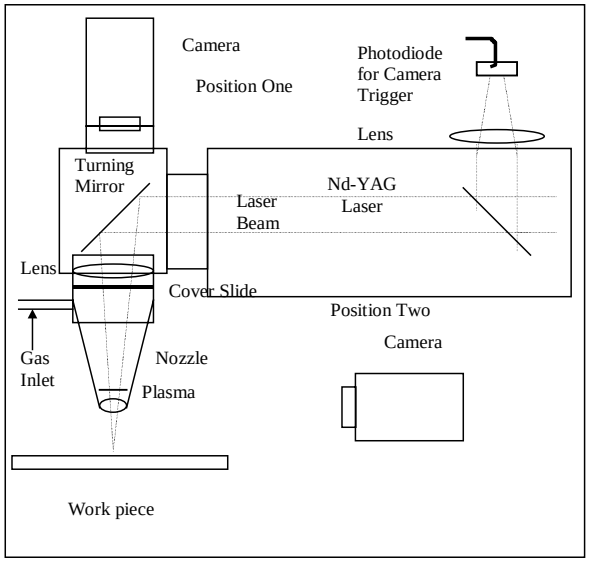

Figure 1. Schematic diagram of the experimental arrangement.

The laser used for drilling in this experiment was a Lumonics 704 TR which has a beam quality M^2 of 24, for laser pulse lengths from 0.3 - 1.0 ms, and peak powers from 4 - 33 kW. A ×2 beam expanding telescope inside the laser head provides an output beam diameter of 18 mm. A 120 mm focal length achromatic doublet lens was used to focus this onto the workpiece, giving a focus spot diameter of 200 μm. In each case, the workpiece material used was a nickel-based super alloy C263, with a thickness of 3 mm. In the experimental set-up in Figure 1, a photodiode was positioned to detect a laser pulse and trigger the high speed camera. For this purpose a low power triggering pulse was programmed into the laser to occur 10 ms before the main drilling pulse. In this way it was ensured that the complete drilling event was captured by the high speed camera.

Drilling events were recorded both with, and without, an assist gas in order that its effect on the process could be observed. In practice, an assist gas is *always* used with this process in order to prevent the high velocity melt which is ejected from the hole contaminating the optics. In addition, it is thought to aid the final hole development, blowing ejecta through the hole and if oxygen is used, to supply energy from an exothermic reaction. In laser *cutting* with oxygen it has been calculated that the laser contributes only 40 % of the energy to the cutting zone the remaining 60 % of the thermal input supplied by the exothermic reaction[3)] . However, with drilling, any change in processing efficiency is much less dramatic, presumably since most of the material is removed from the *top* of the hole and so is opposed by the gas flow.

Results and Discussion

Drilling Mechanism

The material ejection mechanism involved in percussion drilling has three distinct stages, see Figure 2. The first involves material being ejected as a plasma and a liquid conical sheet. This melt cone will continue to be ejected after the plasma has disappeared. The second stage involves material being ejected in a column like structure in a random direction from the hole. In the third stage of hole development 'droplets' of melt can be seen leaving the hole.

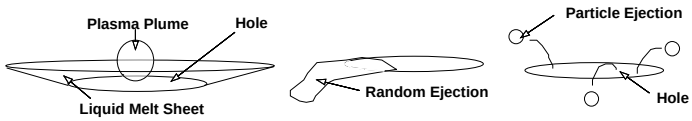

Figure 2. Material removal mechanisms.

Plasma Formation

A simple square shaped laser drilling pulse of width 1 ms was used to determine the times for the laser to generate a plasma plume. With the high speed camera viewing on-axis, the hole development appears as shown in Figure 3. The plasma growth and contraction through the process can be clearly seen.

The time period between the pre-programmed trigger pulse and the appearance of the plasma plume was recorded as a function of pulse energy, both with oxygen-assist at 2.8 bar, and no assist gas, observations show that the time for the plasma plume to appear is dependent on pulse energy, but not assist gas. The time taken to reach the vaporisation temperature t_v is given by [2)] :

$$t_v = \left(\frac{\pi}{4}\right)\left(\frac{\kappa \rho c}{F^2}\right)\left(T_v - T_0\right)^2$$

where κ is the thermal conductivity, T_v is the vaporisation temperature, T_0 is initial temperature, F is the laser flux density, ρ is density, and c is heat capacity per unit mass. The time for a laser pulse with an energy of 3.7 J to reach t_v is 10.5 μs, using the above formula the time for a pulse with a range of energies from 3.7 to 33 J has been plotted in Figure 4.

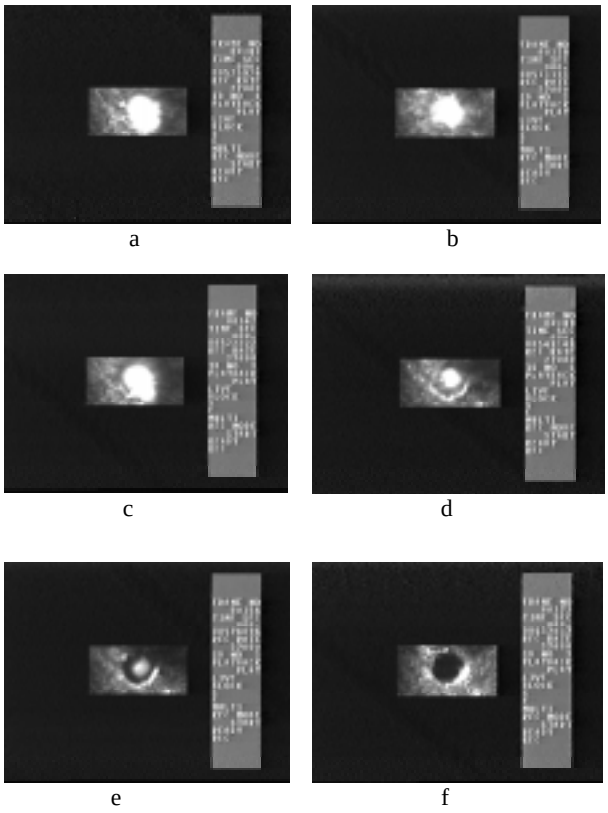

Figure 3. Hole development from initial plasma formation to the stable hole for a simple square 1 ms pulse,(a) 0.11ms, (b) 0.22 ms, (c) 0.26 ms, (d) 0.48 ms, (e) 0.74 ms, (f) 58 ms, after the start of the pulse.

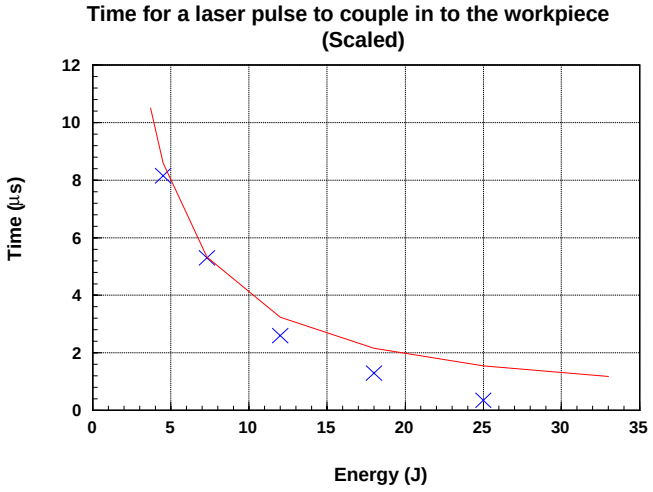

Figure 4. The time taken for laser pulse to reach vaporisation temperature (tv).

In Figure 5 the plasma lifetime is plotted. It is clear that this increases with pulse energy if an oxygen assist gas is used, approaching a maximum of 1 ms (the pulse length) if the energy is in excess of 10 J. With no assist, however, even a low pulse energy gives a plasma lifetime of close to the 1 ms pulse length. This may be explained by the pressure of the assist gas 'blowing away' the plasma. The average lifetime for the plasma plume with no assist gas was 0.92 ms with a standard deviation (s.d) of 0.1 ms.

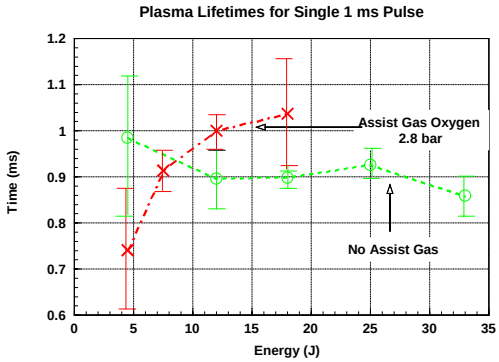

Figure 5. Plasma lifetime for a single 1 ms laser pulse.

It is hard to accurately determine the size of the plasma because its boundary is difficult to see against the expelled melt sheet, however, it is roughly proportional to the pulse energy. Two examples are shown in Figure 6, for different pulse energies. The use of oxygen as an assist gas had no effect on the size of the plasma plume from which the authors concluded that the size of the interaction zone remains roughly constant.

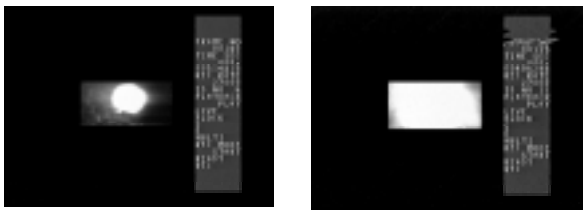

Figure 6. Images of the plasma plume at its maximum size for 7.3 and 18 J pulses.

Melt ejection

(1) Conical ejection

Whilst the plasma is present, liquid melt is expelled in a conical shape from the hole, but this particular ejection mechanism continues for some time after the laser pulse ends and the plasma disappears. We believe that it is during this conical ejection process that the majority of the material is removed. The duration of this process shows no clear dependence on the laser pulse energy as shown in Figure 7. The average time for this type of ejection is 1.7 ms with a standard deviation of 0.5 ms. When an assist gas of oxygen was used this did not effect this average time.

The independence of this liquid melt eject time and the pulse energy may be understood when it is realised that greater the pulse energy, the larger the hole that is drilled—the material is simply removed at a faster rate. The conical shape may result

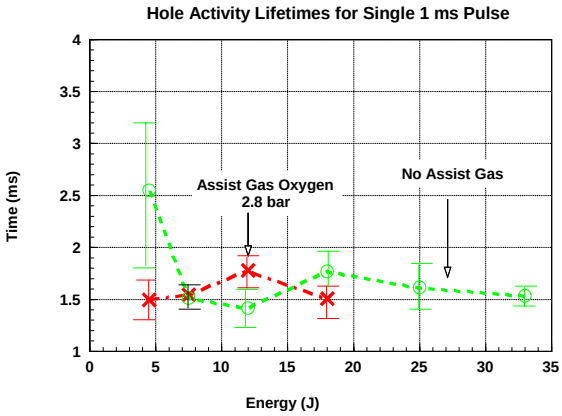

Figure 7. Hole activity lifetime for a single 1 ms pulse.

from a combination of recoil pressure and capillary action, causing the melt to flow up the sides of the hole. Indeed, the camera clearly shows the melt oscillating at the bottom of the hole, see Figure 8.

The velocity of the melt within this conical sheet was estimated from the high speed filming to be in the range 30 - 34 ms^{-1} for the first drilling pulse, and 17 - 27 ms^{-1} for the second pulse. The reason for the difference maybe due to the gas flow impinging on top of the hole. In the first drilling shot material can escape at a large angle to the gas flow. As the hole becomes deeper the material is restricted by the hole walls and the material can only escape directly against the gas flow. In this case the gas pressure was 4 bar. Observations show that the velocity of the liquid melt ejected normal to the workpiece surface is reduced by 50% when the gas pressure is increased form one to six bar. When the gas pressure is in the region of 5-6 bar and above, the liquid melt is clearly deflected from the nozzle exit.

(2) Random Ejection

After ~ 1.7 ms (with both the first and second pulse), the conical ejection process breaks down, and instead the melt ejection becomes much more directional, although the actual direction is random from pulse-to-pulse. The expelled material leaves the hole in a ribbon like structure.

(3) Particle Ejection

The last stage in hole development is when liquid droplets are ejected from the hole.

However, this particular ejection mechanism was only observed when an oxygen assist gas (2.8 bar) was used with sufficient pulse energy (16 J). These droplets move relatively slowly compared with the liquid cone, with velocities in the range 9 - 17 ms^{-1}, and appear to come from deep within the hole, see Figure 9.

This type of material ejection shows no dependence on the energy of the drilling pulse. The oxygen requirement suggests that the mechanism for particle ejection is fuelled by an exothermic reaction. However, if the pressure is increased to ~ 5 bar, this particle emission appears to be suppressed, which may explain why better hole quality is obtained at lower gas pressures.

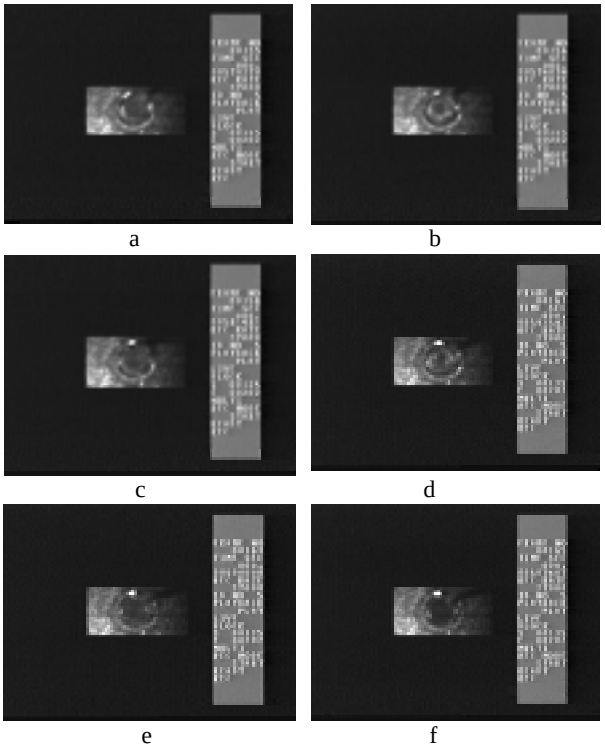

Figure 8. Images showing oscillation of liquid inside the hole, (a) 0.704 ms, (b) 0.741 ms, (c) 0.815 ms, (d) 0.926 ms, (e) 1.0 ms and (f) 1.07 ms after the start of the laser pulse.

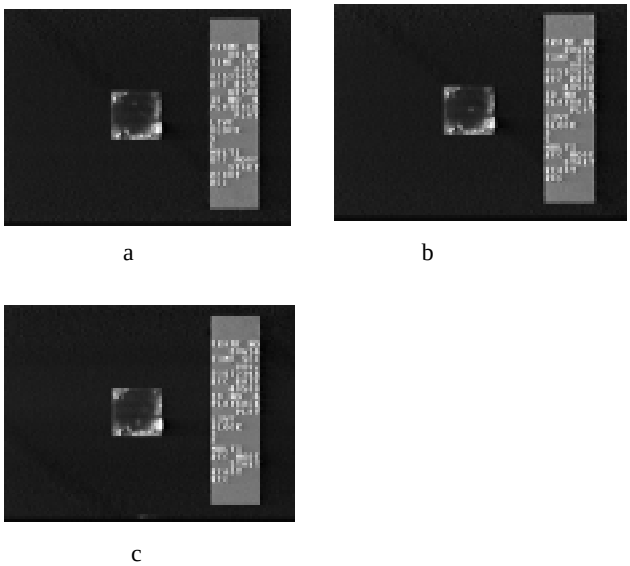

Figure 9. Images of particle ejection at 2.8 bar, 16 J, (a) 9.3 ms, (b) 10.04 ms, (c) 10.23 ms after the end of the laser pulse.

Pulse Shaping

The authors have previously undertaken a detailed study of percussion drilling involving factorial designed experiments. This demonstrated the importance of pulse shaping in the production of high quality holes. The high speed camera was therefore used to study the processes involved with different pulse shapes in more detail. Four different shapes were used, and these are summarised in Table 1. The shapes are very different but in respect of energy and mean power they are very similar. The shapes were filmed at two different values of gas pressure, 1.2 and 6.0 bar. Two different focal positions were also used, + 1.0 mm and + 2.5 mm relative to the workpiece surface.

	Pulse Shape 1	Pulse Shape 2	Pulse Shape 3	Pulse Shape 4
	Two Pulses Low peak power	Two Pulses High peak power	Ramp Down	Ramp Up
Energy J	4.3	3.9	3.9	4.0
Mean Power W	131	144	152	144
Lamp power KW	2.8 – 2.9	2.9 – 3.0	2.9 – 3.0	2.6 – 2.7
Rep Rate Hz	30	37	39	36
Pulse Height %	19	37	32 and 20	17 and 29
Pulse Width ms	1.0	0.3	Both 0.5	Both 0.5
Gap ms	0.6	0.6	//////////////	//////////////

Table 1. Parameters for each different pulse shape.

The camera was used to film the drilling events on-axis. Plasma formation was observed with pulse shapes 2, 3 and 4, having peak powers of 6.5, 4.0 and 4.0 kW respectively. Pulse 1, however, with its low peak power of 2 kW, did not produce a plasma. The lifetime of the plasma plume is plotted for the two different focal positions as a function of pulse shape in Figure 10.

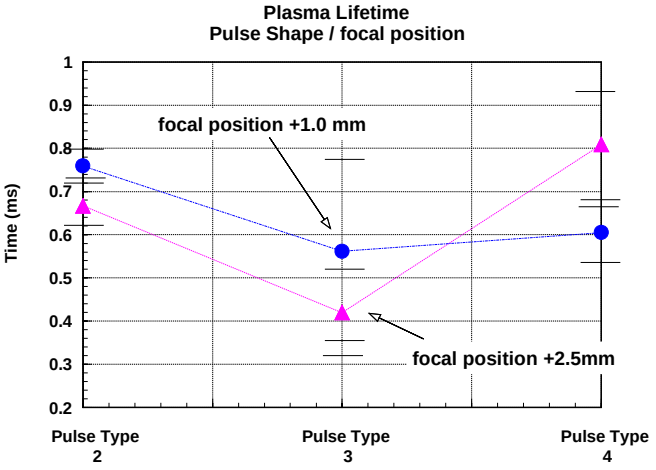

Figure 10. Plasma lifetime as a function of pulse shape.

The lifetime for pulse shape 2 is the combined time for each part of the pulse. For pulse shapes 2 and 3 the + 1 mm focal position produced more plasma than the + 2.5 mm. This is likely to result from the higher power density at the surface with the focus at + 1 mm. Pulse 4, however, showed the opposite effect, which may be due to the higher intensity at the end of the pulse interacting with the vaporised material above the hole. The gas pressure setting did not alter the plasma lifetime for either of the focal settings.

The liquid melt ejection times are plotted as a function of pulse shape in Figure 11, for the two different focal positions. Pulse types 2, 3 and 4, though very different in shape have approximately the same melt ejection time. Pulse shape 1, however, having a low peak power and longer interaction time with the material has the longest melt time for both focal positions. From the video it is also possible to determine the breakthrough of the laser pulse. At the focal position of +1 mm the number of shots to breakthrough was three for pulse shapes 1, 2 and 3, but pulse shape 4 breaks through on the second shot, corresponding to the highest drilling velocity. This maybe due to the initial heating of the material by the leading part of the pulse, which then allows for more efficient drilling by the second part. Pulse 4 also came out favourably in the factorial experimental design study which confirmed this pulse shape as best in terms of taper, hole roundness and hole variation. At the focal position of + 2.5 mm all pulses broke through on the third shot. The decrease in drilling efficiency for pulse shape 4 can possibly be explained by the increased plasma interaction discussed above, and *vice versa* for pulse shapes 1, 2 and 3.

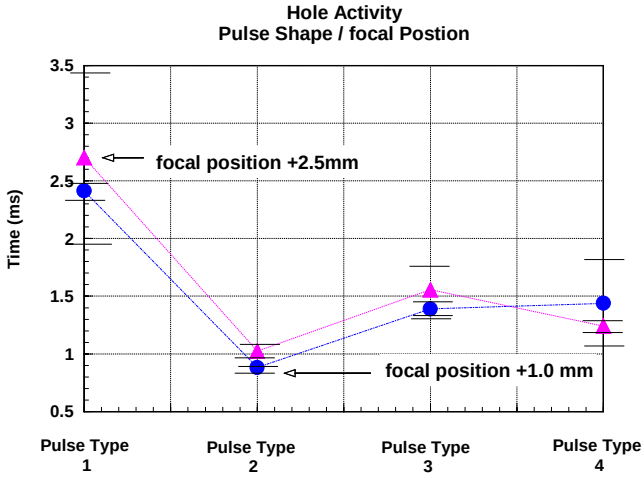

Figure 11. Liquid melt ejection time as a function of pulse shape and focal position.

From the on-axis high speed film, the basic drilling mechanism with each of the pulse shapes 1 - 3 appears almost identical, being similar to the mechanism with the single square pulse discussed earlier in detail (Figure 3). Pulse shape 4, however, has a visibly different drilling mechanism. The initial coupling of the pulse into the surface appears to be more controlled than with the other pulse types. In the first half of the pulse (the 'pre-heat phase'), the growth of the hole is very uniform, and no plasma forms. It is in the second half of the pulse that most material is removed, however, during which time a plasma is excited.

One problem that all of the pulse shapes suffer from, however, is that the material is not expelled in a uniform cone in the melt ejection part of hole development. The melt is instead ejected in one particular random direction, which is thought to affect the hole roundness. This may be due to instabilities in the gas flow, but there may be some contribution from a non-uniform energy distribution of the laser beam.

Conclusions

The laser percussion drilling mechanism in Nickel alloys with pulse energies of up to 30 J in 1 ms has been studied in this experiment. The process has been shown to consist of three stages:

1) Initial coupling of the laser into the surface, breaking down its reflectivity, and giving rise to a plasma plume above the workpiece. This takes ~1 to 10 μs depending on pulse energy.

2) Majority material removal: while the plasma plume is present, the material is generally removed as a liquid in a well-defined 'cone', driven by the vapour pressure inside the hole. The plasma lifetime is typically the same as the pulse length, but this removal process continues for ~ 0.5 ms after the plasma has disappeared.

3) Continued hole development. The material removal continues, firstly as 'ribbons' of melt in random directions, and finally as droplets. These droplets are, however, only seen with an oxygen assist gas with a pressure in the range of 2 - 4 bar, indicating the importance of the assist gas flow and pressure in determining final hole quality. The hole reaches equilibrium after 31 - 70 ms depending on initial conditions.

Pulse shaping can improve hole quality, with the most successful being split into two parts, with the first half at relatively low power. During this part no plasma is produced, and only a small amount of material is removed. The majority of the material is instead removed during the second half of the pulse. It is thought that the preheat provided by the first half of the pulse provides a more controlled coupling into the material.

Acknowledgements

The authors gratefully acknowledge the support of the Engineering & Physical Science Research Council, UK and Lumonics Ltd (Rugby, UK)

References

1. M H H van Dijk, G de Vlieger, J E Brouwer
Proc, 6th Int. Conf, Lasers in Manufacturing Page 237-247
May 1989. ISBN 1-85423-047-6.

2. J F Ready
Effects of High Power Laser Radiation Academic Press
1971

3. Library of Congress Catalog Card Number 77-137597,
Page 101.

4. A Ivarson, J Powell, L Ohlsson, C Magnusson
Optimisation of the Laser Cutting Process for Thin Section
Stainless Steels ICALEO 1991 page 211.

Laser engineering for manufacturing applications: phase 3, stream A, 'precision laser drilling'

D P Hand, W S O Rodden, J D C Jones

Heriot-Watt University, Department of Physics, Riccarton, Edinburgh EH14 4AS

Main contact email address: *D.P.Hand@hw.ac.uk*

Introduction

As part of the long term Laser Engineering for Manufacturing Applications (LEMA) programme, funded by EPSRC, we are researching into the Precision Laser Drilling process; in particular how the efficient (in terms of cost per hole) Nd:YAG single-shot drilling process can be improved in terms of its reliability and repeatability. If sufficient improvements can be achieved, then the process has significant potential in an aerospace application; the generation of large arrays of small (50 μm diameter) holes in the 1 mm thick titanium and aluminium used in the leading edges of aircraft wings and tail-fins. These hole arrays will have the effect of reducing turbulence around the wing, leading to potential fuel savings of at least 7%. At present, methods for doing this by percussion drilling using excimer lasers are available, but this is a slow and hence relatively costly process.

In order to improve the single-shot Nd:YAG drilling process, however, we need to better understand its dynamics. This can be partly achieved by the use of single-point optical measurements, but in order to obtain a more complete picture a full-field imaging technique is essential. The process is however too fast for standard digital cameras, with holes being formed in less than 100 μs. We therefore applied to the EPSRC Engineering Loan Pool to borrow a high-speed camera (Kodak Ektapro HS Motion Analyzer Model 4540, which operates at up to 40,500 frames per second). In order to reduce the glare due to plasma generation, however, it was essential to use an intense narrow-band illumination light source, together with a corresponding narrow-band filter in front of the camera. The most convenient light source to use was an Argon ion laser, and so in conjunction we obtained a Spectra-Physics 2025-05 (CWL1) laser from the Central Laser Facility.

Experimental

A schematic diagram of the experimental arrangement is shown in Figure 1. Light from the Argon-ion laser was coupled into a large core multimode optical fibre. This fibre was used both to guide the light to the region where illumination was required, and to diffuse the light to some extent, thereby reducing the laser speckle. The camera viewed the process from two different angles, using either mirror A on its own (shallow angle to the workpiece surface), or both A and B together (near normal to workpiece surface). Filming was also attempted from the rear, but very little could be seen, as most of the material is removed from the front of the hole.

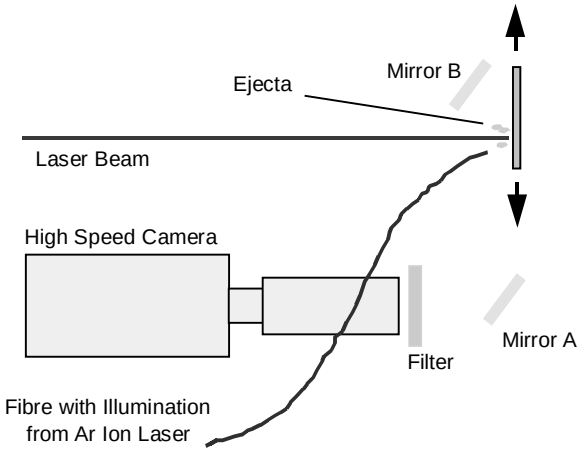

Figure 1. Schematic of experimental arrangement.

Filming from the near normal angle was found to produce poor images due to the low level on contrast between the ejected material and the metallic workpiece behind it. Filming from the side at a shallow angle, in which the workpiece is only visible from the side rather than behind the ejecta, was found to be more satisfactory.

Results

Example results are shown in Figure 2, filmed at 27,000 frames/s, illustrating the process by which material is removed from the hole by a liquid ejection process. It can be seen that the molten metal is initially ejected as an approximately conical spray of small particles with a later, considerably larger particle of melt being expelled in the final stages of the drilling pulse. This final large piece of melt, unlike the earlier small particles which were ejected in an approximately symmetrical manner, was found to be expelled in a random direction.

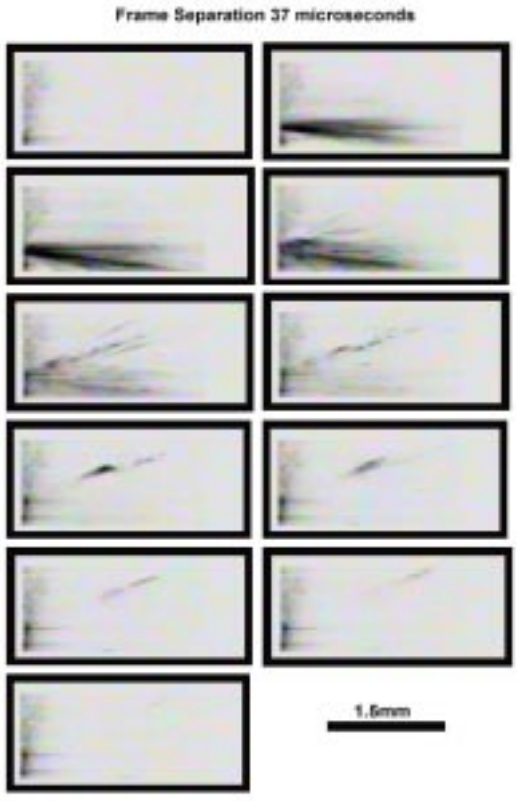

Figure 2. Melt ejection filmed at 27,000 frames/s.

Figure 3 shows a sequence filmed at 13,500 frames/s without the narrow bandpass interference filter. The very bright light from the plasma generated during the drilling is clearly visible and completely obscures the melt ejected during this stage of the process (cf Figure 4). However, in the final stages of the drilling pulse, as the light from the plasma diminishes, it is possible to identify the ejection of the large, randomly directed particle of melt discussed above (frames 6-9).

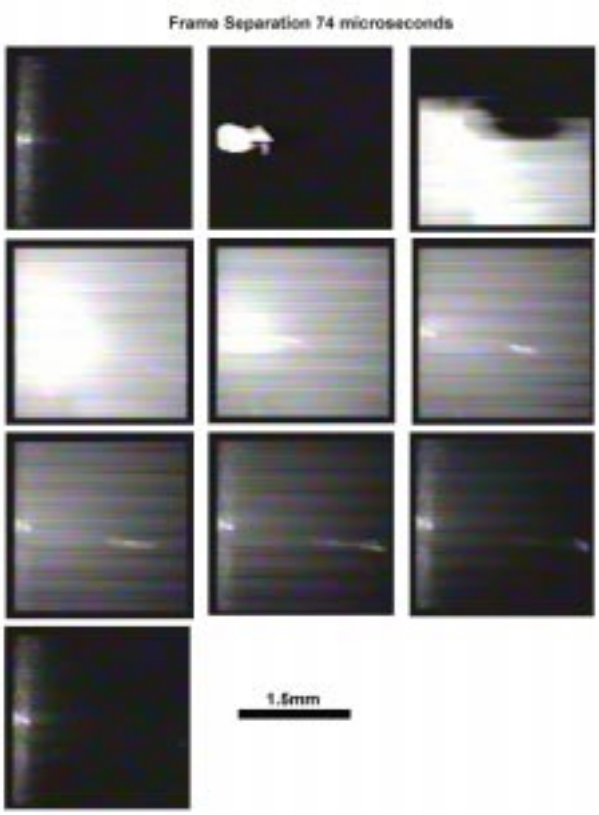

Figure 3. Sequence filmed at 13,500 frames/s without interference filter.

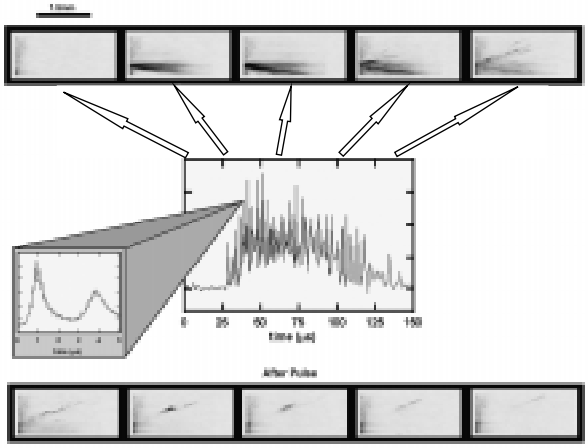

Figure 4. Melt ejection at various stages of the drilling pulse.

Figure 4, meanwhile, illustrates the melt ejection that occurs at different stages of the drilling pulse. By measuring the positions of the ejected particles in successive frames it was possible to estimate the ejection velocities to be within the 6 to 14 ms^{-1} range. A rough error estimate based on the uncertainties in the angles of ejected material would suggest possible errors as large as 30%.

Summary and Conclusion

High speed filming of the laser drilling process has allowed two significant results to be obtained. Firstly, two distinct ejection processes occur. An initial approximately conical ejection of small particles followed, at the end of the pulse, by the expulsion of a larger particle in a random direction. Secondly, the ejection velocities of the melt were estimated to be in the 6-14ms^{-1}range.

Observation of Ultrafast Demagnetisation in a Nickel Foil

J Wu, R Wilks, R J Hicken

School of Physics, University of Exeter, Stocker Road, Exeter EX4 4QL.

Main contact email address: *R.J.Hicken@exeter.ac.uk*

Introduction

Recent observations of optically induced ultrafast demagnetisation in magnetic metals[1-3] have caused great excitement in the Magnetism community. The principles that govern spin dynamics on femto and picosecond time scales are not yet fully understood and there is the promise of technological applications in which magnetic components are switched on and off by direct optical excitation. Nickel was considered to be an ideal candidate for such studies because its Curie temperature is the lowest of the ferromagnetic 3d transition metals. In previous pump-probe studies of Nickel, optical excitation was performed with micro-joule pulses at repetition rates of less than 100 kHz. In this report we describe the experimental procedures that must be used when working with nano-joule pulses at a repetition rate of 82 MHz. We demonstrate that ultra-fast demagnetisation may be observed in a Nickel foil under such conditions.

Experimental method

A schematic of the optical pump-probe apparatus is shown in Figure 1. The light source was a mode-locked Ti:sapphire laser. The optical pulses had a width of the order of 100 fs and a repetition rate of 82 MHz. The bandwidth of the pulses was monitored continuously with a spectrum analyser. Each pulse was split into two parts and the path length of the more intense pump pulse was varied by reflecting the beam from a corner cube mounted on a stepper motor driven translation stage. The probe beam was intensity stabilised and both beams were passed through Glan-Taylor polarisers before being focused and overlapped on the surface of the sample. Earlier reports have suggested that a pump fluence of the order of 1-10 mJ/cm^2 is required in order to observe a significant demagnetisation effect in Nickel. This implies a spot size of the order of 100 μm for the 1 μJ pulses used in earlier reports, but a spot size of just 10 μm for the 10 nJ pulses used in this study.

In principle one may focus and overlap the pump and probe beams using a single lens. However, the focal length must be short if the beam divergence, of less than 0.6 mrad, is not to limit the spot size. It is then difficult to separate the two beams and to obtain a large angle of incidence, as is required if the sample is to be probed by means of the longitudinal Magneto Optical Kerr Effect. We therefore chose to focus pump and probe beams with separate lenses. Both beams were expanded by a factor of 10 to reduce the beam divergence and then focused with achromatic lenses of focal length 16 cm that were chosen for their reduced level of aberration. All studies were performed at a wavelength of 800 nm. The focused spots were viewed from a distance of greater than 16 cm with a CCD camera fitted with a zoom lens that gave a magnification factor of approximately x100. The focus and position of the beams were adjusted by moving the final lenses on XYZ stages. We found that the initial focusing and overlap were most easily achieved by using a piece of clean commercially polished GaAs wafer as a target. This was then replaced with the Nickel sample which was moved to the focal plane by means of an XYZ stage that had a resolution of better than 10 microns. As a check on the overlap and focusing of the beams, the sample was also replaced with a pinhole of 12.5 μm diameter. A simultaneous transmission of 30% and 60% was achieved for the pump and probe beams respectively. These figures are consistent with a spot size of the order of 10 μm when we remember that the two beams were obliquely incident upon the pinhole.

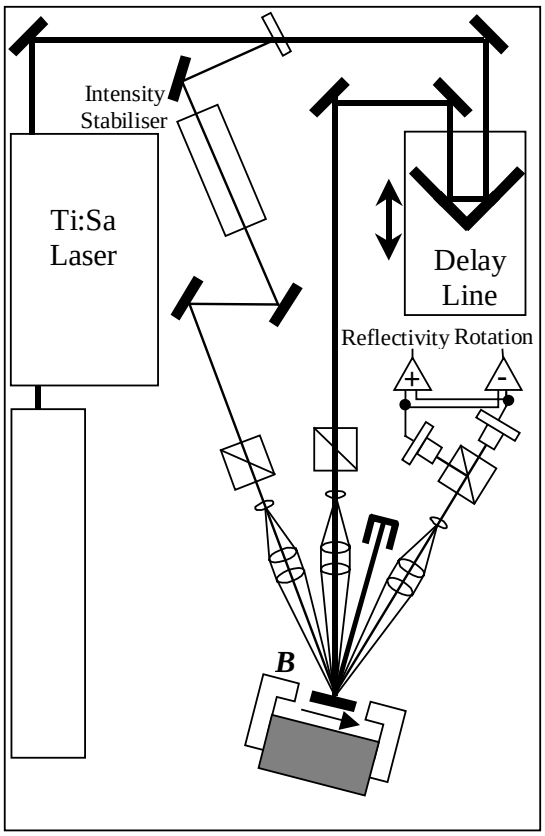

Figure 1. Schematic of the experimental apparatus.

When studying processes that occur on time scales of approximately 1 ps it is necessary to know precisely at which position of the translation stage the optical path lengths of the pump and probe beams are equal. To determine this position we placed a thin β-BBO crystal, cut for non-collinear doubling, at the sample position and monitored the intensity of the frequency doubled beam as the translation stage was scanned. The results of such a measurement are shown in Figure 2(a). Coherence effects are also observed when there is temporal overlap between the pump and probe pulses at the surface of an opaque sample. Light is diffusely scattered from the pump beam into the probe beam path, leading to interference in the measured probe beam intensity. Figure 2(b) shows the variation in intensity observed for a Ni(1000Å)/Cu sample when both pump and probe beams were p-polarised. The intensity is expected to oscillate with a period corresponding to one optical cycle (2.67 fs). The rapid variations in Figure 2 (b) are consistent with this behavior. The scan was made at the resolution limit of our stage so that the time delay was incremented by 1.67 fs between successive data points. This increment is clearly too large for us to fully resolve the oscillations.

The full width at half maximum (FWHM) of the curve in Figure 2 (a) is approximately 400 fs. Treating this as a true autocorrelation curve we would expect a FWHM of 280 fs for a Gaussian pulse shape. This value probably reflects the extent of

the group velocity dispersion incurred in the optics external to the laser, although we note that the pump and probe pulses follow different paths and so may have different pulse widths at the sample.

With a repetition rate of 82 MHz, our tightly focused pump beam delivers a much larger CW-equivalent power per unit area to the sample than do the lasers used in previous studies[1-3]. Indeed we found that thin films grown on glass substrates suffer irreversible damage due to heating by the pump beam. In this report we present results obtained from a polished Nickel foil of thickness 500 μm. The surface oxide layer is assumed to be sufficiently thin that it does not significantly affect the magnetic signal from the underlying metal. The electromagnet in the experiment was specially designed to allow wide field optical access and angles of incidence of 20° and 60° were used for the pump and probe beams respectively. The corresponding CW equivalent power values for the two beams were 300 mW and 5 mW.

In our experiment the incident probe beam is p-polarised. The longitudinal Magneto Optical Kerr Effect causes the reflected beam to become elliptically polarised. To first order both the rotation and ellipticity are proportional to the component of magnetisation that lies in the plane of incidence. We have previously demonstrated that the rotation angle may be measured to an accuracy of 1 μdeg by using the optical bridge shown in Figure 1 and by employing a suitable modulation technique[4]. However it is first necessary to obtain a hysteresis loop from the sample with the pump beam blocked so that a suitable bias field can be chosen for the time resolved measurement. Recording a hysteresis loop is essentially a dc measurement and in these circumstances the optical bridge becomes susceptible to low frequency noise. A better signal to noise ratio may be obtained by setting the polariser in the bridge so that the intensity at one of the two detectors is almost zero. When the magnetic field is swept, the change in intensity at this detector is proportional to the rotation induced by the sample[5].

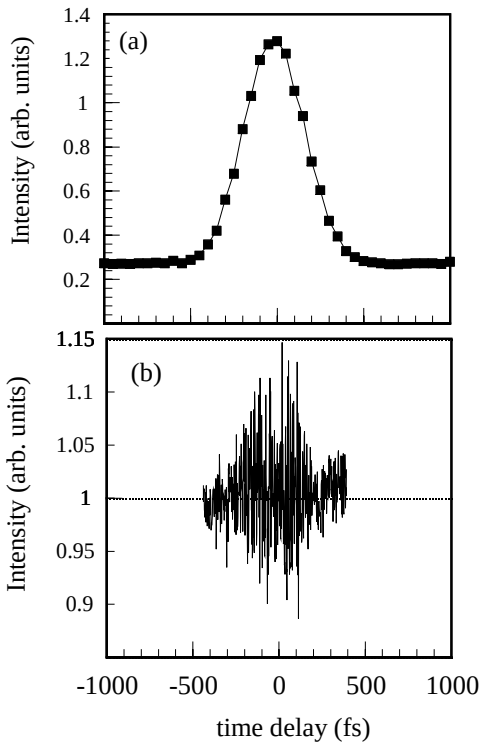

Figure 2. (a) A non-collinear doubling crystal was placed at the sample position. The intensity of the frequency doubled beam is shown. (b) the interference of diffusely scattered pump light with the probe beam is shown for a Ni (1000 Å)/Cu sample.

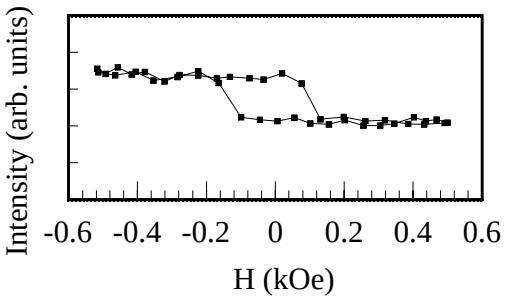

Figure 3. A hysteresis loop is shown for a Nickel foil sample.

A hysteresis loop obtained by this method is shown in Figure 3.

In previous time resolved measurements of ferromagnetic resonance oscillations[4] we found that the best signal to noise ratio was obtained by modulating the pump mechanism and measuring the response of the probe beam with a phase sensitive detector. In the present study, where the pump and probe spots were overlapped on the surface of the sample, this method proved to be inappropriate. A background signal due to diffusely scattered pump light masked any signal from the probe beam. We have therefore investigated a number of other modulation schemes. The first of these involved applying an ac voltage to the electromagnet and driving the sample around the hysteresis loop shown in Figure 3. The height of the hysteresis loop was measured in a phase sensitive manner. The results of such a measurement are shown in Figure 4(a) and the ultrafast demagnetisation effect is clearly seen. There is a single data point at zero delay that is off scale which occurs because of the coherence effects described previously. The signal was again derived from a single photodiode with the polariser in the optical bridge set close to the extinction condition. We also set the polariser to balance the optical bridge. The variation of the difference signal with time delay was similar to that in Figure 4(a). The disadvantage of the field modulation method is that the modulation frequency is limited to about 10 Hz by the self-inductance of the magnet. Also it is not possible to discern the effect of a particular value of the applied magnetic field upon the ultrafast demagnetisation.

We investigated other measurement schemes in which one or both beams were chopped. We found that this placed additional demands upon the detector circuitry. The square wave signals from the sum and difference amplifiers in Figure 1 were found to possess overshoots that arose from variations in gain and slew rate between the two photodiode pre-amplifiers. While the circuitry has since been modified, we found that the difference signal could be reliably obtained by connecting the outputs of the two photodiodes in anti-parallel into a single amplifier. Chopping the probe beam eliminates background signals resulting from stray light, but does not eliminate the low frequency drift in the bridge detector. Chopping only the pump beam is unhelpful as we have already discussed. We found that the best approach was to chop both beams synchronously at different frequencies, using a dual blade chopper, and to then phase detect at the sum frequency. The results of such a measurement, with a bias magnetic field of 300 Oe, are shown in Figure 4(b). The signal was derived from a single photodiode with the polariser set close to the extinction condition. Again similar results were observed by taking the difference signal from the balanced optical bridge. The signal in Figure 4 (b) is saturated at three points about zero delay and again we believe that coherence effects were responsible.

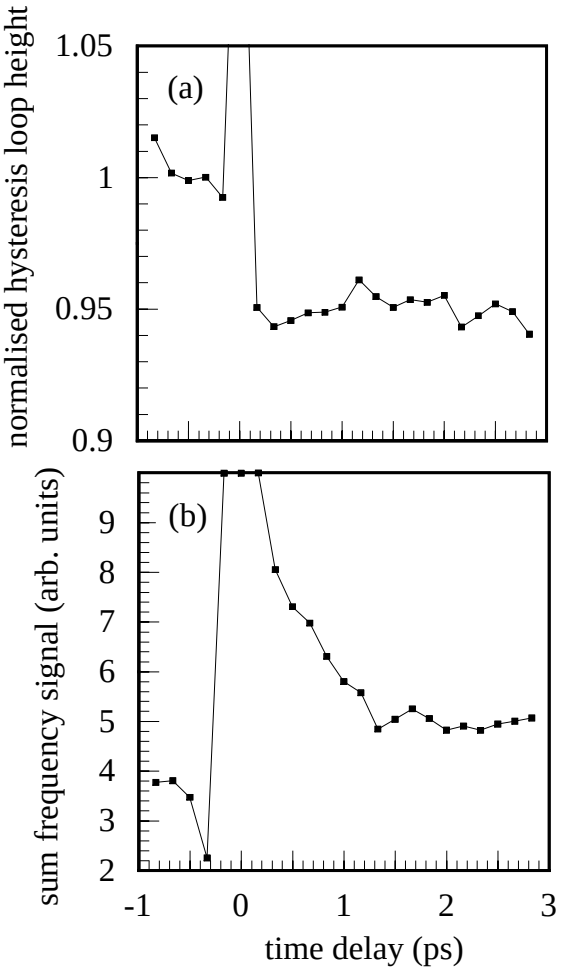

Figure 4. The results of optically pumped measurements on a Ni foil are shown. In (a) the foil was driven through a full hysteresis loop at a frequency of about 10 Hz, while in (b) the pump and probe beams were chopped synchronously at different frequencies and the signal measured at the sum frequency.

However a change in signal level is also observed over longer time scales which we attribute to an ultrafast demagnetisation. The origin of the signal at negative delay times is still under investigation but we point out that diffusely scattered pump light could give rise to this effect if there is any non-linearity in the response of the detection electronics.

Discussion

The ultrafast demagnetisation process begins with electrons in the nickel being excited to a non-thermal distribution. According to the latest reports[3], after thermalisation the electron and spin systems are described by the same temperature which is higher than the temperature of the lattice. The thermalisation time has been reported to be about 250 fs for a pump fluence of approximately 7 $mJcm^{-2}$. However this time depends upon the pump fluence and is expected to be longer for smaller fluences[6]. We suspect that our pump has a smaller fluence and larger pulse width than those used in earlier reports.

Due to the presence of coherence effects in our experiments we are currently unable to comment on the value of the time required for thermalisation. However we expect that, with the use of compression optics, the pulse width at the sample can be reduced to less than 100 fs so that the electron thermalisation time can be explored. Furthermore the use of shorter pulses might also yield an increased demagnetisation effect. The two curves in Figure 4 are seen to have a somewhat different form at time delays beyond the region in which coherence effects are observed. Changes in reflectivity of close to 1 % have been reported in recent pump probe studies of Nickel[3]. We suspect then that the curves in Figures 4(a) and 4(b) might represent different combinations of rotation and reflectivity signals.

So far the large cw equivalent power of the pump beam has limited our studies to samples of high thermal conductivity. However thin films may still be studied if they are deposited on to suitable substrates and the cw equivalent power could easily be reduced by using a pulse picker. In summary, we have shown conclusively that the ultrafast demagnetisation effect in Nickel can be observed with only a mode-locked Ti:Sapphire laser. While we are still developing the experimental technique, we expect that it will be applicable to a wide range of samples in future.

References

1. E. Beaurepaire et al.
Phys. Rev. Lett. 76, 4250 (1996).

2. J. Hohlfeld et al.
Phys. Rev. Lett. 78, 4861 (1997).

3. J. Hohlfeld et al.
Appl. Phys. B 68, 505 (1999).

4. R. J. Hicken and J.Wu,
J. Appl. Phys. 85, 4581 (1999).

5. J. A. C. Bland et al.
J. Phys. E:Sci Instrum. 22, 308 (1989).

6. J. Hohlfeld et al.
Ch. 4 “Nonlinear Optics in Metals”, OUP (1998).

Upgrade of Vulcan to 1 Petawatt

C B Edwards, M H R Hutchinson, C N Danson, D Neely, B E Wyborn

Central Laser Facility, CLRC Rutherford Appleton Laboratory, Chilton, Didcot, Oxon, OX11 0QX, UK

Main contact email address: *C.Edwards@rl.ac.uk*

The CLF has been awarded a grant of £3.3M by EPSRC (the Engineering and Physical Science Research Council) to upgrade the Vulcan high power neodymium glass laser facility. Over the course of the 3 year project, the output of Vulcan's ultra-short pulse beam will be increased to 500 J in a pulse of 500 fs duration giving a power on target of 1 Petawatt (10^{15} Watts). With the use of adaptive optics to correct wavefront errors, the Vulcan beam will be focussed to a near diffraction limited focal spot, producing irradiance on target of 10^{21} Wcm^{-2}.

This level of performance will open up new regimes of plasma physics to the UK scientific user community and their international collaborators including photon induced nuclear reactions, studies of relativistic effects in ultra high fields and new schemes for the acceleration of charged particles.

In addition to funding from EPSRC, the upgrade is benefiting from components which have been made available by the U.S. Department of Energy following the closure of the NOVA laser at Lawrence Livermore National Laboratory in May '99. This includes 20 cm disc amplifiers, large aperture beam delivery optics and a number of high energy density capacitors. In return, scientists from Livermore will receive access to beam time, either as sole investigators or in collaboration with the UK user community.

The most visible sign of the upgrade will be the construction of a new target area on the east side of R1 adjoining TA East as shown below. This new building will be approximately equal in size to target areas East and West combined, slightly higher and equipped with a 5 ton crane to enable the major pieces of equipment to be moved quickly and safely. The size of the building is set by the length of the vacuum spatial filter beam expander and relay, and the size of the pulse compression system. The latter comprises a pair of diffraction gratings 92 cm in diameter with a separation of 13 m and housed in an ultra-clean vacuum chamber. At the time of writing of this report, planning permission has been obtained and it is hoped that building work will begin at the end of 1999.

From the above it will be appreciated that this upgrade represents a significant increase in the scale size of components routinely handled within the CLF. This will affect all aspects of the operation of Vulcan from the cleaning of components, optical metrology and testing, assembly and alignment. It will also necessitate some changes in the way of working in the new target area. For example, with a beam diameter approaching 70 cm, the weight of a turning mirror alone is 360 kg and major changes to the optical configuration of an experiment will require considerable planning.

A major factor in the planning and organisation of the upgrade is the determination to maintain full operational capability of Vulcan throughout the project, with the exception of a 14 week closure for modifications to the power supply and pulsed power systems. This clearly requires additional staff effort and recruitment of scientists and engineers on fixed term contracts is already underway.

The Petawatt Upgrade represents a very exciting opportunity to enhance still further the scientific profile of the facility and its user community. It is an extremely demanding undertaking and presents many challenging objectives; technical, financial and organisational. When these objectives are met the challenge will pass to our user community to exploit the new facility in the most imaginative, competitive, and cost effective ways possible!

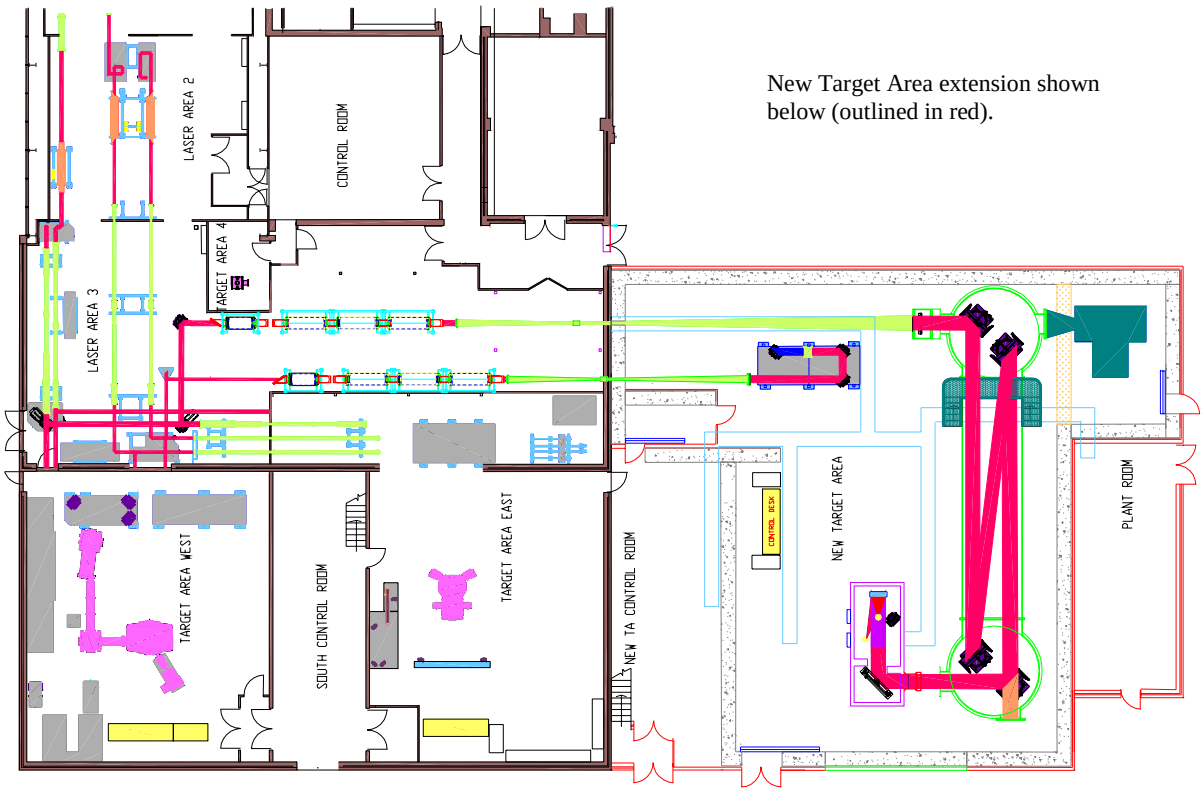

Figure 1. Proposed floor plan of Vulcan Upgrade.

Vulcan Computer Control System Upgrade

D Pepler

Central Laser Facility, CLRC Rutherford Appleton Laboratory, Chilton, Didcot, Oxon, OX11 0QX, UK

Main contact email address: *D.A.Pepler@rl.ac.uk*

Historical Perspective

The Vulcan high power Nd:glass laser facility at the Rutherford Appleton Laboratory has had since it's infancy (some 22 years previous) some form of computer control for operating the laser and for collecting, collating and archiving of the data obtained from the laser operations. The computer control has changed over the intervening years but initially the computer was a GEC 4080 'mini' computer which despite it's classification completely took up two 6' high 19" racks. To enable this computer to control the laser it was interfaced into a series of CAMAC crates placed around the laser system.

The GEC 4080 was quite advanced for it's time and was able to run up to 256 concurrent processes but was quite restricted in the memory available both for RAM and for hard disc space. Two 20 MB Winchester discs were available which had to be backed up onto magnetic tape at least once a week. The computer was programmed in the high-level assembly language BABBAGE that also had its restrictions.

With the advent of the single board computer, the LSI 11, the target areas of Vulcan were computerised using the MicroPower PASCAL programming language again with these computers interfaced into CAMAC for target area control and communication with the GEC 4080. Using the experience gained from this and with the introduction of the personal computer (PC), the GEC 4080 was replaced by two networked PC's. These were 286 processor-based computers both with their own monochrome displays and 20 MB hard discs. Each computer, through a PASCAL application, performed it's own independent function but communicated with the other via file sharing. The first computer was interfaced to CAMAC so as to be able to control the laser and obtain data. The second computer was used to obtain and archive data (onto a 200 MB optical disc) and also to display (via an external graphics controller) a colour schematic diagram of the laser system for the benefit of the laser operator.

This system was extremely reliable for many years but being only a 286-based computer now has problems in serviceability.

The Upgrade

The current laser control system is heavily reliant on the CAMAC and on several items that have far exceeded their normal expected lifetime. Apart from the 286 based computers themselves these obsolete pieces of equipment include data acquisition systems, the graphics controller, video character generators and the file-sharing network.

A solution was therefore required to address these and other issues such as the fact that the facility downtime should be minimal.

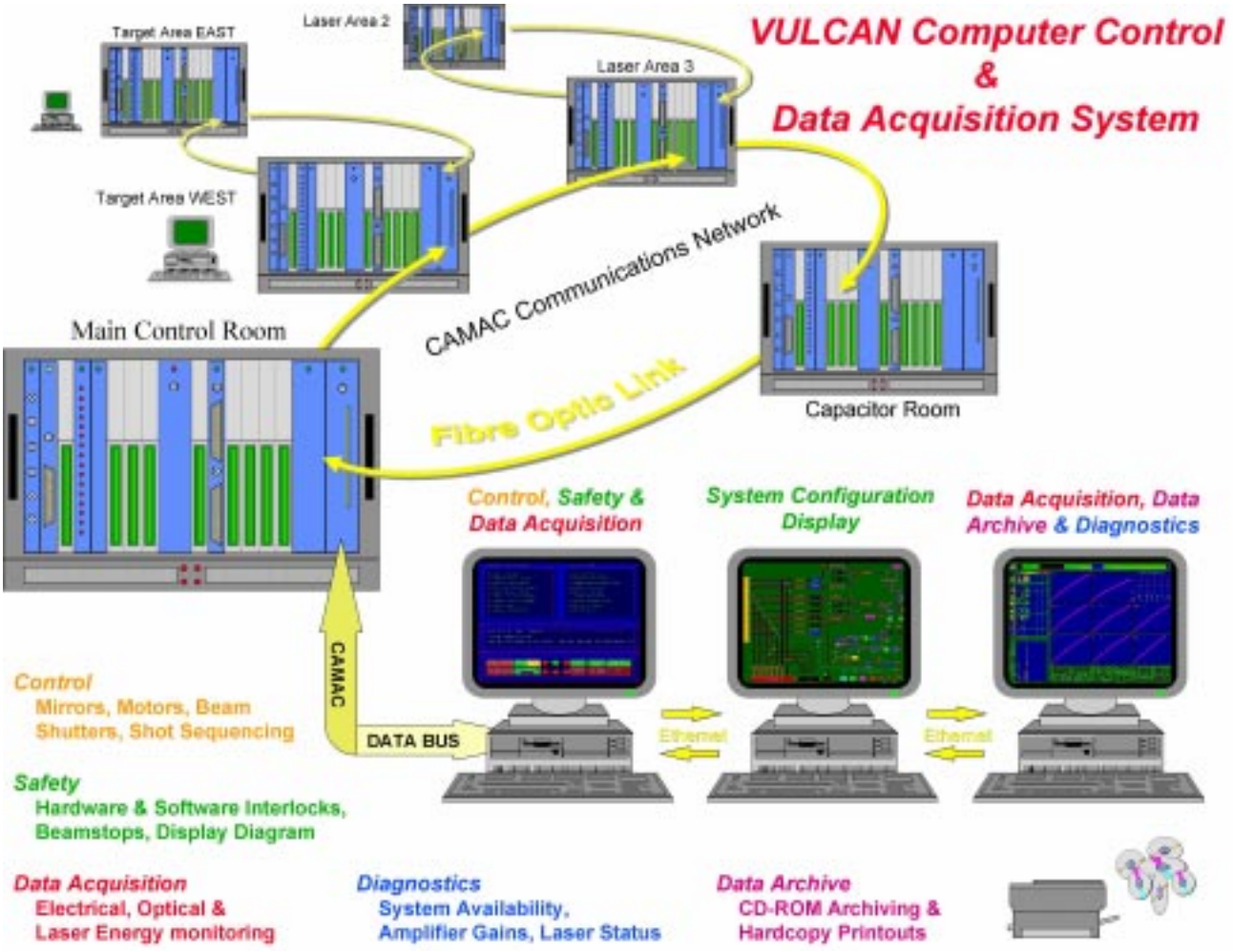

Figure 1. Schematic of the CAMAC communications network.

Figure 2. Sequence of menus controlling laser operation :- Lower screen area contains interlock status indicators. Upper screen area changes to charging histogram on shots. (see Figure 3).

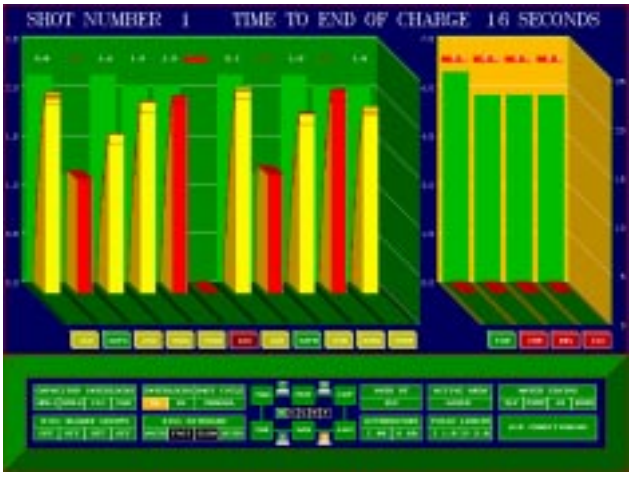

Figure 3. Charging diagram, indicating voltage levels on all selected amplifiers. This display reverts to menu screen after shot firing sequence is complete (see Figure 2).

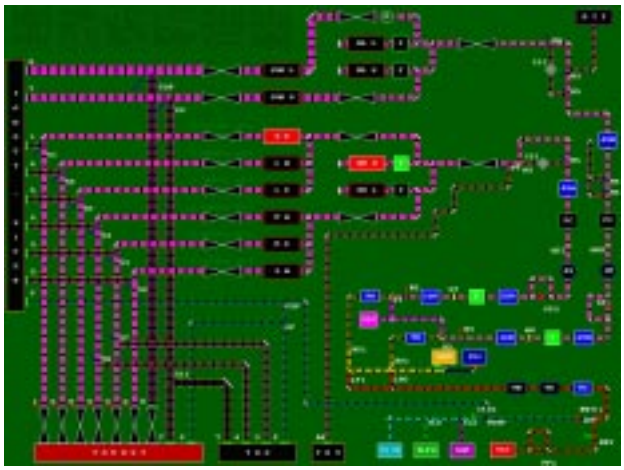

Figure 4. Continuously updated safety diagram indicating the status of the laser system configuration.

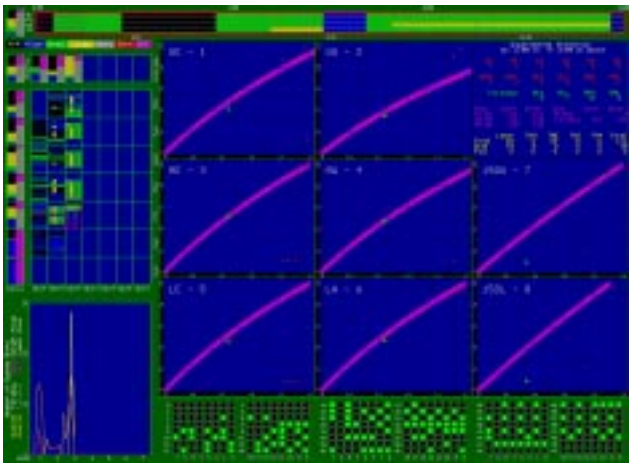

Figure 5. On full laser shots, this display converts to a sequence of shot data screens for archiving and hardcopy printout.

Obviously the computers needed to be replaced with modern equivalents but it quickly became apparent that any solution required a complete restructuring of the functions of the computers and the way in which they would communicate.

Because of this, a number of avenues were explored as to whether or not some radically new control system should be implemented. LabView in particular was looked at in some detail but despite the attractiveness of some of it's features, there were difficulties in duplicating the working schematic diagram, also, very few of the LabView drivers that would have been necessary to control the varied CAMAC modules existed. These facts meant a considerable amount of work would have been necessary to write the required drivers and to develop the graphical display.

The solution was therefore to use the 17,000 lines of PASCAL programs that already existed on the 286 based PC's, as the basis of a re-structured control system. The new system would have to duplicate and enhance the control, display and archiving functions of the previous system and be capable of using modern data acquisition devices such as analogue to digital converters (ADC), GPIB services and video framestores.

The video framestores, best suited for the present laser application along with other interface cards, are based on the standard ISA bus. As more modern computers are restricting the number of ISA slots in favour of PCI slots, this dictated that three computers would be necessary to house all the required interface cards. The chosen devices were Viglen P5 200 MHz computers, (medium specification computers at the time of starting this project). The primary functions of these three computers are Control, Display and Data Archive.

Control

The Control computer, in order to operate the laser system, has to be interfaced in a number of ways to the specialised hardware that actually runs and fires the laser. This is achieved through the CAMAC communications network. Figure 1 shows the schematic of the whole computer control system with the three computers linked via ethernet and the additional CAMAC network connections. The CAMAC system comprises of six individual interface crates; one in the main control room; two inside the main laser area; one in the high voltage power area and one in each of the two main target areas. Each of these crates contains a number of modules for digital input / output (IO), ADC or similar interfacing functions. The separate zones are fibre-optically coupled to eliminate any electrical interference.

All three computers are situated in the main control room with the Control computer being linked directly to the CAMAC via a 1330 PC / CAMAC interface module (Hytec Electronics Ltd).

Figure 2 shows the main menu screen. This was deliberately chosen to be as similar as possible to the previous control menus so that operator training / errors could be minimised, but with significant operational enhancements as well. A key feature of the new control screen is the continuously updated

colour coded interlock status indicator panel, filling the lower part of the screen. This enables the laser operator to see, at a glance, the status of the most important hardware interlocks - the simple colour coding giving indication of definite hazards (red), possible hazards (yellow) and clear interlocks (green).

In normal operations this indicator panel is on display all the time with the middle screen area also giving extra information concerning the time and date and laser ready status. The upper screen area is normally reserved for the menus, which are several layers deep. Through the use of these menus the operator can control and monitor most aspects of the laser's operations.

It should be noted that although the menu screen appear in part to be text based, in fact all the elements on screen are drawn in high resolution graphics mode, namely 1024 x 768 pixels in 256 colours. This method was chosen simply to eliminate the screen flicker that is common when changing from graphics mode to text mode and vice versa. Graphics mode is essential not only for the interlock status indicators but also for displaying electrical waveforms.

When the laser is required to fire, an extra screen display is needed to show the laser operator the voltages of all of the selected amplifiers. Since when firing a shot the menus are no longer required to be active, the upper part of the control screen is replaced by a pseudo 3D histogram of the charging voltages. Figure 3 shows this in operation. After the laser has fired the histogram is replaced by a number of other screens which give details of the post-shot data collection, for example the retrieval of energy calorimetry. After the data collection is completed the main control menu screen is redisplayed.

Display

The data obtained from the control computer is sent via ethernet to either (or both) of the other computers. For example, the state of all the micro-switches indicating safety shutter Open / Closed statuses is obtained via Control and is used by the second computer to generate a continuously updated safety diagram which indicates the current state of the laser. Figure 4 shows this diagram giving clear indication of the status of particular laser amplifiers being selected and the status of an alignment laser beam being directed into one of the four target areas.

The beamlines drawn on the display are continuously rewritten to give an appearance of motion. Other indications are given of special devices such as waveplates, optical pre-pulse generators, vacuum levels, beam smoothing elements etc.

Data Archive

The third computer also displays the micro-switch information for diagnostic purposes but is primarily concerned with data collection and data archival.

Figure 5 indicates the displays that are normally shown, giving the operator details of past shots on any beamline. These indicate the number of shots, the shot rates for low level, medium level and high level shots and the optical laser gain for each beamline. Also, details are given of the system start-up time, the time that has been taken to align the laser, when target areas have used the laser and whether or not any downtime has been experienced. This data is displayed in detail on a daily basis and also for a complete 7-week experimental period. This information is then used as input to check performance against the facility Service Level Agreements (SLA).

When a full laser shot has been fired this computer is also used to collect and to process certain data (for example reading the waveforms from oscilloscopes via GPIB interfaces) and to then produce both a hardcopy printout and to save all the data to disk for archival purposes.

The time taken from firing the shot to producing all hardcopy printouts is about 40 seconds, which is a considerable improvement over the previous 286-based system which used to take some two and a half minutes.

Communications

It has already been stated that the computers communicate with each other and that this information is passed via ethernet. Each computer has an identical PCI ethernet adapter card (Viglen EZ-3200P+), and each of the PASCAL applications uses an identical PASCAL program to access the network. This routine uses the Packet Driver code supplied with the cards and enables data variables to be sent from one computer application directly into another. The routine operates on interrupts and so the data transfer is essentially transparent to the receiving application, it merely uses the current value which is always the most recent. The ethernet packet variable used in this application is declared as follows: a 6-byte address for the destination; a 6-byte address for the source; a protocol type word; a command word; a data length word; then the data itself which can be up to 1496 bytes long. When this packet is received, the computer loads the data into a particular variable according to the command word value.

To make the system as robust and as plug-and-play compatible as possible, the first task on power-up, of each of the computers, is to broadcast a packet containing it's unique identification (ID) number and ethernet address, over the network. It does this by encoding the ID into the command part of the ethernet header, which also includes the senders ethernet address. Each PC repeatedly sends this packet, until it has also received valid ethernet addresses from all the other computers. With this technique even if an ethernet card fails and is replaced with a new one, of the same type, no modification is required in the software as it will automatically pick up and use the ethernet address of the replacement adapter card.

Having established full communications with each other, each PC initialises the variables that it is responsible for and then initialises the graphics display. The Control PC then initialises the CAMAC hardware, updates the status indicator panel and sends the packet containing the IO data to the Display and Archive PC's for them to update their displays as well.

The Control PC then continuously monitors the keyboard and the Laser controls to check for requests to fire the laser, or for changes in system configuration to be made. Because of the speed of the computers, the Control PC is able to check and display the status of a wide range of interlocks, to read large numbers of analogue voltages and to process these requests 2 or 3 times a second. This is more than adequate for operating this real-time system.

The Future

It is anticipated that in the next few years, further enhancements will be made to the control system with touch screen interfacing, additional networking to diagnostics and computerised interlock systems being installed.

Frequency Doubling for Ultra-High Intensity, High Contrast Ratio Plasma Interactions

R M Allott, R J Clarke, D Neely, J L Collier, C N Danson, C B Edwards, C Hernandez-Gomez, M H R Hutchinson, M Notley, D A Pepler, M Randerson, I N Ross, J Springall, M Stubbs, T Winstone

Central Laser Facility, CLRC Rutherford Appleton Laboratory, Chilton, Didcot, Oxon, OX11 0QX, UK.

Main Contact email address: *R.M.Allott@rl.ac.uk*

Introduction

Recently, there has been increased interest in using the second harmonic of the chirped pulse amplified (CPA) Vulcan Nd:glass laser system. With shorter duration pulses and ultra-high intensities, pulse contrast plays a crucial role in many interactions. Due to the non-linear nature of the process, frequency doubling offers one route of reducing any pedestal or laser pre-pulse. In addition, a shorter drive wavelength can be advantageous in some laser-plasma interaction experiments.

This paper describes the frequency doubling of a 140x110 mm, 40 J, sub-picosecond, 1054 nm beam for laser matter interaction studies at the Central Laser Facility. The conversion characteristics including efficiency, beam quality, focusability and pulse length for two large aperture (157 mm diameter) high quality KDP crystals of thickness 2 mm and 4 mm were studied.

Experimental Arrangement

The experimental arrangement is shown in Figure 1. The 850fs, 40J, IR pulse from the TAW CPA compression gratings was directed into the KDP, Type I frequency doubling crystal contained within the target chamber. The use of Type I doubling increases the contrast ratio as it leads to more efficient rejection of the fundamental beam since the fundamental and second harmonic are orthogonally polarised. The frequency doubled beam then reflects off four HR @ 527nm mirrors to maximise the Green/IR contrast ratio (each mirror rejects the IR by a factor of ~ 10^2) and onto the 3m Off Axis Parabola via a final turning mirror. The focussing beam from the parabola was then sent through pinhole targets and onto a large area calorimeter.

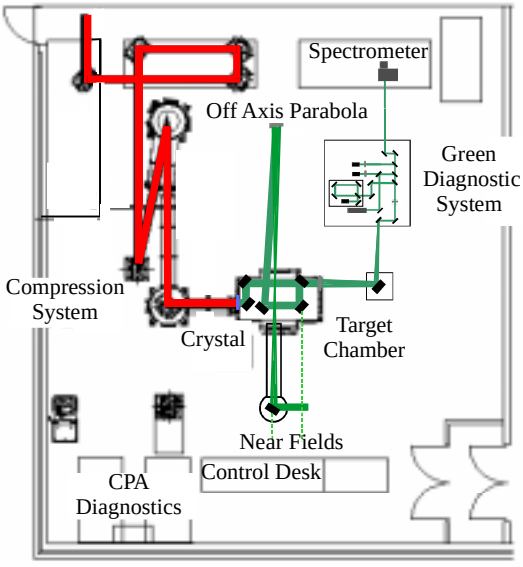

Figure 1. Experimental Layout.

The Green CPA diagnostics were fed from a 0.2% leakage from the 3rd IR rejection mirror, where the green/IR contrast is high. The green leakage from the mirror was sent through a telescope system to de-magnify the beam by a factor of 7 and energy dump to reduce the intensity and prevent build up of B integral before entering the diagnostics suite. The green diagnostics suite consisted of an autocorrelator, interferometer, spectrometer, and farfield monitors providing a full data set for the second harmonic beam on each and every shot.

Initially calorimetry was performed after the CPA compression gratings to determine energy losses in the compression system and the CPA diagnostics feed. This provided a calibrated input energy to the second harmonic crystal. The crystal was then tuned with a series of low energy shots. Once the crystal was optimised, the parabola was replaced by a large area calorimeter and shots were taken over a wide energy range in order to determine the crystal conversion efficiency. All shots provided data on the 1ω and 2ω CPA diagnostics and gave information on beam quality, focusability and pulse length.

Results and Discussion

In order to define the maximum intensity that can be delivered to target the conversion efficiency, pulsewidth and focal spot size (beam quality) must be determined.

The second harmonic conversion efficiency of the 2mm and 4mm crystals is plotted in Figure 2. The 4mm crystal has a peak efficiency of 68% for an incident intensity of 100GWcm^{-2}, whilst the 2mm crystal gave 57% for 120 GWcm^{-2}.

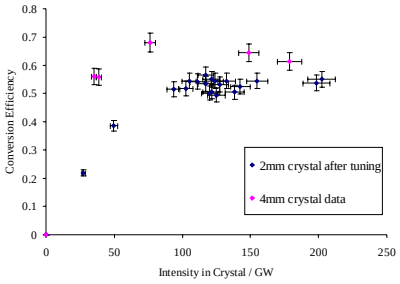

Figure 2. Conversion Efficiency for 2mm and 4mm Crystals.

This very high efficiency allows in excess of 20 J at 527nm to be delivered to target when using the 2mm crystal. Figure 3 indicates the effect of driving the crystals at even higher intensities. The dotted red line indicates the operational region at present and the dotted black line the operating point expected after the installation of the OPCPA front end. It can be seen that as the intensity increases to ~ 400 GWcm^{-2} the conversion efficiency of the 2mm crystal peaks at ~ 70% whilst that of the 4mm crystal appears to drop off rapidly beyond ~ 100 GWcm^{-2}. It should be noted that these data have been scaled from original lower intensity data. It does however show clearly that the 2mm crystal is the optimal thickness for future experiments on Vulcan.

To generate a frequency doubled pulse with minimal energy in the wings, it is essential that the bandwidth of the doubling process supported by a given crystal is sufficiently large. There is therefore a tradeoff between using a thick crystal to improve conversion efficiency and using a thin crystal to increase supported bandwidth. To maintain optimum conversion efficiency for a given crystal thickness L, it has already been shown that the quantity $IL^2 = p$ should be maintained, where I is the incident intensity and p a constant for a given type of crystal and doubling process. Based on the data presented in this paper

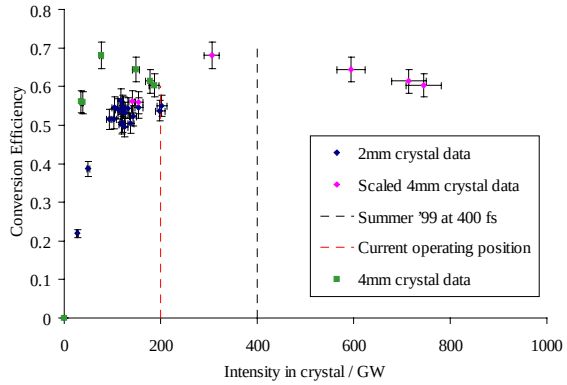

Figure 3. Conversion Efficiency Scaled to indicate Present and Future Operating Points.

a value of $I(GWcm^{-2})L^2(cm) = 14 \pm 6$ for Type I doubling in a KDP crystal is obtained. In a CPA system the energy density $E(J)/A(cm^2)$ which a grating can support before damaging is a limiting operational point (assuming no beam telescoping). Expressing the optimum crystal length in terms of the pulse duration τ, the beam area A and energy E gives:-

$$L = \left(\frac{pA}{E}\right)^{0.5} \tau^{0.5} \quad (1)$$

To preserve a given pulse shape the time bandwidth product $\tau\Delta\omega$ must be maintained as the duration is reduced. However, to obtain phase matching in a crystal the range of wavevectors scales inversely with crystal thickness as $\Delta K \propto L^{-1}$. Therefore, to maintain conversion bandwidth as the pulse duration is reduced the crystal thickness should satisfy :-

$$L \leq N\tau \quad (2)$$

where N is dependent on the pulse shape and desired supported bandwidth. In the case of Type I KDP doubling the ideal crystal thickness for efficient doubling with the Vulcan system at a pulse length of 400 fs and an intensity onto the crystal of 400 $GWcm^{-2}$ is 2 mm. The bandwidth supported by the 2 mm crystal is 28 nm centred at 1054 nm. This is ~ 7 times the pulse bandwidth which is acceptably large to avoid introducing energy into the wings of the pulse. The 2 mm thick KDP Type I crystal therefore satisfies both conditions expressed in equations 1 and 2 and is an ideal choice for 400 fs pulses.

A single shot autocorrelation of the 2ω pulse is given in Figure 4. The FWHM indicates a pulsewidth of 600fs ± 50fs. A slight shortening with respect to the initial pulse is expected due to the non-linear process whereby the wings of the pulse are suppressed.

The farfield was found to have a high degree of astigmatism as is shown in the focal scans in Figure 5. This is confirmed by single shot interferometry of the second harmonic beam.

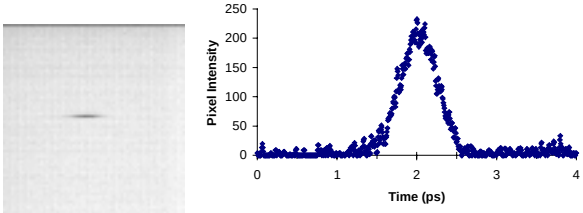

Figure 4. Autocorrelation of 527nm Pulse indicating a FWHM pulsewidth of 600fs ± 50fs.

It was found that by tilting the farfield lens the majority of the astigmatism could be removed.

Figure 5. Focal Scans Showing Astigmatic Farfield.

The same procedure was applied to the F20 off-axis parabola resulting in the spot profile shown above in Figure 6. Using an F20 optical system the spot size is ~50μm which implies a < 4 x diffraction limited performance at 527nm. The farfields taken for low and high energy shots for the 2mm crystal show much less beam breakup than for previous measurements with the 4mm crystal[1] probably due to an improved beam wavefront from the static corrector plate[2].

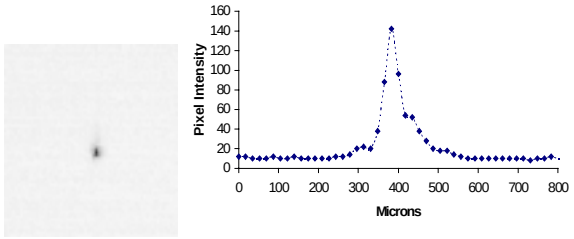

Figure 6. Image and line-out of green focal spot.

The results obtained indicate that an on target intensity of ~10^{19} Wcm^{-2} is achievable with the present system using the 2mm crystal and F3.5 focussing optics. This equates to an $I\lambda^2$ of $3x10^{18}$ $Wcm^{-2}\mu m^2$.

This is a significant result in terms of the high intensity plasma physics on Vulcan. Many experimental schemes rely on a very "clean" pulse with high (>10^{10}) contrast ratio. Such pulses do not form a pre-plasma which in turn decreases the density scale length of the plasma. In particular high harmonic generation is very sensitive to the level of pre-plasma with the greatest efficiency and shortest wavelengths generated via the steepest possible density gradient. In addition it has the added advantage of driving the plasma at twice the frequency.

In summary the frequency doubling of the large aperture CPA beam on Vulcan has been investigated and quantified. The selection of a 2mm Type I KDP crystal has proved to be the optimal choice for the Vulcan system now and after future upgrades. It is believed that ~ 10^{19} Wcm^{-2} can be delivered to target with much enhanced contrast ratio, opening up new plasma physics experiments and improving on existing schemes.

References

1. D Neely et al
Laser and Particle Beams, Vol. 17, No 2, p281-286, 1999

2. C Hernandez-Gomez, J Collier, S Hawkes
CLF Annual Report 1997/98, RAL-TR-1998-080

Materials processing with high power lasers

DA Pepler, R Allott, A Boba, R Clarke, J L Collier, C N Danson, G Hirst, D Neely, M Notley, M Payne, T Winstone
Central Laser Facility, CLRC Rutherford Appleton Laboratory, Chilton, Didcot, OXON, 0X11 0QX. UK

W Cranton, D Koutsogeorgis, E A Mastio
Nottingham Trent University, Nottingham NG7 4BU, UK

Main contact email address: *d.pepler@rl.ac.uk*

Introduction

Materials processing such as the annealing of phosphor thin films deposited (via RF magnetron sputtering) on silicon wafers has traditionally been achieved using time consuming transfers through high temperature cycles in N_2, O_2 or H_2 atmospheres. It should be possible however, to anneal a full-sized silicon wafer, at room temperature, using a single pulse (1 - 20 ns) of high energy ultra-violet laser light, provided that the laser beam is large enough and that the laser energy and beam quality is of a sufficiently high level. It will be shown in this paper that the output from the neodymium glass laser Vulcan can be converted from the fundamental near IR wavelength (1.053 µm) to the fourth harmonic (263 nm). With the use of diffractive optics in the form of phase plates, large focal spots (~ 50 mm diameter) can be achieved with high beam quality.

Previous work on the laser annealing of phosphors on silicon wafers [1, 2, 3] used the output from the Titania KrF laser at the CLF. This work enabled the annealing of small areas (~ 3 mm^2) of ZnS:Mn thin films to be successfully achieved. This was sufficient to prove the technique but the requirement now is to scale up the irradiation to about 2 cm square. However the KrF laser is no longer available and so a new source of UV laser was sought.

The Vulcan high power Nd:glass laser is capable of delivering up to 400 J of energy in a 1 ns pulse in a single beam. The fundamental wavelength of this laser is 1.053 µm, which is not suitable for irradiating silicon phosphors for annealing purposes due to the lack of absorption at this wavelength and the destruction of the surface layer / substrate interface states. However, it is a standard technique within the facility to use KDP crystals to frequency convert to a harmonic wavelength. We commonly convert to the second harmonic ($2\omega_o$, wavelength 527 nm) but for this materials processing experiment the fourth harmonic (263 nm) is required.

Frequency Conversion

The conversion from near-IR to UV requires the use of two KDP crystals, the first (operating in type II mode) to convert the fundamental IR to the second harmonic (green) and the second crystal (operating in type I mode) to convert the green light to the fourth harmonic (UV). Figure 1 shows the crystals installed in the system along with some of the injection optics for the UV CW alignment laser.

Some difficulty has been experienced in optimizing the output of these crystals using the broad band oscillator usually used on Vulcan for the generation of long pulses (ns).

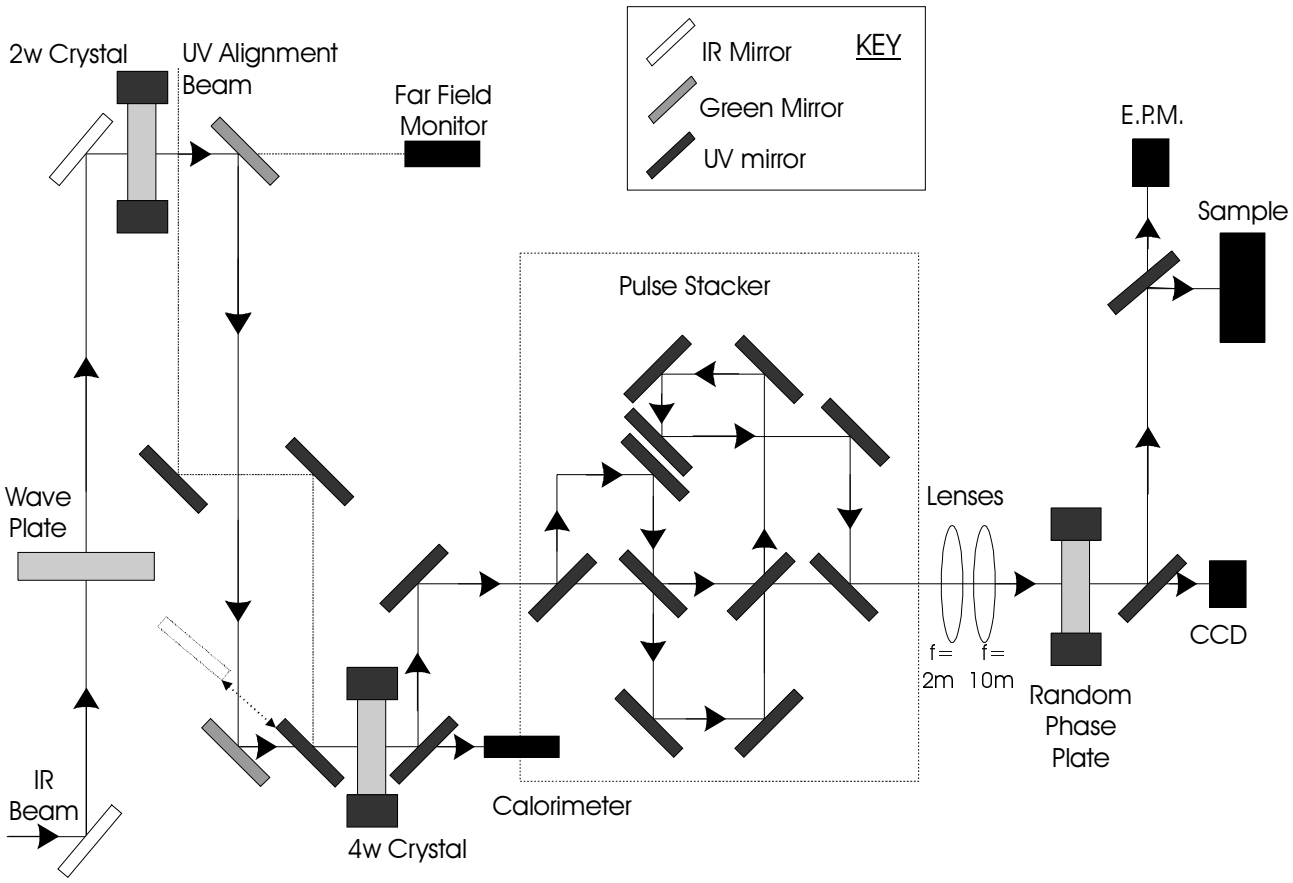

Figure 1. Experimental schematic showing the CW alignment injection optics, the second and fourth harmonic crystals, the pulse stacker arrangement, the position of the random phase plate, the focussing optics and the target.

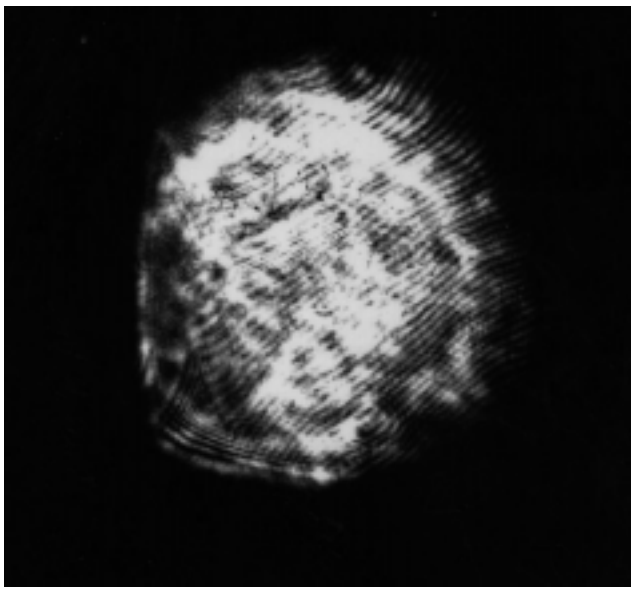

Figure 2. Near-field image of the fourth harmonic beam.

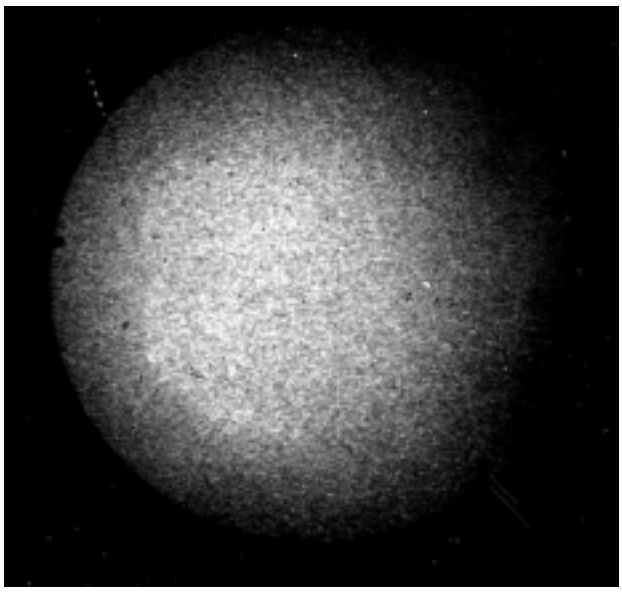

Figure 3. Pseudo far-field image with the RPP in use.

The overall conversion efficiency from the IR to the UV was limited to 3%. This gave fluences up to 240 m J cm^{-2} in an area > 3 cm^2. When the Vulcan seed pulse was generated from the SLM (single longitudinal mode) oscillator the overall efficiency increased to 14% with 20 J generated in the UV for 147 J IR. This is close to that expected theoretically.

Beam Smoothing

The frequency conversion is a highly non-linear process and it therefore enhances any hot spot or beam non-uniformity. This is obviously not desirable and some mechanism for smoothing the beam intensity profile is essential. A simple method of beam smoothing which has commonly been practiced within the CLF is the use of Random Phase Plates (RPP). These devices are diffractive optical elements that impose a particular profile on a far-field intensity pattern. The RPP is used in conjunction with a principal focussing optic and produces a $sinc^2$ intensity profile at nominal focus containing a high spatial frequency speckle pattern. The full width half maximum (FWHM) size of the focus is given by $f\lambda/d$ where f is the focal length of the lens and d is the element size of the RPP structure. In order to obtain a substantially flat intensity profile for irradiating a wafer over a 2 cm diameter circle, a 50 mm FMHM is required. With the wavelength fixed at 263 nm and a RPP structure size of 50 microns being the smallest that could be easily made in-house, a 10 metre focal length lens was therefore required.

Figure 2 shows the near field of the converted fourth harmonic laser beam with significant non-uniformities apparent. Figure 3 was generated with the use of the RPP and shows the corresponding 5 cm diameter far-field. The RPP acts to convert the low frequency spatial modulations of the beam to high frequency spatial modulations at the focus and this is demonstrated in Figure 4 which shows the modal power spectrum for each image. The near field image contains a higher level of low frequency components whereas the RPP image has almost a uniform spread of low and high frequency components as would be expected from a random beam profile. The far field image is made up of a ~26 micron speckle pattern which is believed to be smoothed out by some lateral thermal transport within the phosphor layer.

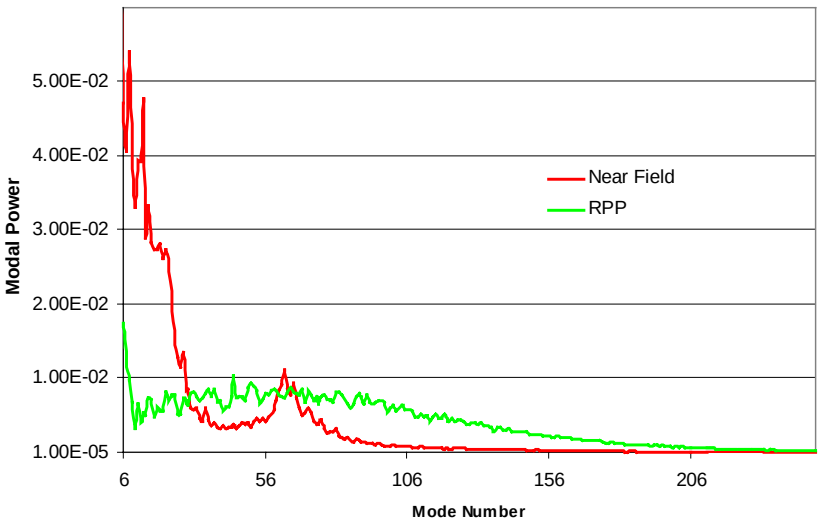

Figure 4. Modal Power Spectrum derived from an FFT of the near and far field images.

References

1. W.M. Cranton, E.A. Mastio, C.B. Thomas, R. Stevens and J.P.O Evans 'Laser annealing for high intensity flat screen displays', CLF Annual Report 1996 / 97.

2. E.A. Mastio, W.M. Cranton, C.B. Thomas 'Phosphor dopant activation using pulsed KrF laser annealing', CLF Annual Report 1997 / 98.

3. E.A. Mastio, W.M. Cranton, C.B. Thomas, E. Fogarassy, S. de Unamuno 'Pulsed KrF laser annealing of RF sputtered ZnS:Mn thin films', Applied Surface Science, Vol 139, pp35-39 (1999)

An F1 on-axis parabola producing focal spots of less than 10 microns on Vulcan

CN Danson, RM Allott, J Collier, CB Edwards, D Neely, PA Norreys, TB Winstone

Central Laser Facility, CLRC Rutherford Appleton Laboratory, Chilton, Didcot, Oxon, OX11 0QX, UK

NS Child, WP Harris, JH Mathers

Optical Surfaces Ltd., Godstone Road, Kenly, Surrey, CR8 5AA, UK

Main contact email address: *C.Danson@rl.ac.uk*

The technique of Chirped Pulse Amplification (CPA) [1] is now in common use on many laser systems and has resulted in massive increases in intensities delivered to target. A fundamental aspect of generating these intensities is the ability to focus the beam. It has been demonstrated that with the standard beam configuration Vulcan operates with approximately three times diffraction limited performance [2] and with the commissioning of an in-house developed static corrector this performance can be improved to 1.5 times diffraction limited [3]. With such a beam it is necessary to use the highest possible quality optic and shortest focal length to generate the smallest focal spot size and hence the highest possible irradiance on target.

The focusing of the beam to target was accomplished using an on-axis parabola. These have the benefit of being able to be made with relatively short focal lengths. The manufacturing limit for these types of parabolas whilst maintaining the optical quality is about F1. With a rectangular shaped beam, as apertured by the grating compressor, the beam is therefore focused onto target using an F1 (vertically) - F1.5 (horizontally) on-axis parabola. The optical testing of one of the on-axis parabolas is shown in Figure 1 resulting in a peak to valley wave-front error of 0.1 λ at 633 nm.

Figure 2 shows focal spot quality measurements using the parabola. The input beam at full energy can be focused giving a central focal spot of approximately 5 microns FWHM as shown in Figure 2(a). The target mounting system will then partially obscure the near field as indicated in Figure 2(b). This will not only reduce the total pulse energy but also introduce additional high spatial frequencies into the near-field, diffracting energy away from the central peak and into side lobes. The recorded far-field with a c.w. alignment beam is shown in Figure 2(c). The on-axis intensity is reduced by approximately 15% with an observed enhancement of the side lobe structure.

Energies of 30 J to target have been delivered in a 750 fs pulse and a focal spot of ~ 5 microns has been obtained using the on-axis parabolic focusing optic. This spot size has been verified from x-ray imaging diagnostics. Assuming 25 % of the energy is contained within the 5 microns spot diameter this gives a focused intensity of 5 x 10^{19} Wcm^{-2}.

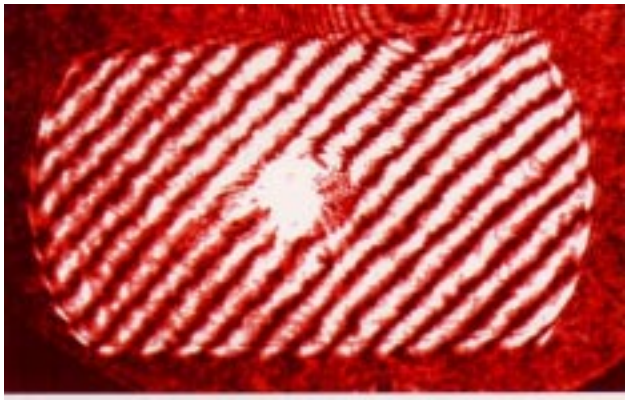

Figure 1. Interferogram showing the wavefront accuracy of the parabola in double pass at 633 nm.

References

1. D Strickland, Mourou, G
Opts. Comm. 56, 219-221 (1985)

2. C N Danson *et al*
J Mod Opt. 45, 8, 1653-1669 (1998)

3. C Hernandez Gomez *et al*
Applied Optics, In Press

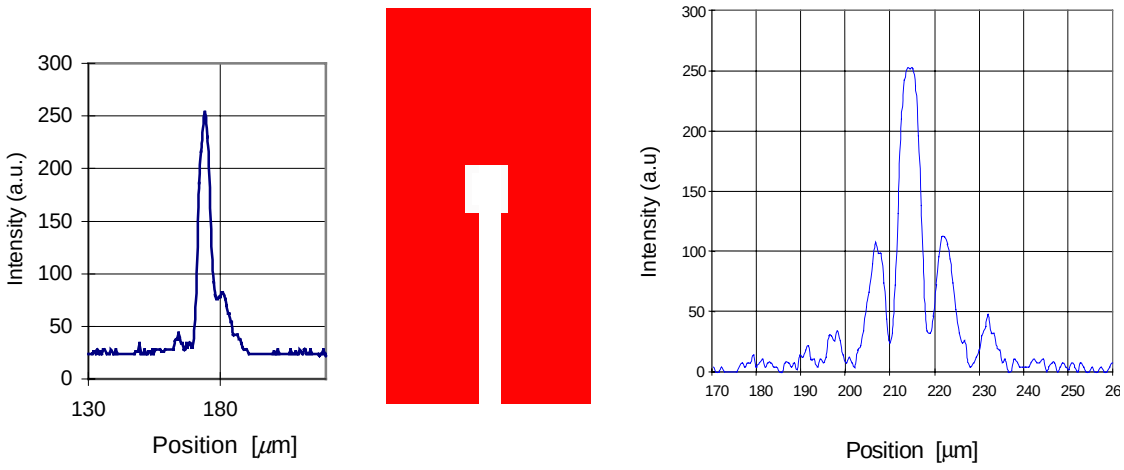

Figure 2. Measurement of the focused intensity. (a) The measured full energy focal profile in an equivalent plane imaging system (b) The simulated near field profile showing the target obscuration and (c) measured CW far-field profile using a retro-reflected image off the target.

Characterisation of Vulcan's Tsunami Oscillator

M Parkinson, A K Kidd, J L Collier

Central Laser Facility, CLRC Rutherford Appleton Laboratory, Chilton, Didcot, Oxon, OX11 0QX, UK

Main contact email address: *j.collier@rl.ac.uk*

Introduction

The Vulcan laser system relies heavily on the performance of the short pulse oscillators that feed the CPA chain. As part of a continuing diagnostic program installation of a number of beam diagnostic systems has begun. One such diagnostic system from the Coherent-Ealing company was used to analyse the performance of the Tsunami mode-locked Ti: Sapphire Laser.

The Tsunami is a commercial Kerr Lens Modelocked (KLM) oscillator using Ti: Sapphire as the active medium. The 80 MHz cavity produces 120 fs pulses at 5 nJ per pulse. It is an integral part of Vulcan's 'Front End' system being the main oscillator that seeds the CPA chain.

Beam Diagnostic System

The commercial Beam diagnostic system used was the Coherent LaserGauge[1]. This system consists of a colour CCD camera and a self-contained computer-based frame-grabber unit. Using the RS-232 interface a computer program was written using both Qbasic and the object-orientated Pascal language Delphi.

The computer program was designed to capture the centroid, diameter and intensity of a series of pulses over a period of time. The program offers the ability to alter the number of pulses captured either by varying the time or selecting the desired number of shots to be recorded.

Figure 1 shows the computer program interface. The first graph down the right hand side of the screen plots both the x and y axis of the centroid of the pulse. The second graph plots the pulse diameter and the third the intensity of the pulse. The program is also designed to capture a two-dimensional image of a laser pulse and x and y cross-section profiles on an individual shot basis.

The diagnostic equipment was set up as shown in Figure 2. The Ti: Sapphire beam was focused down using a 3m focal length lens. A length of C-tube was used to cut out any background light affecting the image on the camera. To avoid saturation or damage to the camera the laser was attenuated using a λ/2 waveplate and ND filters.

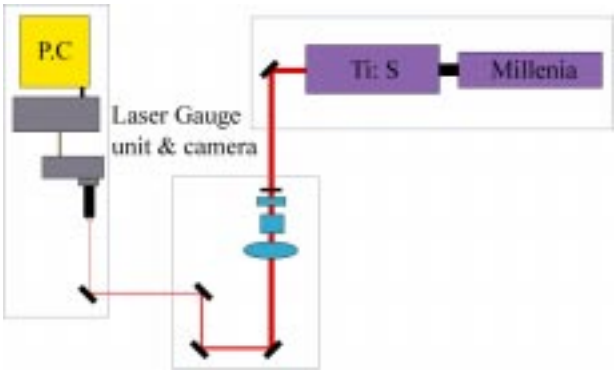

Figure 2. Experimental setup.

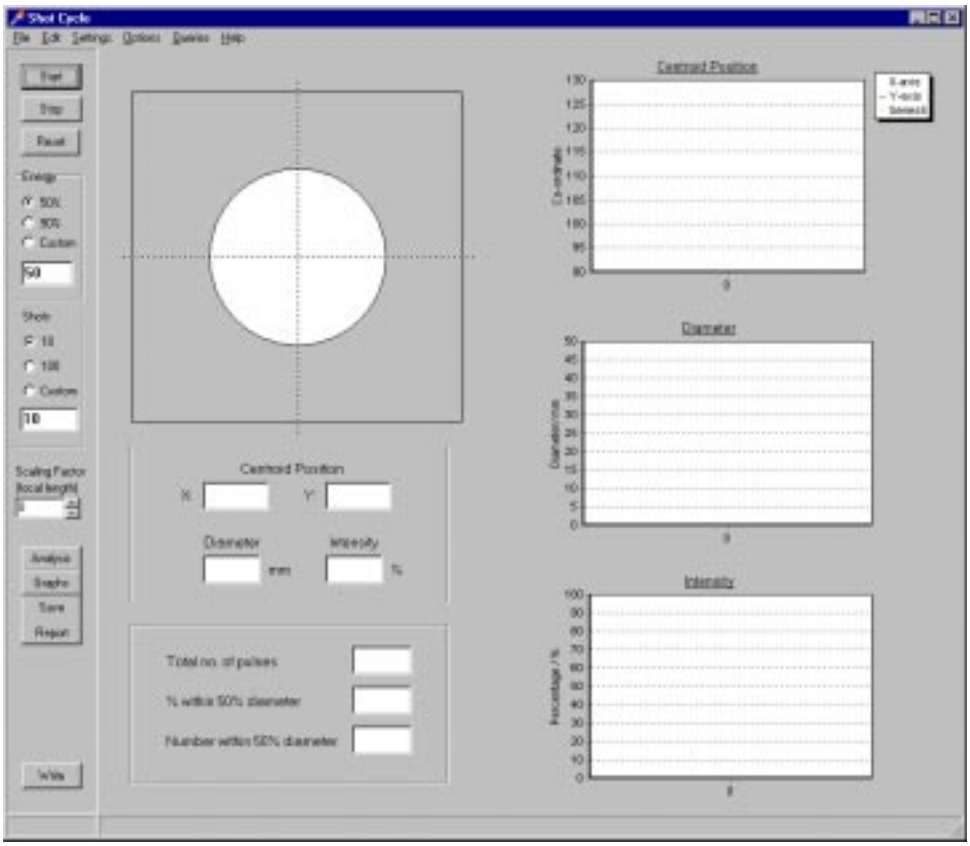

Figure 1. Computer program interface.

Beam Stability

Figure 3 shows the change in the x and y coordinates of the Ti: Sapphire centroid over a period of 3 hours. 2160 data points were sampled at an interval of 5 seconds. The upper series represents the y-coordinate and the lower series represents the x-coordinate of the centroid.

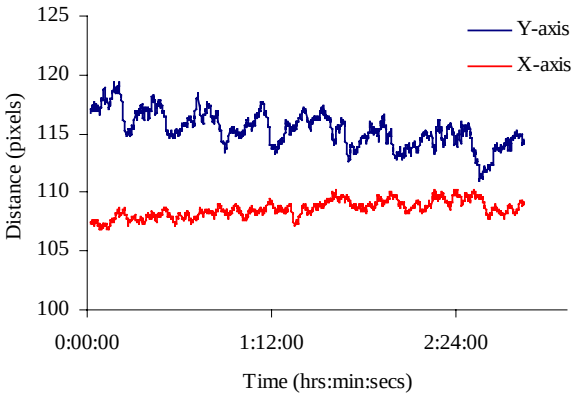

Figure 3. X and Y coordinates for centroid.

As the data was given in pixels the camera was calibrated using 1mm^2 grid mesh at the focus giving a calibration of 1 pixel to 10µm.

Figure 3 shows that there is a drift in both the x-coordinates and the y-coordinates of the centroid over 3 hours. There is a downward drift in the y-coordinates and a drift to the right in the x - coordinates.

The overall drift in the centroid is:

Y-axis = 40µm giving a standard deviation of 27µm

X-axis = 17µm giving a standard deviation of 17 µm

Beam Intensity

Over the same 3-hour period that the centroid data was collected the intensity of each pulse was also captured and recorded.

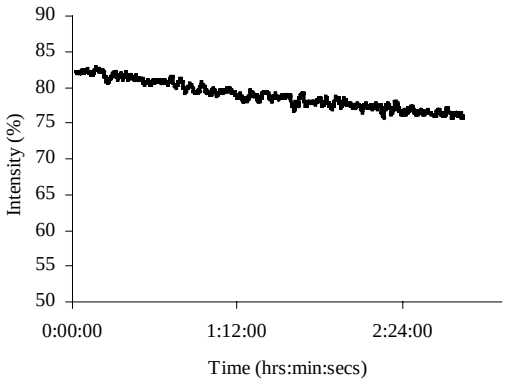

Figure 4. Change in intensity.

Figure 4 shows a steady 10 % drop in intensity over the 3-hour period. The specification of the Tsunami Laser[2)] states a percent power drift in any 2-hour period of <5%.

Beam Profiling and image capture

Figure 5 represents the profile in the X-axis of a single pulse of the Ti: Sapphire.

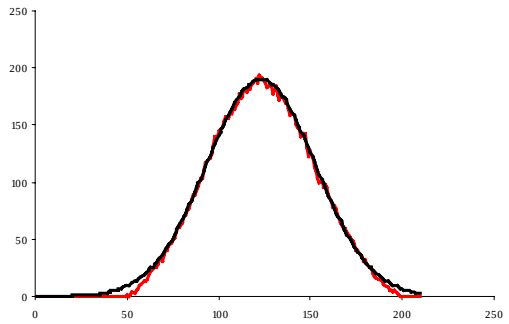

Figure 5. Beam profile in the X-axis.

The distribution of energy across the profile is stated to be Gaussian[1)], that is,

$$I(r) = I(0)\exp(\frac{-2r^2}{w^2}) \qquad (1)$$

where the parameter *w* is referred to as the mode field radius or the spot size. The Gaussian fit to the X-axis profile in Figure 6 shows a beam waste of 1500µm or spot size of 1.5mm. The specification of the Tsunami Laser[2)] stated a beam diameter at 1/e^2 points to be less than 2mm. This shows that after 3 years the laser is still performing to its specification.

Figure 6 shows the two-dimensional image of the captured Ti: Sapphire pulse.

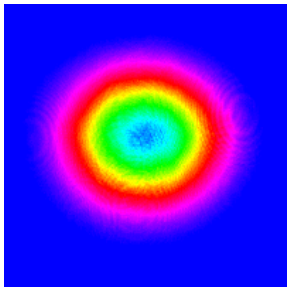

Figure 6. Image of Ti: Sapphire pulse.

Conclusion

The Coherent Laser Gauge diagnostic system has proved to be useful in the characterisation of a short pulse oscillator. The ability to monitor the pointing stability and intensity over a period of time will be used to characterise the 3 remaining short pulse oscillators in Vulcan. The beam profiling and image capture will be useful in monitoring both the alignment and performance of the rod amplifier chain on two-minute shots into Vulcan.

References

1. Coherent Auburn Group, 2303 Lindbergh Street, Auburn, CA

2. Spectra-Physics, Tsunami Mode-Locked Ti: Sapphire Laser User's Manual

Development of a Multi-Terawatt, Femtosecond Laser Facility - Astra

A J Langley, E J Divall, N Girard, C J Hooker, M H R Hutchinson, A Lecot, D Marshall, D Neely, P F Taday

Central Laser Facility, CLRC Rutherford Appleton Laboratory, Chilton, Didcot, Oxon, OX11 0QX, UK

Main contact email address: *A.J.Langley@rl.ac.uk*

The development of Astra will provide the research community with one of the world's most powerful and versatile femtosecond laser facilities. The project, which is set for completion by January 2000, brings together expertise which exists within the Central Laser Facility (CLF) in High Power Lasers (HPL) and within the Lasers for Science Facility (LSF) to develop a laser system which is capable of producing ultra high intensities (~10^{19} Wcm^{-2}) at the repetition rate of 10 Hz. The multi-output laser will provide a range of energies and wavelengths into two experiment areas simultaneously. This will support all the CLF's new and existing femtosecond users within one facility, offering both an economy of scale by multi-user access and encouraging cross-fertilisation between different research programmes.

The combination of very high intensities, ultrashort pulse duration (<50 fs) and high repetition rate opens up new and important opportunities. For example, the generation of X-ray pulses of femtosecond duration will enable time-resolved studies with temporal resolutions of <100 fs of molecular and solid-state structures to be undertaken. The ability to study a broad range of chemical and biological processes on such short time-scales is of wide applicability and should significantly increase the number and range of users of the facility.

Specific areas of interest to users of the new facility are:

- Time-resolved X-ray absorption and diffraction studies
- Laser plasma interactions
- Atomic molecular and cluster physics
- VUV generation via high harmonics
- Laser acceleration of particles
- Nuclear interactions

A schematic diagram of the Astra facility is shown below. Phase 1 of the development programme is now complete and became operational in September 1998. This consists of two Nd: YAG laser pumped titanium-sapphire (TiS) amplifiers that provide sufficient energy to generate TW, 50 fs pulses at 10 Hz after compression. Operationally, however, the beam has normally been split and energies in excess of 10 mJ in 50 fs made available to researchers in both target areas simultaneously.

The Phase 2 of the development programme to generate multi-terawatt pulses is now underway and involves building a third TiS amplifier pumped by a 5 J (532 nm) Nd:YAG laser. The system is designed to provide at least 500 mJ in 50 fs at 800 nm after compression. It is proposed to make this available for user experiments in early 2000.

A more detailed description of the Phase 1 TW development is presented in the following article. The third article in this series considers the design of the multi-terawatt amplifier to be built during Phase 2 of the development programme.

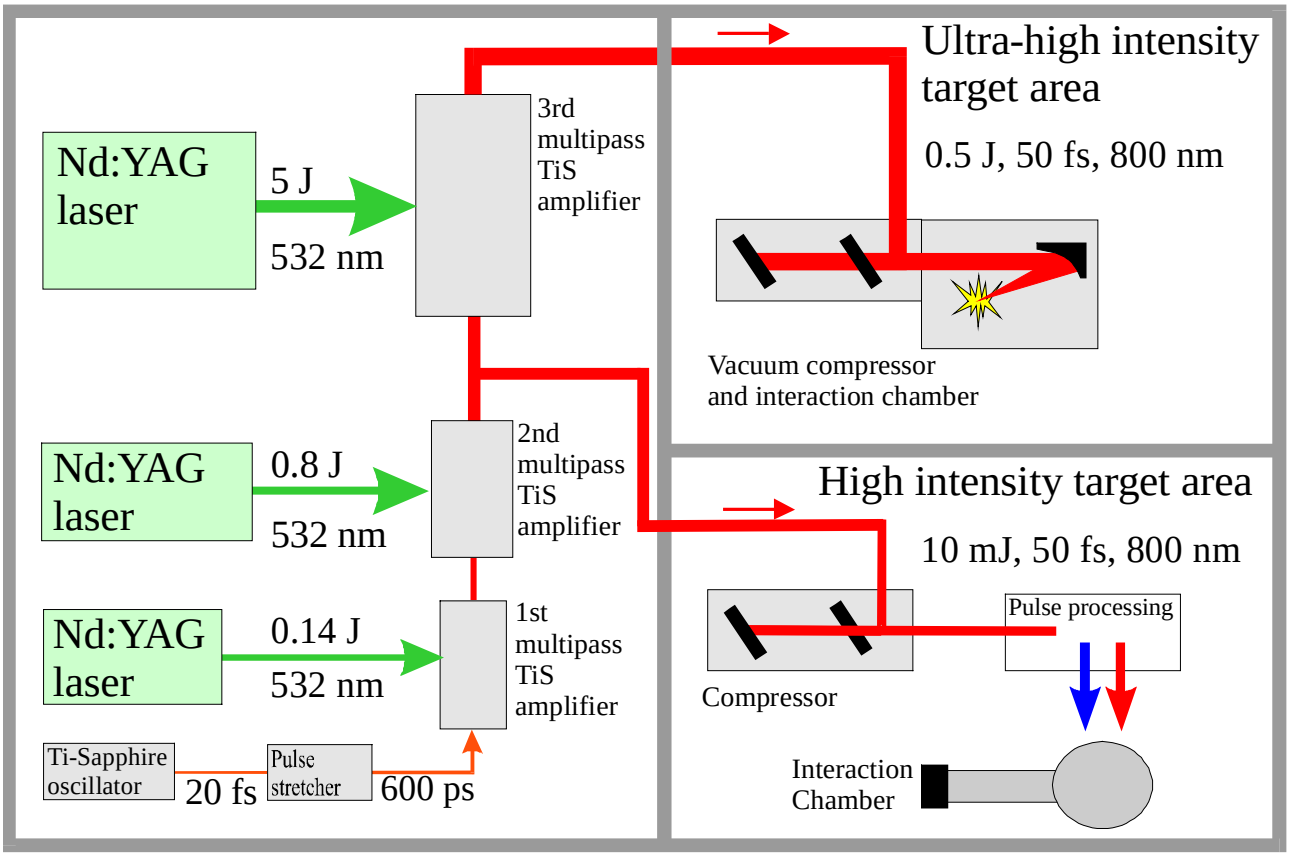

Figure 1. Schematic diagram of Astra – the CLF's new multi-terawatt, ultrahigh intensity femtosecond laser facility.

Astra Development Phase 1 - a Femtosecond Terawatt Laser

A J Langley, N Girard, I Mohammed, I N Ross, P F Taday

Central Laser Facility, CLRC Rutherford Appleton Laboratory, Chilton, Didcot, Oxon, OX11 0QX, UK

Main contact email address: *A.J.Langley@rl.ac.uk*

Introduction

During the 18 month period of the EPSRC funded development programme we have upgraded the intensity of the femtosecond laser facility at RAL by a factor of 500 to provide a laser capable of delivering a focused intensity of 10^{18} Wcm^{-2}.

The development took place over a period of 18 months between April 1997 and September 1998. During stage I of the development, a sub-terawatt single-amplifier system was built delivering 1 mJ, 50 fs pulses to user experiments. This system was used to carry out 22 weeks of user experiments between October 1997 and August 1998. Stage II of the project to upgrade to terawatt performance was carried out in two separate periods in March, June and July 1998. During October 1998 the TW laser was relocated in a new laboratory at RAL and, following the announcement of the grant (GR/M30548), it became part of the EPSRC funded programme to develop a multi-terawatt laser facility to be known as ASTRA. Terawatt experiment operations began on 16 November 1998.

Description of the Femtosecond Terawatt Laser

Figure 1 shows the layout of the newly built femtosecond terawatt laser at RAL. The system is constructed on three 1.5 x 3.0 m optical tables. Pulses for amplification are derived from a mirror-dispersion controlled titanium-sapphire oscillator[1)] (Femto, Technische Universitat, Vienna) pumped by a frequency doubled cw diode-pumped Nd:YVO_4 laser (Millennia, Spectra-Physics).

The Femto laser provides pulses at a repetition rate of 76 MHz centred at 790 nm with sufficient bandwidth for compression to 20 fs. Prior to amplification the pulses are stretched to 300 ps in a pulse stretcher. The stretcher design is shown in Figure 2. This consists only of reflective optics to minimise the contribution of higher order phase terms and thus maintain pulse fidelity. The stretcher is essentially a simple all-reflective analogue of a dual grating stretcher with single relay lens. It is designed with a bandpass 4x the FWHM bandwidth of a 30 fs Gaussian pulse.

The input pulses make a double pass through the stretcher which consists of two 1500 lines/mm gratings (Spectrogon), a large gold coated mirror (ROC = 730 mm) and a gold coated flat mirror (Optical Surfaces). The gratings and mirrors were specified to $\lambda/10$ and $\lambda/20$ flatness respectively. For this design, minimum beam aberration is achieved by retro-reflecting the beam.

It was found necessary to place a Faraday isolator before the stretcher to minimise the likelihood of back reflections disrupting the oscillator.

The stretched pulses are amplified in the first amplifier to an energy up to 2 mJ. This amplifier consists of four confocal mirrors (ROC = 2000 mm) which direct and focus the amplified beam through a 7 mm long Ti:S rod (Crystal Systems, FOM = 150 and α_{514} = 4.7). The rod is pumped with 140 mJ, 20 ns pulses of 532 nm radiation from a 10 Hz Nd:YAG laser (Continuum). The 532 nm beam is image relayed to the rod to provide close to uniform, saturated pump fluence of 2 Jcm^{-2}. After the first 5 passes the pre-amplified pulse train is extracted from the amplifier and passed through a Pockels cell (Leysop) to pulse pick from the 76 MHz pulse train and minimise amplified fluorescence in the high gain first amplifier. The selected pulse is then re-injected into the amplifier to boost its energy to the 1-2 mJ level. The amplifier provides a net gain of 4 x 10^6.

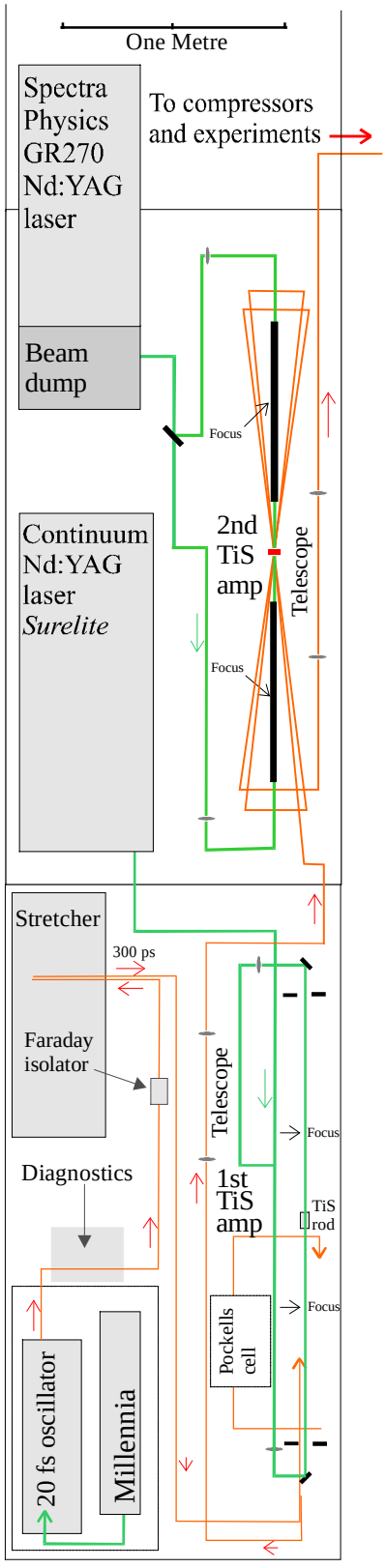

Figure 1. Layout of the femtosecond terawatt laser.

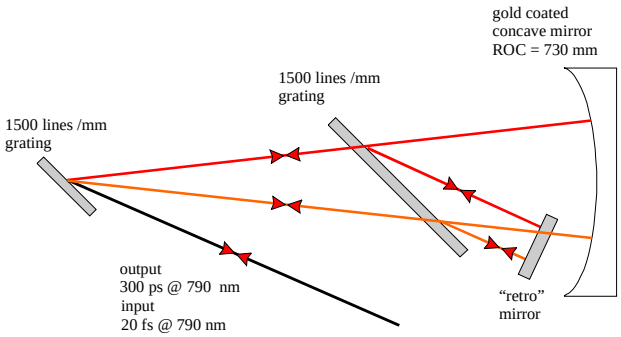

Figure 2. All reflective stretcher.

Prior to building the second amplifier, the first amplifier stage of the femtosecond laser provided output for a series of EPSRC funded user experiments. Pulses were compressed after amplification to 50 fs using a conventional compressor design comprising a pair of 1500 lines/mm gratings (Spectrogon) in a parallel arrangement. The transmission efficiency of the compressor is 50%. During this phase of the development programme an existing Ti:S oscillator (Spectra-Physics, Tsunami) was used as the source of 50 fs pulses for amplification. The stretcher and compressor were set up using rapid-scanning autocorrelators with unamplified oscillator pulses to test that the stretched pulses were successfully recompressed to 50 fs duration. Figure 3 shows autocorrelator

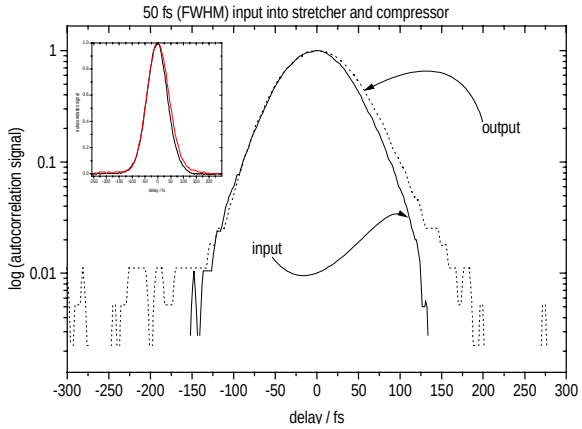

Figure 3. Autocorrelation of unamplified pulses.

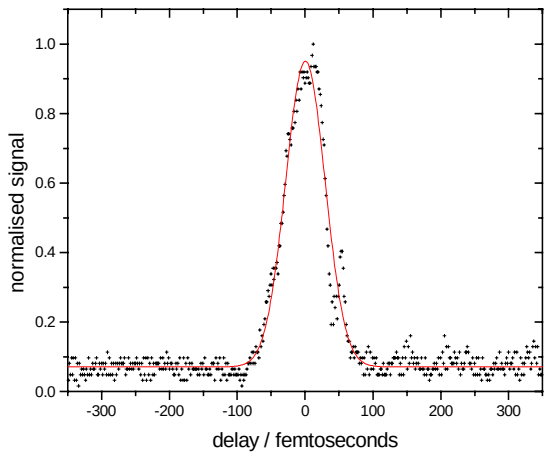

Figure 4. Single-shot autocorrelation of amplified pulses.

traces obtained before stretching and after compression. The small difference is due to different autocorrelators being used for the input and output pulses. Amplified pulses were also monitored on a single-shot autocorrelator. A typical autocorrelation for an amplified pulse of energy 500 μJ is shown in Figure 4. Measurements in the far field of beam transmission through a pin-hole indicated that the amplified beam of compressed pulses was ~ 1.8 times the diffraction limit. Intensities in excess of 10^{16} Wcm^{-2} would be expected with these parameters and this was confirmed by observing up to the 7th ionisation stage of argon in an ion time-of-flight spectrum[2].

The second amplifier is a conventional four-pass bow-tie configuration with a 10 mm diameter 7 mm long Ti:S crystal (Crystal Systems, FOM = 150 and α_{514} = 4.7). The crystal is pumped by an energy of up to 850 mJ in two 532 nm beams from a Q-switched Nd:YAG laser (Spectra-Physics GCR). The maximum measured amplified uncompressed energy derived from this amplifier is 110 mJ per pulse (see Figure 5).

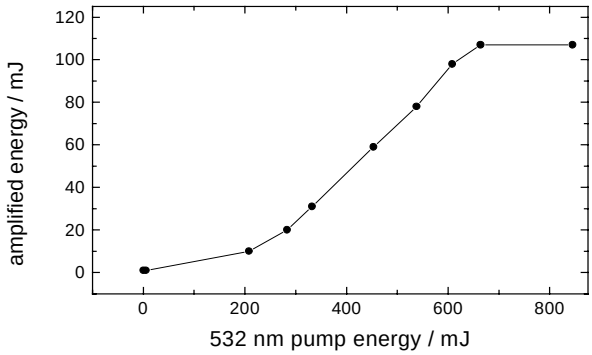

Figure 5. pump versus amplified energy in 2nd amplifier.

However, the expected amplified energy is closer to 200 mJ per pulse based upon the efficiency of Ti:S. Our amplifier modelling analysis indicates that the gain clamping near the 100 mJ level is due to parasitic modes in the rod competing for gain at pump energies in excess of 700 mJ. In due course the rod will be clad with a material of suitable refractive index to minimise this problem. In the mean time the energy obtained is more than adequate for all current applications and allows the system to operate at the intended terawatt level.

Pulses of 50 fs duration are obtained after compression for user scientist experiments. See Figure 6. The FWHM of the spectrum of the amplified pulse, shown in Figure 7, is sufficient to support a 46 fs Gaussian shaped pulse. The fact that we have been able to recompress stretched pulses derived from the Femto oscillator, i.e. without amplification, down to 2 fs suggests that the amplified pulses are subject to gain

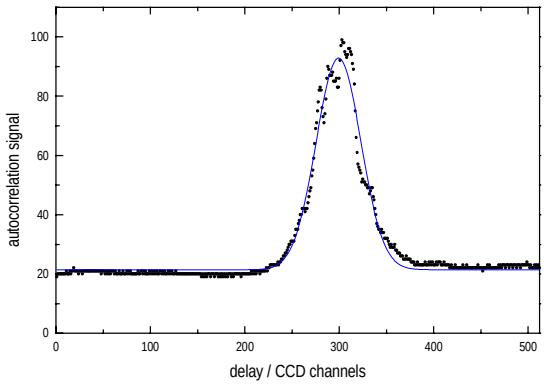

Figure 6. Single-shot autocorrelation.

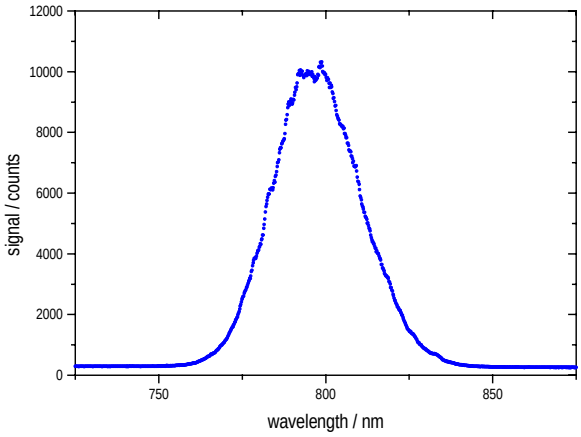

Figure 7. Spectrum of amplified pulse.

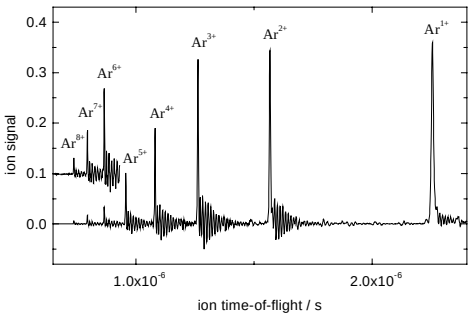

Figure 8. Time-of-flight spectrum of argon.

narrowing in the amplifier. This has been observed by other developers of ultra-short pulse amplifiers[3]. It is intended to explore the effects of saturation on pulse duration when the schedule of user experiments permits. We also plan to undertake high-dynamic range autocorrelation measurements to determine the contrast of the compressed pulse.

In order to obtain an estimate of the maximum intensity available from the terawatt laser, 5 mJ pulses of 50 fs duration were focused with a f/2.5 focusing mirror in an ionisation time-of-flight (TOF) spectrometer containing argon as the test gas. The TOF spectrum is shown in Figure 8 and clearly shows the 8th stage of ionisation.

This indicates that a focused intensity in the region of 10^{17} Wcm^{-2} was obtained. This is consistent with these pulse parameters assuming a 2x diffraction-limited beam.

Since compressed pulse energies in excess of 50 mJ are available, the laser is capable of providing a maximum focused intensity of at least 10^{18} Wcm^{-2}.

Conclusion

An EPSRC funded development programme to upgrade the femtosecond laser at RAL to the terawatt level has been succesfully completed. EPSRC funded research groups are now using the facility for their high-intensity experiment programmes. The facility is currently operating two target areas simultaneously with pulse energies up to 10 mJ per 50 fs pulse at focused intensities >10^{17} Wcm^{-2}. The laser is capable of providing up to 50 mJ per 50 fs pulse at a focused intensity of 10^{18} Wcm^{-2}.

Acknowledgements

The following are acknowledged for their support: the EPSRC for funding the programme, Roy Newell's group from UCL for providing the argon ionisation measurements, and all the users of the CLF's femtosecond facility who supported this facility upgrade.

References

1. Ch Spielman, A Stingl, R Szipocs and F Krausz
Optics Letters 19, 204 (1994)

2. S Augst, D Strickland, D D Meyerhofer, S L Chin and J H Eberly
Phys. Rev. Letts., 63(20), 2212 (1989)

3. A Antonetti, F Blasco, J P Chamberet, G Cheriaux, G Darpentigni, C le Blanc, P Rousseau, S Ranc, G Rey and F Salin
Appl. Phys. B., 65, 197-204 (1997)

Astra Development Phase 2, Design Considerations for a Multi-Terawatt Amplifier

C J Hooker, D Marshall

Central Laser Facility, CLRC Rutherford Appleton Laboratory, Chilton, Didcot, Oxon, OX11 0QX, UK

Main contact email address: *C.J.Hooker@rl.ac.uk*

Introduction

In order to achieve the 1-Joule pulse energies required for multi-terawatt operation, a third amplifier was needed at the end of the Astra laser chain. Preliminary calculations based on the expected intensity showed that the length of the stretched pulse would have to be increased, otherwise nonlinear effects would prevent effective recompression of the amplified pulses. A new stretcher was designed to produce pulses of 600 ps, which was both the shortest acceptable duration and the longest achievable with readily available gratings. The design of this stretcher is not described in this article, which deals with the development of a simulator for the laser chain and the analysis of parasitic modes in the crystal and methods of overcoming them.

Computer modelling of the amplifier chain

The simulator was written in MathCad (from MathSoft), which provides many of the graphical and display tools required for showing the results of the different stages in the simulation. While the code was being written, its scope was extended to include the first two laser amplifiers as well as the final one: this allowed the code to be checked against the known performance of the laser, and ensured the input to the final stage had the correct characteristics. Because Astra is a repetitively-pulsed laser it is possible to simulate its output by modelling a single pulse and assuming steady-state conditions. The input pulses, which are stretched from 20 femtoseconds in the oscillator to 600 picoseconds FWHM length, are modelled as a Gaussian distribution. This shape shows good agreement with the present output. In order to maintain the shape of the pulse it is split into 'slices', each of which represents the energy of a narrow band of wavelengths in the chirped stretched pulse. The envelope of these slices forms a Gaussian distribution containing the appropriate energy for the pulse. The slices are calculated as they are required so that different numbers can be used. The data representing the pulse is then fed through functions representing the Ti:S crystals, Pockel cells, and beam expanders. The equations used to model the amplification were taken from Reference 1. As the pulse data is manipulated, the program builds an array containing data about each of the slices in the pulse. The quantities recorded are the fluence, energy, B integral contributions, and the stored energy in the current amplifier crystal. Each function representing one of the modelled components returns data which fills in the array.

Once the simulated run through the system is finished, the data can be extracted from this array for use elsewhere in the program. The energy outputs can be accumulated along a slice (i.e. one slice is summed up to the current pass for any pass number) to give measures of the change in pulse shape (Figure 1). The sum of all the slices gives the total energy at any point in the laser chain, as shown in Figure 2, where the "system coordinate" is the number of optical components that has been traversed. The B integral is accumulated through the slices and can be mapped in a similar fashion to the energy. The overall B integral for the system is that of the slice of the pulse with the greatest total B integral.

B integral contributions are calculated for the amplifier crystals, Pockels cells, and air paths between passes of the amplifier crystals. These values are displayed in Table 1, which also includes B integrals due to the beam expanders. It can be seen

that the air paths contribute about one-third of the total B of the system.

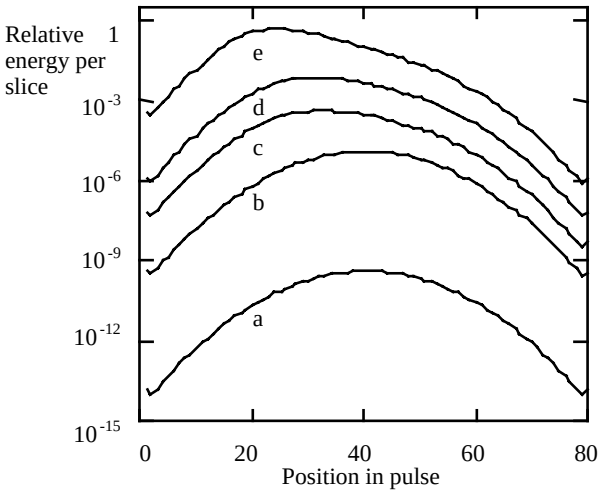

Figure 1. Pulse shapes through the system, showing leading edge steepening: a) Initial pulse; b) After 5 passes of Amp 1; c) After Amp 1; d) After Amp 2; e) After Amp 3.

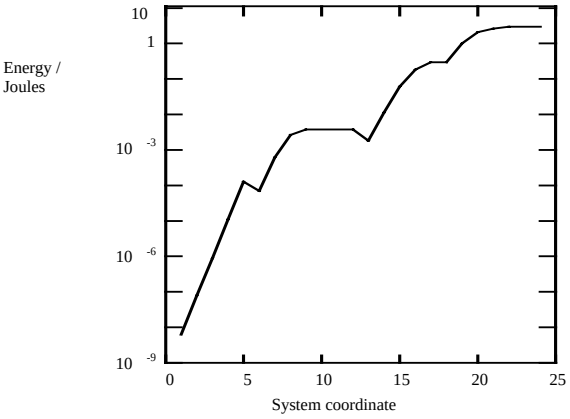

Figure 2. Total pulse energy through system.

B integral due to :	Air path	Material	Total B integral	Cumulative Total
Amp. 1	0.147	0.395	0.542	0.542
Amp. 2	0.055	0.133	0.188	0.730
Amp. 3	0.109	0.323	0.432	1.162

Table 1. B integrals of various parts of the Astra laser.

The program has been written in such a way that it can be expanded to perform extra tasks, such as a calculation of the FWHM of the pulse as it propagates through the system. The simulation agrees well with measurements taken in the current laser system. The energy output of the first amplifier is 3.4 mJ in the simulator and between 3 and 4 mJ measured on Astra.

Design of the amplifier crystal

Several inter-related factors influenced the design of the Ti:sapphire crystal for the third amplifier. The computer model was very important for evaluating different possibilities. Astra has two target areas. One requires most of the output from Amp 2, so only about 10 percent can be used as input to Amp 3. The main variables are the dimensions of the crystal, the dopant concentration, the diameters of the pumped region and the infra-red beam and the number of passes made through the crystal. The first two are constrained somewhat by cost and by the technical limitations of the crystal-growing process. Another important constraint was the thickness of the crystal: as this is the principal contribution to both higher-order dispersion and B-integral in the laser, it was important to keep the total thickness (i.e. physical thickness times the number of passes) to a minimum. Even with a new design of pulse stretcher, giving a pulse length of 600 ps FWHM, the expected increase in output energy to 1 Joule restricted the maximum length of the crystal to around 1 cm if the B-integral was not to exceed unity. Efficient use of the available pump energy was also important. Lastly, the dimensions of the crystal affect the extent of losses resulting from parasitic oscillations. A simple computer model was written to analyse this problem.

The requirements of efficiency and minimum path in the material pushed the design in the direction of a thin, highly-doped crystal with a small number of passes. A long series of code runs with a range of diameters of the pumped region showed that efficient extraction of the energy and good saturation on the fourth pass of the crystal were achievable with the available input, using a pumped region 18 mm in diameter and an extracting beam of 16 mm diameter. The output in this operating regime was reasonably stable with respect to variations in pump energy.

Analysis of parasitic oscillations

The problem with parasitic oscillations is due to the high refractive index of sapphire (n = 1.76 at 800 nm), which means the critical angle for total internal reflection is only 34.6 degrees. The diameter of the crystal must be at least 1.76 times that of the pumped region, otherwise “whisper-mode” parasitic oscillations can build up in the circular cross-sections of the crystal perpendicular to the axis; this dictates a diameter of 32 mm. In rectangular sections of the crystal containing the cylinder axis, there can be closed optical paths for which total internal reflection occurs at every surface, and which also pass through the gain region. Depending on the aspect (length-to-diameter) ratio of the crystal, there can be one, two or even more reflections at the end faces in each path. Examples of these “rectangular” modes are shown in Figure 3.

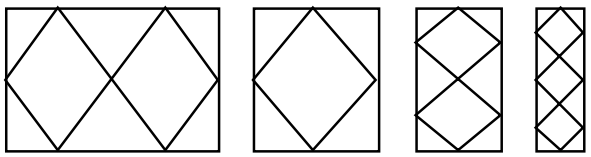

Figure 3. Examples of "rectangular" parasitics and the notation used to describe them.

Parasitic oscillations can also build up between the faces of the crystal, which are normally parallel, if the gain is high enough to outweigh the transmission losses. Anti-reflection coatings on the crystal faces will minimise this type of parasitic loss, as well as reducing the losses of both pump and infra-red energy, but such coatings do not change the critical angle, so they will have no effect on the “rectangular” parasitics. The only way to suppress these is to introduce loss at the cylindrical surface of the crystal, which can be done by coating it with an index-matched absorbing layer. Such a layer will also suppress the whisper modes, hence the pumped region can be a larger fraction of the crystal diameter, allowing the use of a smaller crystal (22 mm if the cladding has n = 1.5). A computer program was written to analyse the different modes, and to calculate the net round-trip gain as a function of the crystal aspect ratio and the refractive index of the absorbing layer.

The results from the code showed that certain values of the aspect ratio are very much better than others, because the effective gains of the different rectangular parasitics vary widely. The absorbing cladding layer was found to be essential, particularly for crystals with an aspect ratio in the region of 0.5, arising from a maximum thickness of around 10 mm combined with a crystal diameter of 22 mm. Some examples of the effects are shown in Figure 4, where two different parasitic modes are plotted as a function of aspect ratio. The net gain must be below 1 to ensure the parasitic mode will not oscillate. For the final design, a diameter of 24 mm was chosen, with an aspect ratio of 0.5 to avoid the gain peak of the [3,1] parasitic at 0.48. The crystal is thus 12 mm thick, which does not compromise the B-integral too seriously. The cladding needs to have a refractive index of at least 1.55 to suppress the parasitic, but this is fairly easy to achieve.

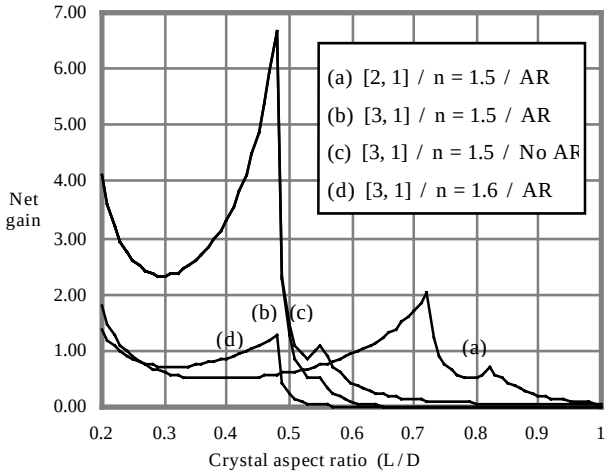

Figure 4. Relative gains of different parasitic modes.

Development of an absorbing cladding

The requirements for the cladding layer can be summarised as follows: the material must have a high refractive index, ideally between 1.6 and 1.9. It must either absorb (or else incorporate another material which absorbs) at 800 nm; it must not break down under intense illumination, must be physically robust and be suitable for coating as a thin, uniform layer on the cylindrical surface of the crystal. The refractive indices of various adhesives and polymer materials were measured, but few were higher than 1.55. After investigating a variety of materials, a photoresist with a refractive index of 1.62 was found to be suitable. For the absorber, powdered copper(II) oxide was used, mixed with the resist to form a kind of black paint, which could be applied to the edge of the crystal. A special jig was built which rotated the crystal slowly during the process, to ensure the layer was uniform.

Reference

1. Catherine Le Blanc Amplification femtoseconde Terawatt basée sur le Titane-Saphir, D. Phil. thesis, Ecole Polytechnique 1993.

Efficient Rejection of Fluorescence from Raman Spectra

P Matousek, M Towrie, A Stanley, A W Parker

Central Laser Facility, CLRC Rutherford Appleton Laboratory, Chilton, Didcot, Oxon, OX11 0QX, UK

Main contact email address: *P.Matousek@rl.ac.uk*

Introduction

Resonance Raman spectroscopy provides a powerful and sensitive analytical tool but is restricted to investigating samples with low levels of fluorescence in the region of the Raman spectra. These problems are exacerbated when performing time-resolved resonance Raman (TR^3) investigations because the pump pulse electronically excites the sample to potentially emissive states. Further problems associated with fluorescence can also come from sample impurities. To apply the technique of ps-TR^3 more widely a method for removing fluorescence has been a major quest and whilst a number of techniques have been proposed and used, no generally applicable solution has been found[1-3]. One of the most promising methods seeks to temporally reject the longer lived fluorescence. Ideally, such a system should achieve the highest possible rejection ratio while having high throughput and have the time resolution, or gating time, of ~1 - 2 ps to match the duration of the Raman flux in typical ps-TR^3 systems. Existing gated CCD cameras and photomultipliers typically operate on nanosecond timescales with the fastest reaching several tens of picoseconds. Streak cameras perform better[1] offering gating times 10 ps, limited by trigger jitter, but these have dynamic range limitations.

Optical parametric amplifiers (OPAs) are becoming the light source of choice for ultrafast spectroscopy. Within such a system the OPAs are driven by an intense ps/fs laser delivering pulses with energies often more than required to drive the experiments. We propose to use this spare capacity to drive a fast optical gate with temporal width comparable with the duration of the laser pulse[10]. The ps-TR^3 spectroscopy technique imposes strict requirements on the performance of such an optical gate. Apart from the need for a fast gating time the gate should also have a high throughput, high contrast to effectively block fluorescence in the closed state, broad bandwidth to transmit the full spectral range of Raman emission (~ 2000 cm^{-1}) and low noise induced by the gating pulse in the Kerr medium. In addition, the gate must not perturb the positions and widths of Raman bands. In our development we have identified the CS_2 based Kerr gate[4,5,6,10] as an optimum choice meeting the above criteria and have characterised and demonstrated the worthiness of such a device for rejecting fluorescence in the presence of Raman scattering.

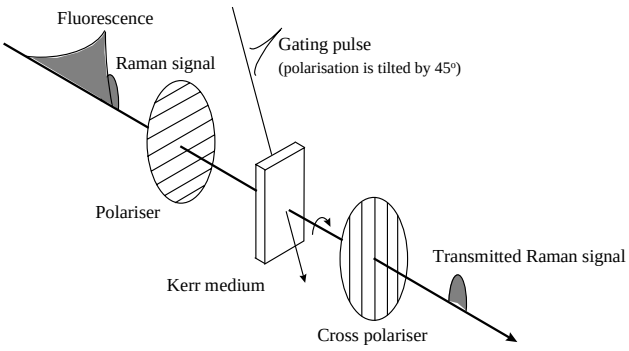

Figure 1. Schematic diagram of the Kerr gate used in the fluorescence rejection system.

A Kerr gate comprises two crossed polarisers and a Kerr medium activated to propagate the light of interest by an intense linearly polarised laser pulse, further referred to as the gating pulse. The relative angle of polarisation between these beams is 45^o (see Figure 1). The interaction of the gating pulse with the Kerr medium induces a transient anisotropy through a nonlinear optical effect. This transforms the polarisation of the light, in this case the fluorescence and Raman scatter, propagating through the medium from linear to elliptical polarisation. The propagation length through the Kerr medium or the strength of anisotropy can be chosen so the polarisation of the Raman light is transformed back to being linearly polarised but rotated by 90^o with respect to its original polarisation direction. In this case the medium acts as a $\lambda/2$ waveplate and the light is transmitted through the cross polariser onto the spectrometer slit. In our application, fluorescence emitted after the gate is closed is efficiently blocked by the polarisers.

Experimental

The system consists of four lenses, acting as collection and relay optics, a Kerr medium and two polarisers. The fluorescence and Raman light scattered from the sample are linearly polarised using a sheet polariser with high throughput before being collimated using a collector lens. The second lens images the light from the sample into the Kerr cell. The rays emerging from the Kerr medium are then re-collimated by another lens before being finally relayed onto spectrometer entrance slit. A cross polariser and two edge filters are placed in front of the spectrometer slit to block the remaining gating pulse and Rayleigh light.

The Raman emission was collected in 90^o geometry. The sample solution was recirculated in an open liquid jet with diameter 0.5 mm. In our experiments the spectral resolution is normally limited by the laser linewidth of 25 cm^{-1}, however for the experiments reported here the spectrometer slit was set to give the spectral resolution of ~ 70 cm^{-1}.

Our ps-TR^3 apparatus uses a regenerative amplifier system providing 800 nm (1 ps, 0.7 mJ) fundamental pulse which is frequency doubled to pump an optical parametric amplifier generating the probe pulse at 0.65 kHz. The 266 nm pump pulse was obtained by frequency mixing a fraction of the frequency doubled beam with the residual fundamental. The Kerr gate was designed to operate with the residual fundamental beam pulse energy of 110 μJ at 800 nm. The gating pulse was focused to a diameter ~ 0.5 - 1 mm using a 150 mm lens. The gate was optimised for the maximum throughput around 650 nm by employing high quality Polarcor polarisers (Newport Ltd) with 80 % throughput and extinction ratio 10^{-4} although an effective performance was also demonstrated with 415 nm probe beam (frequency doubled fundamental) by using sheet polarisers with ~ 30 % throughput. The Kerr medium consisted of a 2 mm-path length cell with static CS_2. A liquid nitrogen cooled, back illuminated CCD camera with an array 2000 x 800 pixels (Instruments S.A. (UK) Ltd) was used to collect Raman spectra. The CCD, with gain of 1 (1 count equals one photo-electron), was binned vertically across the full 800 pixels and horizontally across 10 pixels using purpose written software.

The temporal width of the gate was determined to be 3.2 ps which is consistent with the ~ 2 ps relaxation time[4] of CS_2 anisotropy, the duration of the gating pulse (~ 1 ps) and the Raman flux duration of ~ 2 ps given by the transit time of the probe pulse through the jet stream. As expected the measured curve also exhibited a small degree of asymmetry[4] due to CS_2 relaxation time.

The highest throughput of the Kerr gate with the above gating pulse energy reached 32 % given by incomplete polarisation rotation in the Kerr medium but this figure excludes optical losses. Taking into account transmission losses caused by the optical elements, polarisers and lenses, the overall throughputs for linearly polarised light, in open and closed gate states were 15 % and 0.005 %, respectively. When a higher gating pulse energy was used (~ 250 μJ) the throughput of up to 60 % (excluding optical losses) was obtained.

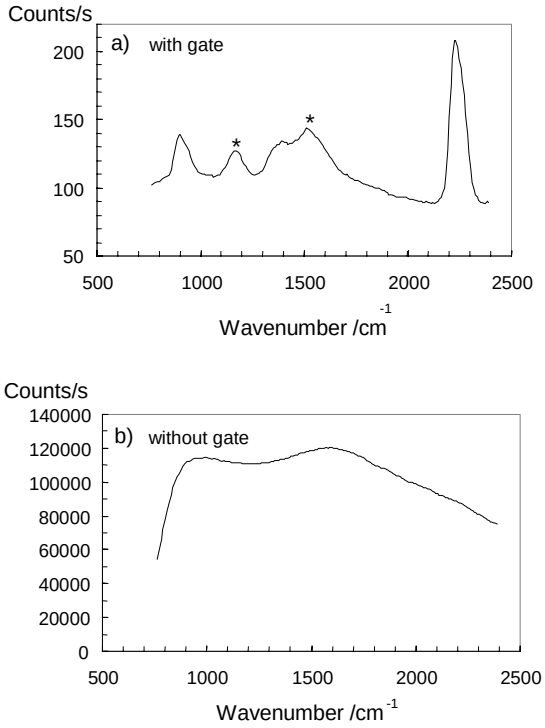

Figure 2. Raman spectra of acetonitrile and the laser dye DCM (*) measured (a) with gate and (b) without gate for 1 mM DCM concentration. The probe wavelength was 588 nm (1 ps, 4.6 μJ) and the accumulation time 400 s.

To characterise the spectral performance of the gate measurements of acetonitrile Raman bands with and without the gate were compared. The results demonstrated that the gate possesses sufficiently broad bandwidth to transmit a broad range of Raman spectra at least 1400 cm^{-1} wide without affecting the band positions and bandwidths which were reproducible to within 2 - 3 cm^{-1} and 5 % of the bandwidth, respectively. The noise induced by the gating pulse within the gate, measured at 650 nm, was 17 counts/s and this is an acceptably low level to avoid seriously affecting Raman data collections which give 10 - 100 counts/s typically. The gate noise gradually increased as the Raman excitation wavelength approached the wavelength of the gating pulse (800 nm). The origin of this noise is attributed to the stimulated anti-Stokes emission induced by the gating pulse within the Kerr gate. This limits the upper usable range of gate to ~ 750 nm. The lower wavelength range is ~ 390 nm and this is determined by the electronic absorption of CS_2. It may be possible to extend the operating range of 390 - 750 nm by using a longer wavelength gating pulse and a different Kerr medium absorbing further towards the ultraviolet.

To demonstrate the effectiveness of the Kerr device to capture Raman spectra from intensely fluorescing samples we have produced Raman spectra of acetonitrile solutions containing the laser-dye DCM[12], ($1x10^{-3}$ mol dm^{-3}) using a laser probe wavelength capable of inducing intense fluorescence emission from the dye (see Figure 2). The fluorescence decay of DCM in acetonitrile is bi-exponential[7] with time constants ~ 2 and 0.2 ns of equal amplitudes. The spectrum obtained with the gate shows well resolved solvent Raman bands and resonant Raman bands of the dye itself. The spectrum measured without the gate (polarisers oriented in parallel) is dominated by massive fluorescence background precluding the observation of the Raman spectrum by conventional means due to photon shot noise and random low frequency distortions of the fluorescence background. The sharp decrease in the intensity profile at low wavenumbers is caused by the edge filter.

The rejection technique was also applied successfully to a ps-TR^3 measurement of S_1 p-quaterphenyl in p-dioxane again with addition of DCM at a concentration inducing an intense fluorescence background. It should also be noted that the ~1 ps time-resolution of the TR^3 apparatus is preserved when using the optical gate[8]. The optical gate has also been used in the time-resolved fluorescent measurements with time-resolution of ~ 3 ps.

In summary, we have developed and demonstrated a practical method for the efficient rejection of fluorescence from Raman spectra based on an optical gate with response time 3 ps. The device has successfully measured Raman and ps-TR^3 spectra in solutions in the presence of intense fluorescence. The characteristics of the gate can be further tailored to the needs of any particular experiment. For example, higher light rejection can be achieved in the closed state by using more polarisers. Also the gate response time can be improved by employing shorter pulses, thinner sample and using Kerr media with faster response time such as optical crystals[9]. The setup can also be converted to an imaging device with 3 ps shutter speed by simply imaging directly onto the CCD.

This work was supported by EPSRC research grant GR/L83943.

References

1. T Tahara and H Hamaguchi
Appl. Spectrosc., 47 391 (1993).

2. P A Mosier-Boss, S H Lieberman and R Newbery
Appl. Spectrosc., 49 630 (1995).

3. T Fujii, K Kamogawa and T Kitagawa
Chem. Phys. Lett., 148 17 (1988).

4. E P Ippen and C V Shank
Appl.Phys.Lett., 26 92 (1975).

5. P P Ho and R R Alfano
Phys. Rev. A, 20 2170 (1979);

6. L M Wang, P P Ho and R R Alfano
Appl. Opt., 32 535 (1993).

7. H Kanbara, H Kobayashi, T Kaino, T Kurihara, N Ooba and K Kubodera
J.Opt.Soc.Am. B, 11 2216 (1994).

8. M Meyer, J C Mialocq and M Rougee
Chem. Phys. Lett., 150 484 (1988).

9. M Towrie, A W Parker, W Shaikh and P Matousek
Meas. Sci. Technol., 9 816 (1998).

10. R Adair, L L Chase and S A Payne
Phys. Rev. B, 39 3337 (1989).

11. A Deffontaine, M Delhaye and M Bridoux
in Time-resolved Vibrational Spectroscopy, A Laubereau and M Stockburger, Eds. (Springer-Verlag, Berlin, 1985), p.20.

12. 4-dicyanomethylene-2-methyl-6-p-dimethylaminostyryl-4-H-pyran

A Single Shot 3rd Order Cross-Correlator for Pulse Contrast and Pulse Shape Measurements

J Collier, C Hernandez-Gomez, I Ross, R.Allott, C Danson, A Hall, T J Spencer.

Central Laser Facility, CLRC Rutherford Appleton Laboratory, Chilton, Didcot, Oxon., OX11 0QX, UK

Main contact email address *: j.collier @ rl.ac.uk*

Introduction

Traditionally, in CPA and short pulse systems temporal pulse characteristics are generally measured using a 2nd order cross correlation, or autocorrelation. However, whilst the use of autocorrelations is widespread, they suffer from a number of drawbacks. If a pulse has an intensity distribution in time *I(t)* then the 2nd order intensity autocorrelation $A_2(\tau)$ can be defined as

$$A_2(\tau) = \int_{-\infty}^{\infty} I(t).I(t+\tau)dt$$

Referring to Figure 1, the function $A_2(\tau)$ is symmetric about τ=0 and as such it is unable to differentiate temporal activity ahead of the real optical pulse from temporal activity behind. This means that pre or post pulses cannot be determined. Furthermore, because of this symmetry, complex or rapidly changing temporal shapes tend to become smoothed and cannot be easily resolved. Finally, optical auto-correlation usually relies on sum frequency mixing of two replicated pulses at a fundamental wavelength producing signals at the second harmonic wavelength[1]. High dynamic ranges are thus not possible because of the additional presence of second harmonic wavelengths from direct second harmonic generation from either or both of the replicated pulses.

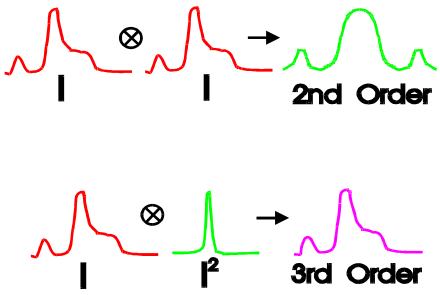

Figure 1. Graphical Comparison of 2nd and 3rd Order Correlation.

3rd order cross-correlation however offers a more attractive proposition and certainly single point (ie single value of τ) devices have been demonstrated before[2]. If a pulse has an intensity distribution in time *I(t)* then its intensity 3rd order cross correlation function $A_3(\tau)$ can be defined as

$$A_3(\tau) = \int_{-\infty}^{\infty} I^2(t).I(t+\tau)dt$$

In contrast to the autocorrelation function $A_2(\tau)$, the 3rd order function $A_3(\tau)$ is asymmetric. It is therefore possible to differentiate temporal activity ahead of the main pulse from temporal activity behind. Furthermore, the smoothing action is much less pronounced and it is therefore able to resolve more complex temporal shapes. And finally in this implementation of the cross correlation, the signal occurs at a wavelength different from either of the replicated pulses or their harmonics and thus high dynamic ranges are in principle possible.

To generate this 3rd order cross correlation function in an optical scheme two non linear processes are required. The first is a process that can produce the $I^2(t)$ response to an *I(t)* stimulus and the second is a process that can produce the $A_3(\tau)$ response that arises from the product of the two arbitary intensity functions $I^2(t)$ and *I(t)*. Additionally, the integral with respect to *t* is needed as is the provision for an arbitary τ. Finally, for true single shot operation, multiple values of τ are required simultaneously on a single shot basis. The first non linear process used to generate $I^2(t)$ from *I(t)* is second harmonic generation and the second process to generate $A_3(\tau)$ from $I^2(t)$ and *I(t)* is sum frequency mixing. Both these processes arise with high efficiency from the second order non linearity found in standard non linear crystals such as β-Barium Borate (BBO).

To generate the sum frequency signal, the fundamental and second harmonic beams are arranged to cross each other at an angle in the mixing crystal. The sum frequency signal is generated at all points in the overlap region and at each point it is proportional to the product of the local intensity in each arm at that point**.** The emission of the sum frequency signal occurs for all points in the overlap region in a direction that bisects the crossover angle. For any line parallel to this bisector a measurement of the total amount of sum frequency signal occurring along that line represents the time integral of the local intensity products. The beams cross at an angle and thus for different measurement lines the intensity product integral occurs for a different relative delay τ between each arm. Therefore, the spatial distribution of the emitted light is the time integrated intensity product of the two pulses evaluated at different delays which is the intensity 3rd order cross correlation as defined above. As time progresses the two pulses move through each other but if the temporal pulse shape in each arm is constant spatially then the overlap region will remain identical in form and location.

Description

A schematic of the device is shown in Figure 2. It is based on an autocorrelator design previously reported by ourselves[3]. The linearly polarised input pulse at the fundamental wavelength enters the device and is focussed into a suitable Type I frequency doubling crystal, such as BBO. The action of the Type 1 crystal is to convert part of the input pulse to its second harmonic. Importantly, this second harmonic version is generated with a polarisation orthogonal to the original pulse polarisation. Both are then recollimated with an achromatic lens. The two pulses at the fundamental and second harmonic frequency are separated into two “arms” by the Woolaston Prism. A Woolaston Prism is a bi-refringent device that splits an arbitrarily polarised beam into two beams that are orthogonally polarised. Both beams emerge at an approximately equal angle with respect to the input beam axis which is not significantly dependent on wavelength. As such, the fundamental and second harmonic beams, given their

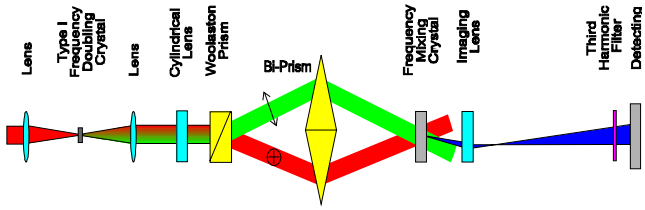

Figure 2. Schematic diagram of the device.

orthogonal polarisation, are split.

The Woolaston Prism is constructed from Calcite with an internal cut angle of 25 degrees. Each beam is then redirected towards the axis of the device by a bi prism. The bi-prism is contructed from BK7 and has an apex angle of 30 degrees. The combination of the Woolaston prism and bi-prism ensures that the two beams cross the axis at approximately ±10 degrees.

At the crossover point a Type II mixing signal is located. The crystal is cut for the third harmonic generation from the two first and second harmonic beams through sum frequency mixing. In order to increase the intensity available for the process both beams are focussed onto the crystal by the cylindrical lens located prior to the Woolaston Prism, and therefore also produce two horizontal line focii. The spatial extent of the third harmonic signal that is generated is then imaged onto a CCD detector by an imaging lens with an appropriate magnification. The entrance to the CCD camera is heavily filtered using band pass filters for the third harmonic wavelength to completely reject fundamental and second harmonic. One point to note which needs to be accommodated in the imaging system is that due to the necessary conservation of momentum for sum frequency generation in the mixing crystal, the emission of the third harmonic radiation is at an angle to the optic axis and so the aperture of the imaging lens needs to be sufficiently large to accommodate this.

Calibration of the device is achieved by the insertion of a BK7 etalon of known thickness, and the corresponding group delay into either arm, and recording the spatial shift of the signal.

Results

Figure 3 illustrates a typical output of the device when imaged directly onto a CCD camera and a line out performed. The data in Figure 4 was produced using a seed pulse that had been amplified in an Optical Parametric CPA system (OPCPA) [4]. It had a top hat spectral profile and was approximately compressed to its temporal Fourier transform limit. Centered at 1053 nm with a top hat bandwidth of 6 nm, its expected pulse duration at the 50% points is expected to be ~ 1 ps as shown.

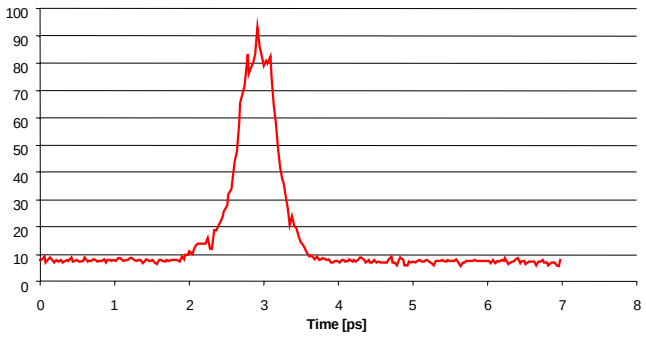

Figure 3. Line out of a CCD image.

However, because of the top hat nature of the spectral profile, significant temporal wings are produced on the pulse that extend for many tens of ps. Thus a high dynamic range cross correlation of the same pulse is shown in Figure 4. Figure 4 is constructed by recording the cross correlation measured by the device in the time window available (~2.5 ps) and then displacing this time window temporally by inserting into either arm a BK7 etalon of known thickness. By using different thickness etalons the time window may be displaced to different temporal points in the pulse, either before the peak (delay fundamental arm) or after (delay harmonic arm). The Figure shows the long temporal wings with a pulse length at the 10^{-3} level of some 15 ps, consistent with the spectral profile.

Furthermore, also shown is the effect of directly inserting into the input beam an uncoated BK7 etalon, thus producing, through a double 4 % reflection, a post pulse at the ~1.5×10^{-3} level. This is clearly recorded by the device and appears only on one side of the peak illustrating the asymmetric nature of the process thus enabling the direct distinction of pre or post pulses.

Finally, Figure 5 illustrates the ability of the cross-correlator to resolve more complex temporal shapes on a single shot basis. The temporal shape in the Figure was generated by applying "square wave" spectral amplitude mask to the seed pulse prior to amplification. This complex temporal shape would not have been resolved by an autocorrelation

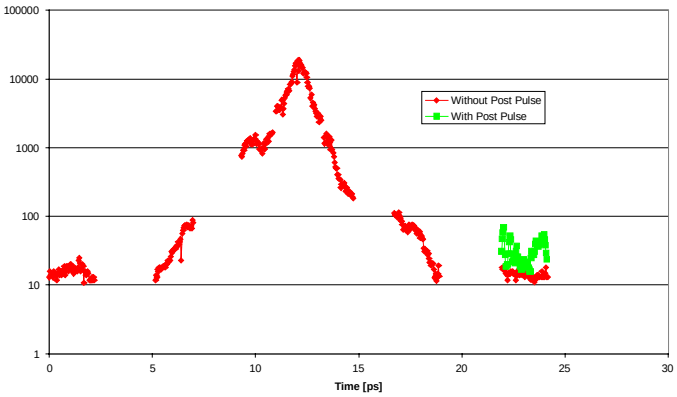

Figure 4. Composite graph showing the same optical pulse of Figure 3 over several orders of magnitude. Also shown is the effect of inserting a BK7 etalon into the beam to produce a post pulse.

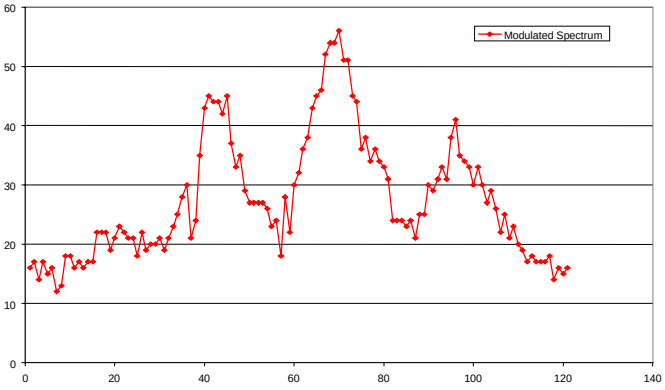

Figure 5. Resolution of a complex temporal shape.

Conclusion

We have presented a design of a 3rd order single shot cross correlator that is no more complex or difficult to operate than a 2nd order device yet has a number of distinct advantages. On a single shot basis we have demonstrated its use to determine pulse shape over several orders of magnitude, showed that it is possible to detect without ambiguity pre or post pulses and have also used it to better resolve more complex temporal shapes.

References

1. J Jansky, G Corradi, R N Gyuzalian,
Optics Communications, 23, No. 3, 293 (1977).

2. S Luan, M H R Hutchinson, R A Smith, F Zhou,
Meas. Sci. Technol. 28, 1426 (1993).

3. J Collier, C Danson, C Johnson, C Mistry
Rev. of Sci. Inst., Vol. 70, No. 3, 1599-1602 (1999a).

4. J. Collier, C Hernandez-Gomez, I Ross, P Matousek,
C Danson, J Walczak
To be published in Applied Optics (1999b).

Production of nickel targets for X-ray laser experiments

N M Prior, M A Stubbs, T Stinson, D Shepherd, D Neely

Central Laser Facility, CLRC Rutherford Appleton Laboratory, Chilton, Didcot, Oxon, OX11 0QX, UK

Main contact email address: *D.Neely@rl.ac.uk*

Introduction

The target preparation laboratory within the Central Laser Facility is responsible for the production of interaction targets used during Vulcan experiments. In recent years the efficiency of X-ray lasers has improved significantly and the wavelength range has been increased by using a broader range of different atomic number targets from titanium (Z=22) to tantalum (Z=73).

The targets used in these experiments consist of a single stripe 100 μm wide, normally required to be around 0.6 μm thick with a top-hat profile, coated onto a flat glass substrate by thermal deposition. In this process, material is loaded into a tungsten filament, which is heated by a low voltage current source causing evaporation. The evaporated material travels in straight lines from the source and coats all exposed surfaces of the substrate. A mask made of two razor blades separated by the stripe width is placed over the substrate to produce a clean edged stripe. Razor blades have been found to be ideal for producing straight edges of the stripe to within 5-10 μm. The thermal evaporation method is not appropriate for high boiling point materials such as nickel, as there is a physical limit to the current that can be passed through the tungsten filament. An alternative method of coating such materials is the use of the magnetron sputtering plant.

The sputter plant uses a potential voltage applied across an argon plasma to dislocate ions of coating material and to transfer them to the substrate. Due to the presence of the argon buffer gas, the material can often "seep" forming diffuse edges. The aim of this experiment was to investigate and compare ways of optimising the coating of nickel stripes using the sputtering technique to obtain top-hat coating profiles.

Experimental Schemes

Three mask geometries were tried in order to achieve a clean 100 μm stripe across the surface of the glass, as shown in Figure 1.

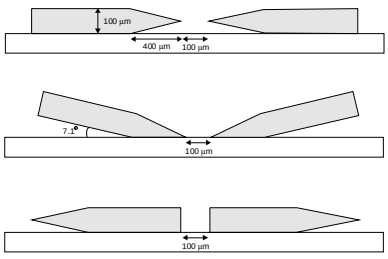

Figure 1. Three experimental mask designs for the orientation of the obscuring razor blades. The blades were arranged (i) flat against the glass, (ii) angled so that the sloped underside was parallel with the substrate and (iii) reversed so that the rectangular edge of the blade formed the obscuration.

The first scheme demonstrates the traditional method used in the thermal evaporation coating plant. The blades are placed against the surface of the glass leaving a 100 μm gap, tip to tip. The second scheme employs angling the blades at 7°, ensuring that the blades are flat against the glass. This was achieved by packing the underside of the blades. The third design was implemented using the blades backwards, so that the rectangular edges sat square on the surface of the glass.

All three samples were coated at the same time to avoid variations in temperature and coated thickness. The sputtering was carried out in three periods of fifteen minutes with a cool down period of twenty minutes between each. The argon pressure was regulated between 4 and 5 millitor. The masks were arranged as directly as possible beneath the source at a distance of 115mm.

Results

After coating an interferogram of each stripe was taken and the thickness profile across the stripe width calculated. Figure 2 shows an interferogram of the stripe which was coated with the third scheme and the profiles of all three results are in the attached graph. The first scheme, using the blades flat against the substrate, produced a wide stripe with a thickness of ~ 130 μm and diffuse edges. The second scheme, using angled blades produced a stripe of around 175 μm with reasonably straight edges. Although this geometry appears to be the most sensible, it proved extremely difficult to implement mechanically. The third scheme, using the rectangular edge of the razor blades, resulted in a clean edged stripe of around 110 μm, closest to the desired profile, as shown by the interferogram.

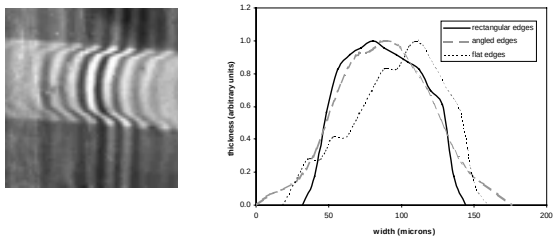

Figure 2. (a) Interferogram showing the nickel stripe coated in the third scheme, using the rectangular edges of the blades as an obscuration. (b) Plotted profiles of all three resultant stripes.

Conclusions

Using the rectangular edges of the blade to form an obscuration produced the closest match to a top-hat shaped profile. This was also the simplest method to implement and is readily reproducible. Therefore it is recommended that this method is used in future for the production of stripe targets which are to be coated using the magnetron sputter plant.

A cheap CCD for measuring hot electron temperatures

S. J. Pestehe, G. J Tallents[1], R. Smith

Department of Physics, University of Essex, Colchester CO4 3SQ, UK

[1]Now at Department of Physics, University of York, York YO1 5DD, UK.

Main contact email address: *sjpest@essex.ac.uk*

Introduction

Superthermal electrons are produced in large irradiance x-ray laser experiments (>10^{14} $Wcm^{-2}\mu m^{-2}$), harmonic generation from solid target and laser fusion experiments. These hot electrons can accelerate fast ions and cause target preheating, production of x-ray continuum and K line emission. The hard x-ray (5-50 keV) continuum slope has been used to measure the hot electron temperature[1,2]. In this paper we demonstrate the diagnosis of moderate-energy electron temperatures generated by irradiating multi-layered disc targets with 248nm, 350 fs, ~10^{17} Wcm^{-2} Titania KrF laser pulses. The moderate-energy electron temperatures up to 10 keV have been measured by a photon counting technique using an inexpensive CCD. The relation of the hot electron temperature to the time interval between the start of a pre-pulse and the 300 fs pulse and irradiance has been investigated. The self-calibration of the CCD with this technique and its comparison with the calibration of the same CCD with a standard x-ray tube will be illustrated.

Experimental setup

A CPA beam of 248 nm wavelength from the Titania KrF laser at Rutherford Appleton Laboratory (RAL) with duration 350 fs (FWHM) superimposed on an inherent flat top amplified spontaneous emission (ASE) prepulse was used to irradiate multi-layered targets. The laser beam was focussed onto the target using a f/5.27 parabola to produce a ~25 μm diameter spot size giving an irradiance of ~10^{17} W/cm ^{2} with the average energy of ~ 300 mJ. Inserting a random phase plate (RPP) into the beam line increased the uniformity of the intensity profile of the focussed spot size. The size and uniformity of the focal spot was monitored in each shot using an x-ray pinhole camera. The incident beam qualities were measured by setting up near and far field monitors. A potassium acid phthalate (KAP) (2d=26.6Å) time integrated crystal spectrometer with a spectral resolution of ($\lambda/\Delta\lambda\approx200$) was employed to record the spectrally resolved x-ray emission in the range 6-12 Å range. In the 6-6.4 Å spectral range a Von-Hamos spectrometer with a cylindrically curved Pentaerythritol (PET) (2d=8.742 Å) was used to record the output x-ray emission. To monitor the hot electrons, a windowless 6CN CCD camera with suitable Al filter was employed. A schematic experimental set up is shown in Figure 1.

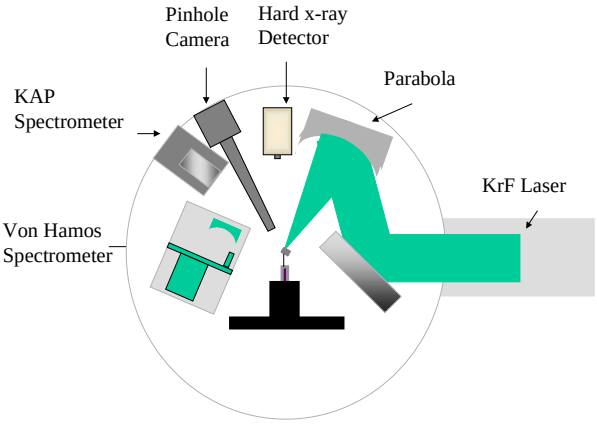

Figure 1. A schematic experimental set up.

Method

The ability of charge coupled devices (CCDs) to operate in the x-ray photon counting mode has been confirmed by Catura et al[3] and Schwartz et al[4]. They are sensitive to single x-ray photons with each electron-hole pair generated in a CCD pixel representing 3.65 eV of absorbed energy[1,2]. A photon with high energy excites an inner shell electron, which loses energy to valence band electrons enabling the excitation of electrons to the conduction band. The number of electrons collected in a pixel is proportional to the energy of the incident photon if the possibility of finding more than one photon in the pixel is negligible[7]. The pulse height (h) in a CCD and the number of exposed pixels can be assumed, respectively, to be proportional to the incident photon energy (E_p) and the number of photons (N). We can then histogram the counts from the pixels and obtain a spectrum of detected photons. A common front illuminated CCD where the incident light has to cross the whole gate structure and a silicon oxide layer of about a few hundred angstroms is suitable for hard x-ray photon detection and hence suitable for hot electron temperature measurements[5]. We have used a common cheap, 752×582 pixels, 6CN CCD to monitor the superthermal electrons. The quantum efficiency of the CCD can be written as

$$Q_E(\lambda) = [1-r_G(\lambda)]\exp[-\alpha_G(\lambda)t_G]\exp[-\alpha_{OX}(\lambda)t_{OX}]\{1-\exp[-\alpha(\lambda)t]\} \quad (1)$$

where r_G, α_G, t_G, α_{OX}, t_{OX}, α, t are , respectively, the reflectivity at the gate surface, the absorption coefficient of the gate, the thickness of the gate, the absorption and thickness of the oxide layer and the absorption and thickness of the active region. The first three terms represent the fraction of photons reaching the active region, while the last term is the absorption in the active region. In this expression we have neglected the electron collection efficiency of the CCD, but as we shall show, this can be taken into account by calibration.

A series of null shots with only the ASE pre-pulse were taken and analyzed. A correction for the null shot background has been undertaken by subtracting the averaged spectrum of two such failed shot images from the analyzed spectrum of data shots. This corrects for dark current effects and statistical noise. We have compared the second and third pixel heights around each peak event and binned them together, when the second peak had an intermediate value. This corrects for the generation of charge between two or more pixels by a single photon and the effect of the disparity between the digital converter system with 768×576 pixels and the image grabbing system with 752×582 pixels.

Electron-ion collisions result in charge acceleration and the emission of continuum Bremsstrahlung radiation. Spectrally resolving the energetic Bremsstrahlung photons can provide a technique to monitor the superthermal electron temperature. As Bremsstrahlung emission decays exponentially with photon energy, the product of an exponential decay function, filter transmission, T_f, and the CCD quantum efficiency, QE(E), can give the expected spectrum ,S_{th}. To a good approximation

$$S_{th} = T_f\left(1-\exp[-\alpha(\lambda)t]\right)\exp\left(-\frac{E_p}{KT_{he}}\right) \qquad (2)$$

where T_f is the filter transmission, $\alpha(\lambda)$ and t are the absorption coefficient and depletion layer thickness of the CCD substrate, respectively. In writing Eq. **(2)** we have neglected the CCD gate and oxide layer reflection and absorption coefficient. We have assumed a thickness t=40μm for the depletion layer[8]. Expected spectra for different temperatures are shown in Figure 2. The peak position in the theoretical spectrum does not change significantly with temperature. Calibrating the CCD camera using the spectrum peak position is therefore feasible.

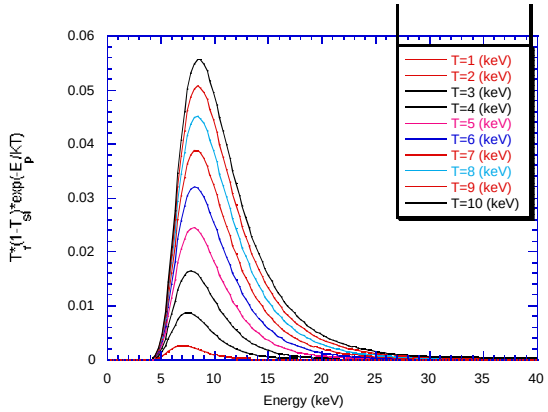

Figure 2. Theoretical Bremsstrahlung spectra for different detection temperatures as would be measured by the CCD after fitting with 100 μm Al filtering.

Fitting the theoretical curves to the experimental spectra completes the measurement of the hot electron temperatures. To fit the experimental and theoretical spectrums, we found the best position for the peak of the spectrum. The CCD has been, thus, self-calibrated by this fitting. A typical fitted spectrum is shown in Figure 3.

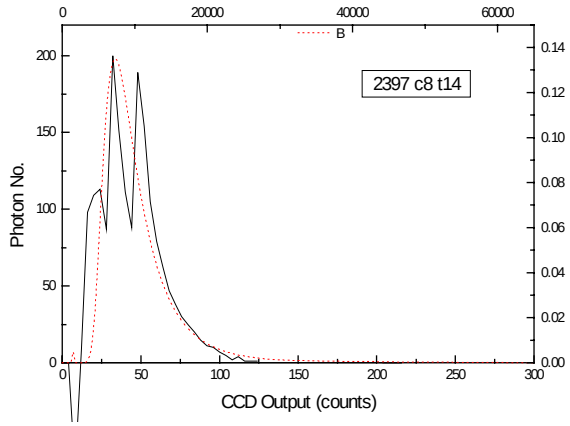

Figure 3. A typical fitted experimental (solid) and theoretical (dotted) spectrum.

The CCD has also been calibrated using an electron beam x-ray source. We have used the peak energy of emitted photons, which is equal to the applied accelerating voltage for the calibration. The calibration results for both self and x-ray source calibrations are illustrated in Figure 4.

Results

Using this technique we have measured moderate electron temperatures up to 10 keV in the Titania experiment. Putting the origin of the time axis at the half rise time point of the ASE pulse, we varied the time interval between the ASE and CPA pulses. The distribution of hot electron temperature versus this time interval is shown in Figure 5. Usually, the hot electron temperatures measured are compatible with the thermal electron temperature (≤1 keV), but for some shots higher temperatures were measured (Figure 5). It is clear that at $I\lambda^2 \approx 10^{15}$ $Wcm^{-2}\mu m^2$ for the Titania experiment with the ASE prepulse, the production of superthermal electrons is usually small.

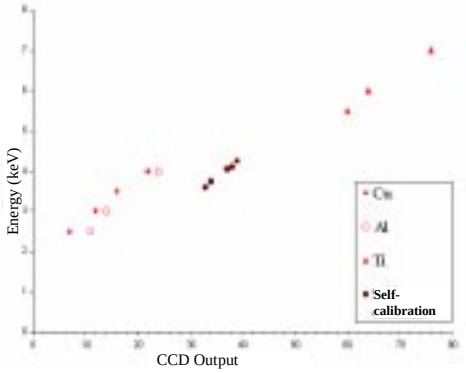

Figure 4. Photon energy as a function of the CCD count for different x-ray source voltage and targets and the self-calibration results (as labeled).

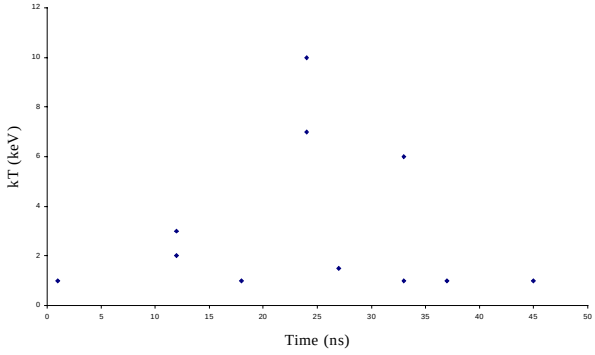

Figure 5. The hot electron temperature variation with the time interval between ASE and CPA pulses

References

1. D.W. Forslund, J.M. Kindel, and K. Lee, Phys. Rev. Lett. 39, 248 (1977).
2. J.W. Shearer et al., Phys. Rev. A 6, 764 (1972).
3. R.C. Catura, R.C. Smothson. Rev. Sci. Inst. 50, 219 (1977).
4. D.A. Schwartz, et al.. Proc. SPIE, 184, 247 (1979).
5. Yuelin Li, G.D. Tsakiris, and R. Sigel, Rev. Sci. Instrum. 66 , (1995).
6. D. Riley, N.C. Woolsey, and D. McSherry, CLF Annual Report (1997/98).
7. E.G. Chowanietz, et. al. Proc. SPIE. 597, 381 (1985).
8. C.M. Castelli, G.W. Fraser, Nuc. Inst. Meth. Phys. Res. A, 376, 298 (1996) .

A Closed-Loop Adaptive Optical System for Laser Wavefront Control

C J Hooker, E J Divall, W J Lester, K Moutzouris, C J Reason, I N Ross

Central Laser Facility, CLRC Rutherford Appleton Laboratory, Chilton, Didcot, Oxon, OX11 0QX, UK

Main contact email address: *C.J.Hooker@rl.ac.uk*

Introduction

The R&D programme to develop an adaptive optical system for the control of laser beam quality has continued throughout the year. Since the publication of the previous report[1)], we have changed the experimental configuration of the testbed, to allow monitoring of the focus after the adaptive mirror; the current setup is shown in Figure 1. After changing the way in which the control matrix is generated, we have successfully operated the system in closed-loop mode, and achieved substantial improvements in the far field of an aberrated beam. We have also begun construction of a larger-aperture mirror for off-line trials on Vulcan, which we intend to conduct in TA2 later in the year.

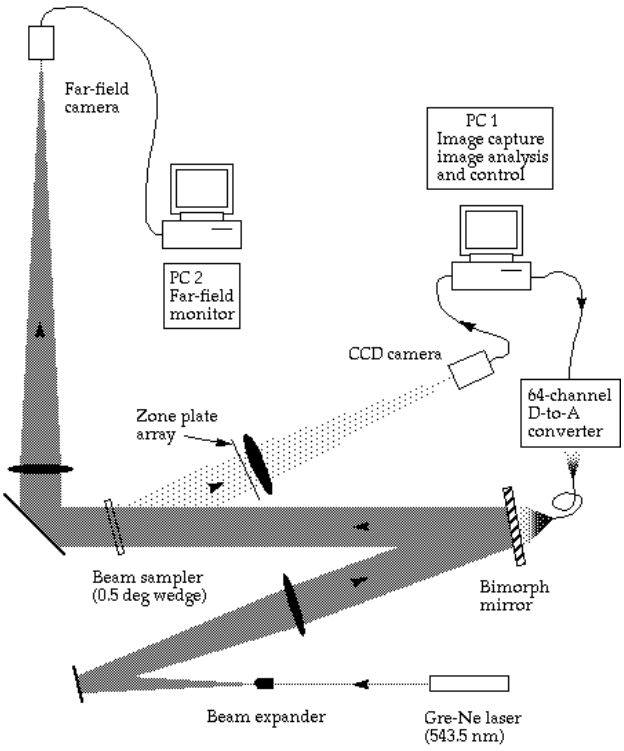

Figure 1. Adaptive optics test configuration.

Closed-loop operation of the adaptive mirror

To operate the mirror in a closed loop we had first to correct a number of errors in the software, but even after resolving those problems, the mirror would still not work properly in closed loop. The reason was that the curvature produced by the bimorph elements is highly localised, and twenty-four of the sixty actuators lie outside the area of the beam that is monitored by the Hartmann pattern. When the response matrix of the mirror is measured by applying a voltage to each element in turn, these exterior actuators produce almost no curvature in the measured area, and hence the entries for those actuators in the response matrix are dominated by noise. The pseudo-inverse matrix calculated from the curvature data did provide some control of the mirror in the central regions where the curvatures can be measured, but the edges became severely distorted. However, it was clear from observations of the Hartmann spots during the matrix-generation process that the exterior actuators do have an effect on the spot pattern. We therefore decided to switch from curvature to slope as the measured quantity, as the slope produced by an actuator extends several centimetres from the actuator itself. As a result, every actuator contributed real data to the response matrix, and the resulting control matrix was able to provide reasonably good closed-loop control of the mirror for the first time. A further refinement has been added recently, in which the centroid positions measured from ten image frames are averaged to obtain better-quality slope data, and each actuator is operated three times, with relaxation cycles in between. This change produced much cleaner data for the response matrix, and has reduced the number of cycles required to reach the full correction.

Optimisation of the control matrix

The computation of the control matrix was described in Reference 1. In its most basic form, the Pseudo-Inverse function in *Mathematica* is applied to the measured response matrix, but the result is not satisfactory. A more sophisticated approach involves decomposing the response matrix into the product of three square matrices, one of which is diagonal and contains the so-called singular values (SVs) of the original matrix. After inverting these matrices individually, they are multiplied together in reverse order to generate the control matrix. The singular values reflect the sensitivity of the mirror to different possible modes: those at the top left correspond to the lowest, and those at the bottom right to the highest spatial frequencies. By modifying the singular values before the final multiplication is carried out, it is possible to suppress any tendency the mirror may have to try and generate large amplitudes at high spatial frequency. With no modification, the mirror rapidly becomes severely deformed, with adjacent elements driven to the maximum voltages of opposite sign; the control program then halts because many of the Hartmann spots have moved too far from their original positions to be located correctly. The simplest approach to modifying the SVs is to set some number

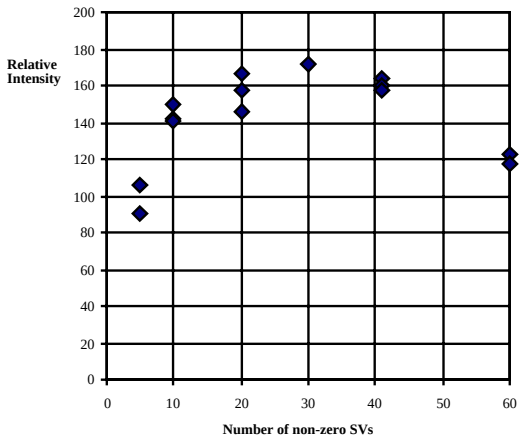

Figure 2. Effect of truncation of the singular values on focal spot intensity.

of them to zero, beginning on the lower right of the diagonal so as to suppress the highest frequencies first: the modifying function is then a simple step. Using the peak intensity in the far-field spot as a diagnostic, we found that the control matrices generated with between twenty and forty non-zero SVs all gave fairly good results, whereas those with either fewer or more failed to reach maximum intensity in the focal spot (Figure 2). A 1/10th-wave flat mirror was substituted for the adaptive mirror to record an "ideal" far-field spot using the same

imaging system; the ratio of peak intensities in this spot and in the corrected spot from the adaptive mirror is a good approximation to the Strehl ratio. The same mirror is used to generate a reference wave-front which is the target of the closed-loop control: changes to the applied voltages are calculated from the differences between the measured Hartmann spot positions and those in the stored reference. The FWHM of the focal spot was also measured in each instance, but the variations were too small for it to be a useful diagnostic of the degree of correction. We found that the most basic level of correction would produce a reasonably good focal spot; subsequent refinements caused a redistribution of intensity within the focal pattern without greatly affecting the overall structure.

A variety of other modifying functions has been applied to the SVs, to investigate the effects of a gradual smooth or stepwise reduction in their values over some range. Modifying functions that have been tried include linear scaling from 1 to 0 between selected values and smoother gradations using a $\cos^2$ function. In each case the modifying function is calculated in *Mathematica* as a table of 60 values between 1 and 0, and the Nth SV is then multiplied by the Nth entry in the modifying table. The results from this investigation are not very conclusive: the peak intensity achieved appears relatively insensitive to the details of the modifying function provided the first 10 SVs are included and the last 10 are reduced to some extent. Only minor differences were observed between linear and $\cos^2$ scaling.

Enhancement of the closed-loop response

When closed-loop operation of the mirror was first achieved, the cycle time was close to 700 milliseconds. To discover how this time was split between image capture, analysis, voltage output, etc., software commands were added to the program to apply a series of alternating positive and negative voltage steps to one of the output channels at different points in the cycle. By monitoring that channel with an oscilloscope, the timings of the different stages were measured. The most time-consuming steps were found to be the centroiding of the Hartmann spots, which took 500 ms, grabbing the frame from the camera (160 to 200 ms) and the voltage output to the driver box (90 ms). The first effort at reducing the cycle time was aimed at speeding up the centroiding, a part of the code not originally written with efficiency as a priority. Some very simple changes reduced the centroiding time to 90 ms, of which half involved the finding of the brightest grouping of pixels in each cell of the Hartmann pattern. Once the initial correction has been applied to the mirror, the spots should move very little, so the previous positions of the centroids can be used as a starting point for the next cycle, instead of locating all the spots afresh. The code for integrating the x- and y-projections of the individual spots, in order to determine the coordinates of the centroids, was also rewritten to increase its speed. This modification further reduced the cycle time to 130 ms, of which the calculation of the centroids now accounts for 6.5 ms: the image analysis and voltage calculation sequence takes 24 ms in total. With the screen display of the Hartmann pattern turned off, the cycle time is reduced to 93 ms, corresponding to a frequency of 10.7 Hz. The cycle time is now dominated by the hardware, in particular the voltage output stage, so attention has been switched to ways of reducing that part of the cycle. At a frequency of 10 Hz, however, the mirror can already correct for slowly-varying components of atmospheric turbulence.

Large adaptive mirror for use on Vulcan

The success of the prototype mirror has generated interest in the possibility of using adaptive optics in the high-power laser systems. A larger-aperture mirror suitable for use on the 108 mm beams of Vulcan has been designed and is under construction. Most of the residual aberrations on the Vulcan beams occur at the edges, and typically include coma and higher orders of astigmatism. The mirror layout was designed to allow for this, with 48 of the 64 actuators around the periphery of the mirror, half inside and half outside the beam footprint, and relatively few in the centre (Figure 3a). The substrate material (Pyrex) and the PZT are the same as on the prototype, the new substrate being 3 mm thick and 150 mm in diameter to have the same maximum deflection as the prototype. The piezo material is in four quadrants, as the largest available pieces are 70 mm square. The major change in construction is that the electrodes have been etched in a layer of nickel plated onto the PZT, rather than printed with conductive ink as before. The adhesion of the ink to the PZT is poor, and at various times the wires have become detached from the back of the prototype, bringing part of the ink with them. The bonding of the nickel to the PZT should be far stronger, which will solve this problem. Potential stress deformation of the mirror will be avoided by coating the reflecting surface with gold instead of a multilayer: the laser fluence in the planned position for the mirror, after the first pass of the disk preamplifier, is low enough for a gold mirror to survive.

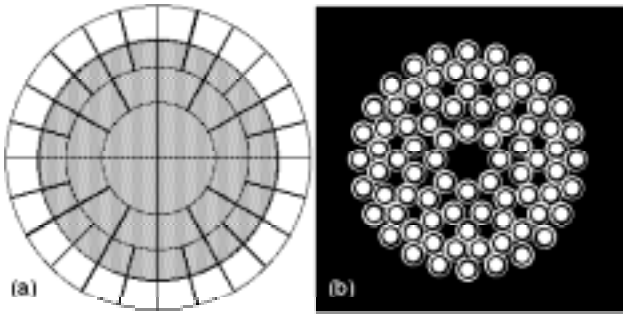

Figure 3. (a) Electrode layout for the 150 mm adaptive mirror. The grey circle represents the 108 mm diameter beam footprint. (b) New design of Hartmann zone plate array.

A new Hartmann array has been developed to complement the new mirror, and the design of this is shown in Figure 3b. Each of the 80 sensing elements consists of a small Fresnel zone plate with two transparent zones, having a focal length of approximately four metres. The elements lie within the beam footprint on the boundaries between actuators, to maximise the sensitivity to “ripple” modes around the circumference of the beam; consequently, like the actuators, the Hartmann spots are concentrated towards the edge of the beam. The existing software is based on the use of a 10-by-10 grid of sensing apertures, and is being rewritten to allow the use (in principle) of any arbitrary Hartmann array. The new sensor array and revised software will first be tested on the prototype mirror: the performance of the prototype may improve if the entire 70 mm diameter area of the beam is measured, instead of just a central 55 mm square as at present.

References

1. C J Hooker, C J Reason, I N Ross, M J Shaw and N M Tucker
CLF Annual Report 1997-98, pp175-76, (1998)

An experimental investigation of OPCPA on the Vulcan laser

I N Ross, J L Collier, P Matousek, C N Danson, D Neely, R M Allott, D A Pepler, C Hernandez-Gomez
Central Laser Facility, CLRC Rutherford Appleton Laboratory, Chilton, Didcot, Oxon, OX11 0QX, UK

K Osvay
Department of Optical and Quantum Electronics, JATE University, Szeged, Hungary

Main contact email address: *I.N.Ross@rl.ac.uk*

Introduction

Following new ideas by the authors[1)], which showed that a combination of the two techniques of optical parametric amplification and chirped pulse amplification offers exciting prospects for a major enhancement to laser facilities, a programme was set up to develop this technique (called optical parametric chirped pulse amplification or OPCPA) and apply it to the CLF's lasers. This report describes the second phase of this programme following earlier experiments at low power using millijoule lasers which verified the basic properties and performance of the scheme.

The rationale for the experiment was to investigate a scheme as close as possible to a full design for the Vulcan laser without incurring large equipment costs. The resulting scheme was a two stage OPCPA, scaled to operate at the joule level. This enabled a study of the ability of the OPA amplifiers to give very high gain, efficiency and beam quality for chirped pulses, and to give pulses free of phase and spectral errors which might affect the ability to recompress them with good fidelity.

General Description

The OPCPA scheme amplified a chirped and stretched 'signal' pulse from the sub-nanojoule to the joule level requiring a total gain of about 10^{10} to achieve good energy extraction. This required a two stage OPA and we use LBO for the high gain first stage followed by KDP as the power amplifier.

The signal is derived from the TSUNAMI Ti:sapphire '150fs' oscillator, chirped and stretched using a lens/grating stretcher and propagated to the OPCPA system through a single mode fibre. The power in the stretched pulse was insufficient to lead to significant self-phase-modulation in the fibre and the fibre was not so long as to give significant spectral phase errors through group velocity dispersion. The fibre provided a diffraction-limited beam for injection into the first OPA.

A beam from Vulcan containing a few joules at 527nm was required to pump the OPAs, and was obtained by aperturing the output beam of one of the 108mm amplifiers down to 20mm. This provided a beam with a uniform top-hat profile which was converted to the second harmonic in a KDP crystal, and subsequently imaged into each of the OPA crystals. This arrangement resulted in good pump beam uniformity and insensitivity to pump beam-pointing errors.

Pump and stretched signal pulse durations were set at about 0.5ns, similar to expected values for a full Vulcan scheme, with the pump pulse slightly longer to try to reduce spectral narrowing resulting from pump intensity variations, without reducing the ability to transfer energy efficiently from pump to signal. These durations were altered during the experiment for reasons discussed below.

A non-collinear geometry was employed with 0.5deg between pump and signal beam in each OPA. This enabled the proper isolation of pump, signal and generated 'idler' beams after each OPA, especially necessary since the idler had the same wavelength as the signal.

Output amplified pulses were re-compressed using a grating compressor with 20cm gratings matched in groove density (1740l/mm) and angle to the stretcher.

Experimental details

Figure 1 shows a schematic layout of the OPCPA system.

The pump beams are relayed to each of the two OPAs using vacuum telescopes. These de-magnify the pump beam to generate the correct pump intensity in the crystal and act as an image relay to ensure good pump beam uniformity in the crystals.

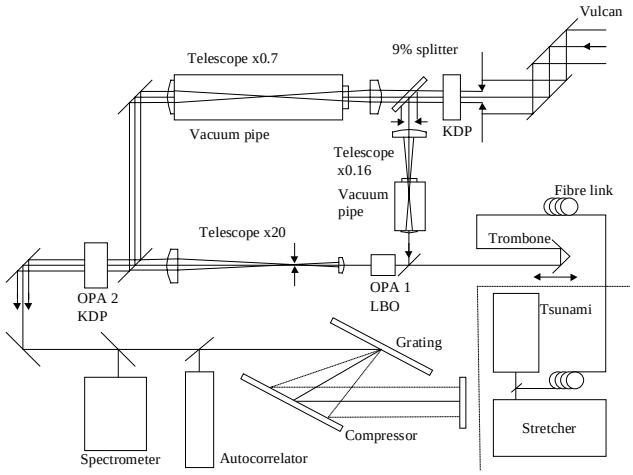

Figure 1. Schematic of the OPCPA experiment.

The design calls for a pump intensity of up to 4 GW/cm^2 and a pump beam size of 1mm and 14mm respectively in the two crystals. The pump injection mirrors immediately before each crystal serve to protect them from damage since the mirror damage threshold is less than that of the crystals. The signal beam is injected from its single mode fibre using a microscope objective to project a beam focus of size 0.5mm into the first OPA (OPA1) and via an optical trombone for fine tuning of the timing, coarse tuning being accomplished by adjusting the length of the fibre. A x20 telescope between the two OPAs ensures that the signal beam overfills the second OPA (OPA2) and that the output of OPA1 is imaged to the input of OPA2.

Crystal alignment is accomplished by injecting a separate alignment laser into the system via a moveable mirror and using a far field monitor at the injection point to ensure co-linearity between the beam from this laser and the Vulcan pump beam. This alignment laser produces 200mj in 5ns at 532nm and can generate sufficient intensity at the two OPAs to give a measurable gain on the 1053nm signal beam. The crystals are aligned by adjusting their angle for maximum gain followed by making a correction to account for the slight difference in wavelength between this beam and the Vulcan second harmonic (526.5nm).

Alignment monitoring is necessary to maintain phase-matching in the OPAs, in particular in OPA2 for which the tolerance is 100μrad. A far field CCD monitor on the input beam from Vulcan and a second far field CCD after OPA2 to monitor the directionality of both the pump beam and signal beam are used. The mechanical stability of the arrangement and the short-term directionality of the pump beam proved to be sufficiently stable

to ensure good gain. Longer term drift of the Vulcan beam required a correction to be made before each shot.

Timing was measured by reflecting a fraction of the pump and signal pulses onto a single photodiode, leading to a measurement accuracy of 50ps. Timing, once corrected, proved to be sufficiently stable with a shot-to-shot jitter of 100ps.

Gain was measured by reflecting a fraction of the output signal beam onto a fast photodiode. This was sufficiently sensitive to record the unamplified signal pulses. Measurement of high values of gain was obtained by using calibrated filters.

Experimental data

Data was acquired during the experiment:

a) from the direct reading of oscilloscope traces for the measurement of gain,

b) from calorimeters for the measurement of energies

c) from the grabbing of CCD images for the recording of near and far field distributions, for the measurement of spectra and for the recording of autocorrelation traces.

The results of these measurements together with an assessment and discussion of them is set out below.

1) Optical parametric gain

The predicted gain for an OPA under high gain conditions is given by:

$$G \cong \frac{1}{4}\exp 2\gamma L\sqrt{I}$$

For the 20mm LBO and 30mm KDP this reduces to:

$$G_{LBO} \cong \frac{1}{4}\exp 8.4\sqrt{I} \quad \text{and}$$

$$G_{KDP} \cong \frac{1}{4}\exp 4.4\sqrt{I} \quad \text{respectively}$$

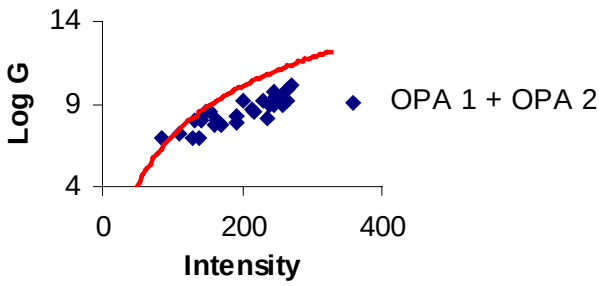

Figure 2. Measured (points) and theoretical (line) values of gain vs intensity for the amplifiers in series.

Figure 2 plots the predicted curve of the two amplifiers in series together with the gain measurements. There is reasonable agreement between the measured and predicted values, sufficient to be confident in the design. A number of points lie significantly below the curve due to the presence of gain saturation. Also there is in general a higher gain for longer pump pulses. This serves to highlight that it is not sufficient to estimate gain from the intensity (as energy divided by pulse duration) since the gain is highly non-linear with intensity and hence very sensitive to the exact value of the peak intensity and its variation near the peak. Vulcan pulse shapes were measured early in the laser system and differ significantly from the output profile as a result of gain saturation in the system. This is thought to be the cause of the systemic change in gain versus intensity for the different pulse durations (which lead to different pulse shapes and levels of saturation in Vulcan).

A positive feature of the measurements is the lack of evidence of gain suppression at high gain resulting from amplified spontaneous emission (ASE) or parasitic generation. This was confirmed by the direct measurement of the level of ASE in the signal direction which was several orders of magnitude below amplified signal values.

2) Efficiency of transfer of energy from pump to signal.

Evidence of the extraction of energy by the amplified signal was obtained from three measurements.

a) Measurement of the signal gain and measurement of the signal energy in the absence of gain. With values of 10^{10} and 0.05nJ respectively for these measurements we obtained an output energy of 0.5J. Estimated pump energy at OPA2 within the area of the signal beam was 2.5J giving an extraction efficiency of 20%.

b) The depletion of the pump intensity was obtained from measurements of the relative values of incident and transmitted pump energy. The pump energy transmitted by OPA2 was noted to fall by 40% for shots giving maximum gain compared to shots at low gain. Since an OPA transfers pump energy to both signal and idler pulses in proportion to their frequency and since their frequencies are equal in this case, the efficiency transfer to the signal is 20%.

c) A measure of the output energy was obtained from a burn-paper recording, the sensitivity of which had been calibrated approximately for the same wavelength and pulse duration. This also indicated an output signal energy of ≈0.5J.

Using the pulse durations of pump and signal and other known parameters, the saturation gain characteristics were computed using the existing simulation code. This gave a predicted value for efficiency of 17% in good agreement with the measurement in view of the assumption that the pulse profiles were gaussian in shape.

Efficiencies higher than 30% can be obtained, and have been noted by other workers, but require heavy saturation of all the amplifiers in the system. The scheme under test would be expected to give higher efficiency if there were heavier saturation in OPA1.

3) Output spectral profile

A key aspect of the OPCPA performance is its ability to amplify a chirped pulse with minimal spectral narrowing, since any spectral narrowing leads to an increase in the pulse duration after re-compression. In an OPCPA spectral narrowing is not a result of the limited OPA spectral gain profile since this is very large (≈100nm) compared to the bandwidth being amplified (≈20nm). However spectral narrowing does occur as a result of the pump-intensity-dependent gain variation with time. For example the small signal gain falls by a factor 2 from 10^{10} for a pump intensity reduction of only 6%. This demonstrates the importance of the profile in the region of the peak intensity. Simulations show that it is not possible to have high efficiency and small spectral narrowing if only the final amplifier is saturated, unless the pump intensity profile is flat to a few percent and this is difficult. The preferable alternative is to saturate all the amplifiers to reduce the sensitivity to pump intensity variations. Under the conditions of this experiment in which OPA2 but not OPA1 is in saturation, some reduction in spectral width on amplification is expected but not easily predictable in the absence of precise information of the temporal profile of the pump pulse (not available). For part of the experiment the pump pulse was made much longer (1.2ns) than the signal pulse (300ps) to try to maximise the amplified spectral width.

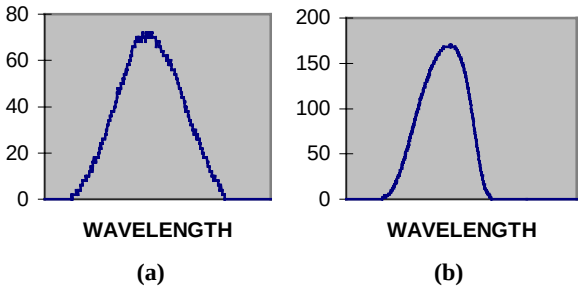

Figure 3. Output spectra for (a) unamplified and (b) amplified pulses.

Unamplified and amplified spectra are shown in Figure 3, and give spectral widths of 108cm^{-1} and 80cm^{-1} respectively. The asymmetry of the amplified spectrum is thought due to the shape of the pump pulse at its peak since this has a fast-rising leading edge followed by an intensity declining over the duration of the pulse. In this case amplification occurs around the relatively sharp peak at the start of the pulse and does not derive benefit from lengthening the pulse at the FWHM.

4) Compressibility of the amplified signal pulse

Re-compression was carried out using a grating compressor optimised to give minimum re-compressed pulse duration for the unamplified pulse train. A single shot autocorrelator was used for measurements of the recompressed pulse profile. The autocorrelation trace for the unamplified pulse is shown in Figure 4(a) and gives a pulse duration of 260fs. With no further adjustment of the compressor and autocorrelator an autocorrelation trace for the amplifed signal was recorded and is shown in Figure 4(b). This gave a pulse duration at FWHM of 300fs, 15% larger than that of the unamplified pulse. This can be explained in terms of the change in spectral profile on amplification indicating, as expected, that there are no spectral phase changes in the OPCPA which significantly affect the pulse compressibility.

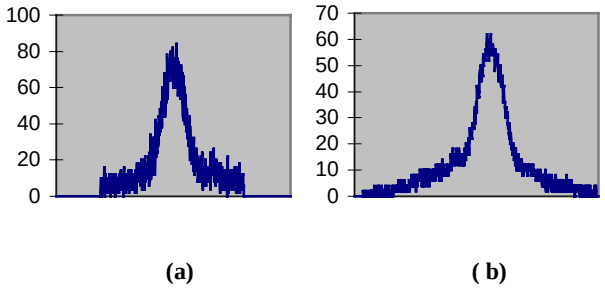

Figure 4. Autocorrelation traces of recompressed pulses (a) unamplified and (b) amplified.

A feature not explained at the present time is the inability to obtain shorter compressed pulses without amplification, these being expected to be given by the Fourier transform of the spectrum. It must be concluded that the discrepancy is caused by a spectral phase aberration, perhaps arising in the lenses of the pulse stretcher.

5) Focusability of the amplified signal

The ability of the OPA to amplify signal pulses without introducing spatial aberration was also tested. Far field profiles of the output signal pulse were recorded for both unamplified and amplified pulses and are shown in Figure 5. Since the unamplified beam is close to the diffraction limit, the amplification process is seen to introduce very little aberration at the aperture used. Within the accuracy of the measurements the FWHM increased by less than 10%, while the Strehl Ratio was calculated to be 0.72.

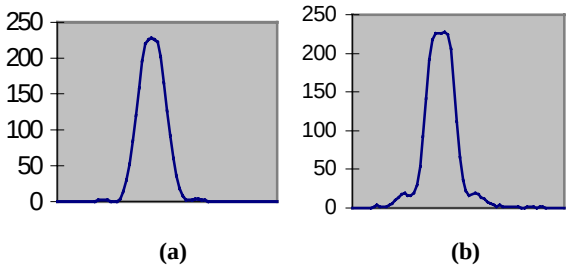

Figure 5. Far-field profiles for (a) unamplified and (b) amplified pulses.

Conclusions

This experiment has investigated the operation of a two-stage OPCPA system operating with similar parameters to those required for a full scheme for the Vulcan laser and at intermediate energy. It has confirmed much of our understanding of the physics and, where performance was limited, it enabled us to understand better the limitations so that these can be overcome. A summary of the results are:

1) High gains as required were achieved without damage in both LBO and KDP and at expected pump intensities.

2) Gains more than 10^{10} were measured for the two-stage OPCPA giving good saturation in OPA2 with output energy of 0.5J and a pump depletion (40%) close to the predicted value.

3) Amplification in the OPAs gave only a small reduction in focusable intensity.

4) Amplified pulses were recompressed to 300fs, 15% longer than was possible for the unamplified pulses.

5) The performance of the Vulcan laser suggested that an OPCPA system could be operated with good reliability and reproducibility.

6) Limitations in amplified spectral width and recompressed pulse duration are understood and have led to an improved design for a full scale Vulcan OPCPA system.

References

1. I.N.Ross, P.Matousek, M.Towrie, A.J.Langley, J.L.Collier, Optics Communications, 144, 125, (1997)

Vulcan Operational Statistics

D Pepler, M Payne, C Danson

Central Laser Facility, CLRC Rutherford Appleton Laboratory, Chilton, Didcot, Oxon, OX11 0QX

Main contact email address: *D.A.Pepler@rl.ac.uk*

Vulcan has completed an extremely productive experimental programme this year, with 14 full experiments taking place in the two main target areas, East (TAEAST) and West (TAWEST).

Table 1 below states the operational schedule for the year, with indications of the shot rate statistics for each experiment. Numbers in parenthesis indicate the total number of shots (includes low energy level alignment / set-up shots), the number of full energy target shots, and the number of these that failed.

In addition, a Direct Access experiment (Optical Parametric Chirped Pulse Amplification (OPCPA) development) was performed in target area 2 (TA2) which had a total of 406 laser shots, 163 target shots and 1 failure.

The total number of shots (inclusive of all types and areas) that have been fired this year is 8,557. Almost half of these (4,147) have been into the target areas. Of these target area shots 1,712 have been full disc amplifier shots with only 92 of these failing to meet user requirements. This gives an overall system reliability figure of 94.6 %. The EPSRC Service Level Agreement (SLA) requires Vulcan to be at least 90% reliable.

The SLA also requires that the laser system be available, during the 4 week periods of experimental data collection, from 09:00 to 17:00 hours, Monday to Thursday, and from 09:00 to 16:00 hours on Fridays, (a total of 156 hours). The laser has not always met the startup target of 9:00 am but it has been common practice to operate the laser well beyond the standard contracted finish time on several days during the week and to operate during some weekends.

On average, Vulcan has been available for each experiment for approximately 137 hours during contracted hours and 213 hours overall. However, each experiment has also experienced an average of 20 hours of laser downtime.

There was a brief break in the experimental programme in June when the Laboratory Open Week took place. Over the week there were several thousand visitors to RAL from schools, businesses and Government, as well as many visitors from the general public. The CLF displays were well received by all and the experimental programme was re-started with no problems.

Although the laser is very reliable, there is still an overall shot failure rate to target of 5.4 %. Analysis of the failure modes of the individual shots enables a breakdown of these modes into specific categories. Chart 1 shows the identified failure modes and their individual failure rates.

This information enables servicing and equipment refurbishment to be focussed on the most serious sources of system downtime. For example, the most significant causes of failed shots were the pre-amplifier stages and the timing of the electrical triggers relative to the laser light pulse. Both of these

PERIOD	TAE	TAW
20 Apr - 31 May	GR/L11540 - *J Wark* X-ray laser Radiography (144, 100, 8)	GR/K93815 - *P Norreys* CPA solid target interactions (140, 79, 1)
8 Jun - 26 Jul	GR/L11779 - *GJ Pert*	GR/L04436 - *O Willi*
	Laboratory Open Days, 29 June - 5 July	
	X-ray laser wave-guiding (133, 87, 10)	CPA channeling (208, 88, 4)
3 Aug -13 Sep	GR/K95543 - *D Riley* X-ray diffraction (305, 125, 6)	GR/L79151 - *AE Dangor* Wake-field acceleration (233, 128, 7)
21 Sep –1 Nov	GR/K57460 - *O Willi* Foams (295, 144, 8)	GR/L12608 - *J Wark* X-ray laser (220, 132, 6)
9 Nov – 20 Dec	GR/L11540 - *J Wark* X-ray laser (176, 139, 13)	GR/K93815 - *P Norreys* Solid target interactions (153, 108, 2)
4 Jan – 15 Feb	GR/L11540 - *J Wark* X-ray laser (182, 119, 17)	GR/K93815 - *P Norreys* Solid target interactions (198, 123, 2)
22 Feb – 4 Apr	GR/K57460 - *O Willi* Foams (428, 93, 7)	Short pulse harmonic generation tests (240, 84, 0)

Table 1. Experimental Schedule for period April 1998 – March 1999.

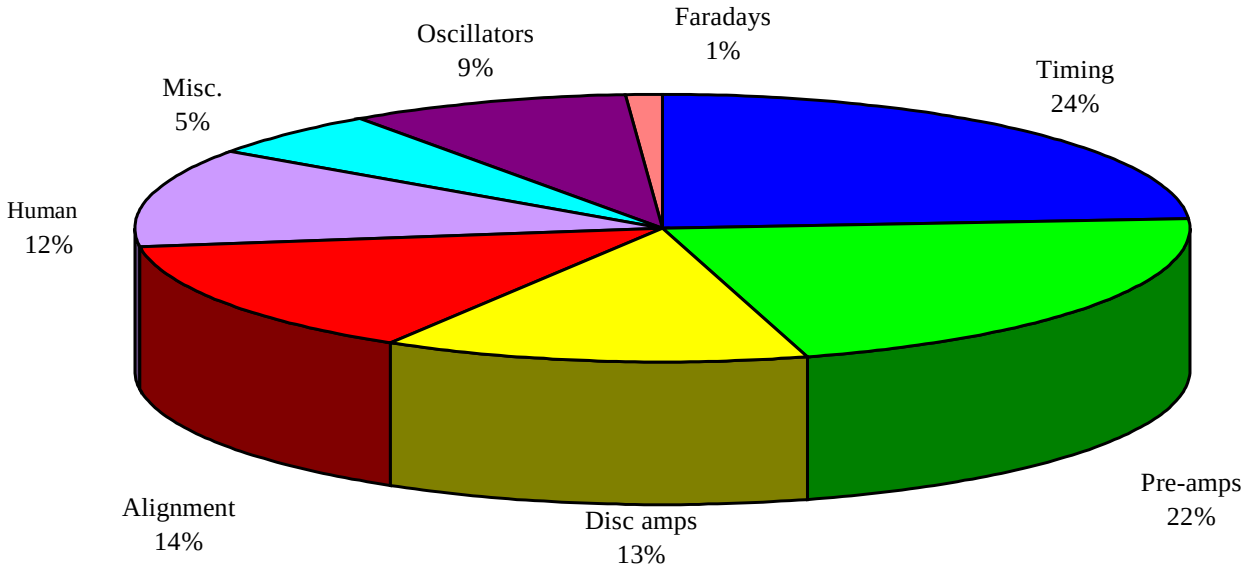

Chart 1. Analysis of Vulcan failure modes.

issues have been addressed with new timing electronics installed and improvements made to the high voltage connectors of the pre-amplifiers.

Additional changes have been made to the system in order to make the laser alignment more reliable and it is planned to replace all disc amplifier high-voltage junction boxes to reduce problems with the disc amplifiers. It is also planned to enhance the computer control system to include more sophisticated error checking to guard against potential operator error.

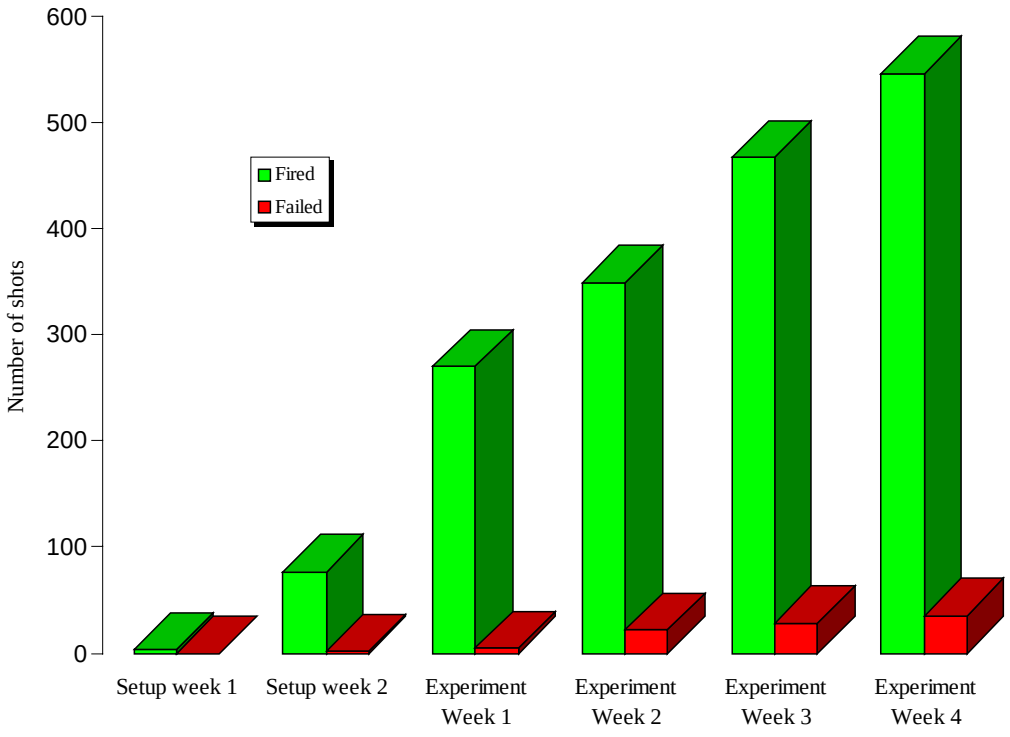

Chart 2. Annual total of disc amplifier shot rates, through a 6 week experimental period.

Chart 2 shows the total number of disc amplifier shots that were fired through the year distributed into individual experimental weeks. This clearly shows the high demand for shots in the final stages of each experiment.

Astra Operations

A J Langley

Central Laser Facility, CLRC Rutherford Appleton Laboratory, Chilton, Didcot, Oxon, OX11 0QX

Contact email address: *A.J.Langley@rl.ac.uk*

A total of 46 weeks of scheduled experiments were carried out using the Astra facility during 1998/99. The majority of these, 38 in total, were ticketed weeks sponsored by the EPSRC which also funded 4 weeks of direct access to the facility. Four weeks of experiment time was sponsored by the European Union. The facility operated within its required specification and there were no significant periods of down-time.

The facility was upgraded to TW performance during the year. See the articles within the development section of this year's annual report. This involved moving and reconstructing the facility in new laboratories. This move occurred in September and enabled us to open a second target chamber for operations from November 1998.

Astra Scheduled Experiments

DATE	TARGET AREA 1	TARGET AREA 2
30-Mar-98		
6-Apr-98	**Kosmidis/Ledingham/ Singhal**	
13-Apr-98	(UoI Greece/Glasgow)	
20-Apr-98	FS laser induced ionization/dissociation of biomolecules	
27-Apr-98		
4-May-98	**Frasinski/Codling**	
11-May-98	(Reading)	
18-May-98	Manipulating the dissociation dynamics of	
25-May-98	simple molecules in intense laser fields	
1-Jun-98		
8-Jun-98		
15-Jun-98		
22-Jun-98	**RAL OPEN DAYS**	
29-Jun-98		
6-Jul-98		
13-Jul-98		
20-Jul-98		
27-Jul-98	**Ledingham/Singhal/Langley/Towrie**	
3-Aug-98	(Glasgow/RAL)	
10-Aug-98	The potential of femtosecond mass spectrometry	
17-Aug-98	for ultra-trace analysis of atoms and molecules.	
24-Aug-98	**Joint RAL-Universities collaborative development**	
31-Aug-98	(RAL/Glasgow/Oxford/UCL/QUB/Reading)	
7-Sep-98	A Femtosecond terawatt laser at RAL	
14-Sep-98		
21-Sep-98		
28-Sep-98		
5-Oct-98		
12-Oct-98		
19-Oct-98		
26-Oct-98		
2-Nov-98		
9-Nov-98		**TARGET AREA 2**
16-Nov-98		**Frasinski/Codling**
23-Nov-98	**Newell/Williams**	(Reading)
30-Nov-98	(QUB/UCL)	Manipulating the dissociation dynamics of
7-Dec-98	Short pulse laser interactions with	simple molecules in intense laser fields
14-Dec-98	positive ions and molecules	
21-Dec-98	**CHRISTMAS**	**CHRISTMAS**
28-Dec-98		
4-Jan-99		
11-Jan-99		
18-Jan-99	**Ledingham/Singhal/Langley/Towrie**	
25-Jan-99	(Glasgow/RAL)	**Frasinski/Codling**
1-Feb-99	The potential of femtosecond mass spectrometry	(Reading)
8-Feb-99	for ultra-trace analysis of atoms and molecules.	Manipulating the dissociation dynamics of
15-Feb-99	**Marangos**	simple molecules in intense laser fields
22-Feb-99	(Imperial College London)	
1-Mar-99	High harmonic generation in organic materials	
8-Mar-99	Direct Access Proposal	
15-Mar-99		
22-Mar-99	**Newell/Williams**	
29-Mar-99	(QUB/UCL)	
5-Apr-99	Short pulse laser interactions with	
12-Apr-99	positive ions and molecules	

Lasers *for* Science Facility Operational Statistics

S M Tavender, A W Parker

Central Laser Facility, CLRC Rutherford Appleton Laboratory, Chilton, Didcot, Oxon., OX11 0QX

Main contact email address: *S.M.Tavender@rl.ac.uk*

RAL-based experiments

In the reporting period (April 1998 to March 1999), 21 different User groups performed a total of 40 experiments in the laboratories at RAL. A total of 4640 hours laser time was scheduled throughout the year and 4744 hours delivered with only 80 hours downtime giving a reliability of 98.6%. Across the funding Councils the weeks scheduled were 100 to EPSRC, 6 to the MRC, 8 to BBSRC, 1 to a commercial User, and 1 to the CREST awards, giving 116 weeks delivered to the User community overall. Once again, a wide spread of disciplines was covered and a breakdown is shown in Figure 1 with the RAL-Based schedule Table 1. There was a total of 26 publications and 11 conference presentations with 4 PhD theses published during the reporting year.

Loan Pool

The Loan pool delivered 356 weeks laser time with only one major laser failure leading to 8 weeks lost time. There were 34 laser loans to 16 different university groups across the UK with the chemistry community once again the biggest user as shown in Figure 2. The Loan pool schedule is shown in Table 2. There was a total of 19 publications, 3 conference proceedings and 1 PhD in the reporting year.

Figure 1. Breakdown by discipline, RAL-Based Experiments

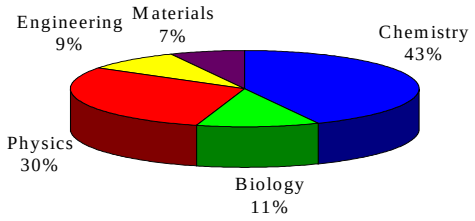

Figure 2. Breakdown by discipline, Loan Pool Experiments

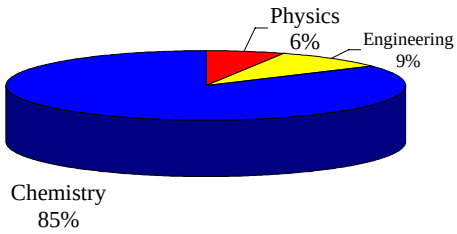

Table 1. RAL-BASED SCHEDULE April 1998 to March 1999

Date	Laser Microscope Laboratory	Nanosecond Science Laboratory	Ultrafast Spectroscopy Laboratory	X-Ray Laboratory
30-Mar 1998			**FREY** (Southampton)	**O'NEILL/MELVIN/PARKER** (MRC) Hole migration in DNA
06-Apr		**COMMERCIAL CONTRACT**	**TAYLOR** (Oxford)	**SHAIKH/TURCU/ ALLOTT/FOLKARD**
13-Apr				High throughput VUV source XU5P3/97
20-Apr		**CRANTON** TFEL devices XU2M3/97	Dynamics in Wide-bandgap III-V Materials	**CAIRNS/FITZGERALD LAWRENSON**
27-Apr		**TRUSCOTT** (Keele)		(Dundee) Manufacture of next
04-May	**MacROBERT/ PHILLIPS**	Time resolved resonance Raman of carotenoid radicals	US4P3/97	generation photomasks XU3P3/97
11-May	(UCL/IC) Confocal	formed from reactions with oxy-radicals	**VLCEK** (Queen Mary)	**MICHETTE/ BUCKLEY/TURCU**
18-May	fluorescence lifetime imaging microscopy	NL 3/97 DA	Charge Transfer Excited States of Organometallics	(KCL/RAL)
25-May	LM4B2/97	**MAINTENANCE**	US5C3/97	Laboratory scanning
01-Jun			**BISBY** (Salford)	Soft X-Ray microscope
08-Jun	**JONES/MOUNT** (Edinburgh) Photophysics		Ultrafast Studies of the Photochemistry of	
15-Jun	of novel electropolymerised Indolines LM2C3/97		Phenols US1C3/97	XU3P3/97
22-Jun	**RAL OPEN DAYS**			
29-Jun				
06-Jul	**JONES/MOUNT** (Edinburgh)	**CREST 1998**	**REID** (Nottingham)	**SHAIKH/TURCU/ ALLOTT/FOLKARD**
13-Jul	LM2C3/97		Depolarization Mechanisms studied by	**CRANTON** TFEL devices XU2M3/97
20-Jul			Time and Angle Resolved Photoelectron Spectroscopy	**REEHAL** (South Bank) Silicon Solar cells
27-Jul		**CRANTON** TFEL devices XU2M3/97	US3C/97	**MAINTENANCE**

Date	Laser Microscope Laboratory	Nanosecond Science Laboratory	Ultrafast Spectroscopy Laboratory	X-Ray Laboratory
03-Aug		**MAINTENANCE**		
10-Aug	**JONES** (Edinburgh)			
17-Aug	Development of the time correlated single			
24-Aug	photon counting system LM3/98		**MAINTENANCE**	
31-Aug				**CAIRNS** (Dundee)
07-Sep				Photomasks for electronic devices and sensors XU2/98
14-Sep		**DEVONSHIRE** (Sheffield) High	**BENNISTON** (Glasgow)	
21-Sep		resolution studies of nuclear hyperfine	TR^3 studies on electron transfer	**MICHETTE** (King's London)
28-Sep		population distributions in photo dissociation	processes in metallo-based cyclophanes	Laboratory scanning X-ray microscope
05-Oct		reactions using a novel OPA NL4/98	and catenanes US1/98	XU1/98
12-Oct				
19-Oct	**MAINTENANCE**			
26-Oct				
02-Nov	**MACROBERT** (UCL) Confocal fluorescence	**ZARBAKHSH** (Durham)		
09-Nov	lifetime imaging microscopy LM1/98	Study of amphiphilic polymers at oil/water	**VLCEK** (Queen Mary)	
16-Nov		interfaces using vibrational sum frequency generation	Ultrafast electron transfer in Rhenium Complexes	
23-Nov		NL1/98	US3/98	**TALLENTS/HILL** (Essex,MRC,RAL)
30-Nov			**MAINTENANCE**	X-ray Source Development XU3/98
07-Dec	**MAINTENANCE**		**MATOUSEK** (RAL)	**MICHETTE** (King's London) XU8/98
14-Dec			Kerr Gated TR^3 of TICT State Molecules	**REEHAL** (South Bank) Solar Cells XU5/98
21-Dec	**CHRISTMAS/NEW YEAR**			
28-Dec				
04-Jan 1999			US6/98	**MICHETTE** (King's London)
11-Jan		**PHILLIPS** (IC) US8/98	**TAYLOR** (Oxford)	
18-Jan		**DEVONSHIRE** (Sheffield) Studies of	Hot-carrier and Exciton Dynamics in Wide-Bandgap	Laboratory Scanning Soft X-ray
25-Jan		nuclear hyperfine population distributions	III-V Materials	Microscopy XU8/98
01-Feb	**CRANTON** (NTU) TFEL devicesCM2/98	**MAINTENANCE**	US7/98	**HILL** (MRC)
08-Feb		**BENNISTON** (Glasgow)	**STEVENS** (Oxford)	X-ray Source Development XU6/98
15-Feb		Time-resolved studies of ruthenium	Quasiparticle Dynamics in High	**O'NEILL** (MRC)
22-Feb		intercalates NL6/98	Temperature Superconductors	Nucleic Acid Modifications XU7/98
01-Mar	**BEEBY** (Durham) Lanthanide complexes		US5/98	**MICHETTE** (King's London)
08-Mar	**MACROBERT** (UCL)	**GEORGE** (Nottingham)	**PHILLIPS** (Imperial College)	
15-Mar	Confocal fluorescence lifetime imaging microscopy	TR^3 studies on solvent effects on	Reorganisation Dynamics of Charge Transfer Reactions	Laboratory Scanning Soft X-ray Microscopy
22-Mar	CM1/98	organometallic and organic charge-transfer excited states	US8/98	
29-Mar		NL5/98	**BENNISTON** (Glasgow) US9/98	XU8/98

Table 2. LOAN POOL SCHEDULE April 1998 to March 1999

Date	NSL1 GCR-11/PDL-3		NSL2 Spectron SL805G/PDL	NSL3 Spectron SL805/PDL-2	NSL4 Continuum 8010/ND6000	NSL5 Fluoride excimer	NSL6 Nd:YAG/Dye/ SHG	CWL1 2025 Argon Ion	CWL2 3900 Ti:S
Apr 6	**ELLIS**		**POWIS**	**GEORGE**	**SMITH**	**SIMS**	**HANCOCK**	**FRENCH**	**HICKEN**
13	**Leicester**		**Nottingham**	**Nottingham**	**Birmingham**	**Birmingham**	**Oxford**	**Liverpool**	**Exeter**
20					MAINTENANCE				Optically triggered
27					AND REPAIR				magnetic field
May4	**WAYNE**						**SIMONS**		pulses
11	**Oxford**		LP7C2/97				**Oxford**	UNALLOCATED	
18									
25				Time-resolved					**KUCERNAK**
Jun 1				IR					**TAYLOR**
8	Investigations of		**SIMS**	spectroscopy in					**IC**
15	I_2,		**Birmingham**	conventional and					
22	BrO and IO		SL805G/SIRAH	supercritical	State-selected		Conformational		
29	reactions using		installed	fluids	dynamics of		Landscapes in		
July 6	LIF				reactions	Reactive processes	Molecular &		Optical SHG
13			Reactive		between	in the gas phase at	Biomolecular		studies of
20			processes		triatomic	Ultra-low	Systems	**BLEWETT**	electrocatalytic
27			in the gas		molecules	Temperatures:		**Heriot-Watt**	oxygen
Aug 3	LP11C3/97		phase at		and radical	Reactions of		High speed	reduction
10			Ultra-low		atoms	C-atoms		filming	
17			Temperatures:					LP1P1/98	
24			Reactions of						
31	**WAYNE**	**DENNIN**	C-atoms						
Sept 7	**Oxford**	**Oxford**	Nd:YAG/	LP4C3/97			LP8C3/97	**DEVONSHIRE**	
14	*GCR-11*	*PDL*	Dye/SHG	**GEORGE**	LP10C3/97			**Sheffield/RAL**	LP7C3/97
21	*YAG*	*Dye*		**Nottingham**	**SMITH**			OPA	
28	*Laser*	*Laser*			**Birmingham**		**LEVY**	development	
Oct 5				LP8C1/98		LP9C3/97	**Northumbria**		
12	Investig	The	LP9C3/97						**HICKEN**
19	ations	correlation		Time-resolved					**Exeter**
26	of I_2,	crystal		IR			State to state		
Nov 2	BrO	field in	**ELLIS**	spectroscopy in		MAINTENANCE	Chemi-		
9	and IO	lanthanid	**Leicester**	conventional and	Vibrational	(RAL)	Luminescence	UNALLOCATED	
16	reaction	compounds		supercritical	relaxation	**BROUARD**	excitation		
23	using			fluids	in polyatomic	**Oxford**	Functions for		Stimulation of
30	LIF				molecules		Mn atom		Non-linear
Dec 7						Product	reactions		Ferromagnetic
14			Stimulated			rotational			Resonance
21			emission			polarisation in			Oscillations in
28		LP6C1/98	pumping			elementary			Ferromagnetic
Jan 4			spectroscopy		LP4C1/98	biomolecular			Thin film
11			of alkali			chemical		**DEVONSHIRE**	
18	**WAYNE**		monoxides	**GEORGE**		reactions		**Sheffield**	LP5P1/98
25	**Oxford**			**Nottingham**	**SIMONS**		LP2C1/98	High resolution	
Feb 1					**Oxford**			Spectroscopic	
8					Structural			studies	
15	Coupled chemistry		LP7C1/98	Nanosecond time	landscapes			Of nuclear -fine	
22	of bromine in			resolved IR	in hydrogen		**SIMS**	Population	**KUCERNAK**
Mar 1	stratosphere			spectroscopy using	bonded		**Birmingham**	hyper	**TAYLOR**
8	Investigation of the			a commercial	clusters:		Reactive	distributions	**IC**
15	kinetics of some		**HINDS**	step-scan	resonant ion -dip		in the gas phase at	using	In situ optical
22	Reactions of the		**Sussex**	interferometer	Spectroscopy		Ultra-low	a novel OPA	SHG Studies
29	IO radicals			LP13/98		**LANGRIDGE-SMITH**	Temperatures:		of semiconductor
									growth

Science – High Power Laser Programme

JOURNAL PUBLICATIONS, BOOKS AND PUBLISHED PROCEEDINGS

P Argitis, A C Cefalas, Z Kollia, E Sarantopoulou, T W Ford, T Stead, A Marranca, C N Danson, J Knott, D Neely
Single-pulse high-resolution x-ray contact microscopy with an advanced epoxy novolac resist
Second GR-I international conference on new laser technologies and applications, Ed P di Lazzaro, SPIE **3423** 411-415 (1999)

D Batani, A Bernardinello, V Masella, F Pisani, M Keonig, J Krishnan, A Benuzzi, S Ellwi, T A Hall, P A Norreys, A Djaoui, D Neely, S Rose, P Fews, M H Key
Propagation in compressed matter of hot electrons created by short intense lasers
Superstrong Fields in Plasmas, Eds M Lontano, G Mourou, F Pegoraro, E Sindoni AIP Conf Proc **426** 372-376 (1998)

A R Bell, J R Davies, S M Guerin
Magnetic field in short-pulse high-intensity laser-solid experiments
Phys Rev E **58** (2 Pt B) 2471-2473 (1998)

M Borghesi, A J MacKinnon, A R Bell, R Gaillard, O Willi
Megagauss magnetic field generation and plasma jet formation on solid targets irradiated by an ultraintense picosecond laser pulse
Phys Rev Letts **81** (1) 112-115 (1998)

M Borghesi, A J Mackinnon, R Gaillard, O Willi, A A Offenberger
Guiding of a 10-TW picosecond laser pulse through hollow capillary tubes
Phys Rev E **57** (5 Pt A) R4899-R4902 (1998)

M Borghesi, A J Mackinnon, R Gaillard, O Willi, A Pukhov, J Meyer-ter-Vehn
Large quasistatic magnetic fields generated by a relativistically intense laser pulse propagating in a preionized plasma
Phys Rev Letts **80** (23) 5137-5140 (1998)

R E Burge, G E Slark, M T Browne, X C Yuan, P Charalambous, X H Cheng, C L S Lewis, G F Cairns, A G MacPhee, D Neely
Dependence of spatial coherence of 23.2-23.6 nm radiation on the geometry of a multielement germanium x-ray laser target
JOSA B-Optical Physics **15** (10) 2515-2523 (1998)

R E Burge, G E Slark, M T Browne, X C Yuan, P Charalambous, Z An, X H Cheng, C L S Lewis, A G MacPhee, D Neely
Time dependence of the spatial coherence of the 23.6 and 23.2 nm radiation from the germanium soft-x-ray laser
JOSA B-Optical Physics **15** (5) 1620-1626 (1998)

A C Cefalas, P Argitis, Z Kollia, E Sarantopoulou, T W Ford, A D Stead, A Marranca, C N Danson, J Knott, D Neely
Laser plasma x-ray contact microscopy of living specimens using a chemically amplified epoxy resist
Appl Phys Letts **72** (25) 3258-3260 (1998)

C E Clayton, K-C Tzeng, D Gordon, P Muggli, W B Mori, C Joshi, V Malka, Z Najmudin, A Modena, D Neely, A E Dangor
Plasma wave generation in a self-focused channel of a relativistically intense laser pulse
Phys Rev Letts **81** (1) 100-103 (1998)

C N Danson, J Collier, D Neely, L J Barzanti, A Damerell, C B Edwards, M H R Hutchinson, M H Key, P A Norreys, D A Pepler, I N Ross, P F Taday, W T Toner, M Trentelman, F N Walsh, T B Winstone, R W W Wyatt
Well characterized 10^{19} W cm^2 operation of VULCAN - an ultra-high power Nd:glass laser
J Mod Opt **45** (8) 1653-1669 (1998)

C N Danson, P V Nickles, R Allott, A Behjat, J Collier, A Demir, M P Kalachnikov, M H Key, C L S Lewis, D Neely, D A Pepler, G J Pert, M Schnurer, W Sandner, V N Shlyaptsev, G J Tallents, P J Warwick, E Wolfrum, J Zhang
Implementation of a CPA line focus travelling-wave for highly efficient saturated lasing of Ne-like Ti and Ge
Superstrong Fields in Plasmas, Eds M Lontano, G Mourou, F Pegoraro, E Sindoni AIP Conf Proc **426** 473-478 (1998)

T Ditmire, P K Patel, R A Smith, J S Wark, S J Rose, D Milathianaki, R S Marjoribanks, M H R Hutchinson
keV x-ray spectroscopy of plasmas produced by the intense picosecond irradiation of a gas of xenon clusters
J Phys B-Atomic Molecular and Optical Physics **31** (12) 2825-2831 (1998)

L A Doyle, G W Martin, A Al-Khateeb, I Weaver, D Riley, M J Lamb, T Morrow, C L S Lewis
Electron number density measurements in magnesium laser produced plumes
Appl Surf Sci **127-129** (1-4) 716-720 (1998)

L A Doyle, G W Martin, T P Williamson, A Al-Khateeb, I Weaver, D Riley, M Lamb, T Morrow, C L S Lewis
Three-dimensional electron number densities in a titanium PLD plasma using interferometry
IEEE Trans Plasma Sci **27** (1) 128-129 (1999)

P Gauthier, S J Rose, P Sauvan, P Angelo, E Leboucher-Dalimier, A Calisti, B Talin
Modeling the radiative properties of dense plasmas
Phys Rev E **58** (1) 942-950 (1998)

A Giulietti, A Macchi, E Schifano, V Biancalana, C Danson, D Giulietti, L A Gizzi, O Willi
Stimulated Brillouin backscattering from underdense expanding plasmas in a regime of strong filamentation
Phys Rev E **59** (1 Pt B) 1038-1046 (1999)

E T Gumbrell, R A Smith, T Ditmire, A Djaoui, S J Rose, M H R Hutchinson
Picosecond optical probing of ultrafast energy transport in short pulse laser solid target interaction experiments
Physics of Plasmas **5** (10) 3714-3721 (1998)

T A Hall, S Ellwi, D Batani, A Bernardinello, V Masella, M Koenig, A Benuzzi, J Krishnan, F Pisani, A Djaoui, P Norreys, D Neely, S Rose, M H Key, P Fews
Fast electron deposition in laser shock compressed plastic targets
Phys Rev Letts **81** (5) 1003-1006 (1998)

E Ivanova, I P Grant, S J Rose
Gain evaluation for the Ni-like tantalum X-ray laser
X-ray lasers 1998, Eds Y Kato, H Takuma, H Daido, IOP Conf Series **159** 383-386 (1999)

K A Janulewicz, P V Nickles, M P Kalachnikov, M Schnurer, W Sandner, S B Healy, G J Pert, P J Warwick, C L S Lewis, C N Danson, D Neely, E Wolfrum, A Behjat, A Demir, G J Tallents
Saturation in transient gain scheme of collisionally pumped germanium X-ray laser
Superstrong Fields in Plasmas, Eds M Lontano, G Mourou, F Pegoraro, E Sindoni AIP Conf Proc **426** 491-496 (1998)

M P Kalachnikov, P V Nickles, M Schnürer, W Sandner, V N Shlyaptsev, C Danson, D Neely, E Wolfrum, J Zhang, A Behjat, A Demir, G J Tallents, P J Warwick, C L S Lewis
Saturated operation of a transient collisional x-ray laser
Phys Rev A **57** (6) 4778-4783 (1998)

C L S Lewis, R Keenan, A G MacPhee, R M N O'Rourke, G J Tallents, G Eker, J Y Lin, S J Pestehe, R Smith, J S Wark, E Wolfrum, J Zhang, G J Pert, S P McCabe, P A Simms, R E Burge, M T Brown, P Charalambous, D Neely, J Collier, C N Danson
Overview of X-ray laser research in the UK
X-ray lasers 1998, Eds Y Kato, H Takuma, H Daido, IOP Conf Series **159** 1-8 (1999)

J Y Lin, G J Tallents, R Smith, A G MacPhee, E Wolfrum, J Zhang, G Eker, R Keenan, C L S Lewis, D Neely, R M N O'Rourke, G J Pert, S J Pestehe, J S Wark
Optimization of double pulse pumping for Ni-like Sm x-ray lasers
J Appl Phys **85** (2) 672-675 (1999)

J Y Lin, G J Tallents, J Zhang, A G MacPhee, A Demir, C L S Lewis, G J Pert, R M N O'Rourke, D Ros, R Smith, E Wolfrum, P Zeitoun
Gain saturation and travelling-wave effects for collisional excitation X-ray lasers
X-ray lasers 1998, Eds Y Kato, H Takuma, H Daido, IOP Conf Series **159** 79-82 (1999)

J Y Lin, G J Tallents, J Zhang, A G MacPhee, C L S Lewis, D Neely, J Nilsen, G J Pert, R M N O'Rourke, R Smith, E Wolfrum
Gain saturation of the Ni-like X-ray lasers
Opt Comm, **158**, No.1-6, 55-60 (1998)

A Lorenz, N J Peacock, M G O'Mullane, D Neely
Diagnostic characterization of a prepulsed carbon fiber Z pinch using spectral line intensity analyses
Rev Sci Instr **70**, No.2 1425-1429 (1999)

A J Mackinnon, M Borghesi, A Iwase, M W Jones, O Willi
Interaction of intense laser pulses with neutral gases and preformed plasmas
11th APS topical conference on atomic processes in plasmas, Eds E Oks, M S Pindzola, AIP Conf Proc **443** 229-238 (1998)

A J Mackinnon, M Borghesi, A Iwase, O Willi
Interaction of intense laser pulses with preformed density channels
Phys Rev Letts **80** (24) 5349-5352 (1998)

A G MacPhee, R M N O'Rourke, C L S Lewis, J Y Lin, A Demir, G J Tallents, J Collier, D Neely, D Ros, P Zeitoun, S P McCabe, P Simms, G J Pert
Transient gain in travelling wave pumped Ni-like X-ray lasers
X-ray lasers 1998, Eds Y Kato, H Takuma, H Daido, IOP Conf Series **159** 75-78 (1999)

G W Martin, T P Williamson, A Al-Khateeb, L A Doyle, I Weaver, D Riley, M Lamb, T Morrow, C L S Lewis
Two-dimensional imaging of low temperature laser-produced plasmas
IEEE Trans Plasma Sci **27** (1) 130-131 (1999)

E Nardi, Z Zinamon, D Riley, N C Woolsey
X-ray scattering as a dense plasma diagnostic
Phys Rev E **57** (4) 4693-4697 (1998)

P A Norreys, M Bakarezos, L Barringer, M Borghesi, F N Beg, M Castro-Colins, D Chambers, A E Dangor, C N Danson, A Djaoui, A P Fews, R Gaillard, P Gibbon, L Gizzi, M E Glinsky, B A Hammel, M H Key, P Lee, P Loukakos, A J MacKinnon, C Meyer, J Meyer-ter-Vehn, S Moustaizis, S G Preston, A Pukhov, S J Rose, M Tatarakis, J S Wark, O Willi, M Zepf and J Zhang
Studies of the fast ignition route to inertial confinement fusion at the Rutherford Appleton Laboratory
Fusion Eng and Design **44** (1-4) 239-243 (1999)

R M N O'Rourke, C L S Lewis, A Hibbert
Near frequency doubling through four wave mixing in a plasma
X-ray lasers 1998, Eds Y Kato, H Takuma, H Daido, IOP Conf Series **159** 687-690 (1999)

D Riley
Time dependent modelling of K-shell emission lines from laser produced plasmas
J Quant Spectr & Rad Trans **60** (2) 221-230 (1998)

S J Rose
The non-LTE excitation/ionization code GALAXY
J Phys B-Atomic Molecular and Optical Physics **31** (9) 2129-2144 (1998)

S Sebban, F Albert, A Belsky, M Boussoukaya, A Carillon, S Hubert, P Jaegle, G Jamelot, D Joyeux, I Kamenskikh, A Klisnick, C L S Lewis, D Phalippou, A G MacPhee, D Ros, B Rus, R Smith, G J Tallents, P Zeitoun, A Zeitoun-Fakiris
Collisional X-ray-UV lasers and their applications
Ann de Physique **23** (C1) 81-88 (1998)

R Smith, G J Tallents, J Zhang, G Eker, S McCabe, G J Pert, E Wolfrum
Saturation behavior of two x-ray lasing transitions in Ni-like Dy
Phys Rev A **59** (1) R47-R50 (1999)

G J Tallents, J Y Lin, R Smith, A G MacPhee, E Wolfrum, J Zhang, G Eker, R Keenan, C L S Lewis, D Neely, R M N O'Rourke, G J Pert, S J Pestehe, J S Wark
Characterization of X-ray lasers at short wavelengths
X-ray lasers 1998, Eds Y Kato, H Takuma, H Daido, IOP Conf Series **159** 59-66 (1999)

M Tatarakis, J R Davies, P Lee, P A Norreys, N G Kassapakis, F N Beg, A R Bell, M G Haines, A E Dangor
Plasma formation on the front and rear of plastic targets due to high-intensity laser-generated fast electrons
Phys Rev Letts **81** (5) 999-1002 (1998)

P J Warwick, C L S Lewis, M P Kalachnikov, P V Nickles, M Schnurer, A Behjat, A Demir, G J Tallents, D Neely, E Wolfrum, J Zhang, G J Pert
Observation of high transient gain in the germanium x-ray laser at 19.6 nm
JOSA B-Optical Physics **15** (6) 1808-1814 (1998)

I Weaver, L A Doyle, G W Martin, D Riley, M J Lamb, W G Graham, T Morrow, C L S Lewis
Mapping neutral, ion and electron number densities within laser-ablated plasma plumes
ALT'97 international conference on laser surface processing, Ed V I Pustovoy, SPIE **3404** 341-350 (1998)

O Willi
Inertial confinement fusion with fast ignition
Phil Trans R Soc Lond **A357** (1752) 555-574 (1999)

K Witte, M Basko, H Baumhacker, A Boswald, K Eidmann, R Fedosejevs, E Fill, V Kondrashov, A Kendl, T Lower, Y Li, P X Lu, J Meyer-ter-Vehn, G Pretzler, A Saemann, R Siegel, D Beretta, C Danson, T Hall
Experiments with ASTERIX and ATLAS
Fusion Eng and Design **44** (1-4) 239-243 (1999)

E Wolfrum, J S Wark, J Zhang, N O'Rourke, R Keenan, C L S Lewis, A G MacPhee, D Kalantar, M H Key, B A Remington, D Neely, A Djaoui, S J Rose, G Eker, J Lin, R Smith, G J Tallents
X-ray laser radiography of hydrodynamic perturbations due to laser imprint
X-ray lasers 1998, Eds Y Kato, H Takuma, H Daido, IOP Conf Series **159** 657-664 (1999)

J Zhang, E Wolfrum, J Lin, A Djaoui, C L S Lewis, A MacPhee, G Cairns, R M N O'Rourke, R Smith, G J Tallents, J S Wark
KeV spectroscopic diagnostic for the performance of Ni-like X-ray lasers
X-ray lasers 1998, Eds Y Kato, H Takuma, H Daido, IOP Conf Series **159** 471-474 (1999)

J Zhang, E Wolfrum, A MacPhee, J Lin, M H Key, C L S Lewis, J Nilsen, R M N O'Rourke, R Smith, G J Tallents, J S Wark
Experiments of the saturated Ni-like X-ray lasers driven by a double 75 ps laser pulse
X-ray lasers 1998, Eds Y Kato, H Takuma, H Daido, IOP Conf Series **159** 67-70 (1999)

M Zepf, G Pretzler, U Andiel, D M Chambers, A E Dangor, P A Norreys, J S Wark, I Watts, G D Tsakiris
Optimising harmonics from solid targets
Superstrong Fields in Plasmas, Eds M Lontano, G Mourou, F Pegoraro, E Sindoni AIP Conf Proc **426** 264-269 (1998)

M Zepf, G D Tsakiris, G Pretzler, I Watts, D M Chambers, P A Norreys, U Andiel, A E Dangor, K Eidmann, C Gahn, A Machacek, J S Wark, K Witte
Role of the plasma scale length in the harmonic generation from solid targets
Phys Rev E **58** (5 Pt A) R5253-R5256 (1998)

M Zepf, J Zhang, D M Chambers, A E Dangor, A G MacPhee, J Lin, E Wolfrum, J Nilsen, T W Barbee Jr, C N Danson, M H Key, C L S Lewis, D Neely, P A Norreys, S G Preston, R M N O'Rourke, G J Pert, R Smith, G J Tallents, I F Watts, J S Wark
Recent progress in coherent XUV generation at RAL
Superstrong Fields in Plasmas, Eds M Lontano, G Mourou, F Pegoraro, E Sindoni AIP Conf Proc **426** 499-508 (1998)

PUBLISHED DURING 1997/1998

D M Chambers, P A Norreys, A E Dangor, R S Marjoribanks, S Moustaizis, D Neely, S G Preston, J S Wark, I Watts, M Zepf
Feasibility study of high harmonic generation from short wavelength lasers interacting with solid targets
Opt Comm **148** (4-6) 289-294 (1998)

PUBLICATIONS IN PRESS AT END OF 1998/1999

M Borghesi, A J MacKinnon, R Gaillard, O Willi, D Riley
Absorption of subpicosecond UV laser pulses during the interaction with solid targets
Phys Rev E [accepted for publication]

R E Burge, X C Yuan, G E Slark, T Browne, P Charalambous, C L S Lewis, G F Cairns, A G MacPhee, D Neely
Optical source models for the 23.2-23.6 nm radiation from the germanium soft X-ray laser
Opt Comm [accepted for publication]

A C Cefalas, P Argitis, Z Kollia, E Sarantopoulou, T W Ford, A D Stead, A Marranca, C N Danson, J Knott, D Neely
Laser plasma x-ray contact microscopy of living specimens
Tenth international school on quantum electronics, Eds P A Atanasov, D V Stoyanov, SPIE **3571** 388-391 (1999)

A Djaoui
Time-dependent hydrogenic ionization model for non-LTE mixtures
J Quant Spectr & Rad Trans **62** (3) 303-320 (1999)

D Hoarty, L Barringer, C Vickers, O Willi, W Nazarov
Observation of transonic ionization fronts in low-density foam targets
Phys Rev Letts **82** (15) 3070 3073 (1999)

K Krushelnick, E L Clark, Z Najmudin, M Salvati, M I K Santala, M Tatarakis, A E Dangor, V Malka, D Neely, R Allott, C Danson
Multi-MeV ion production from high-intensity laser interactions with underdense plasmas
Phys Rev Letts **83** (4) 737-740 (1999)

C L S Lewis, I Weaver, L A Doyle, G W Martin, T Morrow, D A Pepler, C N Danson, I N Ross
Use of a random phase plate as a KrF laser beam homogenizer for thin film deposition applications
Rev Sci Instr **70** (4) 2116-2121 (1999)

J Y Lin, G J Tallents, A G MacPhee, A Demir, C L S Lewis, R M N O'Rourke, G J Pert, D Ros, P H Zeitoun
Travelling wave chirped pulse amplified transient pumping for collisional excitation lasers
Opt Comm **166** (1-6) 211-218 (1999)

A J Mackinnon, M Borghesi, R Gaillard, G Malka, O Willi, A A Offenberger, A Pukhov, J Meyer-ter-Vehn, B Canaud, J L Miquel, N Blanchot
Intense laser pulse propagation and channel formation through plasmas relevant for the fast ignitor scheme
Physics of Plasmas **6** (5 Pt 2) 2185-2190 (1999)

G W Martin, I Weaver, T P Williamson, A H El-Astel, D Riley, M J Lamb, T Morrow, C L S Lewis
Study of ground state titanium ion velocity distributions in laser-produced plasma plumes
Appl Phys Letts **74** (23) 3465-3467 (1999)

P A Norreys, M Santala, E Clark, M Zepf, I Watts, F N Beg, K Krushelnick, M Tatarakis, A E Dangor, X Fang, P Graham, T McCanny, R P Singhal, K W D Ledingham, A Cresswell, D C W Sanderson, J Maghill, A Machecek, J S Wark, R Allott, B Kennedy, D Neely
Observation of a highly directional γ-ray beam from ultrashort, ultraintense laser pulse interactions with solids
Physics of Plasmas **6** (5 Pt 2) 2150-2156 (1999)

CONFERENCE PRESENTATIONS

25th IOP plasma physics conference, Oxford, UK (April 1998)

D M Chambers, G D Tsakiris, I Watts, U Andiel, A E Dangor, K Eidmann, C Gahn, A Machacek, P Norreys, G Pretzler, J S Wark, K Witte, M Zepf
Harmonic generation from the interaction of an ultra-short-pulse laser with a solid target

E L Clark, A E Dangor, K Krushelnick, A Machacek, R Marjoribanks, D Neely, P A Norreys, M Santala, M Tatarakis, J S Wark, I Watts, M Zepf
Electron and ion emission from solid targets at intensities up to 10^{19} W/cm^2

A Djaoui
Pulse shaping for ignition and gain of an indirectly driven target

A Loveridge, J S Wark, S V Weber, A Hauer, G Kyrala, B A Remington, D H Kalantar, M Meyers, G Ravichandran, E A Chandler, J D Colvin, R Lee, L G Wiley, B Failor
Simulations of x-ray diffraction from hohlraum shocked crystals

A C Machacek, D M Chambers, J S Wark, M Zepf, A E Dangor, E Clark, K Krushelnick, M Santala, M Tatarakis, I Watts, P Norreys, R Allott, C N Danson, D Neely, R S Marjoribanks
Observation of scattered radiation in the vicinity of the fundamental in ultra high intensity laser-solid interactions

P A Norreys, A P Fews, F N Beg, A R Bell, A E Dangor, P Lee, M B Nelson, H Schmidt, M Tatarakis, M D Cable
Neutron production from picosecond laser irradiation of deuterated targets at intensities of 10^{19} W cm^{-2}

P K Patel, E Wolfrum, O Renner, A Loveridge, R Allott, D Neely, S J Rose, J S Wark
Line profile modelling in expanding laser-produced plasmas

M Tatarakis, J R Davies, K Krushelnick, P A Norreys, A R Bell, E L Clark, A Machacek, R Marjoribanks, M Santala, J S Wark, I Watts, M Zepf, M G Haines, A E Dangor
Fast electron transport into thick solid targets in high intensity, short pulse laser-solid interactions

N C Woolsey, D McSherry, E Nardi, D Riley
Recent X-ray scattering measurements of strongly coupled plasmas

M Zepf, D M Chambers, E Clark, A E Dangor, K Kruselnick, A Machacek, P A Norreys, I F Watts, J S Wark
Harmonic generation from laser-solid target interactions at intensities up to 10^{19} Wcm^2

J Zhang, E Wolfrum, A MacPhee, J Lin, J Nilsen, T W Barbee Jr, C Danson, M H Key, C L S Lewis, D Neely, S J Rose, R M N O'Rourke, G J Pert, R Smith, G J Tallents
Demonstration of saturation in Ni-like x-ray lasers

Workshop on the operation of large laser fusion facilities, Livermore CA, USA (April 1998)

C Danson, C B Edwards, B Wyborn
Operational experience and practice on the Vulcan Nd:glass laser

25th ECLIM, Formia, Italy (May 1998)

M G Haines
Overview of laser-matter interaction studies at the Blackett Laboratory

E Wolfrum, J Zhang, J S Wark, M H Key, T W Barbee Jr, D H Kalantar, B A Remington, C L S Lewis, R Keenan, R M N O'Rourke, A G MacPhee, P J Warwick, G Eker, J Lin, R Smith, G J Tallents
Measurement of direct drive laser imprint in thin foils by XUV laser radiography

G J Tallents, R Smith, J Pestehe, J Lin, M Tagviashvili, S J Rose, A Djaoui, D Neely, K Nazir
The production of high energy density x-ray sources

P A Norreys, D Neely, A R Bell, E Clarke, J Davies, M G Haines, K Krushelnick, M Tatarakis, I Watts, M Zepf, A E Dangor, D M Chambers, A Machacek, J S Wark, A P Fews, S Moustaizis, R Marjoribanks
Solid target interaction physics with relativistic laser irradiances

G D Tsakiris, M Zepf, G Pretzler, I Watts, U Andiel, D M Chambers, A E Dangor, K Eidmann, C Gahn, A Machacek, P A Norreys, J S Wark, K Witte
Influence of the density scale-length on the harmonic generation from solid targets

D Batani, A Bernardinello, V Masella, F Pisani, M Koenig, J Krishnan, A Benuzzi, S Ellwi, T Hall, P Norreys, A Djaoui, D Neely, S Rose, P Fews, M Key
Fast electron propagation and energy deposition in laser shock compressed plasmas

N C Woolsey, D McSherry, E Nardi, D Riley
Experimental measurements of x-ray scattering cross-sections from dense plasmas

F Dorchies, F Amiranoff, D Bernard, B Cross, F Jacquet, V Malka, J R Marques, G Matthieussent, Ph Mine, A Modena, P Mora, J Morillo, Z Najmudin, A Solodov
Observation of laser wakefield acceleration of electrons

Z Najmudin, V Malka, R Allott, F Amiranoff, E L Clark, A E Dangor, C N Danson, P Flintoff, D Gordon, C Joshi, K Krushelnick, G Malka, A Modena, D Neely, M Santala, M Tatarakis
High intensity laser interactions with a gas jet

T J M Boyd, A Dyson
Interaction of intense laser light with super-critical density plasma

J R Davies, A R Bell
Fast electron transport in solid targets

M Tatarakis, J R Davies, K Krushelnick, A R Bell, E L Clark, A Machacek, R Marjoribanks, P A Norreys, M Santala, J S Wark, I Watts, M Zepf, M G Haines, A E Dangor
Fast electron generation and propagation into thick solid targets in high intensity laser-solid interactions

N C Woolsey, C A Back, J K Nash, A Calisti, C Mosse, R Stamm, B Talin, A Asfaw, L S Klein, R W Lee
Ar Heβ line shape and line shifts at high density

E L Clark, A E Dangor, K Krushelnick, A Machacek, R Marjoribanks, D Neely, P A Norreys, M Santala, M Tatarakis, J S Wark, I Watts, M Zepf
Electron and ion emission from solid targets at intensities up to 10^{19} W/cm^2

M Salvati, R Allott, F Amiranoff, E L Clark, A E Dangor, C N Danson, P Flintoff, D Gordon, K Krushelnick, V Malka, G Malka, A Modena, Z Najmudin, D Neely, M Santala, M Tatarakis
High intensity laser interactions with a gas jet at 527 nm

M G Haines
On magnetic fields in short laser pulse interactions with overdense plasmas

F Pisani, M Koenig, J Krishnan, D Batani, V Masella, A Bernardinello, T A Hall, S Ellwi, P Norreys, D Neely, A Djaoui, S Rose, P Fews, M Key
Hot electrons deposition in laser shock compressed matter

CLEO/EUROPE'98, Glasgow, UK (September 1998)

A C Cefalas, Z Kollia, T W Ford, A D Stead, A Marranca, C N Danson, J Knott, D Neely
Fast, chemically amplified epoxy novolac photoresist for soft x-ray contact microscopy of living biological species

EQEC'98, Glasgow, UK (September 1998)

D Neely C N Danson, R Allott, J L Collier, A E Dangor, C B Edwards, P Flintoff, P Hatton, Z Najmudin, K Krushelnick, D A Pepler
Simultaneous dual wavelength high energy, picosecond pulses for novel particle acceleration experiments

J Larsson, A Lindenberg, P A Heimann, P H Bucksbaum, R W Lee, J S Wark, R W Falcone
Investigation of disordering and reordering

D Neely, C L S Lewis, J Lin, A MacPhee, R M N O'Rourke, G J Pert, R Smith, G J Tallents, J S Wark, J Warwick, E Wolfrum, J Zhang, M Key, R Allott, C Danson
X-ray lasers - state of the art in the UK

3rd international workshop on the fast ignition of fusion targets, RAL, Didcot, UK (September 1998)

R Bingham
A review of electron acceleration mechanisms with short pulse, ultra-intense laser pulses

M Borghesi, A MacKinnon, O Willi
Channelling in pre-formed plasmas and propagation in capillaries

J Davies, A R Bell
The effects of magnetic fields in collimating electron flows in ultra-intense interactions

E Clark
A comparison of temperatures derived from measurements of the x-ray bremsstrahlung emission with those from escaping electrons generated during ultra-intense interactions with solids

M Tatarakis
Observations of collimated electron flows in ultra intense laser interactions with thick foils

T A Hall
X-ray and fast particle preheat in femtosecond laser driven transport experiments

M Tatarakis
Fast electron generation and propagation into thick solid targets in high intensity laser-solid interactions

F Pisani, L Gremillet, M Koenig, F Amiranoff, E Martinolli, P Norreys, A Djaoui, T Hall, D Batani, A Antonucci. C Rousseaux, H Pepin, H Bandulet, P Fews
Fast electrons deposition experiment with the new LULI 100 TW laser, Part I: K_α spectroscopy

F Amiranoff, L Gremillet, M Koenig, F Pisani, E Martinolli, P Norreys, A Djaoui, T Hall, D Batani, A Antonucci. C Rousseaux, H Pepin, H Bandulet, P Fews
Fast electrons deposition experiment with the new LULI 100 TW laser, Part 2: Shadowgraphy through transparent targets

D Batani, A Bernardinello, M Koenig, F Pisani, J Davies, T Hall, P Norreys, A Djaoui, D Neely, S Rose
Explanations for the increased range of fast electrons in shock compressed plasmas

T Hall
Femtosecond laser driven transport experiments

K Ledingham, P Graham, X Fang, R P Singhal, T McCanny, J Maghill, A Creswell, D Sanderson, R Scott, R Allott, D Neely, P Norreys, M Santala, M Zepf, I Watts, E Clark, K Krushelnick, A E Dangor, M Tatarakis, A Machacek, J Wark
Laser induced fission

A Machacek, D M Chambers, J S Wark, I Watts, M Zepf, A E Dangor, E Clark, K Krushelnick, M Santala, M Tatarakis, P A Norreys, R Allott, C N Danson, D Neely, R S Marjoribanks
Observation and discussion of stimulated optical scattering in ultra-intense laser-solid interactions

P A Norreys, A Djaoui, S J Rose
Developments in the fast ignition conical implosion concept

8th international workshop on the radiative properties of hot dense matter, Sarasota, USA (October 1998)

M E Beer, P K Patel, S J Rose, J S Wark
Calculations of the modal photon densities and gain in a K/CL resonantly photopumped x-ray laser

N C Woolsey, C A Back, R W Lee, A Calisti, C Mosse, R Stamm, B Talin, A Asfaw, L S Klein
Experimental results on line shifts from dense plasmas

D Riley, N C Woolsey, D McSherry, E Nardi
X-ray scattering from plasmas

P K Patel, E Wolfrum, O Renner, A Loveridge, R Allott, D Neely, S J Rose, J S Wark
High-resolution lineshape measurements from a rapidly expanding laser-produced plasma

S J Rose
Comptonisation of x-ray line features in laser-driven implosion experiments

S Davidson, G J Tallents
Experimental design issues for short pulse opacity experiments

40th annual meeting of the APS division of plasma physics, New Orleans, USA (November 1998)

D Hoarty
Observation of ionization fronts in low-density foam targets

A Mackinnon
Intense laser pulse propagation and channel formation through plasmas relevant to the fast ignitor scheme

26th IOP plasma physics conference, Pitlochry, UK (March 1999)

M H R Hutchinson
High power laser research at the Central Laser Facility

G Pert
Development in x-ray lasers

K Ledingham
Nuclear physics merely using a light source

D Riley, N C Woolsey, D McSherry, E Nardi
X-ray scattering from plasmas

J S Wark, M E Beer, I Almiev, P K Patel, S J Rose
Revisiting photopumped X-ray lasers

REPORTS

P Sauvan, P Angelo, E Leboucher-Dalimier, P Gauthier, S J Rose
Traitment alternatif de l'elargissement de la raie Ar He α emise lors d'implosions de capsules d'argon
LULI Annual Scientific Report 1998 (1998)

SEMINARS

S J Rose
Inertial confinement fusion
The Central Laser Facility (November 1998)

S J Rose
Astrophysics with high-power lasers
Physics and applied physics department, University of Strathclyde (March 1999)

PHD THESES

M Borghesi
The interaction of ultra intense laser pulses with solid targets and preformed plasmas
Ph D, 1998

R Gaillard
The interaction of picosecond high intensity laser pulses with preformed plasmas and solid targets
Ph D, 1998

A Iwase
Studies of shock propagation and thermal smoothing in laser irradiated foam targets
Ph D, 1999

Science – Astra Facility Programme

JOURNAL PUBLICATIONS, BOOKS AND PUBLISHED PROCEEDINGS

C Kosmidis, K W D Ledingham, H S Kilic, T McCanny, R P Singhal, D Smith, A J Langley
Molecular fragmentation induced by a femtosecond laser
Second GR-I international conference on new laser technologies and applications, Eds P di Lazzaro, A Torre, G Baldacchini, SPIE **3423** 204-208 (1998)

K W D Ledingham, R P Singhal, D J Smith, T McCanny, P Graham, H S Kilic, W X Peng, S L Wang, A J Langley, P F Taday, C Kosmidis
Behaviour of polyatomic molecules in intense infrared laser beams
J Phys Chem A **102** (18) 3002-3005 (1998)

J H Posthumus, J Plumridge, L J Frasinski, K Codling, A J Langley, P F Taday
Double pulse measurements of laser-induced alignment of molecules
J Phys B-Atomic Molecular and Optical Physics **31** (24) L985-L993 (1998)

J H Posthumus, J Plumridge, K Codling, L J Frasinski, A J Langley, P F Taday
Alignment of molecules on a vibrational timescale
Laser Physics **9** (1) 163- (1999)

J H Posthumus, J Plumridge, P F Taday, J H Sanderson, A J Langley, K Codling, W A Bryan
Sub-pulselength time resolution of bond softening and Coulomb explosion using polarization control of laser-induced alignment
J Phys B-Atomic Molecular and Optical Physics **32** (5) L93-L101 (1999)

J H Posthumus, J Plumridge, M K Thomas, K Codling, L J Frasinski, A J Langley, P F Taday
Dynamic and geometric laser-induced alignment of molecules in intense laser fields
J Phys B-Atomic Molecular and Optical Physics **31** (13) L553-L562 (1998)

J H Sanderson, R V Thomas, W A Bryan, W R Newell, A J Langley, P F Taday
Alignment and bending of CO_2 by intense femtosecond laser pulses
J Phys B-Atomic Molecular and Optical Physics **31** (14) L599-L606 (1998)

R P Singhal, H S Kilic, K W D Ledingham, T McCanny, W X Peng, D J Smith, C Kosmidis, A J Langley, P F Taday
Comment on "On the ionisation and dissociation of NO_2 by short intense laser pulses"
Chem Phys Letts **292** (4-6) 643-646 (1998)

D J Smith, K W D Ledingham, R P Singhal, H S Kilic, T McCanny, A J Langley, P F Taday, C Kosmidis
Time-of-flight mass spectrometry of aromatic molecules subjected to high intensity laser beams
Rapid Communications in Mass Spectrometry **12** (13) 813-820 (1998)

PUBLICATIONS IN PRESS AT END OF 1998/1999

K W D Ledingham, D J Smith, R P Singhal, T McCanny, P Graham, H S Kilic, W X Peng, A J Langley, P F Taday, C Kosmidis,
Multiply charged ions from aromatic molecules following irradiation in intense laser fields
J Phys Chem A **103** (16) 2952-2963 (1999)

J H Sanderson, A El-Zein, W A Bryan, W R Newell, A J Langley, P F Taday
Geometry modifications and alignment of H_2O in an intense femtosecond laser pulse
Phys Rev A **59** (4) R2567-R2570 (1999)

I D Williams, B Srigengan, P McKenna, W R Newell, J H Sanderson, W A Bryan, A El-Zein, P F Taday, A J Langley
Short pulse laser interaction with positive ions
Physica Scripta **T80B** 534-535 (1999)

Science - Lasers *for* Science Facility Programme

JOURNAL PUBLICATIONS, BOOKS AND PUBLISHED PROCEEDINGS

G J Berry, J A Cairns, M R Davidson, D R G Rodley, J Thomson, I C E Turcu, W Shaikh
1 nm X-ray lithography using novel mask fabrication technique
Rev Sci Instr **69** (9) 3350-3352 (1998)

R H Bisby, S A Johnson, A W Parker, S M Tavender
Time resolved resonance Raman spectroscopy of the carbonate radical
J Chem Soc Faraday Trans **94** (15) 2069-2072 (1998)

R H Bisby, S A Johnson, A W Parker, S M Tavender
Time resolved resonance Raman studies of radicals from 4-aminoresorcinol as models for the active site radical intermediate in copper amine oxidases
Laser Chemistry **19** (1-4) 201-208 (1999)

D Chastaing, P L James, I R Sims, I W M Smith
Neutral-neutral reactions at the temperature of interstellar clouds: rate coefficients for the reactions of C_2H radicals with O_2, C_2H_2, C_2H_4 and C_3H_6 down to 15 K
Faraday Discussions **109** 165-181 (1998)

J M F Elks, R T Kroemer, J McCombie, E G Robertson, J P Simons, M Walker
Conformational landscapes in flexible organic molecules: 3-phenylpropanol
Phys Chem Comm **3** (1998)

T Fournier, G D Scholes, I R Gould, S M Tavender, D Phillips, A W Parker
Triplet 1-nitronaphthalene and competitive energy and electron transfer reactions with trans-stilbene
Laser Chemistry **19** (1-4) 397-401 (1999)

S Hess, R A Taylor, J F Ryan, B Beaumont, P Gibart, N J Cain, V Roberts, J S Roberts
Time-resolved bandgap renormalization and gain in GaN epilayers
Proceedings of the second international symposium on blue laser and light emitting diodes, Chiba, Japan, 673, (1998)

S Hess, F Walraet, R A Taylor, J F Ryan, B Beaumont, P Gibart
Dynamics of resonantly excited excitons in GaN
Phys Rev B **58** (24) R15973-R15976 (1998)

R J Hicken, J Wu
Picosecond optical pump-probe spectroscopy of spin dynamics in ferromagnetic thin films
Acta Photonica Sinica **27** 95 (1998)

M R Hockridge, E G Robertson, J P Simons
Ion-dip spectroscopy and structure of 5-phenyl imidazole, 4-phenyl imidazole and its 1:1 hydrate
Chem Phys Letts **302** (5,6) 538-548 (1999)

P L James, I R Sims, I W M Smith, M H Alexander, M Yang
A combined experimental and theoretical study of rotational energy transfer in collisions between NO($X^2\Pi_{1/2}v$=3,J) and He, Ar and N_2 at temperatures down to 7 K
J Chem Phys **109** (10) 3882-3897 (1998)

P Jennnings, A C Jones, A R Mount
Fluorescence properties of electropolymerised 5-substituted indoles in solution
J Chem Soc Faraday Trans **94** (24) 3619-3624 (1998)

G R Kennedy, C-L Ning, J Pfab
The 355nm photodissociation of jet-cooled CH_3SNO: alignment of the NO photofragment
Chem Phys Letts **292** (1,2) 161-166 (1998)

R T Kroemer, K R Liedl, J A Dickinson, E G Robertson, J P Simons, D R Borst, D W Pratt
Conformationally induced changes in the electronic structures of some flexible benzenes: a molecular orbital model
J Am Chem Soc **120** (48) 12573-12582 (1998)

I K Lednev, T-Q Ye, P Matousek, M Towrie, P Foggi, F V R Neuwahl, S Umapathy, R E Hester, J N Moore
Femtosecond time-resolved UV-visible absorption spectroscopy of trans-azobenzene: dependence on excitation wavelength
Chem Phys Letts **290** (1-3) 68-74 (1998)

A Magunov, A Faenov, I Skobelev, T Pikuz, D Batani, M Milani, M Costato, A Pozzi, E Turcu, R Allot, M Koenig, A Benuzzi, F Flora, A Reale
Formation of the X-ray line emission spectrum of excimer laser-produced plasmas
Laser and Particle Beams **16** (1) 61-70 (1998)

A Masini, D Batani, F Previdi, A Pozzi, E Turcu, S Huntington, H Takeyasu
Yeast cell metabolism investigated by CO_2 production and soft X-ray irradiation
European Physical Journal – Applied Physics **5** (1) 101-109 (1999)

E A Mastio, W M Cranton, C B Thomas, E Fogarassy, S de Unamuno
Pulsed KrF laser annealing of RF sputtered ZnS:Mn thin films
Appl Surf Sci 138-139 (1-4) 35-39 (1999)

P Matousek
Regenerative amplifier revolutionizes Raman spectroscopy
Laser Focus World **34** (5) 124 (1998)

P Matousek, G Gaborel, A W Parker, D Phillips, G D Scholes, W T Toner, M Towrie
ps-TR^3 spectroscopy of S_1 cis-stilbene in solution
Laser Chemistry **19** (1-4) 97-100 (1999)

T Melvin, S M T Cunniffe, P O'Neill, A W Parker, T Roldan-Arjona
Guanine is the target for direct ionisation damage in DNA, as detected using excision enzymes
Nucleic Acids Research **26** (21) 4935-4942 (1998)

M Milani, M Ballerini, G Baroni, D Batani, S Cozzi, L Ferraro, M Costato, F Salsi, A Pozzi, F Squadrini, I C E Turcu, R Allot, N Lisi, W Shaikh, S Hughes
Differential two colour X-ray radiobiology of membrane/cytoplasm in yeast cells and lymphocytes
Advances in optical biophysics, Eds J R Lakowicz, J B A Ross, SPIE **3256** 195-205 (1998)

M Milani, A Conte, M Costato, F Salsi, G Baroni, D Batani, L Ferraro, I C E Turcu
NMR and pressure correlated analysis of metabolic changes in soft-X-rays irradiated yeast cells
European Physical Journal D **5** (2) 267-270 (1999)

I D Morrison A J Berry, R G Denning
Energy levels of terbium(III) in the elpasolite $Cs_2NaTbCl_6$
Mol Phys **96** (1) 43-51 (1999)

A W Parker
Preface to the proceedings of the eighth conference on time-resolved vibrational spectroscopy
Laser Chemistry **19** (1-4) ix-x (1999)

G D Scholes, I R Gould, A W Parker, D Phillips
Time-resolved resonance Raman and molecular-orbital studies of charge-separation and intramolecular reorganisation
Chem Phys **234** (1-3) 21-34 (1998)

G D Scholes, T Fournier, D Phillips, A W Parker
Solvent-dependent resonance Raman excitation profiles of 9,9'-bianthryl
Laser Chemistry **19** (1-4) 51-56 (1999)

A D Scully, R B Ostler, A J MacRobert, A W Parker, C de Lara, P O'Neill, D Phillips
Laser line-scanning confocal fluorescence imaging of the photodynamic action of aluminium and zinc phthalocyanines in V79-4 Chinese hamster fibroblasts
Photochem and Photobiol **68** (2) 199-204 (1998)

D J Smith, K W D Ledingham, H S Kilic, T McCanny, W X Peng, R P Singhal, A J Langley, P F Taday, C Kosmidis
Ionization and dissociation of benzaldehyde using short intense laser pulses
J Phys Chem A **102** (15) 2519-2526 (1998)

I W M Smith
Molecules in space: the chemical laboratory at the end of the universe
Chemistry Reviews **7** (3) 2-6 (1998)

S M Tavender, S A Johnson, D Balsom, A W Parker, R H Bisby
The carbonate CO_3^- in solution studied by resonance Raman spectroscopy
Laser Chemistry **19** (1-4) 311-316 (1999)

R J Tompkins, I P Mercer, M Fettweis, C J Barnett, D R Klug, G Porter, I Clark, S Jackson, P Matousek, A W Parker, M Towrie
5-20 keV laser-induced X-ray generation at 1 kHz from a liquid-jet target
Rev Sci Instr **69** (9) 3113-3117 (1998)

W T Toner, P Matousek, A W Parker, M Towrie
Picosecond Raman excitation profile and transient absorption spectrum of S_1 quaterphenyl in solution
Laser Chemistry **19** (1-4) 79-82 (1999)

M Towrie, G Gaborel, P Matousek, A W Parker, W Shaikh, R H Bisby
Tunable picosecond optical parametric amplifiers for time resolved resonance Raman spectroscopy
Laser Chemistry **19** (1-4) 153-159 (1999)

I C E Turcu, B Dance
X-rays from laser-plasmas: generation and applications
Publ John Wiley & Sons (1998)

PUBLISHED DURING 1997/1998

A A Anderson, R W Eason, L M B Hickey, M Jelinek, C Grivas, D S Gill, N A Vainos
Ti:sapphire planar waveguide laser grown by pulsed laser deposition
Opt Letts **22** (20) 1556-1558 (1997)

D Batani, M Milani, G Leoni, A Conti, A Masini, F Pisani, M Costato, A Pozzi, E Turcu, R Allott, N Lisi, F Cotelli, C Lora Lamia Donin, M Moret
Yeast cells response to soft X-rays from laser-plasmas
Vuoto Science and Technology **XXVI** 3-8 (1997)

A J Berry, R G Denning, I D Morrison
Two-photon excitation spectroscopy of lanthanide elpasolites - implications for the correlation crystal field
Chem Phys Letts **266** (1,2) 195-200 (1997)

A J Berry, R G Denning, I D Morrison
Two-photon Zeeman spectroscopy of terbium (III) elpasolites
J Chem Phys **106** (22) 8967-8973 (1997)

A J Berry, I D Morrison, R G Denning
Energy levels of terbium(III) in the elpasolite Cs_2NaTbF_6
Mol Phys **93** (1) 1-14 (1998)

R G Denning, A J Berry and C S McCaw
Ligand dependence of the correlation crystal field
Phys Rev B **57** (4) R2021-R2024 (1998)

J A Dickinson, M R Hockridge, R T Kroemer, E G Robertson, J P Simons, J McCombie, M Walker
Conformational choice, hydrogen bonding and rotation of the $S_1 \leftarrow S_0$ electronic transition moment in 2-phenylethyl alcohol, 2-phenylethylamine and their water clusters
J Am Chem Soc **120** (11) 2622-2632 (1998)

J A Dickinson, P W Joireman, R T Kroemer, E G Robertson, J P Simons
Conformationally induced transition moment rotations in the $S_1 \leftarrow S_0$ electronic spectra of n-propylbenzene and n-butylbenzene
J Chem Soc Faraday Trans **93** (8) 1467-1472 (1997)

I W M Smith, I R Sims, B R Rowe
Gas-phase reactions at low temperatures: towards absolute zero
Chemistry: A European Journal **3** (12) 1925-1928 (1997)

PUBLICATIONS IN PRESS AT END OF 1998/1999

A C Benniston, P Matousek, A W Parker
Kerr-gated picosecond time resolved resonance Raman spectroscopic probing of the excited states in Λ-[Ru(bipy)2dppz(BF4)2 (bipy = 2,2'-bipyridyl, dppz = dipyrido[3,2-a:2'3'-c])phenazine
J Am Chem Soc [submitted]

I R Farrell, P Matousek, A Vlcek
Femtosecond spectroscopic study of MLCT excited-state dynamics of Cr(CO)(4)(bpy): excitation-energy-dependent branching between CO dissociation and relaxation
J Am Chem Soc **121** (22) 5296-5301 (1999)

S Hess, R A Taylor, K Kyhm, J F Ryan, B Beaumont, P Gibart
Femtosecond exciton dynamics and the Mott transition in GaN
Physica Status Solidi B [accepted for publication]

S Hess, R A Taylor, E D O'Sullivan, J F Ryan, N J Cain, V Roberts, J S Roberts
Hot carrier relaxation by extreme electron-LO phonon scattering in GaN
Physica Status Solidi B [accepted for publication]

R J Hicken, J Wu
Observation of ferromagnetic resonance in the time domain
J Appl Phys **85** (8 Pt 2) 4580-4582 (1999)

M R Hockridge, E G Robertson
Hydrated clusters of 2-phenylethyl alcohol and 2-phenylethylamine; structure, bonding and rotation of the $S_1 \leftarrow S_0$ electronic transition moment
J Phys Chem A **103** (19) 3618-3628 (1999)

P Matousek, M Towrie, A Stanley, A W Parker
Efficient rejection of fluorescence from Raman spectra using picoesecond Kerr gating
Applied Spectroscopy [accepted for publication]

F L Plows, A C Jones
Laser-desorption supersonic jet spectroscopy of phthalocyanines
J Mol Spec **194** (2) 163-170 (1999)

K L Reid, T A Field, M Towrie, P Matousek
Photoelectron angular distributions as a probe of alignment evolution in a polyatomic molecule: picosecond time- and angle- resolved photoelectron spectroscopy of S-1 para-difluorobenzene
J Chem Phys **111** (4) 1438-1445 (1999)

G D Scholes, T Fournier, A W Parker, D Phillips
Studies of charge localisation and inertial solvent timescales: non equilibrium resonance Raman excitation profiles of 9, 9'-bianthyl
J Chem Phys [accepted for publication]

R A Taylor, S Hess, K Kyhm, J Smith, J F Ryan, G P Yablonskii, E V Lutsebko, V N Pavlovskii, M Heuken
Stimulated emission and excitonic bleaching in GaN epilayers under high-density excitation
Physica Status Solidi B [accepted for publication]

CONFERENCE PRESENTATIONS

193rd meeting of the Electrochemical Society, San Diego, USA (May 1998)

P Jennings, A C Jones, A R Mount
Luminescence of electrochemically generated indole polymers

15th international symposium on gas kinetics, Bilbao, Spain (September 1998)

C E Canosa-Mas, N J Hendy, D Shah, A Vipond, R P Wayne
Discharge flow studies of some reactions of BrO'

CONFERENCE PRESENTATIONS 1999/2000

COBRA meeting, Lausanne, Switzerland (April 1999)

C E Canosa-Mas, N J Hendy, D Shah, A Vipond, R P Wayne
Kinetic studies of the reactions of CH_3O and CH_3O_2 with Br and BrO

In-fibre Bragg gratings and special fibres, IOP half-day meeting, London, UK (May 1999)

R J Potton
Spectral and time response of photochromic glasses and their application to adaptive filtering

9th international conference on time-resolved vibrational spectroscopy (TRVS IX), Tuscon, USA (May 1999)

P Matousek, M Towrie, A Stanley, A W Parker
Novel method for efficient rejection of fluorescence from Raman spectra

M Towrie, M W George, D C Grills, P Matousek, A W Parker
A development of a new IR picosecond time resolved facility

A W Parker
Early relaxation processes of photoexcited states

American Geophysical Union spring meeting, (June 1999)

C E Canosa-Mas, N J Hendy, D Shah, A Vipond, R P Wayne
Discharge flow studies of the reactions of Br, BrO, Cl and ClO with CH_3O

SEMINARS

A W Parker
Ultrafast chemistry: investigations performed at the Central Laser Facility
National Centre for Ultrafast Processes, University of Madras, India (April 1998)

A W Parker
So little time for chemistry
Open Day Public Lecture, RAL, Chilton, UK (June 1998)

A W Parker
Picosecond time-resolved Stokes and anti-Stokes Raman spectroscopy of photoexcited molecules using optical parametric lasers
Invited presentation in honour of retirement of Dr Albrecht Lau, Max-Born Institute, Berlin, Germany (August 1998)

A W Parker
Applications of time-resolved resonance Raman spectroscopy
Chalmers University of Technology, Sweden (February 1999)

THESES

N J Hendy
A discharge flow study of some reactions of brominated species of atmospheric relevance
M Chem, 1999

S A Johnson
Spectroscopic studies of copper amine oxidase
Ph D, 1998

F L Plows
Supersonic jet spectroscopy of laser-desorbed molecules
Ph D, 1998

P Jennings
A photophysical study of electropolymerised indoles
Ph D, 1999

Facility Developments

JOURNAL PUBLICATIONS, BOOKS AND PUBLISHED PROCEEDINGS

J L Collier, C N Danson, R M Allott, M H R Hutchinson, C L S Lewis, D Neely, D A Pepler, T B Winstone, J Zhang
Ultra-short pulse line focus travelling-wave implementation on the Vulcan laser
X-ray lasers 1998, Eds Y Kato, H Takuma, H Daido, IOP Conf Series **159** 649-652 (1999)

J Collier, C Danson, C Johnson and C Mistry
Uniaxial single shot autocorrelator
Rev Sci Instr **70** (3) 1599-1602 (1999)

C N Danson, J Collier, D Neely, L J Barzanti, A Damerell, C B Edwards, M H R Hutchinson, M H Key, P A Norreys, D A Pepler, I N Ross, P F Taday, W T Toner, M Trentelman, F N Walsh, T B Winstone and R W W Wyatt
Well characterized 10^{19} W cm^2 operation of VULCAN - an ultra-high power Nd:glass laser
J Mod Opt **45** (8) 1653-1669 (1998)

C B Edwards, C N Danson, M H R Hutchinson, D Neely, B Wyborn
200 TW upgrade of the Vulcan Nd:glass laser facility
Superstrong Fields in Plasmas, Eds M Lontano, G Mourou, F Pegoraro, E Sindoni AIP Conf Proc **426** 485-490 (1998)

D Neely, D M Chambers, C N Danson, P A Norreys, S G Preston, F Quinn, M Roper, J S Wark, M Zepf
A multi-channel soft X-ray flat-field spectrometer
Superstrong Fields in Plasmas, Eds M Lontano, G Mourou, F Pegoraro, E Sindoni AIP Conf Proc **426** 479-484 (1998)

K Osvay, I N Ross, J M Lister, C J Hooker
High-dynamic-range measurement of the temporal contrast of ultrashort UV pulses
Second GR-I international conference on new laser technologies and applications, Eds P di Lazzaro, A Torre, G Baldacchini, SPIE **3423** 179-183 (1998)

M J Shaw, I N Ross, C J Hooker, J M Dodson, G J Hirst, J M D Lister, E J Divall, A K Kidd, S Hancock, A R Damerell, B E Wyborn
Ultrahigh-brightness KrF laser system for fast ignition studies
Fusion Eng and Design **44** (1-4) 209-214 (1999)

M Towrie, A W Parker, W Shaikh, P Matousek
Tunable picosecond optical parametric generator-amplifier system for time resolved Raman spectroscopy
Measurement Science & Technology **9** (5) 816-823 (1998)

H L Offerhaus, C B Edwards, W J Witteman
Single shot beam quality (M^2) measurement using a spatial Fourier transform of the near field
Opt Comm **151** (1-3) 65-68 (1998)

PUBLICATIONS IN PRESS AT END OF 1998/1999

C N Danson, R Allott, G Booth, J Collier, C B Edwards, P S Flintoff, S J Hawkes, M H R Hutchinson, C Hernandez-Gomez, J Leach, D Neely, P Norreys, M Notley, D Pepler, I N Ross, J Walczak, T Winstone
The generation of focused intensities of 5x10^{19} Wcm^{-2}
Laser and Particle Beams 17 (2) 341-347 (1999)

C L S Lewis, I Weaver, L A Doyle, G W Martin, T Morrow, D A Pepler, C N Danson and I N Ross
Use of a random phase plate as a KrF laser beam homogenizer for thin film deposition applications
Rev Sci Instr **70** (4) 2116-2121 (1999)

D Neely, C N Danson, R Allott, F Amiranoff, J L Collier, A E Dangor, C B Edwards, P Flintoff, P Hatton, M Harman, M H R Hutchinson, Z Najmudin, D A Pepler, I N Ross, M Salvati, T Winstone
Frequency doubling of multi terawatt picosecond pulses
Laser and Particle Beams 17 (2) 281-286 (1999)

K Osvay, I N Ross
Efficient tuneable bandwidth frequency mixing using chirped pulses
Opt Comm **166** (1-6) 113-119 (1999)

K Osvay, I N Ross, J M D Lister, C J Hooker
High dynamic range measurement of temporal shape and contrast of ultrashort UV pulses
Appl Phys B **69** (1) 19-23 (1999)

I N Ross, P Matousek, M Towrie, A J Langley, J L Collier, C N Danson, C Hernandez-Gomez, D Neely, K Osvay
Prospects for a multi-PW source using optical parametric chirped pulse amplifiers
Laser and Particle Beams 17 (2) 331-340 (1999)

CONFERENCE PRESENTATIONS

25th IOP plasma physics conference, Oxford, UK (April 1998)

R Allott, S Angood, C Beckwith, G Booth, J Collier, C N Danson, A Damerell, C B Edwards, J Ellwood, P Exley, P Flintoff, J Govans, S Hancock, P Hatton, S Hawkes, D Hitchcock, M H R Hutchinson, M H Key, C Hernandez-Gomez, J Leach, W Lester, D Neely, P Norreys, M Notley, D Pepler, C Reason, D A Rodkiss, M Stainsby, M Trentelman, J Walczak, T Winstone, R Wyatt, B Wyborn
10^{20} Wcm^{-2} for laser plasma interactions with the upgraded Vulcan CPA facility

D Neely, D Chambers, C Danson, P Norreys, S Preston, F Quinn, M Roper, J Wark, M Zepf
A soft x-ray multi-channel flat-field spectrometer

M Notley, A Damerell, C Danson, J Leach, D Neely, J Lin, S J Pestehe, R Smith, G Tallents, M Zepf
Diagnostic instrumentation developments for x-ray emission spectroscopy

25th ECLIM, Formia, Italy (May 1998)

C N Danson, R Allott, S Angood, C Beckwith, G Booth, J Collier, A Damerell, C B Edwards, J Ellwood, P Exley, P Flintoff, J Govans, S Hancock, P Hatton, S Hawkes, D Hitchcock, M H R Hutchinson, M H Key, C Hernandez-Gomez, J Leach, W Lester, D Neely, P Norreys, M Notley, D Pepler, C Reason, D A Rodkiss, M Stainsby, M Trentelman, J Walczak, T Winstone, R Wyatt, B Wyborn
Focused intensities of 10^{20} Wcm^{-2} to target with the upgraded Vulcan CPA interaction facility

D Neely, C N Danson, R Allott, J L Collier, C B Edwards, P Flintoff, M H R Hutchinson, D A Pepler, I N Ross, M Trentelman, T Winstone, Z Majmudin, V Malka, F Amiranoff, E L Clark, A E Dangor, D Gordon, K Krushelnick, G Malka, A Modena, M Salvati, M Santala, M Tatarakis
Multi terawatt frequency doubling of picosecond pulses for plasma interactions

D Neely, C N Danson, R Allott, S Angood, J Collier, A Damerell, C B Edwards, J Govans, S Hancock, M Harman, P Hatton, C Henandez-Gomez, M H R Hutchinson, W Lester, P Norreys, M Notley, D A Pepler, D Rodkiss, R Wellstood, T Winstone, B Wyborn, R W W Wyatt
Design and optimisation of the target interaction facilities on VULCAN

I N Ross, P Matousek, M Towrie, A J Langley, J L Collier, C N Danson, D Neely
Multi-PW source using optical parametric chirped pulse amplifiers

3rd annual international conference on solid state lasers for application (SSLA) to inertial confinement fusion (ICF), Monterey, USA, (June 1998)

C N Danson, R Allott, S Angood, J Collier, A Damerell, C B Edwards, J Govans, S Hancock, P Hatton, M H R Hutchinson, M H Key, C Henandez-Gomez, W Lester, D Neely, P Norreys, M Notley, D Pepler, C Reason, D A Rodkiss, M Trentelman, T Winstone, R Wyatt, B Wyborn
Focused intensities of 10^{20} Wcm^{-2} with the upgraded Vulcan CPA interaction facility

M H R Hutchinson, C N Danson, C B Edwards, D Neely, B Wyborn
Current statuts and future development of the Vulcan high power Nd:glass laser

D Neely, C N Danson, R Allott, F Amiranoff, E L Clark, C Clayton, J L Collier, A E Dangor, A Djaoui, C B Edwards, P Flintoff, D Gordon, M H R Hutchinson, K Krushelnick, G Malka, A Modena, Z Majmudin, D A Pepler, I N Ross, A Santala, M Tatarakis, M Trentelman, T Winstone
Multi terawatt frequency doubling of picosecond pulses for plasma interactions

6th international conference on X-ray lasers, Kyoto, Japan (August 1998)

J L Collier, C N Danson, R M Allott, M H R Hutchinson, C L S Lewis, D Neely, D A Pepler, T B Winstone, J Zhang
Ultra-short pulse line focus travelling-wave implementation on the Vulcan laser

CLEO/EUROPE'98, Glasgow, UK (September 1998)

T B Winstone, C N Danson, R Allott, G Booth, J Collier, A Damerell, C B Edwards, A Frackiewicz, P Flintoff, S Hancock, M Harman, P Hatton, S Hawkes, M H R Hutchinson, C Hernandez-Gomez, J Leach, W Lester, D Neely, M Notley, D A Pepler, C Reason, D A Rodkiss, I N Ross, J Walczak, R Wellstood, R W W Wyatt, B Wyborn
VULCAN: A versatile ultra high power Nd:glass laser system

I N Ross, P Matousek, M Towrie, A J Langley, J L Collier, C N Danson, D Neely
Optical parametric chirped pulse amplifiers for the generation of extremes in power intensity and pulse duration

J Collier, C Hernandez-Gomez, I N Ross, K Osvay, P Matousek, C N Danson, J Walczak
Demonstration of a new ultra short pulse amplification technique – optical parametric chirped pulse amplification

EQEC'98, Glasgow, UK (September 1998)

D Neely C N Danson, R Allott, J L Collier, C B Edwards, P Flintoff, M H R Hutchinson, D A Pepler, I Ross, M Trentelman, T Winstone
Characterisation of large aperture frequency doubled picosecond pulses

J Collier, C Hernandez-Gomez, I N Ross, K Osvay, P Matousek, C N Danson, J Walczak
Demonstration of a new ultra short pulse amplification technique – optical parametric chirped pulse amplification

W Shaikh, R M Allott, I C E Turcu, M Folkard, K Prise, K Ledingham, R Donovan, S Wang, N Takeyasu, S Huntingdon
Plasma light source for the VUV spectral region

3rd international workshop on the fast ignition of fusion targets, RAL, Didcot, UK (September 1998)

P Matousek, M Towrie, A Langley, J Collier, C Danson, D Neely, K Osvay
Optical parametric chirped pulse amplification (OPCPA)

D Neely, C Danson, R Allott, R Clarke, M Notley, P Norreys, I Ross, M Stubbs
'Long' pulse recompression for fast ignitor and interaction studies

Developments in ultra-high peak power laser science, IOP half-day meeting, RAL, Didcot, UK (December 1998)

C N Danson
Developments on Vulcan – an ultra-high peak power laser facility

G J Hirst
Progress towards a petawatt femtosecond blue-green laser based on XeF(C-A)

P Matousek
Prospects for a multi-petawatt source using optical parametric chirped pulse amplifiers (OPCPA)

A J Langley
Development of a terawatt femtosecond Ti:sapphire laser at RAL

Intense laser fields – X-ray generation and applications, Les Houches, France (March 1999)

I N Ross, J L Collier, P Matousek, K Osvay, C N Danson, D Neely, R M Allott, D A Pepler
Experimental investigation of a terawatt OPCPA system

R Allott, R Clarke, J Collier, C N Danson, C B Edwards, A Hall, S Hancock, M Harman, P Hatton, M H R Hutchinson, C Hernandez-Gomez, W Lester, P Matousek, D Neely, P Norreys, M Notley, K Osvay, M Parkinson, M Payne, D A Pepler, M Randerson, C Reason, D A Rodkiss, I N Ross, J Springall, M Stubbs, T B Winstone, R W W Wyatt, B Wyborn
High intensity developments on Vulcan for X-ray generation and nuclear interactions

26th IOP plasma physics conference, Pitlochry, UK (March 1999)

M Notley, R Allott, R Clarke, J L Collier, C N Danson, C B Edwards, P Flintoff, M H R Hutchinson, D Neely, D A Pepler, I Ross, J Springall, T Winstone
Characterisation and application of second harmonic picosecond pulses generated for plasma interactions

PANEL MEMBERSHIP

HIGH POWER LASER DIRECT ACCESS PANEL 1998/99

Professor G J Pert (Chairman)
Department of Physics
University of York

Professor W Graham
Plasma & Laser Interaction Physics
Queens University, Belfast

Dr J-C J Gauthier
LULI
Paris, France

Secretary: Dr G Hirst
Rutherford Appleton Laboratory

Mr P C Thompson
AWE
Aldermaston

Professor S Rose
Clarendon Laboratory
University of Oxford

Professor M G Haines
Plasma Physics Group
Imperial College

Mrs C Exton
Cross Programmes Group
EPSRC

LASERS *for* SCIENCE FACILITY PANEL 1998/99

Professor D Phillips (Chairman)
Department of Chemistry
Imperial College

Dr R Bisby
Department of Biological Sciences
University of Salford

Professor K Codling
Department of Physics
University of Reading

Secretary: Dr I Clark
Rutherford Appleton Laboratory

Dr R Devonshire
Department of Chemistry
Sheffield University

Professor J A Cairns
Department of Applied Physics and Electronic and Mechanical Engineering
University of Dundee

Mrs P Backway, Mrs C Exton
Cross Programmes Group
EPSRC

CLF EURO EXPERIMENTS PANEL 1998/99

Professor C L S Lewis (Chairman)
Department of Pure and Applied Physics
Queen's University of Belfast

Professor C Fotakis
Institute of Electronic Structure and Laser
FORTH, Greece

Professor D Phillips
Department of Chemistry
Imperial College

Secretary: Dr RM Allott
Rutherford Appleton Laboratory

Dr E Rachlew-Kallne
Department of Physics
Royal Institute of Technology, Sweden

Dr G Matthieussent
Laboratoire Physique Gaz et Plasmas, Universite Paris XI - CNRS, France

Dr R Sigel
Max-Planck-Institut fur Quantenoptik
Garching, Germany

CENTRAL LASER FACILITY STRUCTURE